AD-A209 728

UNITED STATES AIR FORCE

1987 RESEARCH INITIATION PROGRAM

Conducted by

UNIVERSAL ENERGY SYSTEMS, INC.

under

USAF Contract Number F49620-85-C-0013

RESEARCH REPORTS

VOLUME III OF IV

Submitted to

Air Force Office of Scientific Research

Bolling Air Force Base

Washington, DC

By

Universal Energy Systems, Inc.

April 1989

REPORT DOCUMENTATION PAGE

Form Approved
OMB No. 0704-0188

REPORT SECURITY CLASSIFICATION UNCLASSIFIED	1b. RESTRICTIVE MARKINGS
2a. SECURITY CLASSIFICATION AUTHORITY	3. DISTRIBUTION/AVAILABILITY OF REPORT Approved for public release; distribution unlimited.
2b. DECLASSIFICATION/DOWNGRADING SCHEDULE	
4. PERFORMING ORGANIZATION REPORT NUMBER(S)	5. MONITORING ORGANIZATION REPORT NUMBER(S) 831 AFOSR-TR- 89-0860
6a. NAME OF PERFORMING ORGANIZATION UNIVERSAL ENERGY SYSTEMS INC.	6b. OFFICE SYMBOL (If applicable)	7a. NAME OF MONITORING ORGANIZATION Air Force Office of Scientific Research/XOT
6c. ADDRESS (City, State, and ZIP Code) 4401 Dayton Xenia Rd Dayton OH 45432		7b. ADDRESS (City, State, and ZIP Code) Building 410 Bolling AFB DC 20332
8a. NAME OF FUNDING/SPONSORING ORGANIZATION AFOSR	8b. OFFICE SYMBOL (If applicable) XOT	9. PROCUREMENT INSTRUMENT IDENTIFICATION NUMBER F49620-85-C-0013
8c. ADDRESS (City, State, and ZIP Code) Building 410 Bolling AFB, DC 20332		10. SOURCE OF FUNDING NUMBERS

PROGRAM ELEMENT NO.	PROJECT NO.	TASK NO.	WORK UNIT ACCESSION NO.
61102F	3396	D5	

11. TITLE (Include Security Classification)

USAF Research Initiation Program   Volume 3 of 4

PERSONAL AUTHOR(S)
Program Director Rodney C. Darrah

13a. TYPE OF REPORT Interim	13b. TIME COVERED FROM _____ TO _____	14. DATE OF REPORT (Year, Month, Day) April 1987	15. PAGE COUNT

16. SUPPLEMENTARY NOTATION

17. COSATI CODES			18. SUBJECT TERMS (Continue on reverse if necessary and identify by block number)
FIELD	GROUP	SUB-GROUP	

19. ABSTRACT (Continue on reverse if necessary and identify by block number)

(SEE REVERSE)

89 6 29 008

20. DISTRIBUTION/AVAILABILITY OF ABSTRACT ☒ UNCLASSIFIED/UNLIMITED ☐ SAME AS RPT. ☐ DTIC USERS	21. ABSTRACT SECURITY CLASSIFICATION UNCLASSIFIED
22a. NAME OF RESPONSIBLE INDIVIDUAL Lt Col Cleude Cavender	22b. TELEPHONE (Include Area Code) (202) 767-4971	22c. OFFICE SYMBOL XOT

INTRODUCTION

Research Initiation Program - 1987

AFOSR has provided funding for follow-on research efforts for the participants in the Summer Faculty Research Program. Initially this program was conducted by AFOSR and popularly known as the Mini-Grant Program. Since 1983 the program has been conducted by the Summer Faculty Research Program (SFRP) contractor and is now called the Research Initiation Program (RIP). Funding is provided to establish RIP awards to about half the number of participants in the SFRP.

Participants in the 1987 SFRP competed for funding under the 1987 RIP. Participants submitted cost and technical proposals to the contractor by 1 November 1987, following their participation in the 1987 SFRP.

Evaluation of these proposals was made by the contractor. Evaluation criteria consisted of:

1. Technical Excellence of the proposal
2. Continuation of the SFRP effort
3. Cost sharing by the University

The list of proposals selected for award was forwarded to AFOSR for approval of funding. Those approved by AFOSR were funded for research efforts to be completed by 31 December 1988.

The following summarizes the events for the evaluation of proposals and award of funding under the RIP.

A. Rip proposals were submitted to the contractor by 1 November 1987. The proposals were limited to $20,000 plus cost sharing by the universities. The universities were encouraged to cost share since this is an effort to establish a long term effort between the Air Force and the university.

B. Proposals were evaluated on the criteria listed above and the final award approval was given by AFOSR after consultation with the Air Force Laboratories.

C. Subcontracts were negotiated with the universities. The period of performance of the subcontract was between October 1987 and December 1988.

Copies of the Final Reports are presented in Volumes I through III of the 1987 Research Initiation Program Report. There were a total of 83 RIP awards made under the 1987 program.

TABLE OF CONTENTS

INTRODUCTION

Research Initiation Program - 1987

AFOSR has provided funding for follow-on research efforts for the participants in the Summer Faculty Research Program. Initially this program was conducted by AFOSR and popularly known as the Mini-Grant Program. Since 1983 the program has been conducted by the Summer Faculty Research Program (SFRP) contractor and is now called the Research Initiation Program (RIP). Funding is provided to establish RIP awards to about half the number of participants in the SFRP.

Participants in the 1987 SFRP competed for funding under the 1987 RIP. Participants submitted cost and technical proposals to the contractor by 1 November 1987, following their participation in the 1987 SFRP.

Evaluation of these proposals was made by the contractor. Evaluation criteria consisted of:

1. Technical Excellence of the proposal
2. Continuation of the SFRP effort
3. Cost sharing by the University

The list of proposals selected for award was forwarded to AFOSR for approval of funding. Those approved by AFOSR were funded for research efforts to be completed by 31 December 1988.

The following summarizes the events for the evaluation of proposals and award of funding under the RIP.

A. Rip proposals were submitted to the contractor by 1 November 1987. The proposals were limited to $20,000 plus cost sharing by the universities. The universities were encouraged to cost share since this is an effort to establish a long term effort between the Air Force and the university.

B. Proposals were evaluated on the criteria listed above and the final award approval was given by AFOSR after consultation with the Air Force Laboratories.

C. Subcontracts were negotiated with the universities. The period of performance of the subcontract was between October 1987 and December 1988.

Copies of the Final Reports are presented in Volumes I through III of the 1987 Research Initiation Program Report. There were a total of 83 RIP awards made under the 1987 program.

STATISTICS

Total SFRP Participants   159

Total RIP Proposals submitted by SFRP   117

Total RIP Proposals submitted by GSRP   7

Total RIP Proposals submitted   124

Total RIP's funded to SFRP   81

Total RIP's funded to GSRP   2

Total RIP's funded   83

Total RIP's Proposals submitted by HBCU's   11

Total RIP's Proposals funded to HBCU's   7

Laboratory	SFRP Participants	RIP's Submitted	RIP's Funded
AAMRL	13	12 (2 GSRP)	6
AFWAL/APL	8	6	4
ATL	9	8 (1 GSRP)	6
AEDC	6	4	3
AFWAL/AL	9	9 (1 GSRP)	5
LC	1	1	1
ESMC	1	0	0
ESD	1	1	0
ESC	8	8	6
AFWAL/FDL	9	8 (1 GSRP)	6 (1 GSRP)
FJSRL	9	5	5
AFGL	13	10 (1 GSRP)	7
HRL/OT	2	2	1
HRL/LR	3	3	2
HRL/MO	3	2	2
HRL/ID	0	0	0
LMC	3	1	0
AFWAL/ML	13	11 (1 GSRP)	6 (1 GSRP)
OEHL	5	3	3
AL	7	4	3
RADC	11	10	7
SAM	16	8	6
DEOMI	2	2	0
WL	7	6	4
Total	159	124	83

LIST OF UNIVERSITY THAT PARTICIPATED

Adelphi University	- 1	Meharry Medical College	- 1
Alabama, University of	- 1	Memphis State University	- 1
Alaska-Fairbanks, Univ. of	- 1	Metropolitan State College	- 1
Alfred University	- 1	Michigan State University	- 1
Arizona State University	- 1	Mississippi State University	- 4
Arkansas State University	- 1	Mississippi, University of	- 1
Arkansas, University of	- 1	Missouri-Kansas City, Univ.	- 1
Auburn University	- 1	Missouri-Rolla, Univ. of	- 3
Bishop College	- 1	Montana, University of	- 1
Capital University	- 1	Montclair State College	- 1
Catholic Univ. of America	- 1	Morehouse College	- 1
Cedarville College	- 1	Nazareth College	- 1
Central State University	- 1	Nebraska-Lincoln, Univ. of	- 2
Cincinnati, University of	- 5	New Mexico State University	- 1
Colorado, University of	- 2	New York State, Univ. of	- 3
Dayton, University of	- 7	N. Carolina A&T State Univ.	- 1
Dillard University	- 1	N. Carolina-Greensboro, Univ	- 1
Drury College	- 1	Northwestern University	- 1
Eastern Illinois University	- 1	Ohio State University	- 5
Eastern Kentucky University	- 1	Ohio University	- 2
Eastern New Mexico University	- 2	Oklahoma State University	- 1
Fairfield University	- 1	Oregon Institute of Tech.	- 1
Florida A&M University	- 1	Oregon State University	- 1
Florida, University of	- 2	Ouachita Baptist University	- 1
Fort Lewis College	- 1	Pace University	- 1
Gonzaga University	- 1	Pennsylvania State Univ.	- 1
Grambling State University	- 1	Point Loma College	- 1
Hampton University	- 1	Puerto Rico-Mayaguez, Univ.	- 1
Houston, University of	- 2	Purdue University	- 1
Howard University	- 1	Rochester Inst. of Tech.	- 1
Idaho, University of	- 1	Rose-Hulman Inst. of Tech.	- 2
Illinois-Chicago, Univ. of	- 2	Saint Paul's College	- 1
Indiana University	- 1	San Francisco State Univ.	- 1
Indiana Univ. of Pennsylvania	- 1	South Dakota State Univ.	- 1
Iowa, University of	- 1	South Florida, University of	- 2
Jackson State University	- 1	Southeastern Mass. Univ.	- 2
Jarvis Christian College	- 1	Southern Illinois University	- 2
Jesm Baromedical Res. Inst.	- 1	Southern Mississippi, Univ.	- 1
John Hopkins Evening College	- 1	Southern University	- 2
Kansas State University	- 1	St. Louis University	- 1
Kansas, University of	- 1	St. Mary's University	- 1
Kentucky, University of	- 1	Talladega College	- 1

Continued

v

LIST OF UNIVERSITY THAT PARTICIPATED
Continued

Lock Haven Univ. of Pennsyl.	- 1	Taylor University	- 1
Long Island University	- 1	Temple University	- 1
Louisiana State University	- 1	Tennessee Technical Univ.	- 1
Louisiana Tech. University	- 1	Tennessee, University of	- 1
Lowell, University of	- 4	Texas A&M University	- 2
Texas Southern University	- 3	Wichita State University	- 2
Texas Technical University	- 2	Wilberforce University	- 1
Texas-Austin, University of	- 1	Wisconsin-Eau Claire Univ.	- 2
Tuskegee University	- 1	Wisconsin-Madison, Univ. of	- 1
Utah State University	- 1	Wisconsin-Whitewater, Univ.	- 1
Walla Walla College	- 1	Wittenberg University	- 1
Washington State University	- 1	Worchester Polytech. Inst.	- 2
West Florida, University of	- 1	Wright State University	- 3
Western Michigan University	- 3	Xavier University	- 1

PARTICIPANTS LABORATORY ASSIGNMENT

PARTICIPANT LABORATORY ASSIGNMENT (Page 1)

AERO PROPULSION LABORATORY
(Wright-Patterson Air Force Base)

Dr. Suresh K. Aggarwal
Univ. of Illinois at Chicago
Specialty: Aerospace Engineering

Dr. Richard Tankin
Northwestern University
Specialty: Mechanical Engineering

Dr. Bryan R. Becker
Rose-Hulman Institute
Specialty: Engineering Science

Dr. Cheng-Hsiao Wu
Univ. of Missouri
Specialty: Solid State Physics

ARMAMENT LABORATORY
(Eglin Air Force Base)

Dr. Charles Bell
Arkansas State University
Specialty: Mechanical Engineering

Dr. Elmer C. Hansen
University of Florida
Specialty:Mechanical Engineering

Dr. Robert W. Courter
Louisiana State University
Specialty:Aerospace Engineering

Dr. James Hoffmaster
Gonzaga University
Specialty:Physics

Dr. Joseph J. Feeley
University of Idaho
Specialty:Electrical Engineering

Dr. James Nail
Mississippi State Univ.
Specialty:Electrical Engineering

Ms. Jennifer L. Davidson (1986), (GSRP)
University of Florida
Specialty: Mathematics

Dr. Meckinley Scott (1986)
University of Alabama
Specialty: Statistics

Dr. Mo Samimy (1986)
Ohio State University
Specialty: Mechanical Engineering

Mr. Jim S. Sirkis (1986),(GSRP)
University of Florida
Specialty: Engineering Mechanics

HARRY G. ARMSTRONG AEROSPACE MEDICAL RESEARCH LABORATORY
(Wright-Patterson Air Force Base)

Dr. Praphulla K. Bajpai
University of Dayton
Specialty: Immunology

Dr. Thomas Nygren
Ohio State University
Specialty: Psychology

Dr. Gwendolyn Howze
Texas Southern University
Specialty: Physics

Dr. Donald Robertson
Indiana University of PA
Specialty: Psychology

HARRY G. ARMSTRONG AEROSPACE MEDICAL RESEARCH LABORATORY
(Wright-Patterson Air Force Base)
(continued)

Dr. Noel Nussbaum
Wright State University
Specialty: Biology

Dr. John Westerkamp
University of Dayton
Specialty: Electrical Engineering

Dr. Jacqueline Paver (1986)
Duke University
Specialty: Biomechanical Engineering

ARNOLD ENGINEERING DEVELOPMENT CENTER
(Arnold Air Force Systems)

Dr. Suhrit K. Dey
Eastern Illinois University
Specialty: Aerospace Engineering

Dr. Surgounda Patil
Tennessee Technical University
Specialty: Math Statistics

Dr. William M. Grissom
Morehouse College
Specialty: Mechanical Engineering

ASTRONAUTICS LABORATORY
(Edwards Air Force Base)

Dr. Gurbux S. Alag
Western Michigan University
Specialty: Systems Engineering

Dr. Lawrence Schovanec
Texas Tech University
Specialty: Mathematics

Dr. John Kenney
Eastern New Mexico University
Specialty: Physical Chemistry

AVIONICS LABORATORY
(Wright-Patterson Air Force Base)

Dr. Vernon L. Bakke
University of Arkansas
Specialty: Mathematics

Dr. Narayan C. Halder
University of South Florida
Specialty: Physics

AVIONICS LABORATORY
(Wright-Patterson Air Force Base)
(continued)

Prof. William K. Curry
Rose-Hulman Inst. of Technology
Specialty: Computer Science

Dr. Alastair McAulay
Wright State University
Specialty: Electrical Engineering

Dr. Verlynda S. Dobbs
Wright State University
Specialty: Computer Science

Dr. John Y. Cheung (1986)
University of Oklahoma
Specialty: Electrical Engineering

Dr. George W. Zobrist (1986)
University of Missouri-Rolla
Specialty: Electrical Engineering

ENGINEERING AND SERVICES CENTER
(Tyndall Air Force Base)

Dr. William W. Bannister
University of Lowell
Specialty: Organic Chemistry

Dr. William Schulz
Eastern Kentucky University
Specialty: Chemistry

Dr. William M. Bass
The University of Tennessee
Specialty: Physical Anthropology

Dr. Joseph Tedesco
Auburn University
Specialty: Civil Engineering

Dr. Peter Jeffers
S.U.N.Y.
Specialty: Chemistry

Dr. Dennis Truax
Mississippi State Univeristy
Specialty: Civil Engineering

Dr. William T. Cooper (1986)
Florida State University
Specialty: Chemistry

Dr. Yong S. Kim (1986)
The Catholic Univ. of America
Specialty: Civil Engineering

FLIGHT DYNAMICS LABORATORY
(Wright-Patterson Air Force Base)

Mr. Thomas Enneking (GSRP)
University of Notre Dame
Specialty: Civil Engineering

Dr. Gary Slater
University of Cincinnati
Specialty: Aerospace Engineering

FLIGHT DYNAMICS LABORATORY
(Wright-Patterson Air Force Base)
(continued)

Dr. Oliver McGee
Ohio State University
Specialty: Engineering Mechanics

Dr. Forrest Thomas
University of Montana
Specialty: Chemistry

Dr. Shiva Singh
Univ. of Kentucky
Specialty: Mathematics

Dr. William Wolfe
Ohio State University
Specialty: Engineering

Dr. George R. Doyle (1986)
University of Dayton
Specialty: Mechanical Engineering

Dr. V. Dakshina Murty (1986)
University of Portland
Specialty: Engineering Mechanics

Dr. Tsun-wai G. Yip (1986)
Ohio State University
Specialty: Aeronautics-Astronautics Engineering

FRANK J. SEILER RESEARCH RESEARCH LABORATORY
(United State Air Force Academy)

Dr. Charles M. Bump
Hampton University
Specialty: Organic Chemistry

Dr. Howard Thompson
Purdue University
Specialty: Mechanical Engineering

Dr. Stephen J. Gold
South Dakota State University
Specialty: Electrical Engineering

Dr. Melvin Zandler
Wichita State Univ.
Specialty: Physical Chemistry

Dr. Henry Kurtz
Memphis State Univ.
Specialty: Chemistry

GEOPHYSICS LABORATORY
(Hanscom Air Force Base)

Dr. Lee A. Flippin
San Francisco State Univ.
Specialty: Organic Chemistry

Dr. Gandikota Rao
St. Louis University
Specialty: Meteorology

GEOPHYSICS LABORATORY
(Hanscom Air Force Base)
(continued)

Dr. Mayer Humi
WPI
Specialty: Applied Mathematics

Dr. Timothy Su
Southeastern Massachusetts Univ.
Specialty: Physical Chemistry

Dr. Steven Leon
Southeastern Massachusettes
Specialty: Mathematics

Dr. Keith Walker
Point Loma College
Specialty: Physics

Dr. Henry Nebel
Alfred University
Specialty: Physics

HUMAN RESOURCES LABORATORY
(Brooks, Williams and Wright-Patterson Air Force Base)

Dr. Patricia A. Carlson
Rose-Hulman Inst. of Technology
Specialty: Literature/Language

Dr. John Uhlarik
Kansas State University
Specialty: Psychology

Dr. Ronna E. Dillon
Southern Illinois University
Specialty: Educational Psychology

Dr. Charles Wells
University of Dayton
Specialty: Management Science

Dr. Michael Matthews
Drury College
Specialty: Psychology

Dr. Charles Lance (1986)
University of Georgia
Specialty: Psychology

Dr. Stephen Loy (1986)
Iowa State University
Specialty: Management Information Sys.

Dr. Jorge Mendoza
Texas A&M University
Specialty: Psychology

Dr. Doris Walker-Dalhouse (1986)
Jackson State University
Specialty: Reading Education

Dr. Billy Wooten (1986)
Brown University
Specialty: Philosophy, Psychology

LOGISTICS COMMAND
(Wright-Patterson Air Force Base)

Dr. Howard Weiss
Specialty: Industrial Engineering
Temple University

MATERIALS LABORATORY
(Wright-Patterson Air Force Base)

Dr. Bruce A. DeVantier
S. Illinois University
Specialty: Civil Engineering

Dr. John W. Gilmer
Penn State University
Specialty: Physical Chemistry

Dr. Ravinder Diwan
Southern University
Specialty: Metallurgy

Dr. Gordon Johnson
Walla Walla College
Specialty: Electrical Engineering

Dr. Bruce A. Craver
University of Dayton
Specialty: Physics

Mr. John Usher (GSRP)
Louisiana State University
Specialty: Chemical Engineering

Dr. Robert Patsiga (1986)
Indiana Univ. of Pennsylvania
Specialty: Organic Polymer Chemistry

Dr. Nisar Shaikh (1986)
University of Nebraska-Lincoln
Specialty: Applied Mathematics

Dr. Gopal M. Mehrotra (1986)
Wright State University
Specialty: Metallurgy

OCCUPATIONAL AND ENVIRONMENT HEALTH LABORATORY
(Brooks Air Force Base)

Dr. Richard H. Brown
Ouachita Baptist University
Specialty: Physiology

Dr. Kiah Edwards
Texas Southern University
Specialty: Molecular Biology

Dr. Elvis E. Deal
University of Houston
Specialty: Industrial Engineering

Dr. Ralph J. Rascati (1986)
Kennesaw College
Specialty: Biochemistry

ROME AIR DEVELOPMENT CENTER
(Griffis Air Force Base)

Prof. Beryl L. Barber
Oregon Institute of Technology
Specialty: Electrical Engineering

Dr. Louis Johnson
Oklahoma State Univ.
Specialty: Electrical Engineering

Dr. Kevin Bowyer
University of South Florida
Specialty: Computer Science

Dr. Panapkkam Ramamoorthy
University of Cincinnati
Specialty: Electrical Engineering

Dr. Ronald V. Canfield
Utah State University
Specialty: Statistics

Dr. David Sumberg
Rochester Institute of Tech.
Specialty: Physics

Dr. Lionel R. Friedman
Worcester Polytechnic Inst.
Specialty: Physics

Dr. Donald Hanson (1986)
University of Mississippi
Specialty: Electrical Engineering

Dr. John M. Jobe (1986)
Miami University of Ohio
Specialty: Statistics

Dr. Stephen T. Welstead (1986)
University of Alabama in Hunts.
Specialty: Applied Mathematics

SCHOOL OF AEROSPACE MEDICINE
(Brooks Air Force Base)

Prof. Phillip A. Bishop
University of Alabama
Specialty: Exercise Physiology

Dr. Ralph Peters
Wichita State University
Specialty: Zoology

Dr. Mohammed Maleque
Meharry Medical College
Specialty: Pharmacology

Dr. Stephen Pruett
Mississippi State University
Specialty: Immunology

Dr. Kurt Oughstun
University of Wisconsin
Specialty: Optical Sciences

Dr. Wesley Tanaka
University of Wisconsin
Specialty: Biochemistry

Dr. Hoffman H. Chen (1986)
Grambling State University
Specialty: Mechanical Engineering

Dr. Vito DelVecchio (1986)
University of Scranton
Specialty: Biochemistry, Genetics

WEAPONS LABORATORY
(Kirtland Air Force Base)

Dr. Jerome Knopp
University of Missouri
Specialty: Electrical Engineering

Dr. Randall Peters
Texas Tech University
Specialty: Physics

Dr. Barry McConnell
Florida A&M University
Specialty: Computer Science

Dr. William Wheless
New Mexico State University
Specialty: Electrical Engineering

Dr. Martin A. Shadday, Jr. (1986)
University of South Carolina
Specialty: Mechanical Engineering

RESEARCH REPORTS

MINI-GRANT RESEARCH REPORTS

1987 RESEARCH INITIATION PROGRAM

Technical Report Number	Title and Mini-Grant No.	Professor
Volume I		
Armament Laboratory		
1	Report Not Available at this Time 760-7MG-025	Dr. Charles Bell
2	Effects of Bending Flexibility on the Aerodynamic Characteristics of Slender Cylinders Determined from Free-Flight Ballistic Data 760-7MG-018	Dr. Robert W. Courter
3	Image Complexity Measures and Edge Detection 760-6MG-024	Ms. Jennifer L. Davidson (1986 GSRP)
4	Report Not Available at this Time 760-7MG-070	Dr. Joesph J. Feeley
5	Advanced Gun Gas Diversion 760-7MG-012	Dr. Elmer Hansen
6	A Physical and Numerical Study of Pressure Attenuation in Solids 760-7MG-002	Dr. James Hoffmaster
7	Pyroelectric Sensing for Potential Multi-Mode Use 760-7MG-026	Dr. James Nail
8	Gaseous Fuel Injection and Mixing in a Supersonic Combustor 760-6MG-059	Dr. Mo Samimy (1986)
9	Systems Effectiveness for Targets with Repair or Replacement Facilities of Damaged Components 760-6MG-025	Dr. Meckinley Scott (1986)
10	A Pattern Recognition Application in Elastic-Plastic Boundary Element, Hybrid Stress Analysis 760-6MG-142	Mr. Jim S. Sirkis (1986 GSRP)

Arnold Engineering Development Center
11   Vectorized Perturbed Functional   Dr. Suhrit K. Dey
            Iterative Scheme (VPFIS): A Large-
            Scale Nonlinear System Solver
            760-7MG-037

12   Liquid Film Cooling in Rocket   Dr. William M. Grissom
            Engines
            760-7MG-022

13   Estimation of Autocorrelation and   Dr. Surgounda Patil
            Power Spectral Density for Randomly
            Sampled Systems
            760-7MG-085

Astronautics Laboratory
14   Report Not Available at this Time   Dr. Gurbux S. Alag
            760-7MG-042

15   Report Not Available at this Time   Dr. John Kenney
            760-7MG-019

16   Fracture in Soild Propellant: Dr. Lawrence Schovanec
            Damage Effects upon Crack
            Propagation
            760-7MG-065

17   Novel Conversion of Organometallics to   Dr. Nicholas E. Takach
            Energetic Nitro Compunds   (1986)
            760-6MG-130

Engineering and Services Center
18   Correlations of Spontaneous   Dr. William W. Bannister
            Ignition Temperatures with Molecular
            Structures of Flammable Compounds
            760-7MG-101

19   The Estimation of Stature from   Dr. William M. Bass
            Fragments of the Femur: A
            Revision of the Steele Method
            760-7MG-014

20   Effects of Water Solubility and   Dr. William T. Cooper
            Functional Group Content on the   (1986)
            Interactions of Organic Solutes
            with Soil Organic Matter
            760-6MG-081

21   Report Not Available at this Time   Dr. Peter Jeffers
            760-7MG-038

FINAL REPORT NUMBER 53
REPORT NOT AVAILABLE AT THIS TIME
Dr. Suresh K. Aggerwal
760-7MG-061

1987 USAF-UES RESEARCH INITIATION PROGRAM

Sponsored by the

AIR FORCE OFFICE OF SCIENTIFIC RESEARCH

Conducted by the

Universal Energy Systems, Inc.

FINAL REPORT

A NUMERICAL STUDY OF THE FLOW FIELD

AND HEAT TRANSFER IN A RECTANGULAR PASSAGE

WITH A TURBULATOR

Prepared by: Bryan R. Becker, Ph.D., P.E.

Academic Rank: Assistant Professor

Department and   Department of Mechanical and
                      Aerospace Engineering

University: University of Missouri-Columbia

Research Location: USAFWAL/POTC
                      Wright-Patterson AFB, OH   45433

USAF Researcher: Richard B. Rivir, Ph.D.

Date: 20 March 1989

Contract No: F49620-85-C-0013

A NUMERICAL STUDY OF THE FLOW FIELD AND HEAT
TRANSFER IN A RECTANGULAR PASSAGE
WITH A TURBULATOR

by

Bryan R. Becker, Ph.D., P.E.

ABSTRACT

A detailed numerical study of the aerothermal mechanics within a
short straight section of a turbine blade internal cooling passage
with a single turbulator is described. The two dimensional,
transient, Reynolds averaged Navier Stokes, continuity and energy
equations are iterated to a steady state solution using the
MacCormack explicit predictor-corrector algorithm. Turbulence
closure is achieved through the use of the Baldwin-Lomax algebraic
two layer eddy viscosity model.

Axial distributions of local skin friction coefficient, local
Stanton number and local Nusselt number are given. Profiles of
velocity and temperature are presented as well as contours of
streamfunction and temperature which display complex details of the
flow structure. It was found that the widely used Reynolds Analogy
greatly underpredicts the heat transfer rate as given by a direct
calculation using Fourier's law. Finally, the numerical results
are found to compare favorably to the experimental results
published by Han et al (1986).

I. INTRODUCTION

Advanced gas turbine engines will be designed for higher thermal
efficiency and specific thrust which will necessitate higher
operating speeds, temperatures, and pressures. As a consequence,
the heat loads on the turbine blades will increase, which can
result in both high metal temperatures and thermal stress
concentrations due to severe thermal gradients. To reduce these
effects, cooling air is extracted from the compressor and is routed
through small rectangular cooling passages within the turbine
blades.

As shown in Figure 1, the cooling air enters the root of each
turbine blade and flows through complex, serpentine passages until
it exits through the blade's surface into the cavity surrounding
the turbine rotor-strator. Since the pressure drop, and thus the
mass flowrate, along these cooling passages is limited by the
pressure differential between the compressor and the turbine stage,
methods other than increased coolant flow, such as the introduction
of turbulators, must be used to enhance the heat transfer. These
turbulators or turbulence promoters, which consist of ribs
protruding from the walls of the internal cooling passages,
increase the turbulence level within the cooling air flow and thus
augment the rate of energy transfer from the turbine blade through
the cooling passage wall and into the cooling air flow. Thus, the
resulting coolant flows contain many complex phenomena which are
not adequately included in the current heat transfer design of
turbine blades.   The detailed modeling of these flows is essential
to the accurate prediction of the distribution of the local heat
transfer coefficient along the cooling passages. Such prediction
is necessary to achieve a thermal design of these components which
incorporates efficient cooling and thereby alleviates the effects
of the increased heat load.

II. OBJECTIVES OF THE RESEARCH EFFORT

There have been numerous experimental and analytical studies of
the flow field and heat transfer within straight rectangular ducts
which simulate the flow within the internal cooling passages inside
a turbine blade. However, there remains work to be done in the
detailed modeling of the heat transfer and fluid flow processes
very near the fluid-solid interface. This paper reports on a two
dimensional modeling effort which begins to address this need.

During my tenure as a Summer Research Fellow in the 1987 Summer
Faculty Research Program (SFRP), I began modeling of the fluid flow
and heat transfer in a straight rectangular passage with a single
turbulence promoter. This work was completed and a technical paper
was written during the Spring 1988 term with funding by the 1987
Mini Grant Program. This paper, "A Numerical Simulation of the
Flow Field and Heat Transfer in a Rectangular Duct with a
Turbulator Using a Predictor-Corrector Algorithm," (AIAA-88-2903),
was presented at the AIAA/ASME/SAE/ASEE 24th Joint Propulsion
Conference, July 11-13, 1988 in Boston, MA [1].

This first objective of this 1987 RIP research effort was to
modify the numerical model developed during the summer of 1987 by
incorporating true symmetry boundary conditions at the upper
boundary of the computational mesh:

$$\frac{\partial \phi}{\partial y} = 0 \qquad (1)$$

for all dependent variables ϕ. The resulting numerical model was
then iterated to a well converged steady state solution.

The second objective was to develop a post processor program to
read and analyze the converged solution. After reading the
solution from an online data file, this post processor first
calculates the L2-Norm of the error in the solution. It then
generates a plot data set which contains the information necessary
to plot nondimensional velocity and temperature profiles. It then
calculates the axial distributions of the local skin friction,
local Stanton Number (via both Reynold's Analogy and Fourier's
Law), as well as the local Nusselt Number scaled by McAdams-Dittus-
Boelter correlation for fully developed Nusselt Number in

rectangular ducts. Following these calculations, the post processor appends the experimental data reported by J. C. Han et al [2] and then generates data sets for plotting all of the above mentioned quantities as a function of distance along the duct. This program then integrates both the calculated and the experimental Nusselt numbers to determine axial average values of these quantities. Finally, the post processor integrates the velocity distribution throughout the computational mesh so as to evaluate the streamfunction. It then writes a third plot data set containing the information necessary for plotting contours of streamfunction and nondimensional temperature.

The third and final objective of the 1987 RIP research period was to begin work on a numerical model of a rectangular passage with four turbulators. The computational grid shown in Figures 2 and 3 was generated for this model. Figure 2 shows the entire computational domain containing an entrance region, four turbulators, and a downstream region. Figure 3 shows details of the first ten rib heights of the mesh. It can be seen that the grid is very fine near the lower boundary and in the vicinity of the top of the rib. The MacCormack Predictor-Corrector algorithm was modified to account for the boundaries of the four turbulator surfaces. Every effort was made to accurately model the exact conditions reported by Han et al [2]. At the close of the 1987 RIP research period this model is still in the "development and check-out" phase. It is intended that this work will be continued at my university with additional funding from the Air Force Office of Scientific Research.

III. DISCUSSION OF RESULTS GENERATED BY THE
IMPROVED SINGLE TURBULATOR MODEL

As stated in Section II, the first objective of this summer's
research was to improve the single turbulator model which was
developed during the 1987 SFRP research period. This imporved
model was then iterated to a well converged solution which was
analyzed by the post processor developed during this 1987 RIP
research period. The computational mesh used in the single
turbulator model is shown in Figure 4.

A. Convergence

Iteration towards the improved solution was begun by using the
earlier solution as an initial condition. The previous solution
was achieved after 100,000 iterations and then an additional
100,000 iterations were performed with the improved single
turbulator model. The convergence of the predictor-corrector
algorithm is measured by the L-2 norm of the change in the
normalized global solution vector. Typically, in the iteration to
a converged steady state solution, the value of this norm will drop
3 orders of magnitude from the initial conditions and then
oscillate about this reduced value, indicating that convergence has
been achieved [3]. In the earlier simulation, the value of this
norm decreased from 7.137 at the outset to 0.002662 after 50,000
iterations and oscillated near that value for the next 50,000
iterations. After the symmetry boundary condition was improved,
the solution was restarted and the norm dropped to less than 0.0008
within the first 50,000 iterations and continued to oscillate just
below that value for the final 50,000 iterations. This behavior is
typical of convergence to the steady state solution.

B. Streamfunction Contours

Streamfunction contours over the entire computational domain are
shown in Figure 5. As shown in this figure, counterclockwise
vortices are present both upstream and downstream of the turbulator
rib. Reattachment of the large separated flow behind the

turbulator occurs approximately nine to ten rib heights downstream
of the rib. Figure 6 shows the size of the counterrotating vortex
upstream of the rib. Figure 7 gives detail of the flow structure
atop the turbulator and shows the presence of a long thin
counterrotating vortex centered over the rib. Detail of the large
counterclockwise recirculation behind the turbulator is shown in
Figure 8. The dividing streamline departs from the rib near the
top corner. The small bubble located at the point where the rib
rejoins the horizontal surface indicates the presence of a small
clockwise rotating vortex at that juncture which is shown in Figure
9.

C. <u>Temperature Contours</u>

The flow field temperature distribution is shown in Figure 10.
Upstream of the turbulator, very little mixing is occurring as
indicated by the concentration of temperature contours near the
horizontal surface. The bulk of the approaching fluid is slightly
warmer than the free stream value, T_∞ , as indicated by the
uppermost contour which attaches at the front corner of the rib.
This slight warming is due to heat conduction from the hot
isothermal wall. Downstream of the rib, the turbulent mixing of
the fluid has greatly diffused the thermal energy upward, well
beyond the first rib height. The thickness of this warm air
region grows downstream of the turbulator. Just behind the rib,
the temperature distribution shown in Figure 11, reflects the
effects of the complex flow structure which exists there.

D. <u>Velocity and Temperature Profiles</u>

Figures 12 through 15 present profiles of u/u_∞ and T/T_∞
plotted against Y/YMAX at 9 streamwise locations, X/H, where H is
the rib height. The profiles at X/H = 0.0 represent the specified
inflow boundary conditions.

At X/H = 3.0 and 4.0, the profiles display the development of the
momentum and thermal boundary layers. At X/H = 4.0, the horizontal
velocity is negative near the solid wall which indicates the
presence of the upstream recirculation zone shown in Figure 6.

The locations, X/H = 5.0, 5.5, and 6.0, are at the front top corner, midline and back top corner of the rib, respectively. At X/H = 5.0, the horizontal velocity has increased dramatically near the solid wall as the flow accelerates over the rib which results in a corresponding decrease in flow field temperature since the total energy of the flow must be preserved. By X/H = 5.5, the flow has begun to decelerate with a corresponding increase in temperature. At X/H = 6.0 these trends continue.

The streamwise locations, X/H = 7.0 and 10.0, are located at the back bottom corner of the rib and at the midline of the large recirculation bubble which exists downwind of the rib. The temperature profiles show that the turbulent mixing behind the rib has greatly diffused the energy from the hot solid wall to form a warm air region which extends more than 1.0 rib height vertically from the solid wall. The horizontal velocity profile is typical of a recirculation zone with a negative upstream flow near the wall changing to a positive downstream flow higher in the flow field.

The profiles at X/H = 20.0, demonstrate that both the momentum and thermal boundary layers are reestablished downstream of the recirculation bubble. However, comparison of these profiles to those upstream of the turbulence promoter, show that the downstream boundary layers are much thicker and well mixed, illustrating the effects of the intense turbulent mixing caused by the flow over the turbulence promoter.

E. Skin Friction and Stanton Number

The axial distribution of the local skin friction, shown in Figure 16, was calculated from the following equation:

$$c_f' = \frac{\tau_{wall}}{\frac{1}{2}\rho_{\infty} u_{\infty}^2} = \frac{u(\frac{\partial u}{\partial y})_{y=0}}{\frac{1}{2}\rho_{\infty} u_{\infty}^2} \qquad (2)$$

The normal derivative of the horizontal velocity was evaluated at the wall using a second order accurate three point difference expression. The viscosity was determined as a function of temperature at the wall. As shown in Figure 16, the skin friction achieves a maximum at approximately X/H = 5.0 which corresponds to the very steep velocity gradient near the wall as the flow

accelerates over the rib. As mentioned earlier, this reduces the
temperature of the fluid near the wall which results in a steep
thermal gradient there and the high heat transfer rate displayed in
Figures 17 and 18.

The axial distribution of the local Stanton Number, given in
Figure 17, was evaluated from the following equation using two
different methods:

$$St = \frac{Q_{wall}}{c_p \rho_\infty u_\infty (T_{wall} - T_\infty)} \qquad (3)$$

In the first method, the Reynolds Analogy was used, in which the
heat transfer rate is related to the skin friction as follows:

$$\text{Stanton Number} = \tfrac{1}{2} c_f' \qquad (4)$$

This method is widely used in turbomachinery calculations but these
calculations greatly underpredict the heat transfer rates measured
experimentally.

In the second method, Fourier's Conduction Law was used to
evaluate the heat transfer rate at the wall, Q_{wall}, which appears
in Equation (3):

$$Q_{wall} = -K \left(\frac{\partial T}{\partial y}\right)_{y=0} \qquad (5)$$

In this calculation, the normal derivative of temperature at the
wall was calculated in a manner similar to that used for the normal
derivative of the horizontal velocity discussed above and the
thermal conductivity was evaluated as a function of temperature at
the wall.

In the convection heat transfer process, the energy is first
transferred by conduction from the solid wall to the fluid
particles adjacent to the wall. These fluid particles are then
transported away from the solid wall by the bulk mixing of the
fluid which results in the diffusion of energy from the solid wall.
The basis for the Reynolds Analogy is the assumption that the same
mechanism is responsible for the exchange of both heat and
momentum. This assumption disregards the details of the energy
transfer process at the solid wall-fluid interface. As shown in

Figure 17, the direct calculation of the heat transfer rates via
Fourier's Law predicts heat transfer rates which can be as great as
3 times that given by the Reynolds Analogy. This discrepancy can
be explained by the fact that the Reynolds Analogy is derived for
laminar or fully turbulent flows over a flat plate with laminar and
turbulent Prandtl number, $Pr = Pr_t = 1.0$. Thus, the Reynolds
Analogy is not applicable to flows with recirculation zones and
flow reversals which cause the normal gradient of velocity to
differ greatly from the normal gradient of temperature.

F. Comparison of Numerical to Experimental Results

In an effort to validate the numerical algorithm, the numerical
results were compared to the experimental results published by Han
et al [2]. In the work by Han et al, parametric studies of the
heat transfer and friction characteristics in rectangular channels
with turbulators were performed. The parameters of the test case
which is most similar to the numerical simulation are as follows:

> Re_D = 60,000
>
> channel width/channel height = 4
>
> rib angle of attack = 90°
>
> rib pitch/rib height = 20

For this test case, Han et al report that reattachment occurs
about two rib heights downstream from separation. As discussed
earlier, the numerical results predict reattachment nine to ten rib
heights downstream of the rib. This great disparity is a result of
the difference in rib shapes. As shown in Fighre 18, the
experimental rib is square in cross section and much smaller than
the "flatten sin curve" used in the numerical model. The gentle
slope of the rib in the numerical solution permits the flow
downstream of the rib to straighten more gently, thus preserving
its horizontal momentum and lengthening the recirculation zone.

In Figure 18, the calculated axial distribution of the Nusselt
Number is compared to experimental results reported by Han et al
[2]. In the calculation of the Nusselt Number the heat transfer at
the wall was evaluated by using Equation (5).

In the comparison of the numerical results to the experimental

54-9

results, it is necessary to take into account the difference in resolution: the experimental results are given as nine data points while the calculated distribution contains 100 data points. Thus, the experimental results represent the local average Nusselt Number distribution which is much smoother than the detailed pointwise distribution given by the numerical calculation.

In spite of this difference in resolution, both the numerical and experimental results show similar trends. Both exhibit high heat transfer near the upstream corner of the rib with minimum heat transfer just behind the downstream edge of the turbulator. Both distributions show the heat transfer first increasing and then decreasing as X/D increases downstream of the turbulator.

The average values of these distributions were determined by integrating along the axis of the rectangular channel. The average of the calculated Nusselt Number was found to be 1.5123 while the average of the experimental Nusselt Number was found to be 2.3028. Thus the average calculated Nusselt Number is approximately 34% lower than the average experimental Nusselt Number.

This difference can be attributed to several factors. Again, the rib shape has a profound effect on the flow field and hence the heat transfer. The experimental data includes 3-d effects which are not present in the numerical model. The Baldwin-Lomax turbulence model may not be adequate to predict the turbulence effects in the recirculation zone. Another important factor may be the difference in free stream velocity. Han et al report an average free stream velocity of approximately 70.0 ft/sec while the corresponding value used in the numerical prediction was 270.0 ft/sec. The Reynolds number based on hydraulic diameter in both cases was 60,000. However, since the numerical model is 2-d, the channel width in the simulation is arbitrary and was chosen to be four times the channel height since that was the highest aspect ratio reported by Han et al. Finally, the experimental test set up included several ribs along the duct while the numerical model contained only a single rib. Han et al [2] report that the heat transfer results do not settle into a periodic pattern until the flow has gone over the first three ribs.

Several of these possible causes of error will be eliminated in
the four turbulator model. Obviously the number of ribs is greater
than the three required to establish the periodic results reported
from the experiment. The free stream velocity will be set equal to
that reported by Han et al. Also the turbulator size, geometry,
pitch and angle of attack will duplicate the experimental
conditions. This work will by continued at the University of
Missouri with funding from the Air Force Office of Scientific
Research.

G. Conclusions

In conclusion, the flow field and heat transfer along a turbine
blade internal cooling passage was numerically simulated using a
two dimensional geometry. Attention was focused on the flow along
a short straight section of a rectangular passage with a single
transverse mounted turbulator protruding from its floor.

In contrast to the work done by earlier investigators, this study
was performed using a computational mesh which had very high
resolution. There were 100 grid lines in the horizontal (axial)
direction clustered around the turbulator and 60 grid lines in the
vertical direction with 44 within the first rib height which was
well within the turbulent boundary layer. This high resolution
mesh revealed considerable detail of the flow field and heat
transfer near the turbulator.

The calculation revealed a flow structure near the turbulator
which is more complex than is ordinarily expected for such a simple
passage/turbulator geometry and has a pronounced effect upon the
heat transfer as shown in Figures 17 and 18. This significant
insight indicates that further study is needed into the effects of
turbulator geometry and spacing (or pitch) as a means of heat
transfer enhancement. Furthermore, this calculation revealed a
considerable difference between the heat transfer rate calculated
by using the Reynolds Analogy and that given by a direct
calculation using Fourier's law. This discrepancy results from the
complex flow structure near the turbulator which causes the normal
gradient of velocity to differ greatly from the normal gradient of

temperature. Similar flow structures exist throughout many turbomachinery components, and therefore, corresponding heat transfer effects may occur in those components which would also be inadequately predicted by the Reynolds Analogy. This significant insight may lead to remedies for the underprediction of heat transfer rates in many turbomachinery calculations.

Finally, the numerical results were found to compare favorably with reported experimental results. Both sets of results display similar trends. Comparison of the axially averaged Nusselt Number shows 34% error which is reasonable considering the difference in rib geometry, number of ribs, and free stream velocity as well as the absence of 3-d effects in the numerical model.

IV. RECOMMENDATIONS

As outlined in Section II of this report, work has begun on a four turbulator model and as discussed in the conclusions of Section III, this model will remove many of the causes of discrepancy between the numerical results and the experimental results. It is recommended that this modeling effort be completed and the algorithm validated by comparison with experimental results. After this has been done several parametric studies can be performed.

First, a grid resolution study will be done by producing a converged solution using a course mesh formed by omitting every other grid line shown in Figures 2 and 3. This converged solution will then be interpolated to the fine mesh of Figures 2 and 3. Iteration will then be restarted. Thus, the grid dependence of the solution can be determined. Also, this should produce an efficient solution strategy since part of the iteration will be done using only a quarter of the total grid points.

Second, using the refined mesh, parametric studies of the effects of Reynolds Number and rib pitch can be done and compared to the experimental results.

Third, the ribbed surface could be reflected about the duct line of symmetry and the effects of top and bottom rib alignment studied.

Fourth, various turbulence models could be incorporated in the algorithm and these effects upon flow field structure and heat transfer ascertained.

Finally, this work should eventually progress towards a full 3-d Navier Stokes solution which could then include effects of rib angle of attack and duct rotation.

REFERENCES

1. Becker, Bryan R. and Richard B. Rivir, "A Numerical Simulation of the Flow Field and Heat Transfer in a Rectangular Duct with a Turbulator Using a Predictor-Corrector Algorithm," AIAA-88-2903, AIAA/ASME/SAE/ASEE 24th Joint Propulsion Conference, Boston, MA, 1988.

2. Han, J. C., J. S. Park and M. Y. Ibrahim, "Measurement of Heat Transfer and Pressure Drop in Rectangular Channels with Turbulence Promoters," NASA Contractor Report 4015, 1986.

3. Personal communication with Dr. Donald P. Rizzetta, Flight Dynamics Laboratory, Wright Patterson AFB, Ohio, 1987.
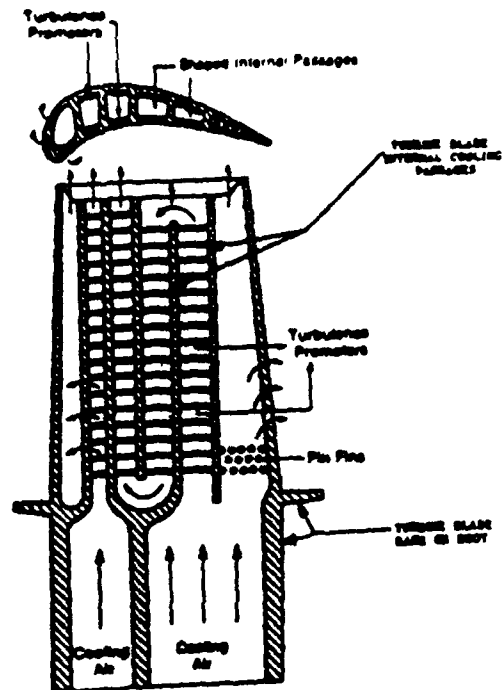
Figure 1. Cross section (cutaway) view of a turbine blade
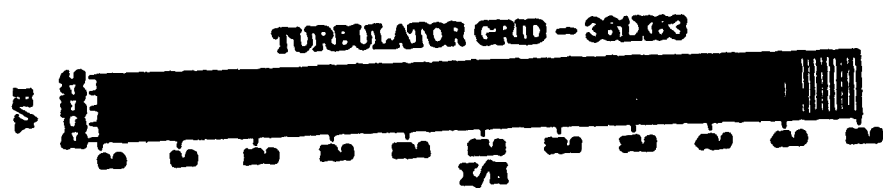
Figure 2. Computational domain for the four turbulator model.

TURBULATOR GRID – 361X83
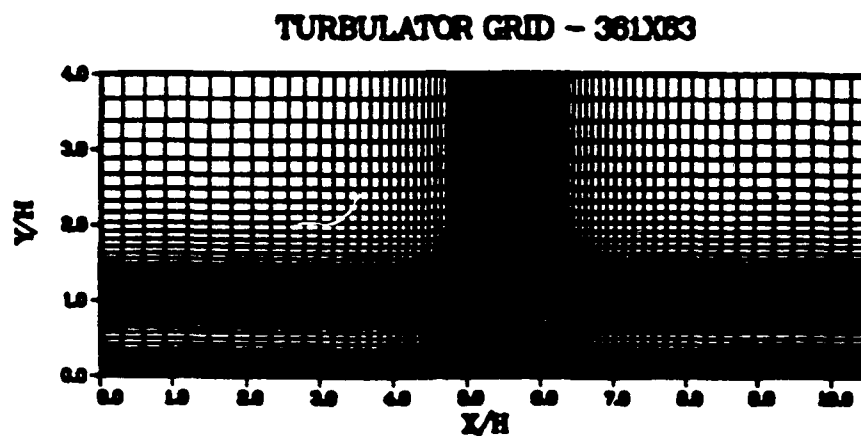
Figure 3. Detail of the computational domain near the first
turbulator of the four turbulator model.
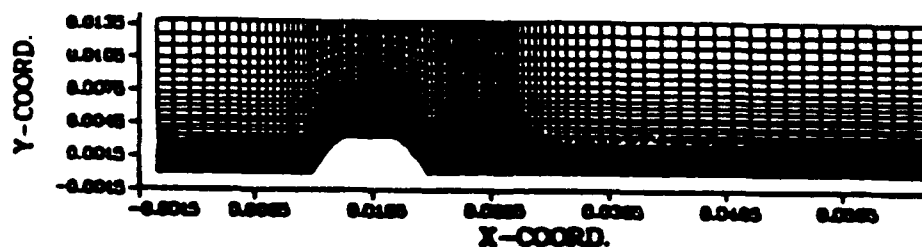
Figure 4. The 100 by 60, (X,Y), computational mesh used in the
single turbulator model.

STREAMFUNCTION CONTOURS
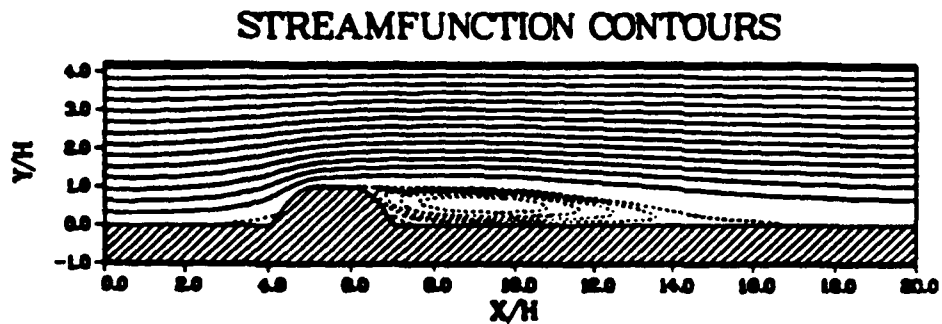
Figure 5. Calculated streamfunction contours. Counterclockwise
rotation is indicated by dashed streamlines.

STREAMFUNCTION CONTOURS
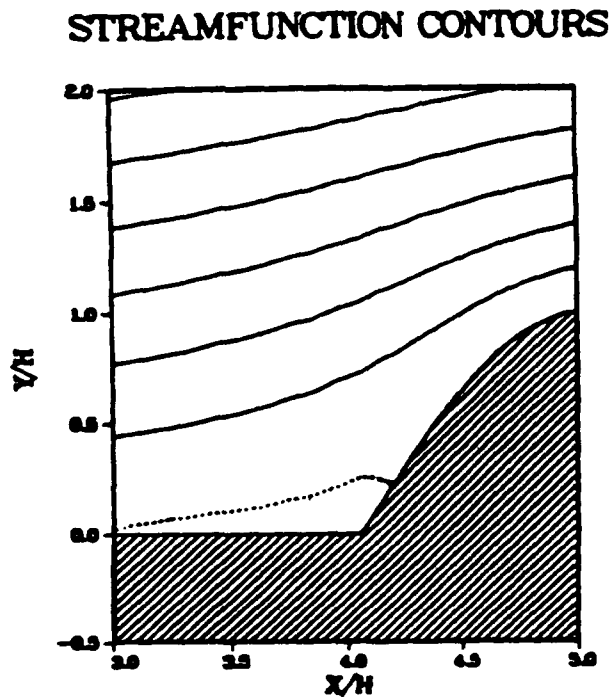
Figure 6. Detail of the streamfunction contours upstream of the
turbulator. Counterclockwise rotation is indicated by the
dividing streamline which appears as a dashed line.

STREAMFUNCTION CONTOURS
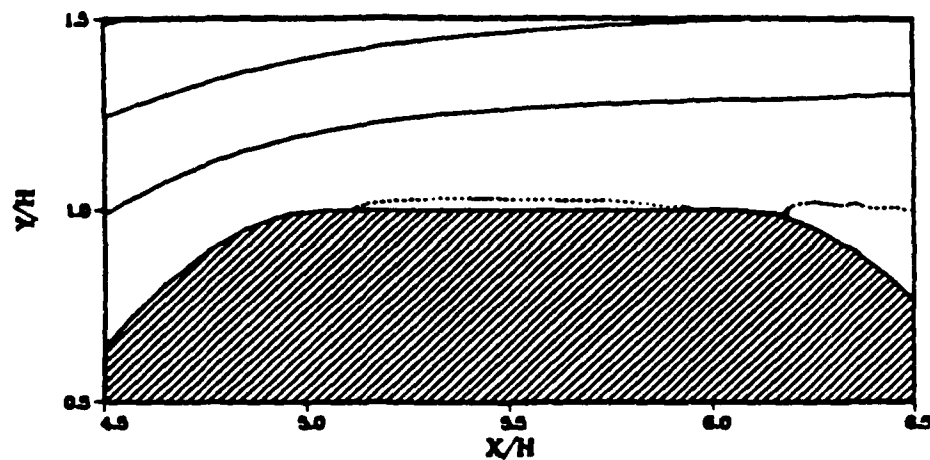
Figure 7. Detail of the streamfunction contours atop the turbulator. Counterclockwise rotation is indicated by the dividing streamline which appears as a dashed line.

STREAMFUNCTION CONTOURS
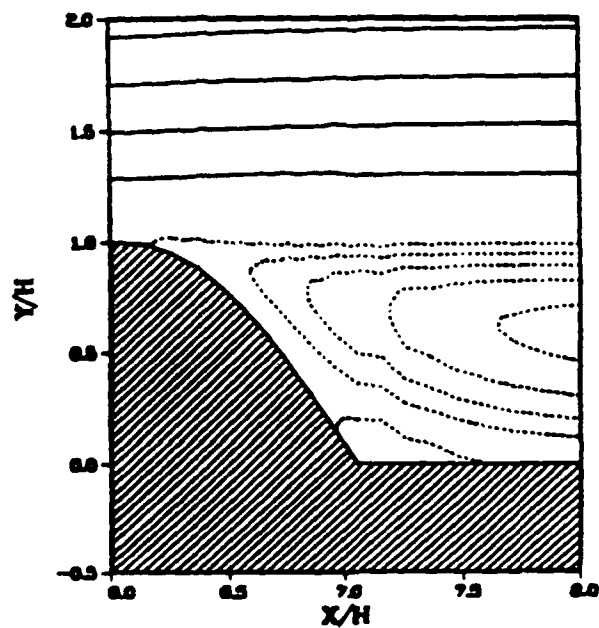
Figure 8. Detail of the streamfunction contours downstream of the turbulator. Counterclockwise rotation is indicated by dashed streamlines.

STREAMFUNCTION CONTOURS
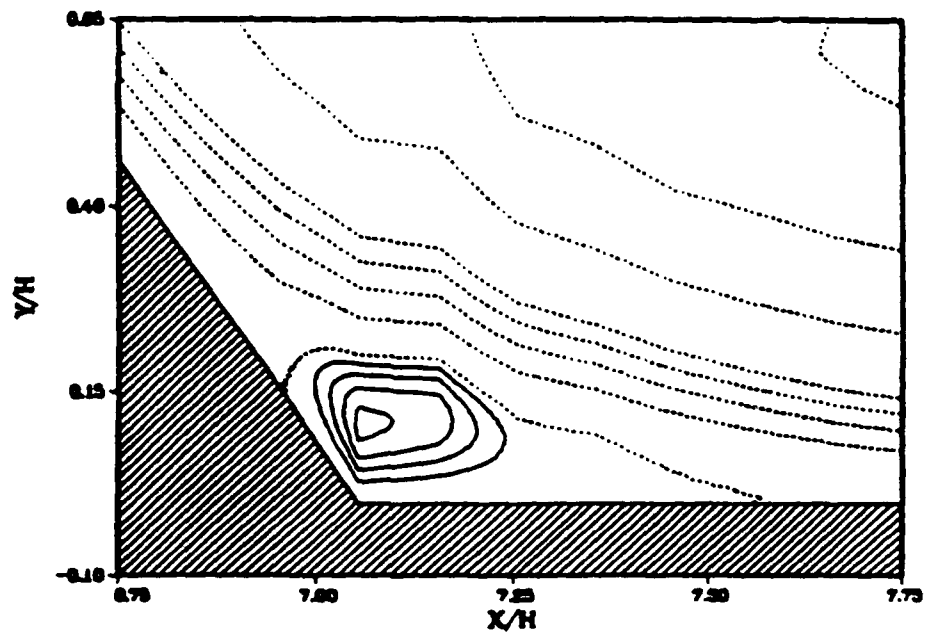
Figure 9. Streamfunction contours near the base of the
turbulator. The clockwise rotating vortex is indicated by the
solid streamlines.

TEMPERATURE CONTOURS
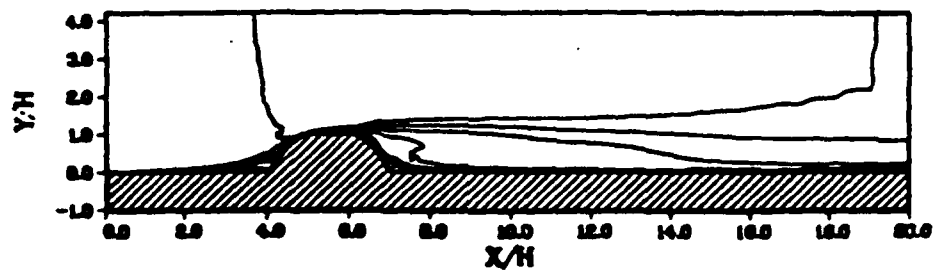
Figure 10. Calculated temperature contours.

TEMPERATURE CONTOURS
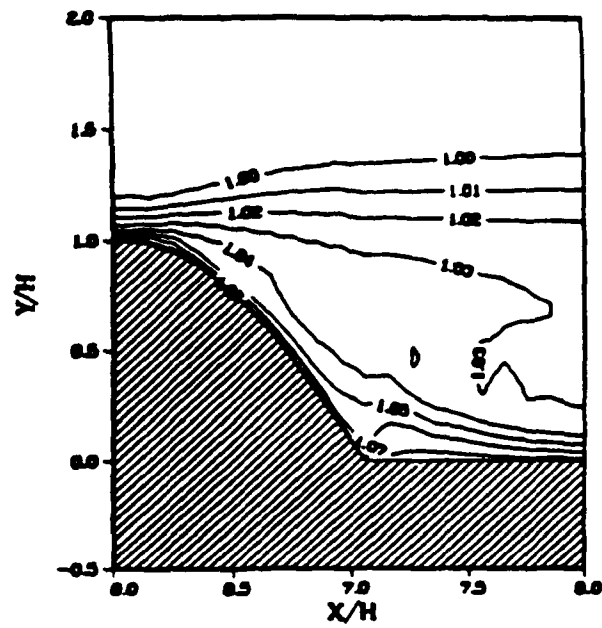
Figure 11. Detail of the temperature distribution downstream of the turbulator. Values of T/T are indicated.

VELOCITY PROFILES UPSTREAM OF RIB
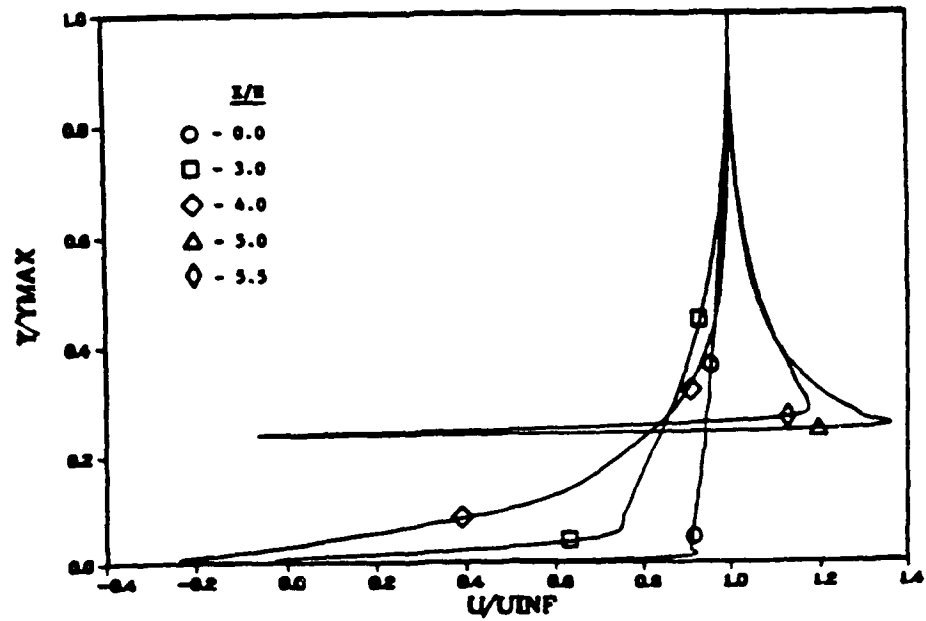
Figure 12. Calculated velocity profiles, upstream of the turbulator.

VELOCITY PROFILES DOWNSTREAM OF RIB
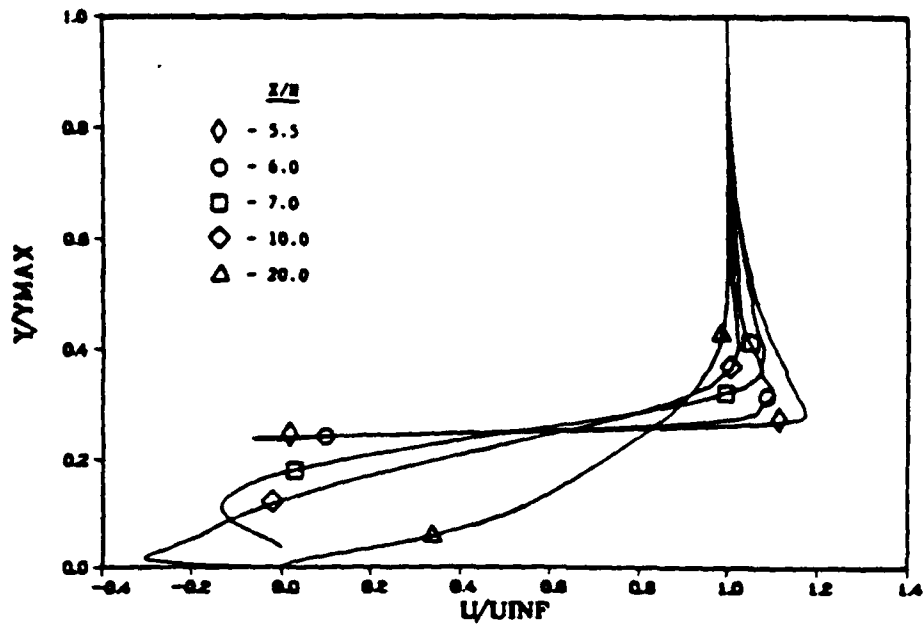
Figure 13. Calculated velocity profiles, downstream of the turbulator.

TEMPERATURE PROFILES UPSTREAM OF RIB
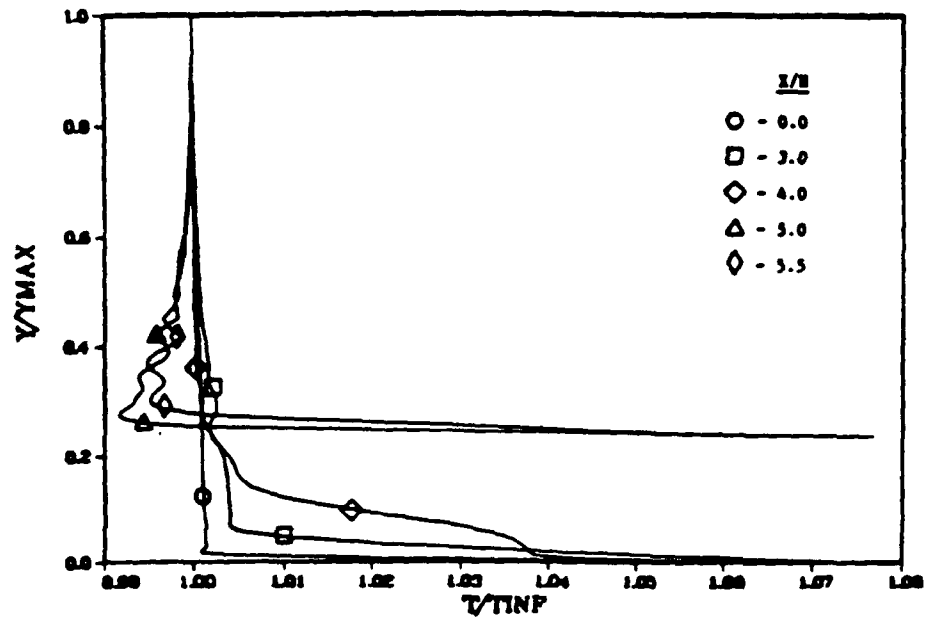
Figure 14. Calculated temperature profiles, upstream of the turbulator.

TEMPERATURE PROFILES DOWNSTREAM OF RIB
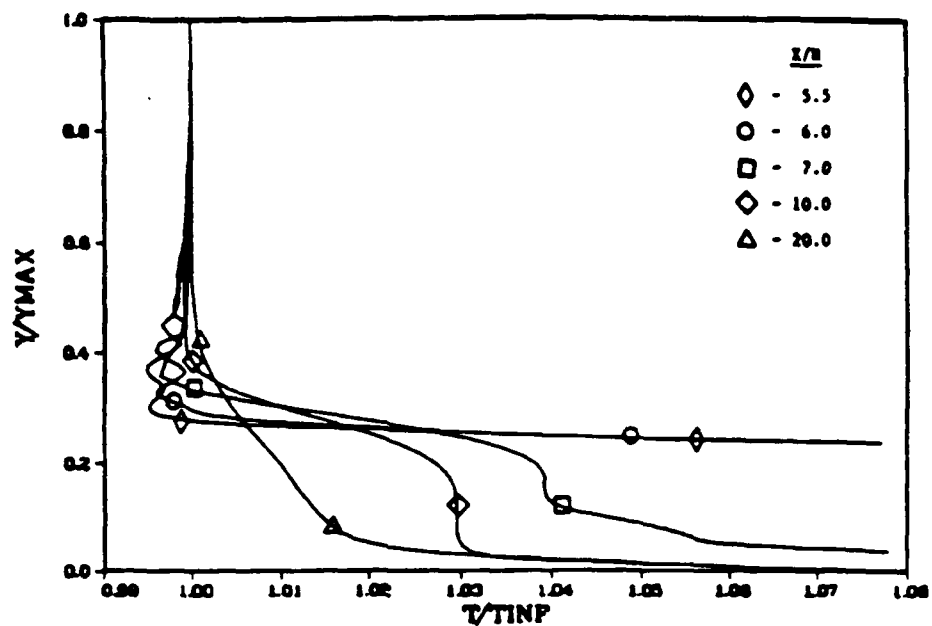
Figure 15. Calculated temperature profiles, downstream of the turbulator.

LOCAL SKIN FRICTION
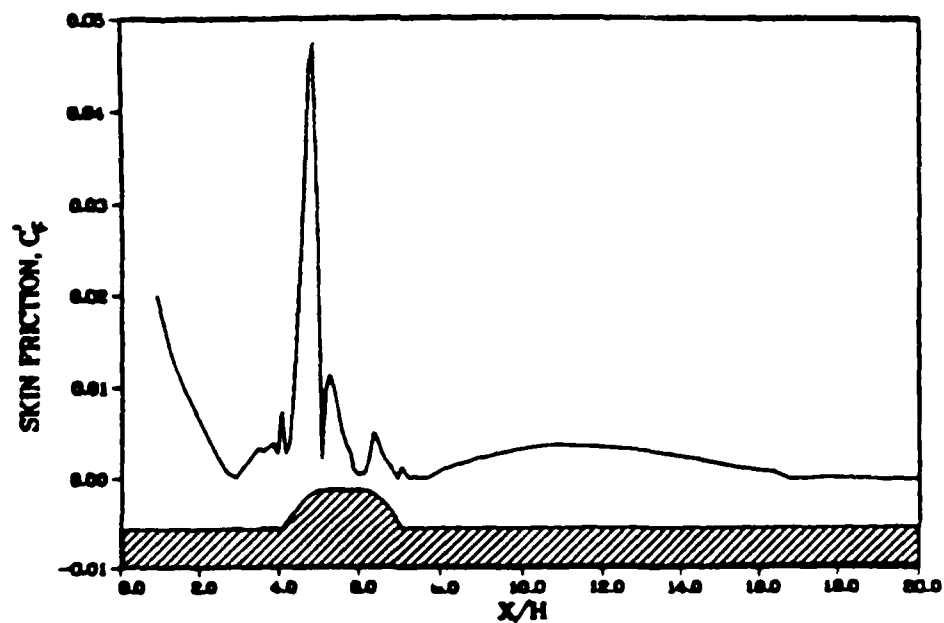
Figure 16. Calculated axial distribution of local skin friction coefficient.

LOCAL HEAT TRANSFER RATE
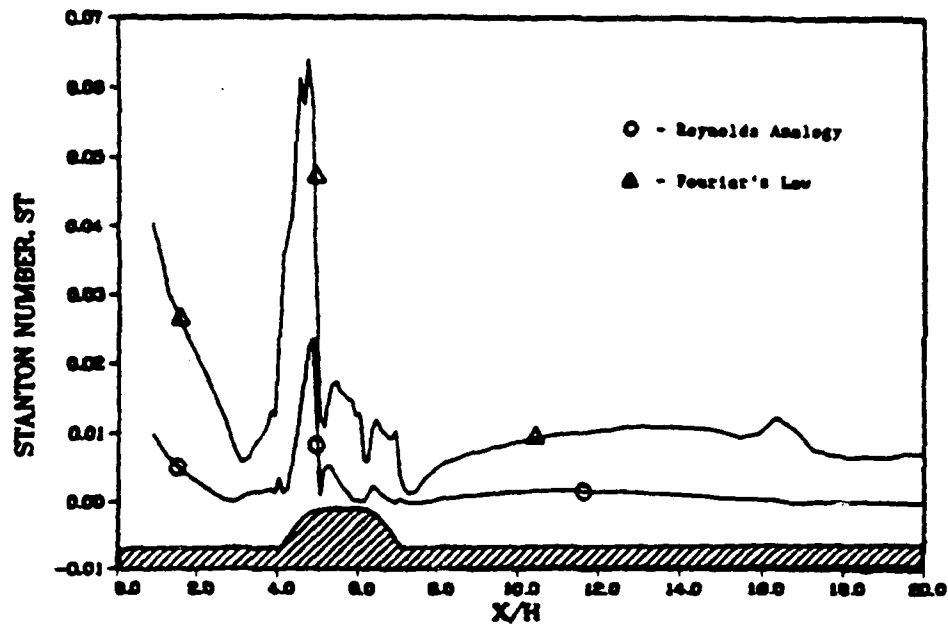
Figure 17. Calculated axial distribution of local Stanton Number.

NUSSELT NUMBER VERSUS X/D
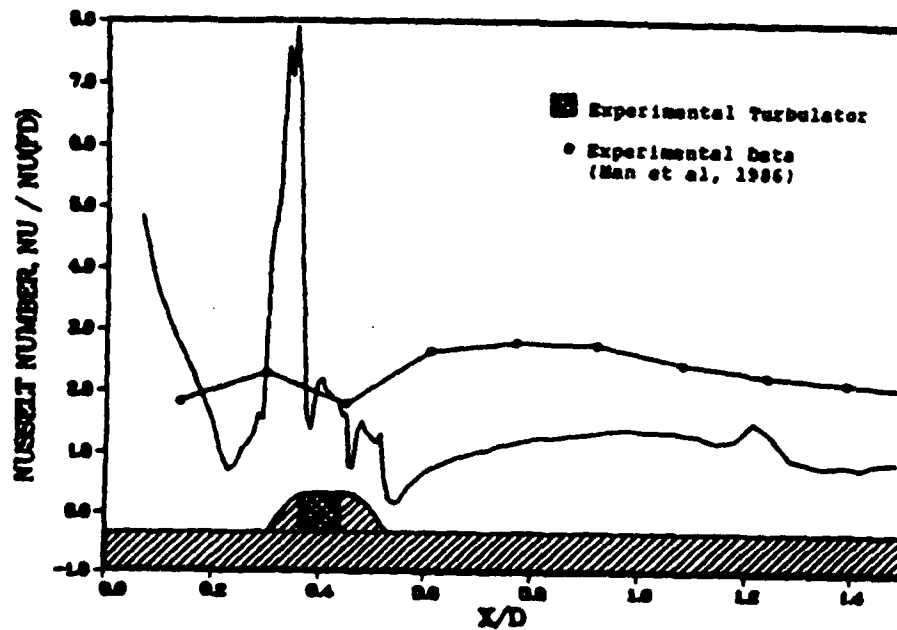
Figure 18. Calculated axial distribution of local Nusselt Number.

FINAL REPORT NUMBER 55
REPORT NOT AVAILABLE AT THIS TIME
Dr. Richard Tankin
760-7MG-051

FINAL REPORT NUMBER 56
REPORT NOT AVAILABLE AT THIS TIME
Dr. Cheng-Hsiao Wu
760-7MG-093

Analysis of an Algorithm for

Multiple Frequency Resolution

By

Vernon L. Bakke

Department of Mathematical Sciences
University of Arkansas
Fayetteville, Arkansas 72701

December, 1988

ABSTRACT

This report describes work on an algorithm constructed in
connection with the estimation of frequencies in radar signals.
In the event multiple frequencies are present in a signal, the
Prony method is applied using sampled data with a time lag large
enough so that direct calculation of the frequencies is possible
only up to modulus the principal value. The algorithm discussed
here is an attempt to resolve this problem. Since the problem is
shown to be inherently unstable, several adaptations are proposed
to overcome some of the sources of error.

1. Introduction.

The problem of estimating frequency of radar pulses has received considerable attention (see, e.g., [5] and the bibliography). Methods of collecting the data from a signal vary, and in all cases numerical software must be constructed to estimate the associated frequencies.

Once the data has been collected, some numerical scheme or schemes are employed to derive estimates for parameters related to the signal frequency, phase or amplitude. The most popular tools are related to transform techniques, such as the Fourier Transform or the Walsh Transform. For a high level accuracy, however, a large number of sample points is necessary. Another numerical method which can be adapted for this problem is the Prony method [3]. In this report, the Prony method and its relation to the problem at hand will be discussed. In [1] an algorithm for implementation of the Prony method was proposed and this report presents further study of the problem and adaptations in the algorithm. In particular the problem of computing estimates of several frequencies occuring in a signal will be examined, and the stability of the method will be studied.

Section 2 outlines the Prony method for approximating the frequencies in a signal. In section 3 a discussion of the unstable nature of this algorithm is presented by deriving a factorization of the system. Section 4 contains a discussion of the adaptations to these instabilities and the algorithm for pairing is discussed. Some examples are presented in section 5 and a scheme for the reduction of the sensitivity to error is proposed. Concluding remarks follow in section 6.

2. THE GENERAL METHOD

In this section we examine the process after the data has been collected. Thus, assume we have a signal $S(t)$ which is of the form

$$(1) \qquad\qquad S(t) = \sum_{k=1}^{p} P_k e^{2\pi i (\omega_k t + \varphi_k)}$$

where P_k , ω_k and φ_k are the amplitudes, frequencies and phase angles, respectively. The digitized data is collected via an IFM receiver by passing the signal pulse through a time delay of known length τ . This is essentially equivalent to viewing the signal as being sampled at times $0, \tau, 2\tau, \ldots, N\tau$. Thus, we may use (1) to write

$$(2) \qquad S(n\tau) = \sum_{k=1}^{p} P_k e^{2\pi i (\omega_k n\tau + \varphi_k)} = \sum_{k=1}^{p} q_k e^{2\pi i \omega_k n\tau} ,$$

$n = 0, 1, \ldots, N\tau$, where $q_k = P_k e^{2\pi i \varphi_k}$, $k = 0, 1, \ldots, p$. Since we are interested in calculating the unknown values ω_k , $k = 1, 2, \ldots, p$, we then use these sampled values to construct a polynomial $P(z)$ which has roots $z_r = e^{2\pi i \omega_r \tau}$, $r = 1, 2, \ldots, p$. The following method, called the Prony method (see [3]) is a scheme to obtain these values.

If $P(z) = z^p + a_1 z^{p-1} + \ldots + a_p$ is the polynomial we seek, it follows that since

$$a_p S(t_k) = a_p \sum_{n=1}^{p} q_n e^{2\pi i \omega_n k \tau}$$

$$a_{p-1} S(t_{k+1}) = a_{p-1} \sum_{n=1}^{p} q_n e^{2\pi i \omega_n (k+1) \tau}$$

$$\vdots$$

$$a_1 S(t_{k+p-1}) = a_1 \sum_{n=1}^{p} q_n e^{2\pi i \omega_n (k+p-1) \tau}$$

then

$$S(t_{k+p}) + a_1 S(t_{k+p-1}) + \ldots + a_p S(t_k)$$

$$= \sum_{n=1}^{p} q_n e^{2\pi i \omega_n k \tau} P(e^{2\pi i \omega_n \tau}) = 0$$

Hence, we may construct the sequence of equations

$$a_1 S(t_{k+p-1}) + a_2 S(t_{k+p-2}) + \ldots + a_p S(t_k) = -S(t_{k+p})$$

$$a_1 S(t_{k+p}) + a_2 S(t_{k+p-1}) + \ldots + a_p S(t_{k+1}) = - S(t_{k+p+1})$$

(3)

$$\vdots$$

$$a_1 S(t_{k+2p-2}) + a_2 S(t_{k+2p-3}) + \ldots + a_p S(t_{k+p-2}) = -S(t_{k+2p})$$

If we solve (3) for the coefficients a_i, $i = 1,2,\ldots,p$, we have the

polynomial $P(z)$ and we can find the roots of $P(z)$ using a method

such as Newton's method. In general, the system (3) will be low order

(p < 10) and a direct method such as Gaussian Elimination will be suitable for solving (3). In practice, the system (3) corresponds to the autoregressive model, where the matrix coefficients $S(t_i)$ are the auto-correlation coefficients. Thus with a matrix of this type one could use a factoring algorithm designed for symmetric, positive definite matrices, such as a Cholesky Decomposition. In all the examples, a Gaussian Elimination code for complex matrices was used.

The polynomial $P(z)$ now has complex coefficients, and for $p > 2$ an iterative method (Newton's method) of order 2 is used. Generally, these methods are sensitive to starting data, and for complex polynomials the regions of convergence can be quite complicated.

3. STABILITY OF THE METHOD

In order to investigate the stability of such an algorithm, we use the matrix form of (3) and write

$$(4) \qquad\qquad Ax = b$$

where

$$A = \begin{bmatrix} S(t_{k+p-1}) & S(t_{k+p-2}) & \cdots & S(t_k) \\ S(t_{k+p}) & S(t_{k+p+1}) & \cdots & S(t_{k+1}) \\ \vdots & \vdots & & \vdots \\ S(t_{k+2p-2}) & S(t_{k+2p-3}) & \cdots & S(t_{k+p-1}) \end{bmatrix},$$

$x = (a_1, a_2, \ldots, a_p)^T$, and $b = -(S(t_{k+p}), S(t_{k+p+1}), \ldots, S(t_{k+2p-1}))^T$. Here the superscript T denotes the transpose operation. The elements of A are given by (2), which we may rewrite as $S(k\tau) = Q^T E_k$, where

$$Q^T = (q_1, q_2, \ldots, q_p)$$

and

$$E_k = (e^{2\pi i \omega_1 \tau k}, e^{2\pi i \omega_2 \tau k}, \ldots, e^{2\pi i \omega_p \tau k})^T.$$

The structure of the matrix allows us to write the ith row as

$$(S(t_{k+p+i-1}), S(t_{k+p+i-2}), \ldots, S(t_{k+i}))$$

and the jth column as

$$S(t_{k+p-j}), S(t_{k+p-j+1}), \ldots, S(t_{k+2p-j-1}))^T,$$

hence the element $a_{ij} = S(t_{k+p+i-j-1})$, and we may express this as

$$a_{ij} = Q^T E_{k+p+i-j-1}.$$

The matrix A may be written in factored form as

$$
\begin{bmatrix}
q_1 e^{2\pi i \omega_1 \tau(k+p)} & q_2 e^{2\pi i \omega_2 \tau(k+p)} & . & . & . & q_p e^{2\pi i \omega_p \tau(k+p)} \\
q_1 e^{2\pi i \omega_1 \tau(k+p+1)} & q_2 e^{2\pi i \omega_2 \tau(k+p+1)} & . & . & . & q_p e^{2\pi i \omega_p \tau(k+p+1)} \\
& & \vdots & & & \\
q_1 e^{2\pi i \omega_1 \tau(k+2p-1)} & q_2 e^{2\pi i \omega_2 \tau(k+2p-1)} & . & . & . & q_p e^{2\pi i \omega_p \tau(k+2p-1)}
\end{bmatrix}
$$

$$
\times
\begin{bmatrix}
e^{-2\pi i \omega_1 \tau} & e^{-2\pi i \omega_1 2\tau} & . & . & . & e^{-2\pi i \omega_1 p\tau} \\
e^{-2\pi i \omega_2 \tau} & e^{-2\pi i \omega_2 2\tau} & . & . & . & e^{-2\pi i \omega_2 p\tau} \\
& & \vdots & & & \\
e^{-2\pi i \omega_p \tau} & e^{-2\pi i \omega_p 2\tau} & . & . & . & e^{-2\pi i \omega_p p\tau}
\end{bmatrix}
$$

Note also that the first matrix may be factored as

$$
(5)
\begin{bmatrix}
1 & 1 & . & . & . & 1 \\
e^{2\pi i \omega_1 \tau} & e^{2\pi i \omega_2 \tau} & . & . & . & e^{2\pi i \omega_p \tau} \\
& & \vdots & & & \\
e^{2\pi i \omega_1 \tau(p-1)} & e^{2\pi i \omega_2 \tau(p-1)} & . & . & . & e^{2\pi i \omega_p \tau(p-1)}
\end{bmatrix}
$$

$$
\times
\begin{bmatrix}
q_1 e^{2\pi i \omega_1 \tau(k+p)} & 0 & . & . & . & 0 \\
0 & q_2 e^{2\pi i \omega_2 \tau(k+p)} & . & . & . & 0 \\
& & \vdots & & & \\
0 & 0 & . & . & . & q_p e^{2\pi i \omega_p (k+p)}
\end{bmatrix}
$$

We observe that the right hand side of (4) also has such a factorization, and it follows that we may rewrite (4) as

(6) $$W \tilde{Q} \tilde{E}_{k+p-1} W^* x = - W \tilde{Q} \tilde{E}_{k+p-1} v$$

where W is the left factor in (5), $\tilde{Q} = \text{diag}(q_1, q_2, \ldots, q_p)$, $\tilde{E}_{k+p} = \text{diag}(e^{2\pi i \omega_1 \tau (k+p)}, e^{2\pi i \omega_2 \tau (k+p)}, \ldots, e^{2\pi i \omega_p \tau (k+p)})$, W^* is the conjugate transpose of W, and $v = (e^{2\pi i \omega_1 \tau}, e^{2\pi i \omega_2 \tau}, \ldots, e^{2\pi i \omega_p \tau})^T$. This decomposition makes the analysis relatively plain, since the existence of a unique solution depends on the nonsingularity of the matrix W and the nonvanishing of the components of $\tilde{Q}$.

REMARK 1. The matrix W is in the form of the Vandermonde matrix, so it is obvious that W is nonsingular if the product $\prod_{k \neq j} (e^{2\pi i \omega_j \tau} - e^{2\pi i \omega_k \tau})$ does not vanish (see [3]).

REMARK 2. Since $q_k = p_k e^{2\pi i \varphi_k}$, $k = 1, 2, \ldots, p$, the matrix $\tilde{Q}$ is nonsingular as long as the signal S consists of the frequencies ω_k, $k = 1, 2, \ldots, p$.

As pointed out in [1] and [6], if τ is chosen sufficiently small so that for the frequencies ω which are in an interval (α, β), we have $(\beta - \alpha) \tau < 1$, then the above method is stable since the values $e^{2\pi i \omega_j \tau}$ will all be distinct. However this choice of τ leads to inaccuracies in data collection, and as a result it is necessary to choose a larger value

for τ. In light of this, we now have two problems: namely the
instability of the above method and the determination of the correct
frequency from ambiguous information. Note that the method is now
inherently unstable because for a given frequency ω such that $\omega + a \, \epsilon$
(a,b), if $\tau > \dfrac{1}{b-a}$, then $\tau\omega > \dfrac{\omega}{b-a}$ and it follows that it is possible to
find values ω_1 and ω_2 for which $\tau\omega_1 > 1$ and $\tau\omega_1 = j + \tau\omega_2$, hence
$e^{2\pi i \omega_1 \tau} = e^{2\pi i \omega_2 \tau}$. In this case, the product mentioned in Remark 1
vanishes and the matrix W is singular.

The problem may be complicated further by the assumption that there
exist p frequencies while $\tilde{p}$ frequencies are present and $\tilde{p} < p$. This
is the point made by Remark 2. Although this leads to an instability, one
may evade this problem by a proper strategy in the implementation of the
algorithm. In this case, the Gaussian Elimination routine in which the
coefficient matrix is triangularized has a built-in check to determine
whether the rank $\tilde{p}$ is less than p. If so, the autocorrelation matrix
is recalculated assuming $\tilde{p}$ frequencies are present.

In addition to the above mentioned problems associated with this
scheme, it is clear that the addition of signal noise and computation
error may lead to large errors. In general, since the coefficient matrix
consists of the autocorrelation coefficients, one expects the noise to
perturb the diagonal of the matrix (see [5]).

4. ALGORITHM

Once a value of τ has been selected, the algorithm is clear until we must decide the true values of the frequencies $\omega_1, \omega_2, \ldots, \omega_p$. Thus, with the scheme we have up to this point, we may obtain a solution to the system (4) as long as a unique solution exists, and then employ a root-finding technique to get values μ_k, $k=1,2,\ldots,p$, which are the zeros of the polynomial $P(z)$. These values satisfy $\mu_k = e^{2\pi i \omega_k \tau}$.

REMARK 3. It is worth mentioning at this point that root-finding techniques for complex polynomials are inherently unstable and extremely sensitive to starting points. In [3], iteration schemes for methods of this nature are pointed out to be related to chaos, which arises from the complicated regions of convergence of this method in the complex plane.

Now that the values of $e^{2\pi i \omega_k \tau}$ have been obtained, we only know the principal value of $\omega_k \tau$. That is, we know a value θ_k, where $\theta_k + M_k = \omega_k \tau$ for some integer M_k. This problem of ambiguity has been the subject of research by the author (see [1]) and others (see [6,7]). Clearly, an error made in the value of M_k can lead to rather disastrous results, since the calculated value for ω_k will be off by at least $1/\tau$, where τ is relatively small (0.015, for some examples given below).

Errors arising from computation or noise can degrade the values of θ_k, and since the bandwidth is quite large, we are still working with quite small values of τ, hence these errors tend to be magnified when we

solve for ω_k. Thus, to explain the algorithm, we first assume we are working with the true values of θ and follow this by altering the algorithm in an effort to compensate for the errors.

Suppose the width of the interval containing the frequencies is a given integer B (band width) and assume that $\omega \, \epsilon \, (0,B)$. Note that for the practical case, $\omega \, \epsilon \, (A,A+B)$, where $A = 2Ghz$ and $B = 2Ghz$. Let K_1, K_2, and K_3 be given integers so that

(6)
$$K_1 + K_2 - K_3 = 0$$

and K_1, K_2, K_3 are relatively prime. Further assume that B is a prime integer. These assumptions will be helpful in damping errors.

If we define $\tau_1 = K_1/B$, $\tau_2 = K_2/B$ and $\tau_3 = K_3/B$, we apply the above scheme to obtain three sets: T_1, T_2, and T_3, where, if $\theta \, \epsilon \, T_1$, then for some M, and some ω $\theta + M = \tau_1\omega$, if $\varphi \, \epsilon \, T_2$ then there is an integer N and some ω such that $\varphi + N = \tau_2\omega$, and if $\psi \, \epsilon \, T_3$ then there is an integer P and an ω such that $\psi + P = \tau_3\omega$.

Define the set $\Omega = \{\omega_1,\omega_2, \ldots ,\omega_p\}$ to be the set of frequencies actually represented in the signal. Now if $\omega \, \epsilon \, \Omega$, then there exist values $\theta \, \epsilon \, T_1$, $\varphi \, \epsilon \, T_2$ and $\psi \, \epsilon \, T_3$ and integers M, N, and P such that

$$\theta + M = \tau_1\omega \, , \quad \varphi + N = \tau_2\omega \quad \psi + P = \tau_3\omega.$$

From the property (6), it follows that

$$(\theta + M) + (\varphi + N) - (\psi + P) = 0$$

hence

$$\theta + \varphi - \psi = P - N - M.$$

Now θ, φ, and ψ all lie in the interval $(0,1)$, so the inequality

$$-1 < \theta + \varphi - \psi < 2$$

must be satisfied, and since $P - N - M$ is an integer, the only candidates for this combination are 0 and 1. This forms a necessary condition for proper association of the triple (θ, φ, ψ), hence we have the following definition:

<u>Definition</u>. We say that the triple (θ, φ, ψ) is a properly associated candidate if the condition

(7)
$$\theta + \varphi - \psi = \begin{cases} 0 \\ 1 \end{cases}$$

holds.

We use the term 'candidate' here because it is possible to satisfy (7) and yet be an improperly associated triple. Thus, the algorithm for proper association is aimed at collecting all triples satisfying (7) and then eliminating the improper associations, as illustrated in the examples below.

Now suppose we have a properly associated triple. Then since

$$\frac{\theta+M}{\tau_1} = \frac{\varphi+N}{\tau_2}$$

we have the relation

(8) $K_2\theta - K_1\varphi = K_1N - K_2M.$

We are looking for a solution pair (N,M) where $0 \leq M < K_1$ and

$0 \leq N < K_2$ (note that we may have used a combination with ψ and P, where

$0 \leq P < K_3$). Since K_1 and K_2 are relatively prime, there exists a

unique pair (N,M) for which (8) is satisfied (see , e.g. [8]).

It should be pointed out here that the above scheme is rather

delicate. Consider the following example.

Example 1. Suppose $\omega_j = \omega_k + \alpha$, where $\alpha = B/K_1$. Then while $\theta_j + M_j =$

$\tau_1\omega_j$, we find that $\theta_k + M_k = \tau_1\omega_k = \tau_1\omega_j + 1 = \theta_j + M_j + 1$. So if (7) is

satisfied by the triple (θ_j,φ,ψ), it will also be satisfied by (θ_k,φ,ψ).

Note, however, that for these values of ω the matrix W in (6)

would be singular, and some adaptation must be made. To account for this

singularity we make the observation that the contribution of ω_j and ω_k

in the values of $S(n\tau)$ given by (2) result in

$S(n\tau) = q_1e^{2\pi i\omega_1 n\tau} + \ldots + q_je^{2\pi i\omega_j n\tau} + \ldots + q_ke^{2\pi i\omega_k n\tau} + \ldots + q_pe^{2\pi i\omega_p n\tau}$

and since

$$q_j e^{2\pi i \omega_j n \tau} + q_k e^{2\pi i \omega_k n \tau} = (q_j + q_k) e^{2\pi i \omega_j n \tau}$$

then the rank of the original system corresponding to τ is reduced. Thus, by solving a system (4) which has been reduced to a system which has rank $p_1 \leq p$, we generate a set T_1 with p_1 distinct values.

So the first adaptation we make is to calculate the rank of the system (4) for each τ_i and find the three sets T_1, T_2 and T_3 with p_1, p_2 and p_3 distinct elements, respectively.

In the next example, we see how it is possible for a false association in another way. We first note that for each $\theta \in T_1$ there exist values φ and ψ in T_2 and T_3 respectively, for which (7) is satisfied.

Example 2. If (θ, φ, ψ) is a properly associated triple corresponding to ω, suppose that $\omega_2 = \omega + \alpha$ and $\omega_3 = \omega + \beta$, where $\tau_2 \alpha + \tau_3 \beta$ is an integer. Then (7) will be satisfied by $(\theta, \varphi_2, \psi_3)$ since

$$\tau_1 \omega + \tau_2 \omega_2 - \tau_3 \omega_3 = \tau_1 \omega + \tau_2 \omega - \tau_3 \omega + J$$

from which it follows that $\theta + \varphi_2 - \psi_3 = 0$ or 1. Note also that this may happen even if the system (4) has a unique solution for τ_1, τ_2 and τ_3.

In order to adapt to this problem, we first consider the case in which all three sets T_1, T_2, and T_3 have p elements. This means that for each $\theta \in T_1$, there exists exactly one φ and one ψ for which the

triple (θ, φ, ψ) is properly associated. Similarly, for $\varphi \in T_2$ there

exists exactly one element $\theta \in T_1$ and one element $\psi \in T_3$ for which the

triple (θ, φ, ψ) is properly associated. The same statement may be made

for $\psi \in T_3$. If either φ or ψ appears in no other triple, then

(θ, φ, ψ) is correctly associated. In this manner we may collect those

triples for which (7) is satisfied and for which any one of θ, φ, or ψ

appear only once.

Before proceeding, the algorithm should be illustrated for the case

$p = 2$. In this case, we generate the three sets

$$T_1 = \{\theta_1, \theta_2\}, \quad T_2 = \{\varphi_1, \varphi_2\}, \quad T_3 = \{\psi_1, \psi_2\}$$

and the matrices $M(\theta_i)$ are formed in which a 1 is placed in the j,kth

position if $(\theta_i, \varphi_j, \psi_k)$ satisfies condition (7). Note that if each set

consists of 2 elements we then have two 2×2 matrices indicating the

candidates for proper association. We must determine the candidates which

are correctly associated. We have two cases which can occur:

Case 1: $M(\theta_1) = \begin{bmatrix} 1 & 0 \\ 0 & 0 \end{bmatrix}$ and $M(\theta_2) = \begin{bmatrix} 0 & 0 \\ 0 & 1 \end{bmatrix}$.

Case 2: $M(\theta_1) = \begin{bmatrix} 1 & 0 \\ 0 & 1 \end{bmatrix} = M(\theta_2)$

It is easily seen that there are no other combinations possible. For

example, if $M(\theta_1) = \begin{bmatrix} 1 & 1 \\ 0 & 0 \end{bmatrix}$, then both $(\theta_1, \varphi_1, \psi_1)$ and $(\theta_1, \varphi_1, \psi_2)$

would satisfy (7), and from that relation, it follows that $\psi_1 = \psi_2$, which

is not the case. Note that in Case 2 it may appear that there are 4

possible associations, but when equation (8) is solved using K_2 and K_3, it

follows that there are only two values of ω calculated.

If one of the sets only has one element, say $T_1 = \{\theta_1\}$, then we have

the matrix $M(\theta_1) = \begin{bmatrix} 1 & 0 \\ 0 & 1 \end{bmatrix}$ and both $(\theta_1, \varphi_1, \psi_1)$ and $(\theta_1, \varphi_2, \psi_2)$ are

correctly associated triples. It is impossible for either of the other

elements to be nonzero, for if this were the case, then we have, say

$M(\theta_1) = \begin{bmatrix} 1 & 1 \\ 0 & 1 \end{bmatrix}$, which implies $(\theta_1, \varphi_1, \psi_1)$ and $(\theta_1, \varphi_1, \psi_2)$ both

satisfy equation (7). But this means that $\psi_1 = \psi_2$, which is not the

case. Note that here there may only be one set with one element, and the

other two sets must have 2 elements. This is because if, in addition,

$T_3 = \{\psi_1\}$, since $\omega_2 = \omega_1 + \alpha$, where $\tau_1\alpha \in \mathfrak{F}$ (the integers), then we also

must have $\tau_3\alpha \in \mathfrak{F}$. Hence $\alpha = I/\tau_1 = J/\tau_3$, where $I, J \in \mathfrak{F}$. Since $\alpha <$

B, we must have $0 < I < K_1$ and $0 < J < K_3$ satisfying $K_1 J = K_3 I$, where

K_1 and K_3 are relatively prime. But since this cannot happen, then T_3

must have two distinct elements.

In theory, it has been shown that this scheme works for all

situations of order 2. Experiments show however, that the method works

best if there are no errors, either due to roundoff or to noise. It is

the purpose of the next section to show how this may be improved to avoid the catastrophic errors.

5. ERROR COMPENSATION.

The problem of non exactness in the algorithm has been the subject of much study both by the author and by McCormick (see [1],[6,7]) and the source of many huge errors, hence illustrating the non-Lipshcitzean nature of this problem. It was McCormick/Tsui [7] who finally saw a means to reduce the sensitivity of the algorithm to noise. If we take the data obtained by the Prony method and form the sets T_1, T_2 and T_3, then quantize these values, by assuming β bits of accuracy, we can replace the calculated values by quantized values and apply the algorithm to the new sets of quantized estimates to the principal values. Thus, denote by θ_t, θ_c and θ_q the true, calculated and quantized values. This means that

$$\theta_q = \frac{\text{nint}(\theta_c 2^\beta)}{2^\beta} ,$$

so

$$|\theta_q - \theta_c| < \frac{1}{2^{\beta+1}} \quad \text{and} \quad |\theta_t - \theta_c| < \varepsilon,$$

where ε is a bound on the error due to roundoff and noise. In the algorithm, the first thing necessary is to see if an ordered triple satisfies (7). If $\theta_t + \Psi_t - \Psi_t = \delta$, where $\delta = 0$ or 1 from equation (7),

then

$$|\theta_q + \varphi_q - \psi_q - \delta| < 3\left[\frac{1}{2^{\beta+1}} + \varepsilon\right].$$

Using this bound as a guide, although a bit pessimistic, from practice it has been found that a criterion for acceptance, i.e., that $(\theta_q, \varphi_q, \psi_q)$ satisfy (7) is if $|\theta_q + \varphi_q - \psi_q - \delta| < \frac{1}{2^{\beta-1}}.$

Once we have determined that such a triple is properly associated, the question is, how severe an error is possible. From (8) we have

$$K_2\theta_q - K_1\varphi_q = K_2(\theta_q - \theta_t + \theta_t) - K_1(\varphi_q - \varphi_t + \varphi_t)$$

$$= K_1N - K_2M + K_2(\theta_q - \theta_t) - K_1(\varphi_q - \varphi_t)$$

and since

$$|K_2(\theta_q - \theta_t) - K_1(\varphi_q - \varphi_t)| < \frac{K_1 + K_2}{2^{\beta+1}}$$

then we should require that $\frac{K_1 + K_2}{2^{\beta+1}} < \frac{1}{2}$. This being the case, we may replace the left side of (8) by $\text{nint}(K_2\theta_q - K_1\varphi_q)$, and solve the resulting equations for the appropriate integer values of M and N. Furthermore, since the values K_1, K_2 and K_3 must be ordered in some way, say $K_1 < K_2 < K_3$, a method to control the error would be to use the equation (8) with K_3. There are two possiblities, namely:

(10a) $$\text{nint}(K_3\theta_q - K_1\psi_q) = K_1 P - K_3 M$$

or

(10b) $$\text{nint}(K_3\varphi_q - K_2\psi_q) = K_2 P - K_3 N$$

The reason for this is that once a pair (P,M) has been determined, the solution ω is of the form

$$\omega_c = \frac{1}{\tau}(\psi_q + P) = \frac{B}{K_3}(\psi_q + P)$$

so that

$$|\omega_c - \omega| = \frac{B}{K_3}|\psi_q - \psi_t| < \frac{B}{K_3}\left[\frac{1}{2^{\beta+1}} + \varepsilon\right].$$

The requirement that $|\omega_c - \omega| < 1$ imposes the final restriction on the number of bits β, the size of K_3 and the accuracy of the calculation of ψ_q. for example, if $\varepsilon < \dfrac{1}{2^{\beta+1}}$, then the requirement on K_3 is that

$K_3 > \dfrac{B}{2^\beta}$. As an illustration with $B \sim 2000$, if $\beta = 7$ then $K_3 \geq 16$.

In order to discuss the error ε we first recall that in equation (6) the existence of a unique solution x depends on the nonvanishing of the product given in Remark 1. Suppose that the values $\omega_j \tau$ are all distinct, $j = 1,2,\ldots,p$. Then to simplify, the solution of (6) is also a solution of

(11) $W^* x = -v$.

Errors from noise and roundoff will also occur in the product $W \tilde{Q} \tilde{E}_{k+p-1}$,

however as a point of illustration, it will suffice to look at (11).

Since W^* is the conjugate transpose of W, the existence of a unique

solution of (11) depends on the non-vanishing of the determinant, which is

given by

$$\det(W^*) = \prod_{k \neq j} (e^{-2\pi i \omega_k \tau} - e^{-2\pi i \omega_j \tau}).$$

It is evident that as this value gets near zero, the sensitivity to

perturbations in the data increases. It is also clear, that since the

error in computation of the solution to (6) under perturbations of the

matrix A, say $\triangle A$ satisfies the inequality

(12) $\|x_c - x_t\| \leq \dfrac{\|A^{-1}\|}{1 - \|A^{-1}\| \, \|\triangle A\|} \left[\|\triangle A\| \, \|A^{-1}\| \, \|v\| \right]$

(see [9]), it is possible that the denominator in (12) cannot be

guaranteed to be positive, hence it is possible for the computed values of

the coefficients of $P(z)$ to contain enough error so that the roots

obtained cannot be trusted. Here, the norm $\| \cdot \|$ is taken to be $\| \cdot \|_\infty$,

where

$$\|x\|_\infty = \sum_{i=1}^{p} |x_i|, \quad \text{and} \quad \|A\|_\infty = \max_i \sum_{j=1}^{p} |a_{ij}|.$$

As a final comment, the error in x_c will degrade the accuracy in the computed values of the roots of $P(z)$. As an estimate via first-order expansion, take the case of $p = 2$ and let the error in a_i be given by δ_i, $i = 1,2$. Then the error in the roots can be estimated by

$$\bar{\varepsilon} = \delta_1 + \frac{2\delta_1 (e^{2\pi i \omega_1 \tau} + e^{2\pi i \omega_2 \tau}) + \delta_1^2 - 4\delta_2}{e^{2\pi i \omega_1 \tau} - e^{2\pi i \omega_2 \tau}}.$$

Note again, the error is related to the closeness of the values of $\omega_1 \tau$ and $\omega_2 \tau$.

Example 3. Suppose we have $p = 3$, $K_1 = 13$, $K_2 = 21$, $K_3 = 34$, $\beta = 7$ and $B = 2143$. If we know that the signal contains the frequencies 3000, 3170, and 3042, all in the range $[2000, 2000+B]$, then through scaling to the interval $[0,B]$, we are searching for the frequencies 1000, 1170 and 1042. With these values known, we check the algorithm to see if it is possible to retrieve these values, and follow through the steps. Once the roots of the polynomials have been found and the arguments quantized, we have the following table:

	K_1/B			K_2/B			K_3/B	
τ	c	$2^\beta q$		c	$2^\beta q$		c	$2^b q$
θ	.066	8		.098	12		.321	41
φ	.790	102		.465	60		.211	27
ψ	.866	111		.563	72		.532	68

Table 1.

$$T_1 = \left| \frac{8}{128}, \frac{12}{128}, \frac{41}{128} \right| \quad T_2 = \left| \frac{27}{128}, \frac{60}{128}, \frac{102}{128} \right| \quad T_3 = \left| \frac{68}{128}, \frac{72}{128}, \frac{111}{128} \right|$$

The indicator matrices are:

$$M(\theta_1) = \begin{bmatrix} 1 & 0 & 0 \\ 0 & 0 & 0 \\ 0 & 0 & 1 \end{bmatrix} \quad M(\theta_2) = \begin{bmatrix} 0 & 0 & 0 \\ 0 & 1 & 0 \\ 0 & 0 & 0 \end{bmatrix} \quad M(\theta_3) = \begin{bmatrix} 1 & 0 & 0 \\ 0 & 0 & 0 \\ 0 & 0 & 0 \end{bmatrix}$$

The triples satisfying (7) are:

$$(\theta_1, \varphi_1, \psi_1), \quad (\theta_1, \varphi_3, \psi_3), \quad (\theta_2, \varphi_2, \psi_2), \quad (\theta_3, \varphi_1, \psi_1)$$

Note that we eliminate $(\theta_1, \varphi_1, \psi_1)$ since all three entrys occur in other triples and the T_i all contain p distinct elements.

Using equation (10b), we have

$$\text{nint}(K_3\varphi_3 - K_2\psi_3) = 9 = 21P - 34N; \quad P = 15 \text{ and } N = 9$$

$$\text{nint}(K_3\varphi_2 - K_2\psi_2) = 4 = 21P - 34N; \quad P = 18 \text{ and } N = 11$$

$$\text{nint}(K_3\varphi_1 - K_2\psi_1) = -4 = 21P - 34 N; \quad P = 16 \text{ and } N = 10$$

With these values we solve for ω :

$$\omega_1 = \frac{2143}{34} \left(\frac{111}{128} + 15 \right) = 1000.09$$

$$\omega_2 = \frac{2143}{34} \left(\frac{72}{128} + 18 \right) = 1169.98$$

$$\omega_3 = \frac{2143}{34} \left(\frac{68}{128} + 16 \right) = 1041.95$$

6. CONCLUSIONS

From the above discussions, it is evident that the algorithm including the prony method and Newton's method for finding roots along with the adaptations is unstable. The reasons for this instability lie in the problem itself, namely that if two frequencies occur in a certain combination and if there is noise present, the calculated values can be degraded to the extent that computed values are unacceptable. In spite of this undesirable aspect of the problem, the case for p=2 is probably best since an iterative technique is not necessary for computation of roots. Perturbations of the diagonal of the matrix A of the order of 1% are allowable, and in some cases, even larger perturbations can be tolerated. Experiments with higher order systems, say order 5 or so have shown an extreme sensitivity to noise, and perturbations of the diagonal on the order of about .1% are near the intolerance level.

The algorithm represented here is an improvement over the original (see [1]), perhaps mainly due to the technique communicated by McCormick in [6] regarding the quantization of the values prior to applying the association algorithm.

REFERENCES

1. Bakke, Vernon L., Frequency Estimation in the Analysis of Radar Signals, Final Report, USAF – UES Summer Faculty Research Program/Graduate Student Summer Support Program, 1987.

2. Danby, J. M. A., Computing Applications to Differential Equations, Reston Publishing Co., Reston, VA., 1985.

3. Hildebrand, F. B., Introduction to Numerical Analysis, 2nd Ed., McGraw-Hill, 1956.

4. Isaacson, Eugene and H. B. Keller, Analysis of Numerical Methods, John Wiley & Sons, Inc., New York, 1966.

5. Kay, Steven M. and Stanley Lawrence Marple, Spectrum Analysis – A Modern Perspective, Proceedings of the IEEE, Vol. 69, No. 11, November, 1981.

6. McCormick, William S., Design of a Digital EW Passive Receiver, AFOSR – 85 – 045.

7. McCormick, William S. and James L. Y. Tsui, A Noise Insensitive Solution to a Simultaneous Congruence Problem in Real-Time Spectral Estimation, Manuscript in preparation for publication, 1988.

8. Niven, Ivan and H. S. Zuckerman, An Introduction to the Theory of Numbers, John Wiley & Sons, New York, 4th Ed., 1980.

9. Stewart, G. W., Introduction to Matrix Computations, Academic Press, New York, 1973.

FINAL REPORT

SIGNAL PROCESSING IN EW ENVIRONMENT

BY

JOHN Y. CHEUNG
SCHOOL OF ELECTRICAL ENGINEERING AND COMPUTER SCIENCE,
UNIVERSITY OF OKLAHOMA,
202 W. BOYD, CEC 219,
NORMAN, OK 73019.

JUNE 20, 1988.

SIGNAL PROCESSING IN EW ENVIRONMENT

By John Y. Cheung

ABSTRACT

This is the final report performed for the contract entitled "Signal Processing in EW Environment". Activities related to this contract can be summarized in three main areas as outlined in the proposal: theoretical development and simulation of the direct adaptive frequency estimation (DAFE) algorithm, theoretical development and simulation of the effect of partially received signals on frequency estimation methods, and performance comparisons through simulation of various frequency estimation methods. These three areas are conducted by the the principal investigator, a visiting scholar, and numerous graduate students throughout the contract period.

ACKNOWLEDGMENT

SIGNAL PROCESSING IN EW ENVIRONMENT

By John Y. Cheung

1. Introduction

This is the final report on the work performed related to the contract entitled "Signal Processing in EW Environment." The application of signal processing techniques in detection and estimation of the spectral contents, particularly the harmonic components of the received signal is an important process in the defense related environments. The problem is further complicated by many additional constraints in the electronic warfare (EW) arena. The purpose of the present contract is to analyze current frequency estimation techniques and to develop new techniques that are applicable for EW environments.

There are many constraints in the EW environments. Received signals are often complex, of short durations, of relatively high signal to noise ratio, overlapping, of varying types, and of different origins. Complex signals are often obtained thus providing both magnitude and phase characteristics. Though the signal received is of relatively high signal to noise ratio, processing is extrememly difficult because the signal duration is extremely short. Additional factors further complicates the effectiveness of many conventional techniques. For example, stationary conditions are often violated because there are many overlapping signals beginning and ending within the same block of sampled data. The sampled data often include different types of signals and signals from many different directions.

There are a number of conventional techniques currently proposed for frequency es-

timation such as Prony's method and other spectral estimation methods. Most of these techniques require a tremendous amount of computations and are of less practical value in EW environments. Furthermore, due to the above mentioned constraints, many conventional techniques cannot be applied when the stationary condition is violated. The concept of adaptive techniques for spectral estimation has been under investigation for the last two decades. The goal of the present research is to adapt and modify the adaptive techniques for spectral estimation for use specifically in frequency detection and estimation environments.

The primary area of investigation during the present contract period is frequency estimation. However, the research effort has been concentrated in three directions:

1. The development of a new adaptive frequency estimatior method for complex signals

2. An evaluation of performance degradation in partially received signals

3. A comparison of performance for various frequency estimation methods

Each of these three areas are now discussed in more details in the following sections.

2. The DAFE algorithm

There are a number of conventional frequency estimation techniques. These can be categorized into two main categories:

1. Direct frequency estimation methods such as Prony's method

2. Spectral methods by means of spectral estimation

Direct frequency estimation methods uses the original signal to directly calculate the magnitudes and phases of any frequency components present in the signal. No intermediate parameters are used. Methods in this category include Prony's method and its variants. In a somewhat indirect way, some methods use the eigenanalysis of the covariance matrix to estimate the frequency contents of the received signal. The second category of frequency estimation methods are actually adapted from spectral estimation methods. After the spectrum is estimated, a threshhold is used to identify the peaks. The locations and heights of the peaks correspond to the frequencies and magnitudes of the harmonic components.

Several problems exist with these conventional techniques. First, Prony's method requires a procedure for finding the roots of a polynomial. The order of this characteristic polynomial is determined by the number of signals present. Rooting a polynomial is an open ended problem. It is not a particularly easy task and requires a fair amount of computations. Secondly, Prony's method requires prior knowledge of the order of the system, i.e. the number of frequencies present. Incorrect order gives grossly inaccurate estimation results. If the order is unknown a priori, then Prony's method must be solved for each order. A selection criterion is used to choose the proper order.

For spectral estimation methods, the amount of computation is also extensive. Most spectral methods require the computation of the covariance matrix from which the auto-regressive and moving average (ARMA) coefficients are estimated. (Depending on the algorithms, sometimes may be strictly AR or MA coefficients that are estimated.) Some methods only yield the auto-regressive coefficients while others give both sets of coefficients. After the coefficients are obtained, a Fast Fourier transform is usually used to generate an estimate of the power spectral density from which the frequency peaks are identified and located. Even though many iterative algorithms can be used to solve for a set of linear equations, the whole process is still quite time consuming. Furthermore, the magnitude estimate is quite unreliable.

In view of the above limitations of conventional methods, the present research uses an adaptive approach for frequency estimation. The adaptive approach has several advantages. First, an adaptive approach can be more effectively applied when the received signal is not stationary but is slowly varying. An adaptive approach can not only detect the presence or absence of a particular frequency component, but also track signals with slowly varying frequencies. This is the basic motivation for developing the direct adaptive frequency estimation (DAFE) method to estimate the magnitude and phase of any frequency components.

The DAFE algorithm is effective for detecting and estimating the frequency and corresponding complex (or real) amplitudes from complex (or real) input signals. There are no theoretical limits as to the total number of frequencies present in the signal. There may be a practical limit depending on the availability of hardware and computation time.

The DAFE algorithm requires simple computations and many of the calculation can be performed in parallel further speeding up the total process. In addition to applying the DAFE algorithm in parameter estimation problem where the model order is known, the algorithm can also be applied in system identification environments where the model order is not known.

There are two versions of the DAFE algorithm. The first and simplest one of the two makes use the least means square (LMS) adaptive algorithm. The second and more complex one makes use of the recursive least square (RLS) technique. The basic principle of both versions is the same. The steps can be itemized as follows:

1. From the original signal, use the property of a sine wave to successively generate intermediate signals each with one sinusoid removed. If all sinusoids have been removed, the signal must be the noise sequence with all sinusoidal components removed.

2. Use the error signal to adaptively change the frequency estimates in such a way that the magnitude of the error signal is minimized.

3. Use the error signal at the same time to adaptively estimate the complex amplitudes of each corresponding frequency components.

4. Repeat steps 1 through 3 for each new data point received.

The detailed analytical development of the LMS version of the DAFE algorithm is given in two papers. The first paper entitled "A Direct adaptive frequency estimation technique" contains preliminary information and has been presented in the 30th Midwest Symposium on Circuits and Systems in Syracuse, NY on August 17-18, 1987. The paper

is also published in the conference proceedings. A reprint of this paper has been included in this report as Appendix A. A second paper entitled "A structured adaptive frequency estimation technique" has been prepared and submitted to the IEEE Transactions on Acoustics, Speech, and Signal Processing. The second paper is more complete in the analytical developments and is included in this report as Appendix B.

The first two papers only include the development of the DAFE algorithm using the LMS method. A third paper is being prepared at this point containing the analytical development and simulation results using the RLS algorithm. Proper acknowledgment to the support of this contract will be given when the third paper is submitted as with the first two papers. The use of the RLS method for adaptation reduces the adaptation time by one half. This reduction in adaptation time is expected.

Estimating Frequencies and Real Amplitudes by The RLS Algorithm

Assume the input signal is real and is represented as follows:

$$x(n) = \sum_{j=1}^{M} a_j(n)u_j(n) \qquad (2\text{-}1)$$

where M is the number of discrete frequencies, a_j's are the real–valued amplitudes, and $u_j(n)$'s are the individual sinusoids, i.e.,

$$u_j(n) = \sin(w_j n) \qquad (2\text{-}2)$$

Using the property of a sine wave, we have $\sin wn - w \sin w(n-1) + \sin w(n-2) = 0$. Let

us then define the following:

$$x_1(n) = x(n) - \hat{w}_1 x(n-1) + x(n-2)$$

$$x_2(n) = x_1(n) - \hat{w}_2 x_1(n-1) + x_1(n-2)$$

$$x_3(n) = x_2(n) - \hat{w}_3 x_2(n-1) + x_2(n-2) \qquad (2\text{-}3)$$

$$x_4(n) = x_3(n) - \hat{w}_4 x_3(n-1) + x_3(n-2)$$

$$\vdots$$

$$x_M(n) = x_{M-1}(n) - w_M x_{M-1}(n-1) + x_{M-1}(n-2) \qquad (2\text{-}4)$$

In 2–2, the first operation effectively removes the sinusoidal component of w_1, the second removes the next sinusoidal component of w_2, etc. Since there are only M discrete frequencies present, $x_M(n)$ must contain noise alone because all M sinusoids have been removed. This error can be expressed in a slightly different form as follows:

$$e(n) = x_M(n) = d(n) - X_M^T(n)\hat{W}_M(n) \qquad (2\text{-}5)$$

where:

$$d(n) = x(n) + x(n-2) + x_1(n-2) + x_2(n-2) + \ldots x_{M-1}(n-2)$$

$$X_M^T(n) = [x(n-1) \quad x_1(n-1) \quad x_2(n-1) \quad \ldots \quad x_{M-1}(n-1)]$$

$$\hat{W}_M(n) = [\hat{w}_1 \quad \hat{w}_2 \quad \hat{w}_3 \quad \ldots \quad \hat{w}_M]$$

The weighted squared error can immediately be found by squaring the expression for the error above:

$$\epsilon(n) = \sum_{i=1}^{n} \lambda^{n-i} e^2(i) \qquad (2\text{-}6)$$

In the gradient search method, the minimum error location can be found by setting $\frac{\partial \epsilon(N)}{\partial W_M(N)} =$ to zero, then

$$R_{MM}(n)\,\hat{W}_M(n) = P_M(n) \tag{2-7}$$

where

$$R_{MM}(n) = \sum_{i=1}^{n} \lambda^{n-i} X_M(i) X_M^T(i)$$

$$P_M(n) = \sum_{i=1}^{n} \lambda^{n-i} d(i) X_M(i)$$

The above matrix equation gives the expression for the optimal weights:

$$\hat{W}_M(n) = R_{MM}^{-1}(n) P_M(n) \tag{2-8}$$

But to get an estimate of the weights, we must know the inverse of the covariance matrix $R_{MM}^{-1}(n)$. To do this, we observe from the definition that $R_{MM}(n)$ can be written as:

$$R_{MM}(n) = \lambda R_{MM}(n-1) + X_M(n) X_M^T(n) \tag{2-9}$$

Using the matrix inverse lemma, a recursive update for $R_{MM}^{-1}(n)$ in terms of the previous inverse, $R_{MM}^{-1}(n-1)$, and the new data acquired at time n can be obtained:

$$R_{MM}^{-1}(n) = \frac{1}{\lambda}\left[R_{MM}^{-1}(n-1) - \frac{R_{MM}^{-1}(n-1) X_M(n) X_M^T(n) R_{MM}^{-1}(n-1)}{\lambda + X_M^T(n) R_{MM}^{-1}(n-1) X_M(n)} \right] \tag{2-10}$$

Define $G_M(n)$, $C_{MM}(n)$, $q(n)$ as below:

$$C_{MM}(n) = R_{MM}^{-1}(n) \tag{2-11}$$

$$G_M(n) = \frac{C_{MM}(n-1) X_M(n)}{\lambda + q(n)} \tag{2-12}$$

$$q(n) = X_M^T(n) R_{MM}^{-1}(n-1) X_M(n) \qquad (2\text{-}13)$$

Now (2-8) can be rewritten as:

$$C_{MM}(n) = \frac{1}{\lambda}[C_{MM}(n-1) - G_M(n) X_M^T(n) C_{MM}(n-1)] \qquad (2\text{-}14)$$

Likewise $P_M(n)$ can also be expanded as:

$$P_M(n) = \lambda P_M(n-1) + d(n) X_M(n) \qquad (2\text{-}15)$$

Substituting (2-11), (2-12), (2-13), and (2-14) into (2-9), we obtain the following expression for $\hat{W}_M(n)$:

$$\hat{W}_M(n) = \frac{1}{\lambda}[C_{MM}(n-1) - G_M(n) X_M^T(n) C_{MM}(n-1)][\lambda P_M(n-1) + d(n) X_M(n)]$$

$$= \hat{W}_M(n-1) + G_M(n) X_M(n) \qquad (2\text{-}16)$$

From (2-15), the frequencies f_j can readily be obtained:

$$\hat{f}_j = (\cos^{-1} \frac{\hat{w}_j}{2})/(2\pi) \qquad (2\text{-}17)$$

Now that we have found the frequencies embedded in the input signal; we next turn our attention to finding the real-valued amplitudes of these frequencies. Rewriting (2-1),

$$x(n) = \sum_{j=1}^{M} a_j(n) u_j(n) \qquad (2\text{-}18)$$

We have an estimate of $u_j(n)$ using (2-2) and $\hat{w}_j$ in (2-15). We now need to estimate a_j. Let the error of estimating the amplitudes be defined as:

$$\bar{e}(n) = x(n) - \hat{U}_M^T(n) \hat{A}_M(n) \qquad (2\text{-}19)$$

where:

$$\hat{U}_M^T(n) = [\hat{u}_1(n), \hat{u}_2(n), \ldots, \hat{u}_M(n)]$$

$$A_M(n) = [\hat{a}_1(n), \hat{a}_2(n), \ldots, \hat{a}_M(n)]$$

Defining the squared error as:

$$\bar{\epsilon}(n) = \sum_{i=1}^{n} \lambda^{n-i} \bar{\epsilon}^2(i) \tag{2-20}$$

We will now use the gradient search method again to obtain an estimate of the amplitudes:

$$\frac{\partial \bar{\epsilon}(n)}{\partial \hat{A}_M(n)} = \sum_{i=1}^{n} \lambda^{n-i} \bar{\epsilon}(i) \hat{U}_M(i) = 0 \tag{2-21}$$

and

$$\hat{A}_M(n) = \overline{R}_{MM}^{-1}(n) \overline{P}_M(n) \tag{2-22}$$

Where

$$\overline{R}_{MM}(n) = \sum_{i=1}^{n} \lambda^{n-i} \hat{U}_M(i) \hat{U}_M^T(i)$$

and

$$\overline{P}_M(n) = \sum_{i=1}^{n} \lambda^{n-i} d(\cdot) \hat{U}_M(i)$$

Following the same developments as the frequency estimation case, we again use the same matrix lemma to obtain an RLS solution to the amplitude estimation.

$$\overline{R}_{MM}(n) = \lambda \overline{R}_{MM}(n-1) + \hat{U}_M(n) \hat{U}_M^T(n) \tag{2-23}$$

$$\overline{R}_{MM}^{-1}(n) = \frac{1}{\lambda} \left[\overline{R}_{MM}^{-1}(n-1) - \frac{\overline{R}_{MM}^{-1}(n-1) \hat{U}_M(n) \hat{U}_M^T(n) \overline{R}_{MM}^{-1}(n-1)}{\lambda + \hat{U}_M^T(n) \overline{R}_{MM}^{-1}(n-1) \hat{U}_M(n)} \right] \tag{2-24}$$

Define

$$\overline{C}_{MM}(n) = \overline{R}_{MM}^{-1}(n) \tag{2-25}$$

$$\overline{G}_M(n) = \frac{C_{MM}(n-1)\hat{U}_M(n)}{\lambda + \overline{q}(n)} \tag{2-26}$$

$$\overline{q}(n) = \hat{U}_M^T(n)\overline{R}_{MM}^{-1}(n-1)\hat{U}_M(n) \tag{2-27}$$

Substituting (2-25), (2-26), and (2-27) into (2-24) and amplifying, we obtain:

$$\overline{C}_{MM}(n) = \overline{C}_{MM}(n-1) - \overline{G}_M(n)\hat{U}_M^T(n)\overline{C}_{MM}(n-1) \tag{2-28}$$

We now have an estimate of the amplidue by putting (2-28) into (2-22):

$$\hat{A}_M(n) = \overline{C}_{MM}(n)\overline{P}_M(n) \tag{2-29}$$

or

$$= A_M(n-1) + \overline{G}_M(n)\overline{e}(n) \tag{2-30}$$

Estimating frequencies and complex amplitudes for complex signal by the RLS algorithm

In the previous case, we have shown how the RLS algorithm can be used to estimate real-valued frequencies and real-valued amplitudes from real-valued input data. In this section, we will further extend the RLS algorithm for complex input data to obtain real-valued frequencies and complex valued amplitudes. The basic algorithm is the same as the previous case in principle except caution must be exercised to distinguish real-valued parameters from complex parameters.

To represent the complex input data, we will use the complex exponential format rather than the simple sine function format:

$$x(n) = \sum_{\ell=1}^{M} a_\ell e^{jw_\ell n} \tag{2-31}$$

The removal of a complex exponential is accomplished by the same operation. We define the following:

$$x_1(n) = x(n) - \hat{w}_1 x(n-1) + x(n-2) \tag{2-32}$$

$$x_2(n) = x_1(n) - \hat{w}_2 x_1(n-1) + x_1(n-2)$$

$$\vdots$$

$$x_M(n) = x_{M-1}(n) - \hat{w}_{M-1} x_{M-1}(n-1) + x_{M-1}(n-2) \tag{2-33}$$

If there are only M complex exponentials, the $nx_M(n)$ would represent the noise signal after all M sinusoids have been removed. This error signal can now be rewritten in matrix format:

$$e(n) = x_M(n) = d(n) - X_M^T(n)\hat{W}_M(n) \tag{2-34}$$

where

$$d(n) = x(n) + x(n-2) + x_1(n-2) + x_2(n-2) + \ldots + x_{M-1}(n-2)$$

$$X_M^T(n) = [x(n-1) \quad x_1(n-1) \quad x_2(n-1) \quad \ldots \quad x_{M-1}(n-1)]$$

$$\hat{W}_M(n) = [\hat{w}_1 \quad \hat{w}_2 \quad \hat{w}_3 \quad \ldots \quad \hat{w}_M]^T$$

The squared error for the frequency estimation is real-valued and can be expressed as follows:

$$\varepsilon(n) = \sum_{i=1}^{n} \lambda^{n-i} e^*(i) e(i) \tag{2-35}$$

The asterisk indicates a complex conjugate operation. The gradient of the squared error in terms of the frequency vector $\hat{W}_M$ can be found by differentiating the above equation.

Setting the gradient to zero, we have the optimal solution for the weight vector:

$$\frac{\partial \varepsilon(n)}{\partial \hat{W}_M} = \sum_{i=1}^{n} \lambda^{n-i} [e^*(i) X_M(i) + e(i) X_M^*(i)] = 0 \qquad (2\text{-}36)$$

or

$$\hat{W}_M(n) = R_{MM}^{-1}(n) P_M(n) \qquad (2\text{-}37)$$

where

$$R_{MM}(n) = \sum_{i=1}^{n} \lambda^{n-i} [X_M(i) X_M^{*T}(i) + X_M^*(i) X_M^T(i)]$$

$$P_M(n) = \sum_{i=1}^{n} \lambda^{n-i} [X_M(i) d^*(i) + X_M^*(i) d(i)]$$

Note that $R_{MM}(n)$ is a real–valued and symmetric covariance matrix. We want to evaluate $R_{MM}^{-1}(n)$ in a recursive manner. Rewriting the above definition for $R_{MM}(n)$ in an iterative manner, we obtain:

$$R_{MM}(n) = \lambda R_{MM}(n-1) + X_M(n) X_M^{*T}(n) + X_M^*(n) X_M^T(n) \qquad (2\text{-}38)$$

$$= R'_{MM}(n-1) + X_M^*(n) X_M^T(n) \qquad (2\text{-}39)$$

Since there are three terms on the right hand side in (2–38), the matrix inversion formula must be applied twice. In other words, we first find the inverse of $R_{MM}^{-1}(n)$ in terms of $R'^{-1}_{MM}(n-1)$, then we find the inverse of $R'_{MM}(n-1)$ in terms of $R_{MM}^{-1}(n-1)$. First, we will find $R_{MM}^{-1}(n)$ in terms of $R'^{-1}_{MM}(n-1)$ using (2–39):

$$R_{MM}^{-1}(n) = R'^{-1}_{MM}(n-1) - \frac{R'^{-1}_{MM}(n-1) X_M^*(n) X_M^T(n) R'^{-1}_{MM}(n-1)}{1 + X_M^T(n) R'^{-1}_{MM}(n-1) \hat{X}_M^{*}(n)} \qquad (2\text{-}40)$$

If we now define the parameters as follows:

$$C_{MM}(n) = R_{MM}^{-1}(n)$$

$$C'_{MM}(n) = R'^{-1}_{MM}(n) \qquad (2\text{-}41)$$

$$q'(n) = X_M^T(n) R_{MM}'^{-1}(n-1) X_M^*(n)$$

$$G_M'(n) = \frac{C_{MM}'(n-1) X_M^*(n)}{1 + q'(n)}$$

then

$$C_{MM}(n) = C_{MM}'(n-1) - G_M'(n) X_M^T(n) C_{MM}'(n-1) \tag{2-42}$$

Next we need to find the inverse of $R_{MM}'^{-1}(n-1)$ in terms of $R_{MM}^{-1}(n-1)$. From (2–38) and (2–39), we have the expression for $R_{MM}'(n-1)$:

$$P R_{MM}'(n-1) = \lambda R_{MM}(n-1) + X_M(n) X_M^{*T}(n) \tag{2-43}$$

and

$$P_M'(n-1) = \sum_{i=1}^{n} \lambda^{n-i} X_M(i) d^*(i)$$

The iterative expression for $R_{MM}'^{-1}(n-1)$ is:

$$R_{MM}'^{-1}(n-1) = \frac{1}{\lambda} R_{MM}^{-1}(n-1) - \frac{1}{\lambda} \frac{R_{MM}^{-1}(n-1) X_M(n) X_M^{*T}(n) R_{MM}^{-1}(n-1)}{\lambda + X_M^{*T}(n) R_{MM}^{-1}(n-1) X_M(n)} \tag{2-44}$$

If we now further define additional parameters as follows:

$$q(n) = X_M^{*T} C_{MM}(n-1) X_M(n) \tag{2-45}$$

$$G_M(n) = \frac{C_{MM}(n-1) X_M(n)}{\lambda + q(n)}$$

Then $C_{MM}'(n-1)$ in (2-44) can be expressed as follows:

$$C_{MM}'(n-1) = \frac{1}{\lambda} [C_{MM}(n-1) - G_M(n) X_M^{*T}(n) C_{MM}(n-1)] \tag{2-46}$$

Substituting (2-42) and (2-46) into (2-37), we obtain an iterative expression for the frequency vector:

$$W_M(n) = C_{MM}(n)P_M(n)$$

$$= [C'_{MM}(n-1) - G'_M(n)X_M^T(n)C'_{MM}(n-1)][P'_M(n-1) + X_M^*(n)d(n)]$$

$$= W'_M(n-1) + G'_M(n)X_M(n) \tag{2-47}$$

But from (2-46) we have:

$$W'_M(n-1) = C'_{MM}(n-1)P'_M(n-1)$$

$$= \frac{1}{\lambda}[C_{MM}(n-1) - G_M(n)X_M^{*T}(n)C_{MM}(n-1)][\lambda P_M(n-1) + X_M(n)d^*(n)]$$

$$= W_M(n-1) + G_M(n)X_M^*(n) \tag{2-48}$$

Substituting (2-48) into (2-47), we obtain the final expression for the optimal weight vector:

$$W_M(n) = W_M(n-1) + G_M(n)X_M^*(n) + G'_M(n)X_M(n) \tag{2-49}$$

Close examination of the above equation shows that the last two terms are real–valued vectors thus always making the $W_M(n)$ vector real-valued. The elements of $W_M(n)$ vector are exactly the frequencies of the complex sinusoids.

Next, we proceed to estimate the complex amplitudes by the same RLS algorithm. The derivation parallels that of the real–valued case developed in the previous section. Let the input and the estimation signal be given as follows:

$$x(n) = \sum_{\ell=1}^{M} a_\ell e^{jw_\ell n} \tag{2-50}$$

$$\hat{x}(n) = \sum_{\ell=1}^{M} \hat{a}_\ell e^{j\Phi_\ell n} = \hat{A}_M^T \hat{U}_M(n) \tag{2-51}$$

The estimation error is:

$$\bar{e}(n) = x(n) - \hat{A}_M^T \hat{U}_M(n) \tag{2-52}$$

and the squared error is:

$$\varepsilon(n) = \sum_{i=1}^{n} \lambda^{n-i} e(i) e^*(i) \tag{2-53}$$

Since the amplitudes are complex, we must treat the real and imaginary part separately. The gradient of the real–valued square error with respect to the real and imaginary past of the complex amplitudes are:

$$\frac{\partial \varepsilon(n)}{\partial \hat{A}_R(n)} = \sum_{i=1}^{n} \lambda^{n-i} [e(i)(-\hat{U}_M^*(i)) + e^*(i)(-\hat{U}_M(i))] \tag{2-54a}$$

$$\frac{\partial \varepsilon(n)}{\partial \hat{A}_I(n)} = \sum_{i=1}^{n} \lambda^{n-i} [e(i)(j\hat{U}_{M}^*(i)) + e^*(i)(j\hat{U}_M(i))] \tag{2-54b}$$

Combining the real and imaginary parts, we have:

$$\frac{\partial \varepsilon(n)}{\partial \hat{A}_M(n)} = \frac{\partial \varepsilon(n)}{\partial \hat{A}_R} + j\frac{\partial \varepsilon(n)}{\partial \hat{A}_I} = \sum_{i=1}^{n} \lambda^{n-i} e(i) \hat{U}_M^*(i) \tag{2-55}$$

The optimal estimation for $\hat{A}$ is found by setting the above gradient to zero. This results in the following:

$$\sum_{i=1}^{n} \lambda^{n-i} [d(i) - A_M^T(n)\hat{U}_M(i)]\hat{U}_M^*(i) = 0 \tag{2-56}$$

or

$$\hat{A}_M(n) = \overline{R}_{MM}^{-1}(n)\overline{P}_M(n) \tag{2-57}$$

where

$$\overline{R}_{MM}(n) = \sum_{i=1}^{n} \lambda^{n-i} \hat{U}_M^*(i)\hat{U}_M^T(i)$$

$$\overline{P}_M(n) = \sum_{i=1}^{n} \lambda^{n-i} d(i) \hat{U}_M^*(i)$$

Using the same principles as before to arrive at an iterative solution, $\overline{R}_{MM}(n)$ can be rewritten as:

$$\overline{R}_{MM}(n) = \lambda \overline{R}_{MM}(n-1) + \hat{U}_M^*(n)\hat{U}_M^T(n) \qquad (2\text{-}58)$$

$$\overline{P}_M(n) = \lambda \overline{P}_M(n-1) + \hat{U}_M^*(n)d(n) \qquad (2\text{-}59)$$

The inverse of $\overline{R}_{MM}(n)$ can be found in similar fashion:

$$\overline{R}_{MM}^{-1}(n) = \frac{1}{\lambda}\overline{R}_{MM}^{-1}(n-1) - \frac{1}{\lambda} \cdot \frac{\overline{R}_{MM}^{-1}(n-1)\hat{U}_M^*(n)\hat{U}_M^T(n)\overline{R}_{MM}^{-1}(n-1)}{\lambda + \hat{U}_M^T(n)\overline{R}_{MM}^{-1}(n-1)\hat{U}_M^*(n)} \qquad (2\text{-}60)$$

where

$$\overline{q}(n) = \hat{U}_M^T(n)\overline{R}_{MM}^{-1}(n-1)\hat{U}_M^*(n)$$

$$\overline{G}_M(n) = \frac{\overline{R}_{MM}^{-1}(n-1)\overline{U}_M^*(n)}{\lambda + \overline{q}(n)}$$

and

$$\overline{C}_{MM}(n) = \overline{R}_{MM}^{-1}(n)$$

then

$$\overline{C}_{MM}(n) = \frac{1}{\lambda}[\overline{C}_{MM}(n-1) - \overline{G}_M(n)\hat{U}_M^T(n)\overline{C}_{MM}(n-1)] \qquad (2\text{-}61)$$

Substituting (2-61) into (2-57), we obtain an expression for the complex amplitudes:

$$\hat{A}_M(n) = \overline{R}_{MM}^{-1}(n)\overline{P}_M(n)$$

$$= \frac{1}{\lambda}[\overline{C}_{MM}(n-1) - \overline{G}_M(n)\hat{U}_M^T(n)\overline{C}_{MM}(n-1)][\lambda\overline{P}_M(n-1) + \hat{U}_M^*(n)d(n)]$$

$$= \hat{A}_M(n-1) + \overline{G}_M(n) \cdot e(n) \qquad (2\text{-}62)$$

Simulation Results

The DAFE algorithms using the LMS or RLS method has been simulated on the IBM 3081 computer using single precision arithmetic. For the present report, we only include the results of a single test case based on real-valued data. Other simulation runs nevertheless have shown that indeed the algorithm does converge correctly for complex input data when estimating the real-valued frequencies end complex amplitudes.

Figure 2.1 shows the learning curve for the DAFE–LMS and DAFE–RLS methods in a sample individual run. Note that though the DAFE–LMS curve seemingly has a lower error magnitude at the beginning, the convergence rate is nevertheless very slow at the end. For this particular simulation run, the DAFE–LMS algorithm converges rather rapidly after 500 iterations rotate the DAFE–RLS algorithm takes twice as many interations. Figure 2.2 and 2.3 shows the trajectories of frequency estimations of all four frequencies as a function of the number of points for the DAFE–LMS and DAFE–RLS algorthims, respectively.
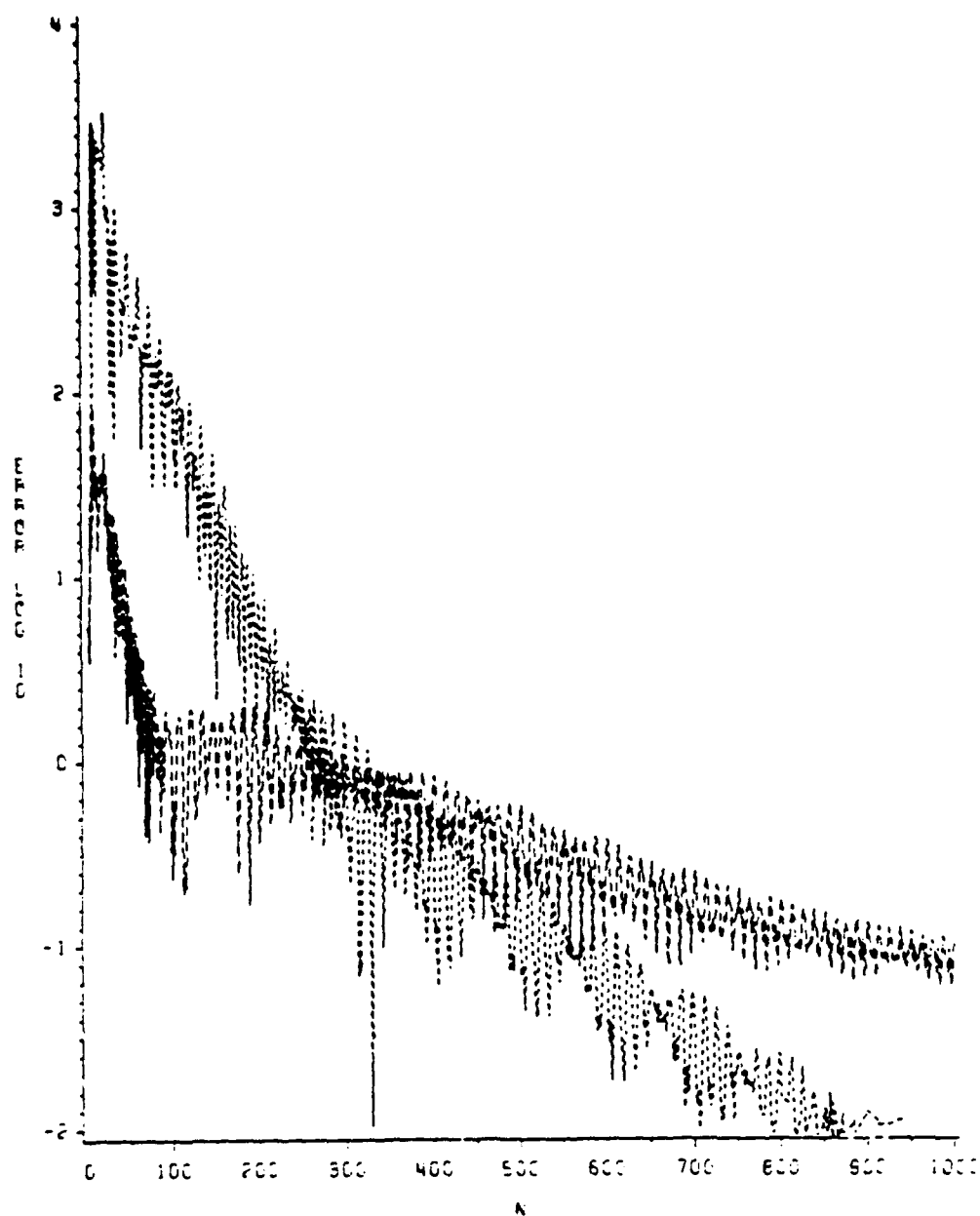
Figure 2.1 Learning curve for the DAFE–LMS and DAFE–RLS algorithms
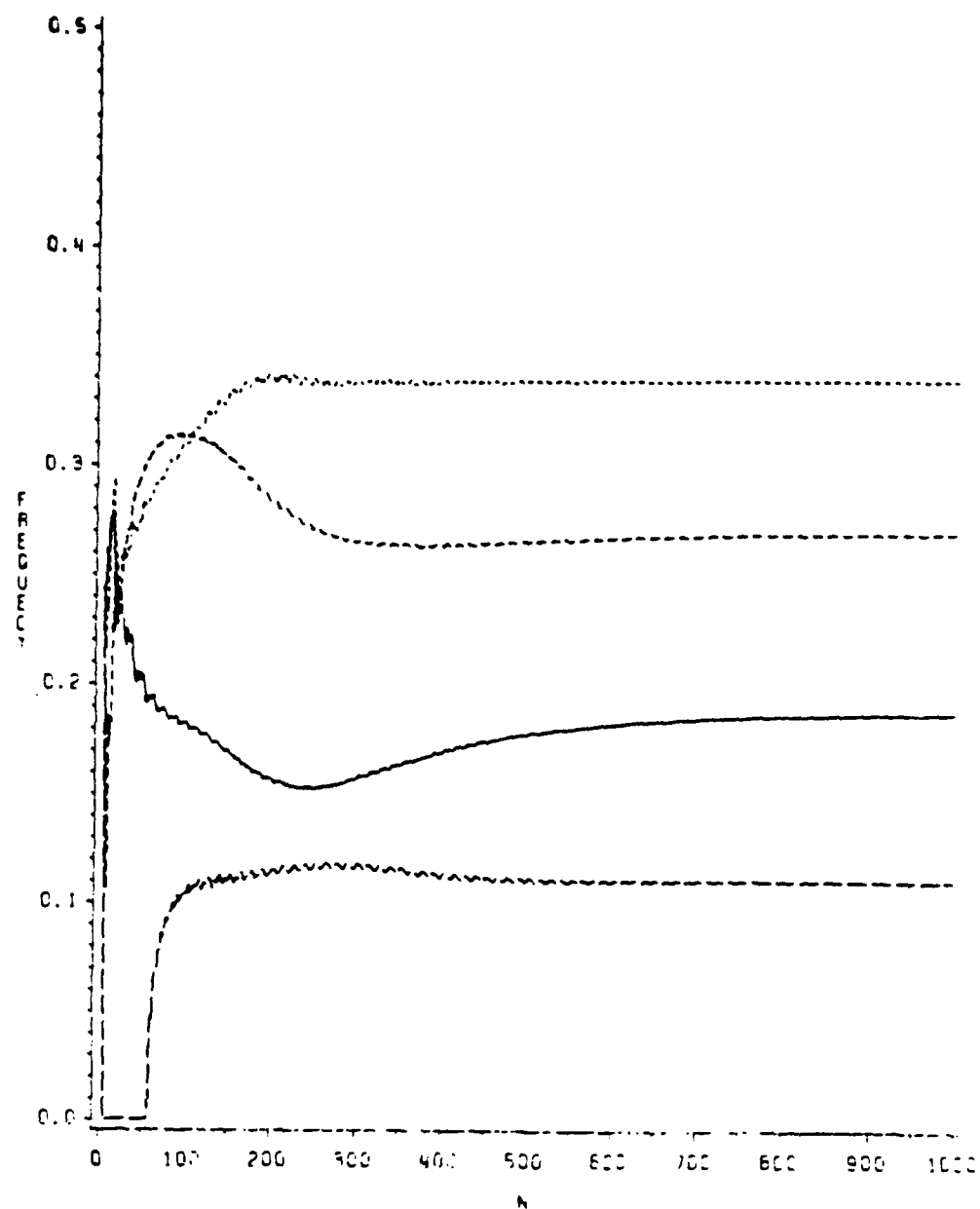
Figure 2.2 Trajectories of frequency estimation for the DAFE–LMS algorithm
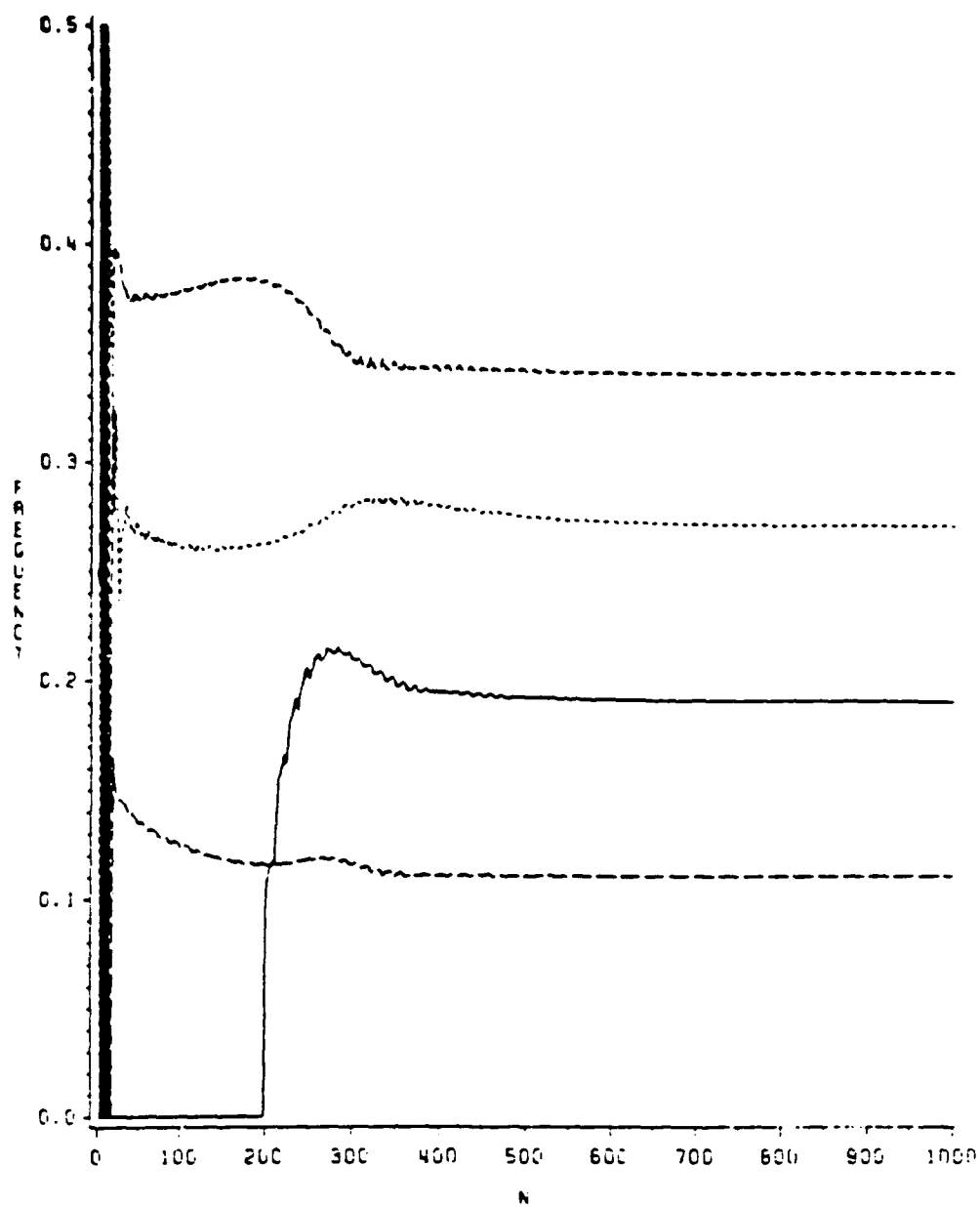
Figure 2.3 Trajectories of frequency estimation for the DAFE-RLS algorithm

8. Effects of partially received signals

The second aspect of this contract is to investigate the effects of partially received signals on various frequency estimation methods. A partially received signal is a short signal that begins or ends during a block of sampled data, i.e. within a sampling window. In other words, because the signal duration is so short, some signals would always start during the sampling window while others would always end during the sampling window. In real life situations, it may not often be possible to capture a signal that lasts longer than the sampling window. Even then, other signals present would often not be present for the whole sampling window unless the sampling window is trivially short.

The effect of partially receiving a signal during the sampling window is equivalent to windowing the fully received signal by a small rectangular window. In the periodogram, the windowed signal has the effect of convolving the spectral estimate with the transform of the windowing function. The result of this convolution is a loss of frequency resolution. This effect should be the same for the other frequency estimation methods.

Detailed theoretical analyses for the periodogram and the modified covariance method is given in the master thesis of Mr. Gopinath Benigeri who has also carried out the simulation of partially received signals for different frequency estimation methods.

A ρ percent window is defined as follows. Let there be M points in the window function with non-zero values such that

$$\frac{M}{N} \times 100\% = \rho\%$$

For example in an 80% window ($\rho = 80\%$) we have

$$\frac{M}{N} \times 100 \quad \text{or} \quad M = \frac{8N}{10} = \frac{4N}{5}$$

so there are $\frac{4N}{5}$ values in a rectangular window of width N with values $= 1$ and the rest are zero.

The rectangular data window is defined as

$$w(n) = \begin{cases} 1 & 1 \leq n \leq N-1 \\ 0 & \text{elsewhere} \end{cases} \qquad (3\text{-}1)$$

The fourier transform of the rectangular data window $w(n)$ is

$$W(f) = \sum_{n=-\infty}^{\infty} w(n)e^{-j2\pi fn}$$

$$= e^{-j2\pi f(N-1)/2} \frac{\sin \pi f N}{\sin \pi f} \qquad (3\text{-}2)$$

$W(f)$ is known as the Dirichlet kernel.

Equivalent Noise Bandwidth:

The equivalent noise bandwidth of a window is the width of a rectangular window with peak signal power gain that would accumulate the same noise power. The accumulated noise power of a window is defined by

$$\text{Noise Power} = N_o \int_{-\pi/T}^{\pi/T} |W(w)|^2 \frac{dw}{2\pi}, \quad w = 2\pi f \qquad (3\text{-}3)$$

where N_o is the noise power per unit bandwidth. Assuming $T = 1$, and using Pareval's Theorem, we get

$$\text{Noise Power} = N_o \int_{-\frac{1}{2}}^{\frac{1}{2}} |W(f)|^2 df = N_o \sum_{n=-\infty}^{\infty} |w(n)|^2 \qquad (3\text{-}4)$$

The peak signal gain and the peak power gain both occur at $f = 0$. Therefore, the peak signal gain $W(o)$ and the peak power gain $W^2(o)$ can be expressed as follows:

$$W(0) = \sum_{n=-\infty}^{\infty} w[n]$$

$$W^2(0) = \left[\sum_{n=-\infty}^{\infty} w[n] \right]^2$$

So the equivalent noise bandwidth is given as follows after normalizing by N_o:

$$ENBW = \frac{\text{Noise Power}}{\text{Peak Power Gain}} = \frac{\sum\limits_{n=-\infty}^{\infty} (w(n))^2}{\left[\sum\limits_{n=-\infty}^{\infty} w(n) \right]^2} \tag{3-5}$$

The limits of n are assumed to be, in general, from $-\infty$ to ∞. When $w(n)$ is substituted by a particular window, the values of n are bounded by the region where the window is defined.

Let us assume that we have a $\rho\%$ rectangular window. The $\rho\%$ rectangular window is defined as

$$W[n] = \begin{cases} 1 & 0 \leq n \leq M-1 \\ 0 & M \leq n \leq N-1 \end{cases} \tag{3-6}$$

The equivalent noise bandwidth for this window is as follows:

$$\begin{aligned} ENBW(M) &= \sum_{n=0}^{M-1} W^2(n) / \left[\sum_{n=0}^{M-1} W(n) \right]^2 \\ &= M/M^2 \\ &= \frac{1}{M} \end{aligned} \tag{3-7}$$

The $ENBW$ is now seen to be a function of the width M of the window.

Scalloping Loss:

Let us assume that we have a signal consisting of a complex sinusoid and additive noise. The signal can be represented as follows:

$$f(n) = Ae^{jw_k nT} + q(n) \tag{3-8}$$

where $q(n)$ is a Gaussian noise process with variance σ_q^2. The Fourier Transform of the signal component of the input after being processed through a window is given by the matched filter output:

$$F(w_k) = \sum_{n=0}^{N-1} w(n) A e^{jw_k nT} e^{-jw_k nT}$$

$$= A \sum_{n=0}^{N-1} w(n) \qquad (3\text{-}9)$$

This is also called the coherent gain. Here we have implicitly assumed that the signal frequency w_k is a multiple of the sampling frequency f_s. If the signal frequency w_k lies midway between the two adjacent sampling frequency multiplies, i.e.

$$w_k = (k + 1/2)\frac{w_s}{N} \qquad \text{where} \qquad w_s = 2\pi f_s$$

Then the change in the coherent gain due to this half bin shift is

$$F(w_{1/2}) = A \sum_{n=0}^{N-1} w(n) e^{-jw_{1/2} nT} \qquad \text{where} \qquad w_{1/2} = \frac{w_s}{2NT} = \frac{\pi}{NT}$$

or

$$F(w_{1/2}) = A \sum_{n=0}^{N-1} w(n) e^{-j\frac{\pi}{N}n} \qquad (3\text{-}10)$$

The scalloping loss, which is defined as the ratio of the coherent gain for a signal frequency located at half a bin away to that located at the DFT bin, is

$$\text{Scalloping loss} \quad = \frac{\left| \sum_{n=0}^{N-1} w(n) e^{-j\frac{\pi}{N}n} \right|}{\sum_{n=0}^{N-1} w(n)} \qquad (3\text{-}11)$$

For a rectangular window, which is $\rho\%$, the scalloping loss will be a function of M. It is given by

$$\text{Scalloping Loss} \quad = \frac{\left| \sum_{n=0}^{M-1} e^{-j\frac{\pi}{N}n} \right|}{M} \qquad (3\text{-}12)$$

Simulation Results

The effect of partially received signals has been simulated in FORTRAN on the IBM 3081 for three methods:

1. The Burg Method

2. The Modified Covariance Method

3. The Adaptive RLS Method

For each method, we have simulated the data for a signal window of 100%, 80%, 60%, 40%, and 20%. Figure 3.1 shows the effect of diminishing window size for the Burg Method. Figure 3.2 and 3.3 shows the same for the modified covariance method and the adaptive RLS method respectively.

4. Performance comparison of frequency estimation methods

The third aspect of the present research effort is to compare the performance of various frequency estimation methods. The methods chosen for this purpose include:

1. The Periodogram

2. The Modified Covariance Method

3. The Burg Method

4. The Adaptive RLS Method

5. Prony's Method

6. The SVD Method

Among these six methods, the periodogram serves as a control for comparison with other methods. The modified covariance method is based on the input covariance matrix. Autoregressive coefficients are estimated directly from the covariance matrix and the power spectral density function is computed from the estimated autoregressive coefficients. The Burg Method gives an estimate of the power spectral density using an estimate of the reflection coefficients. In the adaptive RLS Method, the autoregressive coefficients are computed directly from the input signal in an iterative manner whenever a new sample point is available. In Prony's Method, the input data is reduced into a set of polynominal coefficients. The roots of the characteristic polynomial correspond to the frequencies of the signal. In the signular value decomposition (SVD) method, the eigenvalues of the covariance matrix are related to the desired frequencies.

To test the effectiveness of all these six methods, two standard sets of test data are generated and applied to these methods. In the first test, a single frequency embedded
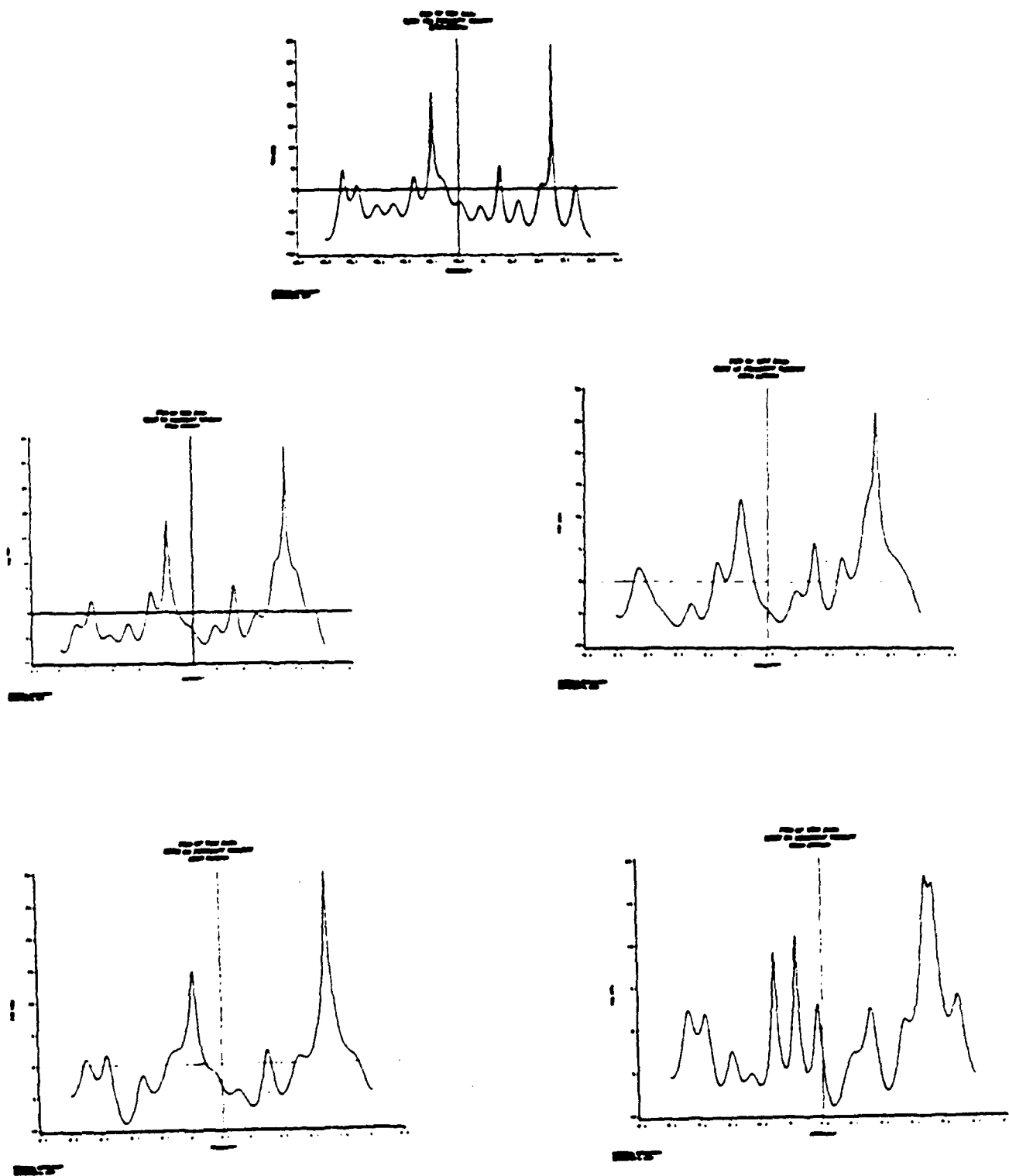
Figure 3.1 Effect of diminishing percentage of received signal in the Burg Method
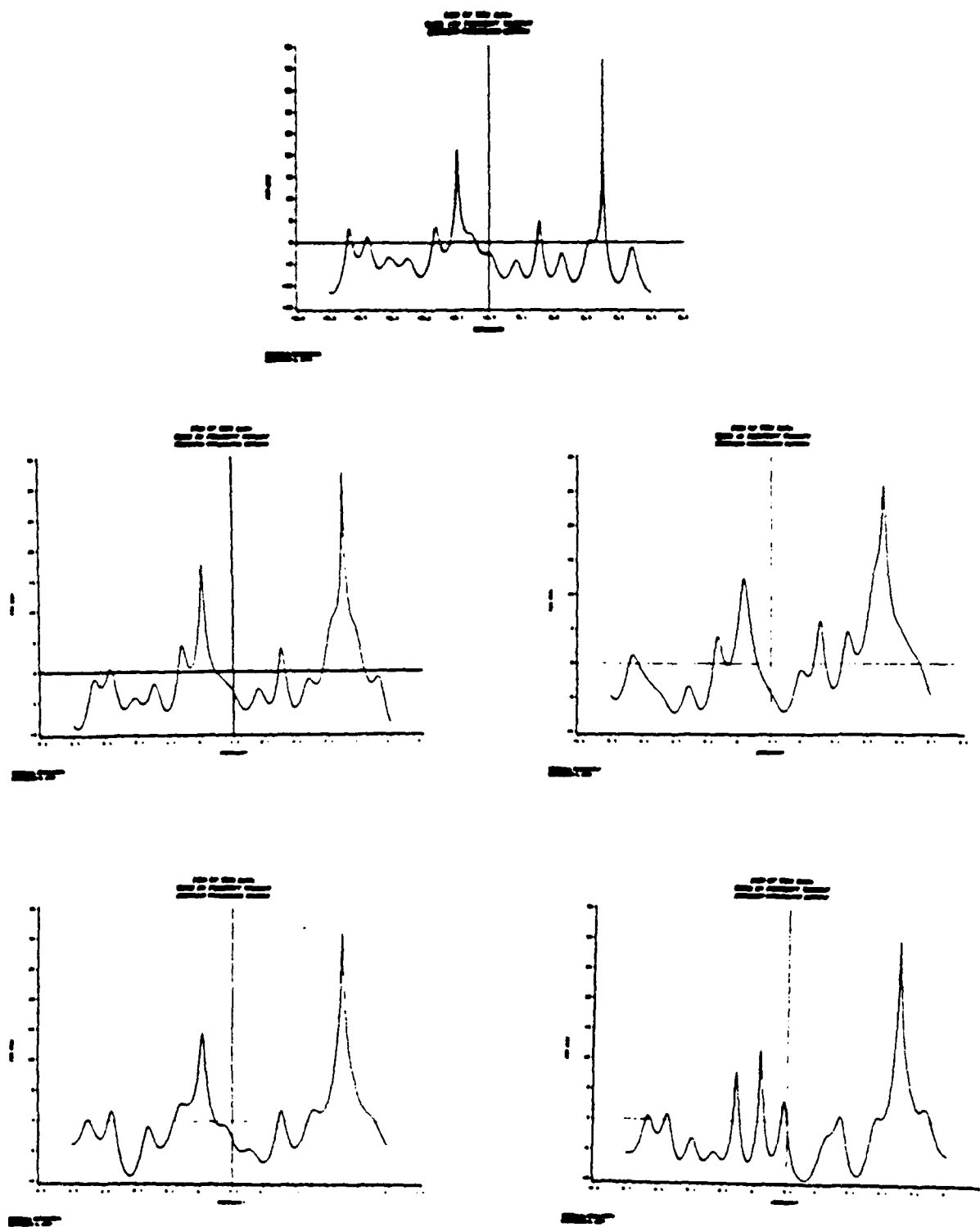
Figure 3.2 Effect of diminishing percentage of received signal in the Modified Covariance Method
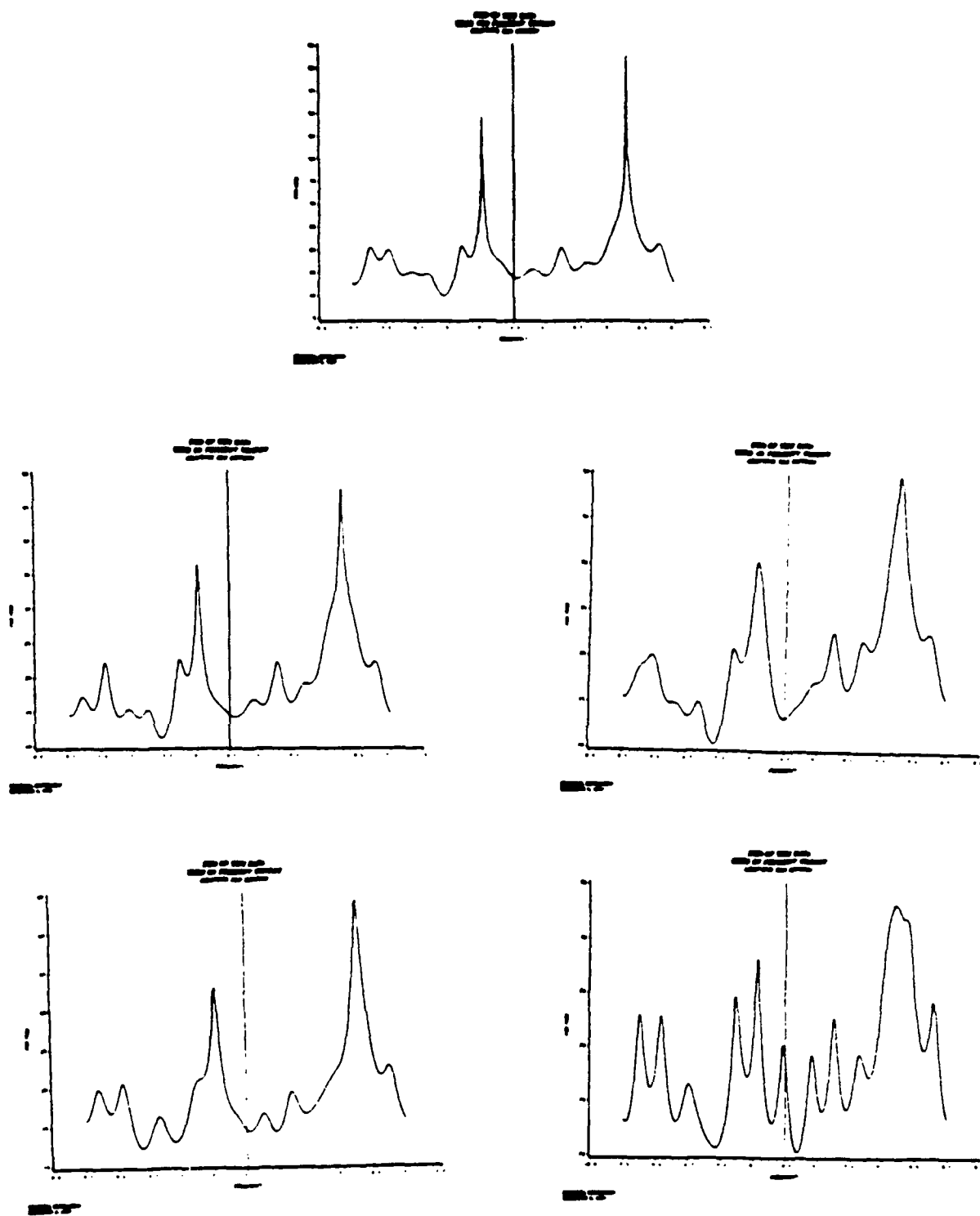
Figure 3.3 Effect of diminishing percentage of received signal in the Adaptive RLS Method

in additive Gaussian noise for testing the performance of the methods including the bias and the mean square error of frequency and amplitude estimation. In the second test, two frequencies are present in the input signal. These two frequencies vary in frequency independently from the low end of the frequency scale to the upper end of the frequency scale. The purpose of this test is to explore the effects of one signal on the other.

Test One: Single Sinusoid in Noise

In the first test case, we have a single sinusoid embedded in white noise. The purpose of this test is to examine the performance of the six methods with respect to various signal to noise ratio. Specifically, we will examine the bias and mean signal error of the frequency and amplitude estimations of these six methods.

Figure 4.1 shows the bias and mean squared error for all six methods. To visualize the effect of noise level on the bias of frequency estimation, we have plotted the frequency bias as a function of signal to noise ratio (SNR). These plots are shown in Figure 4.2. From Figure 4.2, it is evident that the SVD method appears to perform well even in low signal to noise ratio.

From Figure 4.2a, we see that the bias in frequency estimation for the periodogram begins to increase when SNR drops below 10 DB. For the modified covariance method, frequency bias is minimized until the SNR drops below 5 DB. The same is observed for the Burg Method. Somewhat inconsistent results are observed in the adaptive RLS method. This inconsistency is due mostly because a short data sequence (64 points) is used so that convergence was not obtained. The Prony's Method seems to have minimum frequency bias until SNR drops below −5 DB. The same is observed also for the SVD method.

SNR (db)	Bias (Freq.)	Bias (Amp.)	Std. of Mse (Freq.)	Std. of Mse (Amp.)	C.R.B. (Freq.)	C.R.B (Amp.)
35.0	.1953e-3	.1099e-2	.1953e-3	.1254	.9576e-5	.7812e-2
30.0	.1953e-3	.1257e-1	.1953e-3	.1339	.1703e-4	.7812e-2
25.0	.1953e-3	.1907e-2	.1953e-3	.1246	.3028e-4	.7812e-2
20.0	.1953e-3	.7266e-2	.1953e-3	.1112	.5385e-4	.7812e-2
15.0	.1270e-3	.2793e-1	.2797e-3	.1074	.9576e-3	.7812e-2
10.0	.8786e-4	.1752e-1	.4212e-3	.1340	.1703e-3	.7812e-2
5.0	.9589e-1	.1117e+1	.1386	.1628	.5385e-3	.7812e-2
0.0	.1880	.1187e+1	.1939	.1232	.5385e-3	.7812e-2
-5.0	.2000	.6309	.2000	.6362	.9576e-3	.7812e-2
-10.0	.2000	.2901	.2000	.3016	.1703e-2	.7812e-2

a) The Periodogram

SNR (db)	Bias (Freq.)	Bias (Amp.)	Std. of Mse (Freq.)	Std. of Mse (Amp.)	C.R.B. (Freq.)	C.R.B. (Amp.)
35.0	.5176e-3	.7553	.7112e-2	.7371e+1	.9576e-5	.7812e-2
30.0	.1953e-3	.1317e-1	.1953e-3	.1135	.1703e-4	.7812e-2
25.0	.1953e-3	.1605e-1	.1953e-3	.1223	.3028e-4	.7812e-2
20.0	.1953e-3	.2171e-1	.2522e-3	.1296	.5385e-4	.7812e-2
15.0	.1464e-3	.2431e-1	.2584e-3	.9956e-1	.9576e-4	.7812e-2
10.0	.4882e-4	.6416e-2	.3782e-3	.1289	.1703e-3	.7812e-2
5.0	.6837e-4	.1772e-1	.6314e-3	.1280	.5385e-3	.7812e-2
-5.0	.1330	.3976	.1630	.5214	.9576e-3	.7812e-2
-10.0	.1940	.2626	.1970	.2847	.1703e-2	.7812e-2

b) The Modified Covariance Method

Figure 4.1 Bias and mean square error of frequency and amplitude estimation for all six methods

SNR	Bias	Bias	Std. of Mse	Std. of Mse	C.R.B.	C.R.B
(db)	(Freq.)	(Amp.)	(Freq.)	(Amp.)	(Freq.)	(Amp.)
35.0	.1953e-3	.1381e-1	.1953e-3	.1272	.9576e-5	.7812e-2
30.0	.1953e-3	.2229e-1	.1953e-3	.1299	.1703e-4	.7812e-2
25.0	.1885e-3	.1913e-1	.2095e-3	.1172	.3028e-4	.7812e-2
20.0	.3904e-4	.1812e-1	.3601e-3	.1250	.5385e-4	.7812e-2
15.0	.4882e-4	.1326e-1	.5074e-3	.1243	.9576e-3	.7812e-2
10.0	.0000	.1520e-1	.9468e-3	.1295	.1703e-3	.7812e-2
5.0	.3910e-4	.1724e-1	.1237e-2	.1273	.3028e-3	.7812e-2
0.0	.8223e-2	.5083e-1	.4004e-1	.2769	.5385e-3	.7812e-2
-5.0	.1442	.4353	.1697	.5466	.9576e-3	.7812e-2
-10.0	.1980	.2919	.1990	.3077	.1703e-2	.7812e-2

c) The Burg Method

SNR	Bias	Bias	Std. of Mse	Std. of Mse	C.R.B.	C.R.B.
(db)	(Freq.)	(Amp.)	(Freq.)	(Amp.)	(Freq.)	(Amp.)
35.0	.1953e-3	.6601e-1	.1953e-3	.1284	.9576e-5	.7812e-2
30.0	.1953e-3	.1492e-1	.1953e-3	.1280	.1703e-4	.7812e-2
25.0	.2930e-3	.1215e-1	.4143e-3	.1554	.3028e-4	.7812e-2
20.0	.8301e-2	.1351e-1	.2588e-1	.4312e+1	.5385e-4	.7812e-2
15.0	.2363e-1	.1507e+1	.5302e-1	.3314e+1	.9576e-4	.7812e-2
10.0	.2002e-1	.3738	.6325e-1	.1351e+1	.1703e-3	.7812e-2
5.0	.1563e-1	.1115e+1	.1084	.1495e+1	.3028e-3	.7812e-2
0.0	.1311	.8527	.1589	.1045e+1	.5385e-3	.7812e-2
-5.0	.1868	.5986	.1910	.6079	.9576e-3	.7812e-2
-10.0	.1333	.2846	.1770	.2922	.1703e-2	.7812e-2

d) The Adaptive RLS Method

Figure 4.1 (Con't.)

SNR (db)	Bias (Freq.)	Bias (Amp.)	Std. of Mse (Freq.)	Std. of Mse (Amp.)	C.R.B. (Freq.)	C.R.B (Amp.)
35.0	.0000e-0	.7824	.1306e-4	.1021e+1	.9576e-5	.7812e-2
30.0	.1574e-4	.1280e+1	.2553e-4	.1436e+1	.1703e-4	.7812e-2
25.0	.9000e-5	.2510e+1	.4685e-4	.2619e+1	.3028e4	.7812e-2
20.0	.2623e-4	.4352e+1	.9350e-4	.4442e+1	.5385e-4	.7812e-2
15.0	.4244e-4	.5743e+1	.1786e-3	.5774e+1	.9576e-4	.7812e-2
10.0	.8106e-5	.4032e+1	.6325e-1	.4057e+1	.1703e-3	.7812e-2
5.0	.8035e-3	.1996e+1	.1414	.2108e+1	.3028e-3	.7812e-2
0.0	.1795e-2	.8555	.1789	.1231	.5385e-3	.7812e-2
-5.0	.4144e-2	.7965	.1838	.1074e+1	.9576e-3	.7812e-2
-10.0	.5852e-1	.7387	.2174	.9565	.1703e-2	.7812e-2

e) Prony's Method

SNR (db)	Bias (Freq.)	Bias (Amp.)	Std. of Mse (Freq.)	Std. of Mse (Amp.)	C.R.B. (Freq.)	C.R.B (Amp.)
35.0	.1953e-3	.6653e-2	.1953e-3	.1259	.9576e-5	.7812e-2
30.0	.1953e-3	.3972e-1	.1953e-3	.1177	.1703e-4	.7812e-2
25.0	.1953e-3	.6317e-2	.1953e-3	.1047	.3028e-4	.7812e-2
20.0	.1953e-3	.3010e-1	.1953e-3	.9838e-1	.5385e-4	.7812e-2
15.0	.1953e-3	.1869e-1	.1953e-3	.1013	.9576e-4	.7812e-2
10.0	.9763e-4	.3285e-1	.3088e-3	.9504e-1	.1703e-3	.7812e-2
5.0	.2930e-3	.2170e-1	.7437e-3	.9383e-1	.3028e-3	.7812e-2
0.0	.6836e-3	.3285e-1	.1061e-2	.1390	.5385e-3	.7812e-2
-5.0	.1953e-2	.5522e-1	.2576e-2	.1544	.9576e-3	.7812e-2
-10.0	.1409	.1941	.1673	.2648	.1703e-2	.7812e-2

f) The SVD Method

Figure 4.1 (Con't.)
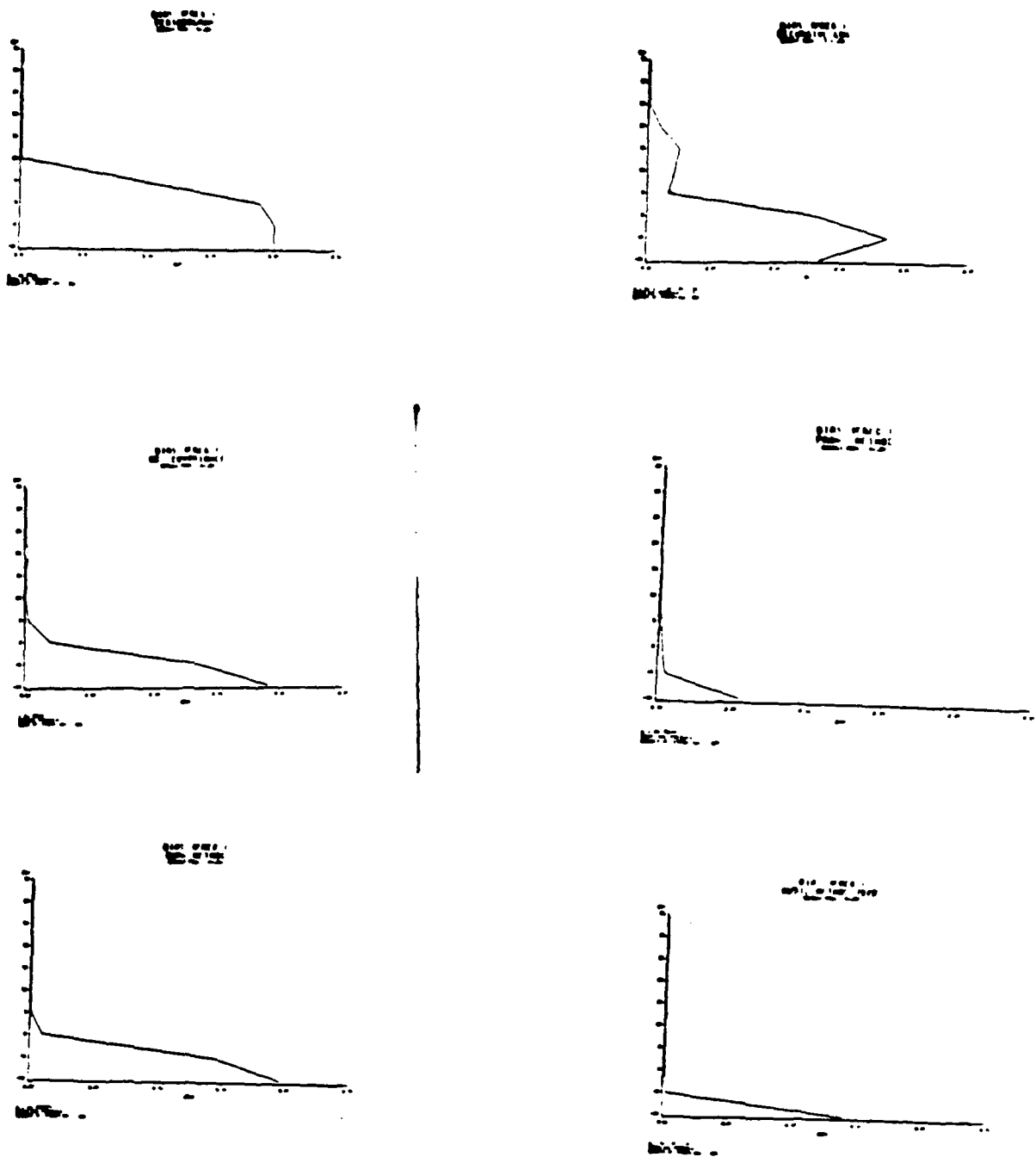
Figure 4.2 Frequency bias as an function of signal to noise ratio for all six methods

To test the consistency of the performance for these six methods the simulation is repeated for 100 independent trials. If the frequency bias is larger than a frequency bin or if the estimated amplitude falls outside 3 DB of the expected amplitude, the estimation run is regarded as an error. We plot in Figure 4.3 the estimation error as a function of SNR and frequency for all six methods. The size of the circle in the plots indicate the percentage of error at that frequency for that SNR. The results shown in Figure 4.3 confirms our observations discussed previously.

We are interested in comparing the mean squared error for frequency estimation of all the methods to the Cramer Rao bound. This is shown in Figure 4.4. It is readily observed from Figure 4.4 that the SVD method performs well particularly in low signal to noise ratio conditions.

Test Two: Two Sinusoids

In the second test case, we use two sinusoids, each with its frequency sweeping from low frequency to high frequency. The results for these simulations are shown in Figures 4.5 and 4.7. We plot the percentage of error as a function of the two varying frequencies for SNR = 25 DB in Figure 4.5, for SNR = 10 DB in Figure 4.6, and for SNR = 5 DB in Figure 4.7. Examination of these three figures shows that the performance of frequency resolution tends to degrade as SNR decreases.

For the sake of comparison, we have selected a single case with frequencies 0.2 and 0.21. These values are chosen in such a way that the frequency 0.2 is right on the frequency bin while 0.21 is not. Again, the mean squared error of the frequency estimation is measured and compared to the Cramer Rao bound. The plot for f = 0.20 is shown in Figure 4.8
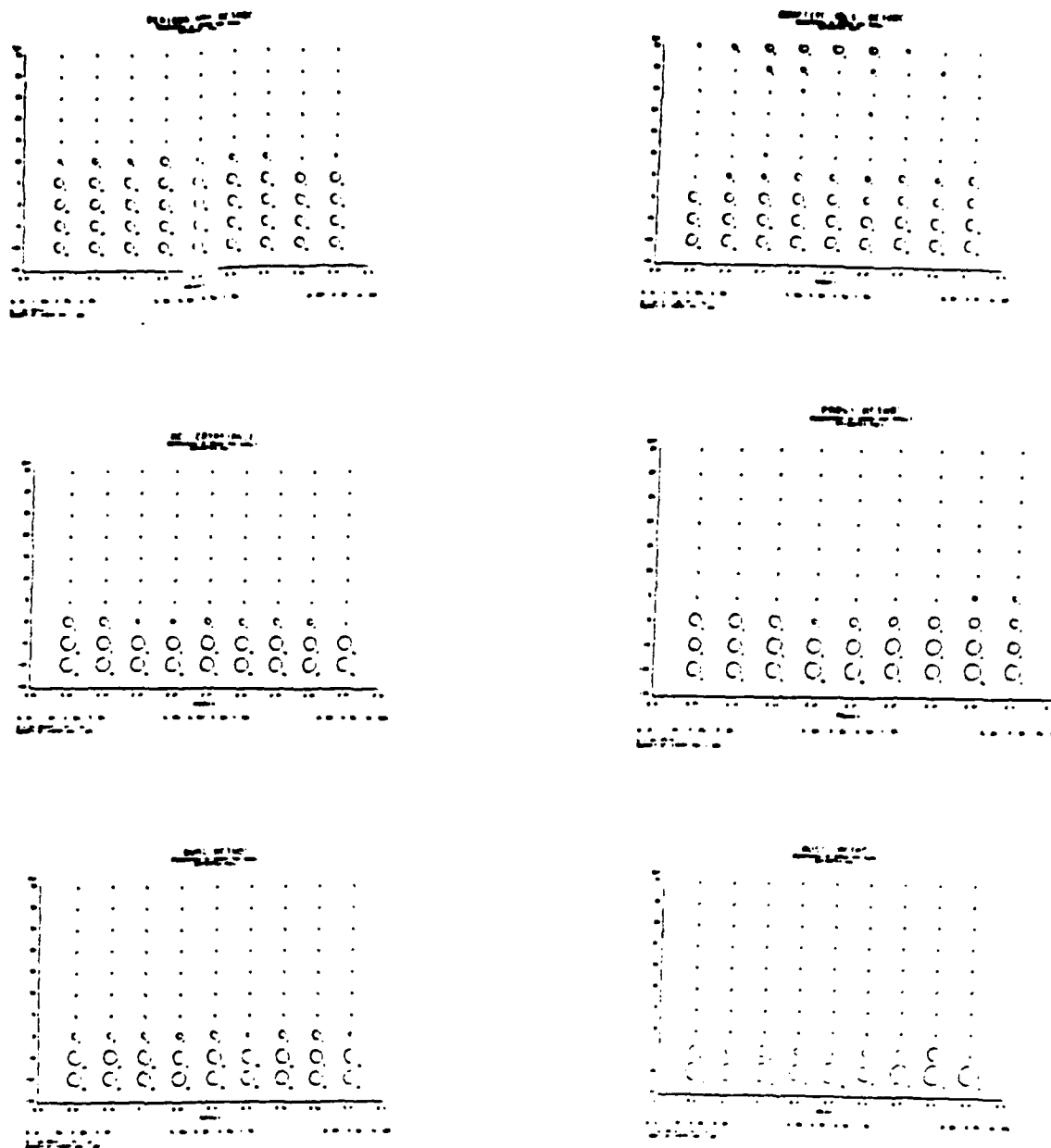
Figure 4.3 Plots of estimation error percentage as a function of SNR and frequency for all six methods
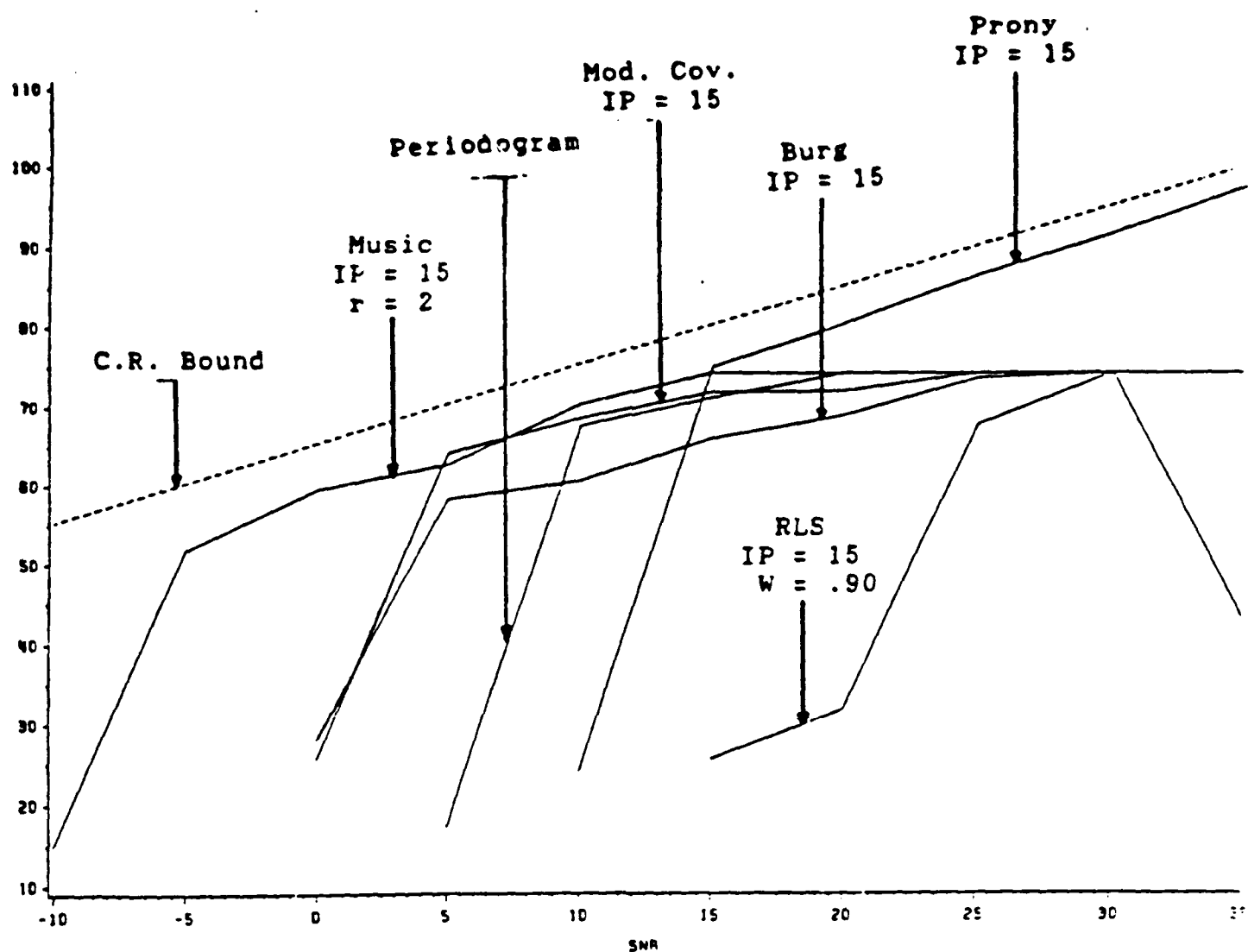
Figure 4.4 Comparison of the mean squared error of all the algorithms to the Cramer Rao Bound for the single sinusoid $(f = .20)$ case
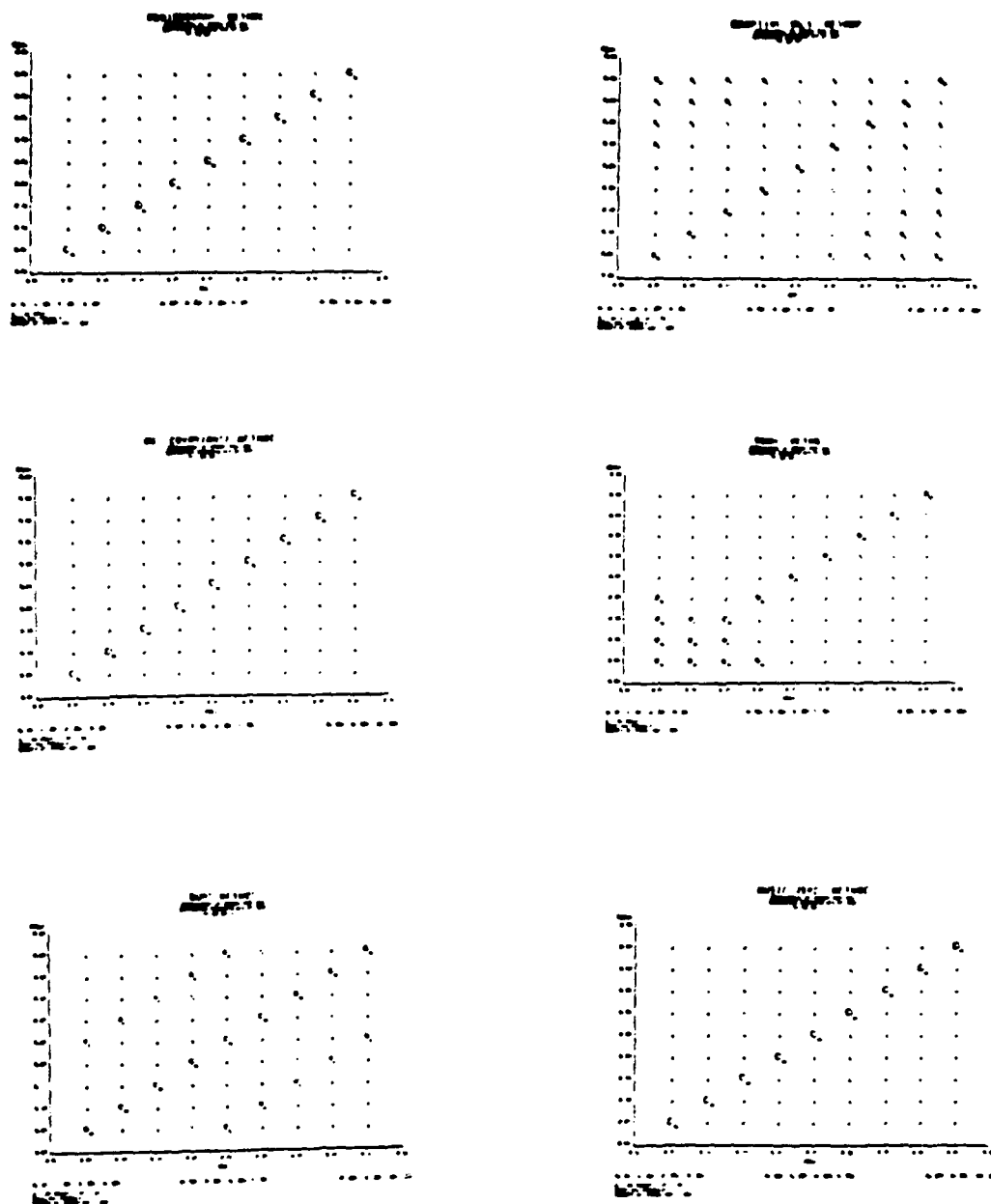
Figure 4.5 Plots of estimation error percentage for all six methods at SNR = 25 DB
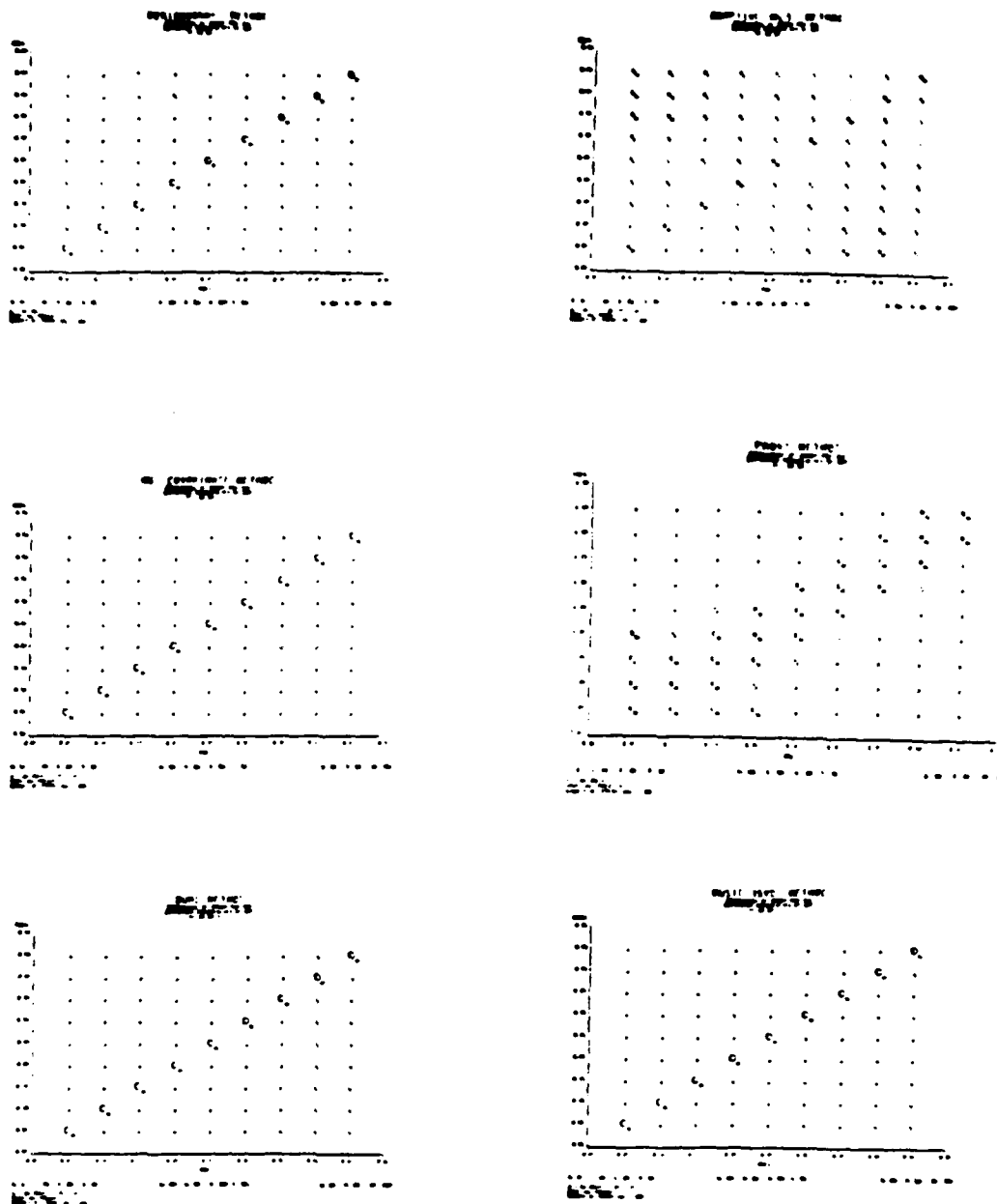
Figure 4.6 Plots of estimation error percentage for all six methods at SNR = 10 DB
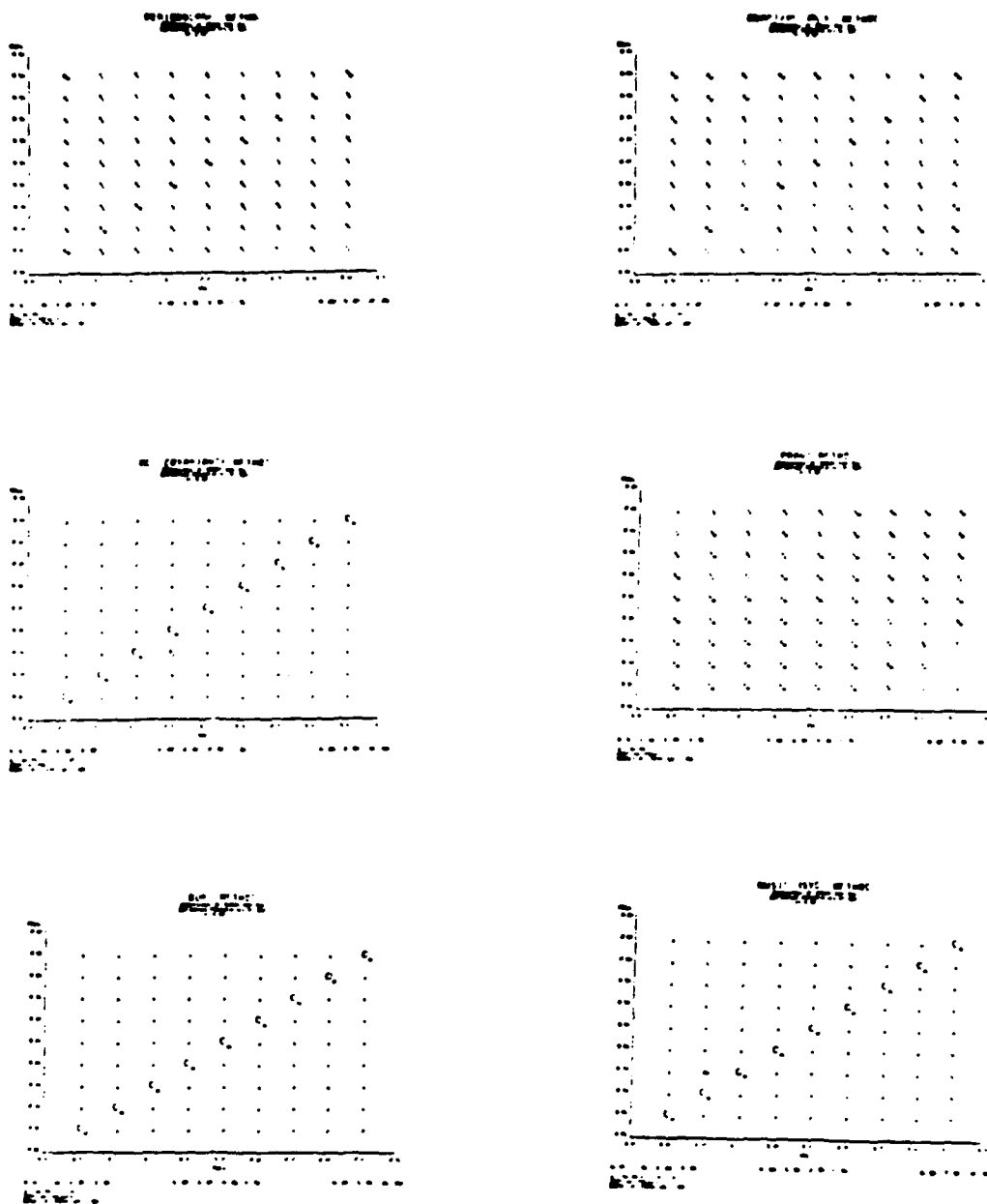
Figure 4.7 Plots of estimation error percentage for all six methods at SNR = 5 DB
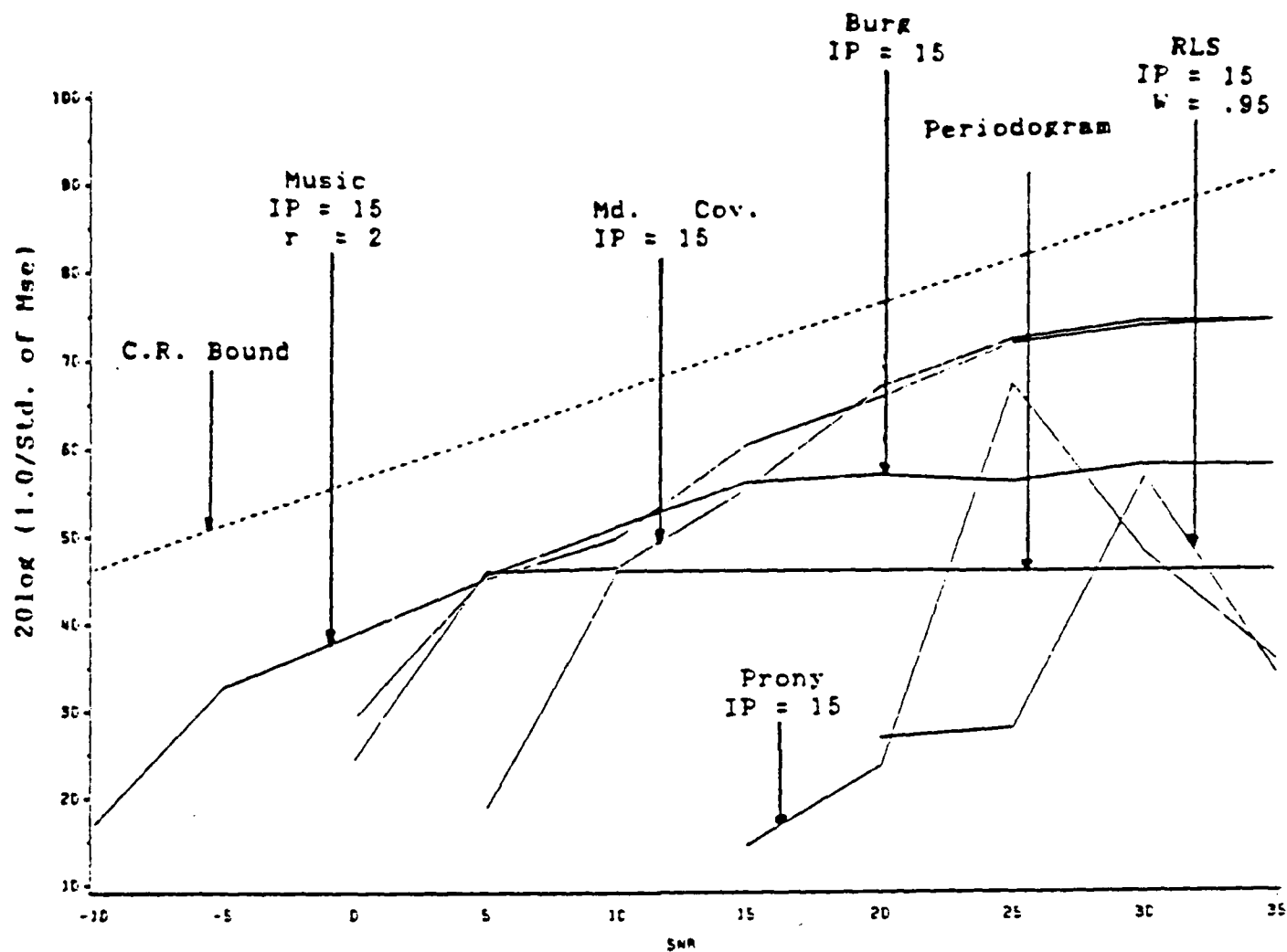
Figure 4.8 Comparison of mean squared error of all the algorithms to Cramer Rao Bound for the $f_1 = 0.20$ in the double sinusoidal test case

while that for $f = 0.21$ is shown in Figure 4.9. Note that when the frequency is on the bin, rather accurate estimation can be obtained. When the frequency is off the bin, poorer estimation is observed.
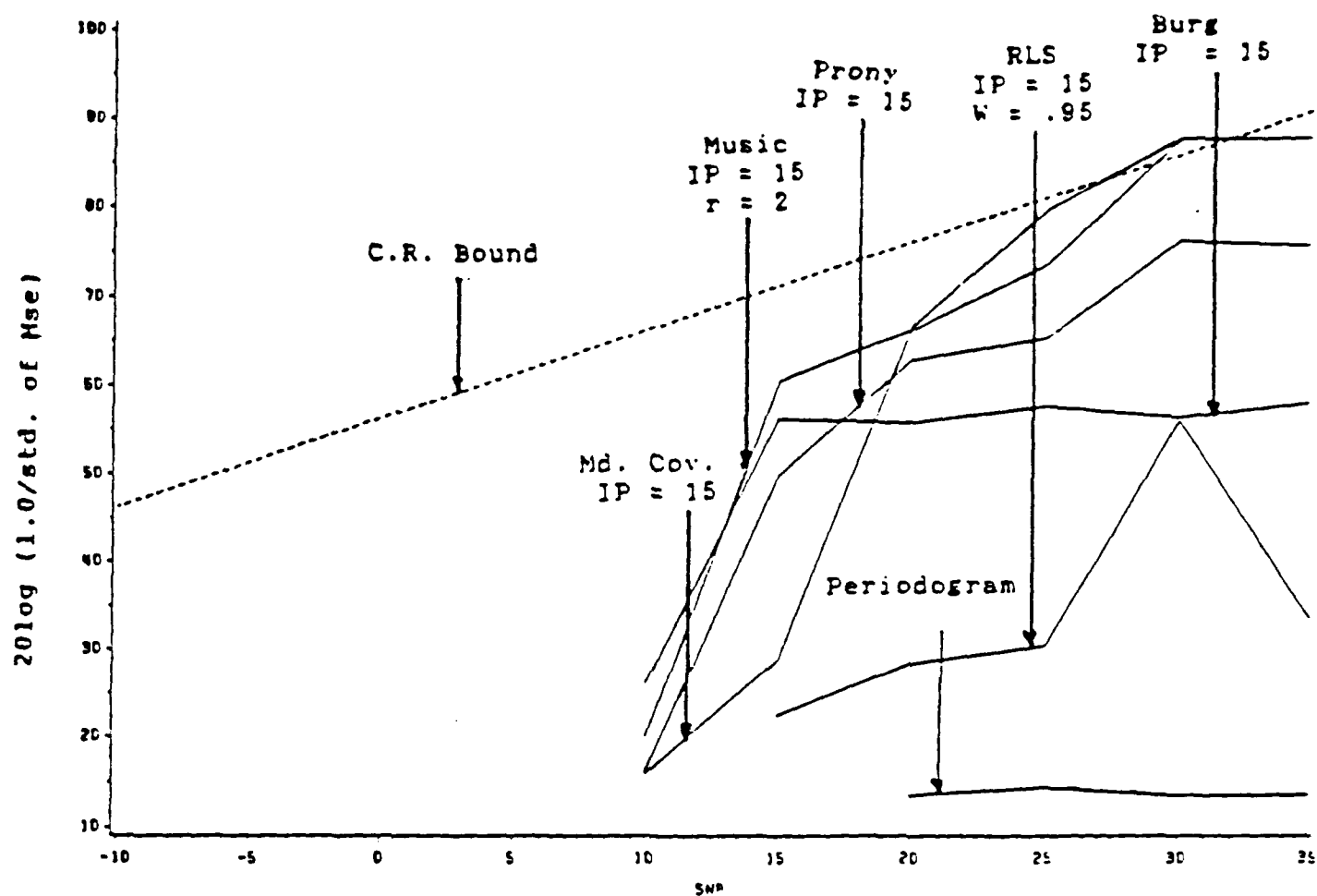
Figure 4.9 Comparison of mean squared error of all the algorithms to the Cramer Rao Bound for $f_1 = 0.21$ in the double sinusoidal test case

REFERENCES

1. Kay, Steven M., <u>Modern Spectral Estimation</u>, Prentice–Hall, Englewood Cliffs, NJ, 1988.

2. Marple, S. Lawrence, Jr., <u>Digital Spectral Analysis with Applications</u>, Prentice–Hall, Englewood Cliffs, NJ, 1987.

3. Khelgati, Hojat, " A Comparison of Modern Frequency Estimation Techniques," M.S. Thesis, School of Electrical Engineering and Computer Science, University of Oklahoma, May 1988.

4. Benigeri, Gopinath, "Effects of Partially Received Signals," M.S. Thesis, School of Electrical Engineering and Computer Science, University of Oklahoma, (to be published).

Appendices can be obtained from
Universal Energy Systems, Inc.

FINAL REPORT NUMBER 59
REPORT NOT AVAILABLE AT THIS TIME
Dr. William Curry
760-7MG-081

Research Initiation Program
Final Report:
Implementation
of
Blackboard Systems in Ada

Pamela P. Cook, Graduate Student
and
Verlynda S. Dobbs, Principal Investigator
Department of Computer Science and Engineering
Wright State University
Dayton, Ohio 45435
513-873-2491

February 9, 1989

1 Introduction

There is increased interest in implementing artificial intelligence applications in Ada. Efforts in this area encompass expert systems [Adk86,LaV86,JLZ87], distributed knowledge based systems [Bra86,Fra86], pattern directed processing [RKW85], semantic networks [SPA86], reusable heuristic search algorithms [Dob88] and others. This paper concentrates on the implementation of blackboard (BB) systems in Ada. It describes the blackboard control model of problem solving, a generic approach to the design and implementation of a blackboard control system, and the application of the approach to a classic defense problem.

2 Blackboard Model

A *problem solving model* is a scheme that constructs a solution by organizing reasoning steps and domain knowledge. A model provides a conceptual framework for organizing knowledge and a strategy for applying that knowledge. Examples of problem solving models include forward reasoning models, backward reasoning models, event driven models, model driven models, etc. In a forward reasoning model, the inference steps are applied from an initial state toward a goal. In a backward reasoning model, problem solving begins by reasoning backward from a goal to be achieved toward an initial state.

The blackboard model [Nii86b,Nii86a], which was developed in the 1970's and has undergone very few changes in the last ten years, uses an opportunistic reasoning model. In an opportunistic reasoning model, pieces of knowledge are applied either backward or forward at the most *opportune* time. This model was first abstracted from the Hearsay-II speech understanding system [Nii82] and applied to the design and implementation of the HASP system for ocean surveillance [EHRLR80]. Many application programs have subsequently been implemented (usually in Lisp) using the blackboard model. These include systems for interpreting electron-density maps, planning errands, understanding military signals, and understanding images.

The basic blackboard model is usually described as consisting of three major components - the knowledge sources, the blackboard data structure, and the control - as shown in the figure on the following page.
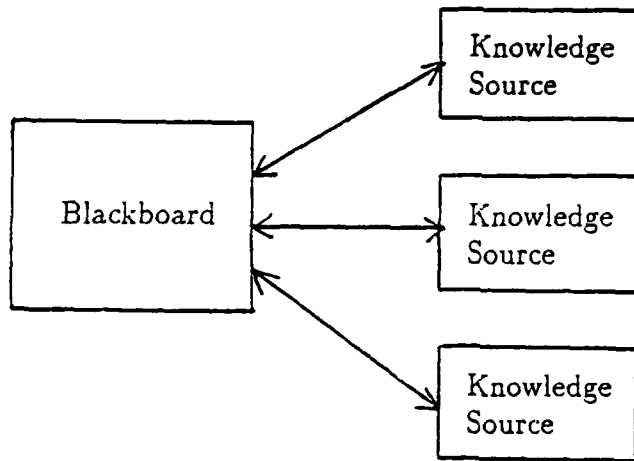
(—— data flow)

The domain *knowledge sources* are partitions formed from the total domain knowledge that can be used to solve the problem. These knowledge sources are logically independent and kept separate. The domain *blackboard data structure* is a global data base that holds the problem solving state data. The solution space is organized into one or more application dependent hierarchies. Information at each level of the hierarchy represents *partial solutions* and is associated with a unique vocabulary that describes the information. The knowledge sources produce changes to the blackboard that lead incrementally to a solution to a problem. Communication and interaction among knowledge sources take place solely through the blackboard. There is no predetermined flow of *control.* The knowledge sources respond opportunistically to changes in the blackboard. The knowledge sources transform information on one level of the hierarchy into information on the same or other levels using algorithmic procedures or heuristic rules that generate actual or hypothetical transformations. Which knowledge source to apply is determined dynamically, one step at a time, resulting in the incremental generation of partial solutions. The choice of a knowledge source is based on the solution

state and on the existence of knowledge sources capable of improving the current state of the solution.

There are at least two different approaches to handling the control. The first has control residing in a set of procedures which monitor the changes on the domain blackboard and trigger appropriate knowledge sources to improve the solution state. In the second approach, control is achieved by placing the strategy on a control blackboard. The decision then as to what to do next is made by control knowledge sources using the control blackboard where data describing the state of the current strategy exists. Strategies can be enabled on the control blackboard to reflect the current state of the problem solution. This second approach is referred to as a blackboard control architecture [HR85].

The blackboard architecture approach improves on traditional expert systems for solving ill-structured problems in the following ways. First, the blackboard approach requires no a priori determined reasoning path. Because ill-structured problems often do not have a predetermined decision path to a solution, the selection of what to do next must be made while the problem is being solved. The capability to do this is provided in blackboard systems by the incremental and opportunistic problem solving approach. Second, vague information and knowledge, which characterize ill-structured problems, need to be made concrete in the process of finding a solution to the problem. The blackboard model is an excellent tool for this knowledge engineering activity. During the initial interactions with an expert, a knowledge engineer tries to find an appropriate conceptual model for the task while trying to understand the domain and the nature of the task. The blackboard approach aids in the problem formulation because it provides some organizational principles that are both powerful and flexible. The blackboard approach is also an excellent tool for exploratory programming, a useful technique for developing solutions to complex and ill-structured problems.

Although blackboard systems are useful for many complex, ill-structured problems, they are generally expensive to build and to use. Therefore, the blackboard approach should not be used when lower cost methods are sufficient. A problem which exhibits some combination of the following characteristics is a good candidate for the blackboard approach:

1. a large solution space

2. noisy and unreliable information

3. a variety of input data and a need to integrate diverse information

4. the need for many independent or semi-independent pieces of knowledge to cooperate in forming a solution

5. the need to use multiple reasoning methods or lines of reasoning

6. the need for an evolutionary solution

A proposed application should be carefully analyzed before a decision to implement a blackboard system is made.

3 Application of BB Systems

The following sections describe the domain analysis, functional requirements, design, and implementation of the prototype system for a classic defense problem.

3.1 Domain Analysis

Functions of a classic defense system include sensing of the environment; interpretation of conflicting, incomplete or corrupted sensory data; integration of sensory data; overall situation assessment; planning and real-time decisions for mission and survival achievement; and control of weapon system functions. These activities, which are currently performed by the crew, would ideally be provided by a ground and/or onboard computer system. The system would be able to function in an environment containing vast amounts of raw data where the data may be unintentionally corrupted via natural phenomena or intentionally corrupted via friendly or enemy jamming and deception missions.

Electronic warfare (EW) processing spans many different disciplines (passive radio frequency (RF) and infrared (IR) sensor interpretation, active RF and IR countermeasures techniques, etc.) where the sensors operate in different environments with different requirements for information extraction, interpretation and reaction. The EW system must respond to a dense and dynamic environment. A priori information is used to distinguish threats to the aircraft from non-threats and also contributes to the system response and

resource allocation strategy. A priori information often does not represent the true state of the environment because of environment noise, intentional deceptive emissions, jamming, etc.

From this description it is easy to see that EW exhibits several of the criteria that make a good candidate for a blackboard system. It has a large solution space that includes knowledge concerning static threats, limited resources, passive sensors, terrain data, platform data, active countermeasures, goals to be accomplished, etc. Some of the data is noisy and unreliable. There is a variety of input data and a need to integrate diverse information. There is also the need for many independent pieces of knowledge to cooperate in forming a solution. The different types of knowledge require different vocabularies and different lines of reasoning. The solution evolves as new pieces of information are sensed, input and derived from existing data.

One EW defense problem is the monitoring of a hostile environment by a moving platform for the purpose of determining the platform's best path through the environment. Emissions are detected and locations and types of emitters are determined. A map is produced which represents a snapshot of the current knowledge about the environment. This map can then be used as input to a program that will determine the best path for the platform through this environment [DDL88]. This monitoring problem was chosen for the prototype of the blackboard control system in Ada. The domain blackboard will contain the current situation board with respect to the environment while the control blackboard will contain data that indicates strategies and reasonings to be employed.

3.2   Functional Requirements

The functional requirements for the prototype include:

1. Process batches of input data at regular intervals of 4 time units. Input data can be either signal data or intelligence reports. Signal data consists of three emitter characteristics - frequency, pulse width and pulse repetition frequency; a location represented by a position on a grid; and a signal detection time. Intelligence report data, which is for threats only, consists of the location and sighting report time.

2. Determine type of emitter from characteristics of each set of signal data.

3. Identify each emitter as threat or nonthreat based on the capabilities of the emitter type.

4. Post to the current situation board (CSB) the locations of known threats and nonthreats and the time of sighting.

5. Eliminate duplicate sightings but keep history information for each location.

6. Keep a list of known friendly locations to determine whether any emitter identified as a threat is a known friend.

7. Output CSB at regular intervals of 10 time units, including location of sighting, threat or nonthreat, history information, and confidence.

8. Output SOS message immediately when possible threat is detected.

3.3 Design

Two different design methods were considered for the system - object oriented and functional. The choice of functional design was based on the fact that blackboard systems and the blackboard control architecture have been described functionally [HR85]. As the system is decomposed, the functional design approach identifies major tasks to be performed. Subprograms (program units) become the building blocks of a functional design. The system is described in terms of the functions that process the data. Functions receive input, transform input, and produce output. The functional requirements define what needs to be done. The functional design includes the requirements as well as the data flow. Pictured below are the various levels of a functional design.

At the highest level, a block diagram of the system showing inputs and outputs would look like this:
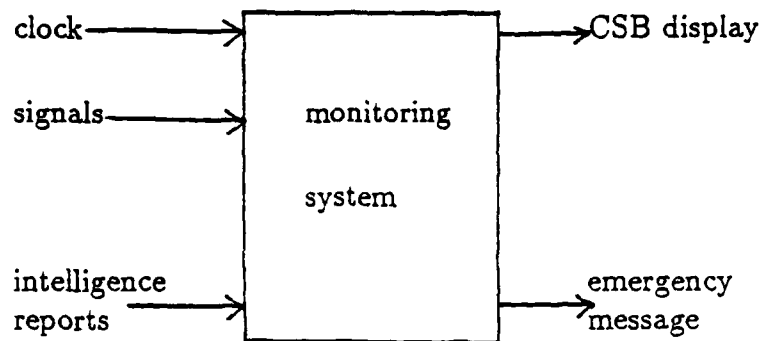
The major function of the monitoring system can then be broken down into a set of functions, each with inputs and outputs.

```
domain                Check           updated
                      for         → domain
blackboard    →       Threats         blackboard


clock    →            Display
domain                CSB         → CSB
blackboard →


domain                Output          SOS
              →       SOS         → message
blackboard            Message
```
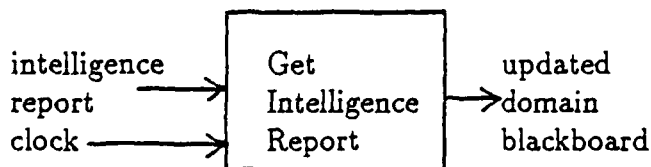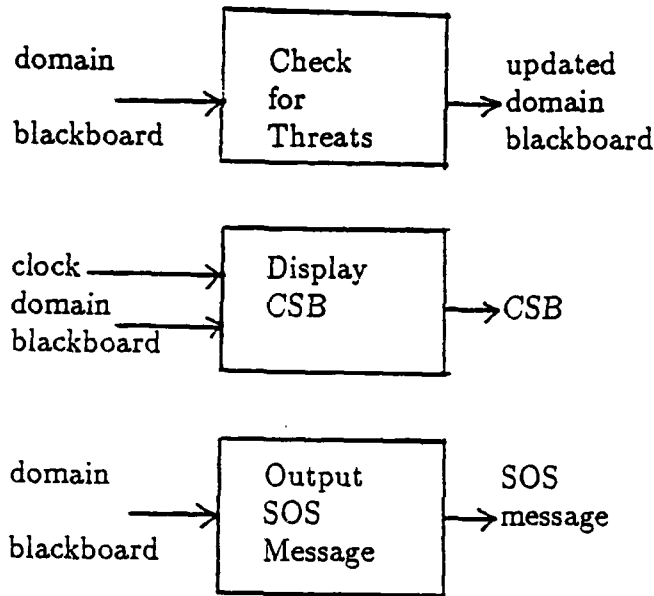
3.4 Implementation

The blackboard control architecture model defines two blackboards, one for the domain and one for control. A set of data structures and a set of knowledge sources are associated with each blackboard. The data structure for each blackboard has its own hierarchy. Each of these components is defined below for the monitoring problem.

3.4.1 Domain Blackboard

The hierarchy for the domain blackboard contains three levels of abstraction: signals, emitters and sites. The domain knowledge sources are listed below:

- **KS0.** Initializes table of locations of known friends on domain blackboard.

- **KS1**. Reads input data, creates signal node on signal level of domain blackboard or creates expectation on site level of domain blackboard.

- **KS2**. Generates emitter node on emitter level of domain blackboard based on characteristics of signal node.

- **KS3**. Generates site node on site level of domain blackboard based on characteristics of emitter node and other information on domain blackboard.

- **KS5**. Handles duplicate emitter nodes on emitter level of domain blackboard, updating history information.

- **KS6**. Initiates termination of system.

- **KS7**. Prints SOS message when possible threat is sighted.

- **KS8**. Outputs CSB and associated information.

Execution of the knowledge sources reflects changes in the environment. Both forward and backward reasoning are used on the domain blackboard. Forward reasoning takes signal input data, creates emitter types from the signal data, and generates threat or nonthreat sites from the emitter types. Backward or model driven reasoning occurs when intelligence reports indicate a threat at a specific location at a specific time. The site can then be verified based on the intelligence report. Discrepancies at this level result from noisy or unreliable data.

Updating the domain blackboard creates events that reflect the updated environment. These events are recorded in knowledge source activation records (KSARs).

3.4.2 Control Blackboard

The control blackboard contains three levels of abstraction that define the strategy used for handling events that occur in the system. These levels are policy, tactic and step. Policy, located on the highest level, determines which blackboard is effected - domain or control. Tactic, on the next level, specifies the category of event to process. The lowest level of abstraction, step, differentiates between the two low level event types.

The control knowledge sources toggle between possible values on each level of abstraction to implement the chosen strategy.

- **KS10.** Initializes the system with problem description from user.

- **KS11.** Initializes control blackboard by setting up policy, tactic and step level for policy being used.

- **KS12.** Generates event to change policy if policy is not "control".

- **KS13.** Toggles tactic setting.

- **KS14.** Toggles step setting.

- **KS20.** Toggles policy setting.

Three additional domain-independent procedures - **update trigger list, choose KSAR, and execute KSAR** - drive an iterative control strategy that operates around three event lists - action, trigger and invocable. **Update trigger list** moves KSARs from the action list to the trigger list. **Choose KSAR** matches conditions of control and the environment with the KSAR and moves the KSAR to the invocable list if the conditions are met. **Execute KSAR** executes the knowledge source of the first KSAR on the invocable list.

3.4.3 Operation

A KSAR contains information on the triggering cycle, triggering event, precondition values, condition values, trigger weight, knowledge source importance, event type, rating and priority. The KSAR is initially placed on the action event list. The action event list contains all KSARs generated by the previous cycle's execution. As KSARs on the action event list are moved to the trigger event list, the events are given a rating based on the current state of the environment and the importance of the associated knowledge source. The KSARs are placed on the trigger event list in descending order by rating points. KSARs are moved to the invocable event list based on the current control strategy. The knowledge source of the first KSAR on the invocable list is executed. If no knowledge source is triggered on a particular cycle, an

event is created that will enable a change in policy, tactic or step level on the control blackboard.

The action, trigger and invocable event lists contain both domain and control events. The policy, tactic and step settings determine which KSARs get moved to the invocable list. Only one event activates a knowledge source (KS) each cycle - the event that is first on the invocable list. The execution of a knowledge source on a cycle generates new KSARs on the action list. A general diagram of the system is shown below.
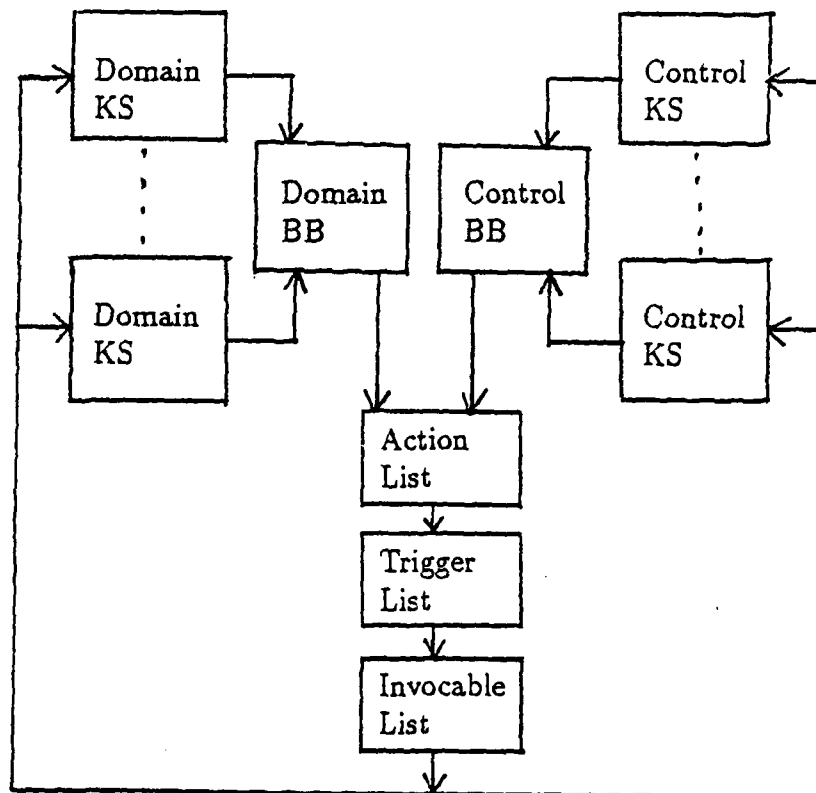
4 Use of Ada

The monitoring system was developed in Vax Ada on a Vax 11/780 running
the VMS operating system. The use of Ada for this prototype presented no
major problems. The resulting system has the structure shown below. (The
arrows indicate required visibility.)
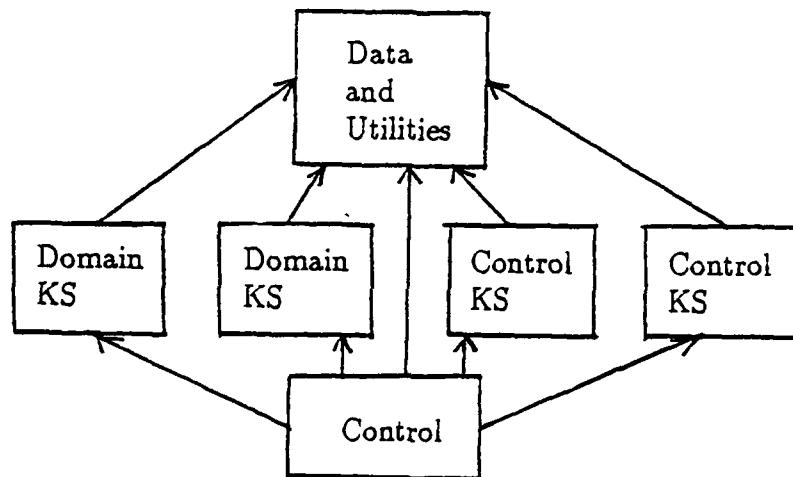
Several of Ada's features greatly facilitated the implementation. The
package concept facilitates data encapsulation, modularity, and locality. Op-
erations on a particular object, for example an event, are contained in a
package with the implementation details hidden from users of the package.
Changes in the implementation will not effect the control structure or the
object's interaction with other objects. The modularity feature of the pack-
age encourages reusability as basic operations can be reused and not repro-
grammed. Packages were used to contain:

- blackboards with associated procedures (data and utilities package)

- procedures to execute cycle for control (control)

- knowledge sources (KSs)

The data and utilities package contains all global structures and utilities. The control and domain blackboards are defined in this package along with procedures that delete information from the domain blackboard as well as create, add and delete nodes from the action, trigger, and invocable event lists. Much of this package is reusable since it manipulates the structures for a blackboard control architecture.

Each knowledge source is contained in a separate package. New knowledge sources can be added and existing ones changed without recompiling the entire system. (Instead of packages, knowledge sources could be contained in separately compilable procedure modules.) Keeping these knowledge sources separate will also facilitate the introduction of concurrency into the system using the tasking feature. More than one knowledge source could then be executed in a cycle.

Other Ada features were also useful in the development of this system. Variant records were used to represent blackboard nodes since the nodes on the different levels of the domain blackboard contained different information fields. Using variant records made it possible to manipulate the nodes on all levels with the same procedures.

The one disadvantage that we encountered resulted from change in the structure or information that was on one of the blackboards. Any changes in the data and utilities package made it necessary to recompile all other units. Changing the tables from static to dynamic and initializing them from files would eliminate many of the changes that were required.

5   Conclusions

A prototype monitoring system based on the blackboard control model of problem solving was successfully implemented in Ada. Blackboard systems exhibit several characteristics that parallel features of Ada. The independent knowledge sources can be developed as program units. Packages can encapsulate operations on specific types of data. The tasking mechanism can

provide the dynamic property required by the control mechanism. The use of Ada tasks will allow a natural movement to multiprocessor systems. These features, along with the capability to incrementally build a solution, make Ada a good choice for a blackboard system.

The incorporation of AI techniques into solutions of real world problems has been hampered by the use of speciality languages for their implementation. Ada provides the vehicle for moving these techniques out of the research laboratories. Successful integration of artificial intelligence techniques into Ada will create adaptable software packages that are highly suitable for solving real world problems.

References

[Adk86]   M. Adkins. Flexible data and control structures in ada. In *2nd Annual Conference on Artificial Intelligence and Ada*, pages 9.1–9.17, 1986.

[Bra86]   D. Brauer. Ada and knowledge-based systems: A prototype combining the best of both worlds. In *First International Conference on Ada Programming Language Applications for the NASA Space Station*, 1986.

[DDL88]   V. Dobbs, H. Davis, and C. Lizza. An application of heuristic search techniques to the problem of flight path generation in a military hostile environment. In *1st International Conference on Industrial and Engineering Applications of Artificial Intelligence and Expert Systems*, 1988.

[Dob88]   V. Dobbs. Reusable ada modules for artificial intelligence applications. In *6th National Conference on Ada Technology*, 1988.

[EHRLR80] L. Erman, F. Hayes-Roth, V. Lesser, and D. Reddy. The hearsay-ii speech understanding system: Integrating knowledge to resolve uncertainty. *ACM Computing Surveys*, 12:213–254, June 1980.

[Fra86]   M. Frank. Using ada to implement the operations management system as a community of experts. In *First International*

Conference on Ada Programming Language Applications for the NASA Space Station, 1986.

[HR85]   B. Hayes-Roth. A blackboard architecture for control. *Artificial Intelligence*, 26:251–321, 1985.

[JLZ87]   A. Jaworski, D. LaVallee, and D. Zoch. A lisp-ada connection for expert system development. In *3rd Annual Conference on Artificial Intelligence and Ada*, pages 74–89, 1987.

[LaV86]   D. LaVallee. An ada inference engine for expert systems. In *First International Conference on Ada Programming Language Applications for the NASA Space Station*, pages E.4.3.1–E.4.3.12, 1986.

[Nii82]   H.P. Nii. Signal-to-symbol transformation: Hasp/siap case study. *AI Magazine*, Spring 1982.

[Nii86a] H.P. Nii. Blackboard application systems and a knowledge engineering perspective. *AI Magazine*, 7(4), August 1986.

[Nii86b] H.P. Nii. The blackboard model of problem solving and the evolution of blackboard architectures. *AI Magazine*, 7(3), Summer 1986.

[RKW85]   L. Reeker, J. Kreuter, and K. Wauchope. Artificial intelligence in ada: Pattern-directed processing. Technical Report AFHRL-TR-12, AFHRL, May 1985.

[SPA86]   D. Scheidt, D. Preston, and M. Armstrong. Implementing semantic networks in ada. In *2nd Annual Conference on Artificial Intelligence and Ada*, 1986.

FINAL REPORT

SURFACE STATES AND ELECTRON TRANSPORT PROPERTIES

IN SEMI- INSULATING GALLIUM ARSENIDE

Sponsored by the

AIR FORCE OFFICE OF SCIENTIFIC RESEARCH

Conducted by the

UNIVERSAL ENERGY SYSTEM, INC.

Prepared by: N.C. Halder
                         Professor of Physics

Department: Physics
University: University of South Florida
                         Tampa, FL   33620

USAF Research: D.C. Look
                         AFWAL/AADR
                         WPAFB,OH, 45433

Date: December 30, 1988

Contract No: S-760-7MG-049

Abstract

The electronic transport properties (electrical conductivity, mobility and carrier concentration) have been measured in undoped, SI-GaAs wafers which have been subjected to various surface treatments. Several samples were selected and measurements have been carried out in the temperature range from 250 to 400°K with gas ambients N_2, He air and vacuum. It has been observed that removal of several microns, before the measurements, and the choice of ambients during the measurements, both can have a substantial effect on the apparent conductivity, concentration and mobility. It is concluded that results are related to the conduction lattice damage (subsurface damage) and surface states (conductive oxide layers) on the surface.

SURFACE STATES and ELECTRON TRANSPORT PROPERTIES IN SEMI-INSULATING GaAs

I.   Introduction

The purpose of this research was to continue and extend the study[1] of the surface states in semi-insulating (SI) GaAs that was (i) initiated at the Avionics Laboratory, Wright Patterson Air Force Base, in May-July, 1987 under USAF-UES Summer faculty Research program, and (ii) subsequently funded by UES/AFOSR under Research Initiation Program. SI-GaAs available from Avionics Laboratory, which were grown by Texas Instruments and Rockwell International, were used. In particular, we have selected random wafers and wafer sections and measured the Hall-the Hall-properties, and dc-conductivities in the temperature range 250 to 400^OK. For ac-properties, we have developed a system suitable for the temperature range 77 to 400^OK and frequency range 10 kHz to 40 MHz. From these measurements, the effect of the surface states have been investigated in various gas ambients (N_2, He, air and vacuum).   The results have been interpreted in terms of recently predicted theories for SI-GaAs.

II. Research Work and Technical Approach

The substrate material for many high performance GaAs device is undoped SI-GaAs. It's usefulness and practical importance are well known. Many studies and results on SI-GaAs have been reported and many problems have been worked out. However, there remain some problems, such as, the effect of nonuniformity a major defect (EL2) and its distribution on the electronic transport properties. The correlations are still not clearly understood and hence all necessary information on this issue is not available.   When SI-GaAs is used as substrate material for devices, after MBE layers are grown, it is believed[2]

characteristics of the devices will heavily depend on the properties of the substrate. The surface states or defects could arise in the samples from absorbed or adsorbed gas molecules. The ionized molecules, in the presence of electric field, could thermally diffuse into the layers immediately below the surface and might interfere with the conduction band electrons. Yeo et al[3]. have investigated the surface effect on Si-implanted GaAs (n-type) and concluded that these surface states could also result from the abrupt termination of the lattice or defects at the semiconductor surface, and therefore, they can pin the Fermi energy within the forbidden gap at the surface, creating a carrier depletion in the region just below the surface. The long range potential fluctuation is a real possibility due to a nonuniform distribution of the impurities.

Many studies[4-8] of the conductivity on SI-GaAs indicate similar interesting results. For example, the ac-conductivity results show that the conductivity is frequency dependent even at high temperatures. Normally, amorphous semiconductors and dielectrics show a strong frequency dependent conductivity, but crystalline semiconductors show somewhat smaller effect at relatively low temperatures. On the other hand, dc-conductivity measurements have been explained in terms of quantum mechanical tunneling between localized gap states in the bandgap. These states are separated by potential barriers which are found to fluctuate with the thermal vibration of the lattice. Other studies[4] indicate that the temperature dependence of the dc-conductivity, especially in the low temperature region, is given by the Berthelot equation. For the ac-conductivity, as well, there are some recent developments[5]. Abdalla and Pistoulet[6] proposed a model based on Gaussian distribution of potential fluctuation suggesting $\sigma \alpha \omega^s$ where $s < 1$ for the intermediate range of $\omega < 10^6$ Hz, but $s = 2$ for $\omega > 10^6$ Hz under some approximations. However, their model depends on a number of unknown input parameters whose justification may be questionable.

In this research we have investigated surface states effect on several SI-GaAs samples. These are illustrated in Table I. These samples are available from WPAFB, and have been studied very extensively. More detailed description of sample growth and characterization are available elsewhere.[9,10]

The TI-samples (Texas Instruments) are low-pressure, liquid-encapsulated Czochralski (LEC), near-tail-end of the boule, which are undoped, but R-samples (Rockwell) are a high pressure LEC, near-seed-end, and doped with In ($2.3 \times 10^{20}/cm^3$ in the melt). For this reason, these sets are contrasting. The methods of sample preparation, polishing and etching, etc. are also described in the above two reports.[9,10]

Our efforts have been directed in two directions: (i) investigation of several samples, both of different wafer numbers and different wafer sections, and the (ii) measurement of dc-conductivities and Hall parameters, especially in the temperature range 250 to 400°K.

III Experimental

In this research we have included, as shown in Table I, two types of SI-GaAs samples (Texas Instruments and Rockwell International). The last number in each sample indicates the location on the wafer section (64 and 65 in the present case)

The Hall-properties and the dc-conductivities were measured at Avionics Laboratory, WPAFB in collaboration with D.C. Look. The experimental setup was a standard van der Pauw configuration and is shown in Fig. 1. For ac-properties, we have developed a compatible system here at USF, which is shown in Fig. 2. As is well known the resistivity of these samples were quite high ($10^8 \sim 10^9$ ohm.cm). This required an impedance measurement of about $500 \sim 800$ MΩ, which was far beyond the limit of our present capability of the HP4275A LCR-meter (limit being 20 MΩ). Hence the present setup could not be used for SI-GaAs samples. We shall discuss later on what improvements would have to be made in the future to overcome these limitations. The results are shown in figs. 3-9.

IV. Results and Discussions

The data from dc-measurements indicate that the resistivity of the samples is quite high $10^8 \Omega$ cm, concentration $10^6/cm^3$ and mobility μ $10^3 cm^2 V\text{-}s$. The conductivity σ is linear with 1/T when plotted on logarithmic scale in the high temperature region, but there is some nonlinearity in the low temperature region, particularly below room temperature. The slopes of the log σ vs 1/T plots are different for different gas ambients, especially below room temperature. The behavior of the concentration plots, i.e., log n vs 1/T is the same as that of log σ vs 1/T plots, since σ is not nearly as temperature-dependent as n. The mobility μ, as expected, increased with 1/T in the high temperature region. The data from ac-measurements are not available for these samples as yet, since the limit of our equipment was 20 m Ω, whereas resistance in these samples ranged between 100 to 800 MΩ. We are, therefore, looking into alternative possibilities, which will be implemented into the second phase of our research.

Kristofik et al[5]. measured the temperature and frequency dependence of electrical conductivity of SI-GaAs and concluded that the surface conductivity is explained by the Berthelot equation, whereas the bulk conductivity has the Arrhenius-type behavior. This type of investigation was followed by Abdalla and Pistoulet[6], and Pistoulet and Hamandjian[6]. They suggested that the long range potential fluctuations can give rise to mixed conductivity due to the accumulation of electrons in potential wells separated in space from holes accumulated in potential hills. They have further carried out a theoretical analysis of the problem by assuming a potential fluctuation with truncated Gaussian distributions, which depended on a number of input parameters (as many as eight parameters). On the other hand, Look[5] had already pointed out earlier the existence of mixed conduction in Cr-doped SI-GaAs from his study of the Hall effect and magnetoresistance. Later on, he has developed[8] an appropriate theory to represent the mixed conduction effect in semiconductors in general. Lo et al[2]. have

demonstrated by a surface property study using cw-electro-optic probing that the EL2 concentration on the surface of SI-GaAs is nonuniform across the wafer, which tends to be depleted near the surface after thermal annealing. This surface depletion of EL2 defect can cause a very leaky substrate surface promoting a serious backgate effect. Very recently Lester et a.[11] have reported studies on ambient-induced surface effects in GaAs, demonstrating sensitivity of the gas environment on the conductivity and photolumiescence. Kuhnel et al.[12] found similar effects on their data of Hall properties.

The plots shown in Figs. 3-9 show marked effects not only from sample to sample, but also from ambient to ambient. The conductivity and concentration data show a gradual, but smooth, variation with temperature, even in the region of low temperature. The mobility data, however, are very sensitive in this region as is evident from Figs. 5-9. The effect of gas molecules apparently do enhance the surface effect more in mobility than in the conductivity or concentration in this region.

The direction of the conductivity changes indicate that the surface charge becomes more negative during exposure to air increasing in positive space charge and moves the surface-Fermi level. Lester et al.[10] have investigated the ambient induced movement of the surface-Fermi level in InP and GaAs. In fact, they have estimated from photoluminescence data that the Fermi level at 0.8 eV below the conduction band in GaAs. Our concentration data further supports this conclusion.

Kuhnel et al.[10] looked at Hall effect and conductivity measurements in SI-GaAs and suggested a correction procedure for the surface effects in their samples. However, Johnson et al.[13] found a nonuniform distribution of charging effect by electron beam in SI-GaAs, which they attributed to the surface effect. This has been interpreted as the interaction between the propagating domains (presumably the gas ambients) and the cellular dislocation structure formation in SI-GaAs. These interactions seemingly produce noise in the current oscillation

waveforms. This has been also interpreted as the fluctuation of the long range potentials by others[5,6].

Our mobility data apparently do not indicate any systematic pattern in the low temperature region except that they are extremely sensitive to the formation of surface states. Another important consideration should be made with regard to the subsurface damage. It has been recently shown by Ives and Leung[14] that a subsurface damage on GaAs wafers (apparently SI) could affect the reliability and performance of a device fabricated on such wafers. We are at present attempting to go still lower in temperature and establish a definite trend with various gas ambients. The frequency dependant data, which are not available as of this moment in our laboratory, will further help to explain this situation.

V. Conclusions

Temperature dependent Hall effect measurements have been carried out on undoped, SI-GaAs wafers, which have been subjected to various surface treatments. It is found that removal of several microns, before the measurements, and the choice of ambients (H_2, He, air and vacuum) during the measurements, both can have a substantial effect on the apparent mobility and carrier concentration. Results are related to conduction lattice damage in the near-surface region, and conductive oxide states on the surface.

VI References

1. N.C. Halder, Final Report, USAF-UES Summer Faculty Research Program, July, 1987, (unpublished); N.C. Halder and D.C. Look, J. Appl. Phys. - to be published.

2. Y.H. Lo, Z.H. Zhu, C.L. Pan, S.Y. Wang, and S. Wang, Appl. Phys. Lett. 50, 1125 (1987).

3. Y.K. Yeo, R.L. Hengehold, and D.W. Elsaesser, J. Appl. Phys. 61, 5070 (1987).

4. B. Pistoulet, P. Girad, and G. Hamamdjian, J. Appl. Phys. 56, 2268 (1984); J. Appl. Phys. 56 2275 (1984); B. Pistoulet, F.M. Rouche, and S. Abdalla, Phys. Rev. b 59, 5987 (1984).

5. J. Kristofik, J.J. Mares, V. Smid, and J. Zeman, Phys. Stat. Sol. (a) 88, K187 (1985); J.J. Mares, J. Kristofik, V. Smid, and J. Zeman, Sol. State Commu. 60, 275 (1986).

6. S. Abdalla and B. Pistoulet, J. Appl. Phys. 58 2646 (1985); B. Pistoulet and G. Hamamdjian, Phys. Rev. B 35, 6305 (1987).

7. D.C. Look, J. Phys. Chem. Solids 36, 1311 (1975).

8. D.C. Look, Phys. Rev. B 25, 2920 (1982).

9. Advanced GaAs Growth, Interim Technical Report Final, No. 10 for Contract NO. F33615-83-C-5072, Sept. 1986.

10. Advanced GaAs Growth, Interim Technical Report NO. 11 for Contract NO. F33615-83-C-5134, Oct. 1986.

11. S.D. Lester, T.S. Kim and B.G. Streetman, J. Appl. Phys. 60, 4209 (1986).

12. G. Kuhnel, W. Siegel, S. Felex and H.A. Schneider, Phys. Stat. Solidi A101, 531 (1987).

13. D.A. Johnson, S. Myhajlenke, J.L. Edwards, G.N. Maracas and R.J. Roedel, Appl. Phys. Lett. 51, 1152 (1987).

14. N.A. Ives and M.S. Leung, Rev. Sci, Instrum 59, 2198 (1988).

Table I: Samples Studied

Lab Code	Texas Inst. Samples	Lab Code	Rockwell Samples
AA	TI 31-41-65	CC	R158-6-65
FF	TI 31-10-64	HH	R158-6-64
GG	TI 31-41-64	II	R158-33-64
EE	TI 31-10-65		
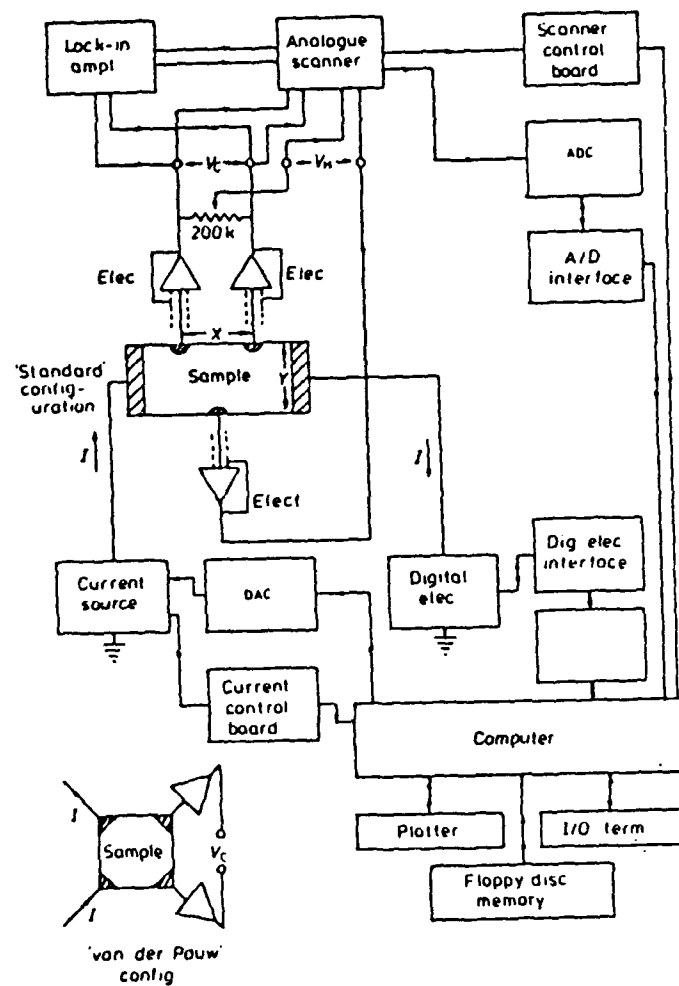
Figure 1

Schematic diagram of the automatic, high resistivity Hall-effect apparatus. A standard van der Pauw configuration is also shown in the diagram.

SST System
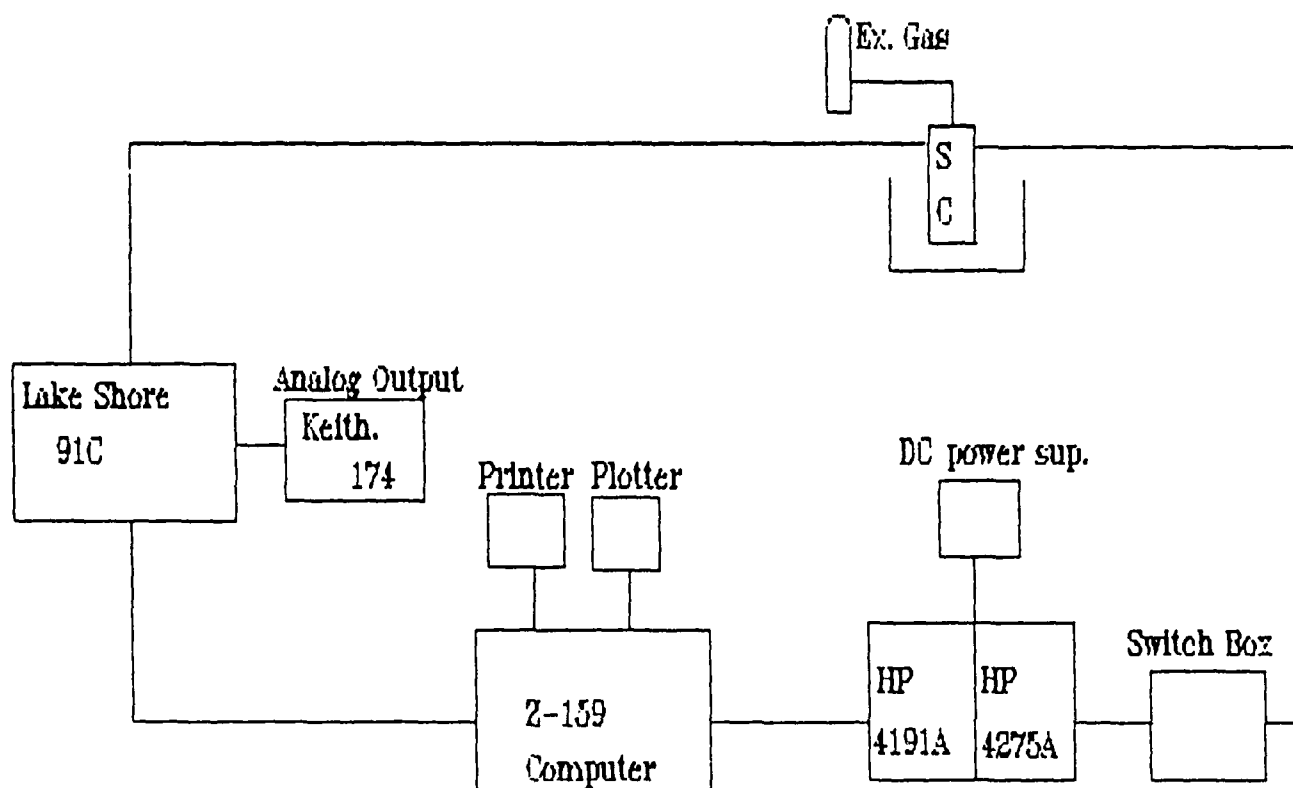
Figure 2

Schematic diagram of the automatic SST-System for the ac-properties.
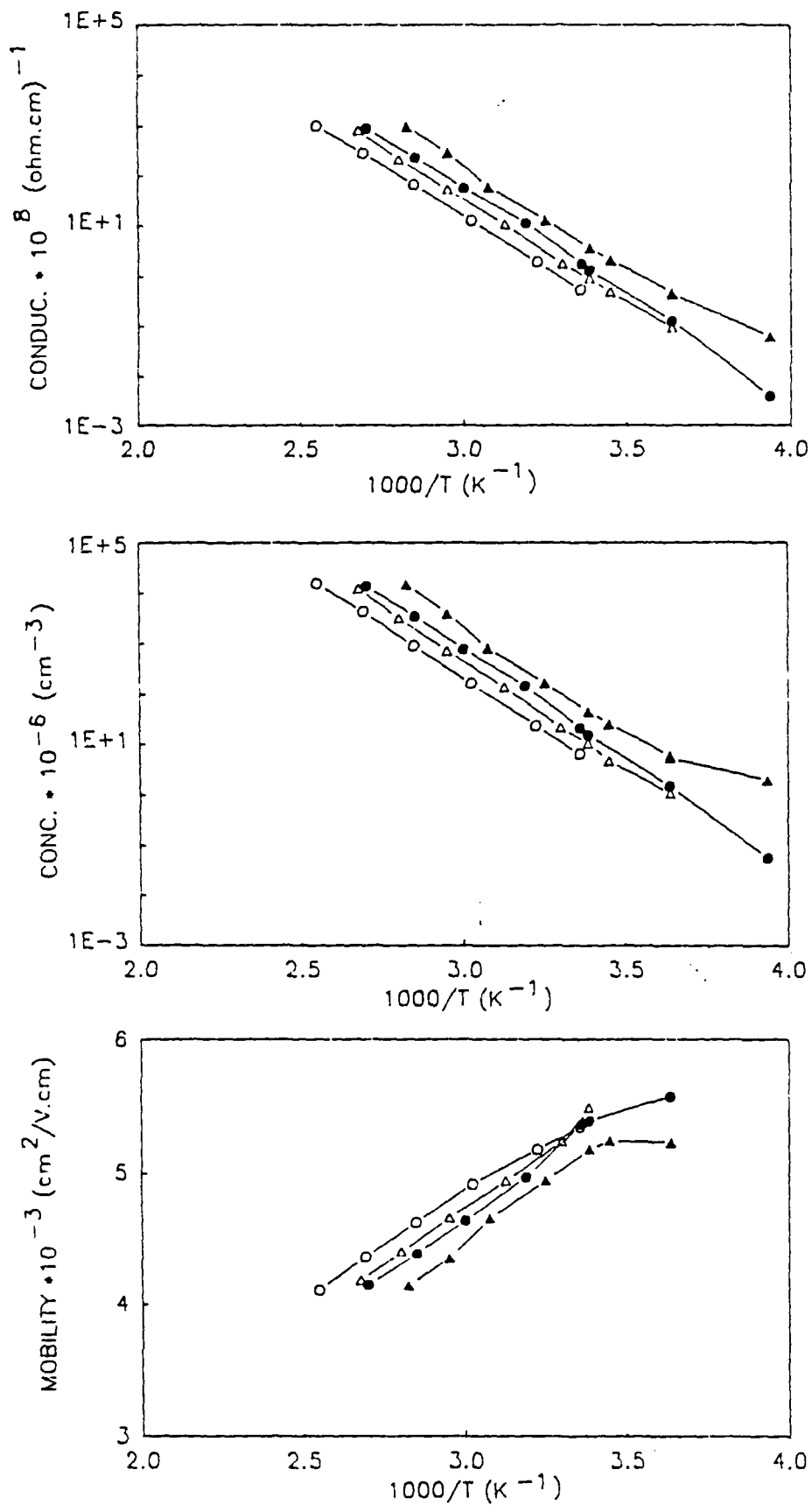
Figure 3.   Sample AA   O:air, △:N$_2$, ●:He, ▲ vacuum
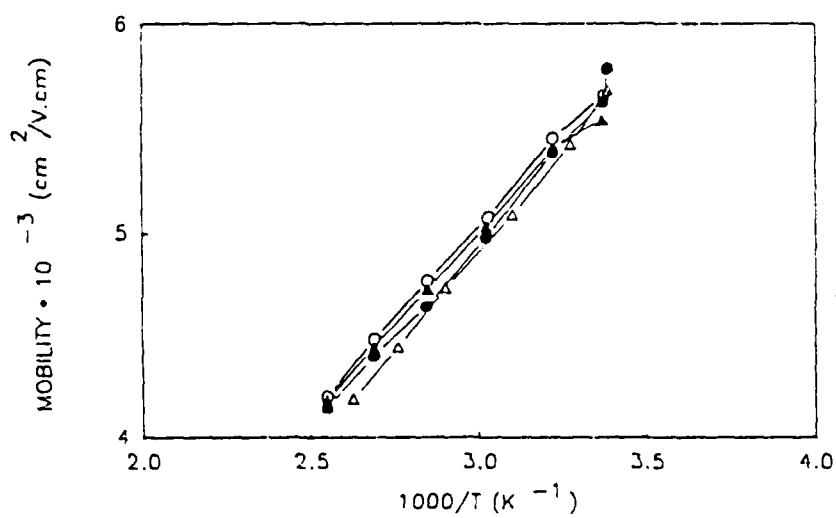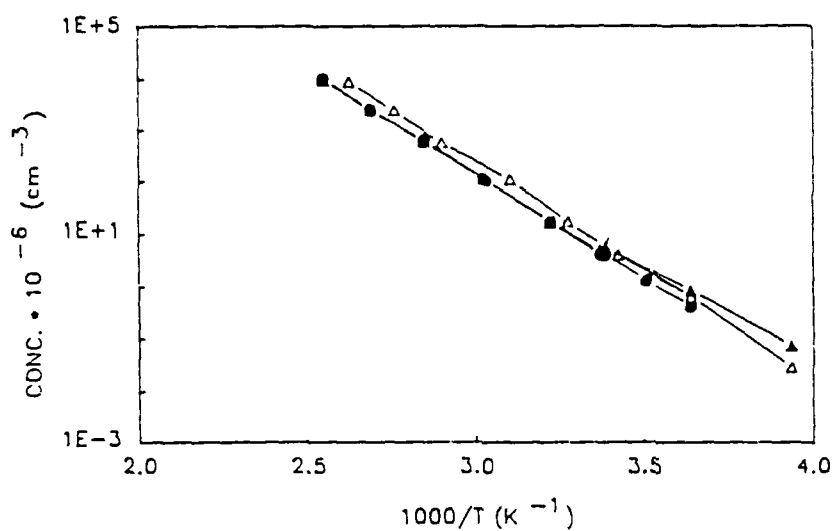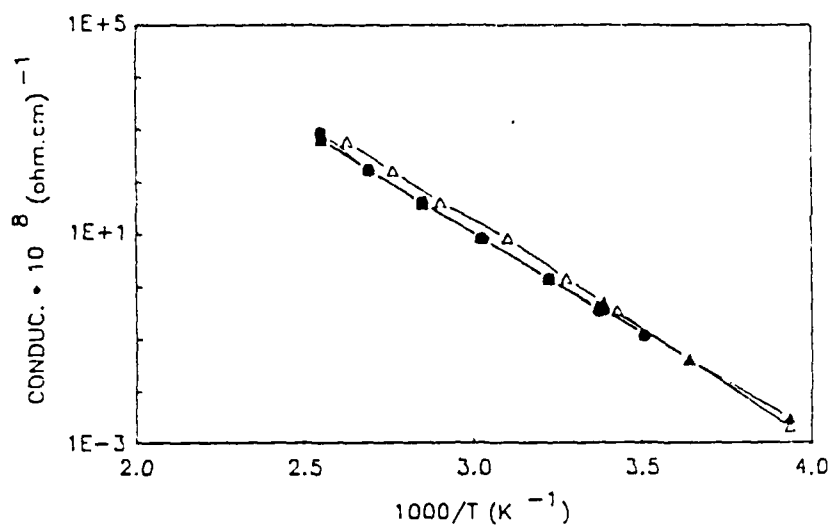
Figure 4. Sample CC
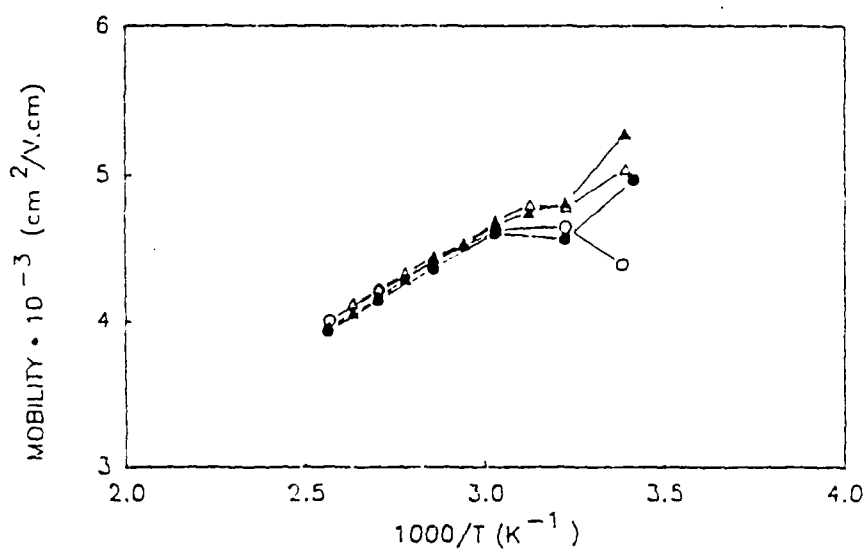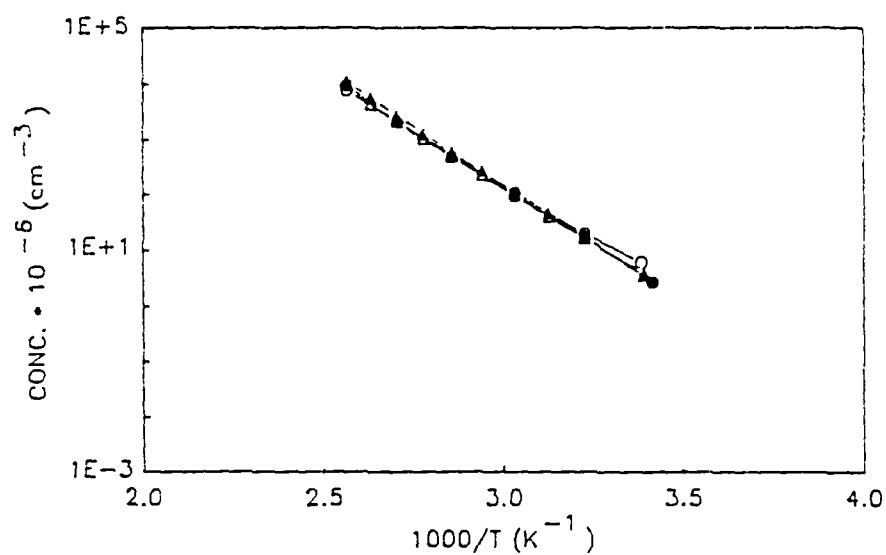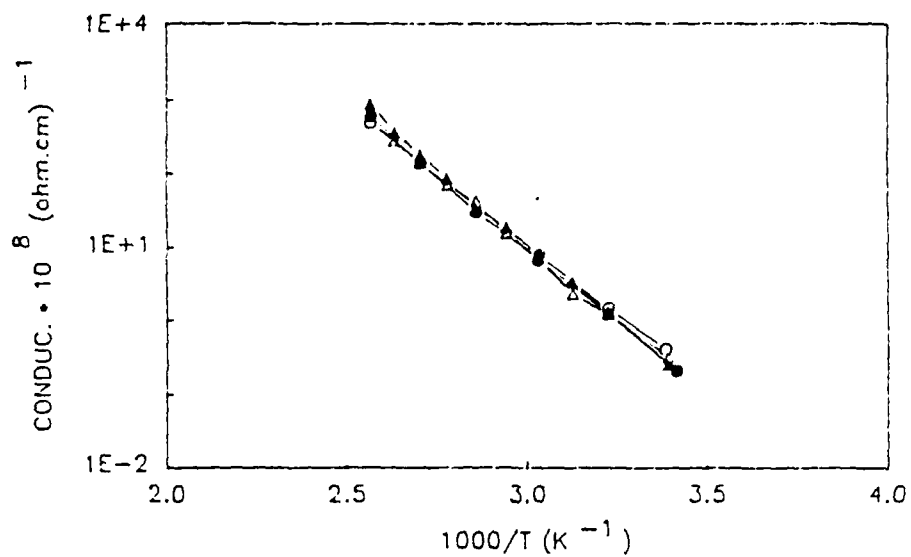
Figure 5. Sample EE

Figure 6. Sample FF

61-16
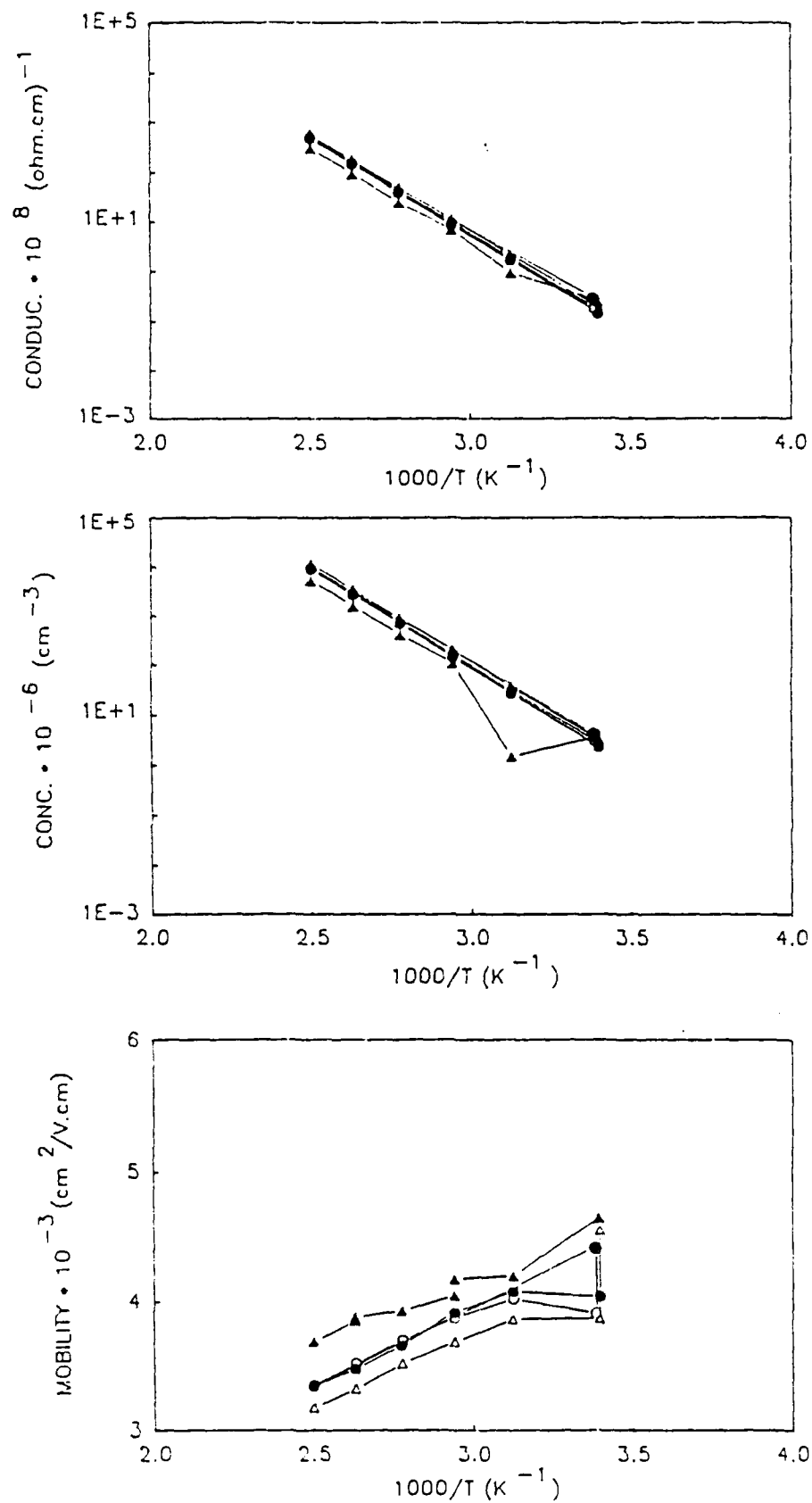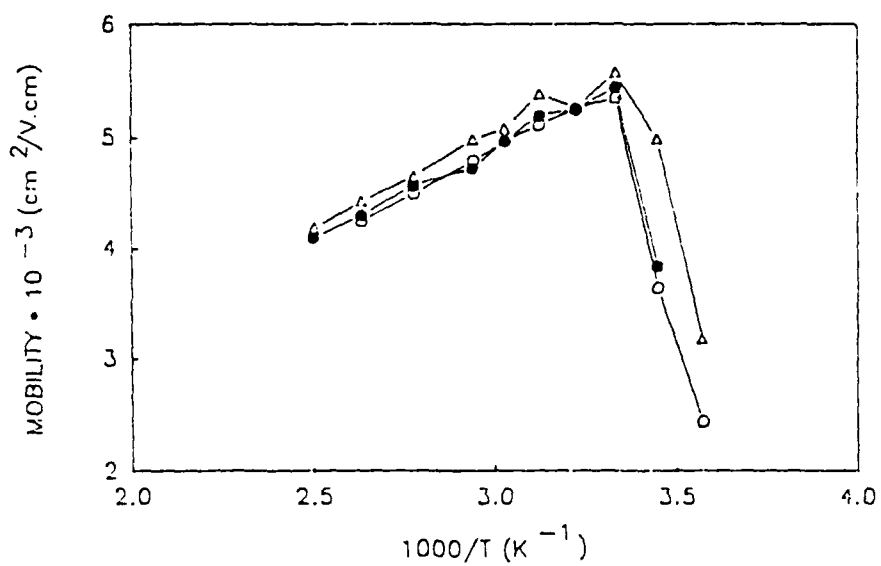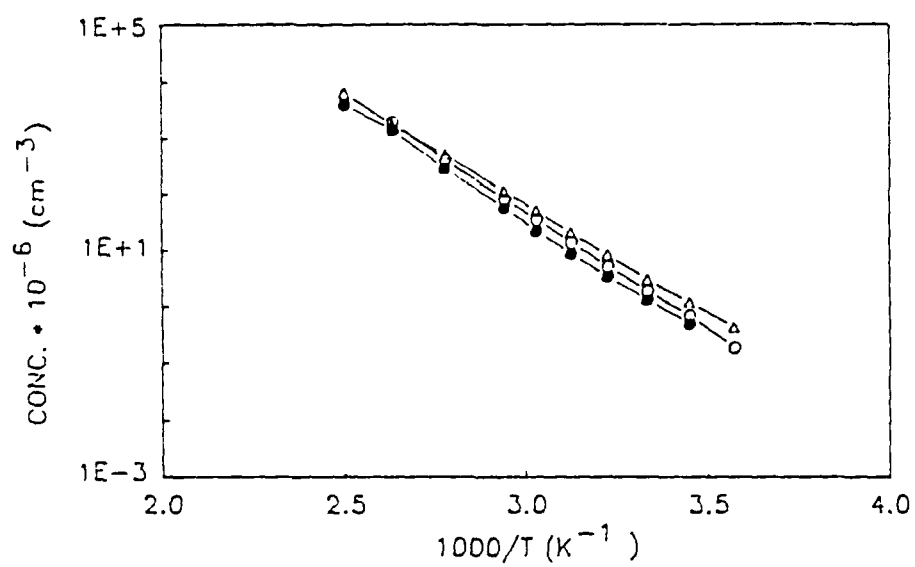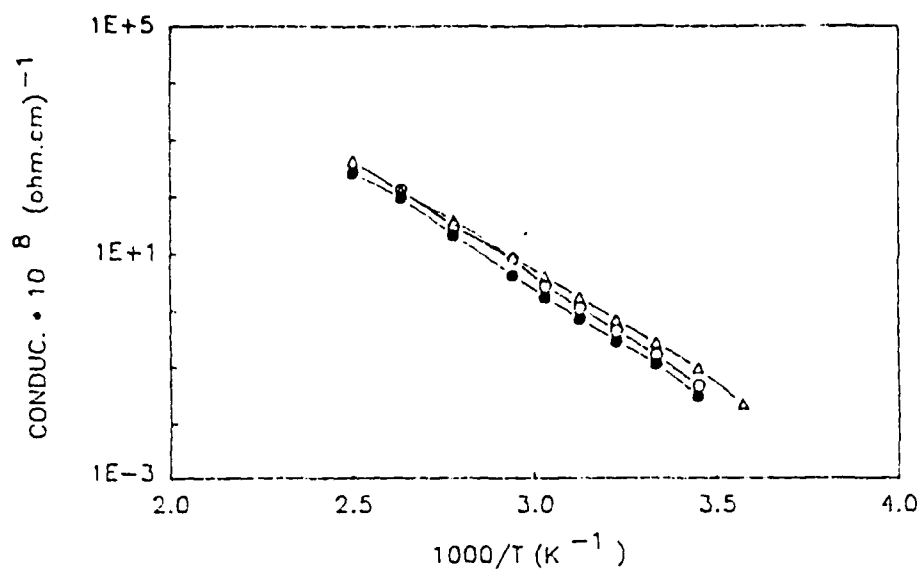
Figure 7. Sample GG

61-17

Figure 8.   Sample HH

51-18
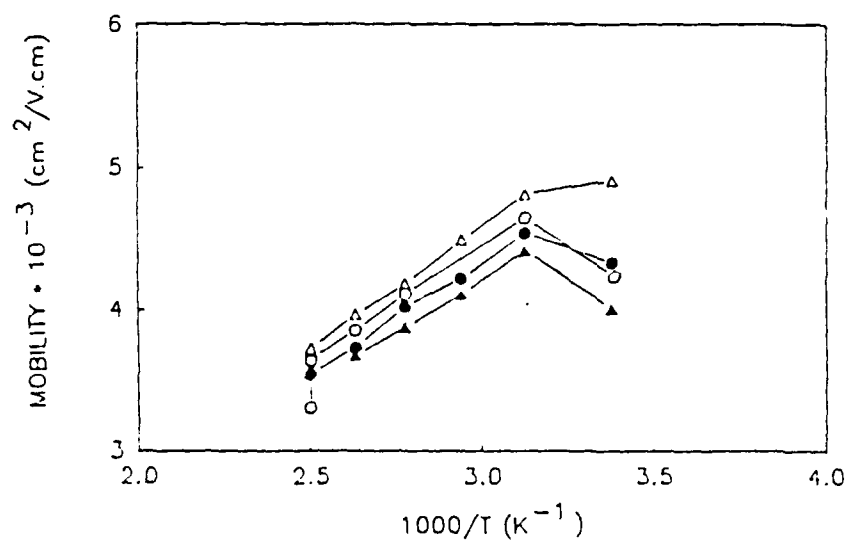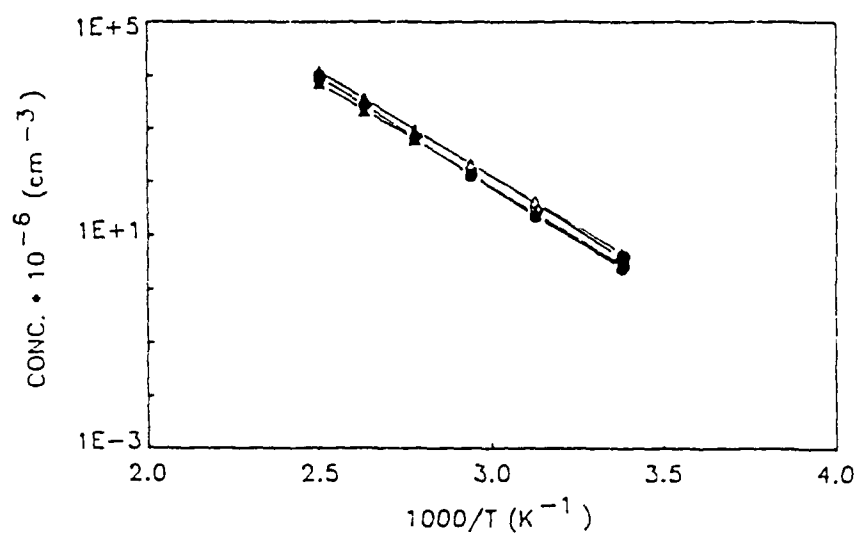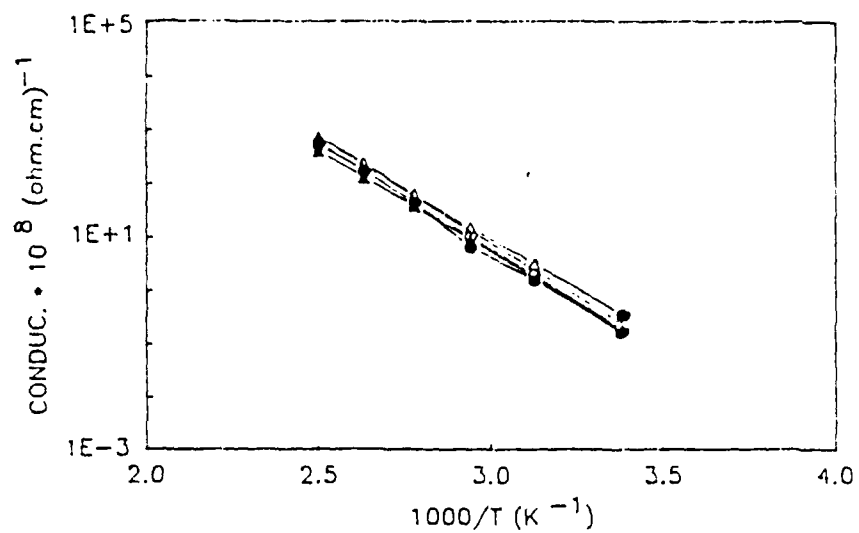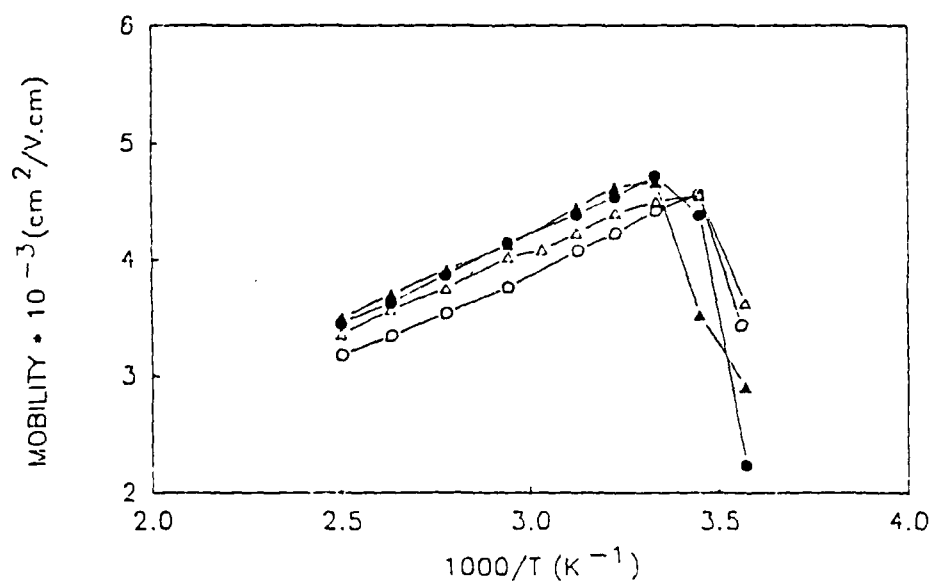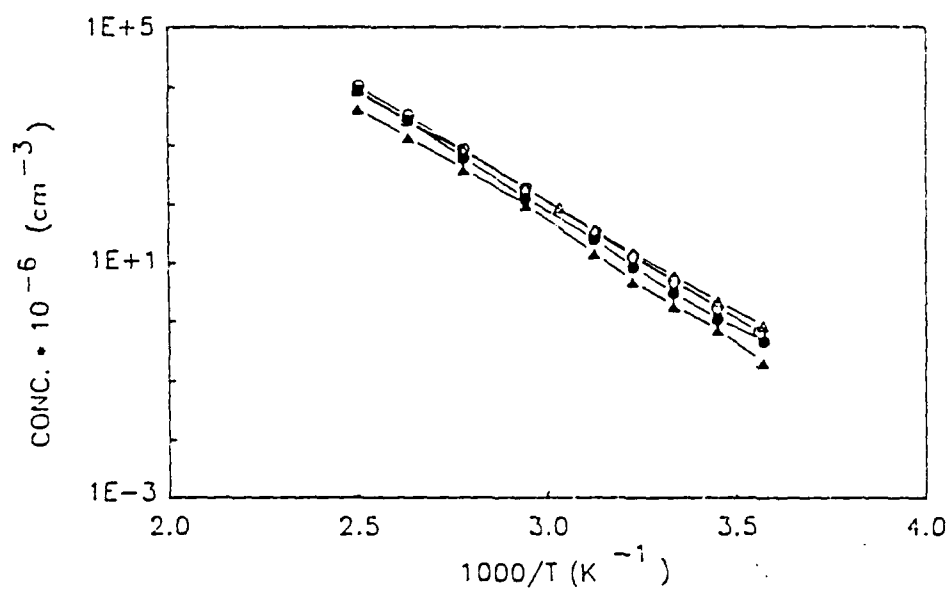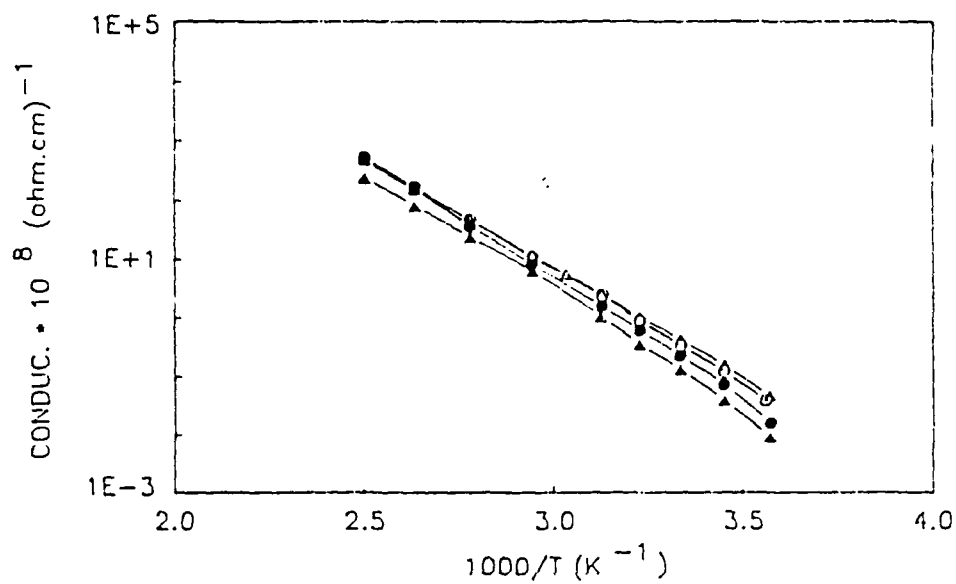
Figure 9. Sample II

MINI-GRANT FOLLOW ON FOR 1987 USAF-UES

SUMMER FACULTY RESEARCH PROGRAM

Sponsored by the

AIR FORCE OFFICE OF SCIENTIFIC RESEARCH

Conducted by the

Universal Energy Systems, Inc.

FINAL REPORT

Investigate feasibility of implementing associative

memories using luminescent rebroadcasting devices

Prepared by:	Alastair D. McAulay, Ph.D.
Academic Rank:	NCR Distinguished Professor
Department:	Computer Science and Engineering
University:	Wright State University
Research Location:	Wright State University, Dayton, Ohio, 45435
USAF Research Contact:	Joseph E. Brandelik
Date:	1 Dec. 1987 to 15 Dec. 1988
Contract No.:	F49620-85-C-0013

Associative memory with LR devices

ABSTRACT

This report describes reasearch performed under a mini-grant resulting from the 1987 Summer Faculty Research Program sponsored by the Air Force Office of Scientific Research. Previously a preliminary characterization was performed for new luminescent rebroadcasting materials developed with support from Wright Patterson Air Force Base. These devices are significant because they have optical disk resolution and potentially nanosecond write-read speed. Basic processing functions were also demonstrated. Experiments performed in this project show for the first time the feasibility of using luminescent rebroadcasting devices for implementing three forms of associative memory: multiple correlations, symbolic substitution, and neural networks. Comparisons between the approaches and their advantages and disadvantages are provided. The results and ease of working with these materials makes this a good area for further research to develop a practical associative memory.

ACKNOWLEDGEMENTS

Chapter 1

Introduction

1.1 Background

This report describes research continuing from a summer faculty research program sponsored by the Air Force Office of Scientific Research performed at Wright Patterson Air Force Base AADO-2 [21]. New luminescent rebroadcasting devices were investigated that had been developed under funding from Wright Patterson Air Force Base. The new materials could result in a breakthrough in write-read memory technologies because resolution approaches that of optical disk, i.e. 0.6 μm, and nanosecond speeds seem possible [5]. In particular, we explore the use of these devices for associative memory (AM) because associative memory appears to be suitable for taking advantage of this potential performance.

Associative memories are an increasingly important computer technology because of the speed obtainable with highly parallel search. In associative memory, data is accessed by specifying part of the contents of the data. The part searched for in the associative memory may be considered the input and the data associated with it may be considered to be the output. When the output includes both the search string and associated data the memory is often referred to as content addressable.

This contrasts with random access memory (RAM) where data is accessed by specifying memory locations or addresses. In AM, data is accessed by specifying part of the contents. A phone directory provides an example. In the case of RAM the information is accessed by remembering that a certain persons information is in a specific location or address, usually encoded in binary. Thus only $log_2 N$ bits will determine one of N locations in memory. In the case of AM the persons data is accessed by providing a part of his name or phone number. The AM then provides

the rest of the information.

RAM is widely used on present day computers because it is much cheaper with existing technologies. It is cheaper because the binary encoding reduces the number of interconnections. However, this results in serial addressing through a single decoder.

AM, in contrast to RAM, operates in parallel and is therefore faster. It is increasingly used in modern computers where speed is necessary, for example, (a), translation look aside buffers for rapidly translating most recently used virtual memory addresses to physical memory addresses, and (b), cache directories for rapid determination of whether data required for subsequent computations is in cache. Another reason for investigating AM is the increasing interest in high speed parallel computing, information storage and retrieval with rapidly changing databases, and real-time AI. An advantage of AM is that it is more forgiving because only part of what is sought needs to be supplied. In this respect it operates more like human memory.

Human experts seem to use *associative memory* (AM) rather than rule based systems most of the time. The expert becomes faster as past experiences accumulate. In contrast, rule based systems become slower as the expertise in the form of more rules is increased.

1.2 Prior optical associative memory implementations

Most optical AM proposed and constructed for experimentation use spatial light modulators (SLMs) to perform correlation or equivalently, matched filtering, of the input against a set of templates. The highest correlation is used to classify patterns. When the template having the highest correlation directly replaces the input, as is often the case in optical designs, the system is referred to as an AM [13],[1]. Parallel correlation against many templates may be performed by generating multiple images of the input [13] or by storing many templates at different angles in a hologram [1]. Sequential correlation is performed by presenting the templates one after the other in a single correlation scheme.

Many systems in optics use Fourier transforms because convolution is transformed to multiplication and the Fourier transform is easily obtained with a thin lens. A Van der Lugt filter is used [8] because the transform of a real image is complex and interference with a plane wave is a holographic method of storing complex functions.

Symbolic substitution may be used for associative memory and simple experiments have previously been performed [3]. A commonly used neural network structure uses

matrix-vector multiplication. Many simple experiments have been performed using matrix-vector multiplication[19],[25],[17],[28],[26].

In this project we explore for the first time the use of luminescent rebroadcasting devices for three associative memory designs: multiple correlations, symbolic substitution, and neural networks. Advantages and disadvantages of each design will be discussed.

Chapter 2

Device characterization

2.1 Samples used

Three types of luminescent rebroadcasting samples are available currently. Sample A is a 2 by 2 inch size thick film in a polymer encapsulation. Sample B is a 0.85 by 0.85 inch thick film bonded to a sapphire window. Sample C is a 0.85 by 0.85 inch thin film bonded to a sapphire window. Sizes refer to active surface area. Thick film is approximately 250 μm and thin film approximately 4 μm. The approach and results of experiments follow in categories of resolution, speed, energy consideration and spectral response.

2.1.1 Resolution

The resolution testing procedure was to first illuminate the device with sufficient infrared (IR) energy at 1064 nm to read out all the stored energy. A resolution chart was attached to the surface of the device. To reach saturation, sufficient energy from a blue Argon laser at 488 nm was used to write uniformly in space on the device. The chart was removed and IR at 1064 nm was then used to cause luminescence. Samples A and C luminesce in orange, while sample B luminesces in green.

Figure 2.1(a) shows the result for the polymer encapsulated thick film, sample A. Based on the center left of this chart the resolution is 125 line pairs per inch. This corresponds to distinguishing an array of at least 200 by 200 for active area of sample A. Figure 2.1(b) shows the result for the thick film on sapphire, sample B. The resolution is higher, at approximately 175 line pairs per inch. This would permit an

array of 150 by 150 to be distinguished with the active area of the sample provided.

Figure 2.1(c) shows that the resolution of the thin film is much higher than samples A and B, at over 275 line pairs per inch. This corresponds to an array of 230 by 230 for the active area of sample C. The improvement in resolution for the thinner sample is obvious from Figure 2.1, but the trade off is that the luminescent intensity of the orange light makes the thinner sample output much harder to detect.

2.1.2 Speed

The free-electron lifetime determines the response time of the luminescence signal to the stimulating laser beam. It has been proved that the response time of the material is less than 50 ns full width at half-maximum[5][2]. In order to use the material for computing continuously, it is necessary to know the photon density required to significantly clear the trap during the short exposure time to the IR laser beam. This photon density combined with the illuminating Ar laser power will decide the cycle time for writing and reading. Generally speaking, the time needed to clean the device for the next operation is longer than reading from or writing to the device. A preliminary experiment concerning the reading and writing speed is reported in [21].

2.1.3 Energy consideration

Figure 2.2 shows an experimental result for the energy response of the device using the encapsulated thick film, sample A. The sample was exposed under different energies of the writing beam and the reading beam power remained constant. Reading occurs following each writing. The sample was cleared completely after each reading. The detector was positioned along a constant angle with respect to normal. Thus output power readings between samples are relative. Also, output power is the reading taken just when the read beam was turned on. A well defined linear area was found where arithmetic operations could be performed [15]. The same experiment was conducted on the thin sample, sample C. A similar result is plotted in Figure 2.3 except that the luminescence of the thin sample was about one order of magnitude lower than the thick sample, which is believed due to the contribution of thickness.

A thicker sample can store more energy in the same spatial location than the thinner sample resulting in a higher energy requirement of saturation. Once the saturation is reached the excess writing energy will penetrate through the sample

(a)

(b)

(c)

Figure 2.1: Resolution tests: (a) for thick film polymer encapsulated material (sample A), (b) for thick film on sapphire (Sample B), (c) for thin film on sapphire material (Sample C).

Relative
Intensity (nW)
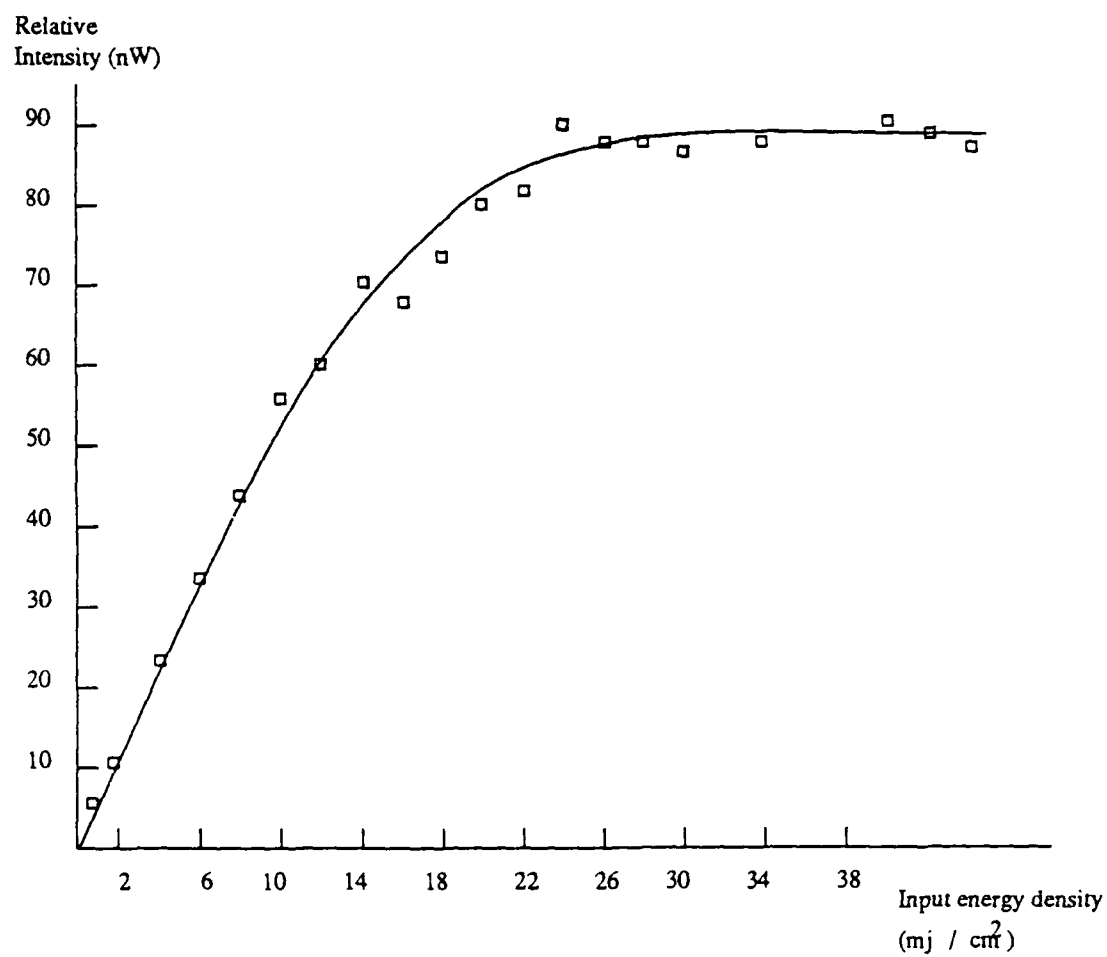
Figure 2.2: Luminescent intensity vs input energy density on thick sample
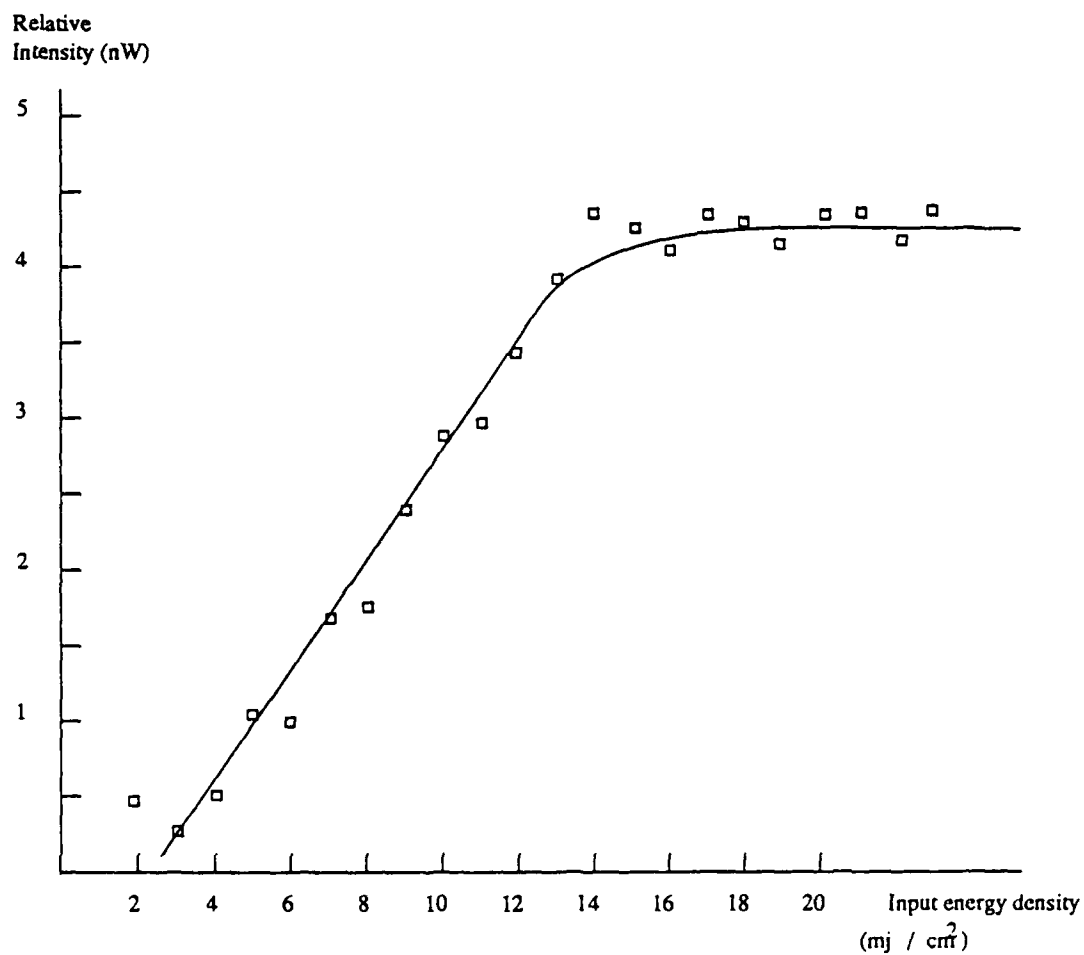
Figure 2.3: Luminescent intensity vs input energy density on thin sample

and logic operations can be performed in this energy region. Figure 2.4 and Figure 2.5 show the luminescent intensity curve from maximum to its stable state for both thick and thin sample. The thin sample, as expected, reached its stable state faster than the thick sample. This implies that the thin sample is more suitable for fast logic operations.

2.1.4   Spectral response

All samples responded to blue and green for writing. Samples A and C emitted orange and sample B emitted green. The luminescence emitted by the thin film material sample C, appeared to be one order of magnitude less than that for the thick films. However, high speed [5] and resolution, comparable to optical disc, are anticipated. Devices with different dopants have different spectral characteristics[11] and quantum efficiencies of photoluminescence[12].

2.2   Arithmetic operations

Analog addition. Analog addition of images A, B, C etc. is performed by writing one image after the other onto a device that was previously cleared by flooding with IR[16]. The images may be considered to be 2-D arrays of elements whose intensities represent analog numbers. The array elements are then added in parallel. The stored energy may be written as

$$S = A + B + C \cdots \qquad (2.1)$$

On reading the device by flooding with IR, the intensity of the luminescence at a pixel is the sum of the energies supplied to the pixel position by each of the images added, provided the operation remains in the linear range of the device. Figure 2.6 shows the result of exposure of the device to a collimated beam at two different positions foι equal time such that the center gets exposed to two times the energy of either side. Note that the intensity of the intersection is about twice as bright as the remaining areas.

Analog multiplication. Parallel multiplication of images A and B is performed by writing one image, say A, onto the device with spatially varying intensities representing one image and then reading with IR having spatially varying intensities

Relative
Intensity (nW)
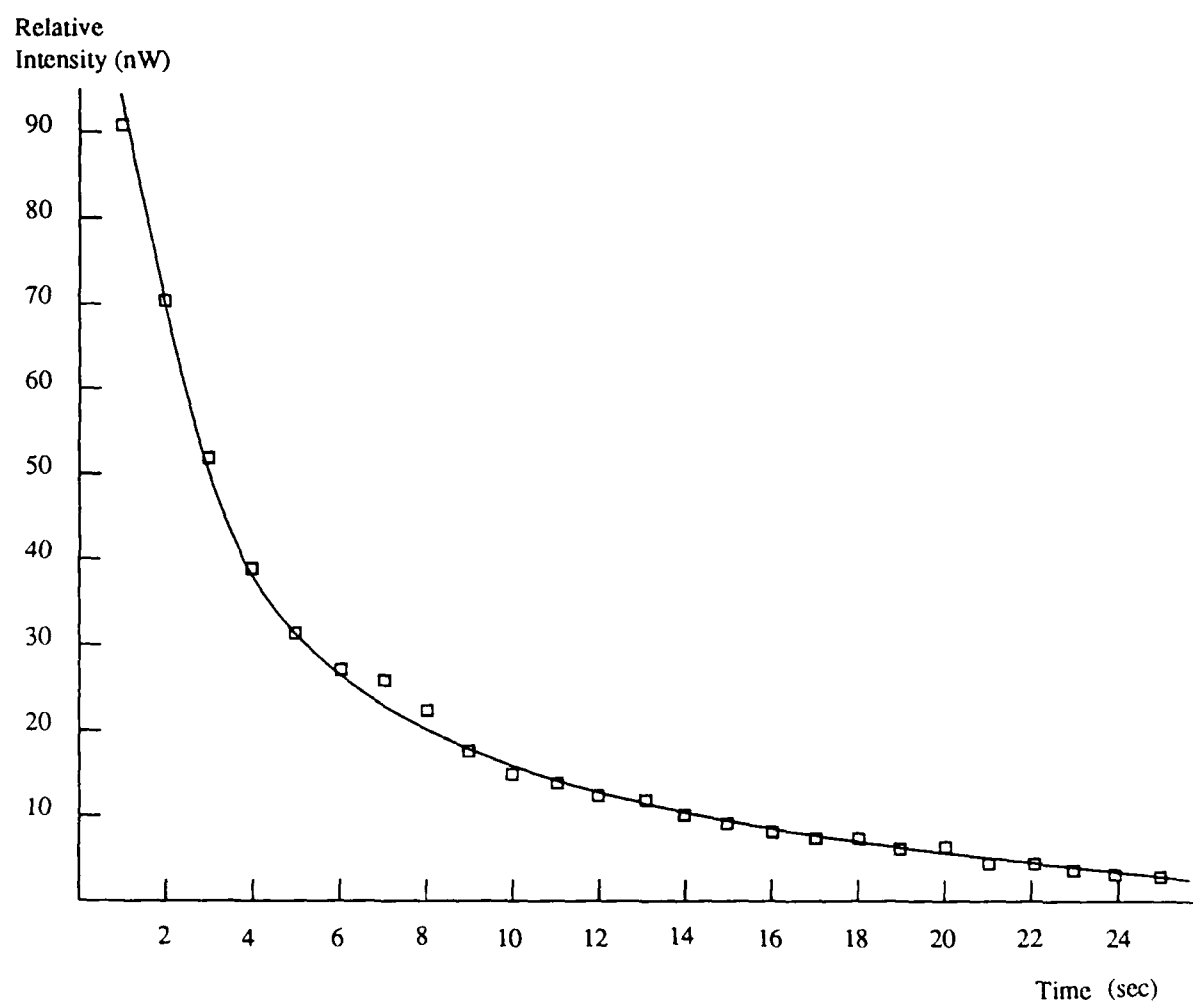
Figure 2.4: Decay of the luminescent intensity vs time on thick sample
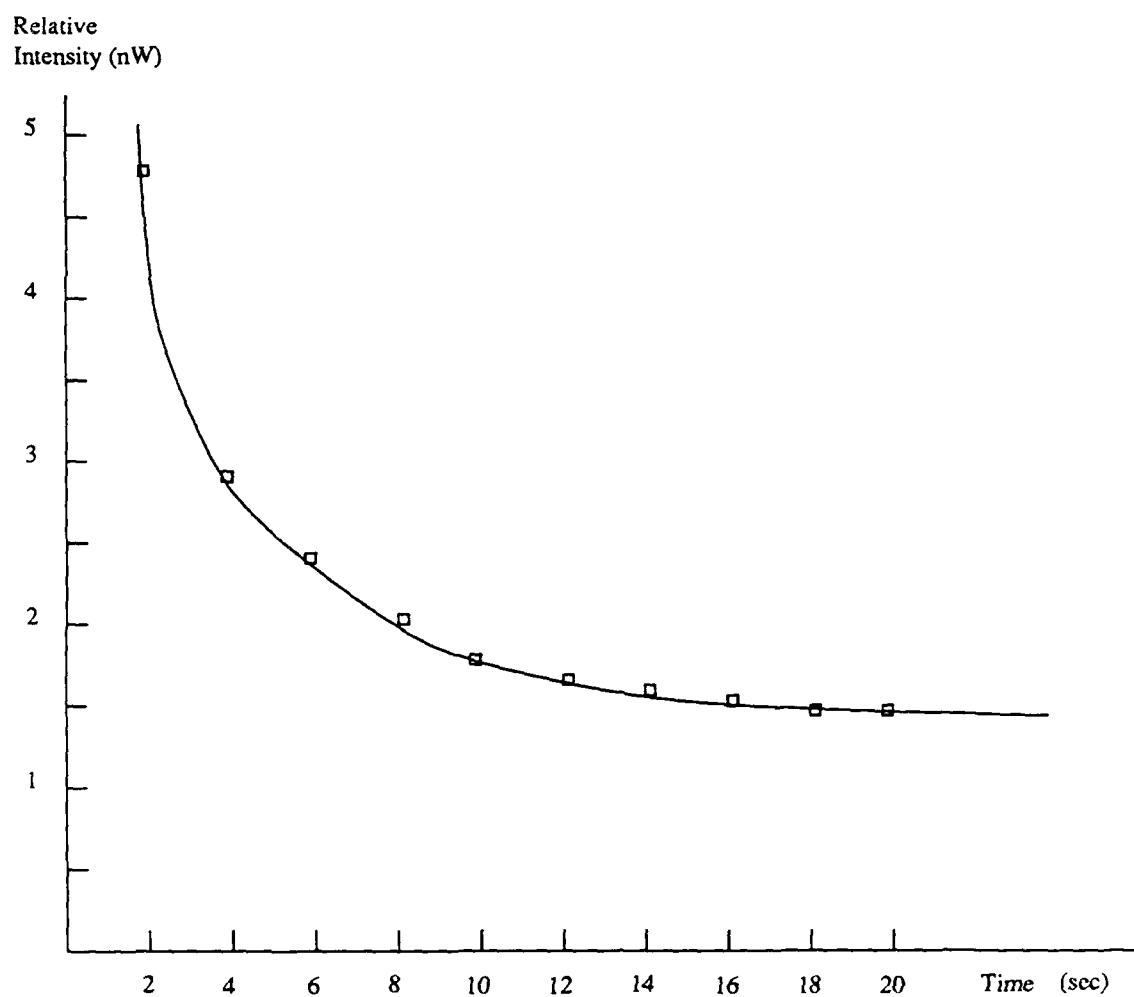
Figure 2.5: Decay of the luminescent intensity vs time on thin sample

Figure 2.6: Illustrating analog addition with luminescent rebroadcasting device.

representing the second image B. The output luminescence at each pixel position is proportional to the analog product of the read intensity at that pixel and the stored value at that pixel

$$Out = A \cdot B \tag{2.2}$$

Figure 2.7 illustrates analog multiplication by reading a previously uniformly written device through a variable density beam splitter. Note the stepped intensities are due to different values of operand B.

The energy that was not read out remains for subsequent operations and equals

$$S = A - (A \cdot B) = A \cdot (1 - B) \tag{2.3}$$

The read out energy A·B is always less than or equal to the stored energy A, hence the value B in equation 2.3 is less than or equal to 1. Consequently, the device must be cleared before further multiplication.

2.3 Logic operations

The device can perform a sequence of OR operations on a sequence of binary arrays by writing the arrays sequentially onto the device with sufficient energy to cause the

Figure 2.7: Illustrating analog multiplication with luminescent rebroadcasting device.

device to saturate. From equation 2.1, addition is now interpreted as OR. The device can also perform a sequence of AND NOTs by successive reads with binary arrays B, C, D, etc. as indicated by equation 2.3 and assuming that A is an array of ones.

$$S = \overline{B} \cdot \overline{C} \cdot \overline{D} \cdots \tag{2.4}$$

Multiplication is now interpreted as AND. As $\overline{B} \cdot \overline{C}$ is equivalent to $\overline{(B + C)}$ or NOR, the system is capable of performing a sequence of NORs.

In some cases, the ability to perform alternative logic operations leads to more efficient implementation than using a simpler set. Table 2.1 shows 14 basic logic operations between two inputs[10]. Two trivial operations are excluded in which the output is zero for any input and for which the output is one for any input. The lower part of the table shows the sequence of incoherent writes and reads required to perform the corresponding logic operations with a single luminescent rebroadcasting device. Exceptions follow: generating exclusive OR (XOR) and exclusive OR negation require either coherent inputs out of phase by 180 degrees, or, like NAND, require multiple rebroadcasting devices. For the NAND, one device is needed to provide a complement of B. "All" refers to saturating the device all over. The "tn" where n = 1,2,3, or 4 refer to the exposure time sequence. Note that all the basic logic functions

CHAPTER 2. DEVICE CHARACTERIZATION

may be performed in four or less time steps.

Every complete logic set involves inversion. This may be performed by flooding the device all over to saturation. The pattern whose inversion is sought is used to spatially modulate the IR in order to remove energy from the device where the pattern is one. Those parts of the device not read out may now be read out with a uniform IR beam and represent the inverse of the pattern.

Figure 2.8 shows the results of 14 basic logic operations between two input patterns A and B. If we encode the patterns to their corresponding binary bit value as suggested in Figure 2.8, then all of those 14 Boolean logic operations can be done within four steps. Figure 2.9 shows an optical set up for implementing those operations. The apparatus is arranged in such a way that the Ar laser and IR laser come from different angles, which reduces the complexity of the experimental procedures.

CHAPTER 2. DEVICE CHARACTERIZATION

Table 2.1: Computing 16 basic Boolean logic functions (except all 0's and all 1's) with luminescent rebroadcasting device
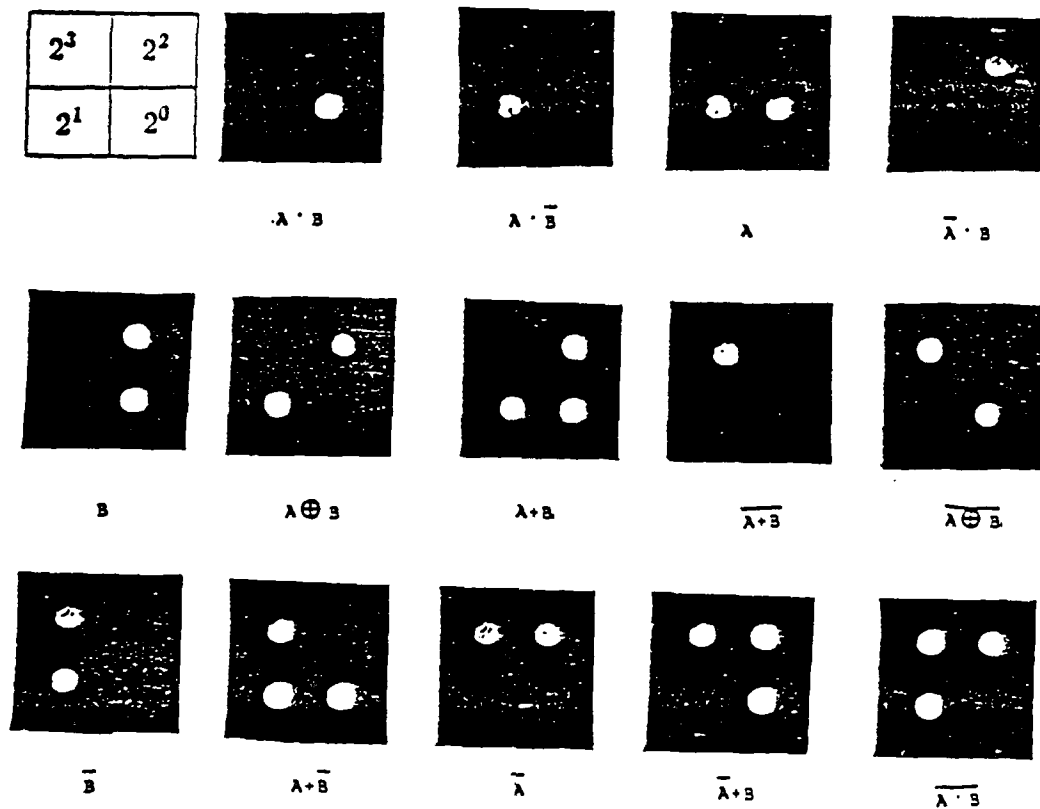
Figure 2.8: Computing 16 basic Boolean logic functions (except all 0's and all 1's) with luminescent rebroadcasting device

S: Shutter, BS: Beam Splitter, M: Mirror

Ar:Argon Laser, IR: Infared Laser

LR: Luminescent Rebroadcasting
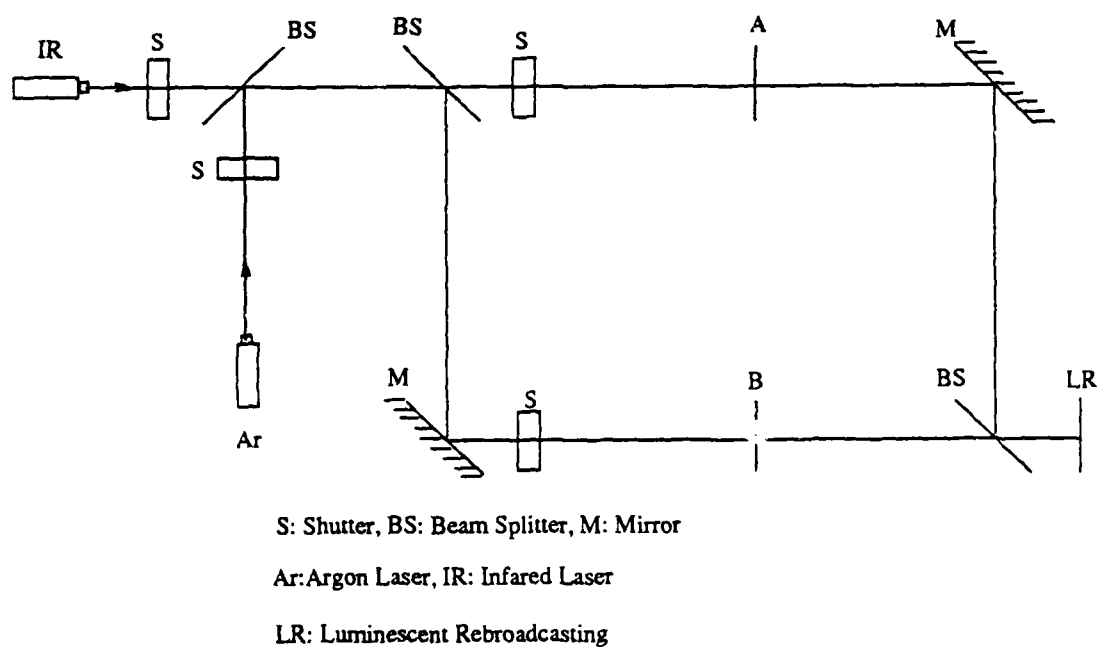
Figure 2.9: Optical set up for arithmetic and logic operations

Chapter 3

Optical LR associative memory

3.1 Correlation with LR devices

3.1.1 Optical dynamic matched filtering

Correlation in space domain

Shadow casting is an effective means of performing correlation[18] in the space domain [10]. The computation performed is

$$z = \sum_{i=1}^{n} \sum_{j=1}^{m} x_{i,j} y_{i,j} \qquad (3.1)$$

The procedure follows. The luminescent rebroadcasting material is cleared with sufficient exposure to IR and kept in the dark. Argon light is used to shadow cast the first image from a piece of film onto the material, Figure 3.1(a).

Writing occurs only where light passes through the film. An IR laser is used to pass light through the second image on a second piece of film so as to cast a shadow of the second image onto the material, Figure 3.1(b). Only where the IR strikes regions where electrons are stored will the material luminesce. A lens is used to collect the luminescent light. Consequently, the output intensity is greater for matching images. For example Figure 3.1(b) provides a greater intensity out than Figure 3.1(c) assuming input image areas are properly normalized.

Figure 3.2(a) shows the results of correlating an X with itself. Figure 3.2(b) shows the results of correlating an X with an O. Only the overlapping regions provide

Figure 3.1: Correlation in spatial domain by shadow casting

luminescence. Figure 3.3 shows the output intensity of correlation between X with X and X with O. Note the much higher peak intensity of correlation between X and X compared to X and O.

However, it is sometimes impossible for multiplicative correlation to distinguish between two similar character images such as E and F. To avoid confusion, a more sophisticated experimental procedure was designed as follows: Figure 3.4 shows that for each character image, two masks, one positive and one negative, were placed side by side. Argon laser light was passed through a writing mask containing both a negative and positive character E. An IR laser was used to pass light through a reading mask containing both a negative and positive character F. Since positive-negative pairs of F's were projected onto negative-positive pairs of E images, the luminescence observed was the bottom horizontal bar and represents a subtractive pattern, or difference, between the images. If and only if the two images are identical will there be no luminescence detected. Figure 3.5 presents experimental results of this subtractive correlation difference between an E and an F.

Matched filtering in the frequency domain

It is preferable to filter in the frequency domain because objects in the two images to be correlated do not have to line up in translation, i.e. the system provides shift invariance. The Fourier transform of a real image is complex so that complex image information must be stored in the filter. The Van der Lugt filter provides this capability [8]. However, it needs an order of magnitude higher resolution materials because the phase is stored by the position of a high spatial frequency carrier. Spatial light modulators available today do not have adequate resolution for this. Consequently, there has been much activity in phase-only filters [9].

Luminescent rebroadcasting materials are considered capable of achieving high enough resolution for storing complex functions. However, there are two difficulties. First the write and read frequencies are different. Second, present samples have too much back scatter to preserve coherence of light passing through the device. The first difficulty can be overcome with proper optical set up. The second problem requires different manufacturing methods and is currently under investigation by Quantex, the manufacturer of the materials.

(a)

(b)

Figure 3.2: Experimental results showing shadow casting results with luminescent rebroadcasting material: (a) X with X, (b) X with O
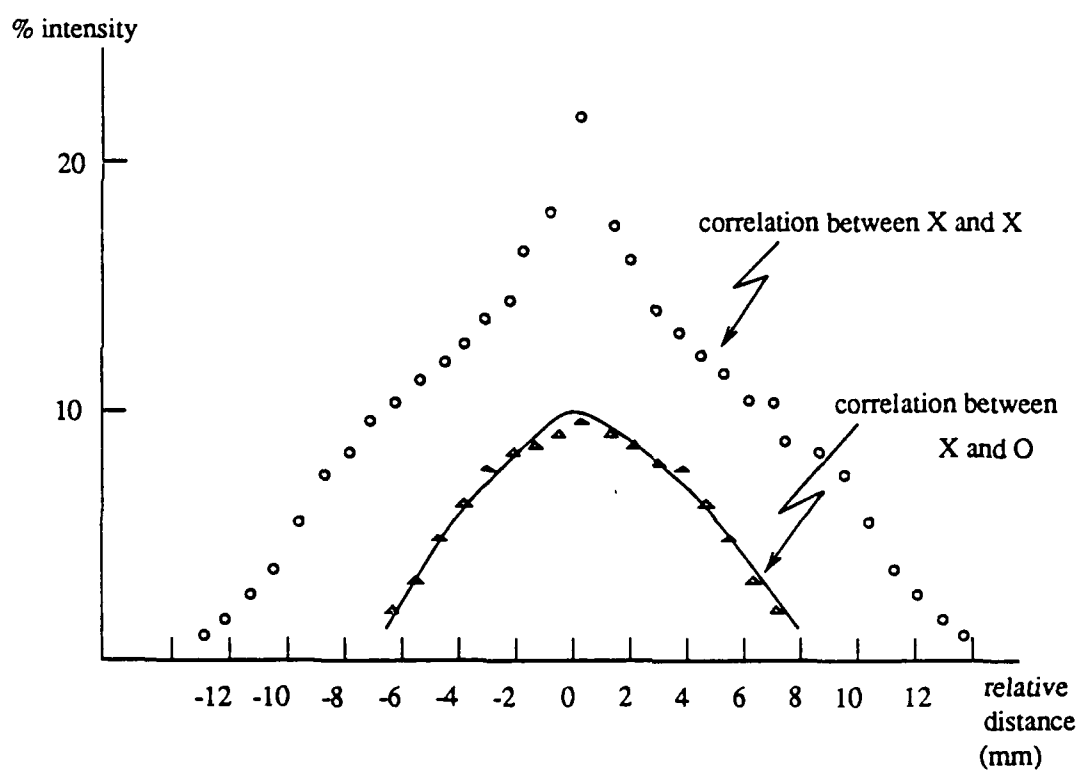
Figure 3.3: Experimental results showing the correlation results of X with X and X with O

Figure 3.4: Shadow casting between E and F with luminescent rebroadcasting device

(a)

(b)

(c)

Figure 3.5: Experimental results showing subtractive shadow casting between E and F
with luminescent rebroadcasting device:(a)image E (b)image F (c)pattern subtraction
between E and F

3.2 Symbolic substitution with LR devices

Search with symbolic substitution

With looping

The luminescent rebroadcasting device has a useful feature in comparison with other SLMs for associative memory search. It stores the current array for successive logic operations of the types discussed in equations 2.1 and 2.4. Figure 3.6 shows an optical system to implement word-parallel, bit-serial associative memory search with looping.

Lenses L_0 through L_5 are for the purpose of directing and collimating the beam through the system, and cylindrical lenses RL_1, RL_2, RL_3 are used for 2-D parallel search. Two luminescent rebroadcasting devices LR_1 and LR_2 are used for storing the database while electronically settable spatial light modulators $ESLM_1$ and $ESLM_2$ serve as IO(input-output) devices. The database is entered on $ESLM_1$ with associated data entered on the same row. For simplicity, frames are considered of fixed bit length and matching is described for which the search bit pattern is exactly one frame long. Blue light is used to image the data onto luminescent rebroadcasting device LR_1. The inverse is imaged onto LR_2 so that inversion is not required at each iteration of the loop shown. This avoids clearing the device frequently which takes a long time, as discussed earlier.

Associative memory search involves performing logic between the bit pattern stored in LR_1 or LR_2 and the output from a previous logic operation that is fed back via mirrors so that it is misaligned by one column. The feedback path has an image intensifier that provides gain and converts light frequency from orange to IR. Consequently, the parallel logic operation performed is AND between the array fed back and that stored.

The location of a linear pattern of bits may be found in parallel anywhere on the 2-D array LR_1 by entering the pattern to be matched in $ESLM_1$ and the inverse pattern in $ESLM_2$. As an example, suppose the pattern to be found in the data is a string of ones. The array ANDed with itself one column right will now have ones out only where there were two ones adjacent horizontally. A further iteration involving a further shift right and an AND will result in an output that has ones only where there were three adjacent ones in a row. This may be repeated a number of times equal to the length of the pattern sought. For a search pattern having ones and zeros the beam path is controlled such that the light will pass through the luminescent rebroadcasting device holding the inverse LR_2 whenever a zero occurs in the search
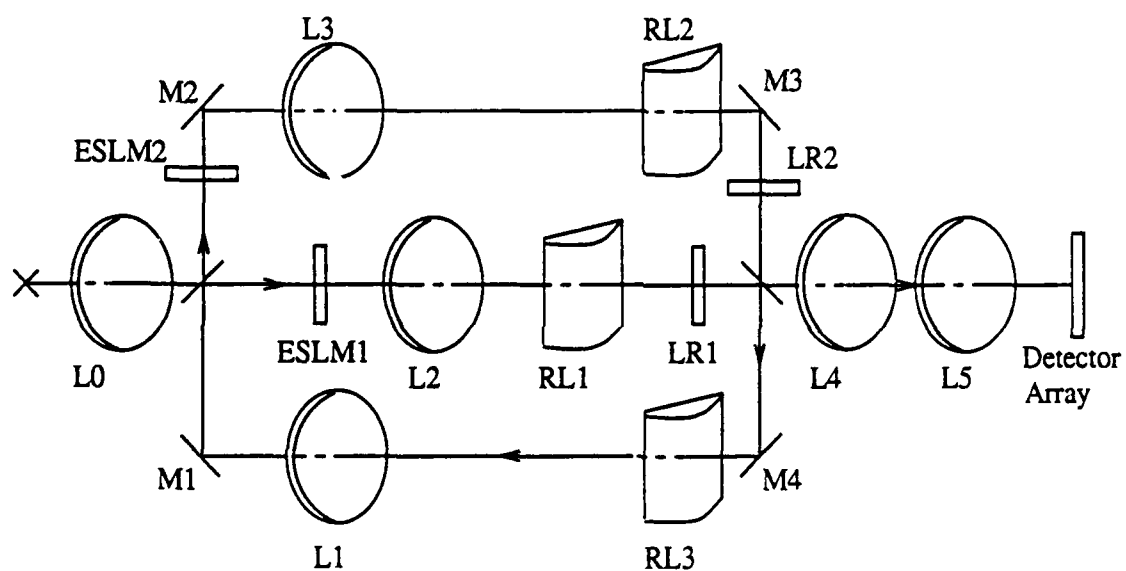
Figure 3.6: Parallel optical associative memory search with looping

pattern and to the device holding the data LR_1 whenever a one occurs in the search pattern.

The output will be one in the right most position of a frame only if the correct pattern is observed, moreover, there will be a one at the right most position for every instance of the pattern on the whole array. In an associative memory application the data corresponding to the lines with matching patterns is read out.

Without looping

The search mechanism described above involved a feedback loop. In order to maintain sufficient intensity of the light beam in consecutive loops, it is necessary to use an image intensifier. However, it is difficult to manufacture an image intensifier working from visible to-IR. Thus a design for associative memory search without looping was tested and the results are presented here. The basic idea here is the same as correlation in the space domain. However, the search pattern is composed of binary digital bits.

Figure 3.7 shows the optical set up of the design. LR_1 and LR_2 store the 2-D database and the inverted 2-D database, respectively. $ESLM_1$ stores the linear search pattern and $ESLM_2$ stores the inverted linear search pattern. LR_1 and LR_2 recorded the database before the search takes place. The cylindrical lens spreads the IR in the horizontal direction through $ESLM_1$ and $ESLM_2$. By precise adjustment of the mirrors those two IR wavefronts will meet in front of the imaging lens. Any matched pattern in the database will show a full range of bright spots in the imaging plane. Figure 3.8 presents the results of searching an 8-bit binary pattern. Note the matching of the fourth row of the database results in an eight-bright-spots pattern in the image plane, only partial or no bright spots appear in unmatched rows.

Substitution with LR devices

It is useful when modifying the database of an associative memory to be able to replace a pattern wherever it occurs in a 2-D array with another pattern [20]. Fig. 3.9 shows an optical system providing this capability for linear patterns. The IR feedback permits searches for a horizontal pattern of consecutive bits as before. After finding all instances of a pattern of bits device LR1 is cleared by flooding with IR and the output, indicating positions of the sought data, is used to write on LR1 via the blue feedback path.

The blue feedback is then used to stretch the isolated ones into a string of ones by writing to adjacent pixels at each iteration. The length of this string is that of the substitution pattern. A linear array of ones occurs on LR1 only where the original array matched the sought pattern. The replacement pattern repeated in every frame
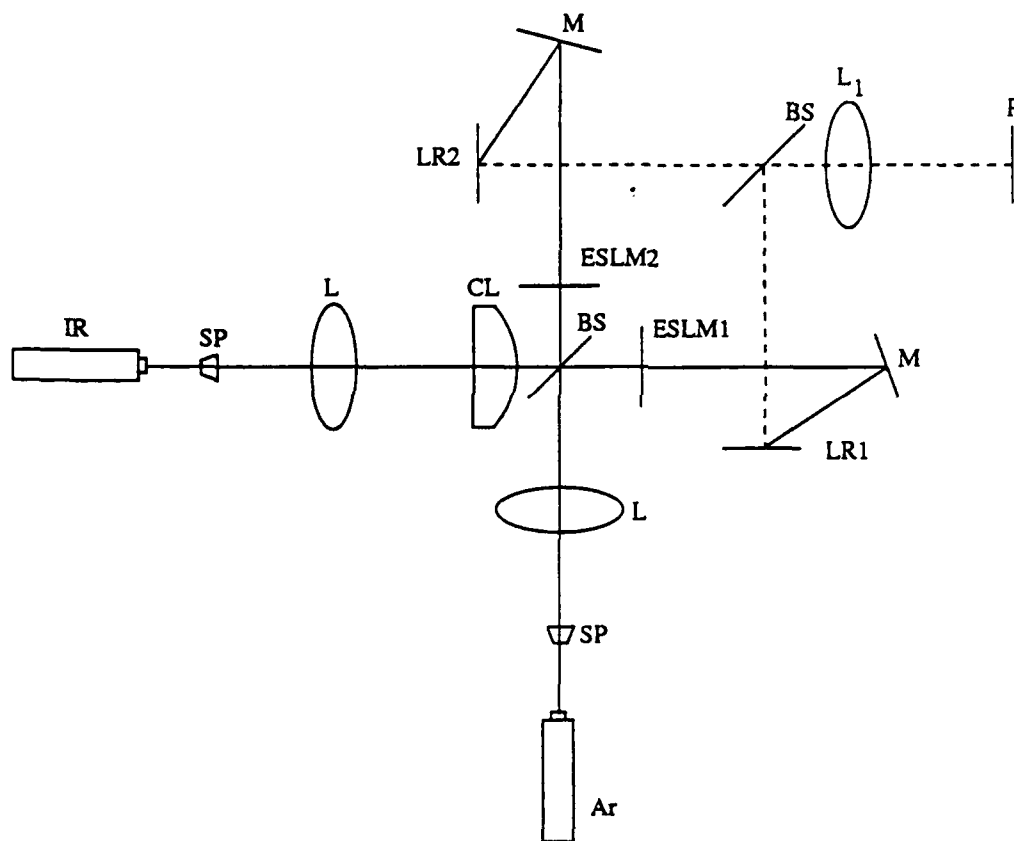
LR: Luminescent Rebroadcasting Material

ESLM: Electrically Addressable Spatial Light Modulator

L: Collimating Lens   SP: Spatial Filter

CL: Cylindrical Lens   BS: Beam Splitter

L_1: Imaging Lens   M: Mirror

P: Image Plane

Figure 3.7: Parallel optical associative memory search without looping

(a)

(b)

(c)

Figure 3.8: Experimental results showing associative memory search without looping: (a)searched pattern (b)database (c)result

Figure 3.9: Symbolic substitution for search and replacement

is entered on the ESLM and IR used to image this onto device LR1. Due to the AND operation the output now has the replacement pattern only in those locations where a match was found earlier. The result is stored in device LR4. The pattern stored on LR1, having ones only where the sought pattern occured, is read out by flooding with IR and is now stored in device LR3. This is replaced by its inverse at LR3 by flooding LR1 with blue, reading LR3, converting to IR and reading LR1, and then reading out the inverse in LR1 into LR3. LR1 can be left cleared. The original data is now entered into the ESLM and imaged onto device LR1 using blue light. Device LR3 is illuminated with IR and the output converted to IR to read device LR1. The stored array on LR1 is replaced with the original pattern modified to have zeroes wherever a pattern existed that matched that sought. Device LR4 is illuminated and the output converted to blue in order to OR with that stored on LR1. The result on LR1 is the original pattern with the new pattern wherever the original pattern matched the sought pattern. This may be used for future operations or read out with uniform IR illumination to the detector array.
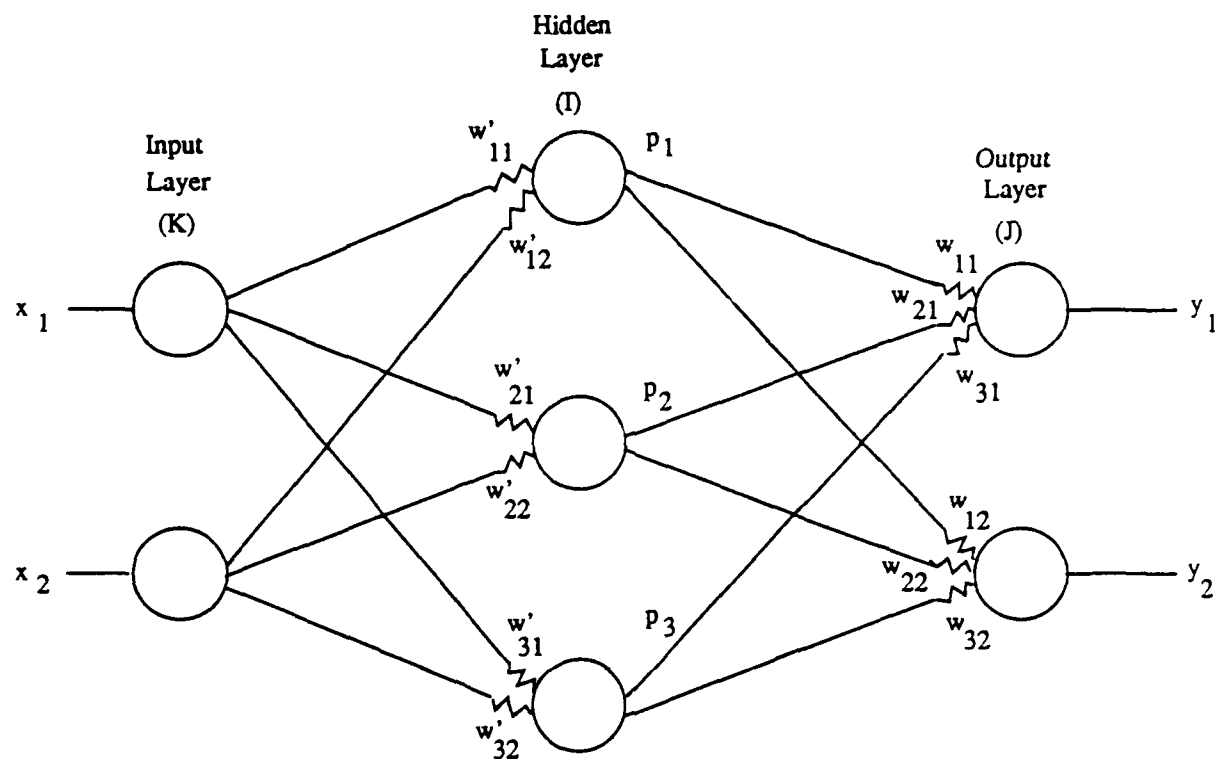
Figure 3.10: Neural network considered

3.3 Matrix-vector multiplication for neural networks

Neural network schemes are aimed at providing more flexible analog processing by means of learning. A popular nonlinear network is considered with J neurons in the output layer, I hidden neurons, and K neurons in the input layer, Figure 3.10.

The equations implemented by this network are

for $j = 1$ to J

$$y_j = f\left[\sum_{i=1}^{I} w_{ij} f\left(\sum_{k=1}^{K} w'_{ki} x_k\right)\right] \tag{3.2}$$

where

$$f(q_j) = (1 + e^{-q_j})^{-1} \tag{3.3}$$

This equation can be implemented using matrix-vector multiplication. An optical design for matrix-vector multiplication with LR devices will be presented in the following sections.

3.3.1 Analog matrix-vector multiplication with LR

To multiply a vector by a matrix, an astigmatic optical processor can be used[4][31][7][14]. The principle of analog matrix-vector multiplication[6][22] is shown in Figure 3.11. Prior to the multiplication, the analog values of the matrix are recorded on the luminescent rebroadcasting device. A low sensitivity film with different grey levels of transparency is created for writing. The film is illuminated by an argon laser to record the analog values of the matrix onto the LR device. The illumination energy must be within the linear operating region of the device in order to perform arithmetic operations. The vector is represented by a row of different grey levels on a film transparency. The cylindrical lens L_1 (Figure 3.11) spreads the IR uniformly in the vertical direction, thus projecting the different analog values of the elements in the vector to the LR device. Since the matrix values have been stored in the LR device earlier, the output luminescence now represents the resulting analog values of the matrix-vector multiplication (Section 2.2). The cylindrical-spherical lens combination L_2 images the results of multiplication and integrates horizontally, providing an output array of strips along a vertical line normal to the optical axis of the system thus forming sums of products. Figure 3.12 shows the details of matrix-vector multiplication while Figure 3.13 presents experimental results of a 3x3 matrix-vector multiplication. The different grey levels represent different analog values of the result.

Within the resolution of the device it is possible to perform matrix-vector multiplication to a much higher order. Figure 3.14 demonstrates the experimental result of a 10x10 matrix-vector multiplication.
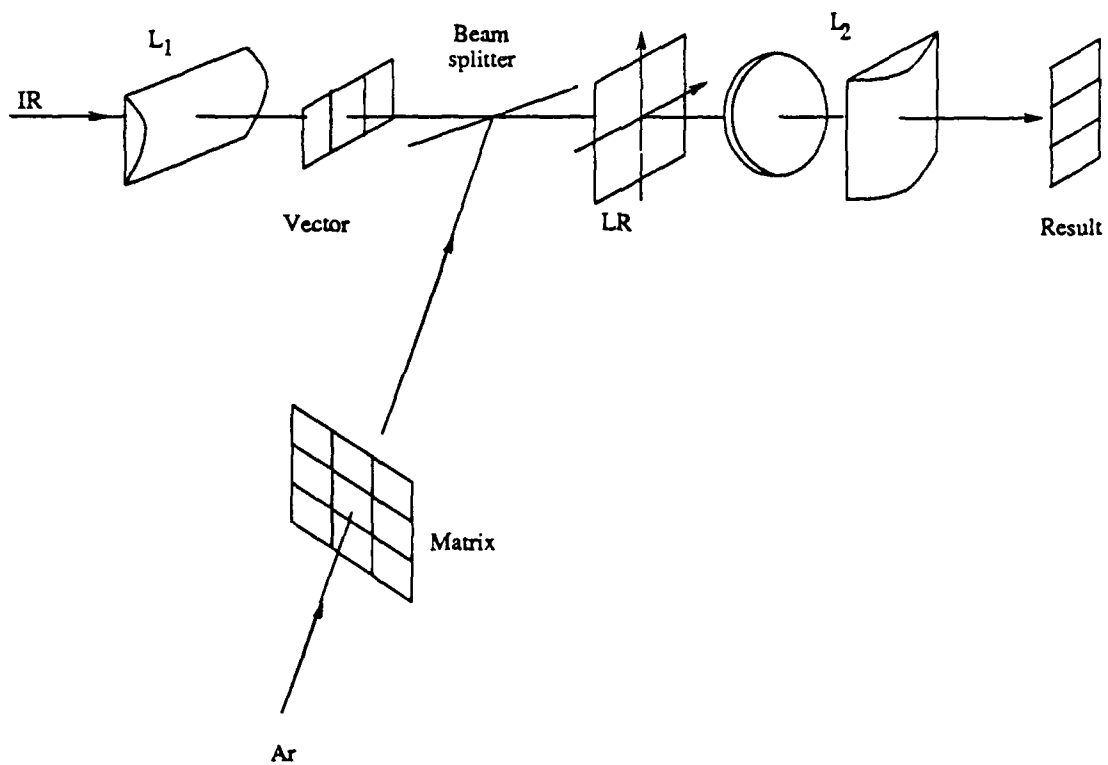
Figure 3.11: Optical set up of matrix-vector multiplication with LR device
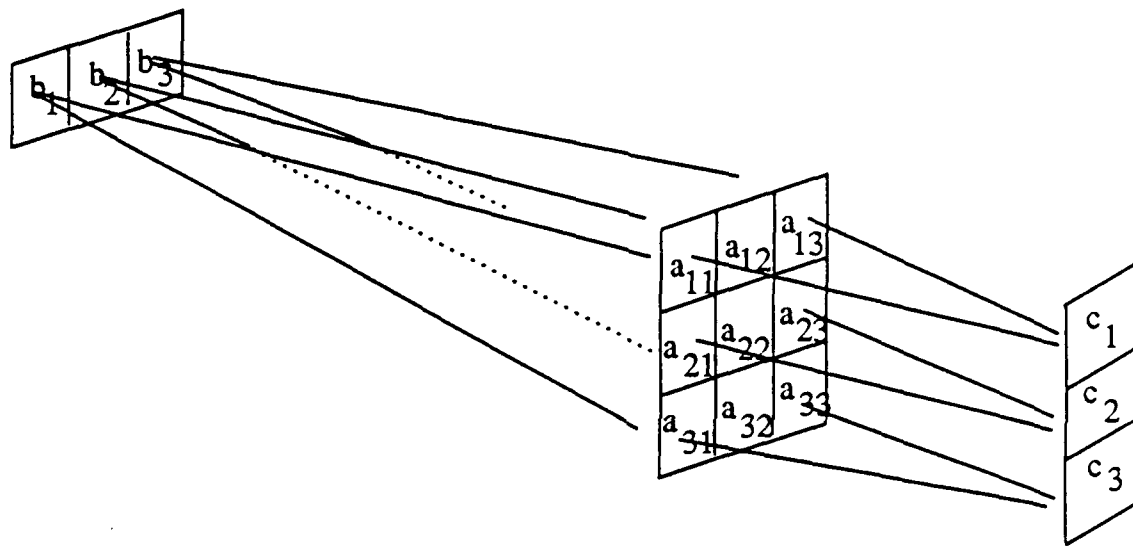
$$c_1 = a_{11}b_1 + a_{12}b_2 + a_{13}b_3$$

$$c_2 = a_{21}b_1 + a_{22}b_2 + a_{23}b_3$$

$$c_3 = a_{31}b_1 + a_{32}b_2 + a_{33}b_3$$

Figure 3.12: Principle of matrix-vector multiplication

(a)

(b)

(c)

Figure 3.13: Experimental result of a 3x3 matrix-vector multiplication (a) vector (b) matrix (c) result of multiplication

(a)

(b)

(c)

Figure 3.14: Experimental result of a 10x10 matrix-vector multiplication (a) vector (b) matrix (c) result of multiplication

Chapter 4

Comparison of AM approaches

Laboratory approaches for three proposed AM's are presented in chapter 3. Each of the approaches has its advantages and disadvantages. Generally speaking, all of the approaches take advantage of the high resolution(0.6 μ), high speed(nsec) and simple operating procedures of the LR. The disadvantage of the devices is that there is no gain so it is necessary to use an image intensifier in feedback optical systems to compensate for energy otherwise lost in propagating through the system. The three different wavelengths involved also pose problems for feedback systems.

4.1 Advantages and disadvantages of correlation AM using LR devices

4.1.1 Advantages

Optics has a distinct advantage in speed for multiple correlations of 2-D images because the correlation for an image is performed in parallel. The high resolution, memory behavior, and high speed of LR devices makes them suitable for highly parallel dynamic correlators or matched filters.

In chapter 3 section 3.1 we described some experimental results for correlation AM using LR devices in the space domain. Because of the fast reading and writing one can perform fast spatial correlation between a series of images against a previously recorded image.

4.1.2 Disadvantages

In order to perform correlation in the frequency domain for shift invariance, *it is* necessary to store complex images in a filter. The high resolution of LR devices makes it possible to store complex images on it. Correlation in the frequency domain requires a transmissive or reflective storage medium for which the output relative phase relationship is preserved. The LR devices available today provide an incoherent orange output and a scattered IR output because they do not have a clear transmissive capability. The scattering of the IR light from the back of the devices make it very hard to observe the correlation results. This is the main reason that the correlation was performed in the space domain for this project. The manufacturer is conducting research on transmissive LR devices and once the device is available, correlation in the frequency domain should be fairly easy to perform based on our experiences.

4.2 Advantages and disadvantages of symbolic substitution AM with LR devices

4.2.1 Advantages

Symbolic substitution differs from neural networks in that the information to be stored is entered directly rather distributed in the database as a result of learning. The difference between the search phase of symbolic substitution and correlation is that a digital technique is used so that an exact match to the input is made. However only part of the information sought need be supplied, e.g. a few consecutive letters anywhere in a name is sufficient to find all names in a database having this sequence of letters. Hence, the inexactness in addressing has a different form to a correlation system where an average correctness is required for the input.

Two optical systems designed to perform the search phase of symbolic substitution were presented in chapter 3, section 3.2. The biggest advantage of these systems is the ability to perform parallel search everywhere in the database. The length of the search pattern with the current designs is unlimited as long as a suitable image intensifier is available. After the search pattern is found one can substitute the desired pattern in a parallel fashion. With the fast reading and writing ability of LR devices one can search and substitute different databases in a rapid way.

4.2.2 Disadvantages

Optical symbolic substitution involves looping during searching and substitution. As the length of the search pattern increases, the number of loop iterations is increased and the intensity of light will decrease very quickly. To insure proper operations it is necessary to incorporate an image intensifier inside the loop. The intensifier is needed to convert luminescent light to IR or to enhance the input IR. Image intensifiers that meet the required specifications were not available for this effort. Available night-vision intensifiers work in the opposite way, i.e. they convert IR to visible light. Without a proper image intensifier the length of the search pattern is constrained. A binary subtractive digital correlator performed similarly to a spatial correlator and avoided the looping. However a row of spots must now be detected rather than a single spot for each match.

4.3 Advantages and disadvantages of neural network AM with LR devices

4.3.1 Advantages

A computer aided design example in structures was illustrated by the principal investigator in Ref. [23]. The AM provides good starting estimates for more accurate subsequent nonlinear parameter estimation in design [29],[30] or in other nonlinear parameter estimation situations [27],[24]. Similarly in complex real-time situations, such as the battle field, AM is expected to be faster than rule based systems.

The neural network AM differs from correlation by using learning to determine the distribution of information stored rather than explicitly storing the information. This permits adaption to the environment and possibly less requirement by the developer to understand the nature of the information stored. The goal of machine learning is to place a greater computational burden on the machine in order to decrease the effort by the human developer. A layer of the network in Fig. 3.10 was implemented using LR devices by means of an analog matrix-vector multiplier. Nonlinearity may be obtained from the natural saturation of the device. The optical system and the results were described in chapter 3, section 3.3. With the design shown in Fig. 3.11, the dimension of the matrix is only limited by the physical size of the lenses. A 100x100 matrix-vector multiplication is currently under investigation by the principal investigator.

The application of matrix-vector multiplication in neural networks is simpler than

for normal arithmetic computation. First, the detectors do not requires a large dynamic range because the network uses a clipping function at each stage. Secondly, high uniformity across the array is not needed because the learning will compensate for spatial differences. Thirdly, the weights representing values to be set on the LR device are adjusted rather than rewritten. Therefore, it is not necessary to clear the device which is time consuming for these devices. Further, the choice of wavelength determines whether the value is adjusted up or down.

4.3.2   Disadvantages

The speed of multiplication is limited by the speed of the electo-optic interface devices. The advantage of optics over electronics is greater for larger matrices because the optics has greater parallelism in the processing step. Larger matrix-vector multiplication, such as 500 by 500, is possible with the same optical approach and materials.

In order to have more than one layer it is necessary to have devices for which the output frequency for one is a match to the input frequency of the other. Such devices are possible but have not yet been constructed. A more expensive alternative is to have a frequency conversion unit such as an image intensifier. Such intensifiers are not presently available.

Chapter 5

Conclusion

Associative memory is becoming increasingly important in computer science because of the need for larger memories with fast recall. Three approaches to optical associative memory using luminescent rebroadcasting devices: correlations, neural networks and symbolic substitution were described. Experimental results and the comparison of advantages and disadvantages of each approach were presented.

Symbolic substitution is useful where a part of the data must be matched exactly while correlation allows an approximate fit to data. Neural networks are useful where interpolation or extrapolation is required or where adaption is needed. For example, where the search is for strings that are between those stored. Further an associated computer is assumed for performing learning.

The performance of the optical systems is severely limited by the availability of optical devices. Without a transmissive LR device, correlation is limited to the space domain which cannot provide shift invariance as would the frequency domain. Without an image intensifier for converting frequency and providing gain the symbolic substitution AM is constrained by the length of the search pattern. The development of transmissive LR devices and suitable image intensifiers is under investigation. Although very large matrix-vector multipliers are possible using LR devices, in order to produce a neural network with more than one layer, matching device pairs or suitable frequency changing intensifiers are needed.

Progress in device technologies suggests that all of the approaches considered may eventually be used for associative memory according to the requirements for the system. Therefore, the development of devices and systems for using such devices is strongly encouraged.

Chapter 6

References

1. Abu-Mostafa Y.S., and Psaltis D., "Optical Neural Networks", Scientific American, 1987.

2. P. Braunlich, J. Gasiot and M. Castagne, Appl. Phys. Lett. 39, 769(1981).

3. Brenner K.H., Huang A., Streibel N, " Digital Optical Computing with Symbolic Substitution," Applied Optics, Vol. 25, Sep. 1986, pp 3054-3064.

4. L. J. Cutrona, in Optical and Electro-Optical Information Processing, J. T. Tippett, D. A. Berkowitz, L. C. Clapp, C. J. Koester, and A. Vanderburgh, Jr., Eds(MIT Press, Cambridge, 1965).

5. Gasiot, J., and Braunlich, P., "Nanosecond Infrared Laser Stimulation of Luminescence in Rare-Earth Doped Sulfides", Appl. Phys. Lett. 40(5), 1982.

6. Goodman, J. W. and Woody, L. M., "Method for Performing Complex-Valued Linear Operations on Complex-Valued Data Using Incoherent Light", Applied Optics., Vol. 16, p. 2611, 1977.

7. J. W. Goodman, P. Kellman, and E. W. Hansen, Appl. Opt. 16, 733(1977).

8. J. W. Goodman, Introduction to Fourier Optics. New York: McGraw-Hill, 1968.

9. J. L. Horner, Ed. "Optical Signal Processing" Academic Press, 1987.

10. Ichioka, Y., and Tanida, J., "Optical Parallel Logic Gates using a Shadow Casting System for Optical Digital Computing", IEEE Proceedings, Vol. 72, 7, 1984.

CHAPTER 6. REFERENCES

11. R. D. Lawangar, C. S. Shalgaonkar, S. H. Pawar and A. V. Narlikar, Solid Commun. 10 (1972)1241.

12. W.Lehmann, J. Electrochem. Soc. 118(1971)1164.

13. Liu H.K., Kung S.Y., Davis J.A., "Real-Time Optical Associative Retrieval Technique" Optical Engineering, **25**, 7, 1986.

14. R. J. Marks, J. F. Walkup, M. O. Hagler, and T. F. Krile, "Ambiguity Function Display: An Improved Coherent Processor", Appl. Opt. 16, 746(1977).

15. McAulay, A.D, Wang, J., and Ma, C.T., "Logic and Arithmetic Operations with Electron Trapping Devices", *To be published.*

16. McAulay, A. D., Ma, Chen-Tai, Wang, Junqing: "Investigation of Luminescent Rebroadcasting Electron Trapping Device for Optical Computing", *to be published*

17. McAulay A. D., "Parallel Modular and Optical Supercomputer Architectures for Seismic Modeling and Inversion", Invited Chapter in Book, *Handbook of Geophysical Exploration*, 1988.

18. McAulay, A.D, Wang, J., and Ma, C.T., "Optical Dynamic Matched Filtering with Electron Trapping Devices", SPIE Real Time Signal Processing Conference, Aug. 1988.

19. McAulay A. D., "Optical Interconnections for Real Time Symbolic and Numeric Processing", Invited Chapter in Book *Optical Computing: Digital and Symbolic*, Marcel Dekker. N. Y. 1988.

20. McAulay A.D., "Optical Prolog Computer using Symbolic Substitution", Digital Optical Computing Symposium, SPIE O-E LASE, Jan. 1988.

21. McAulay, A.D., "Investigation of New Luminescent Rebroadcasting Devices for Optical Information Processing", Final Report, AFOSR USAF-UES Summer Faculty Research Program, 1987.

22. McAulay, A. D., "Spatial Light Modulator Interconnected Computers", IEEE Computer, Oct. 1987.

23. McAulay A. D., "Engineering Design Neural Networks using Split Inversion Learning", IEEE First Internl. Conf. on Neural Networks, 1987.

24. McAulay A. D., "Plane-Layer Prestack Inversion in the Presence of Surface Reverberation", Geophysics, Vol. 51, No 9,(1986).

CHAPTER 6. REFERENCES

25. McAulay A. D., "Optical Crossbar Interconnected Signal Processor with Basic Algorithms", Optical Engineering, Vol. 25, No. 1, 1986.

26. McAulay A. D., "An Extendable Optically Interconnected Parallel Computer", IEEE-ACM Fall Joint Computer Conf., Proceeding, Vol. 1,(1986).

27. McAulay A. D., "Prestack Inversion with Plane-Layer Point Source Modeling", Geophysics, Vol. 50, No. 1, 77-89, Jan. 1985.

28. McAulay A. D., "Predictive Deconvolution of Seismic Array Data for Inversion", IEEE ICASSP, 180-183, 1985.

29. McAulay A. D., "Variational Finite Element Solution of Dissipative Waveguides and Transportation Application", IEEE Trans. Microwave Theory and Techniques Vol. MTT-25, No-5, 382-392(may 1977)

30. McAulay A. D., "The Finite Element Solution of Dissipative Electromagnetic Surface Waveguides", International Journal for Numerical Methods in Engineering Vol. 11, No.1, 11-25, 382-392, (January 1977).

31. P. N. Tamura and J. C. Wyant, in Optical Information Processing, Proceedings of the SPIE, Vol. 83,97(1976).

FINAL REPORT

AUTOMATED TRANSLATION
OF DIGITAL LOGIC EQUATIONS
INTO OPTIMIZED VHDL CODE

Mr. John Evan Stark,   Graduate Research Assistant
Dr. George W. Zobrist,   Principal Investigator

Department of Computer Science
University of Missouri - Rolla
Rolla, Missouri 65401

August 31, 1988

Contract No: F49620-85-C-0013/SB5851-0360

ABSTRACT

It was desired to develop an algorithm for the automated translation of finite state machines from state table form to optimized VHDL form. To do this, algorithms are needed for reducing the state machine to simplest form, making state assignments, producing minimal logic equations to represent the state machine, and producing VHDL code which describes the intended circuit. Various such algorithms were examined and a prototype program written to perform this translation.

A. INTRODUCTION

It was desired to develop an algorithm for the automated translation of finite state machines from state table form to optimized VHDL form. The translation process involves reducing the state machine to its simplest form, making state assignments, producing minimal logic equations to represent the state machine, and producing VHDL code which describes the intended circuit.

A finite state machine is a model of a sequential logic network. The term sequential indicates that its outputs are dependent not just on its current inputs but also on past inputs. This is accomplished by use of a memory. Rather than attempt to keep track of all past inputs, a finite number of states are used, each of which represents an equivalent set of input histories. Each input may cause the machine to enter a new state and affect its output. An electrical circuit for a finite state machine includes inputs, a combinational logic part, a memory, and outputs as shown in figure 1.
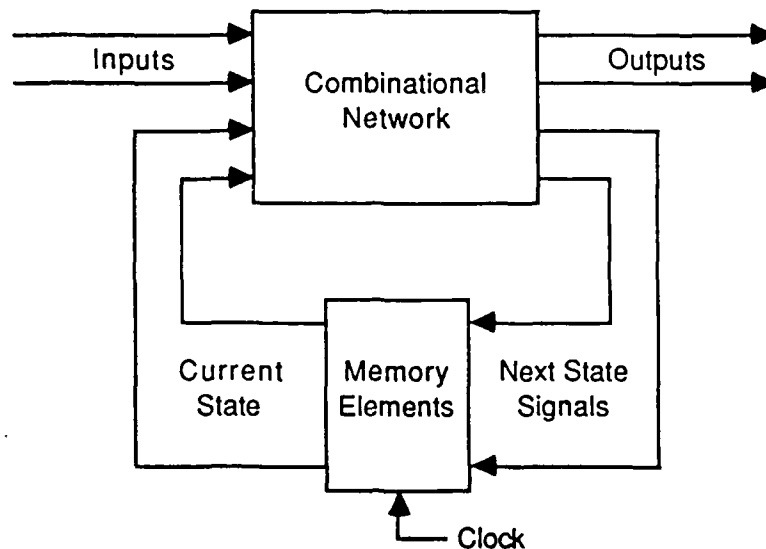
Figure 1.   Sequential Network

VHDL is a hardware description language intended for the design, description, and simulation of electrical hardware systems and components. The description of an object is in two parts, an interface and an architecture. This allows for separation of function and implementation. For versatility objects can be described by behavior, structure, data flow, or any combination of the three. [11, 12] See appendix A for a more detailed description.

Only completely specified, synchronous, single input/single output machines were considered for the translation from state table to VHDL form. A prototype program, FSM, (appendix B) to perform this translation was written using Pascal on an IBM PC. The following sections outline algorithms available and identify those used for the prototype program. Complete examples of the process of translating a state table to logic equations is given in appendix D.

B. FROM STATE TABLE TO LOGIC EQUATIONS

1. State Table Simplification.

A state table is a collection of transitions between states and the outputs produced either at the state (a Moore machine) or on transition between states (a Mealy machine--used by FSM, the prototype program) [3]. Figure 2 shows a transition diagram and corresponding state table for a finite state machine.

Q	Q+		Z	
	X=0	1	X=0	1
0	0	1	0	0
1	2	1	0	0
2	0	1	0	1
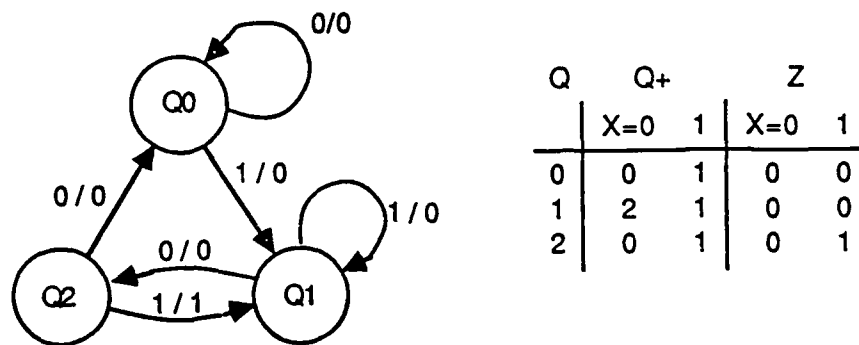
Figure 2.   Transition Diagram and State Table

Input for the prototype program, read from a file, includes a short (80 character) description of the finite state machine, the number of states in the machine, and the state transitions. Each transition is specified by its next state and associated output. Since only completely specified single input/single output machines are considered, there are exactly two transitions for each state. States are initially assumed to be numbered sequentially starting with zero which is assumed to be the initial state. Additional input accepted directly from the user consists of the name the finite state machine is to be given in the VHDL code, the name of the file containing the state transitions, the name of the file to which the VHDL code is to be written, the type of

flipflop to use and its delay time, and the implementation of the combinational logic and its delay.

Reducing the number of states in a state machine can reduce the number of memory elements needed to represent the states of the machine and help minimize the combinational logic used to determine the machine's outputs and next states. To reduce a state table to its simplest form, unnecessary states must be removed. These include redundant, unreachable, and equivalent states. As redundant states are equivalent states they need not be considered separately although algorithms exist for their removal. Unreachable states however can only be equivalent to other unreachable states and must therefore be handled separately.

Removal of unreachable states is accomplished by creating a set of reachable states [4]. Initially only a known reachable state, the initial state, is a member of this set. An iterative process is then set up in which the next states of each member of the reachable set are added to the set (if they are not already members). When no more states can be added, the set is complete and any states not in the set are unreachable and can be removed from the state table. References to these unreachable states as next states of reachable states need not be considered in their removal as there can be none.

Removal of equivalent states can be handled by use of equivalence sets [1] or an implication table [3]. In either case all states are at first considered to be equivalent and equivalences are then ruled out. When the equivalent states of the state table have been identified, all but one of the states in each group of equivalent states are removed from the state table and all references to them as next states are replaced by the state kept.

Q	Q+		Z	
	X=0	1	X=0	1
0	1	7	0	0
1	7	0	0	1
2	8	7	0	1
3	7	4	0	1
4	3	2	0	0
7	3	7	0	1
8	2	0	0	1

a) state table after removal
of unreachable states

b) implication table

$$I = \{\underset{2222}{0\ 4}\} \qquad II = \{\underset{21\ 22\ 21\ 22\ 21}{1\ 2\ 3\ 7\ 8}\}$$

$$I = \{\underset{2323}{0\ 4}\} \qquad II = \{\underset{31\ 31\ 31}{1\ 3\ 8}\} \qquad III = \{\underset{23\ 23}{2\ 7}\}$$

c) equivalence sets

Q	Q+		Z	
	X=0	1	X=0	1
0	1	2	0	0
1	2	0	0	1
2	1	2	0	1

d) with equivalent states removed

Figure 3.   Equivalent State Removal

With an implication table (figure 3b), one entry exists for each possible pairing of states with the exception of pairing a state with itself. A mark is placed in an entry when that pair is known not to be equivalent. The first of these marks are placed on the basis of differing outputs of the states' transitions as states with differing outputs cannot be equivalent. The remaining entries are then checked in repeated passes of the table on the basis of the states' next states. When a pair of next states for an entry have been found not to be equivalent, that entry can be marked. When a pass yields no additional marks, the remaining unmarked entries indicate equivalent states.

When using equivalent sets (figure 3c), the states are first divided into separate sets according to the outputs of their transitions to next states. For the iterative part of this process the states in each set are assigned a subscript for each transition indicating which set its next state is in. Each set is then broken down further into new sets for which the subscripts of all member states match. This is repeated until no new sets are created. At this time, each set contains only equivalent states. The use equivalent sets was chosen over an equivalence table for the prototype program because of the simpler data structure.

2. State Assignment.

In the circuit implementation of a finite state machine each state is represented by a binary n-tuple which is a concatenation of the values of the memory elements when the machine is in that state, n being the number of memory elements. The choice of these n-tuples, or state assignments, can affect the minimization of the combinational logic part of the circuit. For a given machine there are 2^n possible state assignments. Story [10] gives the number of possible combinations of assignments as

$$\frac{(2^n - 1)!}{(2^n - R)!n!}$$

where R is the number of states in the machine. Thus as the number of states grows large, the number of possible state assignments and their possible combinations grows very large. Currently, there is no method for determining an optimal state assignment without comparing the results of assignments through trial and error. Story [10] does offer a method of reducing the number of assignments which need to be checked. The prototype program uses the natural assignment method which consists of numbering the states sequentially starting with zero.

3. Karnaugh Map Production.

Karnaugh map representations of the machine outputs and next state signals are created to help in the production of the logic equations [3]. Two maps are required for each JK or RS flipflop, one is required for each D flipflop, and one for each state machine output. The prototype program can produce VHDL descriptions using JK, RS, or D type flipflops. Maps are represented internally by a list of on-cells and a list of don't-care-cells. All cells not listed are off. Figure 4 shows the production of J and K maps for one memory element of a finite state machine.

Story [10] gave formulas for finding on-cells and don't-care-cells for the Karnaugh maps for JK flipflops:

$$J = \sum_{j=0}^{R-1}(1 - y_j)Q_j\sum_{i=0}^{2^n}y_{ji}X_i + d(\sum_{j=0}^{R-1}y_jQ_j + \sum_{j=R}^{2^m}Q_j)$$

$$K = \sum_{j=0}^{R-1}y_jQ_j\sum_{i=0}^{2^n}(1 - y_{ji})X_i + d(\sum_{j=0}^{R-1}(1 - y_j)Q_j + \sum_{j=R}^{2^m}Q_j)$$

where j is the state table row index, i is the input index, R is the number of states, n is the number of inputs, m is the number of flipflops, y and y represent the current and next state values of the flipflop, QX (rather than SX used by Story) represents the cell number (a concatenation of current state and input), Q represents a grouping of cell numbers (two cells for a single input machine) for when the input values do not matter, and d (Story uses 0.5) indicates don't-care-cells. Formulas for RS and D flipflops can be written similarly:

$$S = \sum_{j=0}^{R-1}(1-y_j)Q_j\sum_{i=0}^{2^n}y_{ji}X_i + d(\sum_{j=0}^{R-1}y_jQ_j\sum_{i=0}^{2^n}y_{ji}X_i + \sum_{j=R}^{2^m}Q_j)$$

$$R = \sum_{j=0}^{R-1}y_jQ_j\sum_{i=0}^{2^n}(1-y_{ji})X_i + d(\sum_{j=0}^{R-1}(1-y_j)Q_j\sum_{i=0}^{2^n}(1-y_{ji})X_i + \sum_{j=R}^{2^m}Q_j)$$

$$D = \sum_{j=0}^{R-1}Q_j\sum_{i=0}^{2^n}y_{ji}X_i + d\sum_{j=R}^{2^m}Q_j.$$

The type of memory element chosen for a circuit can also affect the minimization of the combinational logic part of the circuit. The only method of determining which type will yield minimal results is trial and error. There are however only a limited number of common types available. The decision of which type to use is left to the user of the program, as other factors than just minimization may be relevant. No provision is made for mixing flipflop types in a single machine circuit.

4. Logic Equation Production.

It is desirable that the logic equations describing a finite state machine have both a minimal number of gates and a minimal number of gate levels. Fewer gates means cheaper production costs and fewer gate levels means faster operation.

Q	Q+	
ABC	X=0	1
000	010	010
001	000	000
010	101	011
011	001	001
100	000	000
101	100	001

$$J_A = 1[4] + d[8+9+10+11+12+13+14+15]$$

$$K_A = 1[8+9+11] + d[0+1+2+3+4+5+6+7+12+13+14+15]$$
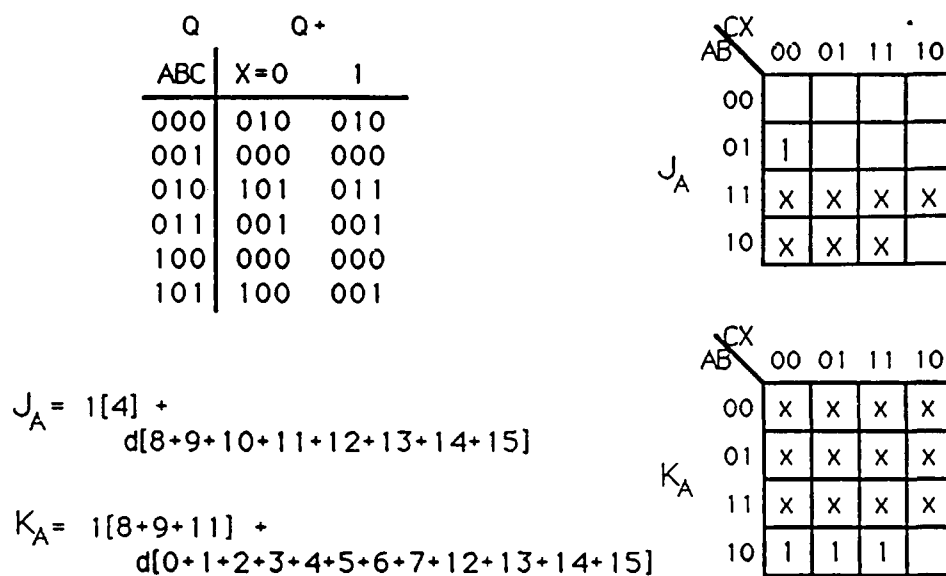
Figure 4.   Karnaugh Maps

Toward these ends the prototype program produces minimal two-level sum of products equations using only NOT, AND, and OR operations.

The standard procedure for producing logic equations from Karnaugh maps is the Quine/McCluskey [5, 7] method (figure 5b). With this method a list of the on-cells and don't-care-cells, called implicants, is made. They are grouped according to the number of 1 bits in their binary representations. Each implicant in a group is combined with as many implicants in the following group (implicants with one more 1 bit) as possible, forming new implicants which are grouped separately according to number of 1 bits. An implicant may be combined with another if their binary representations match except in one position (e.g. 0010 and 0110). The bit position in which the two differ is replaced by a don't-care-symbol (e.g. 0-10 or 0x10). In combinations involving implicants with don't-care positions, the don't-care positions must match exactly in both implicants. The implicants which combine to form a new implicant are marked as such. When no new implicants can be formed, an implicant table is made from the implicants which have not been marked.

$$S_C = 1[0+4+5+8+9] + d[2+7+10+11]$$

a) Karnaugh Map Equation
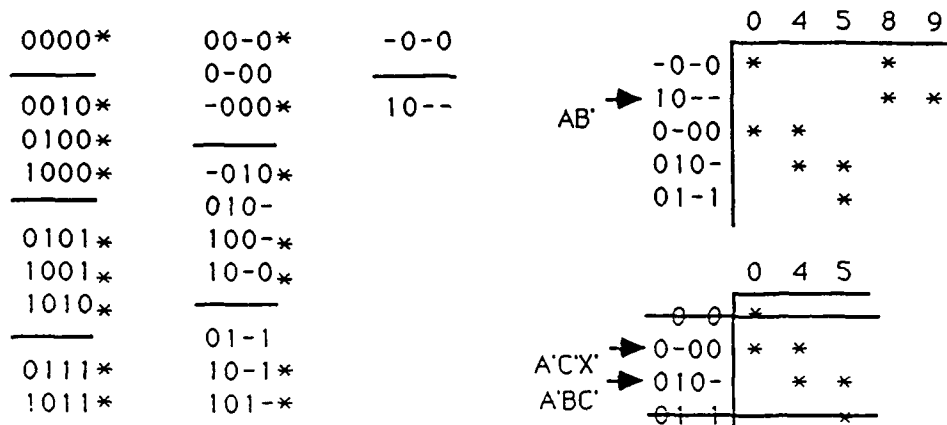
b) Quine/McCluskey method
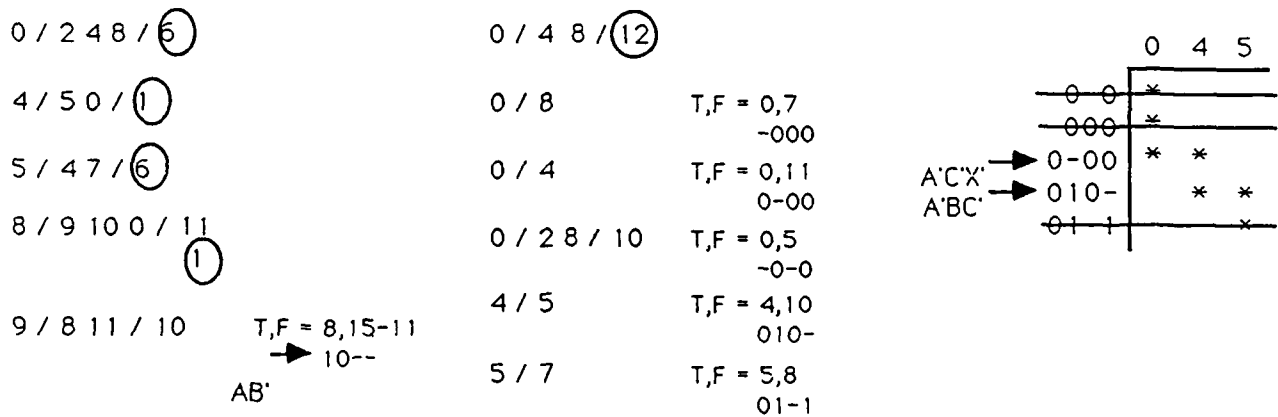
c) Prather Method

$$S_C = AB' + A'C'X' + A'BC'$$

d) Final Logic Equation

Figure 5.   Logic Equation Production

The implicants become the rows of the implicant table arranged so that priority is given to the number of on-cells covered and the number of don't-care positions (indicating fewer literals and thus fewer gate inputs). The columns of the implicant table are labeled by the on-cells of the map. Entries of a row which are in columns that represent on-cells covered by the implicant are marked.

A prime implicant is one which alone covers an on-cell (is the only implicant with an entry in that column marked). Prime implicants are essential to the equation and are removed from the table along with the columns they cover and become the basis of the equation. All remaining columns are now covered by two or more implicants. Implicants may be removed from the table without affecting it if they are dominated. One implicant dominates another if for every column covered by the second, the first also covers that column. If two implicants dominate each other and one has fewer don't-care positions, it should be removed; otherwise the decision is arbitrary. If removing dominance from the table leaves columns which are covered by only one implicant, those implicants should be selected--removed from the table along with the columns they cover and added to the equation. If no columns are covered by only one remaining implicant, then an implicant must be chosen by other means. Normally the implicant chosen is the one highest in the table covering a column having the least number of implicants covering it. The process of removing dominance and chosing implicants is repeated until the implicant table is empty. The equation is now complete. While the equation may not be unique, it is minimal.

A modification of the Quine/McCluskey method was given by Prather [6] (figure 5c). This technique identifies essential cells (prime implicants) by attempting to complete for each on cell the ncell indicated by adjacent on-cells and don't-care-cells. If this ncell can be completed, it is essential to the equation. If not, then the basic (nonessential) cells which cover the first cell can be found by attempting to complete the ncell without one or more of the original adjacent cells.

First all essential ncells are found and the cells they cover marked. Then all basic cells are found for those on cells not yet covered and used to form an implicant table which is reduced as above.

An ncell is completed by checking to see if all the necessary cells are either on or don't-care. The on-cells and don't-care-cells adjacent to the cell to be covered are identified first. The number of these adjacent cells indicates the size of the ncell and, as a power of two, the number of individual map cells covered (e.g. three adjacent cells indicate a 3cell covering eight cells, zero indicates a 0cell covering one cell). The next group of cells are identified by adding the delta of each original adjacent cell to each of the following adjacent cells. New groups of cells are found until one contains only a single cell, at which time the ncell is complete, or until an indicated cell is neither an on-cell nor a don't-care-cell. If the ncell cannot be completed, an attempt to find basic cells can be made by omitting each of the original adjacent cells, one at a time, whose delta was involved in identifying the cell which failed to compete the ncell. The Prather method was the method chosen for the prototype program as it was easier to represent.

C. VHDL DESCRIPTION OF A FINITE STATE MACHINE

The prototype translation program produces two files as output. One is a trace of its operation including the initial state table, simplified state tables, Karnaugh map representations, essential cells and implicant tables for those equations with nonessential cells, complete equations, and timing of operation. The other file is the VHDL source code of the finite state machine, a combination of structural and behavioral descriptions. VHDL version 7.2 was used for this file. Syntax was checked for correctness with the VHDL Analyzer. Sample output for these files can be found in appendix D.

The VHDL code description of the state machine is produced with the use of a template file (appendix C) containing markers indicating the information needed. Markers in the template are set off from the code by brackets. When in copying the VHDL code file from the template a marker is found, it is identified and replaced by its substitution string. Substitution strings, with the exception of the actual logic equations, are determined from parameters prior to writing the VHDL code file. The logic equations are formulated from their internal representation and written when the logic marker is found.

D. CONCLUSIONS

The logic equations for the the finite state machines in the examples shown in appendix D were checked for correctness and if from a text, compared to the solution given where possible. The example solutions were also compared, appendix E, with the output of Meg [9], a state machine equation generator.

The VHDL output of four of the examples in appendix D (examples 1, 5, 6, and 7) was run with the 1076/B VHDL Simulator. As the original VHDL code was version 7.2, some minor changes were required to make the machines run. They did, however, perform as expected.

At present the translation program is not software interfaced to any other programs for input or output. The VHDL output file could be used as a source file for simulation or simply as a circuit description.

Following are some possible extensions to the program. A graphical interface for input would be useful. The handling of asynchronous, multi-input/multi-output, and incompletely specified state machines would make the program more realistic in terms of use. Version 7.2 of VHDL was used for the prototype program as that was the latest version of the analyser available. A more recent version would be desired for actual use. Also, standard library components for the flipflops would make the designs more compatible with existing systems and allow greater device independence. The examination of various state assignments would ensure that the final logic equations were indeed the minimal possible. Interfacing the VHDL with EDIF [2] would allow graphical representation of the electrical circuit.

BIBIOGRAPHY

1. Dietmeyer, Donald L. "Synchronous Sequential Networks", in Logic Design of Digital Systems. Allyn and Bacon, Inc., 2nd ed., 1978.

2. EDIF Electronic Design Interchange Format. Electronic Industries Association, Ver. 2 0 0, May 1987.

3. Hill, Fredrick J. and Gerald R. Peterson. Introduction to Switching Theory and Logical Design. John Wiley and Sons, 3rd ed., 1981, pp. 96-337.

4. Hopcroft, John E. and Jeffrey D. Ullman. "Simplification of Context-Free Grammars", in Introduction to Automata Theory, Languages, and Computation. Addison-Wessley Publishing Company, 1979.

5. McCluskey, Jr., E. J. "Minimization of Boolean Functions", The Bell System Technical Journal. Vol. 35, November 1956, pp. 1417-1444.

6. Prather, Ronald. "Computational Aids for Determining the Minimal Form of a Truth Function", Journal of the Association for Computing Machinery. Vol. 7, No. 4, October 1960, pp. 299-310.

7. Quine, W. V. "The Problem of Simplifying Truth Functions", The American Mathematical Monthly. Vol. 59, No. 8, October 1952, pp. 521-531.

8. Roth, Charles H. Fundamentals of Logic Design. West Publishing Company, 2nd ed., 1979, pp. 221-349.

9. Scott, Walter S., et. al. editors. "Meg", in Berkeley CAD Tools. University of California, 1986 ed., December 1985.

10. Story, James R. et. al. "Optimum State Assignment for Synchronous Sequential Circuits", IEEE Transactions on Computers. Vol. C-21, No. 12, December 1972, pp. 1365-1373.

11. VHDL Language Reference Manual. Intermetrics, Inc., Ver. 7.2, August 1985.

12. VHDL Language Reference Manual. CAD Language Systems, Inc., Ver. 1076/B, May 1987.

Appendices can be obtained from
Universal Energy Systems, Inc.

ANALYTICAL MODEL AND COMPUTER PROGRAM

OF

F-16 NOSE GEAR AND F-16 ALGS

BY

GEORGE R. DOYLE, JR.

UNIVERSITY OF DAYTON

MECHANICAL ENGINEERING DEPARTMENT

300 COLLEGE PARK

DAYTON, OHIO   45469

AUGUST 1988

FINAL REPORT FOR PERIOD APRIL 1987 - JULY 1988

A = amplitude (trough to peak) of versine (1 - cosine), in.

A_i = coefficients of fifth-order polynomial defining force/displacement characteristic

A_h = effective hydraulic piston area, in^2.

A_o = area of hydraulic orifice, in^2.

A_{oe} = effective flow area through hydraulic orifice, in^2.

A_p = effective pneumatic piston area, in^2.

B = bulk modulus of hydraulic fluid, psi

C_d = discharge coefficient for hydraulic orifice

C_h = quadratic hydraulic damping coefficient, $lb-s^2/in^2$.

C_t = effective linear viscous damping coefficient of tire, lb-s/in.

D_b = bottom out deflection of tire, in.

D_e = effective diameter of chamber that will expand due to internal pressures, in.

D_t = deflection of tire (positive for compression), in.

E = Young's modulus of walls of chamber that will expand due to high internal pressure, psi

F_f = sliding friction force between the pneumatic and hydraulic chambers, lb

F_{ge} = stiffness force between the pneumatic and hydraulic chambers when fully extended, lb

F_h = hydraulic damping force, lb

F_{hp} = sum of hydraulic damping and pneumatic stiffness forces, lb

F_1 = length of flat in Class B bump, in.

F_p = pneumatic stiffness force, lb

F_t = compressive (positive) force in tire, lb

F_t' = total force in tire due to tire compression, bottoming out, and damping, lb

K_b = effective linear stiffness of rim when tire bottoms out, lb/in.

L = aerodynamic lift on nose, lb

L_e = effective length of chamber that will expand due to internal pressures, in.

L_w = wavelength of versine, in.

M_n = effective mass of aircraft nose, $lb\text{-}s^2/in.$

M_p = effective mass of floating jump piston, $lb\text{-}s^2/in.$

M_w = effective mass of wheel, $lb\text{-}s^2/in.$

P = pressure, psia

P_a = atmospheric pressure, psia

P_h = pressure in hydraulic fluid, psia

P_i = initial pressure in pneumatic chamber, psia

P_j = pressure under floating jump piston, psia

P_p = pressure in pneumatic chamber, psia

Q_e = effective flow rate of hydraulic fluid through orifice, in^3/s

Q_i = ideal flow rate of hydraulic fluid through orifice, in^3/s

R_h = height of up and down ramps of Class B and E obstacles, in.

R_l = length of up and down ramps of Class B and E obstacles, in.

S = displacement between pneumatic and hydraulic chambers (stroke-positive for compression), in.

S_{pmax} = maximum distance that floating piston can travel when system is in static equilibrium, in.

T = simulation time, s

T_h = temperature of hydraulic fluid, F

t_w = effective thickness of wall of chamber that will expand due to internal pressures, in.

T_o = simulation time at which tire initially contacts the obstacle, s

T_t = simulation time at which the tire has completely traversed the obstacle, s

T_1 = simulation time at which the tire leaves the up ramp of the Class B or E obstacle, s

T_2 = simulation time at which the tire contacts the down ramp of the Class B or E obstacle, s

V = volume, in^3.

V_c = change in hydraulic fluid volume due to high internal pressures, in^3.

V_e = change in pneumatic chamber volume due to high internal pressures, in^3.

V_h = velocity of hydraulic fluid in hydraulic chamber away from orifice, in/s, or volume of hydraulic fluid under 14.7 psia, in^3.

V_i = initial volume of gas in pneumatic chamber, in^3.

V_p = volume of gas in pneumatic chamber, in^3.

V_1 = longitudinal velocity of aircraft, in/s

V_o = velocity of hydraulic fluid through orifice, in/s

W_n = effective weight of aircraft nose, lb

W_p = effective weight of floating jump piston, lb

W_w = effective weight of wheel, lb

Y_o = vertical height (displacement) of obstacle, in.

Y_n = displacement of aircraft nose with respect to static equilibrium position, in.

Y_p = displacement of floating jump piston with respect to static equilibrium position, in.

Y_w = displacement of wheel with respect to static equilibrium position, in.

β = compressibility of a fluid, in^2/lb

γ = polytropic gas constant

ρ = mass density of hydraulic fluid, $lb\text{-}s^2/in^4$.

σ = weight density of hydraulic fluid, lb/in^3.

INTRODUCTION

A primary responsibility of the Mechanical Branch of the Vehicle Equipment Division of the Flight Dynamics Laboratory is to assess the performance of landing gears during taxi, and landing and takeoff. A well-equipped facility is available for testing individual gears. In addition, computer simulations of the dynamics of the complete aircraft are available, and have been used. The disadvantages of using an aircraft simulation to investigate the dynamics of landing gears are two fold. First, aircraft simulations typically simplify the landing gear such that, although the dynamics of the aircraft are reasonably simulated, the particulars of the landing gear may not be well represented. This would be especially true for extreme cases where landing gear nonlinearities are important.

The second disadvantage of a full aircraft simulation is that it simulates the full aircraft, meaning that much more input information is needed to perform the simulation, much more computer time is required, and the results of the full aircraft simulation often do not apply to the test results of a single gear.

To overcome the disadvantages mentioned above, simulations were developed to predict the performance of a single landing gear. The first simulation predicts the pressures and forces in the gear when it is stroked by a well-defined displacement input. It includes several nonlinear phenomena, but no dynamics. The second simulation is that of a cantilevered nose gear traversing

a well-defined obstacle, typical of what would be expected on a bomb-damaged repaired (BDR) runway. It includes several nonlinear phenomena, and the dynamics of the sprung and unsprung masses associated with a landing gear. While the simulation was developed to be generic, it has some specific capabilities associated with the F-16 nose gear, especially the Advanced Landing Gear System (ALGS) that includes the jump capability. If the jump capability is desired, a third degree of freedom is simulated, that of the floating jump piston. The floating jump piston quickly forces the hydraulic fluid into the pneumatic chamber, causing the gear to lift off of its support.

Testing on the standand F-16 gear traversing an obstacle, or on the ALGS during the jump phenomenon has been accomplished by the Mechanical Branch and results can be compared to the simulations developed by this project. The computer simulations can then be used to investigate the effect of varying hardware parameters before actual tests are conducted. Ideally, tests can be used to verify a small number of simulations, and then the simulations can be used to predict a wide variety of conditions.

ANALYTICAL MODELS

There are generally three types of forces that act internally to a strut: pneumatic stiffness, hydraulic damping, and bearing friction. In addition, on the ALGS the jump capability requires the simulation of a pressure buildup that accelerates a floating piston in the hydraulic chamber, causing

the sprung mass (nose weight) to accelerate upward, carrying the unsprung mass (wheel) with it. External forces acting on the system include weight; lift; the force in the tire due to the system's static weight and lift, traversing an obstacle, or being compressed because of the pressure buildup during the jump; and atmospheric pressure.

The pneumatic stiffness is generated by compressing a gas, usually air or nitrogen. Because of the high pressures sometimes generated in a landing gear, the simulations also include the effect of compressing the hydraulic fluid and expanding the chamber. Both of these effects are nonlinear, decrease the pneumatic pressure, and are relatively unimportant at normal pressures in the gear. But they are significant if internal pressures reach several thousand psi.

The hydraulic damping is a result of forcing fluid through one or more orifices. Although the hydraulic force is proportional to the square of the relative velocity between the pneumatic and hydraulic chambers, that proportionality can be a nonlinear function itself.

The bearing friction is produced at the seals between the pneumatic and hydraulic chambers. Associated with the friction force is a stiction force that must be overcome before sliding motion can take place (static friction).

A fourth internal force present in the ALGS is a pressure buildup under a floating piston in the hydraulic chamber that quickly forces all the hydraulic fluid into the pneumatic chamber, causing rapid separation of the two chambers and liftoff of the gear.

A schematic of the F-16 landing gear is shown in Figure 1 with appropriate forces and pressures indicated. In the nonjump mode, the floating piston rests at the bottom of the hydraulic chamber and has no effect on the dynamics of the gear. This is the mode of operation when simulating the motion of the gear traversing an obstacle. On the other hand, if the jump operation is being simulated, the floating piston is accelerated toward the base of the pneumatic chamber when the jump pressure is greater than the hydraulic pressure. The upward motion of the floating piston increases the hydraulic pressure, increasing the flow of oil through the orifices, and causing the pneumatic chamber to extend relative to the hydraulic chamber. If the jump pressure is high enough and is maintained long enough, the tire will be compressed greatly; and when it rebounds, the entire gear may lift off its support.

A summary of the nonlinear phenomena that have been included in this analysis is given in Table 1.

Table 1. Nonlinear capabilities available

1. Polytropic gas in pneumatic chamber.
2. Variable polytropic gas constant.
3. Hydraulic damping proportional to velocity squared.
4. Hydraulic discharge coefficient varies with metering pin location.
5. Hydraulic discharge coefficient varies with compression or extension.
6. Hydraulic fluid density varies with pressure and temperature.
7. Hydraulic bulk modulus varies with pressure and temperature.
8. Hydraulic fluid is compressible.
9. Gear chamber is expandable.
10. Friction and stiction forces differ in compression and extension.
11. Tire can traverse Class B and Class E obstacles.
12. Tire force/displacement relation is fifth order.
13. Tire bottoming-out force is included.
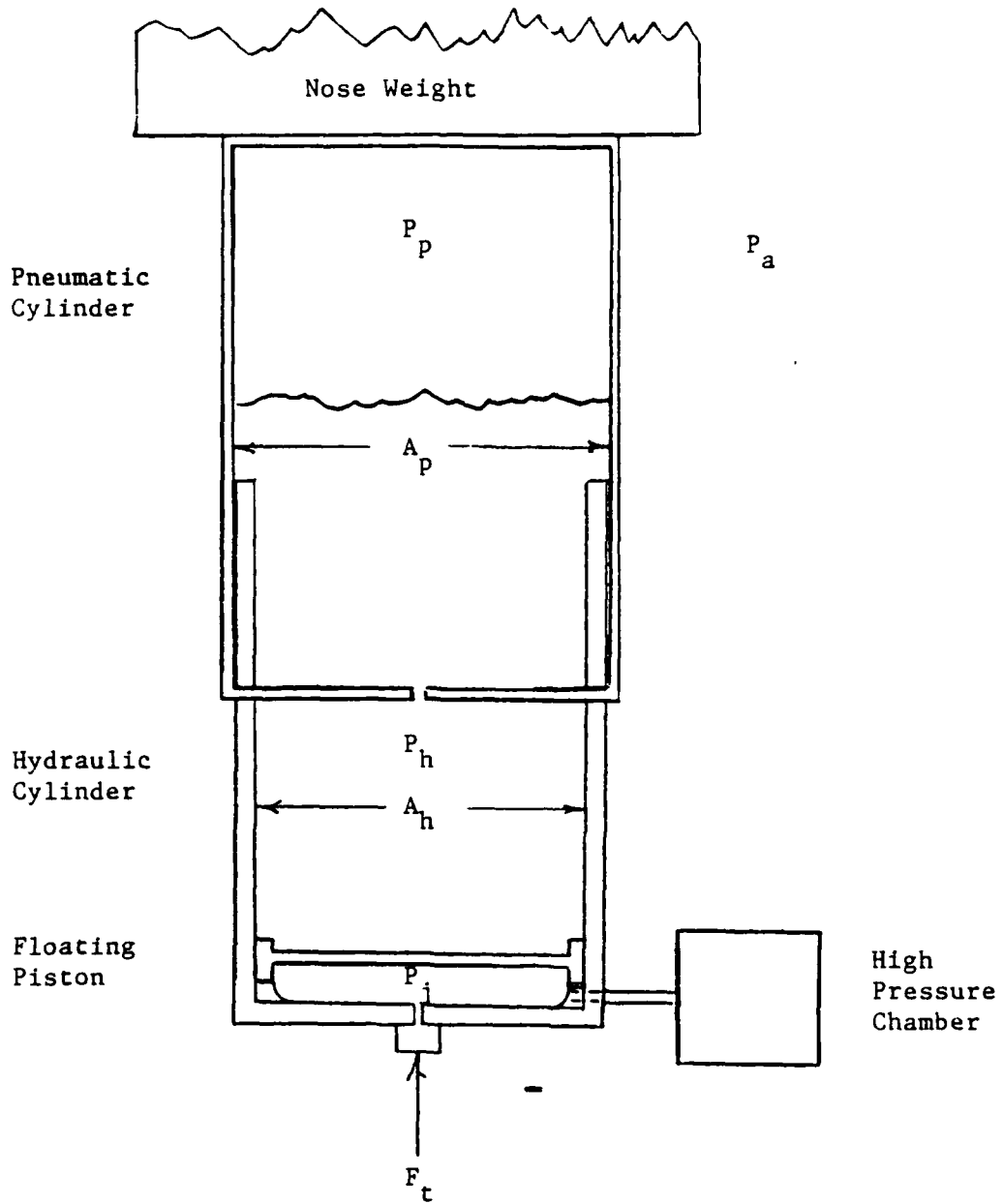
Figure 1. Schematic of F-16 ALGS.

14. Tire lift-off is possible.
15. Metal on metal stiffness force is generated when the chambers' relative position is fully extended.
16. Dynamics of floating jump piston depends on dynamics of hydraulic chamber, the hydraulic and jump pressures, or the dynamics of the pneumatic chamber.

Because of the way the computer code is written, it would be relatively easy to incorporate other nonlinearities into the program. For example, the program uses a constant hydraulic temperature to determine fluid density and bulk modulus. If desired, a variable temperature could be used to affect a change in density and modulus while the simulation is running.

Equations of Motion

The dynamic equations of motion of the system are associated with the mass of the wheel/tire/hydraulic chamber, the effective mass of the nose of the aircraft/pneumatic chamber, and the mass of the floating piston. The equation of motion of the wheel is:

$$M_w \times \ddot{Y}_w = F_t - P_h \times A_h - P_p \times (A_p - A_h) + P_a \times A_p - F_f + F_{ge} - W_w$$

(1)

In the jump mode, if $P_j > P_h$, the floating jump piston will lift off its support in the hydraulic chamber and move toward the base of the pneumatic chamber. For this case, Equation (1) is revised by substituting P_j for P_h.

In Equation (1), the friction force acts in the direction opposing the relative motion between the pneumatic and hydraulic chambers and is typically a different value for compression than for extension. In addition, the friction force is typically high before motion starts and reduces to a lower value once the stiction force has been overcome. The second last term on the

right hand side of Equation (1) is a stiffness force that exists when the pneumatic chamber has fully extended itself with respect to the hydraulic chamber. From a practical standpoint, the two chambers cannot separate indefinitely. When the maximum gear extension is achieved, a very stiff linear spring is engaged, and the upper chamber will attempt to pull the lower chamber off of its support (wheel lift).

The equation of motion for the upper mass (aircraft nose) is given by:

$$M_n \times \ddot{Y}_n = L + P_h \times A_h + P_p \times A_p$$
$$- P_p \times A_h - P_a \times A_p + F_f - F_{ge} - W_n \qquad (2)$$

In the jump mode, if the floating piston contacts the base of the pneumatic chamber, the hydraulic force becomes zero, and the jump pressure acts directly on the pneumatic chamber. For this case, Equation (2) is revised by substituting P_j for P_h.

The equation of motion for the floating piston is given by:

$$Y_p = Y_w \qquad \text{if} \quad P_j < P_h \qquad (3a)$$

$$M_p \times \ddot{Y}_p = (P_j - P_h) \times A_h - W_p \qquad \text{if} \quad P_j > P_h \qquad (3b)$$

$$\text{and} \quad Y_p - Y_w < S_{pmax}$$

$$Y_p = Y_n \qquad \text{if} \quad Y_p - Y_w > S_{pmax} \qquad (3c)$$

The dynamics of the floating piston is equivalent to that of the wheel until the jump pressure is high enough to overcome the hydraulic pressure. As the floating piston moves up, it forces the hydraulic fluid through the orifice in the base of the

pneumatic chamber. When the floating piston makes contact with the base of the pneumatic chamber, its dynamics is assumed to be that of the aircraft's nose. The damping force due to hydraulic fluid flow through the orifice is also set equal to zero at this time.

The pressure terms in Equations (1) and (2) can be rearranged to give the following forces:

$$F_{hp} = (P_h - P_p) \times A_h + (P_p - P_a) \times A_p \tag{4}$$

The first term in Equation (4) is referred to as the hydraulic damping, while the second term is called the pneumatic stiffness. P_h is replaced by P_j during some phases of the jump mode as explained above for Equations (1) and (2).

Hydraulic Damping Force

For an incompressible fluid, Bernoulli's equation relates fluid pressure and velocity at one point in a flow to any other point in the flow. For flow through the orifice:

$$P_h - P_p = \frac{\rho}{2} \times (V_o^2 - V_h^2) \tag{5}$$

For incompressible flow, the volume flow rate is constant. Therefore,

$$V_h \times A_h = V_o \times A_o \tag{6}$$

Substituting V_o from Equation (6) into Equation (3) gives:

$$P_h - P_p = \frac{\rho}{2} \times V_h^2 \times \left[\left(\frac{A_h}{A_o}\right)^2 - 1\right] \tag{7}$$

Since the hydraulic area is much greater than the orifice area, Equation (7) reduces to:

$$P_h - P_p = \frac{\rho}{2} \times v_h^2 \times \left(\frac{A_h}{A_o}\right)^2 \tag{8}$$

If the flow direction changes, the direction of the hydraulic damping force also changes, which can be handled as:

$$F_h = (P_h - P_p) \times A_h = \rho \frac{v_h \times |v_h| \times A_h^3}{2 \times A_o^2} \tag{9}$$

Equation (9) is the hydraulic force for ideal flow. But there are losses depending on the orifice geometry and other factors, which decrease the flow rate. The ratio of the effective flow rate to the ideal flow rate is determined experimentally and is called the discharge coefficient.

$$C_d = \frac{Q_e}{Q_i} = \frac{v_o \times A_{oe}}{v_o \times A_o} = \frac{A_{oe}}{A_o} \tag{10}$$

Typically, the hydraulic force is modified by C_d as follows:

$$F_h = \rho \frac{v_h \times |v_h| \times A_h^3}{2 \times (C_d \times A_o)^2} \tag{11}$$

The expression for the hydraulic force can also be written as:

$$F_h = C_h \times v_h \times |v_h| \tag{12}$$

where: C_h = a function of stroke if one of several devices is used to vary the orifice size or flow characteristic. C_h typically varies as a function of stroke, due to a metering pin and/or the opening of extra orifice holes in extension.

Pneumatic Stiffness Force

The compression of the gas in the pneumatic chamber can be represented by a polytropic process where:

$$P \times V^{\gamma} = \text{constant} \qquad (13)$$

Ideal values for the polytropic constant, γ, are:

.Isothermal: $\gamma = 1.0$

.Adiabatic: $\gamma = 1.4$ (for air or nitrogen)

In actual practice, γ depends on the characteristics of the stroke, e.g. the amount of oil spraying into the gas. From Equation (13) the pneumatic pressure during a stroke is given by:

$$P_p = P_i \times \left(\frac{V_i}{V_p} \right)^{\gamma} \qquad (14)$$

The volume of gas in the pneumatic chamber during a stroke is given by:

$$V_p = V_i - A_p \times S \qquad (15)$$

In Equation (15), S is modified if the floating jump piston causes some or all of the hydraulic fluid to move into the pneumatic chamber. Substituting Equation (15) into Equation (14), the pneumatic force can be written as:

$$F_p = [P_p - P_a] \times A_p = \left[P_i \times \left(\frac{V_i}{V_i - A_p \times S} \right) - P_a \right]^{\gamma} \times A_p \qquad (16)$$

Chamber Expansion - If high pressures are developed in a thin-walled chamber, the expansion of the chamber may be significant. The change in volume in a cylindrical chamber is given by:

$$V_e = \frac{\pi \times P_p \times D_e^3 \times L_e}{4 \times t_w \times E} \qquad (17)$$

Hydraulic Compressibility - At high pressures a hydraulic fluid becomes somewhat compressible, such that the effective pneumatic volume will be increased. The compressibility, which is the inverse of the bulk modulus, is defined as the negative of the fractional change in volume per unit change in pressure, or

$$b = \frac{1}{\beta} = -\frac{V_c}{V_h \times \Delta P} \tag{18}$$

The effective decrease in hydraulic volume is then given by:

$$V_c = -\frac{V_h \times (P_h - P_a)}{\beta} \tag{19}$$

Corrected Pneumatic Force - If both chamber expansion and hydraulic compressibility effects are included in the pneumatic stiffness force, Equation (16) is modified to:

$$F_p' = \left[P_i \times \left(\frac{V_i}{V_i - A_p \times S + V_e - V_c} \right)^\gamma - P_a \right] \times A_p \tag{20}$$

Since both the expansion of the pneumatic chamber and the compressibility of the hydraulic fluid depend on the pneumatic pressure, an iteration procedure is necessary to determine the pneumatic stiffness force in Equation (20).

Friction/Stiction

To analytically define the friction and stiction forces in a gear can be an extremely complex undertaking. The present simulation provides for the specification of different friction and/or stiction forces during compression or extension. If a more exact formulation is required, it can be written in the friction subroutine.

Hydraulic Fluid Density

Typically, the density of the hydraulic fluid is taken as a constant. Actually, over a temperature range of -100 F to 500 F and a pressure range of 0 psi to 5000 psi, the density can vary from .027 to .034 lb/in^3. This variation is represented by:

$$\sigma = 0.03242 - 1.0575 \times 10^{-5} \times T_h$$
$$+ \left(8.6 \times 10^{-8} + 3.3 \times 10^{-10} \, T_h\right) \times P_h \qquad (21)$$

The fluid density affects the hydraulic damping force; see Equation (11).

Hydraulic Fluid Compressibility

The bulk modulus of a hydraulic fluid varies by an order of magnitude over a temperature range of -100 F to 500 F, and a pressure range of 0 to 5000 psi (50,000 to 500,000 psi). This variation for hydraulic fluid MIL-H-5606B is represented by:

$$\beta = 331,000 \times e^{-0.00333 \times T_h} \times \left[1 - \frac{P_h - 2000}{3000} \right]$$
$$+ 372,000 \times e^{-0.00276 T_h} \times \left(\frac{P_h - 2000}{3000} \right) \qquad (22)$$

The bulk modulus affects the hydraulic compressibility volume, Equation (19).

Tire Force

For small tire compression, the force/displacement characteristic can be taken as linear. However, large tire displacements are likely for both motion over obstacles and during the jump mode. Therefore, the characteristic of the tire can be represented by a fifth order relation if desired. The equation is:

$$F_t^! = A_1 \times D_t + A_2 \times D_t^2 + A_3 \times D_3^3 + A_4 \times D_t^4 + A_5 \times D_t^5 \qquad (23)$$

If the tire bottoms out, the stiffness force is assumed to be the series sum of the tire force at its bottomed-out displacement plus the stiffness force caused by deflecting the tire's rim. Also, a linear damping force is produced by a damping coefficient times the relative velocity between the wheel and its support (runway).

$$F_t = F_t^! (D_b) + K_b \times (D_t - D_b) + C_t \times \dot{D}_t \qquad (24)$$

If a linear tire force/displacement relation is desired, use only the A_1 coefficient in Equation (23).

Runway Obstacles

Three types of obstacles have been identified as representative of a BDR runway. A no obstacle case is also available to be used when simulating the jump gear. The type of obstacles are listed below and shown in Figure 2.

    * No obstacle
    * Multiple Versine (1 - Cosine)
    * Class B Bump
    * Class E Bump

The vertical displacement and velocity of the multiple versine obstacle are given by:

$$Y_O = \frac{A}{2} \times \left[1 - \cos\left(\frac{2 \times \pi \times V_1}{L_w} \times (T - T_O) \right) \right] \qquad (25)$$

$$\dot{Y}_O = \frac{A \times \pi \times V_1}{L_w} \times \sin\left(\frac{2 \times \pi \times V_1}{L_w} \times (T - T_O) \right) \qquad (26)$$
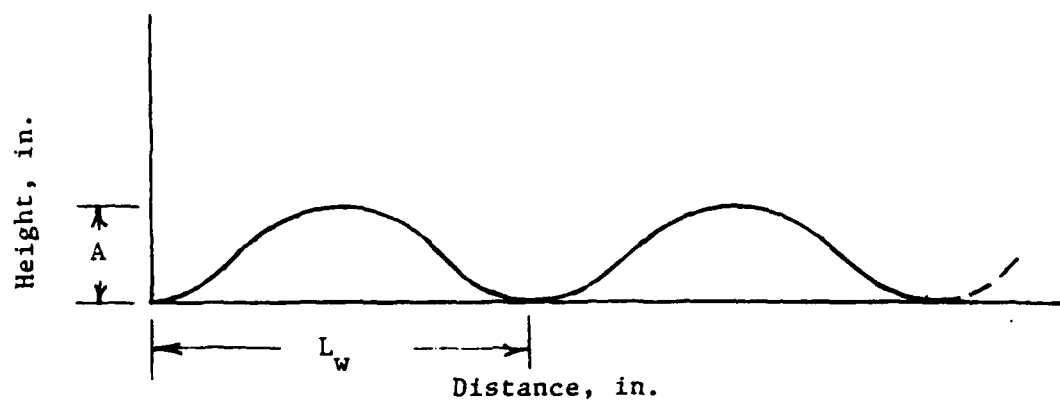
a. Multiple Versines
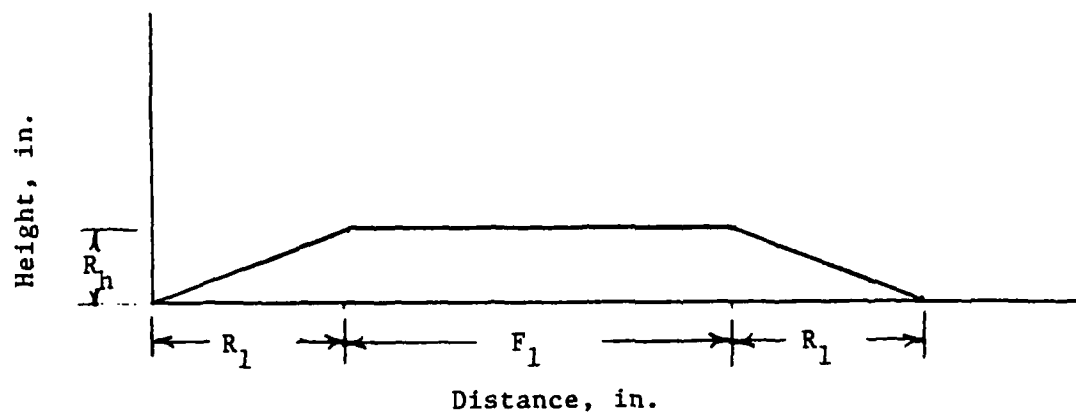
b. Class B Bump
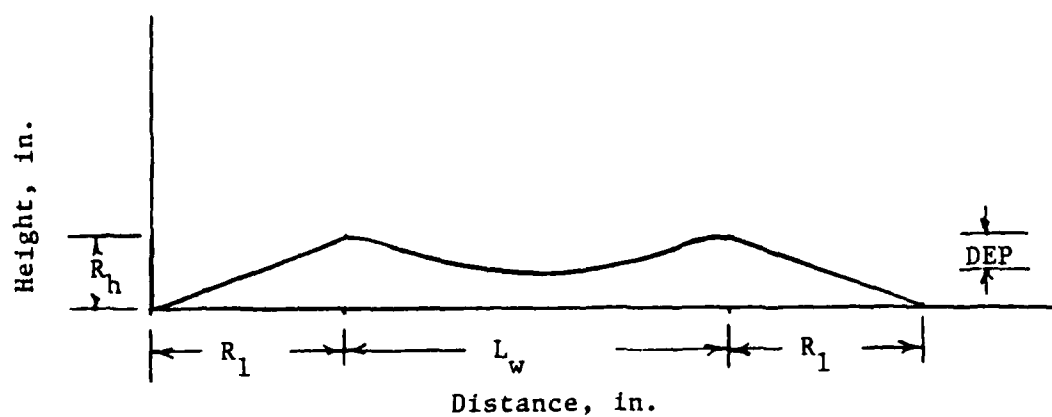
c. Class E Bump

Figure 2. Obstacle profiles for BDR runways.

The vertical displacement and velocity of a Class B obstacle are given by:

For $T_O < T < T_1$:

$$Y_O = \frac{R_h \times V_1}{R_1} \times (T - T_O) \qquad (27)$$

$$\dot{Y}_O = \frac{R_h \times V_1}{R_1} \qquad (28)$$

For $T_1 < T < T_2$:

$$Y_O = R_h \qquad (29)$$

$$\dot{Y}_O = 0 \qquad (30)$$

For $T_2 < T < T_t$:

$$Y_O = R_h - \frac{R_h \times V_1}{R_1} \times (T - T_2) \qquad (31)$$

$$\dot{Y}_O = - \frac{R_h \times V_1}{R_1} \qquad (32)$$

The vertical displacement and velocity of a Class E obstacle are given by:

For $T_O < T < T_1$:

$$Y_O = \frac{R_h \times V_1}{R_1} \times (T - T_O) \qquad (33)$$

$$\dot{Y}_O = \frac{R_h \times V_1}{R_1} \qquad (34)$$

For $T_1 < T < T_2$:

$$Y_O = R_h - \frac{A}{2} \times \left[1 - \cos\left(\frac{2 \times \pi \times V_1}{L_w} \times (T - T_1) \right) \right] \qquad (35)$$

64-18

$$\dot{Y}_O = - \frac{A \times \pi \times V_1}{L_W} \times \sin\left(\frac{2 \times \pi \times V_1}{L_W} \times (T - T_1)\right) \qquad (36)$$

For $T_2 < T < T_t$:

$$Y_O = R_h - \frac{R_h \times V_1}{R_1} \times (T - T_2) \qquad (37)$$

$$\dot{Y}_O = - \frac{R_h \times V_1}{R_1} \qquad (38)$$

Numerical Integration Methods

The equations of motion were reduced to first order differential equations, and can be numerically integrated using one of the following four methods:

* Runge-Kutta-Fehlberg
* Runge-Kutta (fourth-order)
* Adams-Bashforth-Moulton
* Euler

The first three methods incorporate an option to approximate the error and increase or decrease the time increment. Theoretically, this technique can be used to optimize the accuracy and running time. The first three methods can also be run at a fixed time increment by setting an input parameter. Note, automatic time step variation has not worked with this simulation, possibly because of the nonlinearities.

RESULTS

Gear Stroke Simulation

The Gear Stroke Simulation can be used to investigate the pressures and forces in the pneumatic and hydraulic chambers when subjected to relative displacements that represent the motion of a gear over a BDR obstacle. By varying the amplitude, length, or wavelength of the various obstacle profiles provided, different relative displacements and velocities between the pneumatic and hydraulic chambers can be achieved. As a result, different pneumatic and hydraulic forces can be produced.

The program can also be used to investigate the effects of chamber expansion, hydraulic compressibility, changes in hydraulic fluid density, changes in the polytropic constant, various orifice configurations, and the basic geometry of a gear. In addition, the program was written and annotated in such a way that capability or variability can be easily added by the user. The input data are described in APPENDIX A; a set of input data, as it should appear in the data file called GEAR.DAT, is given in APPENDIX B; the output data are described in APPENDIX C; a sample output run, using the data shown in APPENDIX B, is given in APPENDIX D; and a FORTRAN listing of the program is given in APPENDIX E.

The time history of the pneumatic and hydraulic forces are plotted in Figure 3 for the input data given in APPENDIX B. The simulated obstacle was a versine of amplitude 10.32 in. (maximum gear stroke) and a wavelength of 600 in. The simulated velocity was 50 knots. The pneumatic force increases monatonically until
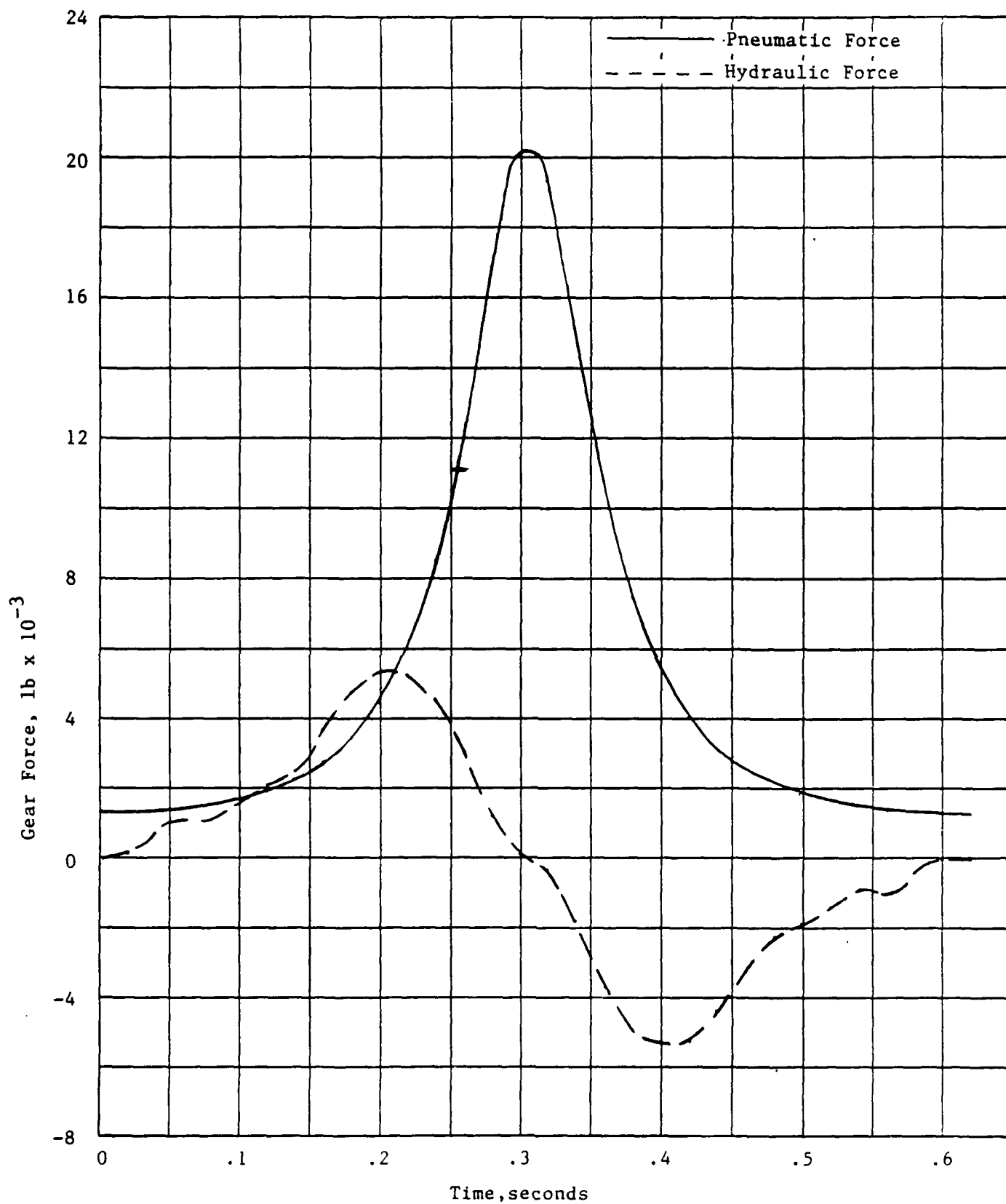
Figure 3. Time histories of pneumatic and hydraulic forces for F-16 nose gear during a 10.32 in. versine stroke.

the stroke reaches its maximum on the F-16 gear. It should be noted that small changes in the polytropic constant have a significant effect on the maximum pneumatic force. The hydraulic force resembles a distorted sine function. The distortion is caused by the fact that the effective quadratic damping coefficient is a function of the stroke. There are times at which the stroke velocity is increasing, but the damping coefficient is decreasing causing a leveling out in the hydraulic force (see Appendix D at times 0.06 and 0.08 s).

F-16 Nose Gear Simulation

The second computer program contains the features of the first program plus much more, including: the dynamics of the wheel and the simulated nose mass, the tire flexibility, and the jump capability. The program runs basically in one of two modes: 1) dynamics of the gear traversing an obstacle, and 2) dynamics of the gear during the jump. Both simulations provide the time history of the dynamics, pressures, and forces in the system. As with the first program, this simulation was written and annotated so that its capabilities could be expanded. The input data are described in APPENDIX F; sets of input, for both modes of operation, are given in APPENDIX G; the output data are described in APPENDIX H; a sample output run for each mode of input data, shown in APPENDIX G, is given in APPENDIX I; and a FORTRAN listing of the program is given in APPENDIX J.

Obstacle Simulation - A sample simulation of the nose gear traversing five versine waveforms was performed. A plot of the time histories of the stroke, pneumatic pressure, hydraulic

pressure, tire load, and obstacle profile are shown in Figure 4, along with a comparison to test data. Of the four comparisons, only tire load is well-correlated. The stroke comparison, Figure 4a, starts out well, but then the simulation oscillates about a mean value that indicates that the pneumatic and hydraulic chambers have separated somewhat beyond their static equilibrium position. The final stroke value is negative because the large stiction force cannot be overcome.

The correlation between test and simulation of the pneumatic pressure, Figure 4b, is also poor because of the low amplitude changes in the simulation. However, a simple calculation with the polytropic gas equation (Equation 14) indicates that a 1.0 in. stroke at 0.15 seconds should correspond to an increase in pneumatic pressure from 937 to 1060 psi, as the simulation results indicates, not 1600 psi as the test data indicate. The lower final pneumatic pressure in the simulation can be attributed to the high stiction force.

In Figure 4c, the hydraulic pressure simulation correlates somewhat better with the test data. It should be noted that the test data for the pneumatic and hydraulic data are almost identical. This does not seem reasonable, because there would be no flow of the hydraulic fluid, and therefore, a constant stroke.

In Figure 4d, the simulated tire load matches very well with the test data, until the fifth versine wavelength is negotiated. For the last half of the simulation the magnitude is similar, but it is out of phase with the test data. The effective frequency of oscillation of the simulated gear system was higher than the test data indicated. This suggests a difference in the
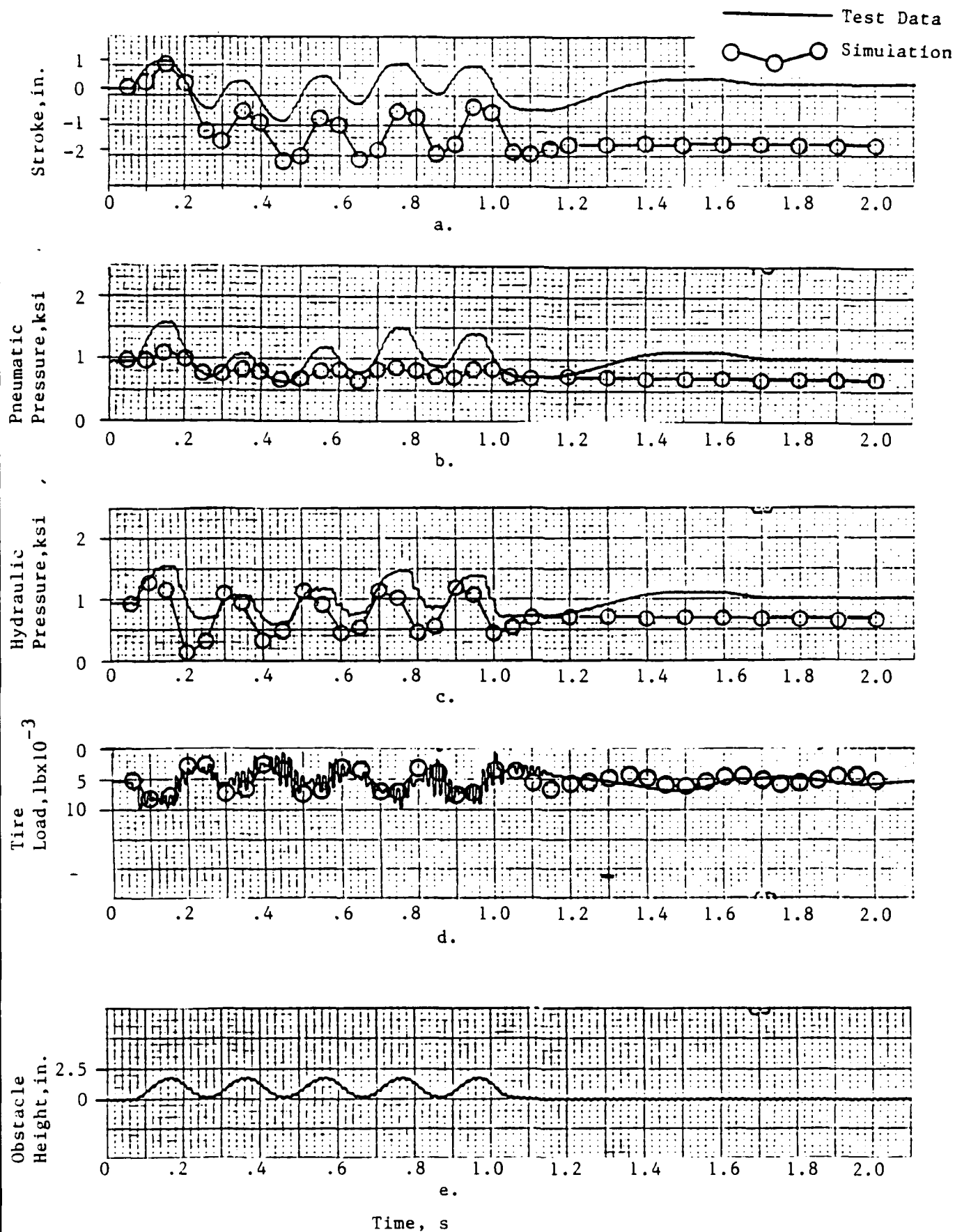
Figure 4. Comparison of test and simulation time histories associated with F-16 nose gear traversing five versine profiles.

stiffness, damping or mass properties assumed for the simulation, and those actually used in the test.

Jump Gear Simulation - Sample data of the simulation of the jump phenomenon is compared to test data in Figures 5 and 6. In Figure 5a, the simulated stroke correlated well with test data, except that the time to full extension was 10 percent quicker. The simulated hydraulic pressure difference across the orifice (Figure 5b) compared well to test data in magnitude, but the predicted time for the floating jump piston to push all the hydraulic fluid into the pneumatic chamber was about 25 percent shorter than actual. The simulated jump pressure (Figure 5c) is input data.

In Figure 6a, the simulated nose velocity increased somewhat quicker, and did not fall off as quickly as the test results. Both of these events can be better interpreted by considering Figure 6b and 6c. The tire load (Figure 6b) displays a large force at 0.028 s. This large force was caused by the tire bottoming out, which apparently did not occur during the test. The large tire force caused a more severe rebound, and therefore, accelerated the nose at a higher rate. The simulated tire load remained consistently above the test results up to 0.22 s, where it fell off rapidly until wheel lift was achieved at 0.25 s, again somewhat sooner than the test results. In Figure 6c, the simulated nose acceleration correlates reasonably well with the high side of the test results. At 0.3 seconds the acceleration test results makes an abrupt increase. Since the system is in free flight at this time, there is no physical justification for this increase. In addition, simple calculations of the system in
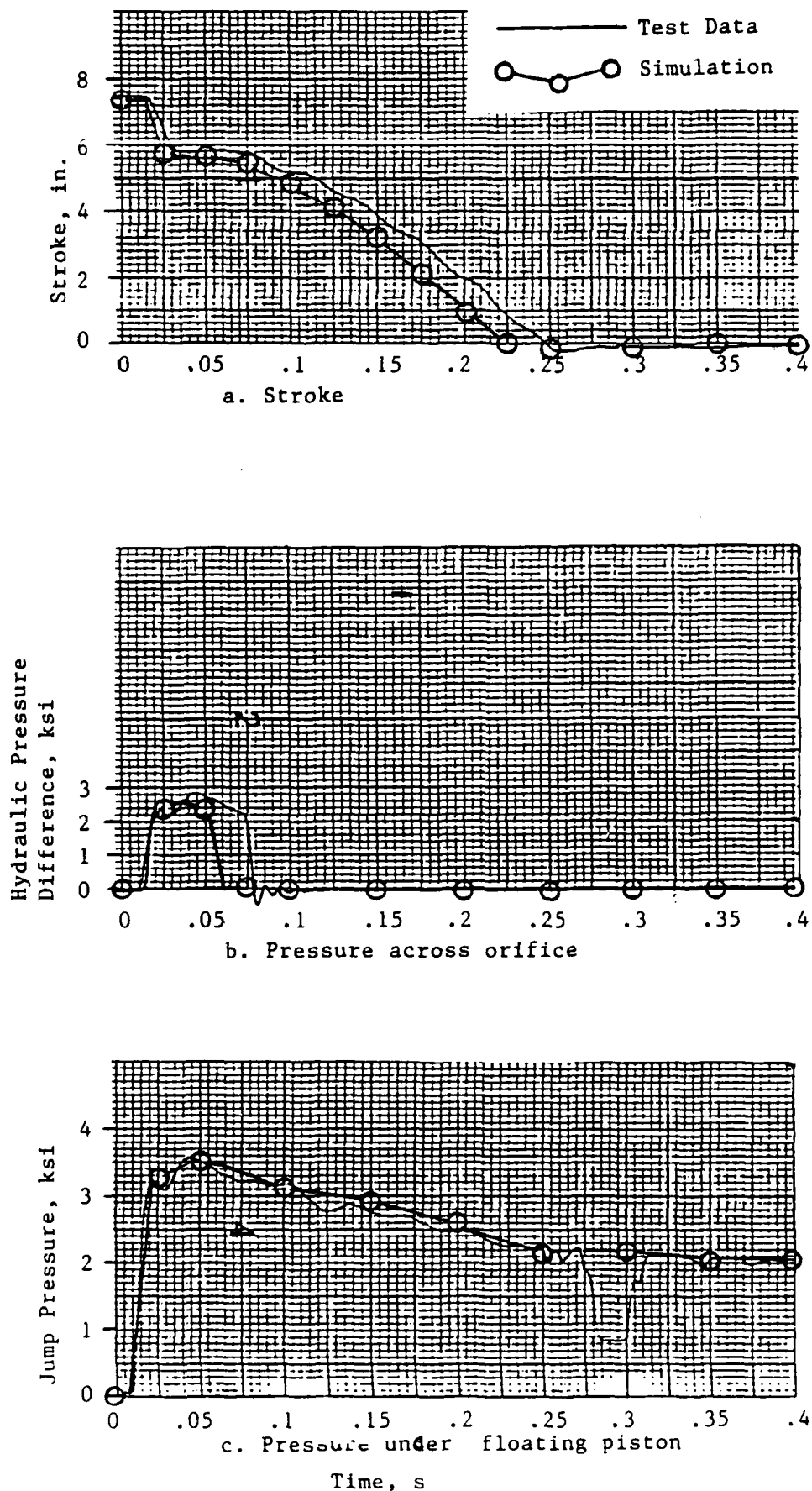
Figure 5. Comparison of test and simulation time histories associated with F-16 ALGS nose gear during a jump.

a. Nose weight velocity

b. Tire load

c. Nose weight acceleration

Time, s
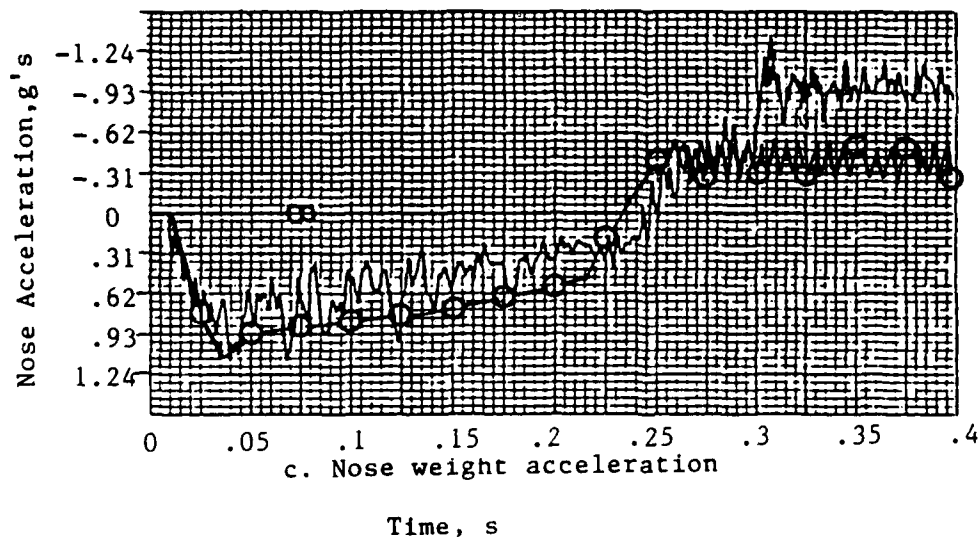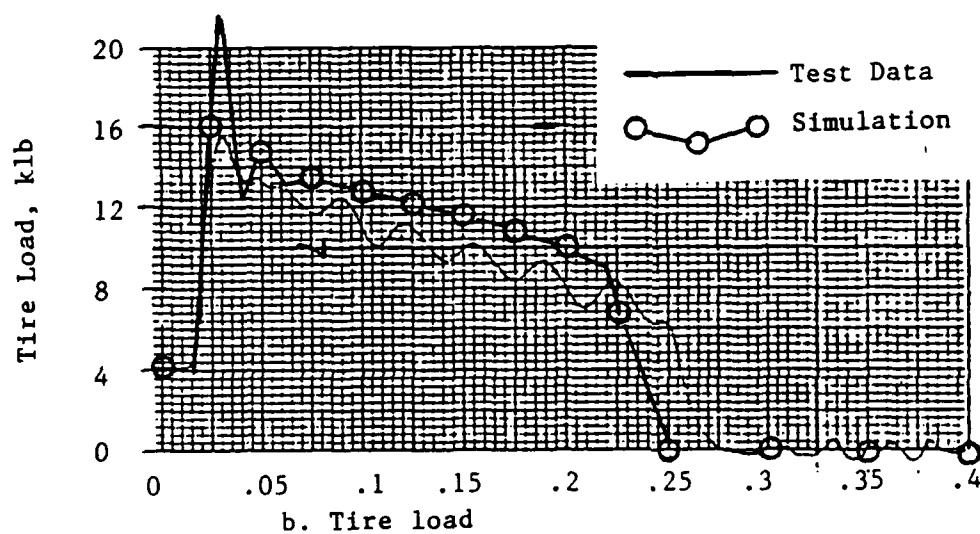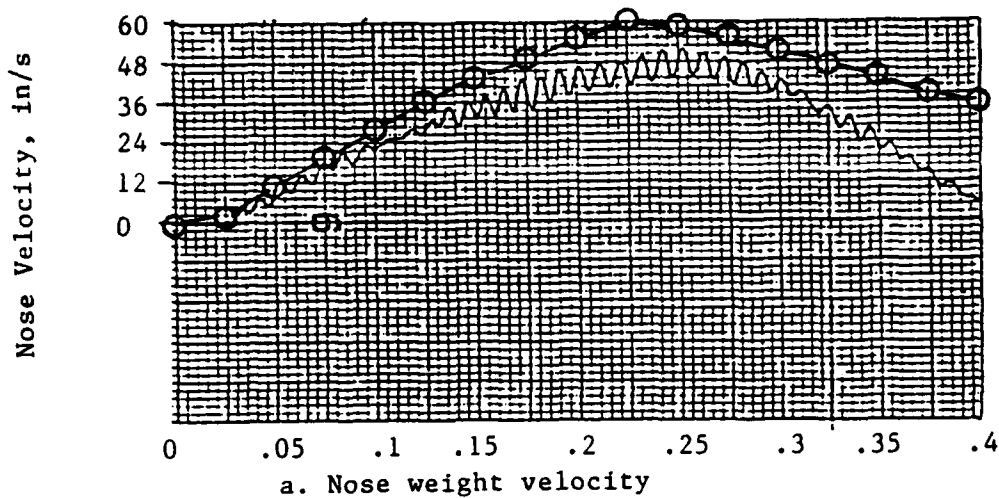
Figure 6. Comparison of test and simulation time histories associated
with F-16 ALGS nose gear during a jump

64-27

free flight indicate that the nose acceleration, with only weight and lift acting, should be about -0.4 g's, as the test results displays between 0.27 and 0.30 seconds. It is at 0.3 seconds that the test nose velocity (Figure 6a) falls off much quicker than the simulation results, indicative of the higher negative nose acceleration shown in Figure 6c.

CONCLUSIONS

Large computer programs that simulate the dynamics of a complete aircraft are often used to investigate or design a landing gear. While this approach is meaningful, it probably should not be used during preliminary design. Typically, an aircraft simulation does not include many of the details of the gear; it is significantly more difficult to use because inputs, not associated with the gear, must be determined; and the output is more difficult to appreciate because much of it is associated with the aircraft rather than the gear. For preliminary design, a detailed model of only the gear will produce greater insight into its performance than a complete aircraft model. Also, a single gear simulation can be used to compare to laboratory test data.

With these incentives in mind, two computer models were developed. While many of the features of both models are generic to landing gears, several of the features are particular to the F-16 nose gear and the ALGS developed for the nose gear of the F-16. The first model is essentially kinematic in nature, i.e., the pneumatic chamber is fixed, and the hydraulic chamber is

stroked according to a well-defined simulated BDR obstacle. The program can be used to investigate basic geometries, varying orifice areas, and several nonlinearities associated with gears. Results of the program can be compared to test data generated on a machine that strokes the gear.

The second computer program simulates the dynamics of a wheel, gear, and effective spring mass. The output is produced by numerically integrating the differential equations of motion. The dynamic model contains all of the features modeled in the first model, plus several additional nonlinearities summarized in Table 1. The model simulates a wheel/gear traversing an obstacle or the jump phenomenon associated with the ALGS.

The results of the first model was shown to produce a realistic pneumatic pressure versus stroke characteristic, Figure 3. Experience with the model quickly gives the user an appreciation that total forces are sensitive to several system parameters which are difficult to determine, e.g., the polytropic gas constant.

The comparison of the dynamic model's results to actual test data were mixed. In several cases the correlation was good; at other times the correlation was poor. However, as was pointed out in the results, the test results seemed to be inaccurate in a couple of places. The simulation results were good enough, however, to encourage further use of the model, and to attempt to determine exactly what caused the difference between the simulation and test results.

RECOMMENDATIONS

The two computer simulations developed on this project seemed to give reasonable results, and in several cases correlated very well with test data. However, there still exists a need to determine the cause of the discrepancies between the test and simulation results. Likely causes are a misunderstanding of the exact nature of the test conditions, and small errors in the analytical model or computer code.

Further efforts should be made to validate the computer codes with well-defined test cases. Working with the codes in conjunction with a test program would provide needed familiarity and give the user a chance to try various options, and possibly add some additional capabilities.

Appendices can be obtained from
Universal Energy Systems, Inc.

FINAL REPORT NUMBER 65
REPORT NOT AVAILABLE AT THIS TIME
Mr. Thomas Enneking (GSRP)
760-7MG-124

FINAL REPORT NUMBER 66
REPORT NOT AVAILABLE AT THIS TIME
Dr. Oliver McGee
760-7MG-115

1986 USAF-UES SUMMER FACULTY RESEARCH PROGRAM/

GRADUATE STUDENT SUMMER SUPPORT PROGRAM

MINI GRANT

Sponsored by the

AIR FORCE OFFICE OF SCIENTIFIC RESE.\RCH

Conducted by the

Universal Energy Systems, Inc.

FINAL REPORT

Development of a Technique for Prediction of Internal

Heat Transfer in Actively Cooled Structures

Prepared by: V. Dakshina Murty

Academic Rank: Associate Professor

Department and   Mechanical Engineering

  University: University of Portland

Research Location: School of Engineering
                                5000 N. Willamette Blvd.
                                University of Portland
                                Portland, OR 97203

Date: April 1988

Contract No: F 496 20-85-C-0013/
                                SB5851-0360

ACKNOWLEGDEMENTS

PREFACE

A summary of the work completed for the minigrant from the Air Force Office of Scientific Research, Cntract No. F49620-85-C-0013/ SB5851-0360, during the period April 1, 1987 to March 31, 1988. The primary aim of the project has been to evaluate actively cooled structures, i.e. convection heat transfer through complex passages. Two geometries have been studied quite extensively. They are pin fin and rectangular plate fin geometries. In addition the mathematical formulation for finite element implementation of the $\tilde{k}-\epsilon$ turbulence model is in place.

NOMENCLATURE

x,y = coordinate directions

u = velocity in direction x

v = velocity in direction y

T = temperature

p = pressure

ρ = density

C_p = specific heat

μ = coefficient of viscosity

k = coefficient of thermal conductivity

Pr = Prandtl number = $C_p \mu / k$

n = number of cylinders

$\hat{p}/D$ = ratio of pitch of cylinders to
       diameter

u_m = Average velocity at minimum cross
       section of cylinders

C_d = Drag Coefficient

Re = Reynolds number = $\rho u_m D / \mu$

s = arc length (measured along the
circumference of each cylinder)

$\underline{\phi}, \underline{\psi}$ = shape functions for velocity,
(temperature) and pressure.

ϵ_o^{-1} = penalty parameter

$\underline{q}$ = vector of unknowns

P_e = Peclet number = $Re\, Pr$

$\Omega, \partial\Omega$ = domain and boundary of a
finite element

$\tilde{k}$ = turbulence kinetic energy

ϵ = dissipation rate of turbulence
kinetic energy

C_1, C_2, C_μ = constants for the $\tilde{k}-\epsilon$ model

L, H = parameters for rectangular fins

θ, a, s = parameters for diamond shape fins

INTRODUCTION

A study of the performance of active cooling devices requires
the solution of Navier Stokes equations including the effects of
turbulence. Since the equations are coupled and nonlinear exact
solutions have been possible only in a few simple cases. For prob-
lems of practical interest, only numerical solutions are possible.
For active cooling devices, because of the complex geometries,
separation, reattachment, and interaction of boundary layers numer-
ical studies have been quite limited. Hence there have been several
studies [1-8] using experimental methods. With the advent of super-
computers, there have also been some studies to utilize the power
of computational fluid dynamics techniques in the modeling of con-
vective heat transfer. The problems addressed were cooling tower
studies [9,10], right angled bends [11,12], rectangular pin
geometries [13-16].

Among the numerical techniques used to solve fluid mechanics
and heat transfer problems finite difference and finite element
methods are most common. Of these, the former because of its sim-
plicity has found wider applicability. However, the finite element
method has some advantages to offer; for example, the ease with
which complex geometries and boundary conditions can be modeled,
sound mathematical foundation, the simplicity with which phase
changes can be included etc. Hence, the use of finite element

methods in increasing in fluid mechanics.

In this report, a summary of the work performed in the study of the application of finite element method to fluid mechanics problems is presented. The project consisted of two phases. The first phase is the numerical computation of the various geometries and the second phase is the inclusion of the turbulence model into the computer code. The computer program used in this study is NON-FLAP, a general purpose finite element program to analyze fluid mechanics and heat transfer problems developed by Murty [17]. The two phases of the project proceeded simultaneously, in that the evaluation of various turbulence models took place in parallel with the computer runs of the fin geometries. In the rest of this report, a description of the governing equations and formulation is presented followed by numerical results and conclusions and recommendations for further work.

GOVERNING EQUATIONS AND FORMULATION

The equations which govern the flow of steady, incompressible, Newtonian, two dimensional flows of Newtonian fluids are the con-servation of mass, linear momentum, and energy. They are given as follows:

$$\frac{\partial u}{\partial x} + \frac{\partial v}{\partial y} = 0 \tag{1}$$

$$\rho \left[u \frac{\partial u}{\partial x} + v \frac{\partial u}{\partial y} \right] = -\frac{\partial p}{\partial x} + \mu \nabla^2 u \tag{2}$$

$$\rho \left[u \frac{\partial v}{\partial x} + v \frac{\partial v}{\partial y} \right] = -\frac{\partial p}{\partial y} + \mu \nabla^2 v \tag{3}$$

$$\rho C_p \left[u \frac{\partial T}{\partial x} + v \frac{\partial T}{\partial y} \right] = k \nabla^2 T \tag{4}$$

The boundary conditions are

$$\underset{\sim}{v} = \hat{\underset{\sim}{f}}(s) \quad ; \quad \underset{\sim}{t} = \underset{\underset{\sim}{\sim}}{T}(s) \, \underset{\sim}{n}(s)$$
$$T = g(s) \quad ; \quad \frac{\partial T}{\partial n} = h(s) \tag{5}$$

The fluid domain and the boundary conditions are shown in Fig. 1. The first step in the solution of Eqs. (1) - (5) using the finite element method is to obtain a variational statement of the problem. This is done by taking the inner product of Eqs. (1) - (4) with $\bar{p}$, $\bar{u}$, $\bar{v}$, and $\bar{T}$ respectively. Thus we get
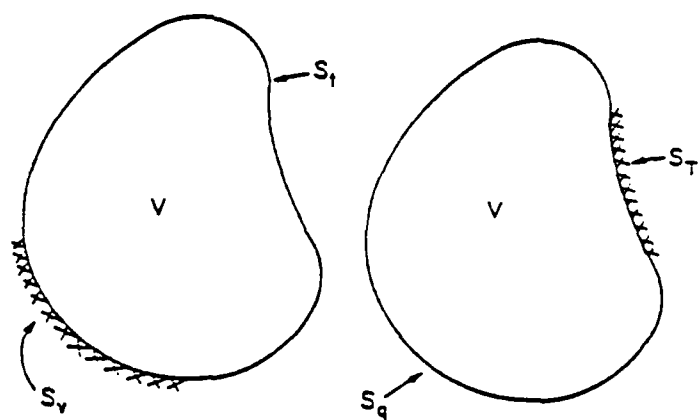
Figure 1: Fluid continuum with boundaries

$$\int_V \bar{P} \left(\frac{\partial u}{\partial x} + \frac{\partial v}{\partial y} \right) dV = 0 \tag{6}$$

$$\int_V \tilde{u} \left\langle g\left[u\frac{\partial u}{\partial x} + v\frac{\partial u}{\partial y}\right] + \frac{\partial p}{\partial x} - \mu \nabla^2 u \right\rangle dV = 0 \tag{7}$$

$$\int_V \tilde{v} \left\langle g\left[u\frac{\partial v}{\partial x} + v\frac{\partial v}{\partial y}\right] + \frac{\partial p}{\partial y} - \mu \nabla^2 v \right\rangle dV = 0 \tag{8}$$

$$\int \tilde{T} \left\langle \rho C_p \left[u\frac{\partial T}{\partial x} + v\frac{\partial T}{\partial y}\right] - k \nabla^2 T \right\rangle dV = 0 \tag{9}$$

Eqs. (7) - (9) can be simplified by using the Gauss divergence theorem on the diffusion terms and written as

$$\int_V \tilde{u} \left\langle g\left[u\frac{\partial u}{\partial x} + v\frac{\partial u}{\partial y}\right] + \frac{\partial p}{\partial x} \right\rangle dV + \mu \int_V \left\langle \frac{\partial \tilde{u}}{\partial x}\frac{\partial u}{\partial x} + \frac{\partial \tilde{u}}{\partial y}\frac{\partial u}{\partial y} \right\rangle dV$$

$$- \int_S \mu \left(\frac{\partial u}{\partial x} n_x + \frac{\partial u}{\partial y} n_y\right) ds \cdot \tilde{u} = 0 \tag{10}$$

$$\int_V \tilde{v} \left\langle g\left[u\frac{\partial v}{\partial x} + v\frac{\partial v}{\partial y}\right] + \frac{\partial p}{\partial y} \right\rangle dV + \mu \int_V \left\langle \frac{\partial \tilde{v}}{\partial x}\frac{\partial v}{\partial x} + \frac{\partial \tilde{v}}{\partial y}\frac{\partial v}{\partial y} \right\rangle dV$$

$$- \int_S \mu \left(\frac{\partial v}{\partial x} n_x + \frac{\partial v}{\partial y} n_y\right) ds\, \tilde{v} = 0 \tag{11}$$

$$\int_V \overline{\tilde{T}} \left\langle \rho C_p \left(u\frac{\partial T}{\partial x} + v\frac{\partial T}{\partial y}\right) \right\rangle dV + k \int_V \left(\frac{\partial \tilde{T}}{\partial x}\frac{\partial T}{\partial x} + \frac{\partial \tilde{T}}{\partial y}\frac{\partial T}{\partial y}\right) -$$

$$- \int_S k \left(\frac{\partial T}{\partial x} n_x + \frac{\partial T}{\partial y} n_y\right) \tilde{T}\, ds = 0 \tag{12}$$

Eqs. (6), and (9) - (11) are valid over the entire fluid domain Ω. In the finite element method the above equations are written for a small subdomain called the finite element (see Fig. 2).

Mixed Method:

The dependent variables to be interpolated in this case are u, v, p, and T. Over each element they are approximated as follows:

$$u = \underset{\sim}{\phi}^T \underset{\sim}{u} \quad ; \quad v = \underset{\sim}{\phi}^T \underset{\sim}{v} \quad ; \quad T = \underset{\sim}{\phi}^T \underset{\sim}{T}$$

$$p = \underset{\sim}{\psi}^T \underset{\sim}{p}$$

(13)

If Eq. (13) is substituted into Eqs. (6), (10) - (12) the following set of matrix equations is obtained

$$[\underset{\sim}{C}(\underset{\sim}{q}) + \underset{\sim}{K}]\{\underset{\sim}{q}\} = \{\underset{\sim}{F}\}$$

(14)

where

$$\begin{bmatrix} \hat{\underset{\sim}{C}}_{11} & 0 & -\underset{\sim}{Q}' & 0 \\ 0 & \hat{\underset{\sim}{C}}_{22} & -\underset{\sim}{Q}^2 & 0 \\ -\underset{\sim}{Q}'^T & -\underset{\sim}{Q}^{2T} & \underset{\sim}{C} & 0 \\ 0 & \underset{\sim}{C} & 0 & \hat{\underset{\sim}{C}}_4 \end{bmatrix} \begin{Bmatrix} \underset{\sim}{u} \\ \underset{\sim}{v} \\ \underset{\sim}{p} \\ \underset{\sim}{T} \end{Bmatrix} + \begin{bmatrix} 2K^{11}+K^{22} & K^{21} & 0 & 0 \\ K^{12} & K^{11}+2K^{22} & 0 & 0 \\ 0 & 0 & 0 & c \\ c & 0 & 0 & L^{11}+L^{22} \end{bmatrix} \begin{Bmatrix} \underset{\sim}{u} \\ \underset{\sim}{v} \\ \hat{\underset{\sim}{p}} \\ \underset{\sim}{T} \end{Bmatrix} = \begin{Bmatrix} F^1 \\ F^2 \\ 0 \\ F^4 \end{Bmatrix}$$
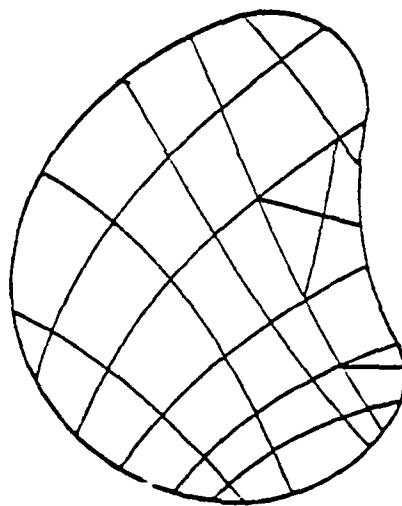
Figure 2: Fluid domain subdivision into finite elements

$$\hat{\underline{\underline{C}}} = \rho \int_{\Omega} \left\langle \underline{\phi}\, \underline{\phi}^T \underline{u}\, \frac{\partial \underline{\phi}^T}{\partial x} + \underline{\phi}\, \underline{\phi}^T \underline{v}\, \frac{\partial \underline{\phi}^T}{\partial y} \right\rangle dV$$

$$\underline{\underline{Q}}^1 = \int_{\Omega} \frac{\partial \underline{\phi}}{\partial x} \underline{\psi}^T dV \quad ; \quad \underline{\underline{Q}}^2 = \int \frac{\partial \underline{\phi}}{\partial y} \underline{\psi}^T dV$$

(15)

$$\underline{\underline{K}}^{11} = \mu \int \frac{\partial \underline{\phi}}{\partial x} \frac{\partial \underline{\phi}^T}{\partial x} dV \quad ; \quad K^{22} = \mu \int \frac{\partial \underline{\phi}}{\partial v} \frac{\partial \underline{\phi}^T}{\partial y} dV$$

$$\underline{K}^{12} = \underline{K}^{21} = \int \frac{\partial \underline{\phi}}{\partial y} \frac{\partial \underline{\phi}^T}{\partial x} dV$$

$$\hat{\underline{\underline{C}}}^1 = C_p \hat{\underline{\underline{C}}} \quad ; \quad L^{11} = k \int \cdot \frac{\partial \phi}{\partial x} \frac{\partial \phi^T}{\partial x} \quad ; \quad L^{22} = \int \frac{\partial \phi}{\partial y} \frac{\partial \phi^T}{\partial y} dV$$

It should be pointed out that since the governing equations are nonlinear, Picard's method of successive substitutions has been used to solve Eq. (14). The starting vectors for the iteration process are creeping flow for the hydrodynamic part and diffusion solution for thermal part. The following convergence criterion has been used for temperature for iteration number j. Similar criteria have been on the other dependent variables also.

$$\max\left\{\left|T_i^{(j)} - T_i^{(j-1)}\right| \Big/ \left|T_{max}^{(j-1)}\right|\right\} \leq 10^{-2}$$

$$1 \leq i \leq \text{No. of Nodes}$$

(16)

$$\left|T_{max}^{(j-1)}\right| = \max \left|T_i^{(j-1)}\right|$$

$$1 \leq i \leq \text{No. of Nodes}$$

The convergence tolerance (= 1% used in this study) can be made as small as necessary. However, it was found during the investigation that smaller values (< 1%) did not significantly improve the solution, but tremendously increased the computational effort.

Penalty Method:

As opposed to the mixed method, here pressure does not appear explicitly as an interpolation variable. Hence this method results in fewer degrees of freedom per element and consequently less computational effort. In this method the continuity equation is treated like a constraint which must be satisfied by the velocity field. By introducing Eq. (13) into the penalized variational statement of Eqs. (1) - (4), we get the following;

$$[\underline{C}(q) + \underline{K} + \epsilon_o^{-1} \underline{K}'] \{q\} = \{F\}$$

(17)

where the matrices $\underline{C}$, $\underline{K}$, $\underline{K}'$, and $\underline{F}$ are given by

$$\begin{bmatrix} \hat{C}_1 & 0 & 0 \\ 0 & \hat{C}_1 & 0 \\ 0 & 0 & \hat{C}_2 \end{bmatrix} \begin{Bmatrix} u \\ v \\ T \end{Bmatrix} + \begin{bmatrix} K^{11}+2K^{22} & K^{21} & 0 \\ K^{12} & K^{11}+2K^{22} & 0 \\ 0 & 0 & L^{11}+L^{22} \end{bmatrix} \begin{Bmatrix} u \\ v \\ T \end{Bmatrix}$$

$$+ \; \epsilon_0^{-1} \begin{bmatrix} K^{11'} & K^{12'} & 0 \\ K^{21'} & K^{22'} & 0 \\ 0 & 0 & 0 \end{bmatrix} \begin{Bmatrix} u \\ v \\ T \end{Bmatrix} = \begin{Bmatrix} F^1 \\ F^2 \\ F^3 \end{Bmatrix} \qquad (18)$$

$$K_{11}' = \int \frac{\partial \varphi}{\partial x} \frac{\partial \varphi^T}{\partial x} dv \qquad\qquad K_{22}' = \int \frac{\partial \varphi}{\partial y} \frac{\partial \varphi^T}{\partial y} dv$$

$$K^{12'} = \int \frac{\partial \varphi}{\partial x} \frac{\partial \varphi^T}{\partial y} dv \qquad\qquad K^{21'} = \int \frac{\partial \varphi}{\partial y} \frac{\partial \varphi^T}{\partial x} dv$$

The matrices $\underline{C}$ and $\underline{F}$ are given in Eq. (15). The integrands in Eqs. (15) and (18) are evaluated numerically due to two reasons: algebraic complexity, and irregularity of the domains. The usual procedure is to use Gaussian quadrature to evaluate them. Any polynomial can be exactly integrated if a high enough order of quadrature is used. However, in the context of penalty methods for incompressible flow problems, a difficulty arises as will be explained below. Eq. (1) which denotes the conservation of mass can be viewed as a constraint to be satisfied by the velocity field. From a computational point of view such constraints can be satisfied by using either the method of Lagrange multipliers or penalty method.

The former results in the mixed method in which the pressure can be identified with the Lagrange multiplier. In the penalty method however, the mass conservation is satisfied by the penalized variational statement for Eq. (1) as given by Eq. (17). The continuity equation is exactly satisfied as the penalty parameter $\epsilon_o^{-1} ---> \infty$. However, as ϵ_o^{-1} increases, the continuity part dominates and we obtain only the trivial result (no flow as can be seen from Eq. (17)). To remedy this, it is necessary to impose a singularity in $\underset{\approx}{K}'$, so that

$$[\underset{\approx}{K}'] \; \{\underset{\sim}{q}\} = 0 \quad \text{but} \quad \{\underset{\sim}{q}\} \neq 0 \qquad (19)$$

Such singularities can be easily introduced by evaluating $\underset{\approx}{K}'$ using low or reduced integration orders. (See Zienkiewicz [18]). Thus while the matrices $\underset{\approx}{C}$ and $\underset{\approx}{K}$ are to be evaluated with a high degree of accuracy, $\underset{\approx}{K}'$ must be evaluated to a lower order. In this study, 3 X 3 integration is used for $\underset{\approx}{C}$, $\underset{\approx}{K}$, and $\underset{\approx}{F}$ while a 2 X 2 scheme is used for $\underset{\approx}{K}'$. This has worked quite satisfactorily in the present study. Finally, the magnitude of penalty parameter should be as large as possible. However, the word length of the computer imposes a limitation on this parameter. For small values (less than 10^6) the solution is effected. For larger values, it is found that convergence becomes difficult. The effects of variation of the penalty parameter on the convergence of the numerical scheme and the overall solution are demonstrated. The convergence criterion is the same as used for the mixed method (Eq. (16))

Turbulence Model:

The need of turbulence modeling in the analysis of heat exchangers can be hardly overemphasized. Usually, higher values of friction drag and pressure drop are associated with turbulent flows, which result in increased mixing and help diffuse a quantity faster in the flow. Besides, it is quite well known in fluid mechanics literature, that laminar flows in nature are more an exception than a rule. Numerical modeling of turbulent flows usually follows the solution of Navier Stokes equations with Reynolds stresses included in them. In order to predict turbulent flows numerically, it becomes necessary to make closure assumptions about the apparent turbulent stresses and heat flux equations. It must be noted however, that all presently known turbulence models have limitations. The ultimate turbulence model is yet to be developed. A good discussion on the various turbulence models and the associated numerical models can be found in references [19-23]. In this investigation, the model adopted is the two equation or $\tilde{k}$-ϵ model (see [19-20] for details). In this model in addition the usual governing equations for pressure, velocities, and temperature (in the form of continuity, linear momentum and energy) two other equations need to be added. They are the turbulence energy $\tilde{k}$, and the dissipation rate ϵ equations which are given as follows:

$$\rho \left[u \frac{\partial \tilde{k}}{\partial x} + v \frac{\partial \tilde{k}}{\partial y} \right] = \frac{\partial}{\partial y} \left(\frac{\mu_T}{Pr_k} \frac{\partial \tilde{k}}{\partial y} \right) - \rho \epsilon + \mu_T \left(\frac{\partial u}{\partial y} \right)^2 \qquad (20)$$

$$\rho \left[u \frac{\partial \epsilon}{\partial x} + v \frac{\partial \epsilon}{\partial y} \right] = \frac{\partial}{\partial y} \left[\frac{\mu_T}{Pr_\epsilon} \frac{\partial \epsilon}{\partial y} \right] + c_1 \frac{\epsilon}{\tilde{k}} \mu_T \left(\frac{\partial u}{\partial y} \right)^2 - c_2 \rho \frac{\epsilon^2}{\tilde{k}} \qquad (21)$$

The finite element analogue to the above is obtained in the usual way. First the variational statement corresponding to the above equations is obtained for the whole domain which is later specialized for a particular element. Then the above equations are combined with Eqs. (10) − (12) to obtain a set of equations. These when combined a suitable set of boundary conditions completes the continuum description. The constants in the $\overline{k}$-ϵ model are as follows:

$$\mu_T = c_\mu \rho \frac{\tilde{k}^2}{\epsilon} \qquad (22)$$

$$c_\mu = 0.09 \qquad c_1 = 1.55 \qquad c_2 = 2.0 \qquad Pr_k = 1.0 \qquad Pr_\epsilon = 1.3$$

Similar to laminar flow formulation wherein the dependent variables were interpolated over a typical element as in Eq. (13), in turbulent flows there are additional nodal point variables corresponding to the turbulence energy $\tilde{k}$ and dissipation ϵ. A typical element

with quadratic interpolation for these variables is shown in Fig. 3. The rest of the formulation follows along the same lines as any other finite element formulation for continuum problems, i.e., generation of the element matrices, assembly, imposition of boundary conditions, solution of the matrix equations, and finally post processing. At present NONFLAP is being modified to include turbulence modeling capability.
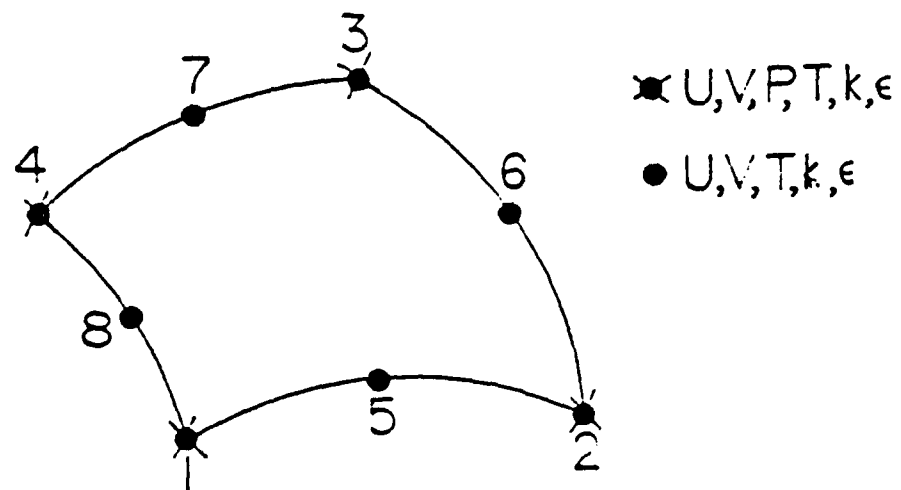
Figure 3: An eight node element for turbulence modeling

NUMERICAL RESULTS

In this section numerical results are presented. This investigation concentrated primarily on the applications of NONFLAP to the numerical solutions of heat exchangers of particular geometries. These include pin-fin, rectangular plate-fin, and diamond shaped fins. Since many of the results from this research will be published elsewhere (some have already been published; see [24-25]), only the highlights of the research will be presented here.

A schematic diagram of the in line and offset pin-fin geometries is shown in Fig. 4. It is to be noted that the lines joining the centres of the cylinders intersect each at right angles for all values of $\hat{P}/D$. The computational domain is denoted by the shaded area. The length of the domain in both case is three rows deep. Three values of $\hat{P}/D$ have been used: 1.5, 1.25, and 1.75 and four different values of Pr : 0.005, 0.7, 5, and 100. The details of the finite element mesh and the boundary conditions are shown in Fig. 5. The mesh consists of 480 eight noded elements for which the velocities and temperatures are interpolated quadratically and the pressure is interpolated linearly. The upstream and downstream lengths were chosen to be about five diameters long. The gradation of the mesh near the cylinders is shown Fig. 5b. A similar grid has been used to investigate offset geometry also, but the total number of elements used was 1224.
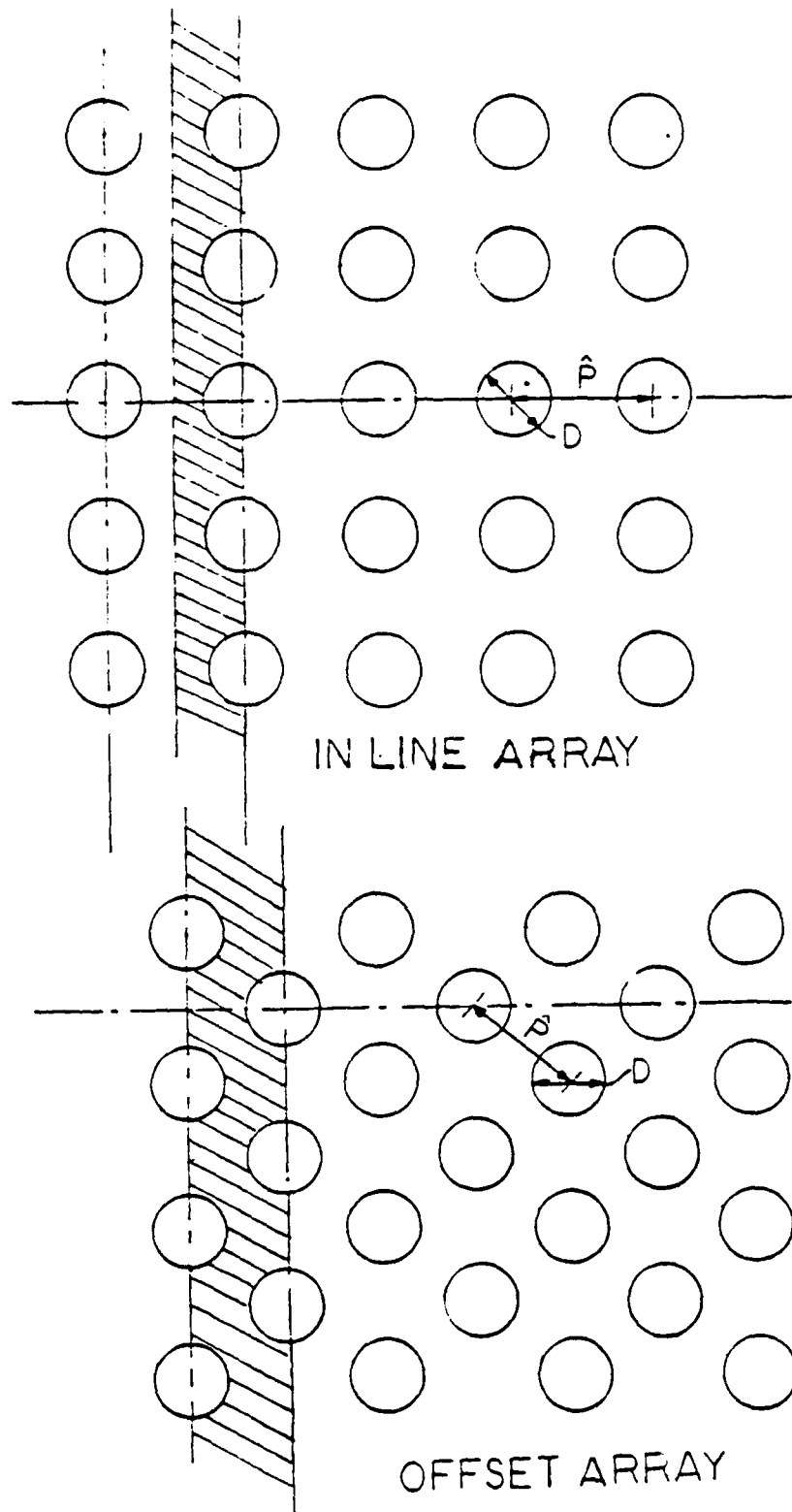
Figure 4: Physical description of the pin fin geometry in line and offset

U,V=O
T=T$_v$

U=O

U=O

U:O,T=T$_i$,
V=V$_o$

U:O

U=O
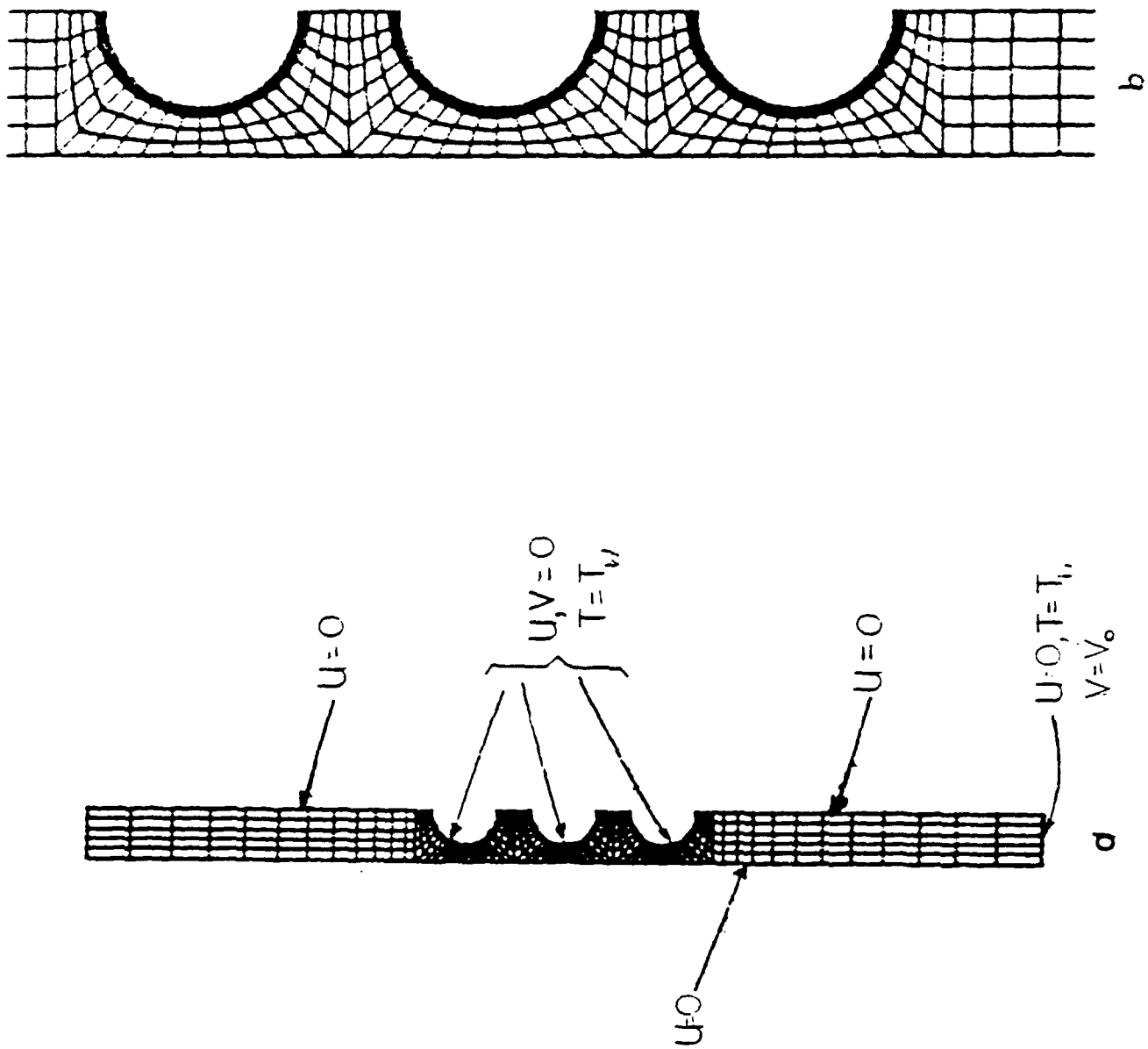
Figure 5: Finite element mesh with boundary conditions:
a) Entire grid and b) Detail near the cylinders.
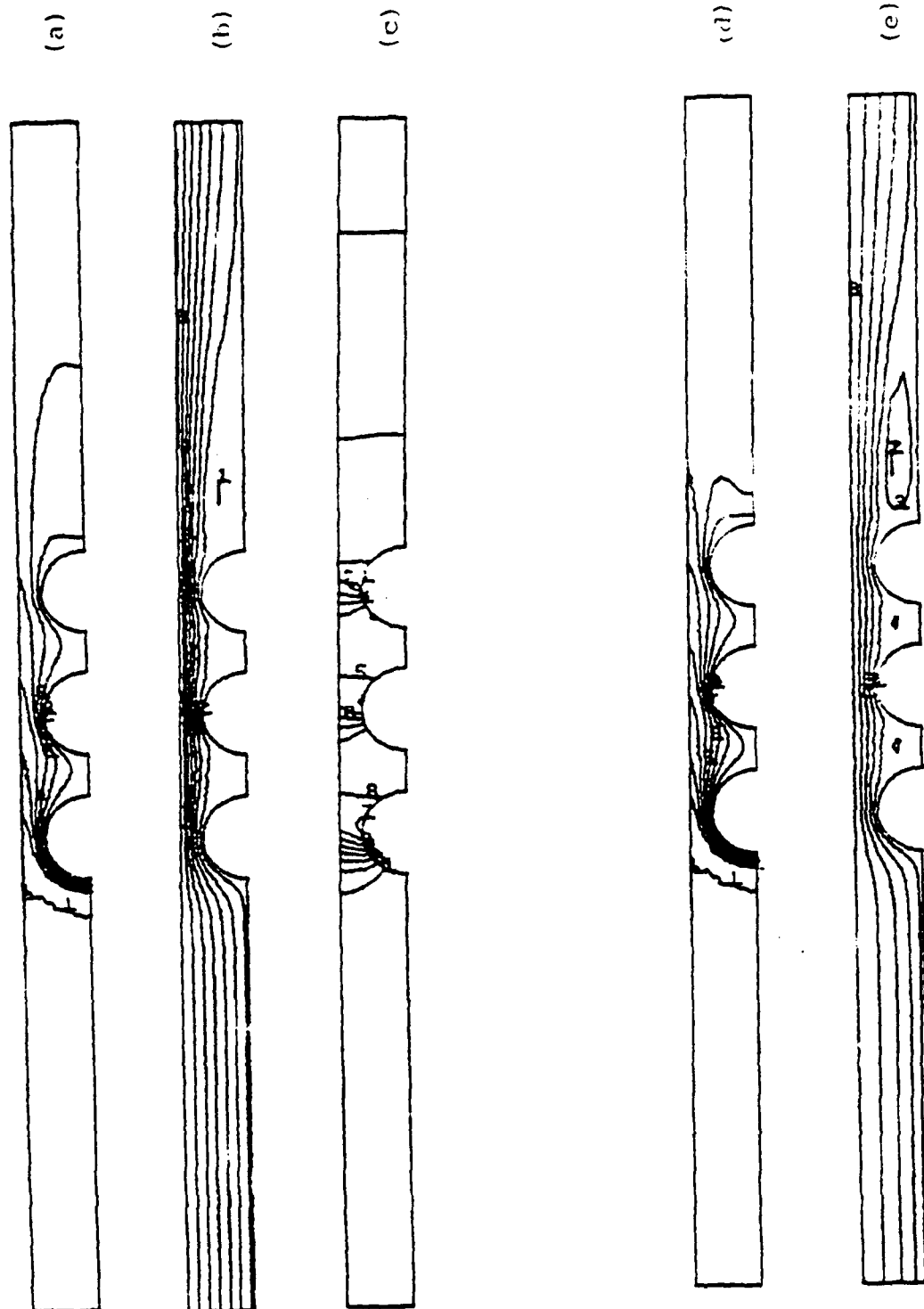
Figure 6: Results for in line geometry for Re = 120, Pr = 0.7, and P/D = 1.5

(a)
(b)
(c)
(d)
(e)
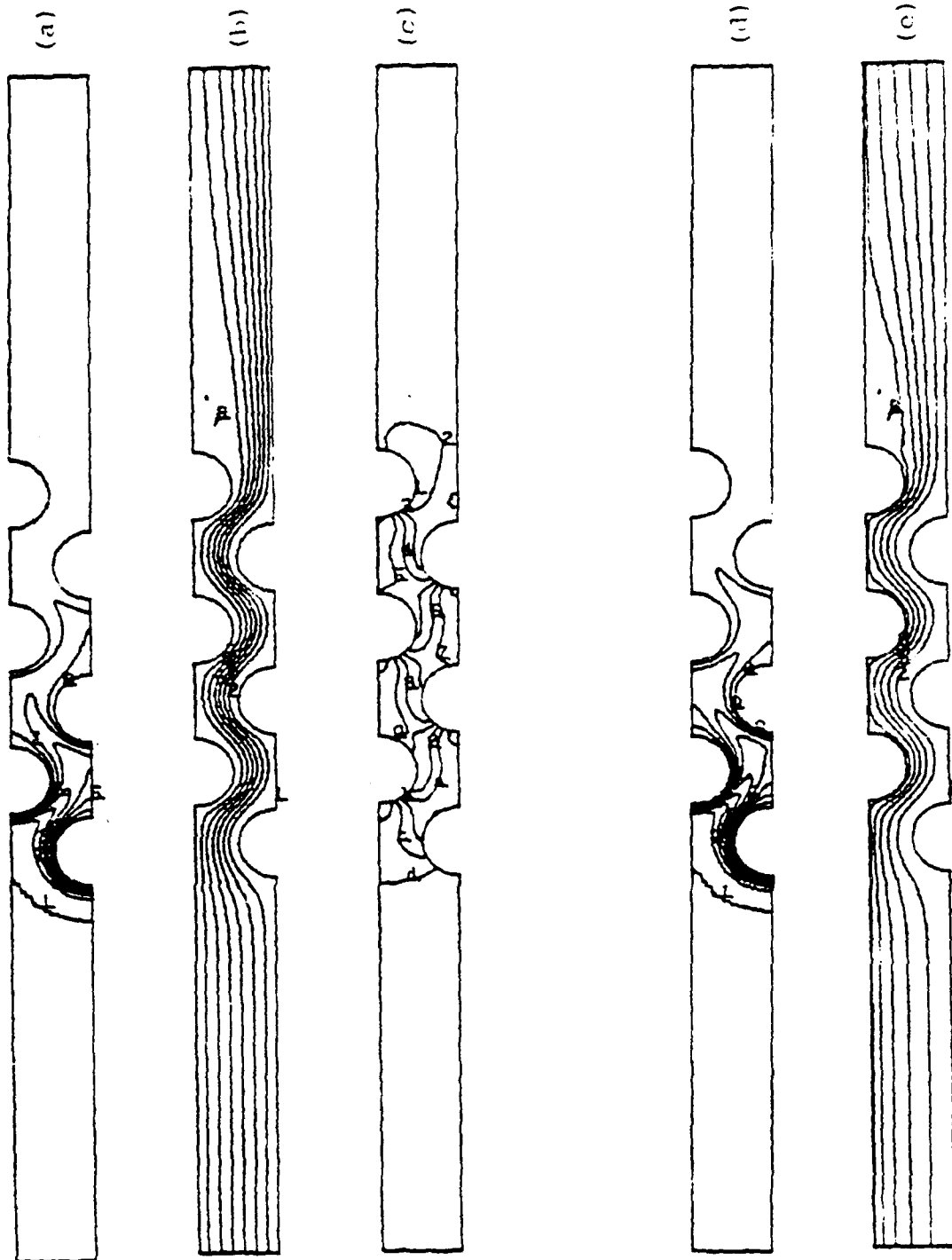
Figure 7: Results for offset geometry for $Pe = 60$, $Pr = 0.7$, and $P/D = 1.5$
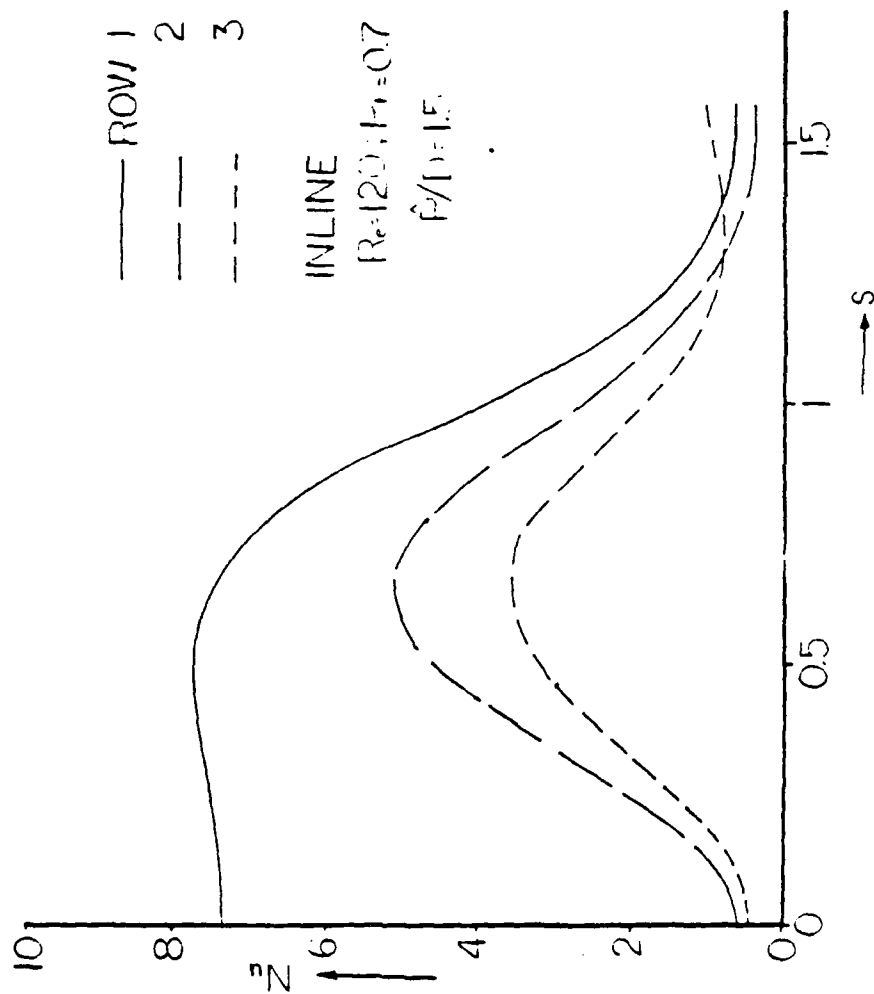
Figure 8: Circumferential variation of Nusselt number for in line geometry for Re = 120, Pr = 0.7, and P/D = 1.5
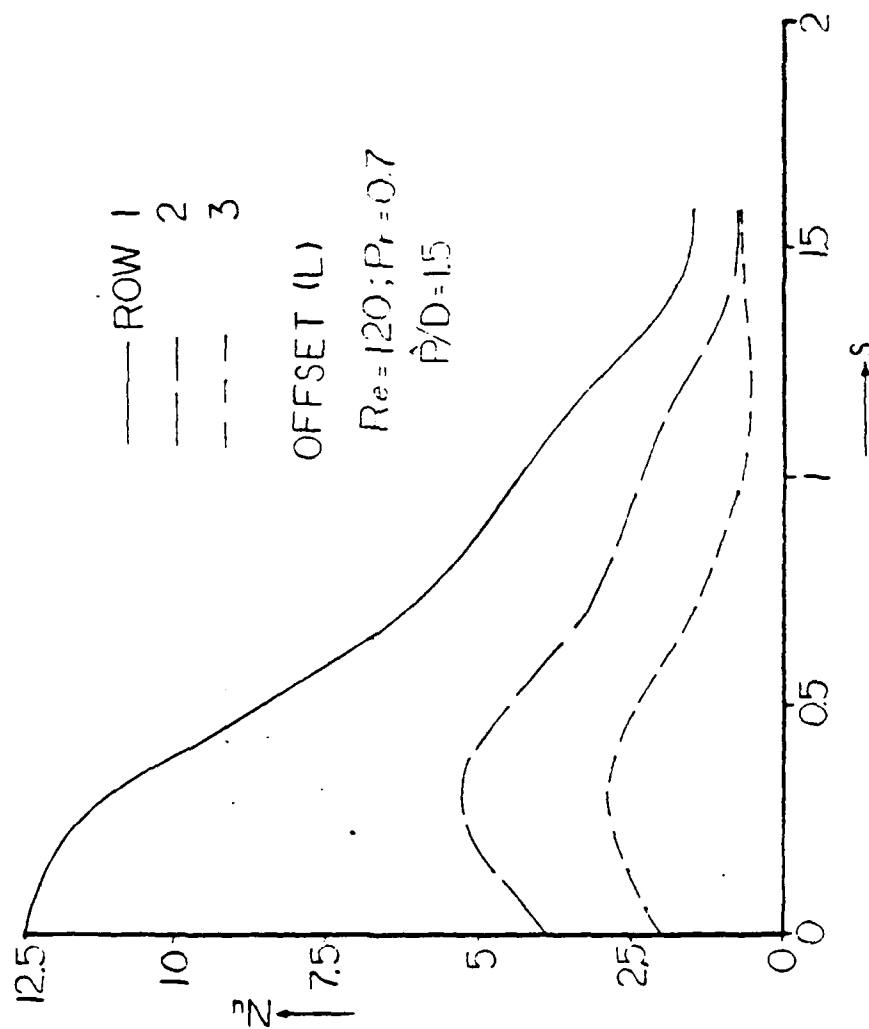
Figure 9a: Circumferential variation of Nusselt number for offset geometry for Re = 120, Pr =,0.7, and P/D = 1.5 ---- left side
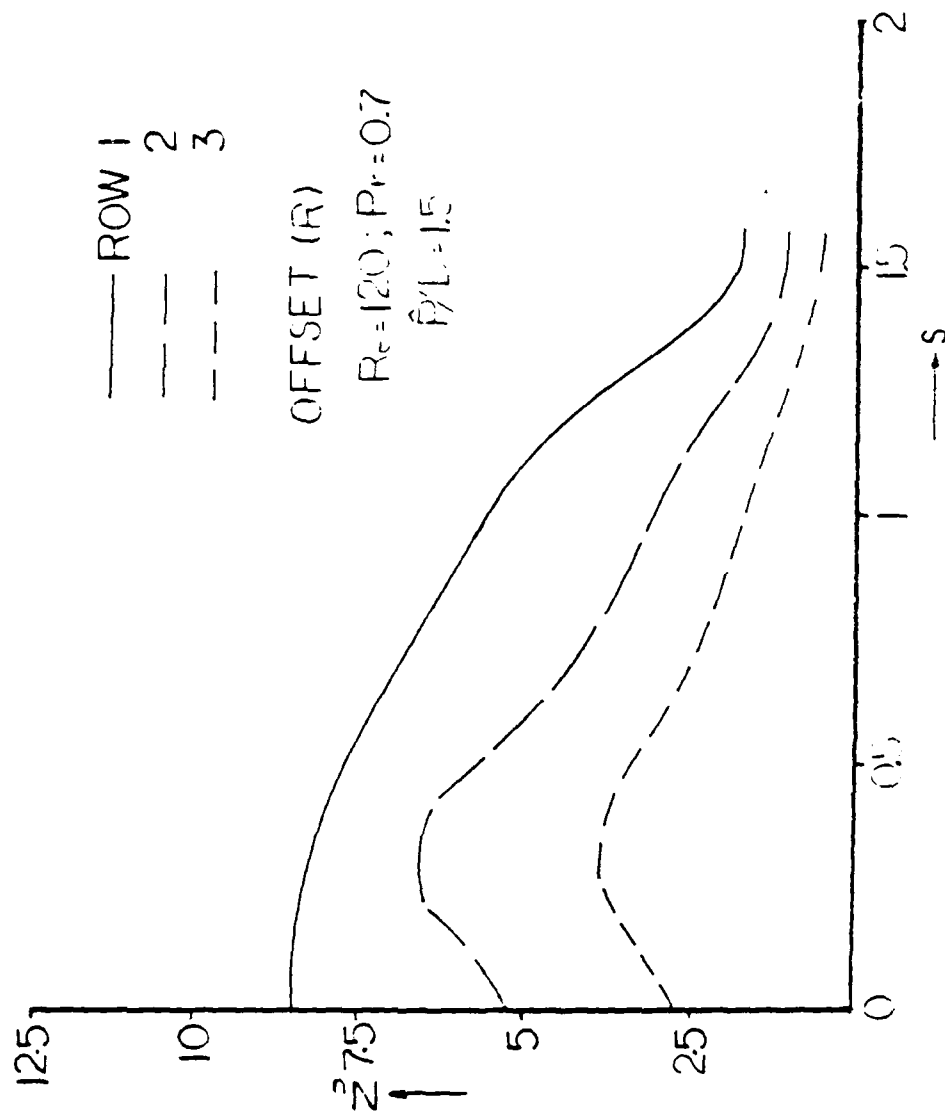
Figure 9b: Circumferential variation of Nusselt number for offset geometry for Re = 120, Pr = 0.7, and P/D = 1.5 ---- right side
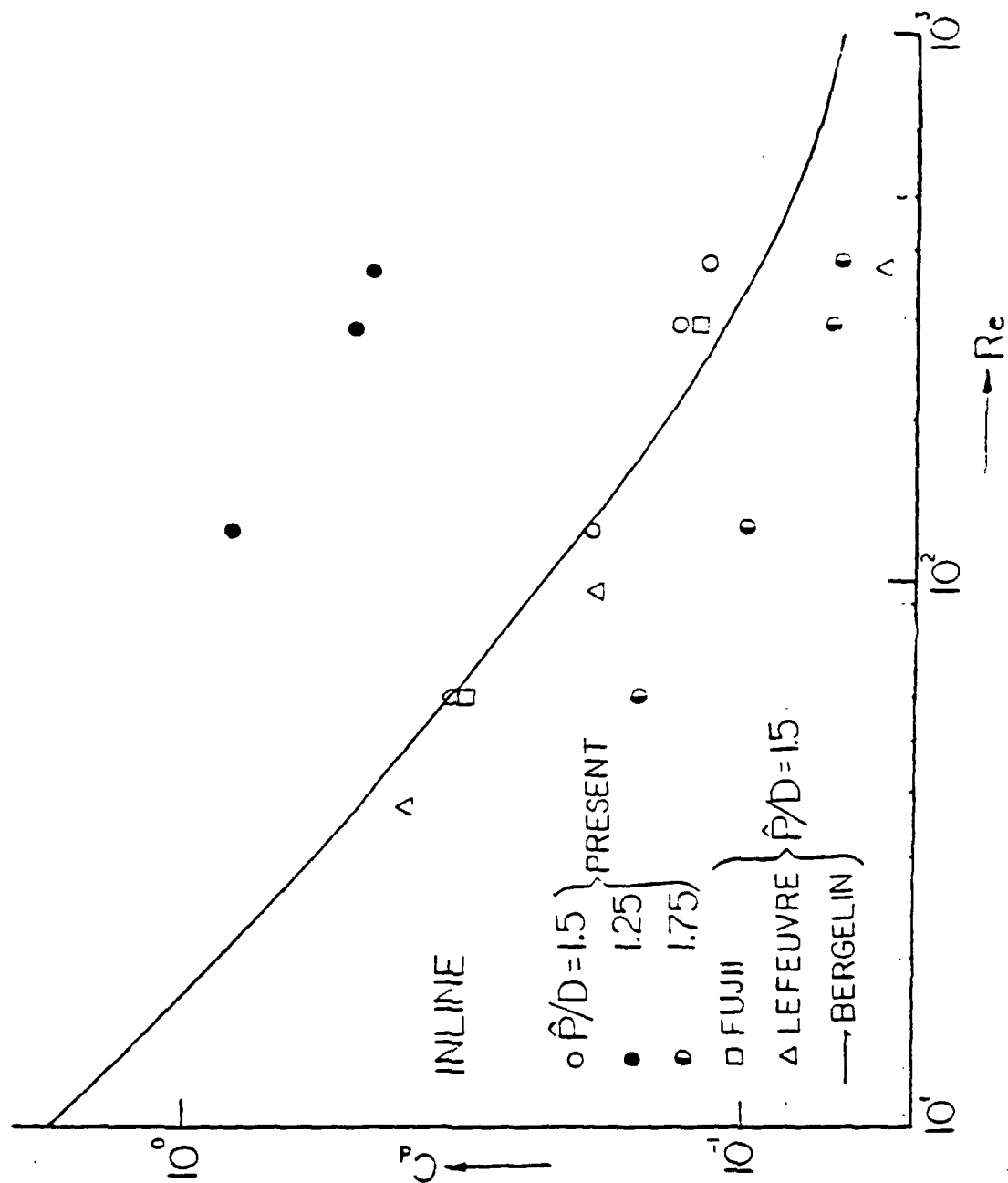
Figure 10a: Variation of drag coefficient vs Reynolds number for in line geometry
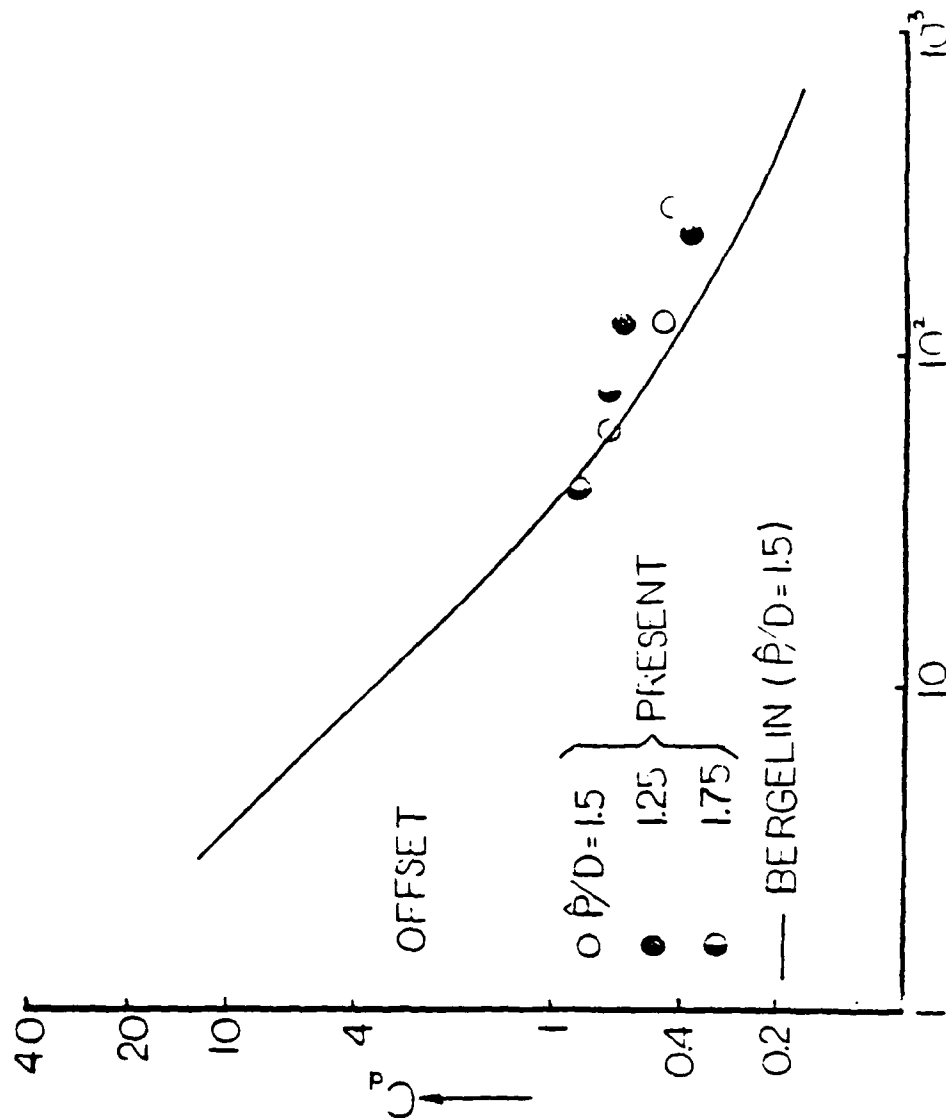
Figure 10b: Variation of drag coefficient vs Reynolds number for offset geometry

The plots of isotherms, streamlines, and isobars for in line geometry for $\hat{P}/D$ of 1.5 and Re and Pr of 120 and 0.7 respectively are shown in Fig. 6. All the plots represent isolines of constant increments. The details of the streamlines and and isotherms near the cylinders are shown in Fig. 6d and 6e. Similar plots are shown in Fig. 7 for offset geometry for Re = 60. The significant feature for this geometry is the near total mixing with practically no stagnant fluid anywhere. Notice the recirculation region here also after the last cylinder. The variation of local Nusselt numbers for each of the three cylinders for in line and offset geometries is shown in Fig. 8 and 9. It can be seen that as opposed to the in line case, the maximum heat transfer occurs upstream of the shoulder and the drop is also more gradual, indicating that the convection mode is quite dominant. The maximum and average values are both higher than the corresponding in line geometry.

An important variable which has an impact on pumping power is the pressure drop between tube rows. The variation of the drag coefficient with Re for both geometries is shown in Fig. 10 and compared with results from other investigators. The agreement is quite reasonable. One trend that can be seen is the increase in the value of drag coefficient as $\hat{P}/D$ decreases especially for the in line configuration. This is not unexpected since the closer the corrugations in a flow, the higher the flow resistance and hence the higher the pressure drop.

The same problem was attempted using the penalty finite element model. The penalty parameter is varied from 10^6 to 10^{15}. It was found that for low values of the penalty parameter (upto 10^{14}) it took six iterations for the method to converge; however, for 10^{15}, the method did not converge in 20 iterations. The difference in the solutions between both the methods was found to be less than half percent. Variations of axial velocity and temperature at different locations in the configuration are shown in Fig. 11. The temperatures are shown at three locations (the shoulders of the three cylinders) while the velocity is shown at only one location. This has been done because the velocity was fully developed for this value of Re after the first cylinder itself. The results plotted are for $\epsilon_0^{-1} = 10^6$ and 10^{14}, and the mixed method. It is clear that the results are identical. As the penalty parameter decreases, the incompressibility condition tends to be violated, the value of $\underset{\approx}{K}'$ would be of the same magnitude of $\underset{\approx}{C}$ and $\underset{\sim}{K}$ and thus would produce erroneous results for the velocity field. The lowest and highest values of ϵ_0^{-1} for which converged results can be obtained for this class of problems are 10^6 and 10^{14} respectively.

Next, rectangular plate fin heat exchangers were analyzed. The geometries of in line and offset fins are shown in Fig. 12. Since it was found that both penalty and mixed methods gave identical results, this problem was solved using the penalty method only. The grids for in line and offset geometries are shown in Fig. 13.
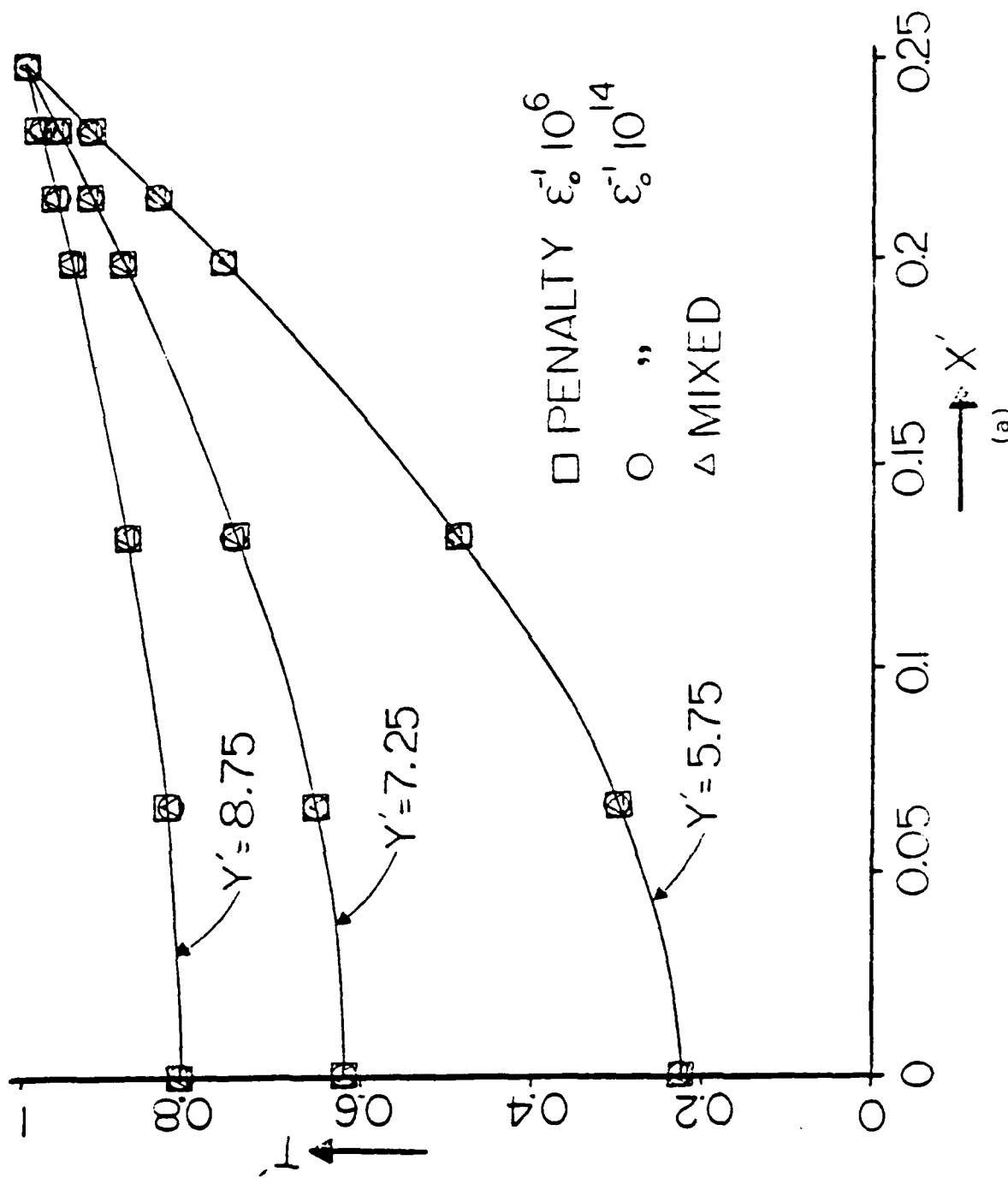
Figure 11: Comparison of results for penalty and mixed methods: Variation of axial velocity
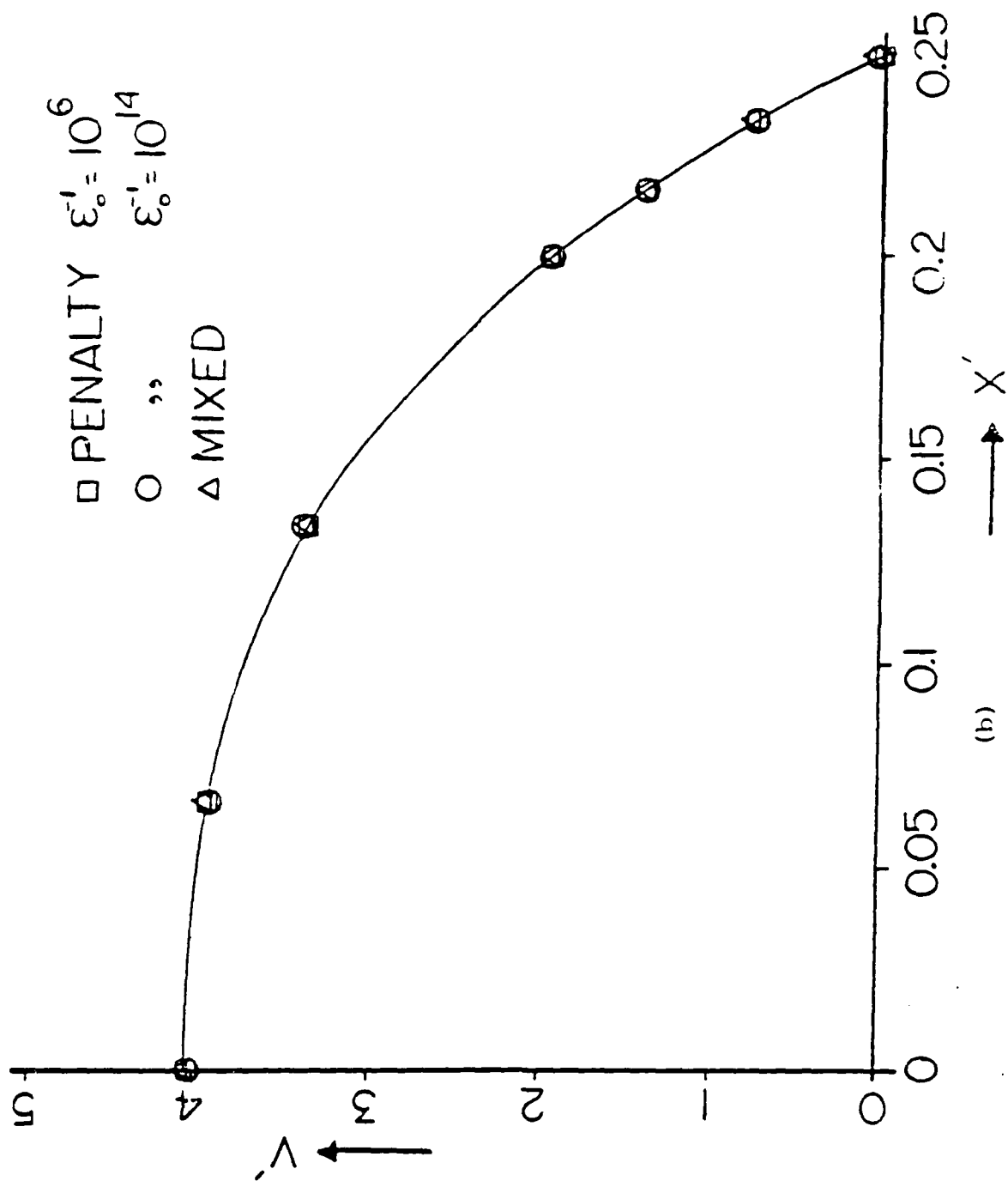
Figure 11: Comparison of results for penalty and mixed methods: variation of temperature at the shoulders of cylinders
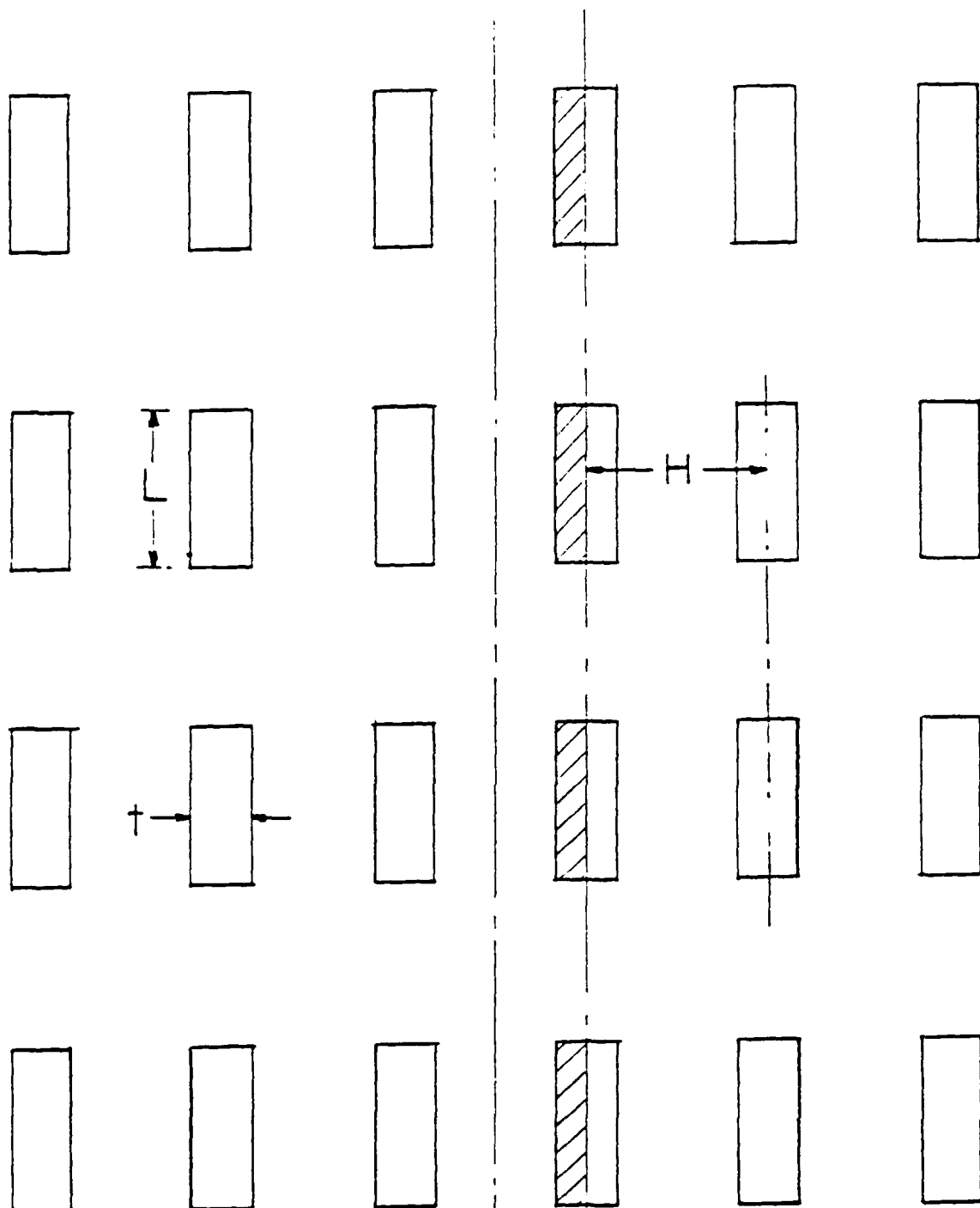
Figure 12a: Physical description of rectangular plate fins
in line geometry
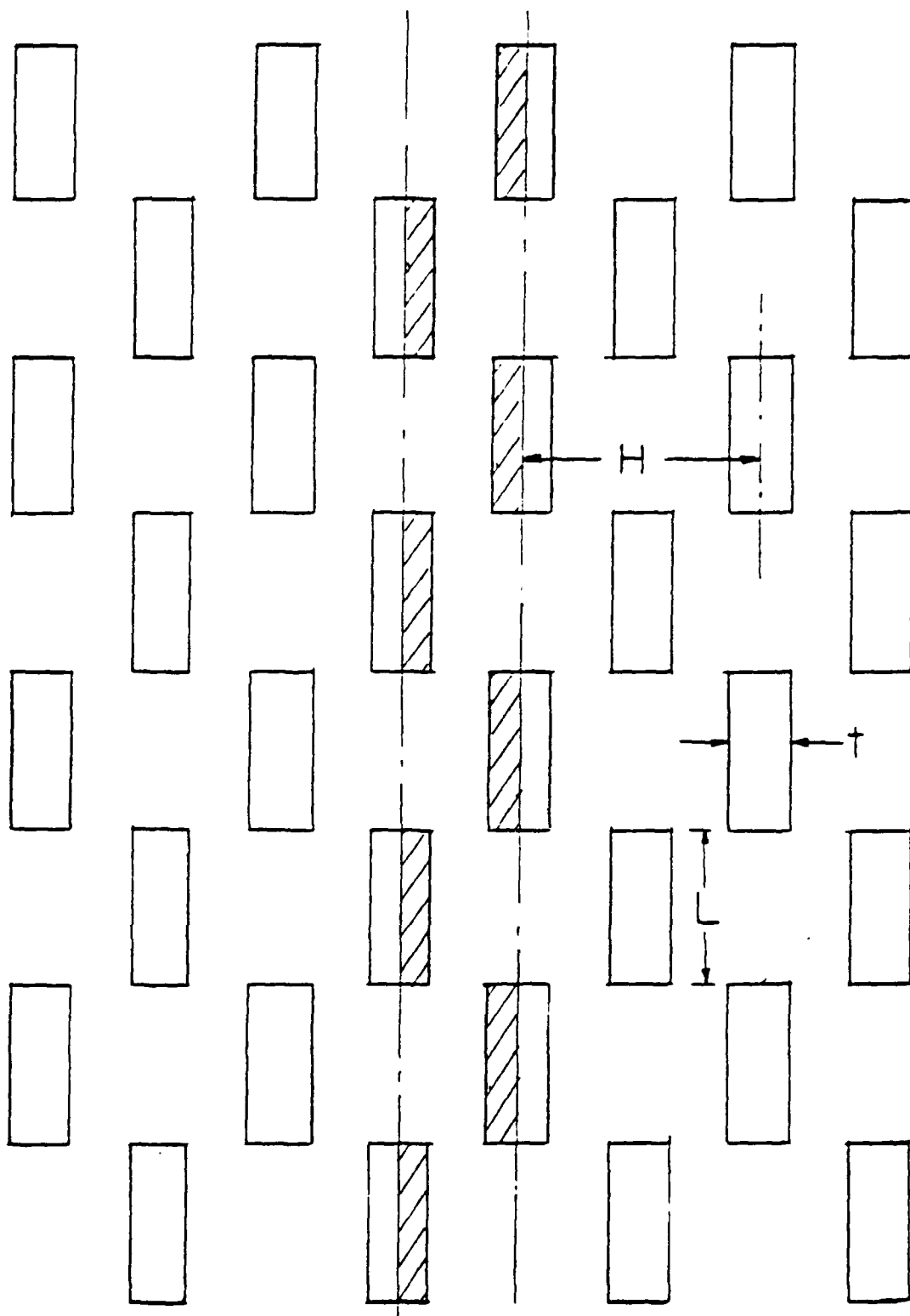
Figure 12b: Physical description for rectangular plate fins offset geometry

(a)

(b)

Figure 13: Finite element meshes for plate fins a) in line and b) offset geometries

The results in the form of streamlines and isotherms are shown in Fig. 14. Notice the boundary layer separation and the wide recirculating region even for low values of Re. Similar results were obtained for offset fin geometry also.

In order to investigate the capabilities of the computer code NONFLAP another problem involving a different geometry was studied. This problem uses fins shaped in the form a diamond placed in an offset array. The physical problem is shown in Fig. 15. Of interest here are the effects of the included angle and aspect ratio s/a on the heat transfer characteristics. This problem was solved for air with Pr = 0.7 and various values of Re. Typical streamlines and isotherms are shown in Fig. 16. Variation of the average Nusselt number with Re is shown in Fig. 17. The last case studied involves the heat transfer characteristics of a fluid through a 180 degree channel. Typical results for this case for different values of Peclet number are shown in Fig. 18. It was found that recirculation eddies formed not only on the inner wall on the exit side but also on the outer wall on the inlet side.

(a)

(b)

(c)

67-38

(e)

(f)

(g)

(d)

(h)
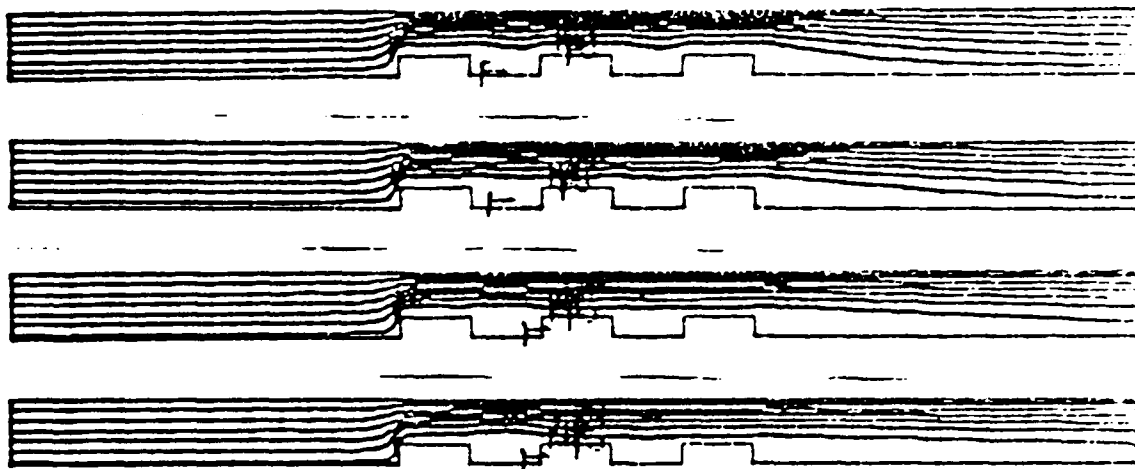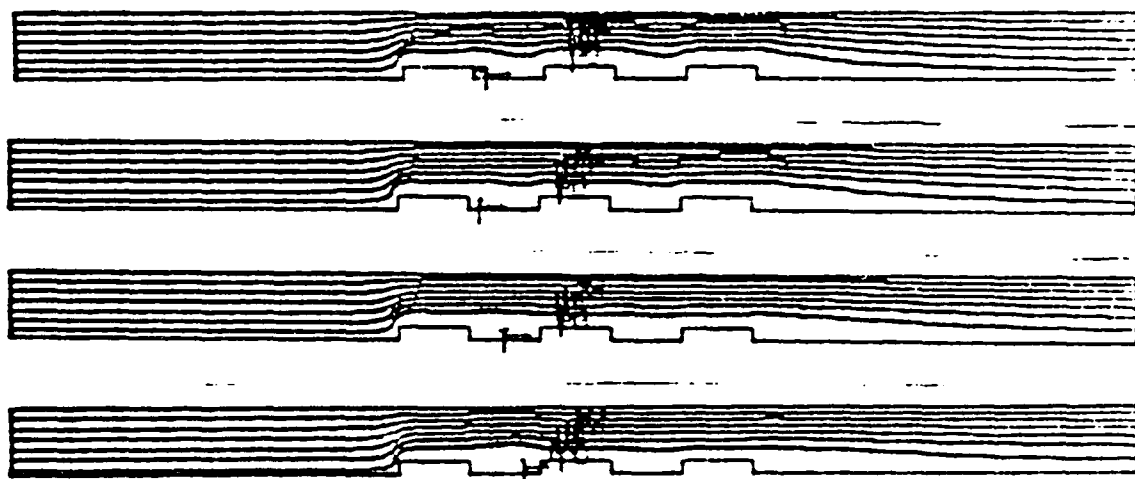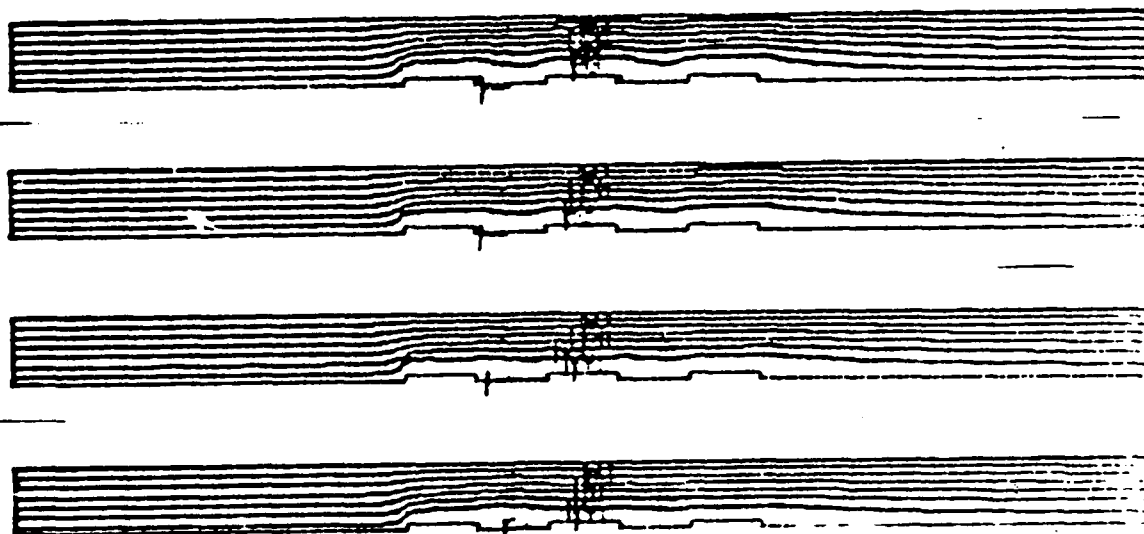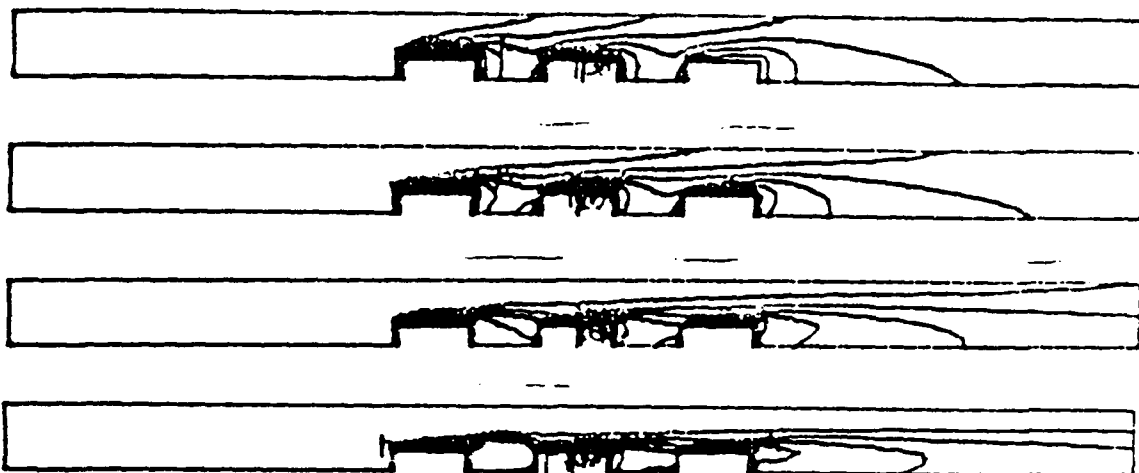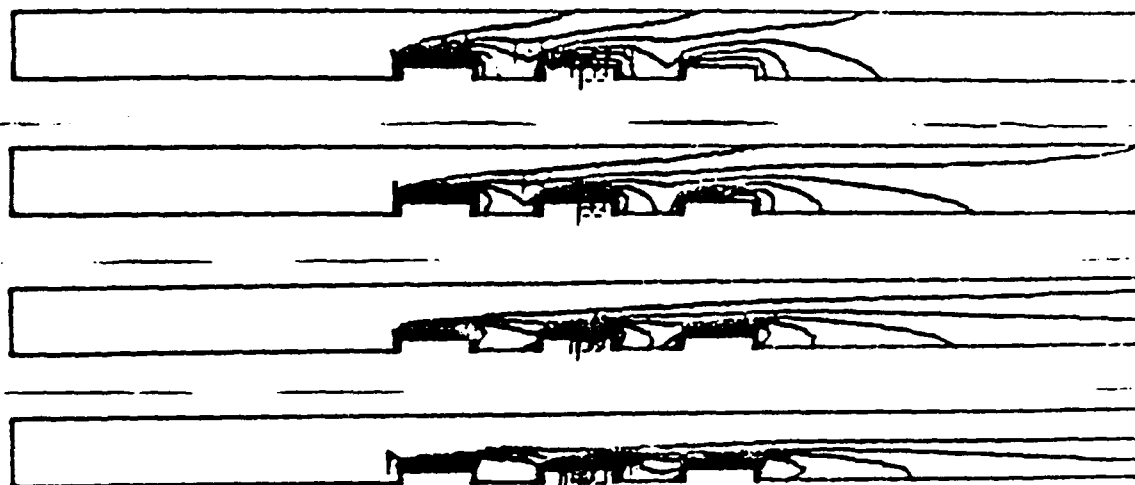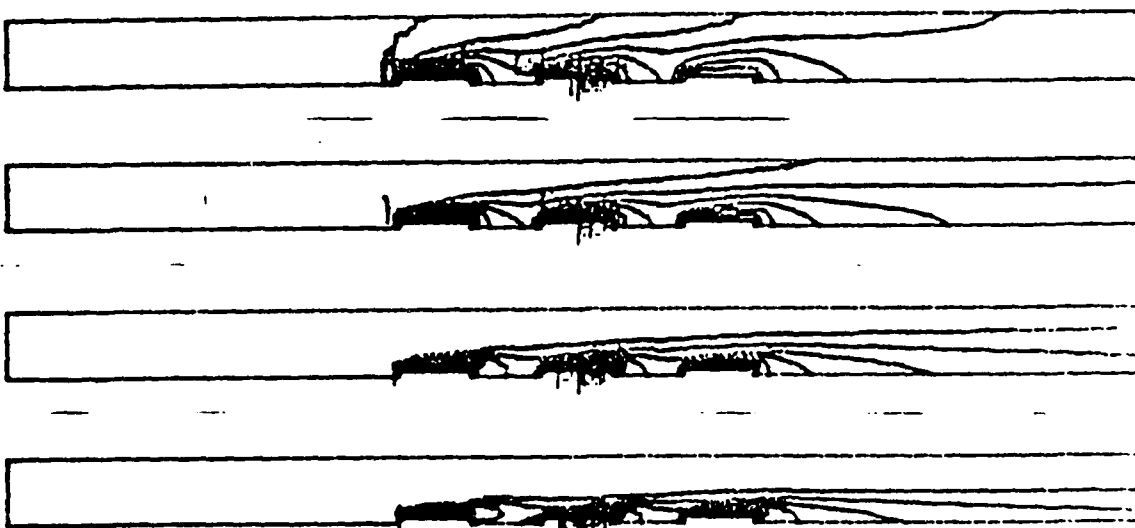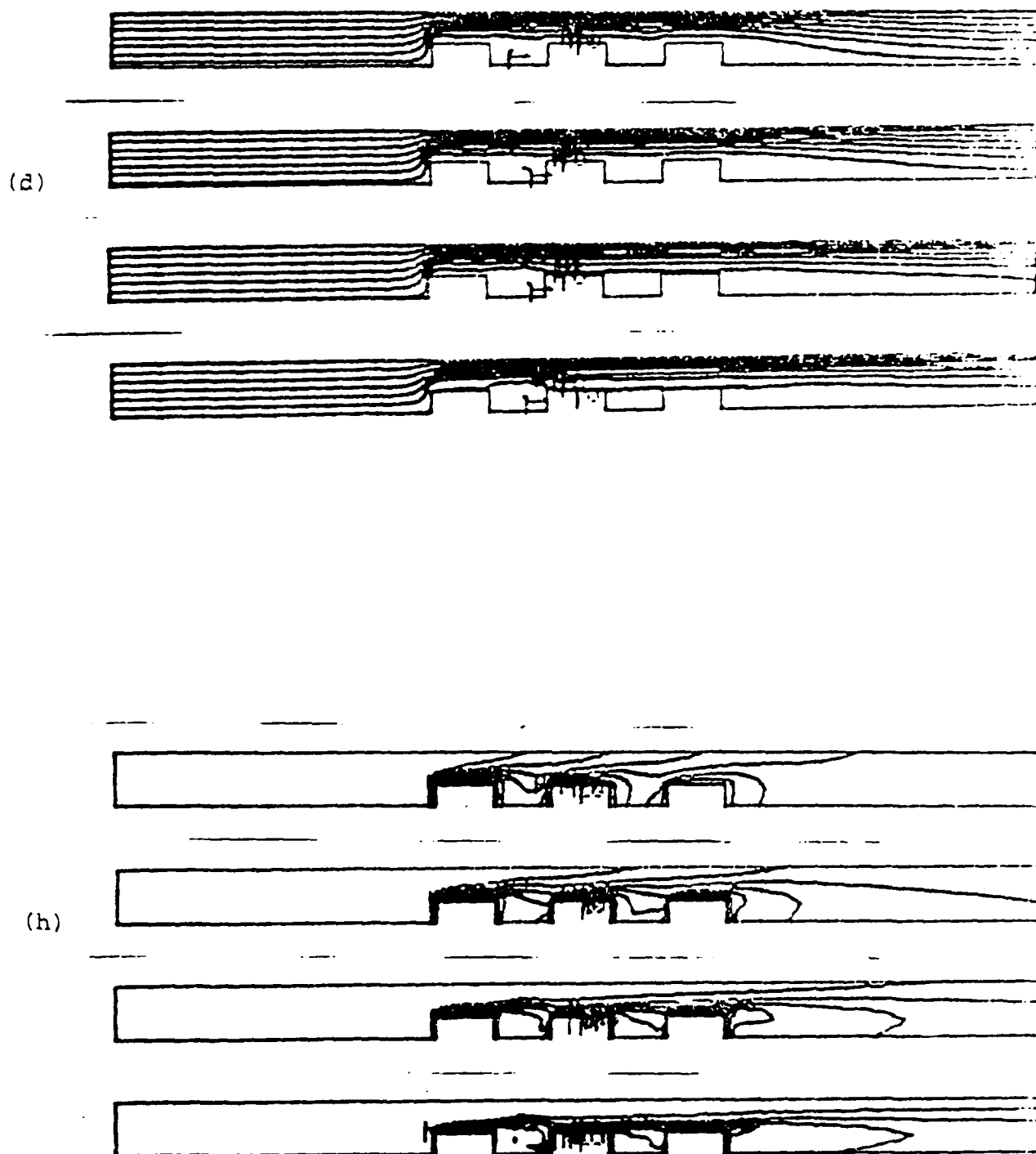
Figure 14: Numerical results for in line plate fins,
a, b, c, d ---- streamlines
e, f, g, h ---- isotherms for different
values of t/L ratios
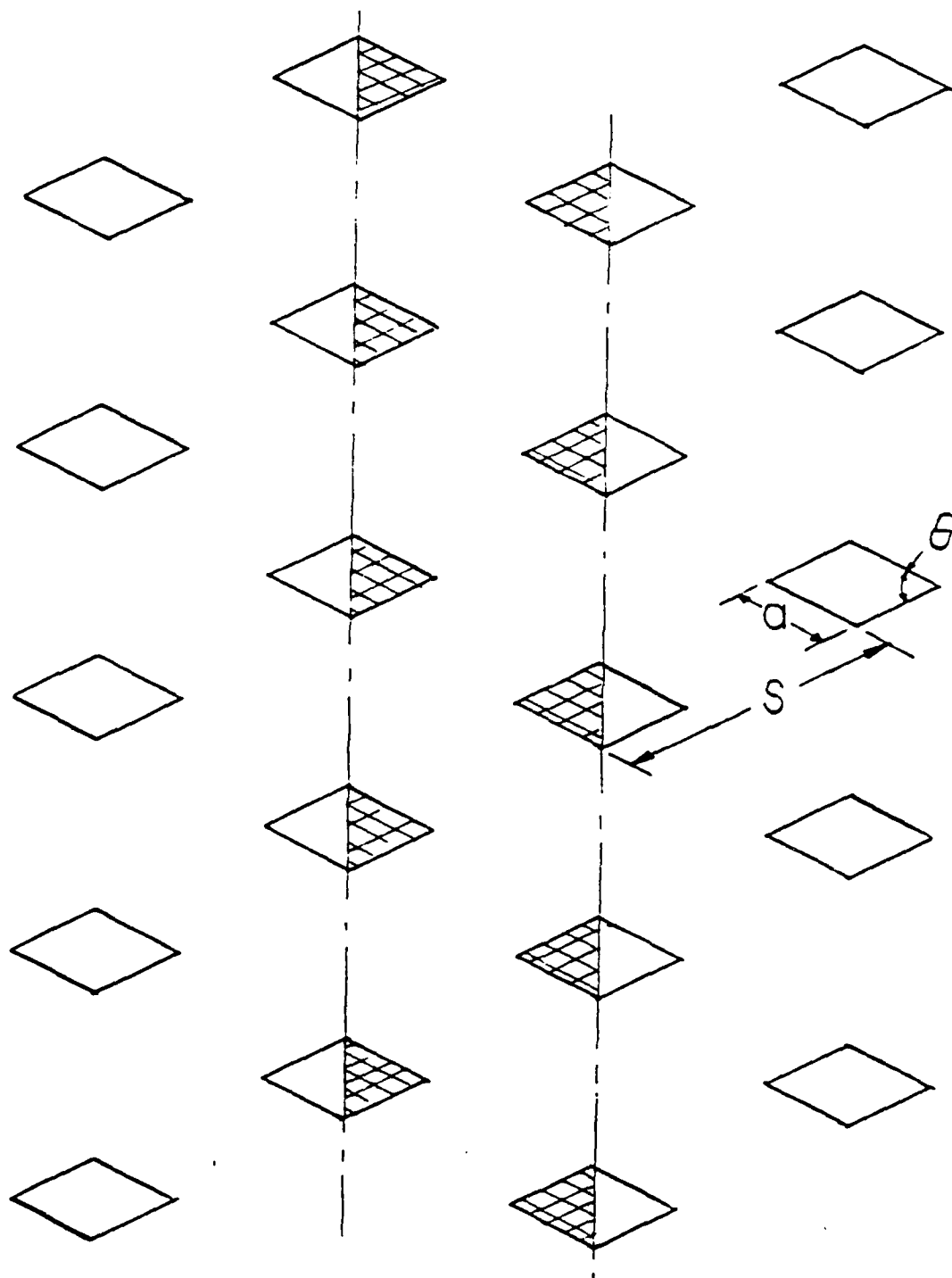
Figure 15: Physical description of diamond shape fin geometry

(a)
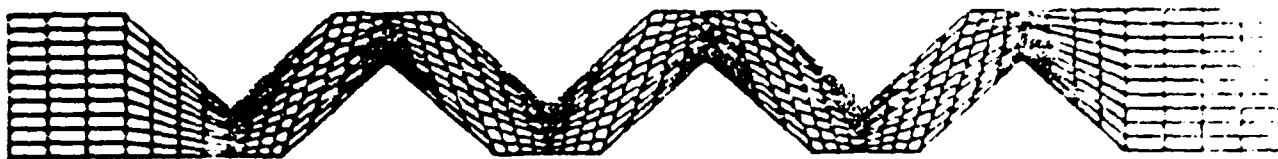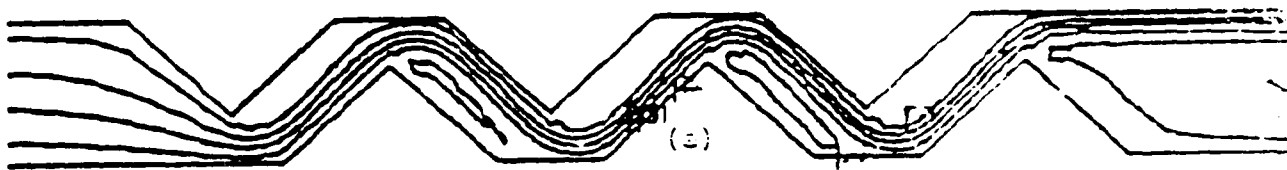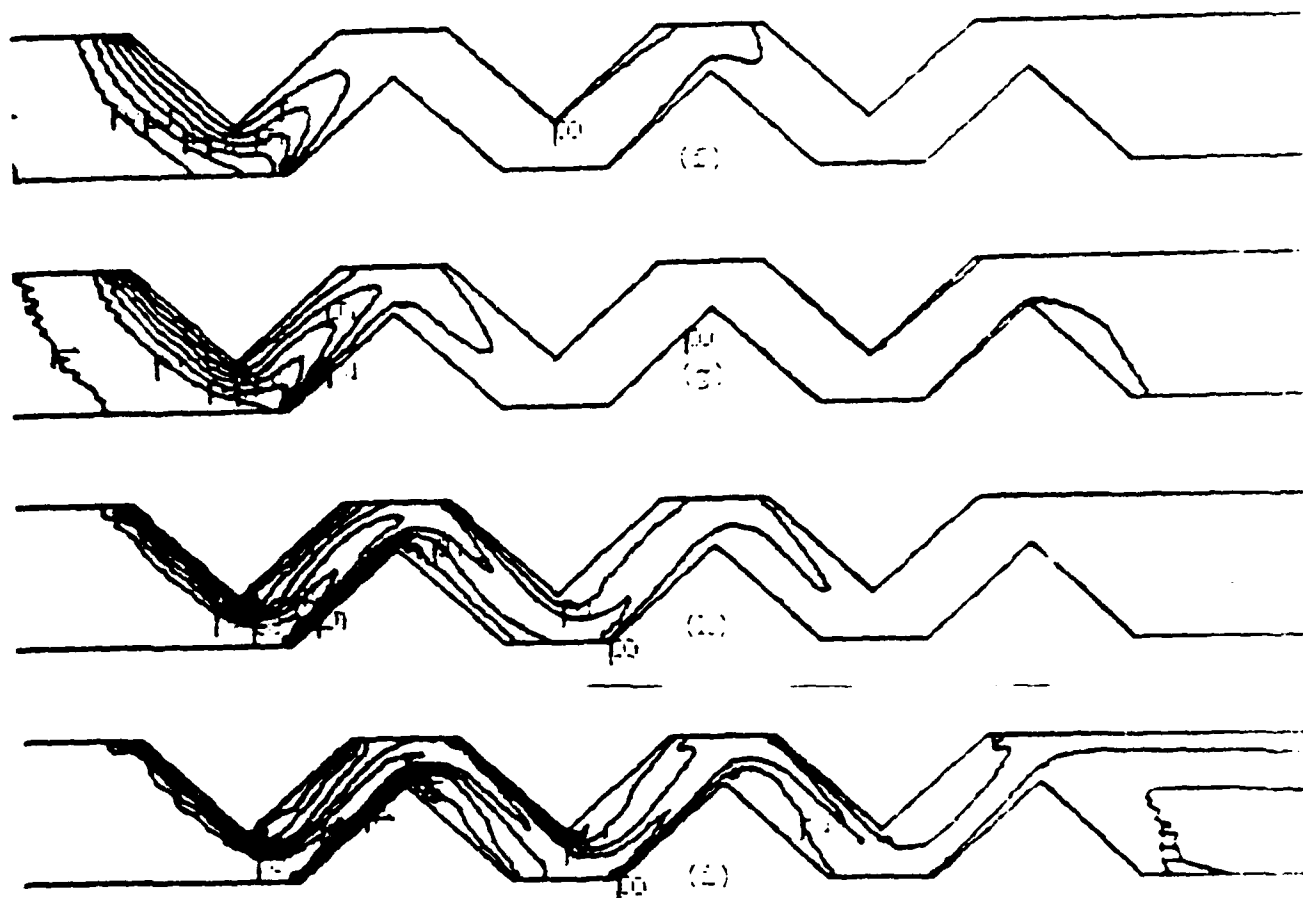
Figure 16: Diamond shape fin problem: a) finite element grid
b) --- i) results for s/a = 1.5, and ϑ = 90 deg.
b) --- e) streamlines and f) --- i) isotherms
for Re = 10, 20, 50 and 100 respectively
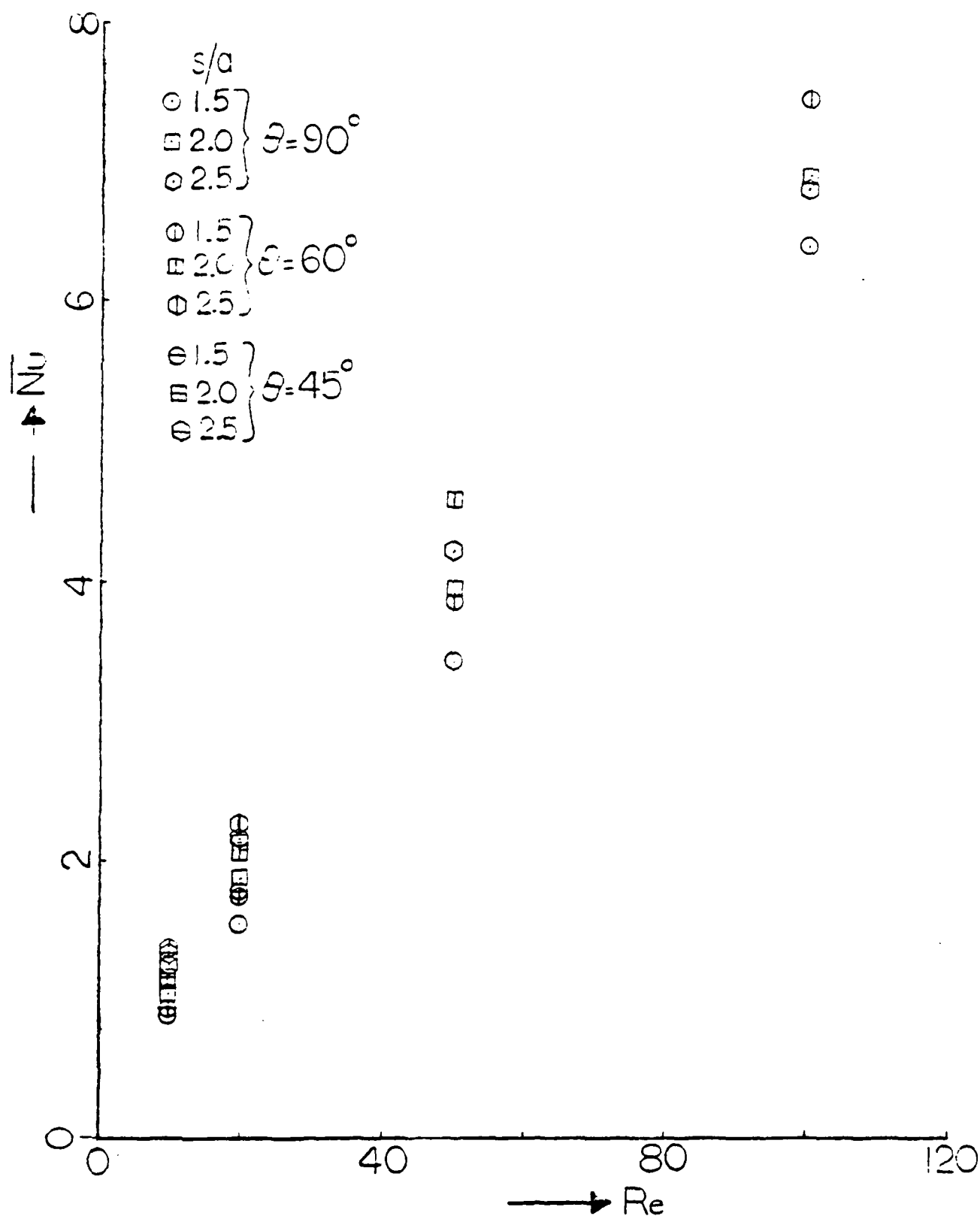
Figure 17: Variation of average Nusselt number with Reynolds number for diamond shape fins.

67-44
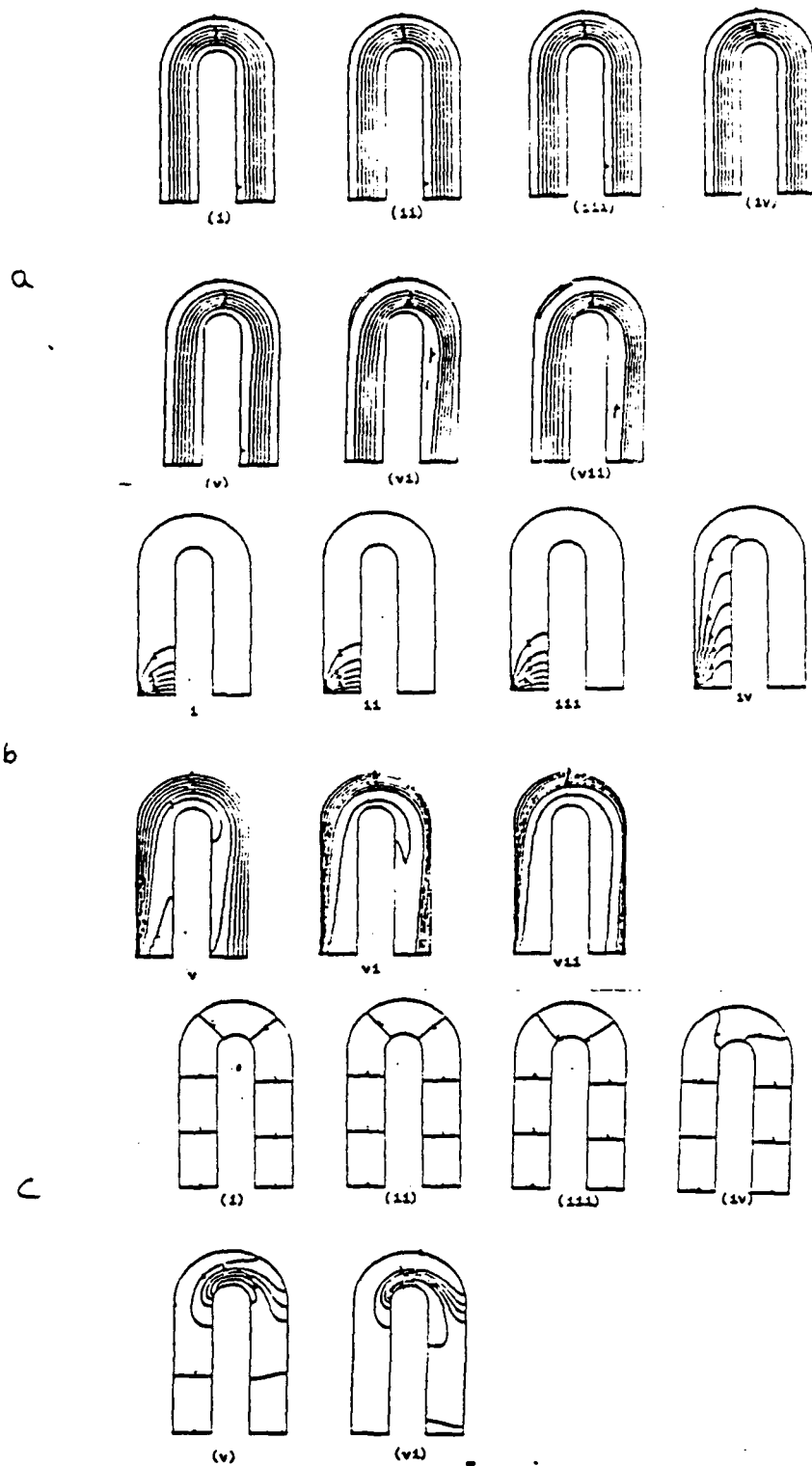
Figure 18: Numerical results for 180 degree U channel,
a) streamlines, b) isotherms, c) isobars

CONCLUSIONS AND RECOMMENDATIONS

The finite element method has been used to analyze active cooling systems. The procedure involved the solution of incompressible and steady Navier Stokes equations for laminar Newtonian fluid flow. Two formulations have been given herein. The first formulation is the mixed or Lagrangian formulation in which pressure appears explicitly as a nodal point variable. The second formulation is the penalty method in which the continuity equation is treated as a constraint on the velocity field. In this formulation pressure does not appear as an interpolation variable. Hence the total degrees of freedom in this case is less. During the course of this investigation, it was found that the highest value of penalty parameter for which converged values were obtained was 10^{14}. When the value was 10^6, the solution was affected. Hence, for the solution of Navier Stokes equations using the finite element method, the penalty method with a penalty parameter of 10^8 to 10^{10} is recommended. The application of the same method to turbulent flows is quite straight forward. However, care must be taken to pick a suitable turbulence model since no single model exists which can accurately and satisfactorily describe turbulent flows. In this study the model which has the widest application in two dimensional flows, namely the $\bar{k}-\epsilon$ model has been used.

Several heat exchanger configurations have been investigated.

It should be pointed out that among all the geometries, the diamond shape is the easiest to manufacture. Although all of the geometries have been studied, a comparison of the heat transfer characteristics remains to be performed so that selection among them could be simplified. From preliminary studies, it can be concluded with confidence that offset geometries give better heat transfer performance.

There are several areas into which this study can be extended. The most immediate and natural extension to the present investigation is the inclusion of natural convection into the model. This is quite important since at low values of inlet flows, natural convection can contribute significantly to the heat transfer. The inclusion of this into the finite element model is very straight forward. When this is accomplished, the various geometries can be studied for several values of Rayleigh numbers, spacing and size of fins, Prandtl numbers, Reynolds numbers, etc. The results presented in this study have a direct bearing on cooling of electronic components. Due to the small size of the passages, the flow is often laminar.

The next area into which this research must be extended is the evaluation of the various turbulence models available in the literature. While the number is large, each model has limited application. A detailed study of these models will yield valuable information as to the uses and limitations of computational fluid

dynamics (involving turbulent flows) in active cooling devices. Because of the versatility of the finite element method, fluid flow and heat transfer through porous media with and without phase change can be easily undertaken. This will facilitate the study several areas of practical interest to aircraft heat exchangers like heat pipes, transpiration cooling, leading edge cooling, etc. If the Navier Stokes equations are combined with equations governing changes of concentration (i.e. mass transfer), boiloff and rollover problems in fuel tanks can be studied. The inclusion of compressibility effects and three dimensional flows is also very important in applying the power of computational methods to solve practical problems.

REFERENCES

1. Zukauskas, A., "Heat Transfer From Tubes in Cross Flow", <u>Advances in Heat Transfer</u>, Vol. 8, pp. 93-160, 1972

2. Aiba, S., Tsuchida, H, and Ota, T., "Heat Transfer Around Tubes in in-line Tube Banks", <u>Bull. JSME</u>, Vol. 25, pp. 919-926

3. Bergelin, O. P., Brown, G. A., Hull, H. L., and Sullivan, F. W., "Heat Transfer and Fluid Friction During Viscous Flow Across Banks of Tubes III: A Study of Tube Spacing and Tube Size", <u>ASME Journal of Heat Transfer</u>, Vol. 72, pp. 881-888

4. Bergelin, O. P., Brown, G. A., and Doberstein, S. C., "Heat Transfer and Fluid Friction During Flow Across Banks of Tubes IV: A Study of Transition Zone Between Viscous and Turbulent Flow", <u>ASME Journal of Heat Transfer</u>, Vol. 74, pp. 953-960

5. Izumi, R., Yamashita, H., and Oyakawa, K., "Fluid Flow and Heat Transfer in Corrugated Channels", <u>Bulletin of the JSME</u>, Vol. 24, 1981a, pp. 1425-1432.

6. Izumi, R., Oyakawa, K., Kaga, S., and Yamashita, H., "Fluid Flow and Heat Transfer in Corrugated Wall Channels", <u>Bulletin of the JSME</u>, Vol. 24, 1981b, pp. 2098-2106

7. Asako, Y., and Faghri, M., "Finite Volume Solutions for Laminar Flow and Heat Transfer in a Corrugated Duct", <u>Fundamentals of Forced an Mixed Convection</u>, ASME HTD-Vol. 42, pp. 43-51, 1985.

8. Suzuki, K., Hirai, E., Miyake, T., and Sato, T., "Numerical and Experimental Studies on a Two Dimensional Model of an Offset-Strip-Fin Type Compact Heat Exchanger Used at Low Reynolds Number", <u>International Journal of Heat and Mass Transfer</u>, Vol. 28, No. 4, pp. 823-836, 1985.

9. Mazumdar, A. K., Singhal, A. K., and Spalding, D. B., "Numerical Modeling of Wet Cooling Towers --- Part 1: Mathematical and Physical Models", <u>ASME Journal of Heat Transfer</u>, Vol. 105, Nov. 1983, pp. 728-735.

10. Mazumdar, A. K., Singhal, A. K., Reilly, H. E., and Spalding, D. B., "Numerical Modeling of Cooling Towers --- Part 2: Application to Natural and Mechanical Draft Towers", <u>ASME Journal of Heat Transfer</u>, Vol. 105, Nov. 1983, pp. 736-743.

11. Amano, R. S., "Laminar Heat Transfer in a Channel With Two Right-Angled Bends", ASME Journal of Heat Transfer, Vol. 106, 1984, pp. 591-596.

12. Amano, R. S., "A Numerical Study of Laminar and Turbulent Heat Transfer in a Corrugated Wall Channel", ASME Paper No. 84-HT-73, ASME/AIChE National Heat Transfer Conference, 1984.

13. Ramadhyani, S., "Numerical Prediction of Flow and Heat Transfer in Corrugated Ducts", Private Communication, pp. 37-43, 1987.

14. Kelkar, K. M., and Patankar, S. V., "Numerical Prediction of Flow and Heat Transfer in a Parallel Plate Channel with Staggered Fins", ASME Paper No. 84-HT-70, ASME/AIChE National Heat Transfer Conference, 1984.

15. Patankar, S. V., and Prakash, C., "An Analysis of the Effect of Plate Thickness on Laminar Flow and Heat Transfer in Interrupted Plate Passage", International Journal of Heat and Mass Transfer, Vol. 24, pp. 1801-1810, 1981.

16. Sparrow, E. M., Baliga, B., and Patankar, S. V., "Heat Transfer and Fluid Flow Analysis of interrupted Wall Channels With Application to Heat Exchangers", ASME Journal of Heat Transfer, Vol. 99, pp. 4-11, 1977.

17. Murty, V. D., "User's Manual for Non-Newtonian Fluid Analysis Program", University of Portland, 1987.

18. Zienkiewicz, O. C., The Finite Element Method, McGraw-Hill, 1977.

19. Anderson, D. A, Tannehill, J. C., and Pletcher, R. H., Computational Fluid Mechanics and Heat Transfer, McGra-Hill, 1984.

20. Launder, B. E., and Spalding, D. B., Mathematical Models of Turbulence, Academic Press, 1972.

21. Jones, W. P, and Launder, B. E., "The Prediction of Laminarization With a Two-Equation Model of Turbulence", Int. Journal of Heat and Mass Transfer, Vol. 15, pp. 301-314.

22. Baker, A. J., Finite Element Computational Fluid Dynamics, McGraw-Hill, 1984.

23. Patankar, S. V, Ivanovic, M., and Sparrow, E. M, "Analysis of Turbulent Flow and Heat Transfer in Internally Finned Tubes and Annuli", ASME Journal of Heat Transfer, Vol. 101, p. 29.

24. Murty, V. D., Paul, D. B., and Pajak, M. E., "A Numerical Study of Heat Transfer and Fluid Friction in Viscous Flow Across Banks of Tubes", *Second International Symposium on Rotating Machinery*, April 3-6, Honolulu.

25. Murty, V. D., Paul, D. B., and Pajak, M. E., "A Comparison of Mixed and Penalty Finite Element Methods in the Analysis of Pin-Fin Heat Exchangers", Accepted for presentation at the *National Heat Transfer Conference*, July 24-28, 1988, Houston.

Radiation Hypersonic Aerodynamics

by

Shiva N. Singh

Department of Mechanical Engineering

University of Kentucky

Lexington, KY 40506

Contents

1. Abstract

Numerical solution of two-dimensional Navier-Stokes equations are presented for flow past a flat plate for Mach numbers equal to 7 and 19.2 and Reynolds numbers in the range 10 to 10^3. The explicit time-dependent MacCormack finite-difference numerical scheme is used to integrate the equations under appropriate velocity-slip and temperature-jump conditions valid for the hypersonic slip-flow regime. It is found that the skin-friction coefficients and Nusselt number results agree reasonably well with other published numerical and experimental results for Reynolds number equal to and or greater than 50, but for less than 50, there is considerable disagreement. The radiation heat transfer effects for thin and gray gas approximations are also discussed.

2. Nomenclature

a	Speed of sound
C_f	Skin friction coefficient
C_v	Specific heat at constant volume
e	Specific internal energy
F,G	Vector fluxes
k	Molecular heat conductivity
M	Mach number
p	Static pressure
q	Heat transfer rate
Re	Reynolds number
t	time
T	Static temperature
u,v	Velocity components in cartesian coordinates
U	Vector flux
x,y	Cartesian coordinates
ξ, η	Transformed coordinate system
ρ	Density
μ	Coefficient of viscosity
τ	Optical thickness
$\tau_{xx}, \tau_{yy}, \tau_{xy}$	Viscous stress components
β	Absorption coefficient
ϵ	Emissivity coefficient

Subscripts

∞	Property evaluated at free stream conditions
w	Property evaluated at the plate surface

3. Introduction

The hypersonic flow problems have recently attracted much attention because of the design of trans-atmospheric vehicles (TAV), the hypersonic boost glide vehicles (HBGV) and the national aerospace plane (NASP). These have been published in five major text books [1-5] and many survey articles [6-9] on the hypersonic flows describe the characteristics in detail.

The problem of rarefield hypersonic flow past a flat plate has been studied by many research workers for more than two decades. Extensive reviews on these studies have been given by Potter [10], Moulic [11], Anderson [6] and Chow [12]. Results for the free molecular flow existing at the very tip of the plate were presented by Schaaf and Chambre [13], Liu [14] and Charwat [15]. The Monte Carlo simulation for the free molecule flat plate flow was carried out by Bird [16]. He indicated that up to the smallest Knudsen number which he investigated, the over-all flow did not show any resemblance to the corresponding continuum state. The effect of velocity-slip and temperature-jump on the wall has been studied by Oguchi [17] and Pan and Probstein [18]. Several authors [19-24] presented their experimental findings for hypersonic flat plate flow, but the experimental results produced from hypersonic low-density wind-tunnel tests on a flat plate do not agree with predictions from existing theories within the slip flow regime. A flow model based on the integral approach was developed by Chow [12] to study hypersonic low-density flow past a sharp leading edge of a flat plate. The disturbed flow field is divided into two subregions, namely, the continuous viscous-conducting region (shock-wave-like region) and the merged layer region (boundary layer like). The Navier-Stokes equation is assumed to be applicable to the wave region and for the merged layer region a cubic-parabolic slip velocity profile is employed and the Crocco integral relationship is adopted

to correlate the velocity and temperature profiles. Davis and Harvey [25] presented the Monte-Carlo direct simulation method for diatomic molecules and compared their results with experimental results for a zero-incidence flat-plate in Mach 21 low Reynolds number flow. The skin friction and drag measurements on flat plates were presented by Boettcher, et all [26], in the range between hypersonic continuum and free molecular flow. In a recent paper [27], Gokcen, MacCormack and Chapman carried out the extensive numerical calculation for hypersonic flow over a flat plate at Reynolds numbers ranging from continuum to the free molecule flow regime. They introduced new slip boundary conditions in the transition flow regime and solved the two dimensional Navier-Stokes equations. Comparison of the computed results with the existing experimental data and Monte-Carlo calculations indicate that the continuum Navier-Stokes equations give surprisingly realistic results throughout the transition regime, when the new boundary conditions are used. Results have been obtained by Hermina [28] for the diverging flow of helium gas along a flat plate using a direct simulation Monte-Carlo technique. Skin friction results are presented for a variety of transverse mesh resolutions corresponding to values of the Knudsen numbers, Ku ranging from 2.452 to 0.1226.

In this report, the main objective has been to obtain the results published in [27], by solving the two-dimensional, unsteady, compressible Navier-Stokes equations numerically under appropriate velocity-slip and temperature-jump conditions for flow past a flat-plate. Calculation were performed for Mach numbers equal to 7 and 19.2 and the Reynolds number varying from 10 to 10^3. The effect of varying the grid size on the skin friction coefficients and the Nusselt number are presented and compared with the existing theoretical and experimental results. The radiation heat transfer

contribution is also considered in this paper.

4. Mathematical Formulation and Numerical Procedure

The equations governing the hypersonic flow in the present analysis are the time-dependent, compressible, two-dimensional Navier-Stokes equations. A general coordinate transformation,

$$\xi = \xi(x), \quad \eta = \eta(x,y) \tag{1}$$

is introduced to take into account the variable grid in the x-y plane. The governing equations can then be written in the so called conservative form [29,30],

$$\frac{\partial U}{\partial t} + \xi_x \frac{\partial F}{\partial \xi} + \eta_x \frac{\partial G}{\partial \eta} + \eta_y \frac{\partial G}{\partial \eta} = 0 \tag{2}$$

where the vector fluxes U, F and G are given by,

$$U = \begin{bmatrix} \rho \\ \rho u \\ \rho v \\ \rho e \end{bmatrix} \tag{3}$$

$$F = \begin{bmatrix} \rho u \\ \rho u^2 + p - \tau_{xx} \\ \rho uv - \tau_{xy} \\ (\rho e + p)u - u\tau_{xx} - v\tau_{xy} + q_x + q_x^R \end{bmatrix} \tag{4}$$

$$
G = \begin{bmatrix}
\rho v \\
\rho uv - \tau_{xy} \\
\rho v^2 + p - \tau_{yy} \\
(\rho e + p)v - u\tau_{xy} - v\tau_{yy} + q_y + q_y^R
\end{bmatrix}
\tag{5}
$$

The components of the shear-stress tensor and heat-flux are given by,

$$
\tau_{xx} = \frac{2}{3}\mu \left(2 \frac{\partial u}{\partial x} - \frac{\partial v}{\partial y} \right)
$$

$$
\tau_{yy} = \frac{2}{3}\mu \left(2 \frac{\partial v}{\partial y} - \frac{\partial u}{\partial x} \right)
$$

$$
\tau_{xy} = \tau_{yx} = \mu \left(\frac{\partial u}{\partial y} + \frac{\partial v}{\partial x} \right)
\tag{6}
$$

$$
q_x = - k \frac{\partial T}{\partial x}, \qquad q_y = - k \frac{\partial T}{\partial y}
$$

and,

$$
\xi_x = \frac{\partial \xi}{\partial x}, \qquad \eta_x = \frac{\partial \eta}{\partial x}, \qquad \eta_y = \frac{\partial \eta}{\partial y}
$$

Derivation of the components of the radiation flux vector q_x^R and q_y^R are discussed in the next section. The equations of state given by the perfect gas law, Sutherland's viscosity law and assigned Prandtl number (0.73) formally close the system of equations. The equations (2) are numerically integrated in the region $0 \le x \le 1$ along the flat plate and $0 < y < 1$ at right angles to the plate. The boundary conditions for the hypersonic flow in the slip flow regime have been discussed by many authors [13,27]. On the plate (y=0), the approximate Maxwell velocity-slip and temperature-jump conditions are given by

$$u(0) = \frac{2 - \sigma}{\sigma} \overline{\ell} \left(\frac{\partial u}{\partial y} \right)_0 \tag{7}$$

$$T(0) - T_w = \frac{2 - \alpha}{\alpha} \frac{2\gamma}{\gamma + 1} \frac{\overline{\ell}}{Pr} \left(\frac{\partial T}{\partial y} \right)_0 \tag{8}$$

where σ is the fraction of diffusely reflected molecules and α, the accommodation coefficient [13,27]. Both σ and α in the present calculations are assumed to be unity. The upstream and initial conditions are prescribed by the values of the unperturbed freestream.

Initial condition:

$$U(\; 0 \; , \; \xi \; , \; \eta \;) = U_\infty \tag{9}$$

Upstream condition:

$$U(\; t \; , \; \xi \; , \; \eta \;) = U_\infty \; , \qquad \xi < 0 \tag{10}$$

The gradients of all the variables U, F, and G are assumed to be zero at x=1, $0 < y < 1$ and $0 < x < 1$, y=1, valid for the far-field boundary.

The whole flow field ($0 \leq x \leq 1$, $0 \leq y \leq 1$) is divided into a M x N mesh such that the mesh is stretched at right angles to the plate exponentially near the plate to provide adequate resolution within the viscous boundary layer, and into uniform mesh size away from the plate. The region along the plate is divided into uniform mesh size. Figure 1 shows a typical 64 x 64 mesh used in the present study.

The explicit MacCormack method [29,30] involving a two-step predictor and corrector finite-difference scheme is used to integrate the system of

equations given by (2). The terms in the flux vectors F and G are approximated by a central, forward and backward differencing scheme in such a fashion that the numerical scheme is second-order accurate both in space and time. The time step Δt is taken to be,

$$\Delta t \leq \frac{\sigma \; (\Delta t)_{CFL}}{(1 + \frac{2}{Re_\Delta})} \tag{11}$$

where σ is the safety factor (≈ 0.9) and $(\Delta t)_{CFL}$ is the inviscid CFL condition [30],

$$(\Delta t)_{CFL} \leq \left\{ \frac{|u|}{\Delta x} + \frac{|v|}{\Delta y} + a \sqrt{(\frac{1}{\Delta x^2} + \frac{1}{\Delta y^2})} \right\}^{-1} \tag{12}$$

Re_Δ is the minimum mesh Reynolds number,

$$Re_\Delta = \min (Re_{\Delta x} , Re_{\Delta y}) \tag{13}$$

where,

$$Re_{\Delta x} = \frac{\rho \; |u| \Delta x}{\mu} , \qquad Re_{\Delta y} = \frac{\rho \; |v| \; \Delta y}{\mu} \tag{14}$$

and,

$$a = \sqrt{\frac{\gamma p}{\rho}}$$

With a given arbitrary initial guess the solution of the time-dependent equations are obtained by an iterative process approaching an asymptotic steady-state.

5. Radiation Heat Transfer

In this section, we will discuss a methodology to solve for the radiation transfer contribution on the energy equation. Consider the fluid flowing over a flat plate, and the medium being absorbing, emitting and semi-infinite. The radiative transfer equation (RTE) and the corresponding boundary condition (b.c.) are given for this problem as,

$$\mu \frac{\partial I(\tau,\xi,\mu)}{\partial \tau} + I(\tau,\xi,\mu) = I_b[\ T(\tau,\xi)] \tag{15}$$

with,

$$I(0,\xi) = \int_0^1 I(0,\xi,\mu)\ d\mu$$

$$= \epsilon_w\ I_b\ [\ T_w(\xi)] + 2\ (1 - \epsilon_w) \int_0^1 I(0,\xi,-\mu')\ d\mu' \tag{16}$$

where I is the radiation intensity,

$$\tau = \int_0^y \beta\ dy' \quad \text{and} \quad \xi = \int_0^x \beta\ dx'$$

are the optical thicknesses in the y-and x-directions, respectively, β is the volumetric extinction (absorption) coefficient (in m^{-1}), $T(\tau, \xi)$ is the medium temperature distribution, $T_w(\xi)$ is the wall temperature distribution, and ϵ_w is the wall emissivity. Here, we will consider only one dimensional radiative transfer primarily in the y-direction (perpendicular to the plate). The ξ-dependance is because of the ξ-dependance of the temperature distribution $T(\tau,\xi)$. It is worth to note that a two-dimensional formulation of the RTE is much more complicated, and we will not treat it here.

The radiation term which appears in the energy equation is the divergence of the radiative heat flux, which can be obtained after solving equation(15) for the radiation intensity. For a gray azimuthally symmetric, planer medium, the radiative flux is give as[31],

$$q^r(\tau,\xi) = 2\pi \int I(\tau,\xi,\mu)\mu \ d\mu \qquad (17)$$

Then, we can write the divergence of the radiative flux distribution in dimensionless form as,

$$\frac{\partial Q^r(\tau,\xi)}{\partial \tau} = \theta^4(\tau,\xi) - \frac{1}{2} \epsilon_w E_2(\tau)\theta_w^2(\xi)$$

$$-(1 - \epsilon_w)E_2(\tau)\int_0^\infty \theta^4(\tau',\xi) \ E_2(\tau') \ d\tau'$$

$$- \frac{1}{2} \int_0^\infty \theta^4(\tau',\xi) \ E_1(|\tau-\tau'|) \ d\tau' \qquad (18)$$

where,

$$Q^r(\tau,\xi) = \frac{q^r(\tau,\xi)}{4n \ \sigma T_\infty} \ , \quad \theta(\tau,\xi) = \frac{T(\tau,\xi)}{T_\infty} \ , \quad \theta_w(\xi) = \frac{T_w(\xi)}{T_\infty}$$

$$E_n(\tau) = \int_0^1 e^{-\frac{\tau}{\mu}} \mu^{n-2} \ d\mu \qquad (19)$$

The boundary condition is given as,

$$Q^r(\tau=0,\xi) = \frac{\epsilon_w}{4} [\{ \theta_w^4(\xi) - 1 \}$$

$$- 2 \int_0^\infty \{ \theta^4(\tau',\xi) - 1 \} E_2(\tau') d\tau'] \qquad (20)$$

These equations are written for a uniform medium refractive index, n.

After the energy equation is solved without including the radiation effect, the temperature distribution is used in equation (4) to obtain the $\partial Q^r/\partial\tau$ variation. This term is used as a source term, and Equation(18) is solved again. This iterative procedure is followed until a preset convergence criteria is satisfied.

Optically Thin-Fluid Approximation

Although many simplified assumptions were introduced in obtaining the RTE, such as planer, one-dimensional system, gray non-scattering medium radiatively, homogeneous fluid layer and uniform-property plate surface, equation(18) is still complicated. We can simplify it further by considering the physical problem. In general, the model developed in this study is applicable to flight-conditions at very high elevations, where gas-density is significantly low. It is, therefore possible to assume that the volumetric extinction (absorption) coefficient is small, which yields τ,

$$\tau_0 = \int_0^{y(L)} \beta \, dy \ll 1 \qquad (21)$$

where y(L) is the upper-limit of the domain we are interested in. Following

this we note that,

$$E_2(\tau) - 1 - O(\tau), \quad e^{-\tau} - 1 - \tau + (\tau^2) \tag{22}$$

where, O denotes the order of the neglected terms. Using these expressions, one can show that for an optically thin gas, equation (18) is rewritten as,

$$\frac{\partial Q^r(\tau,\xi)}{\partial \tau} - [\theta^4(\tau,\xi) - 1] - \frac{1}{2} \epsilon_w[\theta_w^4(\xi) - 1] \tag{23}$$

with the boundary condition,

$$Q^r(\tau-0,\xi) - \frac{\epsilon_w}{4} [\{\theta_w^4(\xi) - 1\} - 2\int_0^\infty \{\theta^4(\tau',\xi) - 1\} \, d\tau'] \tag{24}$$

In order to take into account the spectral nature of the radiation, we may use the Planck mean absorption coefficient in the definition of optical thickness:

$$\tau - \tau_p - K_p y - y \frac{1}{\sigma\theta_m^4} \int_{\lambda-0}^\infty K_\lambda \, I_{\lambda b}(\theta_m) \, d\lambda \tag{25}$$

Where θ_m is the temperature of the fluid layer, and K_λ is the spectral absorption coefficient of the fluid.

Optically Thick-Fluid Approximation

We can simplify the RTE considerably if we assume that the gas (or fluid) is optically-thick. Although it may not be applicable to the practical system of

interest of this study, it is important to analyze the limit, because all practically possible situations will fall between the optically thin and thick approximation results.

For this case, we can write the dimensionless radiative flux as,

$$Q^r(\tau,\xi) = -\frac{1}{3}\frac{\partial}{\partial\tau}[\theta^4(\tau,\xi)] \qquad (26)$$

The divergence of the radiative flux, $\partial Q^r(\tau,\xi)/\partial\tau$ is obtained from Equation (10) readily. It is important to note that for this case the optical thickness, is based on the Rosseland mean absorption coefficient as,

$$\tau = \tau_R = K_R y = y \left[\int_{\lambda=0}^{\infty} \frac{1}{K_\nu} \frac{dI_{\lambda b}(\theta_m)}{dI_b(\theta_m)} d\lambda \right]^{-1} \qquad (27)$$

Solution of the RTE for intermediate optical thickness

If the optical thickness of the medium is neither small nor large, then the radiation contribution is obtained by solving the full RTE. The solution of this integro-differential equation is not easy, and some approximation would be desirable. For this reason, the double spherical harmonics (DP) approximation will be applied to the RTE. This approximation has been developed recently by Menguc and Iyer [32] and has shown to be very reliable for optical thicknes less than 10, and can account for an anisotropically scattering medium.

6. Discussion of results

The numerical calculations have been performed on the IBM 3090 (super) computer, a facility available at the University of Kentucky. To gain

experience in numerical calculations based on the complete Navier-Stokes equations and to test whether the numerical scheme is adequate, it was first attempted to reproduce the results obtained in [27]. In table 1, results for average skin friction coefficients calculations are given for M=7 and R_e=100, 10^3 and 10^4 for flow past a flat plate under the no-slip and adiabatic wall conditions. Number of grid points and the spacing for the first grid in y-direction near the plate are also given in the table The results are compared in Figure (2) with those given in [27], and it is found that the skin friction results based on several variations of number of grids and spacing are a few percent less than obtained in [27].

The local and average skin friction coefficients are defined as,

$$\tau = \mu \ (\frac{\delta u}{\delta y})_{y=0} \ / \ \frac{1}{2} \ \rho \ U_{\infty}^2 \tag{28}$$

$$c_f = \frac{1}{L} \int_0^L [\ \mu \ (\frac{\delta u}{\delta y})_{y=0} \ / \ \frac{1}{2} \ \rho U_{\infty}^2 \ ] \ dx \tag{29}$$

Table 1: Numerical Flow-Field Parameters for M = 7

grid size	64 x 48	64 x 48	64 x 48	64 x 48	96 x 96
δ B-layer	0.5	0.5	0.75	0.75	0.75
$\Delta\eta_{min}$	0.002	0.001	0.001	0.0005	0.0005
Re_{∞}					
100	0.4084	0.4295	0.3776	0.4254	0.4033
1000	0.0794	0.0832	0.0786	0.0848	0.0804
10,000	0.0171	0.0191	0.0178	0.0188	0.0175

For hypersonic flow (i.e. at large Mach numbers), the exchange of heat between surface and gas consists of two components, namely:

(1) Thermal conduction,

(2) work done by shear forces due to the existence of a finite slip velocity at the surface. Then the total heat transfer is given by (+ve into the body),

$$q_{tot} = [\ k \ \frac{\delta T}{\delta y} + u_s \ \mu \ \frac{\delta u}{\delta y} \ ]_{y=0} \tag{30}$$

$$= H \ (\ T_{aw} - T_w \ )$$

where,

$$Taw = T_\infty [1 \ + \ R \ \frac{\gamma - 1}{2} \ M^2]$$

and

$$Nu_x = \frac{Hx}{k} = St_x \ Re_x \ Pr \tag{31}$$

The results for the velocity slip flow conditions have been obtained corresponding to two wall temperature conditions:

(a) $\frac{\delta T}{\delta y} = 0$ on the wall

(b)   temperature jump condition on the wall, $T_w/T_{aw} = 0.7$.

Numerical experiments were run on different grid sizes with varying grid spacing normal to and parallel to the streamwise direction. ΔY_{min}, the minimum grid spacing at the surface of the plate, normal to the flow direction was varied from 0.05 to 0.0005. A value of $\Delta Y_{min} = 0.001$ was selected, as lower values did not have any significant effect on the skin friction coefficient. Three grids of size 64 x 64 and extending 1.4, 3.0 and 6 inches normal to the plate of length 1. inch were studied. These are illustrated in Figures(2a,b,c), respectively. The grid is constructed so as to have an

exponentially increasing grid spacing normal to the wall, and from the leading edge going downstream. This ensures a good definition of the flow field in the immediate vicinity of the wall and in the stagnation region.

For M=7, T_w/T_{aw}=0.7, and velocity-slip, experiments were run for Reynolds numbers=10, 50, 100, and 1000. Figure(3a,b) show the variation of the local skin friction coefficient and the local Stanton number. Two grids, given in Figures(2a,b) were tested in these cases, both giving the same results. As would be expected with the existence of a slip velocity, the heat flux at the wall should follow the same trend as the skin friction coefficient. This is because of the term $u_s\mu\frac{\delta u}{\delta y}$ occurring in equation(30), which contributes to the mechanical heat generation at the wall. The profiles given in figures(3a,b) indicate an increasing trend with 'x', and after passing a maximum begin decreasing again as the boundary layer develops in the downstream direction along the plate. This trend can be explained by considering the mach number contours shown in Figures(4a,b,c). It is noted that in the leading edge region the isomach lines have a higher density in a particular region of the plate, and away from this region, the lines are more spaced out. Such dense regions contribute to larger gradients in the properties of the flow field, leading to higher local skin friction and Stanton number values. Close observation of figures(4a,b,c), reveals that these dense regions compare in location with the occurrence of the maxima in figures(3a,b). For Reynolds number=10, the results proved unsatisfactory, and hence are not presented. Table 2 gives the average value of the skin friction coefficient on the plate. As the Reynolds number increases the skin friction or Stanton number value at any point decreases.

<u>Table 2. M=7: T_w/T_{aw}=0.7; Velocity-slip</u>

Re number	10	50	100
$C_{f_{av}}$	0.552	0.195	0.159
St_{av}	0.74	0.16	0.14

For M=19.2, T_w/T_{aw}=0.7, and velocity-slip, experiments were run for Reynolds numbers=10, 50, and 100. Figure(5a,b,6),show the variation of the local skin friction coefficient and the local Stanton number. Two grids, given in Figures(2a,c) were tested in these cases, both giving the same results. The trends followed are similar to those presented for M=7. The skin friction and stanton values have increased almost proportionally with the increase in mach number. For Reynolds number=10, the results proved unsatisfactory, and hence are not presented. Table 3 gives the average value of the skin friction coefficient on the plate. As the Reynolds number increases the skin friction and Stanton number values decrease at any location, however, downstream of the maxima, the two coalesce to reach an asymptotic value.

<u>Table 3. M=19.2: T_w/T_{aw}=0.7; Velocity-slip</u>

Re number	10	50	100
$C_{f_{av}}$	0.849	0.276	0.212
St_{av}	0.75	0.19	0.13

Numerical experiments were also performed with $\delta T/\delta y = 0$. Even though these computations did stabilise, the resulting flow fields that ensued were

highly disorderd and are currently the subject of study. Further studies are underway to incorporate the radiation transfer equations into the algorithm, and to follow with additional numerical experiments and flow field study.

7. Conclusion

The explicit MacCormack numerical scheme based on the two-dimensional unsteady compressible Navier-Stokes equations gives reasonably comparable results for the skin friction and heat transfer coefficients for Reynolds number equal to and greater than 50. More time and effort are needed to make conclusive statements whether the Navier-Stokes equations are adequate to describe very low density regimes.

ACKNOWLEDGEMENTS

8. References

1. Truitt, R.W., _Hypersonic Aerodynamics_, Ronald Press, New York, 1959.

2. Hayes, W.D., and Probstein, R.F., _Hypersonic Flow Theory_, Academic Press, New York, 1959.

3. Chernyi, G.G., _Introduction to Hypersonic Flow_ (translated from Russion by R.F. Probstein), Academic Press, New York, 1961.

4. Dorrance, W.H., _Viscous Hypersonic Flow_, McGraw-Hill Book Co., New York, 1962.

5. Cox, R.N. and Crabtree, L.F., _Elements of Hypersonic Aerodynamics_, Academic Press, New York, 1965.

6. Anderson, J.D., AIAA, paper No. 85-1578, Jan. 1984.

7. Nagamatsu, H.T. and Sheer, R.E., Jr., AIAA paper No. 85-0999, June 1985.

8. Holden, M.S., AIAA paper No. 86-0267, Jan. 1986.

9. Tirmalesa, D., AIAA, J., 1968, Vol. 6, 369-370.

10. Potter, J.L., _Rarefied Gas Dynamics_, Academic Press Inc., New York, 1967, suppl. 4, Vol. II, pp 881-937.

11. Moulic, E.S., Jr., Space Sciences Lab. Univ. of Calif. Berkeley, TR Series 7, Jan. 1968.

12. Chow, W.L., AIAA, J., 5, 1967, 1549-1557.

13. Schaaf, S.A. and Chambre, P.L., _Flow of Rarefied gases_, Vol. III, Sec. H., 1958, pp 687-793.

14. Liu, V.C., J. Fluid Mech. 5, 1968, 481-490.

15. Charwat, A.F., Rarefied Gas Dynamics, Academic Press Inc., New York 1961, suppl. 1, pp,. 553-578.

16. Bird, G.A., AIAA J., 4, 1966, 55-67.

17. Oguchi, H., Rarefied Gas Dynamics, Academic Press Inc., New York, 1963, suppl, 2, Vol, II, pp. 181-193.

18. Pan, Y.S. and Probstein, R.F., Fundamental Phenomena in Hypersonic Flow, Cornell Univ. Press, Ithaca, N.Y., 1966, Rept. 195 (1952)

19. Ghuan, L. and Waiter, S.A., Rarefied Gas Dynamics, Academic Press Inc., N.Y., 1963, Suppl. 2, Vol. II, pp. 328-342.

20. Vidal, R.J. and Wittliff, C.E., Rarefied Gas Dynamics, Vol, II, 1963.

21. McCrosky, W.J., Bogdonoff, S.M. and McDougall, J., AIAA J. 4, 1966, 1580-1588.

22. Schaaf, S.A., Hurlbut, F.C., Talbot, L. and Aroesty, J., ARS, J., 29, 1959-, 527.

23. Nagamatsu, H.T. and Li, T.Y., J. Aero. Sci, 20, 1953, 345-355.

24. Nagamatsu, H.T. and Sheer, R.E. Jr., Hypersonic Gas Dynamics, AIAA, 20th Thermophysics Conf., June 19-21, 1985, VA.

25. Davis, J. and Harvey, J.K., Rarefied Gas Dynamics, Vol.51, 1976, 335-48.

26. Beottcher, R.D., Koppenwallner, G. and legge, H., Rarefied Gas Dynamics, Vol, 51, 1976, 349-60.

27. Gokcen T., MacCormack, R.W. and Chapman, D.R., Computational Fluid Dynamics Near the Continuum Limit, 1987.

28. Hermina, W.L., J. Thermophysics, Vol. 3, pp. 7-12, 1989.

29. Shang, J.S. and Hankey, W.L., AIAA J., Vol. 15, pp. 1575-1582, 1977.

30. Anderson, D.A., Tannehill, J.C. and Pletcher, R.H., Computational Fluid Mechanics and Heat Transfer, Hemisphere Publ. Corp., NY, pp. 479-489, 1984.

31. Ozisik, M.N., Radiative Transfer and Interaction with Conduction and Convection, Wiley, New York, NY, pp. 314-316 and 485-521, 1973.

32. Menguc, M.P. and Iyer, R.K., J. Quant. Spectrosc. Radiat. Transfer, Vol. 39, pp. 445-461, 1988.
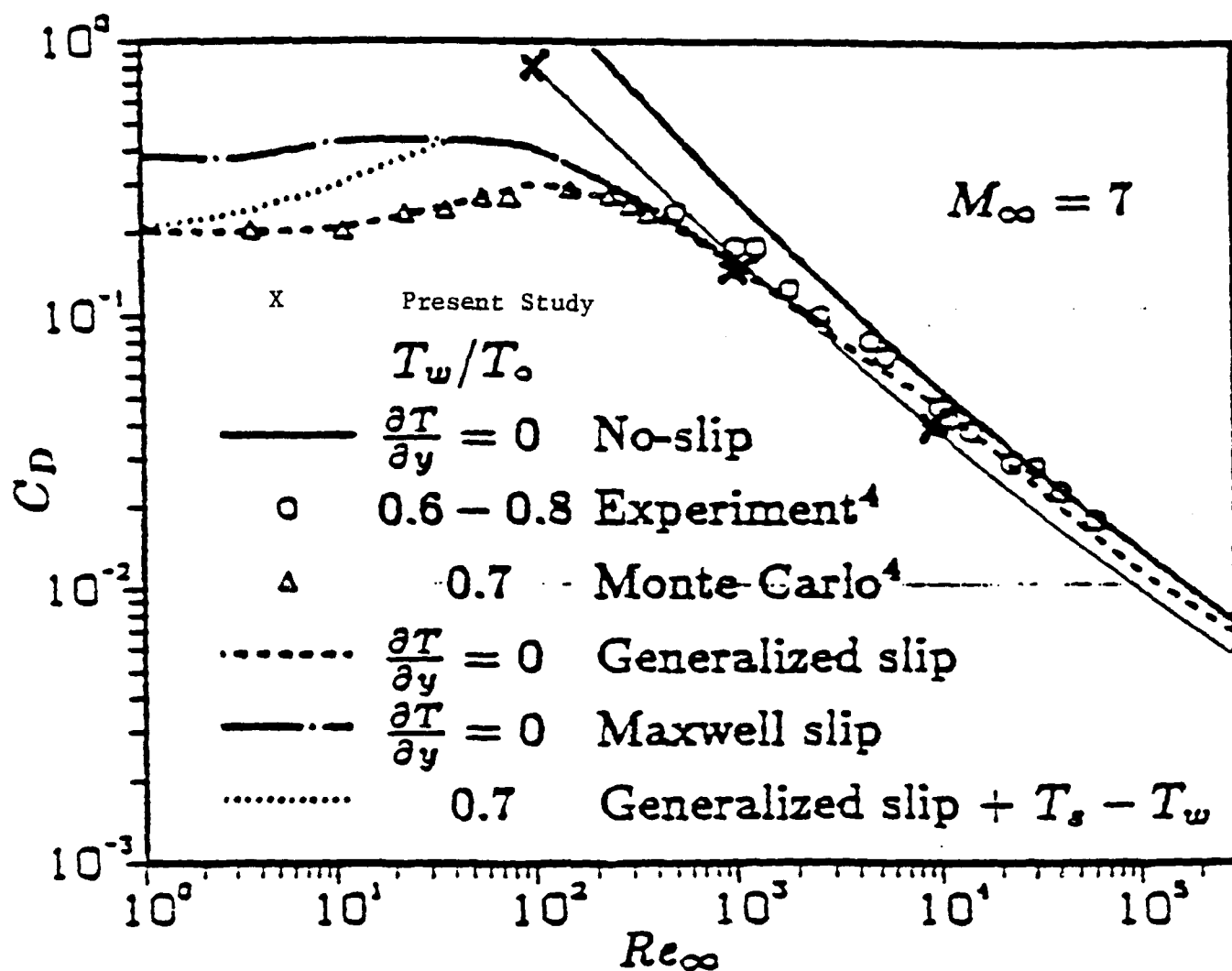
Skin friction drag vs Reynolds number.

Figure(1)

Figure(2)

64 x 64 grid

$Y_{min} = 0.001$

Local Skin Friction Coefficient

M=7., velocity-slip

◇ Re=50 $T_w/T_{aw} = 0.7$

○ Re=100

★ Re=1000

Local Stanton Number

M=7., velocity-slip

◇ Re=50 $T_w/T_{aw} = 0.7$

○ Re=100

★ Re=1000

(a)

(b)

Figure(3)

68-25

Re no. = 1000

Re no. = 100

Re no. = 50

(a)

(b)

(c)
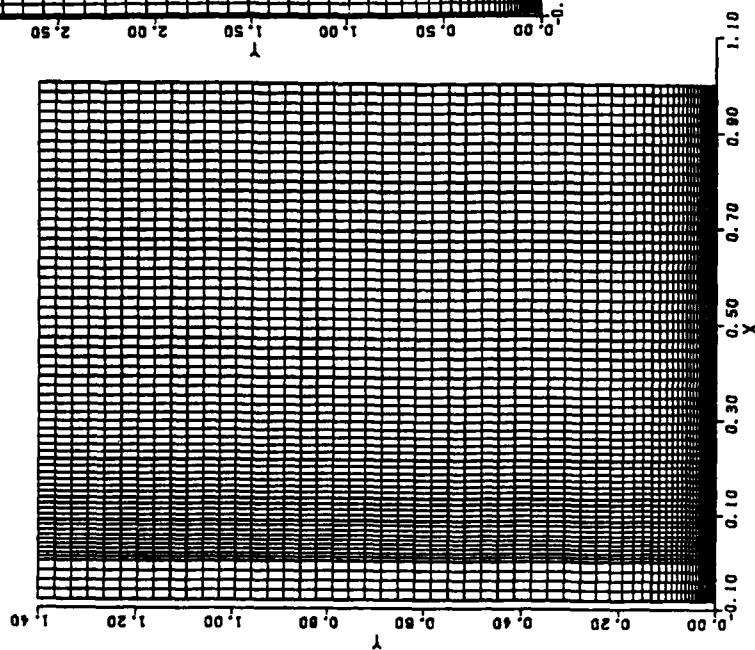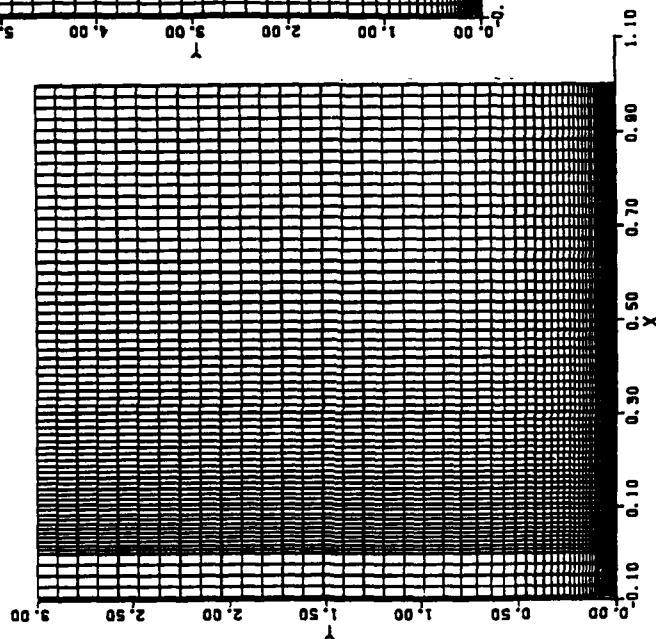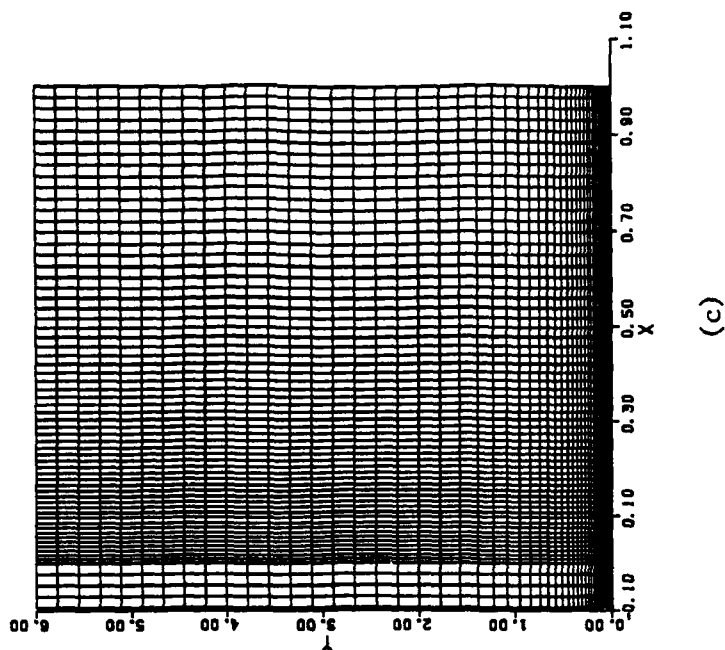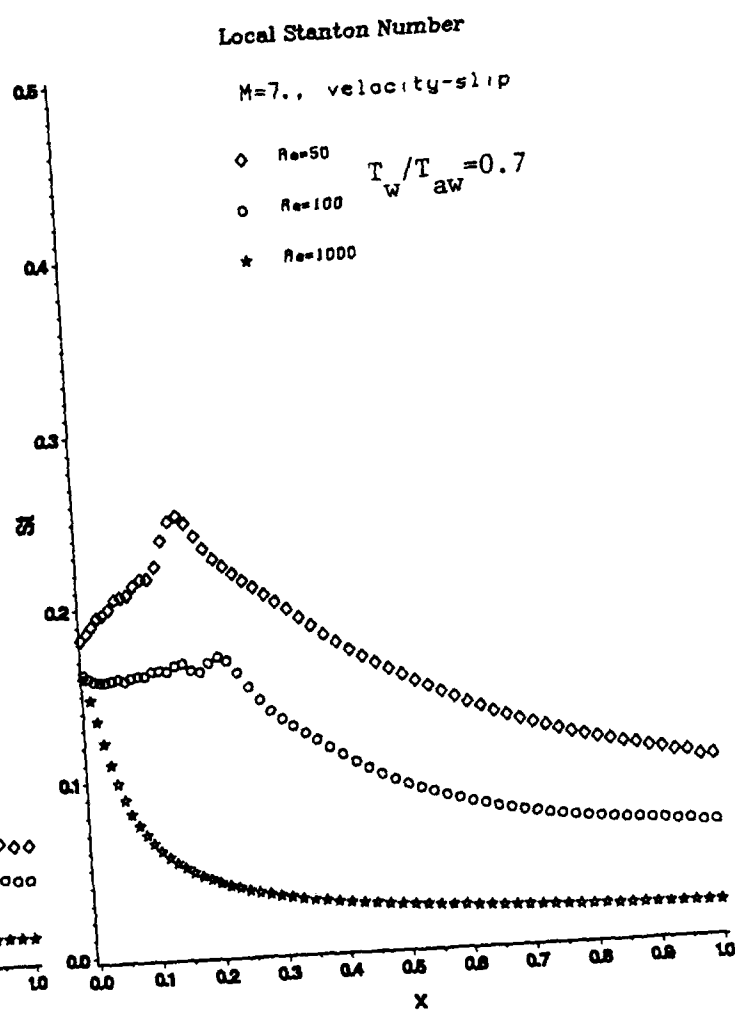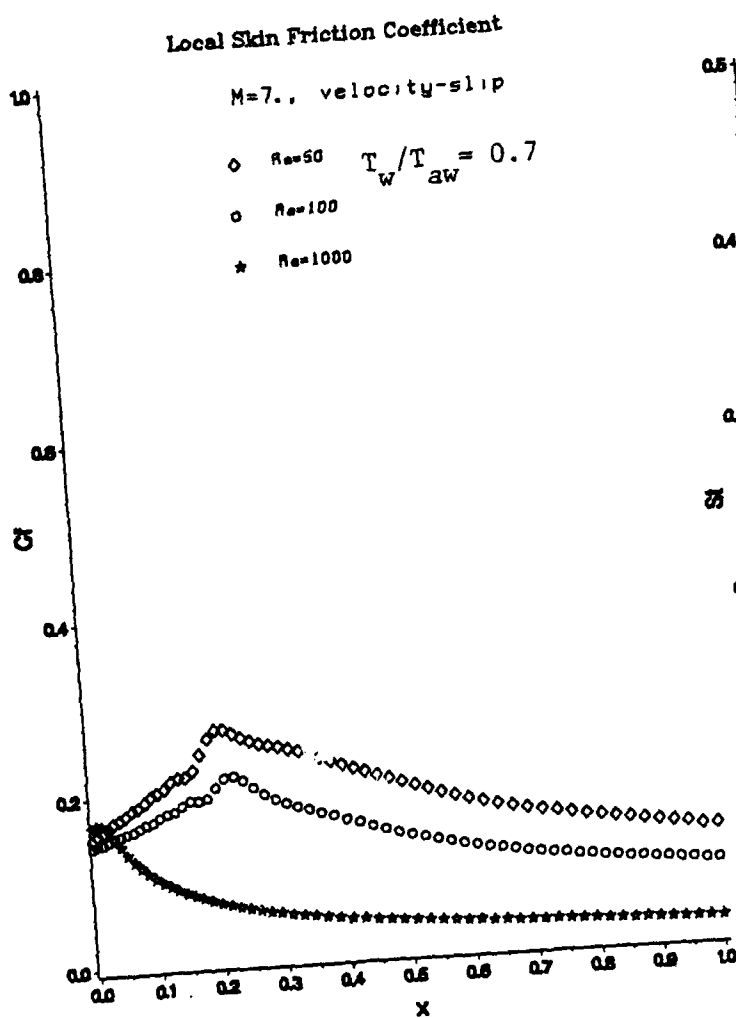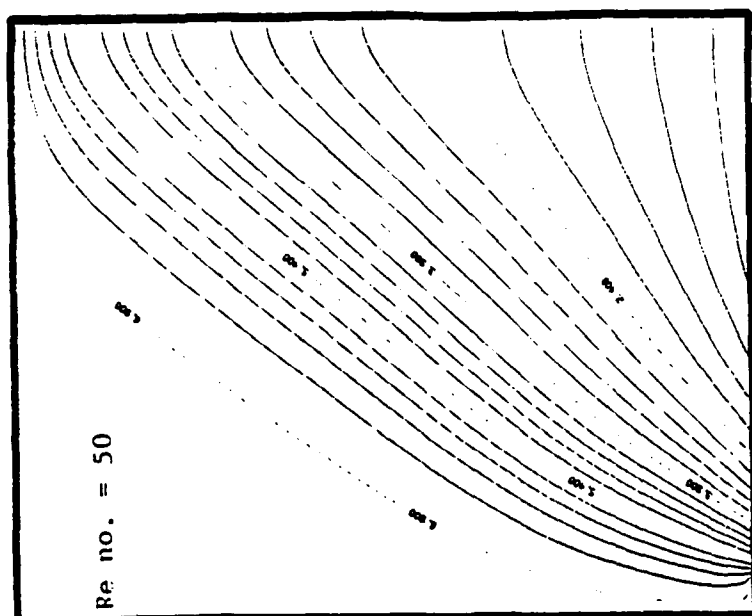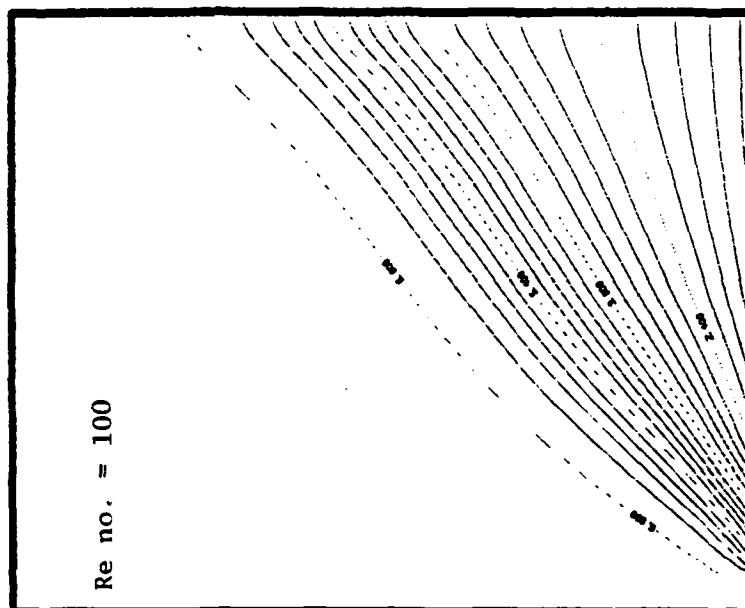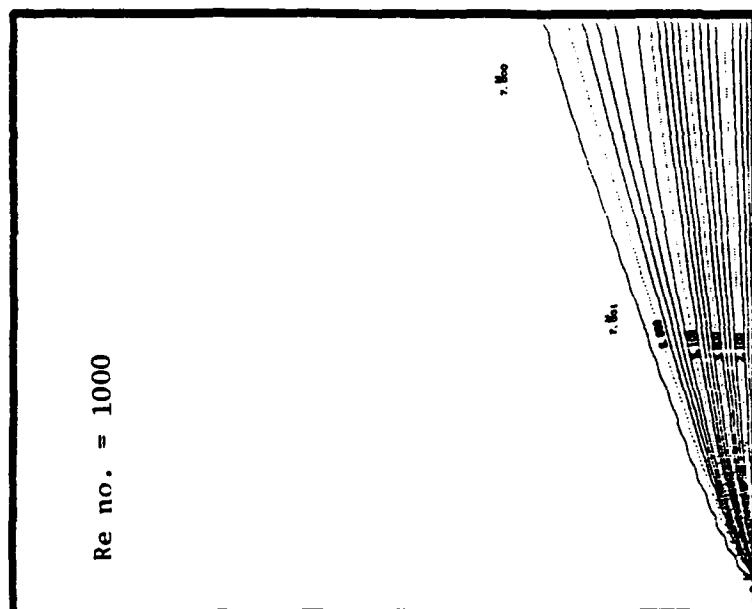
$M = 7$, 64×64 grid $T_w/T_{aw} = 0.7$

Figure(4)

68-26

Local Skin Friction Coefficient

M=19.2, velocity-slip

◇ Re=50

○ Re=100

$T_w/T_{aw}=0.7$

Local Stanton Number

M=19.2, velocity-slip

◇ Re=50

○ Re=100

$T_w/T_{aw}=0.7$

(a)

(b)

Figure(5)

M = 19.2
$T_w/T_{aw} = 0.7$
Velocity-slip
Reynolds no. = 100

15.00
10.00
5.000

15.00
10.00
5.000
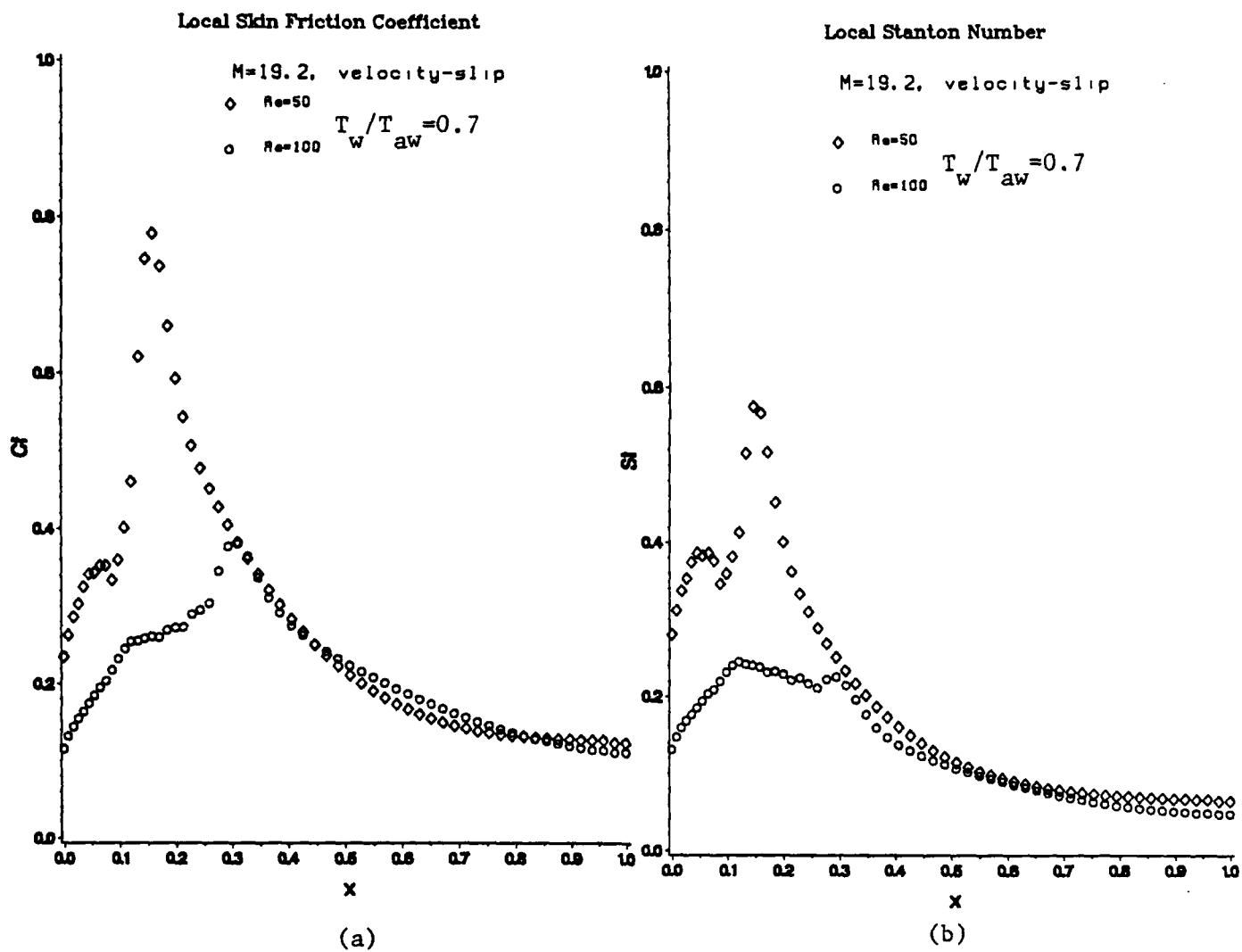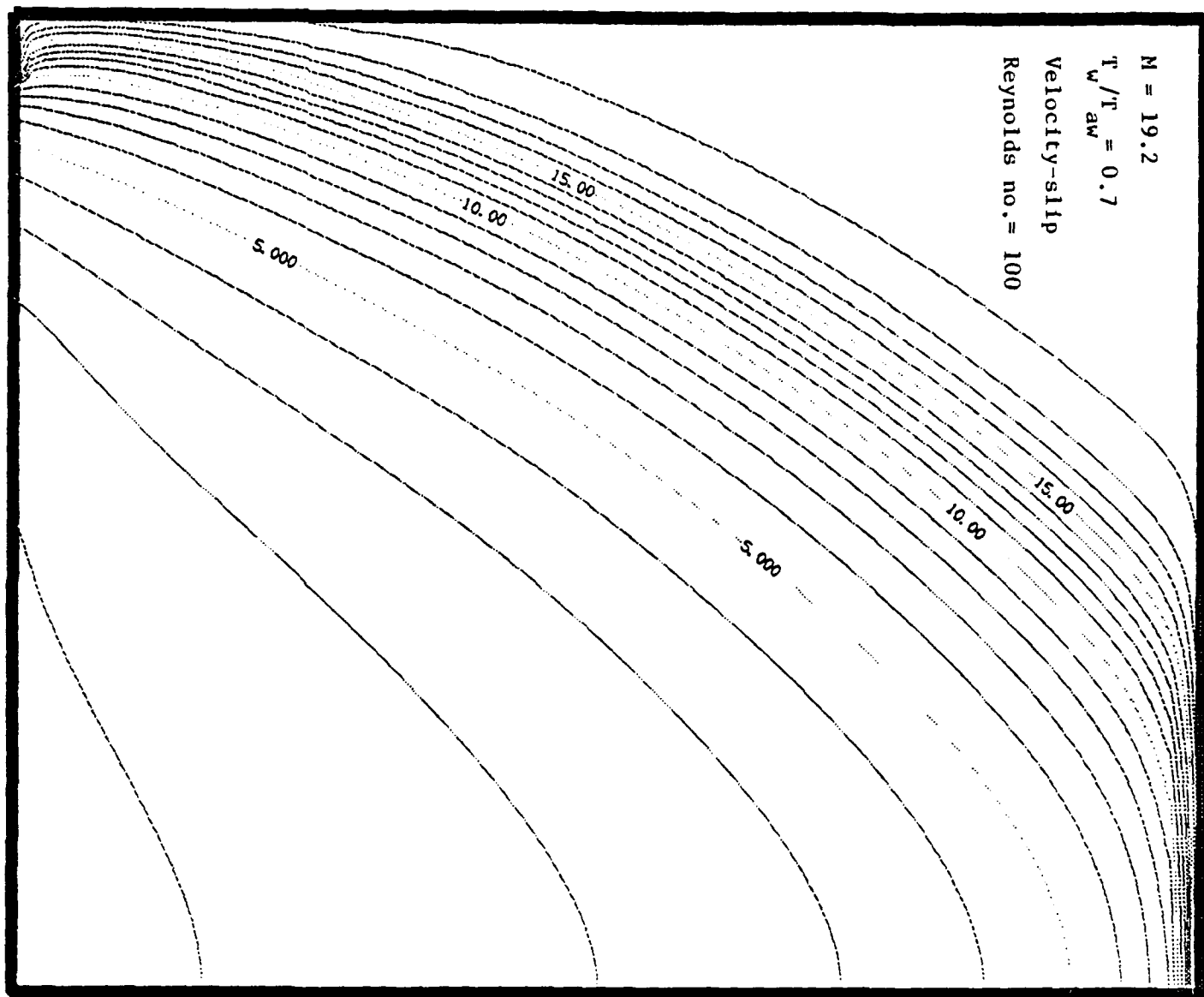
Figure (6)

FINAL REPORT NUMBER 69
REPORT NOT AVAILABLE AT THIS TIME
Dr. Gary Slater
760-7MG-088

FINAL REPORT NUMBER 70
REPORT NOT AVAILABLE AT THIS TIME
Dr. Forrest Thomas
760-7MG-080

FINAL REPORT NUMBER 71
REPORT NOT AVAILABLE AT THIS TIME
Dr. William Wolfe
760-7MG-102

FINAL REPORT

A CHEMICAL KINETICS MODEL FOR

MACH 5 - 14 HYPERSONIC FLOW

T. Gary Yip *

Department of Mechanical Engineering
SANTA CLARA UNIVERSITY
Santa Clara, CA 95053
408 - 554 - 4937

Submitted To

October 5, 1988

* Formerly at the Department of Aeronautical & Astronautical Engineering,
The Ohio State University.

ABSTRACT

This study is aimed to determine the adaquacy of existing chemical kinetics data for numerical predictions of hypersonic flow fields at Mach numbers up to 14, equivalently at temperatures up to 10,000 K. The one-dimensional non-equilibrium flow field behind a normal shock is used here to study the sensitivity of the flow properties to the different reactions and the uncertainties in the values of their rate constants. Known or assumed factors of uncertainty are introduced systematically into a series of flow field predictions. The results are compared to obtain the sensitivity information.

The higher rate of dissociation of O_2, due to the lower dissociation energy of the species, combined with a factor of 2 uncertainty in the rate data have been predicted to cause as much as 1,000 K deviation in the temperature profile. A similar degree of deviation has also been predicted when the dissociation rate constant of NO is assumed to have a factor of 4 uncertainty. Contrarily, the flow properties are found to be much less sensitive to the larger uncertainty in the rate data for the dissociation of N_2. These results suggest that, for Mach 14 or below hypersonic flow fields, the reliability of the predicted flow conditions depends largely on the accuracy of the O_2 and NO data while the existing uncertainty in the N_2 data is expected to introduce relatively insignificant errors.

Identification of the dominant reactions and species in Mach 14 or below flow fields has resulted in two chemistry models which differ by one reaction. The reactions common to both models are the dissociations of O_2, N_2 and NO, and the shuffle reactions $O + N_2 \leftrightarrow NO + N$ and $N + O_2 \leftrightarrow NO + O$. When the objective of a numerical simulation of hypersonic flow is concerned with the presence of free electrons, the ionizing atomic collision $N + O \leftrightarrow NO^+ + e^-$ must be included in the model.

ACKNOWLEDGEMENT

INTRODUCTION

Numerical predictions of chemically non-equilibrium flow fields require an accurate chemistry model and a set of reliable reaction rate data. For high temperature air, a number of models and a wealth of rate data exist in the literature. The resurgence of hypersonic flow research has prompted frequent use of these models and rate data, recently and in the future, to predict the flow conditions about high speed vehicles. Unfortunately, such flow predictions have been and are expected to be received with considerable skepticism about their reliability due to, at least, the following three reasons. The first one is the uncertainties in the rate data. The second is that the rate data are used to predict flow fields at temperatures which are outside the range in which the data were taken. The last reason is the chemistry model may not include all the reactions that are important to the chemistry of air in the temperature range of the predicted flow field. The present study is aimed to ascertain the reliability of the existing chemical kinetics information for the non-equilibrium chemistry of air at temperatures encountered in Mach 14 and below hypersonic flow fields.

SCOPE

The primary objective of this study is to validate a chemical kinetics model for use in predicting Mach 5-14 hypersonic chemically non-equilbrium flow. Validating the model involves identifying the more dominant reactions and species, and determining the sensitivity of predicted flow fields to the uncertainties of the presently available rate data. The less important reactions and species will be eliminated. The study is performed using the one-dimensional chemically non-equilibrium flow field behind normal shocks at Mach numbers 8, 12 and 14. The inviscid flow governing equations and the master rate equations of the non-equilibrium chemistry are solved simultaneously for numerical

solutions. Factors of uncertainty in the rate data are introduced and the numerical results are compared to determine the sensitivity of the flow variables to the chemistry model.

Throughout this study thermal equilibrium is assumed to prevail in the predicted flow fields, hence the effects of vibrational non-equilibrium are not included. While this assumption is in fact consistent with the experimental condition that the rate data were determined for thermal equilibrium, it is intended for the present sensitivity study to be conducted in a manner consistent with the source of the rate data rather than to reduce the importance of vibrational non-equilibrium in a hypersonic flow field.

FLOW MODEL

The flow field considered in this study begins with a steady free stream flowing into a stationary normal shock. Chemical reactions are assumed to be absent from the shock front and the shocked gas at thermal equilibrium behind the shock. The flow properties relax with the non-equilibrium chemistry as the shocked gas is flowing downstream.

The Hugoniot and Rayleigh equations for a normal shock

$$h_2 - h_2 = 1/2 \ p_1 v_1 (p_2/p_1 - 1)(v_2/v_1 + 1)$$

and

$$- \gamma_1 M_1^2 = (p_2/p_1 - 1)/(v_2/v_1 - 1)$$

are solved for the shocked gas conditions, which are also the initial conditions of the non-equilibrium flow field. The symbol v represents the specific volume and the subscripts 1 and 2 the pre- and post-shock conditions, respectively.

The steady, chemically non-equilibrium flow is governed by the following one-dimensional flow equations:

Global Continuity

$$\rho \frac{du}{dx} + u \frac{d\rho}{dx} = 0$$

Species Continuity

$$\frac{dy_i}{dx} = \frac{m_i}{\rho u} \frac{dc_i}{dx}$$

where $i = 1,......, n$

   n = number of species

   y_i = mass fraction of species i

   c_i = concentration of species i

   m_i = molecular mass of species i

Momentum

$$\frac{dp}{dx} = - \rho u \frac{du}{dx}$$

Energy

$$\frac{dh}{dx} - \frac{1}{\rho} \frac{dp}{dx} = 0$$

$$\frac{dh}{dx} = c_p \frac{dT}{dx} + \Sigma h_i \frac{dy_i}{dx}$$

Equation of State $p = \rho RT$

where R is the mixture specific gas constant. There are n+4 equations and the same number of unknowns, namely, $y_1, ... y_n$, u, T, p and ρ. The source term in each of the

species continuity equation is determined from a master rate equation which accounts for the production and consumption of the species by reactions involving that species.

CHEMISTRY MODEL

For a free stream temperature of 300 K, the temperature immediately behind the front of a normal shock in the Mach 5 - 14 range is below 10,000 K. In this temperature range the important reactions needed to properly model the non-equilibrium chemistry of a N_2-O_2 system such as air are rather well known and their rate data are also available. Furthermore, most ionization processes are active at such a low level that only the ionizing collision

$$N + O \rightarrow NO^+ + e^-$$
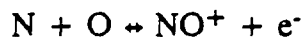
is responsible for the production of the small amount of free electrons in flow fields below Mach 14 [1]. Therefore, limiting the study to the Mach 5 - 14 range helps to reduce the number of reactions to be included in the chemistry model. This plus the fact that the reactions in the model are quite well understood, except for uncertainties in the rate data, ensure a reasonable degree of reliability in the sensitivity results of the present work.

Previous shock tube and chemical kinetics studies suggest that the important reactions in air at temperatures below 10,000 K are:

$$O_2 + M \rightarrow O + O + M \qquad (1)$$
$$N_2 + M \rightarrow N + N + M \qquad (2)$$

$$NO + M \leftrightarrow N + O + M \qquad (3)$$
$$O + N_2 \leftrightarrow NO + N \qquad (4)$$
$$NO + O \leftrightarrow N + O_2 \qquad (5)$$

and
$$N + O \leftrightarrow NO^+ + e^- \qquad (6)$$
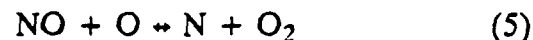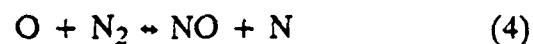
where M can be O_2, N_2, NO, O or N. Beside reactions (3), (4) and (5) other reactions like

$$NO + NO \leftrightarrow N_2O + O \qquad (7)$$

and
$$N_2O + O \leftrightarrow N_2 + O_2 \qquad (8)$$
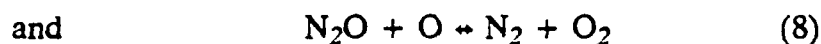
were thought to have significant influence on the overall kinetics of NO. Counting the five collision partners in the three dissociative reactions, a total of twenty reactions are used at the beginning of this study. As will be explained later, the species N_2O and reactions (7) and (8) were included in the study initially and found to have no significant influence on the overall chemical kinetics in the flow fields considered here. Therefore, reactions (1) to (6) are sufficient for modeling Mach 8 -14 hypersonic flow.

RATE DATA

The motivation of this review is to understand the limitations of and the uncertainties in the existing chemical kinetics information. The goal is to obtain a set of rate data appropriate for use in the present sensitivity study. There is no pretense to suggest that the chemical kinetics data mentioned below or those in the open literature are good enough for hypersonic flow research. Instead, it is the purpose of this study to determine which rate constants have unacceptably large uncertainty and therefore requires improvement.

The notation k(A,B) is used below to represent the dissociation rate constant of species A when it collides with species B. Here the unit of concentration is moles/cc and temperature in Kelvins. The rate constant expressions used in this study are summarized in Table I.

Reaction (1): $O_2 + M \rightarrow O + O + M$

Among the aforementioned reactions, the dissociation of O_2 and the reverse three-body recombination reaction are probably the most studied reactions. There is a general consensus on the relative efficiency of the different collision partners in the dissociation of oxygen molecules:

$$k(O_2,O) = 3 \times k(O_2,O_2),$$
$$k(O_2,O_2) = 10 \times k(O_2,Ar),$$
$$k(O_2,N_2) = 1/4 \times k(O_2,O_2),$$
and
$$k(O_2,N) = k(O_2,NO) = k(O_2,Ar).$$

The different rate constants can be determined from $k(O_2,Ar)$.

Figure 1 shows the rate expressions of $k(O_2,Ar)$ from three sources. Wray [2] (1963) fitted data up to 18,000 K to the expression

$$k(O_2,Ar) = 2.5 \times 10^{16} T^{-.5} \exp(-59,400/T).$$

Bortner [4] (1969) later curve fitted data from nine studies. The resulting expression gives a rate value that is a factor of 3 smaller than Wray's at 10,000 K. The difference between the two expressions decreases as the temperature drops. The two agree with one another

at 4,000 K.

The most recent data was reported by Breshares et al [5] in 1972. Using the laser schlieren technique, their data has a factor of two uncertainty and O_2 was found to be 9.6 times more effective than argon. According to the review performed by Boyd and Burns[3] (1982), the rate expression obtained by Breshares et al

$$k(O_2, Ar) = 7.87 \times 10^{13} \exp(-52,760/T)$$

is by far the most reliable with a factor of 2 uncertainty and is used in this study.

Reaction (2): $N_2 + M \leftrightarrow N + N + M$

Only the rate data for $N_2 + N_2 \leftrightarrow 2N + N_2$ and $N_2 + N \leftrightarrow 3N$ are available in the literature. There is no data for the the collision partners NO, O_2 and O. The efficiencies of these three species have often been assumed to be the same as argon.

For $M = N_2$, Bortner [4] (1969) curve fitted the data obtained by Cary [6](1965) and Bryon[7] (1966) at temperatures above 6,000 K and those recorded below 1,000 K by others. The resulting expression agrees very well with the one recommended by Wray [8] (1962). Baulch et al [9] (1973) recommended the expression obtained by Appleton et al [10] (1968) which is known to give much lower values than all the other studies, including a later study by Hanson & Baganoff [11] (1972). All these expressions are plotted in Figure 2. As a result of the higher temperature dependence, the rate by Hanson et al is higher than the ones by Bortner and Wray and the discrepancy increases with decreasing temperature. The expression recommended by Bortner

$$k(N_2, N_2) = 5 \times 10^{18} \ T^{-.75} \exp(-113,200/T)$$

is used in this study.

For M = N, the volume of data is rather small. The rate expressions by Wray[8] (1962), Bortner [4] (1969) and Hanson & Baganoff [11] (1972) agree to within a factor of 2 at temperatures below 10,000 K (Figure 3). The one Bortner obtained by curve fitting data from four studies

$$k(N_2,N) = 3.0125 \times 10^{22} \; T^{-1.5} \; exp(-113,200/T)$$

is used here.

There are contradictory reports on the relative efficiency between N_2 and N in causing the dissociation of N_2. Bryon's results suggest that N is about 10 times more effective than N_2 at 9,000 K and 15 times at 6,000 K. Hanson & Baganoff reported an opposing trend that the relative efficiency is 8 at 12,000 K and it drops to 2 at 6,000 K. Appleton's results suggest a temperature independent ratio of 4. Furthermore, no explanation has been given for the large discrepancy between the data of Appleton et al and the other investigators as mentioned earlier.

For M = Ar, the data obtained by Cary [6] (1965) and Bryon [7] (1966) differ by less than a factor of 2. Bortner curve fitted their data and some other low temperature data. The resulting expression yields rates very close to those of Bryon (Figure 4). For the 6000 -10,000 K range, Bryon's expression

$$k(N_2,Ar) = 1.9 \times 10^{17} \; T^{-0.5} \; exp(-113,200/T)$$

is used here. For the 3,390 K - 6,435 K range, Thielen and Roth [12] (1986) determined the rate expression

$$k(N_2,Ar) = 1.03 \times 10^{28} \ T^{-3.33} \exp(-113,220/T)$$

which has a different temperature dependence from Bryon's. The two expressions agree at 6,210 K. At lower temperatures the dissociation rate of N_2 is so small that the difference between the two expressions is be found in this study to have no significant effect on the overall rate of N_2 dissociation.

In summary, the factor of uncertainty in the rate data for N_2 dissociation is a factor of 2 for the collision partner N and about 3 for the others.

Reaction (3): NO + M → N + O + M

Presently, the dissociation rate data of this reaction is extremely scarce and its reliability is questionable. Freedman & Daiber [19] (1961) studied NO dissociation at 3000 - 4300 K and Wray & Teare [14] (1962) at 3,000 - 8,000 K. Determining the dissociation rate constant of NO is often complicated by the simultaneous presence of other reactions in the test gas. Examples of these reactions include NO + NO → N_2O + O and NO + N → N_2 + O. To circumvent this problem, Wray & Teare had to assume the relative effectiveness of the different collision partners. The rate constant k(NO,NO) was found to be 20 times of k(NO,Ar) with the assumption that O and N are equally effective as NO, and O_2 and N_2 as Ar in causing the dissociation of NO.

In the present sensitivity study, the rate constants recommended by Bortner [4]

$$k(NO,NO) = 8 \times 10^{21} \ T^{-1.5} \exp(-75,400/T)$$
$$k(NO,N) = k(NO,O) = k(NO,NO)$$

$$k(NO,N_2) = 9.0 \times 10^{14} \exp(-75,400/T) = k(NO,O_2)$$

are used. These expressions are essentially the same as those obtained by Wray and Teare. Since no other data is available for comparison, the factor of uncertainty cannot be determined. For the purpose of studying the sensitivity of the flow properties to this reaction, a factor of 4 is used.

Reaction (4): O + N$_2$ ↔ NO + N, and Reaction (5): NO + O ↔ N + O$_2$

The formation of NO at moderately high temperature is primarily controlled by the so-called Zeldovich mechanism which is made up of these two reactions. Their rate determine nature in combustion systems has prompted many studies of their rate constants. By now these rate constants are reasonably well characterised.

Glick et al [17] (1957) and Wray & Teare [14] (1962) determined the forward rate of reaction (4). Their results were later substantiated by a number of combustion studies. Baulch et al curve fitted all the data to produce an expression with a factor of 2 uncertainty in the temperature range 2,000 - 5,000 K. Monat, Hanson & Kruger [15] (1978) used two independent techniques to monitor NO concentration, thus providing a check on the data and reducing experimental uncertainty. The forward rate constant obtained by Monat et al

$$k_f = 1.84 \times 10^{14} \exp(-38384/T)$$

is used. This expression yields rate values close to the upper values of Baulch's expression.

For the reaction NO + O $\leftrightarrow$ N + O$_2$, Wray & Teare [2] reported the only high temperature data at 5,000 K. Hanson et al [16] (1974) reported data in the temperature range 2,500 - 4,100 K and also a rate constant expression that fits all the data from 300 to 5,000 K with extremely small scatter. Therefore, the expression due to Hanson et al is used here:

$$k_f = 2.36 \times 10^9 \, T \, \exp(-19430/T).$$

Presently there is no data available at temperatures above 5,000 K.

Reaction (6): NO + NO $\leftrightarrow$ N$_2$O + O and Reaction (7): N$_2$O + O $\leftrightarrow$ N$_2$ + O$_2$

The reaction NO + NO $\leftrightarrow$ N$_2$ + O$_2$ had been mistaken as the primary NO removal mechanism until Camac and Feinberg [18] (1966) found in a shock tube study of NO decomposition that N$_2$O and O were produced at a rate compatible with the removal rate of NO by the reaction NO + NO $\leftrightarrow$ N$_2$O + O. Other researchers re-evaluated their data and found agreement with the results of Camac and Feinberg. The rate constant expression for reaction (6) derived by Kaufman and Kelso, also recommended by Baulch [9], is used here:

$$k_f = 1.3 \times 10^{12} \, \exp(-32,100/T).$$

The removal of N$_2$O is known to occur via the reactions N$_2$O + O $\leftrightarrow$ N$_2$ + O$_2$ and N$_2$O + O $\leftrightarrow$ NO + NO. The relative efficiency of the two reactions is around unity at temperature above 1000 K. The forward rate expression recommended by Baulch [9]

$$k_f = 1.0 \times 10^{14} \, \exp(-14,100/T).$$

used here.

<u>Reaction (8): N + O → NO$^+$ + e-</u>

. There are different kinds of ionization processes that have been known to occur in high temperature air. The dominancy of the different processes depends largely on temperature. For Mach 5 - 14 flight, the available energy is so small that the ionizing atomic collision

$$N + O \rightarrow NO^+ + e^-$$

is responsible for producing most of the free electrons [1]. This reaction requires less initial energy than the ionization potential of NO by an amount released when NO is formed in the collision of N and O. The rate constant

$$k_f = 5.181 \times 10^{11} \exp(-31900/T)$$

recommended by Bortner [4] is used here. Other ionic species are not included in the present chemistry model because their concentrations have been found to be at least two orders of magnitude smaller [1].

SOLUTIONS

Numerical solutions of the 1-D non-equilibrium flow field have been obtained for Mach 8, 12 and 14 normal shock waves. The free stream conditions are 322 K and 1.216 mmHg and the composition of the free stream air is taken to be 21% O_2 + 79% N_2 by mole.

The governing equations of the chemically non-equilibrium flow field are solved using the DGEAR stiff equation solver of the IMSL. The shock front solutions are the initial conditions. Some of the results are shown in Figures 5 - 12 and will be examined in detail in the next section.

RESULTS AND DISCUSSION

Figures 5, 7 and 9 show the composition profile behind normal shocks at Mach 8, 12 and 14. The length of the relaxation zone has been predicted to reduce significantly with increasing Mach number. It is about 20 meters at Mach 8, 30 cm at Mach 12 and 5 cm at Mach 14.

At all three Mach numbers, the temperature of the flow field is sufficiently high for a very significant degree of O_2 dissociation to occur. At Mach 8 the mole fraction of atomic oxygen increases from zero right behind the shock front to 10 percent at the end of the relaxation zone. At Mach 12 the final mole fraction of O is 25 percent while the mole fraction of O_2 is less than 1 percent. Similar results have been predicted in the Mach 14 case. At all three Mach numbers, the mole fraction of atomic nitrogen is less than or around 1 % indicating the dissociation of N_2 is much less significant than that of O_2.

Figures 6, 8 and 10 show the Mach number, temperature, density and pressure profiles in the chemically non-equilibrium flow fields. The dissociation reactions consume a significant amount of the internal energy of the shocked gas and cause the temperature to drop by almost one half of the beginning value. The pressure varies only slightly within the relaxation zone while the density increases by as much as 50 percent.

Significance of N_2O in the Chemistry of High Temperature Air

At Mach 8 and above, the mole fraction of N_2O in the relaxation zone has been predicted to be very small. When the two reactions involving this species are excluded from the chemical kinetics model, no observable changes in the concentrations of the other species and the flow properties can be found. This is consistent with the experimental results obtained by Myerson [12] that reaction (7) is important for the removal of NO only at low temperatures. Consequently, the reactions

$$NO + NO \leftrightarrow N_2O + O \qquad (7)$$
and
$$N_2O + O \leftrightarrow N_2 + O_2 \qquad (8)$$
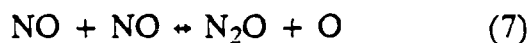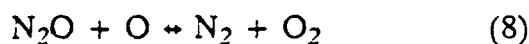
can be eliminated from the chemistry model, which now consists of 6 reactions and 7 species.

Significance of the Reaction $N + O \rightarrow NO^+ + e^-$

As shown in Figures 5, 7 and 9, the concentrations of free electrons and NO^+ ions in the non-equilibrium flow fields are small compared to the concentrations of the neutral species. To test the influence of this reaction on the conditions of the flow fields, this ionizing reaction is excluded from the chemistry model. The predicted flow fields have been found to have no observable changes. Therefore, when the objective of a numerical simulation of Mach 14 or below hypersonic flow does not concern the presence of free electrons, the chemistry model can further be reduced to include only reactions (1), (2), (3), (4) and (5), and the species O_2, N_2, NO, O and N.

Effects of Rate Data Uncertainties on Flow Conditions

The rate constants for the reactions

$$O_2 + M \leftrightarrow O + O + M, \quad N_2 + M \leftrightarrow N + N + M \quad \text{and} \quad NO + M \leftrightarrow N + O + M$$
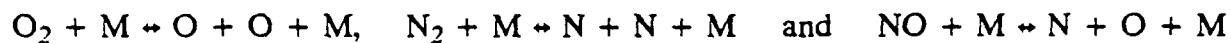
have been varied systematically to study the effects of their uncertainties on the flow properties. The tests performed are listed in Table II below.

Table II

Case	Reaction	Multiply k_f and k_r by
I	$O_2 + M = 2O + M$	2
II	$O_2 + M = 2O + M$	1/2
III	$O_2 + N = 2O + N$	0
IV	$O_2 + NO = 2O + NO$	0
V	$N_2 + M = 2N + M$	3
VI	$N_2 + M = 2N + M$	1/3
VII	$N_2 + N_2 = 2N + N_2$	3
VIII	$N_2 + N_2 = 2N + N_2$	1/3
IX	$N_2 + N = 2N + N$	2
X	$N_2 + N = 2N + N$	1/2
XI	$NO + M \leftrightarrow N + O + M$	4
XII	$NO + M \leftrightarrow N + O + M$	1/4

Reaction: $O_2 + M \rightarrow O + O + M$

The sensitivity of the flow field to the factor of 2 uncertainty in the oxygen dissociation rate constants is examined in the following manner. The flow field is predicted using the upper and lower values of the rate constant. The results from the two cases are compared to determine the effects on the flow properties in the relaxation zone. A comparison of the results of Cases I and II in Table II indicates that a factor of 2 uncertainty is predicted to have significant influence on the temperature profile. The effect becomes larger as the free stream Mach number increases from 8 to 14. At Mach 14 the predicted temperature profile can be off by as much as 1,000 K, based on a pre-shock temperature of 322 K. This can be seen in Figure 11. The least affected is the static pressure.

Cases III and IV are for examining the influence of the less efficient collision partners on the over-all dissociation rate of oxygen. When the reactions $O_2 + N \rightarrow 2O + N$ and $O_2 + NO \rightarrow 2O + NO$ are shut off, no significant changes in the results are found. There are two reasons for the insensitivity of the flow field to these two reactions. The obvious one is NO and N are much less effective than the other collision partners. A more important reason is that the concentrations of NO and N are very small in the early part of the relaxing flow field. The amount of NO and N increase with the distance behind the shock front. By the time they reach a higher concentration, the flow has become closer to equilibrium.

Reaction: $N_2 + M \rightarrow N + N + M$
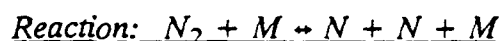
In Cases V through X, the sensitivity of flow properties to the uncertainties in the rate contants for nitrogen dissociation are tested. At Mach 8 and 12, the flow properties appear to be unaffected. At Mach 14, the temperature profile is only slightly sensitive to the uncertainty as shown in Figure 12.

The results presented above suggest that the thermal dissociation of O_2 is much more dominant than that of N_2 in hypersonic flow fields below 10,000 K. Furthermore, the relaxation of the temperature is very sensitive to the uncertainty factor of 2 in the existing rate data for O_2 dissociation. The reason for the high sensitivity is that at the beginning of the relaxation zone the composition is mainly N_2 and O_2. The competing reactions are the dissociations of these two species only. The smaller dissociation energy of O_2, which is about half of that of N_2, allows the dissociation of O_2 to proceed at a much higher rate. Hence the flow properties are more sensitive to this reaction. Consequently, the uncertainties in the O_2 rate constants can cause significant deviations in the temperature of a predicted flow field.

Reaction: $NO + M \rightarrow N + O + M$

The rapid production of oxygen atoms behind the shock front promotes the production of NO via the reactions

$$N_2 + O \rightarrow NO + N$$

and
$$N + O_2 \rightarrow NO + O .$$
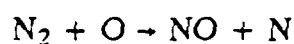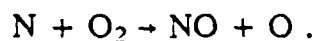
Note that these reactions do not alter the concentration of atomic oxygen. Figure 13 shows the contributions of these two reactions and

$$NO + M \rightarrow N + O + M$$

to the change in the mass fraction of NO with respect to the distance behind the shock front. The results indicate that nitric oxide is produced by the two shuffle reactions and simultaneously consumed in small amount by dissociation. The negative rate of change of the NO mass fraction due to dissociation suggests that NO is not formed from the association of N and O atoms.

The rate constants for $NO + M \leftrightarrow N + O + M$ *have been varied by factors of 1/4 and 4 to study the sensitivity of the flow properties.* As already mentioned in the rate constant review section, the reliability of the existing NO dissociation rate data cannot be determined. The factor of four used here is an assumed factor of uncertainty. Figures 14 and 15 show the sensitivity of the species mole fractions and flow properties, respectively, for a Mach 14 normal shock. Figure 14 indicates that a factor of 4 increase in the dissocation rate reduces the NO peak mole fraction and increases the concentrations of N and O more rapidly. The higher concentration of N atoms at $x = 0.5$ mm to 1 mm enables the reaction

$$N + O_2 \rightarrow NO + O$$
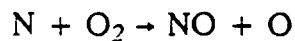
to proceed at a higher rate. This results in a more rapid depletion of oxygen molecules and a higher equilibrium mole fraction of NO.

Figure 15 shows that temperature is very sensitive to the factor of 4 uncertainty in the rate constant of the reaction: $NO + M \leftrightarrow N + O + M$. At Mach 14 the predicted temperature profile deviates by as much as 930 K, based on a pre-shock temperature of 322 K. The least affected is the static pressure. Figure 15 also indicates that the temperature decreases at a higher rate when the dissociation rate of NO is increased by a factor of 4. This is due to the consumption of a larger amount of internal energy when the endothermic dissociation of NO proceeds at a higher rate.

CONCLUSION

The reactions and species that are important to the non-equilibrium chemistry of air at temperatures below 10,000 K have been identified by examining the sensitivity of the flow properties behind a normal shock to the chemistry model. By limiting the maximum post-shock temperature to 10,000 K, equivalently the maximum Mach number of the shock to 14, the reliability of the results is ensured by using a set of reaction rate data taken in the temperature range of the flow fields and a chemistry model made up of reactions known to be important below 10,000 K in air.

The uncertainty factor of 2 in the rate data for oxygen dissociation have been predicted to introduce as much as 1,000 K deviation in the temperature profile. Similar degree of deviation in the temperature has also been predicted when an assumed factor of 4 uncertainty was introduced into the dissociation rate constant of NO. Although the flow in the present study is one-dimensional, the results suggest that comparable deviations in the predicted temperature may occur in the fore portion of the non-equilibrium flow field between a hypersonic vehicle and its leading bow shock.

As a result of lower rate of N_2 dissociation below 10,000 K, the flow properties are much less sensitive to the larger uncertainty in the rate data for this reaction. Thus better rate data for oxygen and nitric oxide dissociations are needed for reliable predictions of hypersonic flow while the existing uncertainty in the nitrogen data is expected to introduce insignificant deviations.

Out of the initial twenty reactions and eight species in the chemistry model, eighteen reactions and seven species have been identified to be essential to the chemistry of air at temperatures below 10,000 K. One of the reactions is the ionizing atomic collision $N + O \rightarrow NO^+ + e^-$. This reaction and the two charged species can be eliminated when the

objective of a numerical simulation of hypersonic flow is not concerned with the presence of free electrons.

Compression or expansion of the flow and vibrational non-equilibrium effects have been neglected in this study. Any attempt to extrapolate the present results to other flow fields should be done with careful consideration of these factors.

REFERENCES

1. Lin, S., Neal, R.A., and Fyfe, W.I., "Rate of Ionization Behind Shock Waves in Air I: Experimental Results," J. Chem. Phy. 5:1633-1648 (1962)

2. Wray, L.K., "Shock Tube Study of the Recombination of O Atoms by Ar Catalysts at High Temperatures," J. Chem. Phy., Vol 38, No. 7, p 1518, 1963

3. Boyd and Burns, Shock Waves in Chemistry, Ed. Assa Lifshitz, p.161, Marcel Dekker Inc., New York, 1981.

4. Bortner, M.H., "Review of Rate Constants of Selected Reactions of Interest in Re-entry Flow Fields in the Atmosphere," NBS Tech Note 484, 1969.

6. Cary, B., Phy. of Fluid, 8:26 (1965)

7. Bryon, S., "Shock-Tube Measurement of the Rate of Dissociation of Nitrogen," J. Chem. Phy,, 4:1378 (1966)

8. Wray,K.L., "Chemical Kinetics of High Temperature Air," Hypersonic Research, Ed. F.R. Ridell, Academic Press, 1962.

9. Baulch, D.L., Drysdale, D.D. and Horne, D.G., Evaluated Kinetic Data for High Temperature Reactions, Vol. 2, Butterworth, London, 1973.

10. Appleton, J.P., Steinberg, M. and Liquornik, D.J., "Shock Tube Study of Nitrogen Dissociation using U.V. Light Absorption," J. Chem. Phy., 48:599 (1968)

11. Hanson and Baganoff, AIAA J., 10:211 (1972)

12. Thielen K. and Roth P., "N Atom Measurements in High Temperature N2 Dissociation Kinetics", AIAA 24:1102-1105, July 1986.

13. Myerson, A.L., "Shock-Tube Atom Kinetics of Nitric Oxide Decomposition", 14th (International) Symposium on Combustion, p. 219-228, 1973

14. Wray, K.L. and Teare, J.D., "Shock Tube Study of the Kinetics of Nitric Oxides at High Temperatures," J. Chem. Phy. 16:2582-2596 (1962)

15. Monat, J.P., Hanson, R.K. and Kruger, C.H., "Shock Tube Determination of the Rate Coefficient for the Reaction $N_2 + O == NO + N$", 17th Symposium (International) on Combustion, p.543, 1978

16. Hanson, R.K., Flower, W.L. and Kruger, C.H., "Determination of the Rate Constant for the Reaction $O + NO == N + O_2$ ", Combustion Sci. and Tech., 9:79-86 (1974)

17. Glick, H.S., Klein, J.J., and Squire, W.J., Chem. Phy., 27:850 (1957)

18. Camac, M. and Feinberg, R. M., "Formation of NO in Shock-Heated Air," 11th Symposium (International) on Combustion, p. 137, 1966.

19. Freedman, E. and Daiber, J. W., J. Chem. Phy., 34:1271 (1961)

TABLE I

RATE CONSTANTS

Reaction	M	Forward Rates	Sources of Forward Rates	Equilibrium Constants
(1)	O_2 O N_2 NO, N	$7.6 \times 10^{14} \exp(-52,760/T)$ $9.6 \times k(M=O_2)$ $0.25 \times k(M=O_2)$ $7.87 \times 10^{13} \exp(-52,760/T)$	See Text	$7.24 \times 10^{26} T^{-.5} \exp(-59,400/T)$
(2)	N_2 N NO,N,O	$5 \times 10^{18} T^{-.75} \exp(-113,200/T)$ $3 \times 10^{22} T^{-1.5} \exp(-113,200/T)$ $1.9 \times 10^{17} T^{-.5} \exp(-113,200/T)$	See Text	$1.08 \times 10^{25} \exp(-113,200/T)$
(3)	O_2,N_2 N,O,NO	$9 \times 10^{14} \exp(-75,400/T)$ $8 \times 10^{21} T^{-1.5} \exp(-75,400/T)$	Wray & Teare [14] (1962)	$1.45 \times 10^{23} \exp(-75,400/T)$
(4)		$1.84 \times 10^{14} \exp(-38,384/T)$	Monat [15] et al (1978)	$4.545 \exp(-38,000/T)$
(5)		$2.63 \times 10^{9} T \exp(-19,430/T)$	Hanson [16] et al (1974)	$2.4 \times 10^{-1} \exp(-16,100/T)$
(6)		$5.18 \times 10^{11} \exp(-31,900/T)$	Bortner (1969)	$3.58 \times 10^{10} T^{1.5} \exp(-31,900/T)$

Concentration in moles/cc, Temperature in Kelvins

$O_2 + Ar \;--\; O + O + Ar$

$M = O_2,\; N_2,\; NO,\; O,\; N$

Wray (1963)

Breshears et al (1972)
(4000 - 8500 K)

Bortner (1969)

k_d ($cm^3/mole\text{-}sec$)

Temperature   (K)
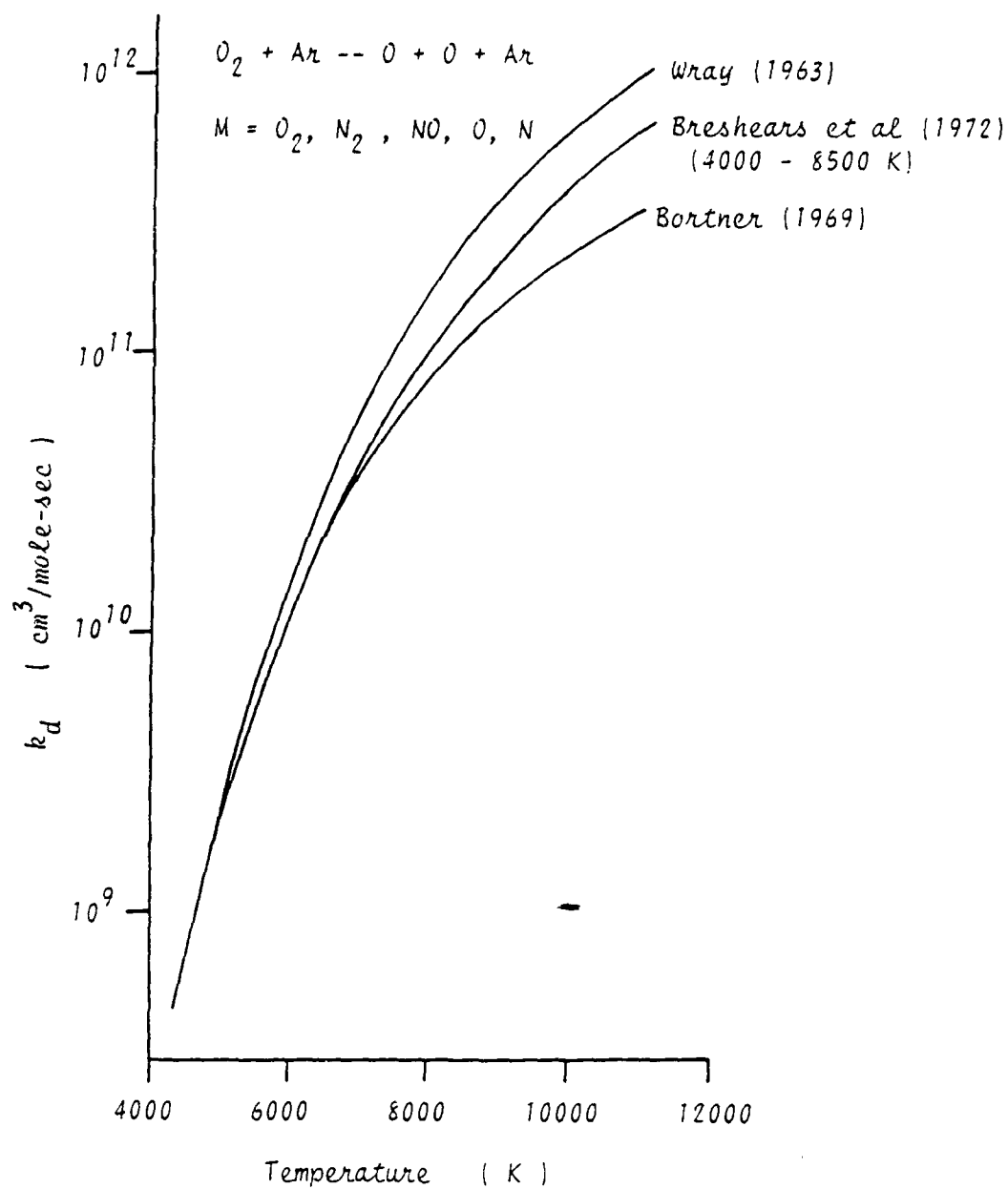
Figure 1 : Comparison of Rate Constants for $O_2 + Ar \rightarrow O + O + Ar$
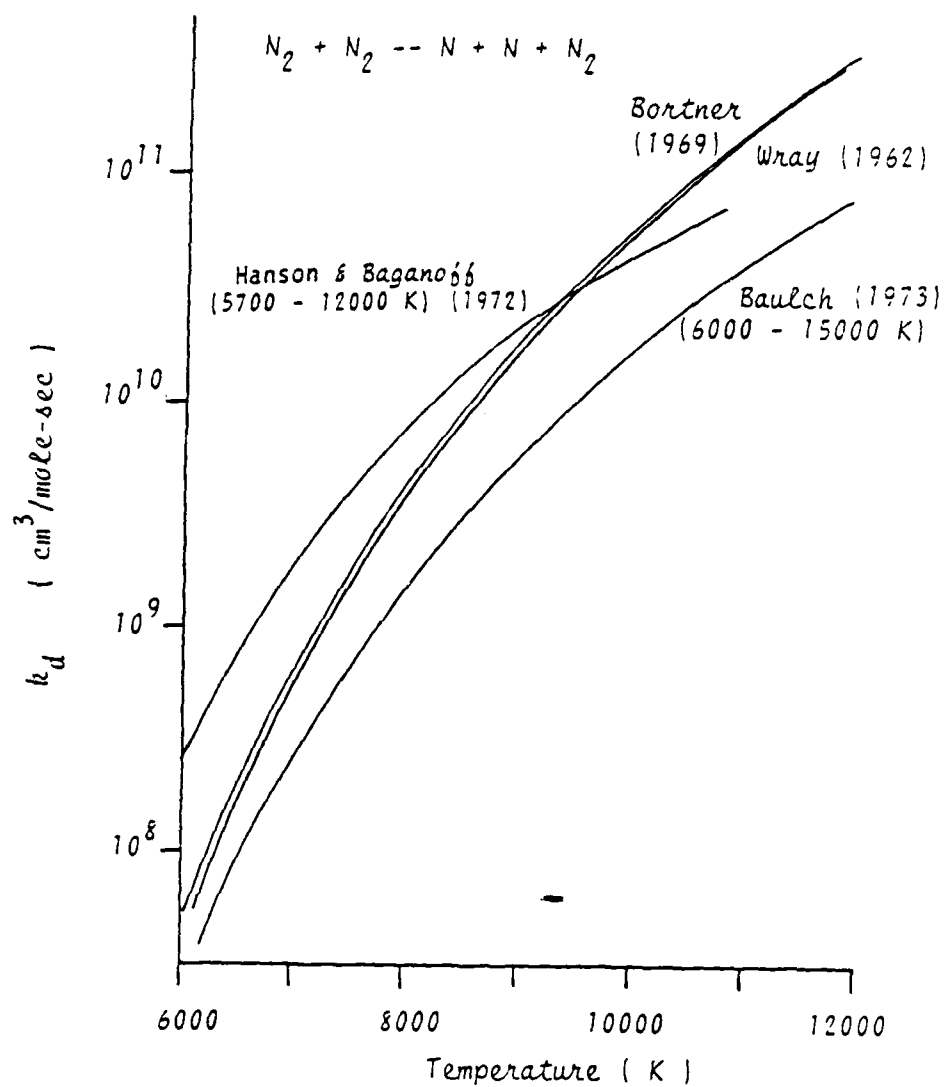
Figure 2 : Comparison of Rate Constants for $N_2 + N_2 \rightarrow N + N + N_2$
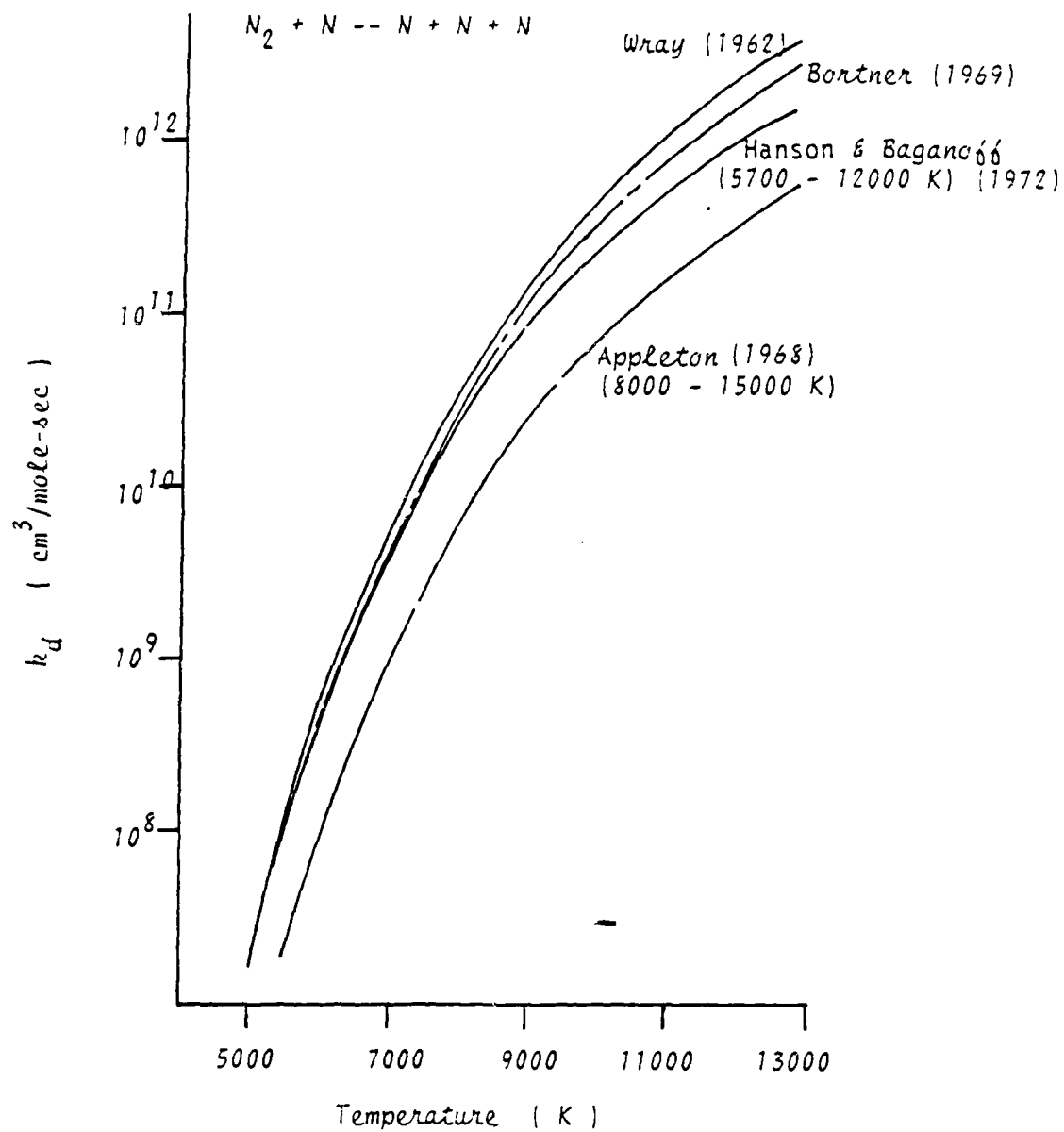
Figure 3 : Comparison of Rate Constants for $N_2 + N \rightarrow N + N + N$
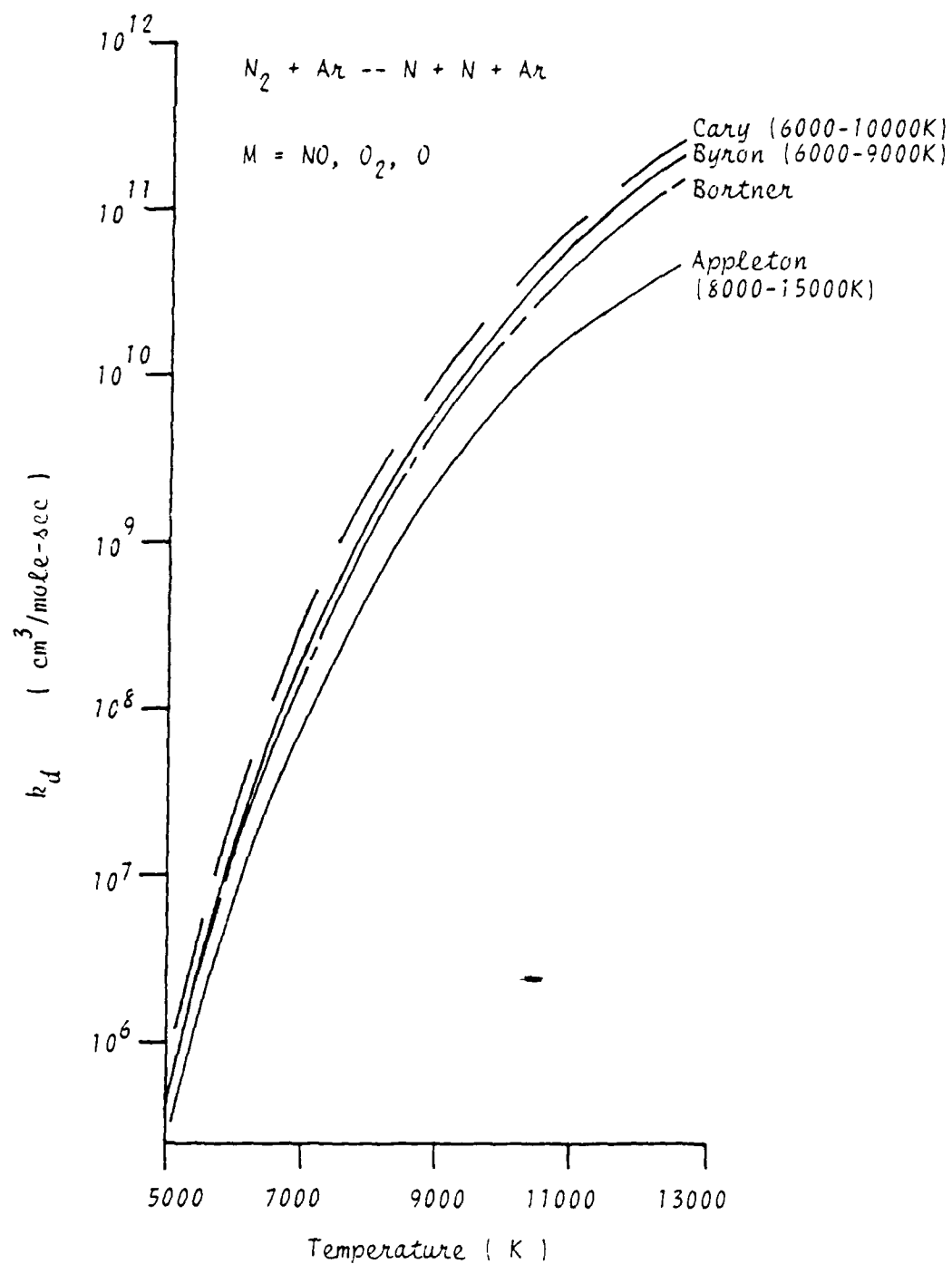
Figure 4 : Comparison of Rate Constants for N_2 + Ar → N + N + Ar
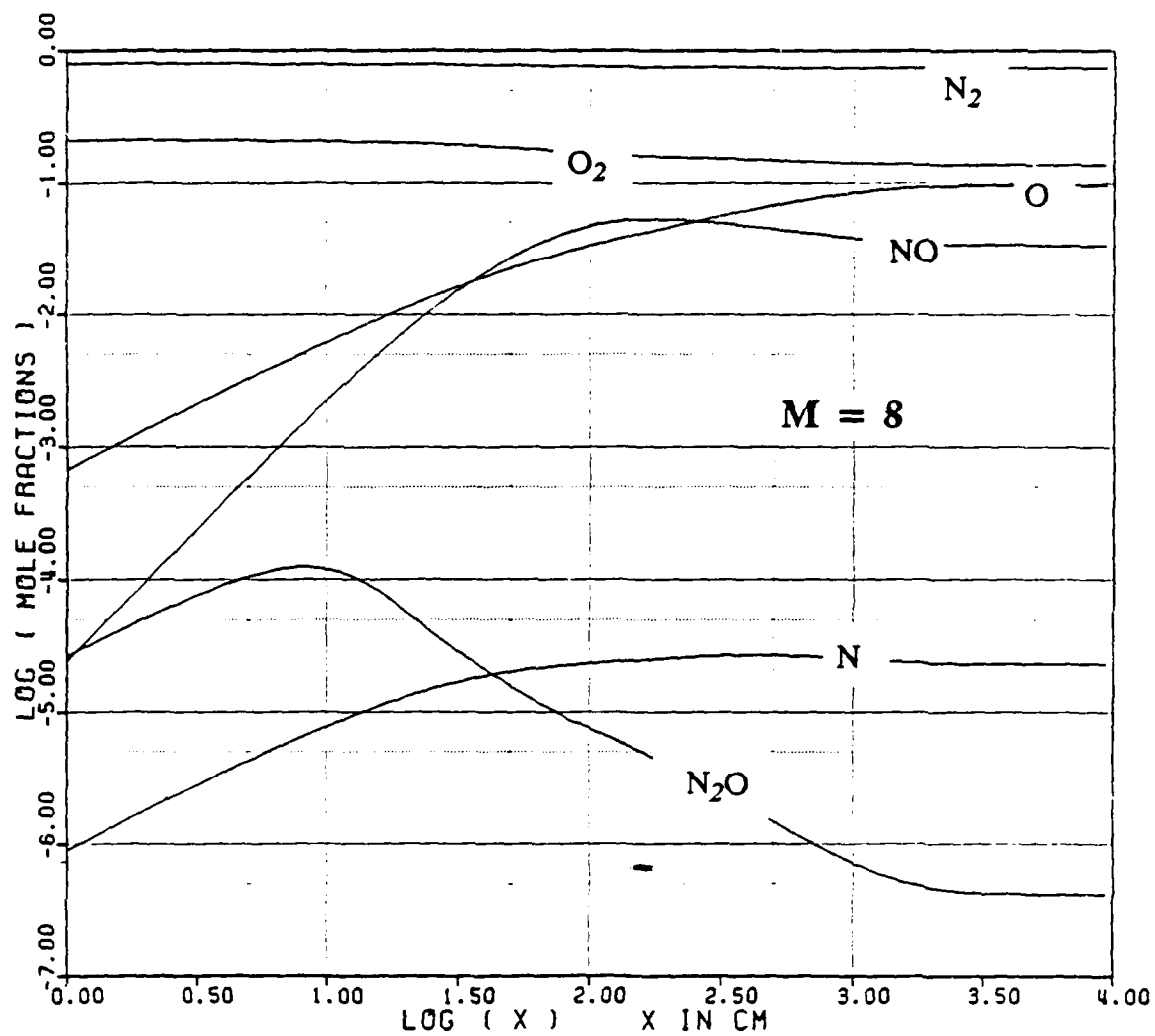
Figure 5 : Species Mole Fractions behind a Mach 8 Normal Shock.
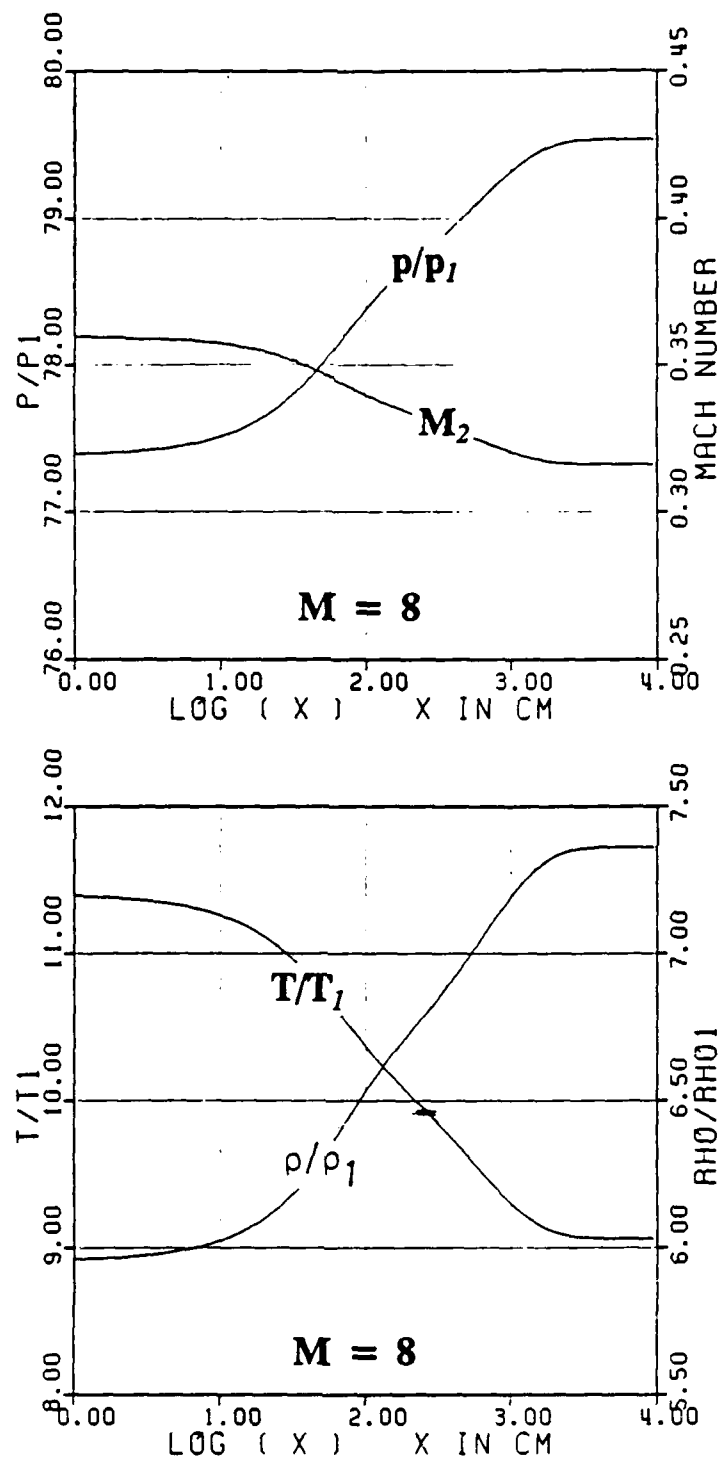
Figure 6 : Profiles of Flow Properties behind a Mach 8 Normal Shock.
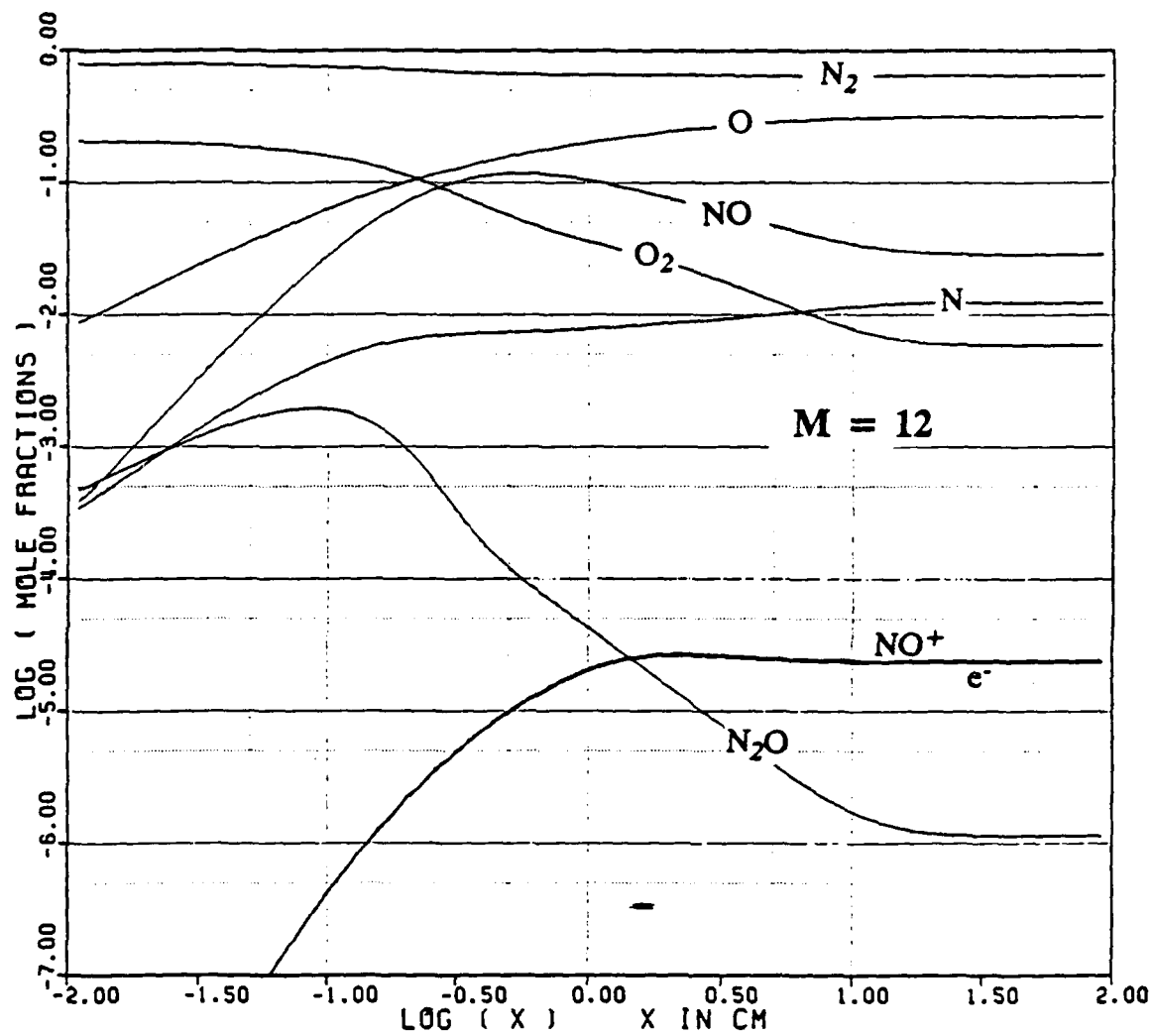
Figure 7 : Species Mole Fractions behind a Mach 12 Normal Shock.
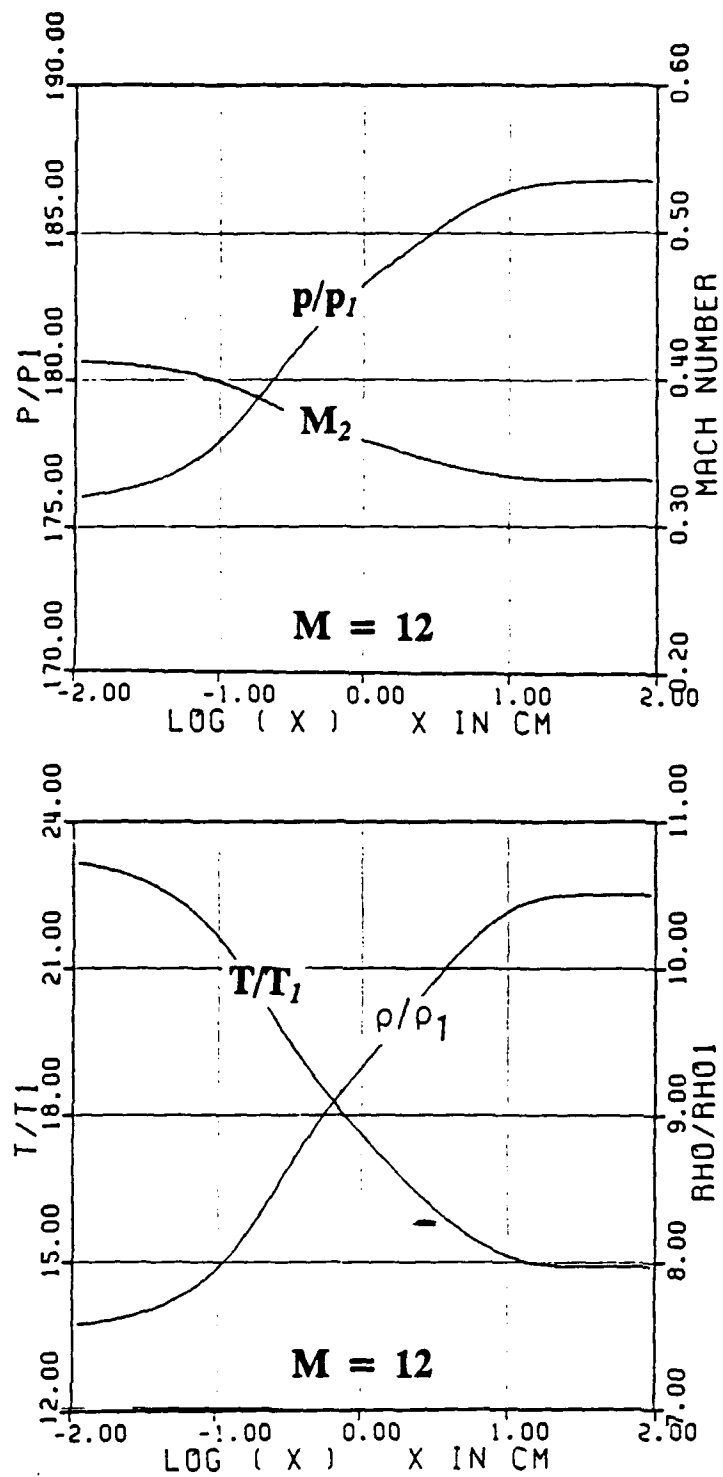
Figure 8 : Profiles of Flow Properties behind a Mach 12 Normal Shock.
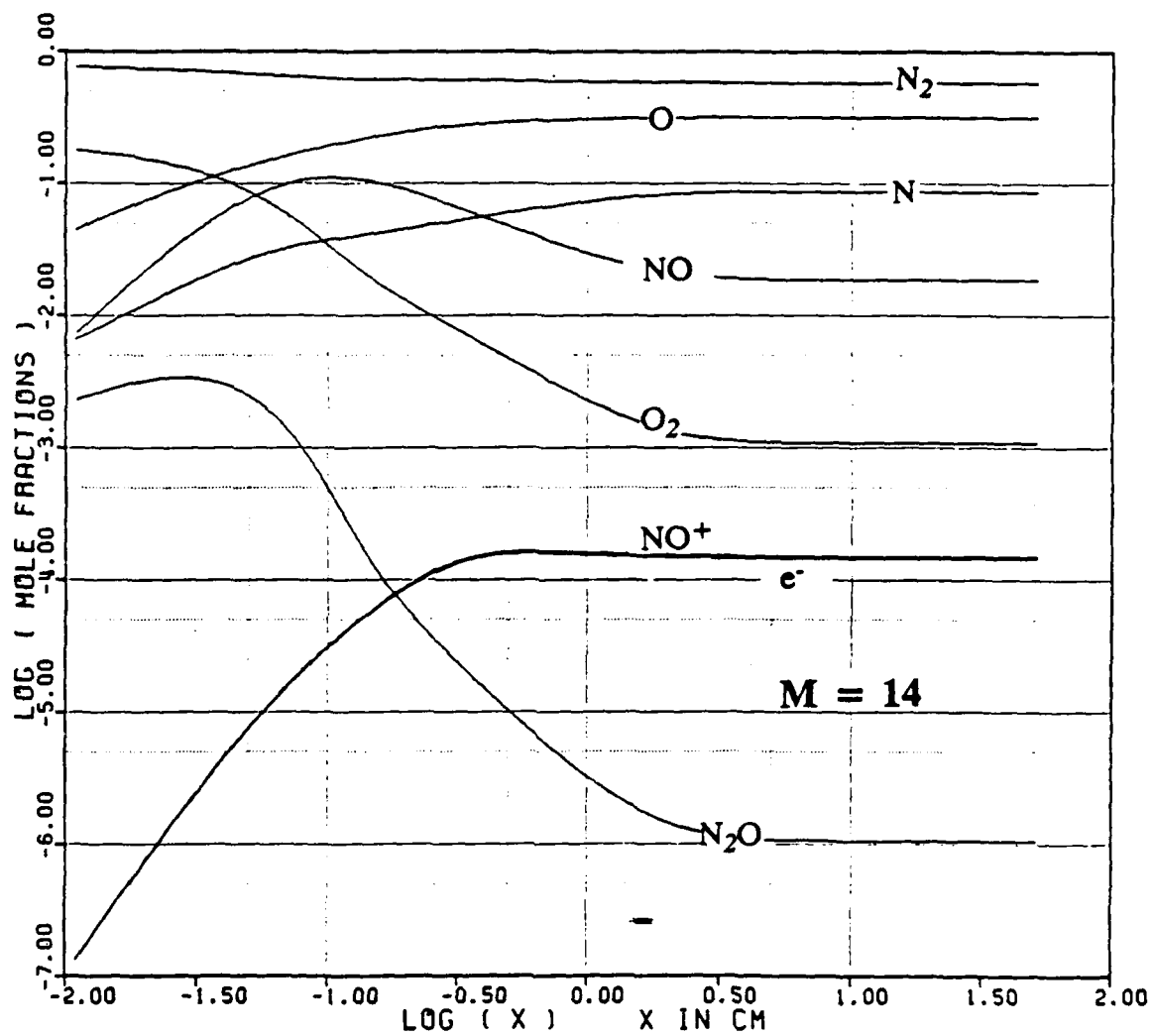
Figure 9 : Species Mole Fractions behind a Mach 14 Normal Shock.
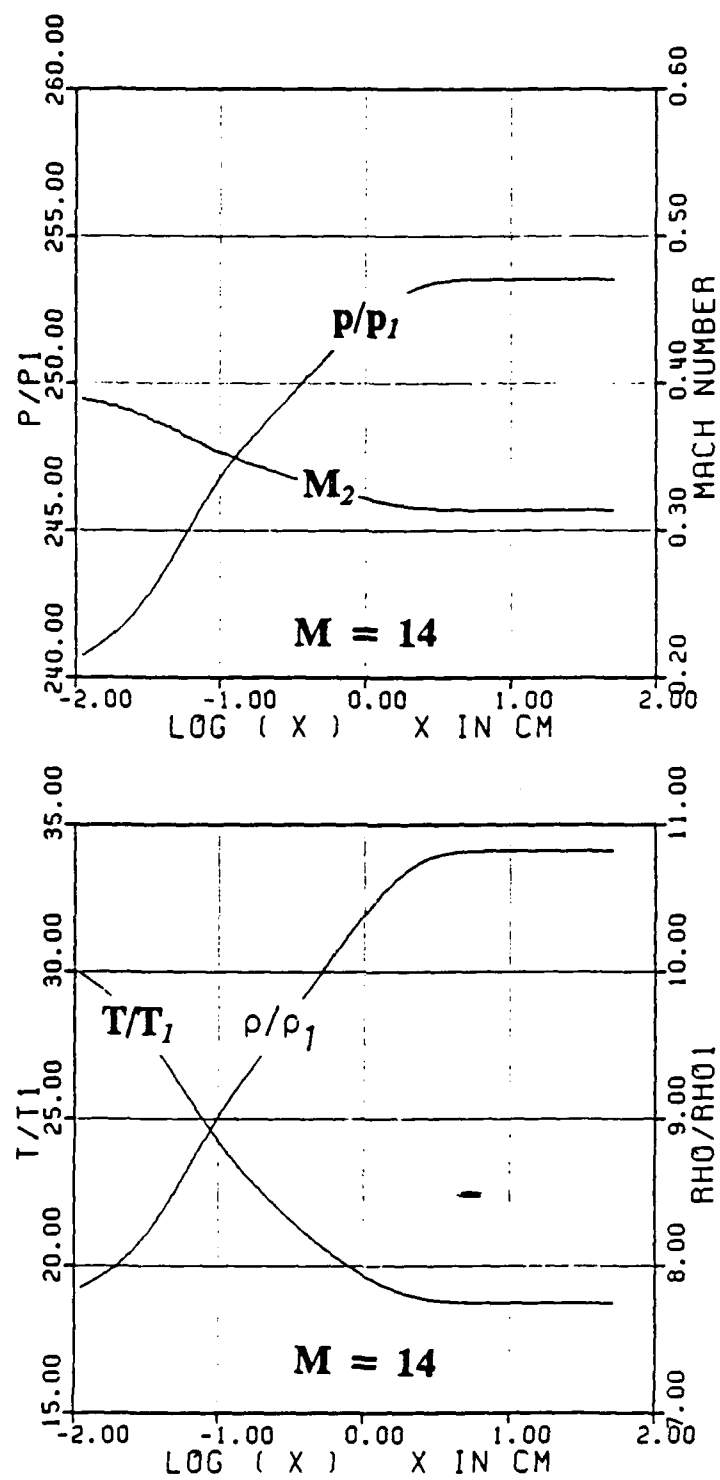
Figure 10 : Profiles of Flow Properties behind a Mach 14 Normal Shock.
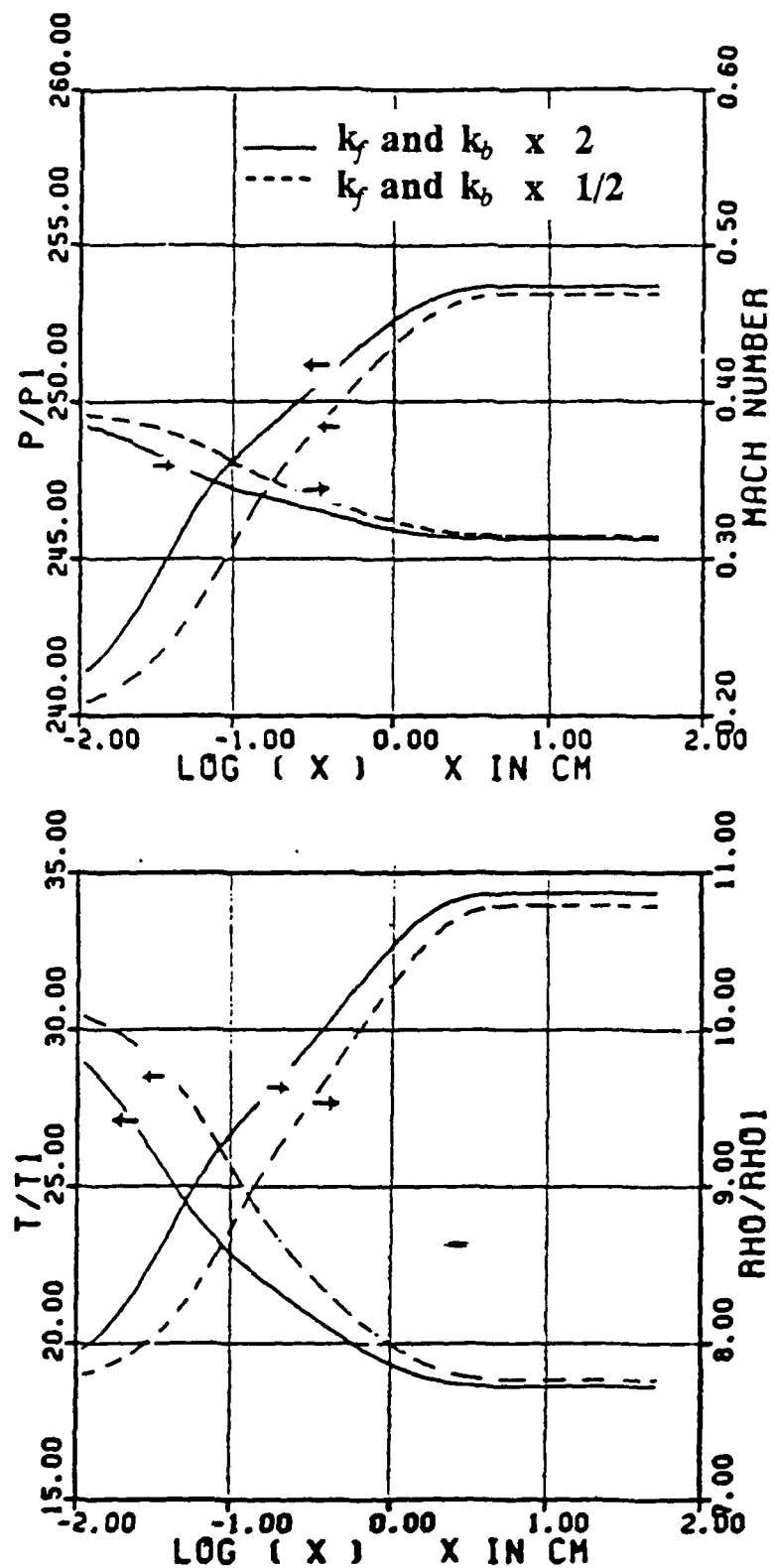
Figure 11 : Effects of the Uncertainty in the Rate Constant for
$O_2 + M \leftrightarrow O + O + M$ on the Flow Properties at M = 14.
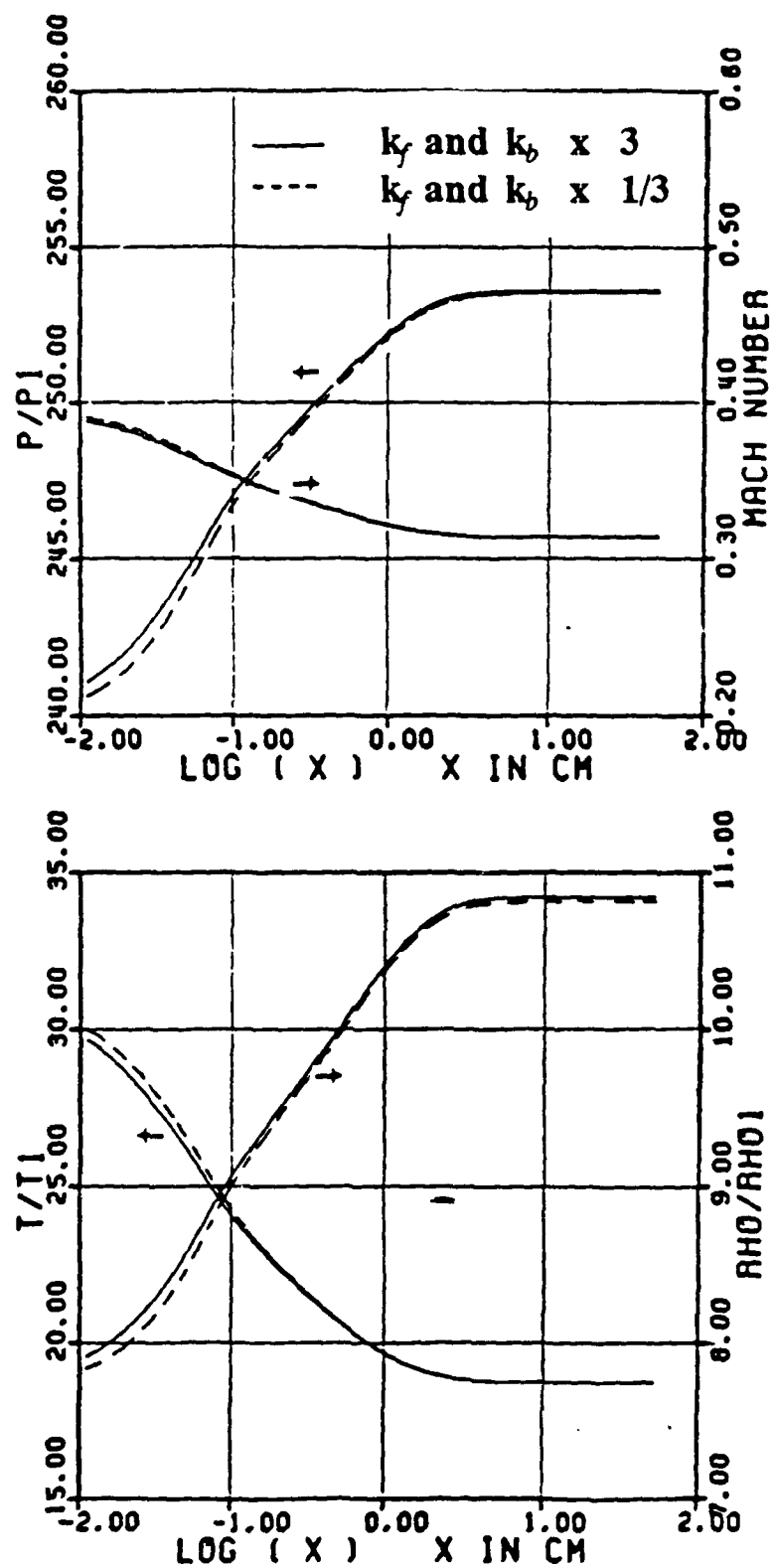
Figure 12 : Effects of the Uncertainty in the Rate Constant for
$N_2 + N_2 \leftrightarrow N + N + N_2$ on the Flow Properties at M = 14.
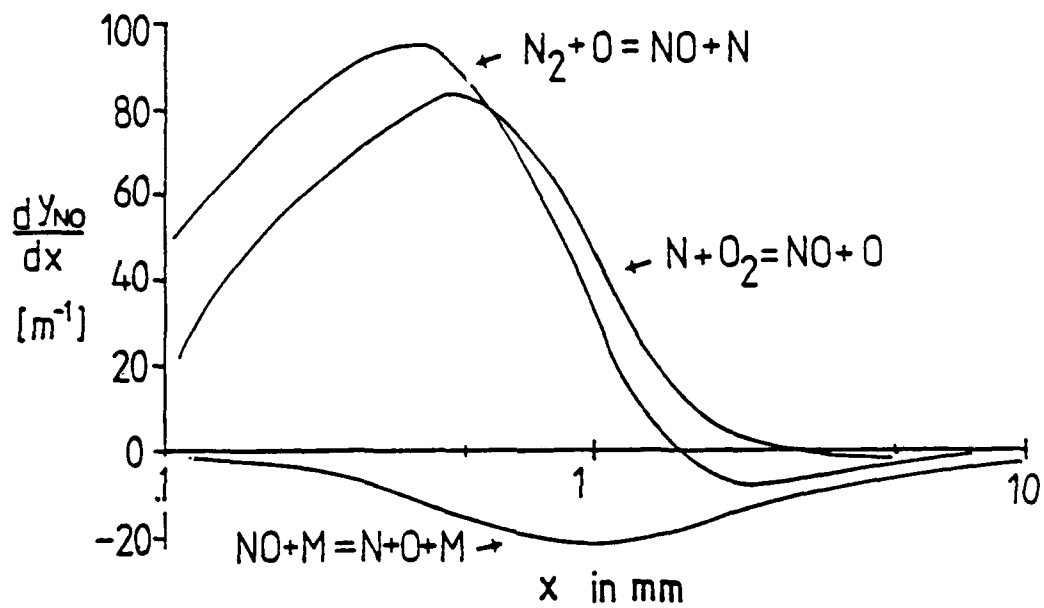
Figure 13 : Change of NO Mass Fraction due to Different Reactions at M = 14.
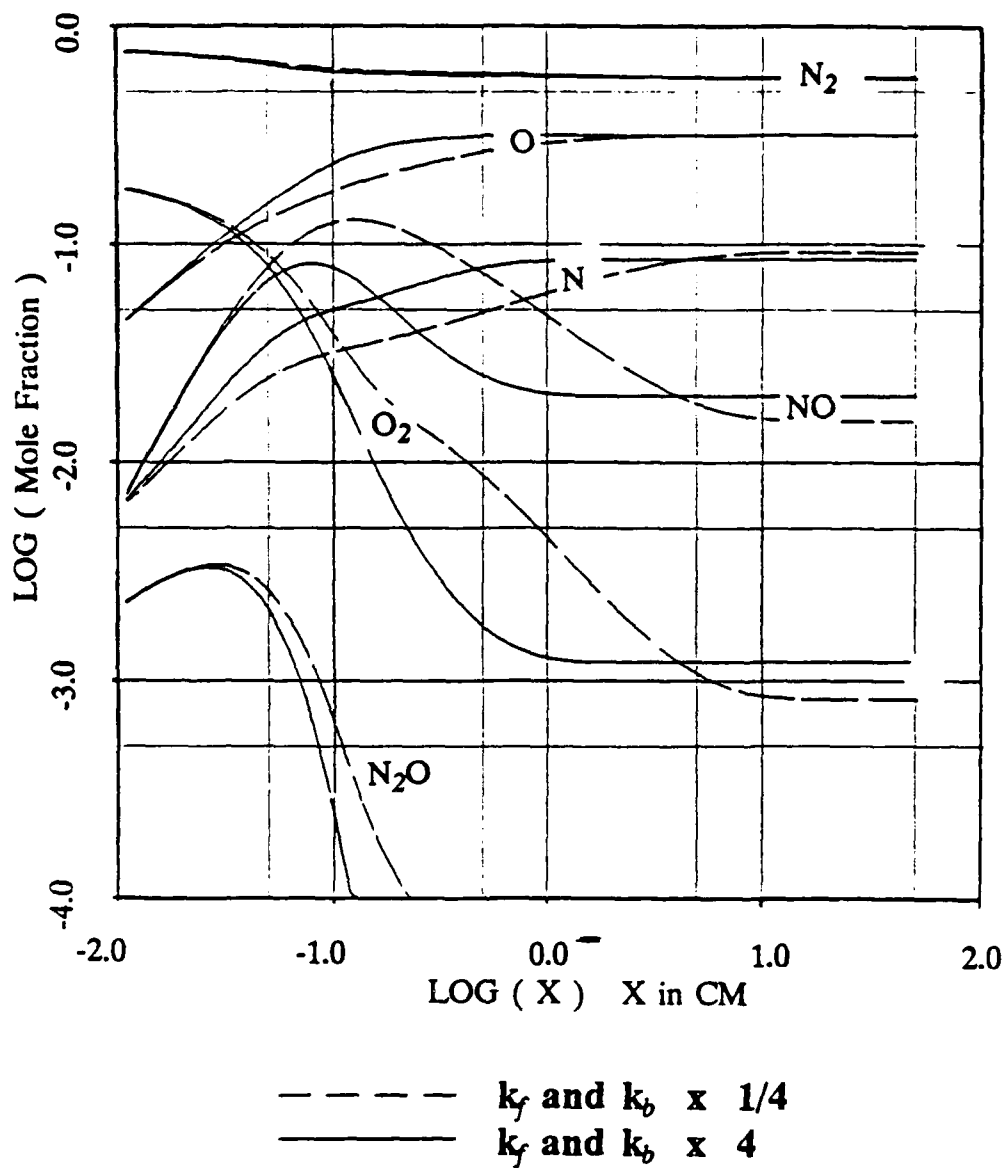
Figure 14 : Deviations in the Predicted Species Mole Fractions due to
a factor of 4 uncertainty in the Rate Data of
NO + M ↔ N + O + M for a Mach 14 Normal Shock.
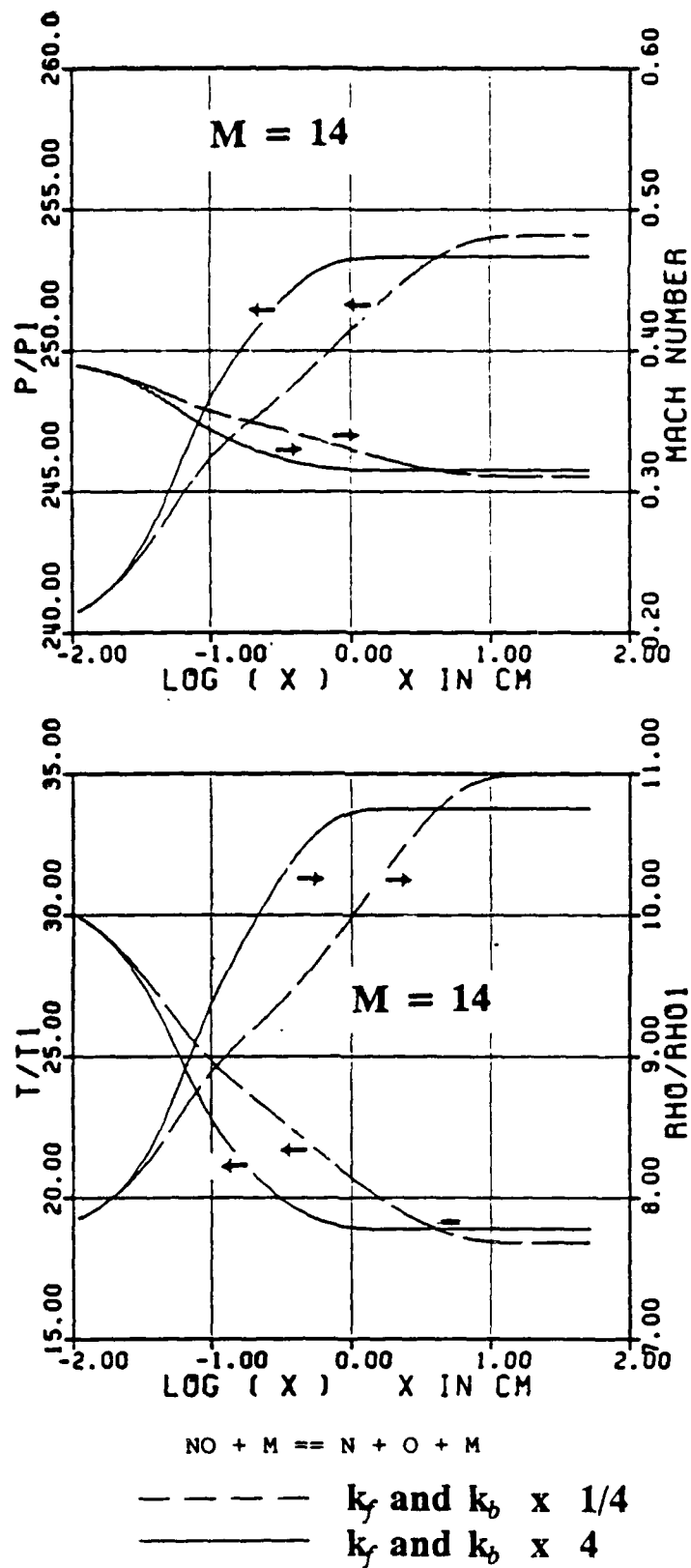
Figure 15 : Effects of the Uncertainty in the Rate Constant of
NO + M → N + O + M on the Flow Properties at M = 14.

Development of a Microcomputer

Lateral Resupply Simulation System

Sponsored by the

AIR FORCE OFFICE OF SCIENTIFIC RESEARCH

Conducted by the

Universal Energy Systems, Inc.

FINAL REPORT

Prepared by: Howard J. Weiss

Academic Rank: Professor

Department and   Department of Management

   University   Temple University

Research Location: USAF/AFLC/XRSA
                    Wright-Patterson AFB
                    WPAFB, Ohio 45433

USAF Researcher: Michael Niklas

Date: 30 Sept 1988

Contract No: F49620-85-C-0013/SB5851-0360

A Microcomputer Lateral Resupply Simulation System

by

Howard J. Weiss

ABSTRACT

A simulation model of lateral resupply of spare parts in a multi-echelon inventory system was developed in order to answer two major questions. What is the effect of any resupply policy on backorders at the bases? What is the optimal lateral resupply policy? Emphasis was placed on the latter question.

ACKNOWLEDGMENTS

I wish to thank the Air Force Logistics Command (AFLC), the Air Force Systems Command and the Air Force Office of Scientific Research for sponsorship of this research. I also wish to thank Universal Energy Systems for their concern and help to me in all administrative and directional aspects of this program.

Within the Directorate of Management Sciences (XRS) at the AFLC there are several people whom I would like to thank. The XRS administrators ,Vic Presutti, Mary Oaks and Curt Neumann were extremely cooperative in making certain that I had all of the information which I needed. Mike Niklas was instrumental in helping me with the development of the model.

I. INTRODUCTION:

The Directorate of Management Sciences (XRS) of the Air Force Logistics Command (AFLC) conducts research on various issues in logistics. In general, XRS relates logistics decisions to peacetime readiness and wartime sustainability. One area in which XRS has become expert is in using, modifying and developing methods and models which are useful for recoverable items. These are items which are repaired rather than discarded upon failure. A major focus of the Assessment Applications Division (XRSA) is on the determination of the capability of the Air Force to fly its planned missions as a function of the spare (recoverable) parts and the repair policies used for spare recoverables. A major tool which is used to provide this assessment is AFLC's Weapons Systems Management Information Systems (WSMIS) and a major component of WSMIS is dyna-METRIC. (dynamic multi-echelon technique for recoverable item control, see Hillestad(1982) and Pyles(1984)).

My expertise is in management science/operations research. In particular I have done a great deal of research on inventory systems, queuing systems and scheduling systems. The recoverable item inventories are a hybrid of inventory, queuing and scheduling systems in that spares (the inventory portion of the hybrid) are provided and failed parts are queued or scheduled for repair (rather than being discarded). Thus,

there is a good fit between my inventory/queueing/scheduling expertise and the problems, methods and models of XRS, in particular, with respect to recoverable items.

II. OBJECTIVES OF THE RESEARCH EFFORT:

The particular problem that I have worked on is the problem of lateral resupply among bases. For the most part, the current models (dyna-METRIC and WSMIS) do not assume that it is possible for bases to supply each other with spare parts. In the current models all spares move up or down the echelons from base to depot and from depot to base. In reality, parts do move within an echelon and this leads to two different problems. The first problem is to determine the best way to move these parts (i.e. determine the optimal lateral resupply policy) and the second problem is to assess the effect of any lateral resupply policy on mission capability. Slay (1986) has worked in the latter area but other than for this paper there has been very little research in the area of lateral resupply. My main concern is with the former problem.

III. MULTI ECHELON INVENTORY SYSTEMS:

One general concern at XRSA is with multi-echelon inventory systems. The major system used to model the multi-echelon inventory systems is WSMIS. Items arrive at the bases in need of repair. If the base has spare items it will provide these items to the customer. If the base has no spares then

the customer waits for either a resupply from the depot or a repair at the base. In either case the item itself is placed in repair either at the base or the depot. While this is the representation of the inventory system as expressed in WSMIS this representation does not allow for the movement of spares within a single echelon in the inventory system. That is, WSMIS does not allow for the movement of spares from base to base or for that matter from depot to depot. This movement can occur and it is precisely this intra-echelon movement of spare parts which has been the focus of my summer research.

The system which needs to be considered is one as follows. Items can move up and down echelons (by moving between the bases and the depot as modelled by WSMIS) and in addition items can move within the same echelon (by moving between bases.) The analysis which is necessary is two-fold. One area of research is to find the optimal policy for the lateral resupply of parts. The second area is to perform the analysis in a fashion similar to Dyna-METRIC. That is, given a set of rules which govern the lateral resupply find the impact on readiness and sustainability of various lateral resupply policies. The latter has been performed to some extent by Slay (1986). My concern is primarily with the former - finding the optimal lateral resupply policy.

IV. THE GENERAL DESCRIPTION OF LATERAL RESUPPLY:

In this section we describe the lateral resupply in operations research terms. The lateral resupply optimization problem is a dynamic program. Unfortunately, as we will discuss shortly the state space for this dynamic program is much too large to yield any useful results. Therefore ultimately, to provide useful rules I have written a simulation which will model lateral resupply.

We make the following definitions:

M = the number of bases

T = the length of time of interest (in days)

$S(i,t)$ = the serviceable stock at base $i = 1,2,\ldots,M$ on day $t=1,2,\ldots,T$.

$X(i,j)$ = the mean length of time to transport the parts from base $i =1,2,\ldots,M$ to base $j \neq i$. As a general rule this length of time is deterministic. It takes 1 day to ship parts from an onshore base to an onshore base or from an offshore base to an offshore base and 3 days to ship parts from an onshore base to an offshore base.

r = mean repair time.

$D(i,t)$ = the number of items due in at base i on day t. These items consist of those which will be repaired as well as those which are arriving due to a lateral resupply from some other base.

The decision which needs to be made on any given day t is denoted by a matrix $d(i,j)$ where $d(i,j)$ is the number of

units shipped from base i to base j . We now can describe the state space for the decision model. On any day t the state is described as

state=(S(i,t),i=1,2,...,M;D(i,z),i=1,2,...,M:z=t+1,t+2,...,T)

That is, the information which is relevant to decision making is the number of units in stock at each base and the number of units that are going to return to the base from the pipeline in future days. This is an unwieldy state space for even the smallest problems. Considering the size of the state space it seems very unlikely that an approach such as dynamic programming can ever find the solution. The problem would have to be very small for DP to work. This leads to two possibilities. One possibility is to simulate the system. The second possibility is to collapse the state space. This second option has been used in perishable inventory where 21 separate days worth of information are collapsed into their sum. (see Nahmias(1975)). The collapsing approach seems unreasonable for the problem of lateral resupply because the structure of the pipeline is critical in determining whether or not items should be shipped from one base to another. We think that by collapsing the state space the distinctions between near and far pipeline items will be lost and ineffective policies will be developed. Even if this is not the case the state space would still be rather large for the size of problem that must ultimately be considered. Therefore we opted for the simulation system.

V. DESCRIPTION

Because an analysis or optimization technique is infeasible it is necessary to use a simulation to determine the effects of policy changes in lateral resupply on backorders. Simulation will not yield the optimal lateral resupply policy but a properly written and properly used simulation should lead us in the direction of the optimal policy.

The first question was whether the simulation should be designed for a micro computer or a main frame. Because the goal of the simulation is to test various lateral resupply operating rules the simulation must be convenient to use and user friendly. This is most easily accomplished if the simulation is written for a micro computer. One concern which we had with using a micro computer was that a simulation program would take too much (real) time. However, this has not been the case and real time has not posed a problem. One problem that arises is the fact that the number of variables is more limited on a micro-computer than on a main-frame. However, keeping in mind that the objective of the simulation is to play with the policies in order to determine useful rules, all runs have been kept relatively small anyway and this was not an issue. (We do feel that after the policies are developed they should be tested on a large scale and this is discussed at the end of this section.)

The simulation system consists of three major portions. The

first part is an editing system which allows quick and easy editing of both the data and the lateral resupply rules which are used as input to the simulation. The second part is the actual simulation itself while the third part is a procedure for taking the output from the simulation and turning the output into useful reports.

The specific data which must be input to the simulation are in accompanying documention and user's guide.

The difficult part of the simulation was setting up the data base and simulation program to handle a wide variety of rules. The rules were organized in order that bases which need units will be given some priority measure and that bases that have excess units will be given some measure. The two are obviously related since the closer that bases are to one another the more likely it is that a lateral resupply will be useful. This is the part of the simulation which required the greatest thought in order to make the simulation useful.

The output reports are described in the accompanying documentation and user's guide.

The long term lateral resupply simulation system which we envision is as follows. Two versions should exist as it should be possible to perform quick experiments on a micro-computer and large experiments on a mainframe computer. There

should be a linking between the data sets so that any data set can be used on either type of computer. This linking is easy to achieve with the use of modems. Similarly output reports from either system should be capable of being produced by either a main frame or microcomputer. Again, this is easy to accomplish with the help of a modem. In addition we envision a linking of WSMIS runs and the lateral resupply simulations. It is possible that WSMIS runs will generate the problem parts which require further study for lateral resupply policies. One additional advantage of having the system on two types of machines is that the accuracy of the results can be checked by running the same data on two different machines.

REFERENCES

Hillestad, R.J., Dyna-METRIC: Dynamic Multi-Echelon Technique for Recoverable Item Control, The Rand Corporation,R-2785-AF,July 1982

Nahmias,S., Optimal Ordering Policies for Perishable Inventory - II, Operations Research, Vol. 23, No. 4, 1975, pp 735-749

Pyles, R., The Dyna-METRIC Readiness Assessment Model: Motivation, Capabilities and Use, The Rand Corporation, R-2886-AF, July 1984

Slay, F.M., Lateral Resupply in a Multi-Echelon Inventory System, Logistics Management Institute, AF 501-2, April 1986

1987-88 RESEARCH INITIATION PROGRAM

Sponsored by the

AIR FORCE OFFICE OF SCIENTIFIC RESEARCH

Conducted by the

Universal Energy Systems, Inc.

FINAL REPORT

Development of Expert System Control
of a Carbon Fiber Production Process

Prepared by:	Bruce A. DeVantier, Principal Investigator
Academic Rank:	Assistant Professor
Department and	Civil Engineering and Mechanics
University:	Southern Illinois University at Carbondale
Location:	Carbondale, Illinois
Date:	January 26, 1989
Contract No.:	F49620-85-C-0013-0360
Purchase Order:	S-760-7MG-027

Acknowledgements

I would like to acknowledge the assistance of Dr. Phillip Wapner of the Department of Mechanical Engineering at Southern Illinois University. The use of his original equipment which was modified in the process of completing this work was key to the work, and his technical suggestions were also very valuable. Assistance with software use and development was provided by Dr. William Lee and Frances Abrams, and it is greatly appreciated.

Development of Expert System Control

of a Carbon Fiber Production Process

by

Bruce A. DeVantier

ABSTRACT

A project to develop hardware and software necessary to control a carbon fiber spinning system using expert system control was completed. The equipment necessary to convert the process to computer control was acquired and tested in the fiber spinning system. Additional software necessary to control the new equipment was developed and tested. Limited scale testing of fiber spinning was accomplished, and additional equipment needs were identified.

I. INTRODUCTION

The development of a microcomputer based system for control of carbon fiber spinning from pitches is of great use, because it allows spinning of a wider variety of carbon fibers, and at the same time allows for the natural variability of pitch feedstocks. Conventional analog control of the process provides less than optimal control of the process and can not easily respond to variability in feedstock. The major effort in this project was in the construction and testing of control units and sensors which were connected to a microcomputer. Thus, a great deal of this report will deal with equipment selection, construction, calibration, and troubleshooting.

II. OBJECTIVES OF THE RESEARCH EFFORT

The objectives of the project included the construction and testing of an the hardware, as well as the development of software, for the expert system control of carbon fiber spinning. The hardware chosen was to be computer controllable, and any necessary interface hardware and software was to be produced. The original fiber spinning equipment did not have the capability of computer interfacing, so selection of equipment for this purpose was important to the project. In evaluating the suitability of the selected equipment, one of the objectives of the project was determination of the interdependence of the control parameters, and their effects upon the quality of the spun fibers. Fiber spinning runs were to be made, and the suitability of the control devices and mechanical equipment selected were to be evaluated.

III. HARDWARE SELECTION AND DEVELOPMENT

The first phase of the project was the selection of hardware necessary to convert existing fiber spinning equipment to allow computer control, and also

the acquisition of the computer control equipment. The computer equipment chosen was a system similar to that used in the development of the Air Force QPA system (Leclair et al., 1987). The main microcomputer computer components are IBM AT compatible computer, a Data Translation 2805 A/D-D/A board, an Omega 2010 temperature controller, and a Mototrolla 68000 coprocessor board. Recent modifications to the QPA expert system shell have allowed the use of a single 68000 board, and with some simple modifications to the code, one board has appeared to be adequate at present. A second 68000 board has been acquired should the single board system prove inadequate in the future.

A schematic diagram of the spinning system modified for computer control is shown in Figure 1 (see Appendix I). The system was modified to accommodate a screw feed and a motor driven pump drive. This allows direct control of feed rate and makes the system essentially a continuous operation. This type of spinning (known as screw melt spinning) requires that the feed pitch be preprocessed to bring it to mesophase, and then cooled and ground to allow dry feeding in the screw feed. The motors which drive the screw feed and melt pump are of the same size and were chosen to provide motor speed on the order of 10 rpm. Bodine motors were chosen, because manufacturer's specifications indicated that both motor speed and torque could be controlled or sensed. The original intent was that the motor speed be controlled and the torque be sensed. It was found however that the torque could not be sensed when speed was controlled, because the speed control degraded the torque signal. Thus the motors required either speed or torque control, but the two modes could not be run simultaneously. A third motor of higher speed rating is connected to the wind up drum. Speed control is important for the wind up, however the tension in draw line is controlled by the torque supplied by the motor. Speed control was chosen, since the same mechanisms of control could be used as for

the other motors, and because speed control can be successful as long as process conditions do not change rapidly.

With the loss of torque measurement ability, the system could not be equipped to sense any measure of the pitch viscosity at the melt-spin stage. Examination of the possibility of in-line viscosity determination with orifice or Poiseulle tube devices led to the conclusion that they could not readily be implemented without seriously reducing the quality of the product as well as control of the process.

Bodine motor controllers were chosen for all of the motors. These controllers are PID based, and are matched to the motors to provide smooth, accurate control. Motor control commands are sent through the DT 2805 board as digital signals. A digital routing network was designed and constructed to allow the available 16 bits of digital output from the DT 2805 to control all three motors with sequential signals. A schematic diagram of the routing network is given in Figure 2. Ten of the sixteen bits of a digital write are used to set the fraction of total output (zero to 1023, with 1023 as full output). The other six bits are used to signal a speed change and to choose the device to be controlled.

The motors were calibrated to relate the speed to the ten bit control signal sent by the routing network. Figures 3 and 4 show the curves for motors A and B which are used by the screw feed and pump. Figure 5 shows both curves plotted on the same graph, and it appears that they respond according to the same curve. When the variation of the combined curves is calculated and compared to a fourth order polynomial fit to the data, the control is found to be accurate to 0.5% as compared to 0.1% suggested by the 10 bit control. Some of the variation can, however be attributed to inaccuracy in the measuring the speed at the low rates of these motors. The speeds could

not be measured by tachometer, because the speeds were on the order of one to ten rpm. The calibration curve of the higher speed windup motor is shown in Figure 6. The apparent jump in the curve at the lower speed is due to switching from manual rotation measurement to tachometer. It is not likely that the motor will run for significant times at these low speeds anyway. It is important to note that all of the motors have a low end clipping of input, so that the lowest few per cent of speed control is not available. This should not cause significant problems.

The other controlled device is a heater in the melt chamber between the screw feed and the pump. The heater is controlled by an Omega CN2010 temperature controller. The CN2010 is equipped with an RS232 interface and an internal microprocessor to direct sensing and control through the serial port as ASCII code signal sequences. Temperature is controlled to the nearest degree over a range of 60 to 500 Celsius.

Pictures of the hardware of the spinning system are shown in Figures 7-10. Figure 7 shows the spin-melt and hot box portions of the top of the apparatus, and Figure 8 shows the bottom half of the hot box and the windup drum with its motor. Figure 9 includes the component parts of the spinneret, and Figure 9 shows the digital routing network (gray box) and motors connected to computers. The controllers are the partially obscured black boxes to the left of the motors.

IV. SOFTWARE DEVELOPMENT

Since the QPA system is written in FORTH language, new control words for the new devices were written in FORTH. All of the changes needed for these control words were made in the source file originally called AUT.SRC. The source file was renamed to DEVICES.SRC, because an autoclave was no longer the

control device. Some words remain from the original source code, and the new code has been documented to aid in understanding of the logic used. The protocol used for the control words used to control the CN 2010 is determined by its internal processor, and so the manual for its operation was used to determine the proper ASCII sequences for reading temperature and writing set points. The protocol for the words sent to the digital routing network for the motors is arbitrary, although it is determined to some degree by the D/A chips used to convert the digital signal to a form acceptable by the controllers.

All of the original FORTH words used to direct the DT 2805 D/A-A/D board in the original QPA implementation for autoclave curing of composites also appear in DEVICES.SRC. Several new words have been added to utilize the digital write capability of the board in the control of the motors. Since testing thus far has only utilized manual control, the words necessary for this control have also been included.

The project did not progress to the point where an expert system rule base could be constructed. Manual control runs were performed using the constructed system, and ongoing work beyond the time frame of this project is continuing toward the development of a workable knowledge base.

V. RECOMMENDATIONS

The difficulties encountered with the inability to sense and control both speed and torque control reduced the ability of the system to sense one of the key parameters of fiber spinning with mesophase pitch. It is clear that some form of viscosity measurement is necessary for successful expert system control. The most easily achievable technique which could be employed is the indirect sensing of torque on the spinning pump. Plans are being drawn to add

torque sensing devices on the shafts of the spinning and wind up motors. These will allow pitch viscosity sensing and draw tension respectively. Furthermore idler tension control is also being examined for use in conjunction with torque measurement.

At present, no in situ viscosity measurement device is commercially available for moving fluids at the temperatures experienced in this setting. Should such a device become available, it would be clearly preferable and should be installed in the system. Along the same lines, research into the development of this kind of device is recommended. Its applicability reaches into all applications dealing with mesophase pitch, one of the more obvious being in the processing of carbon-carbon materials.

It is further recommended that temperature within the hotbox be added as one of the controlled variables. This should be done, however only after many runs have been made without the control for a basis of comparison. The same CN 2010 controller could be used in this temperature control as well as the melt temperature, because the controller is equipped for control of two devices. High intensity lights could be used as heaters to avoid ignition of volatile fumes.

Finally, the expert system rule base should be constructed and tested. Work is continuing in this direction under internal funding of Materials Technology Center of Southern Illinois University at Carbondale.

VI. REFERENCES

1. Leclair, S., Abrams, F., Lee, B. and J. Park, "Qualitative Process Automation for Autoclave Curing of Composites," Wright-Patterson AFB Materials Laboratory, Interim Report, May 1987.

2. Series CN-2010 Programmable Temperature Controllers Operation Manual, Omega Engineering, Inc., 1984.

APPENDIX I. HARDWARE PHOTOGRAPHS AND RELATED GRAPHS AND FIGURES
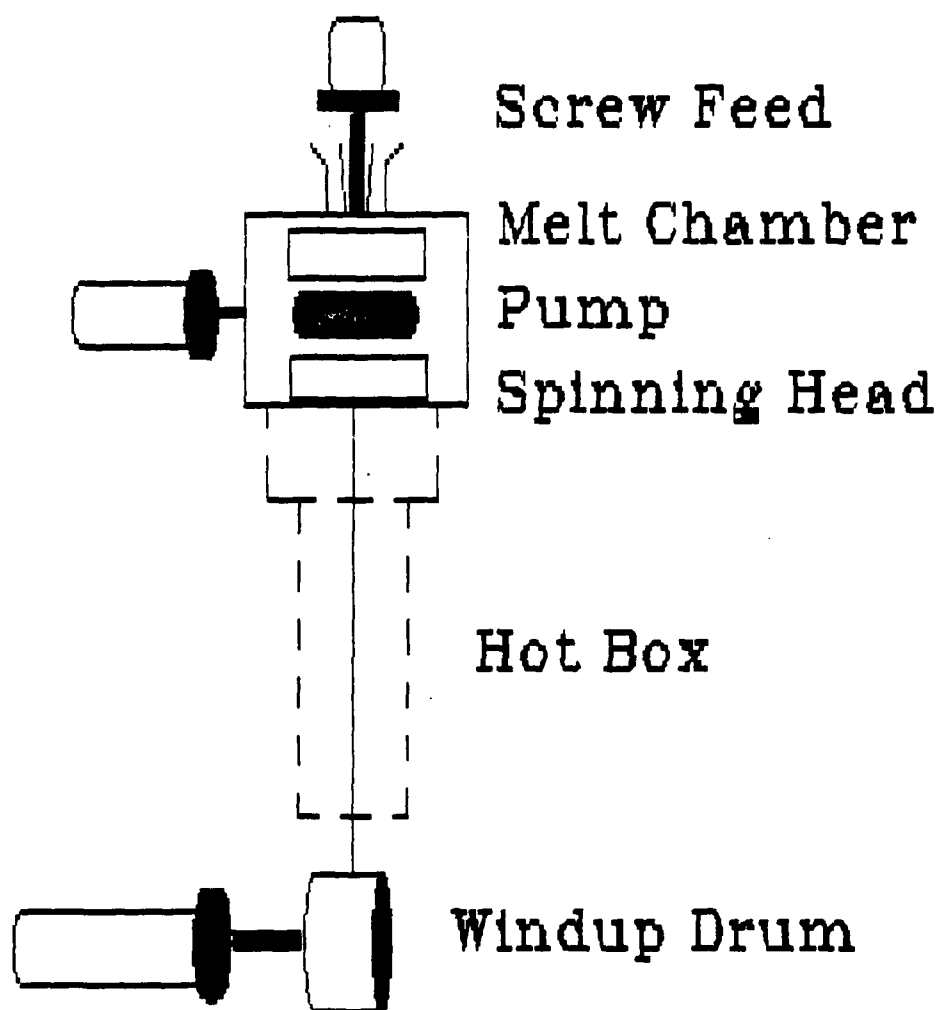
Figure 1. Schematic Diagram of Spinning System

Bits 0-9
(Output Level Control)

Bits 10-11
(Device Select)

Bits 12-14 — X
(Not Used)

Bit 15
(Write Flag)

Multi-plexer

0
1
2
3

D/A Chip

Voltage Isolator

Motor A

Motor B
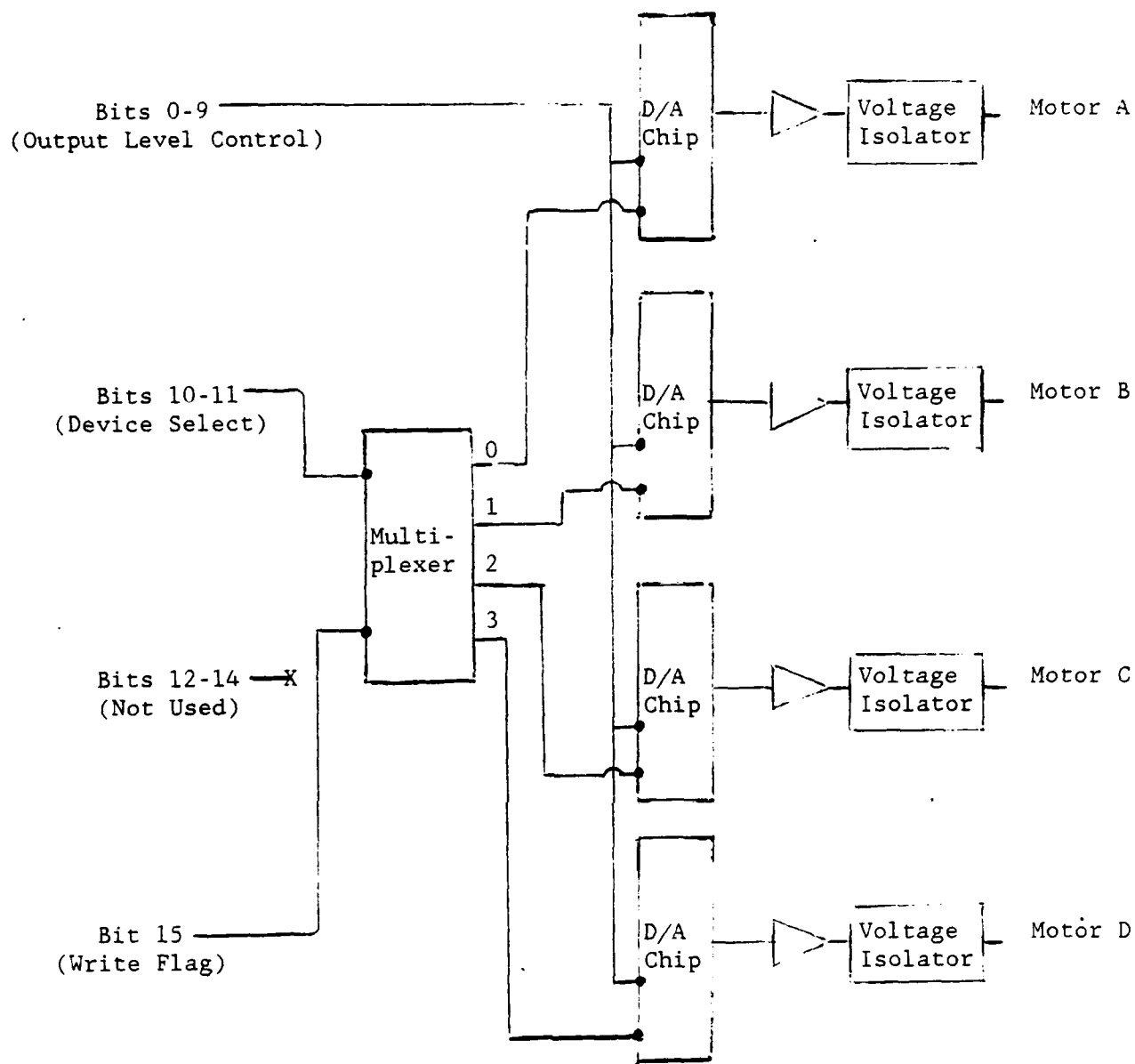
Motor C

Motor D

Figure 2. Digital Routing Network

Calibration Curve

Motor A

RPM
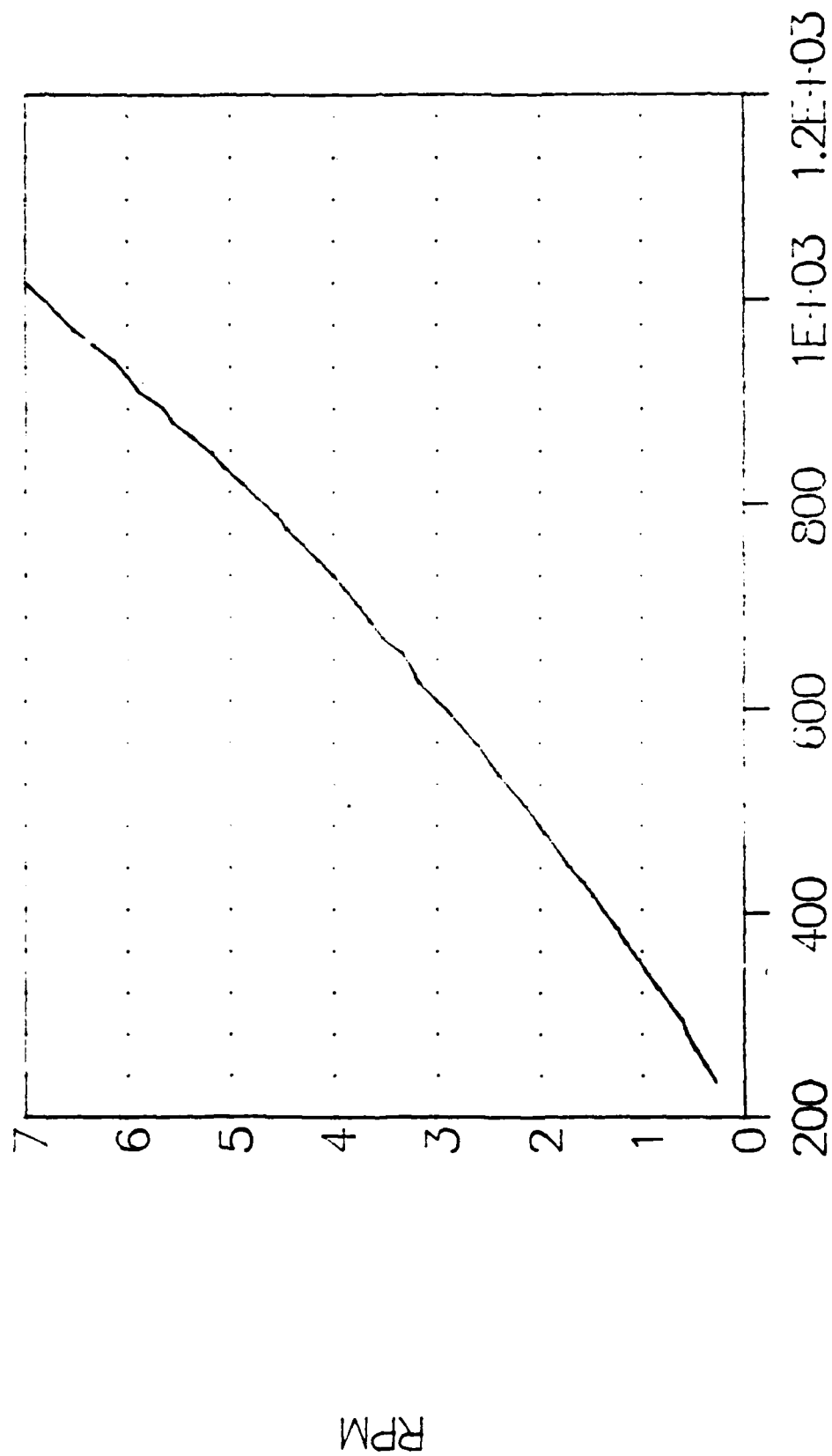
Calibration Curve

Motor B
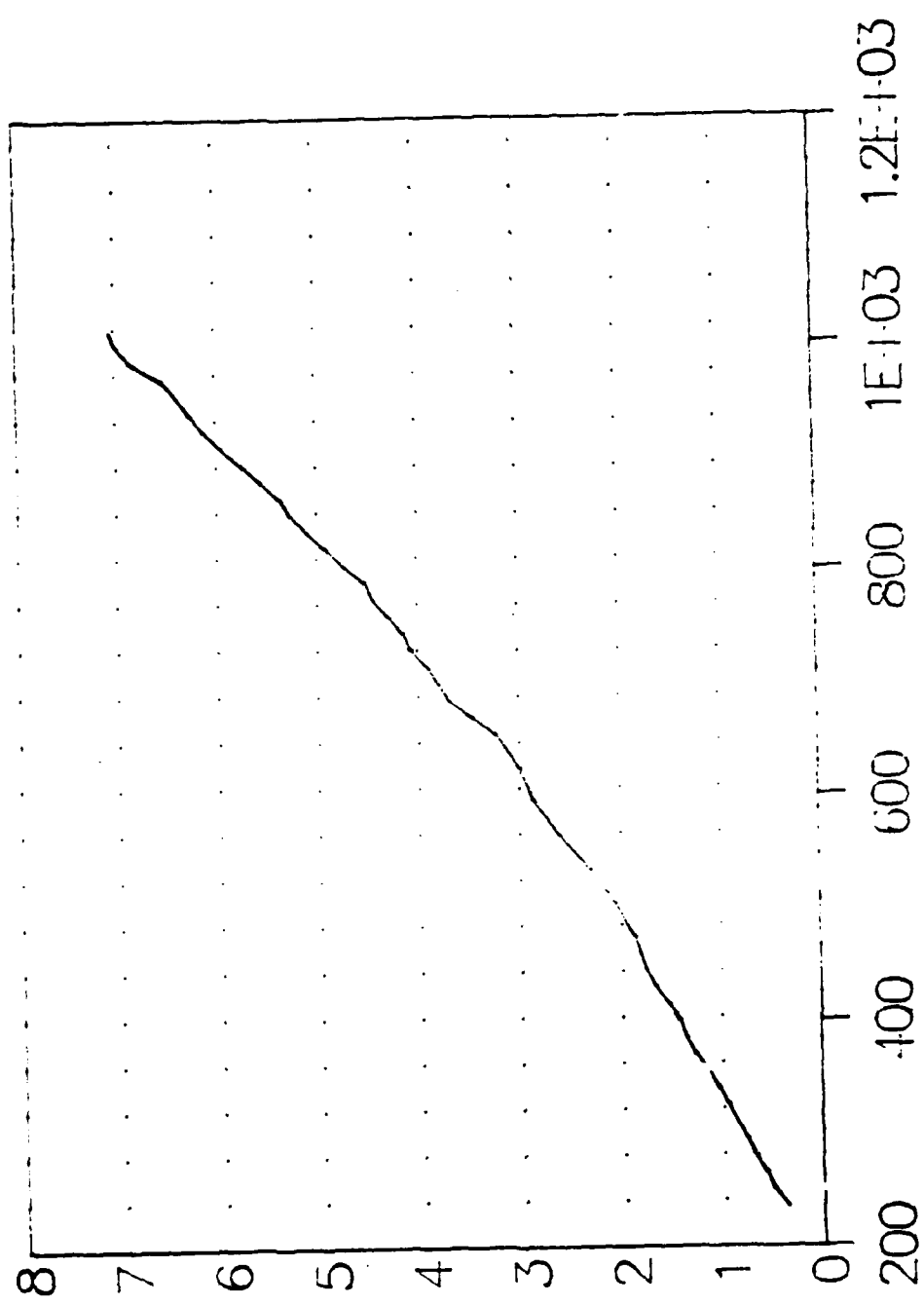
Calibration Curve

Motor A & B

RPM
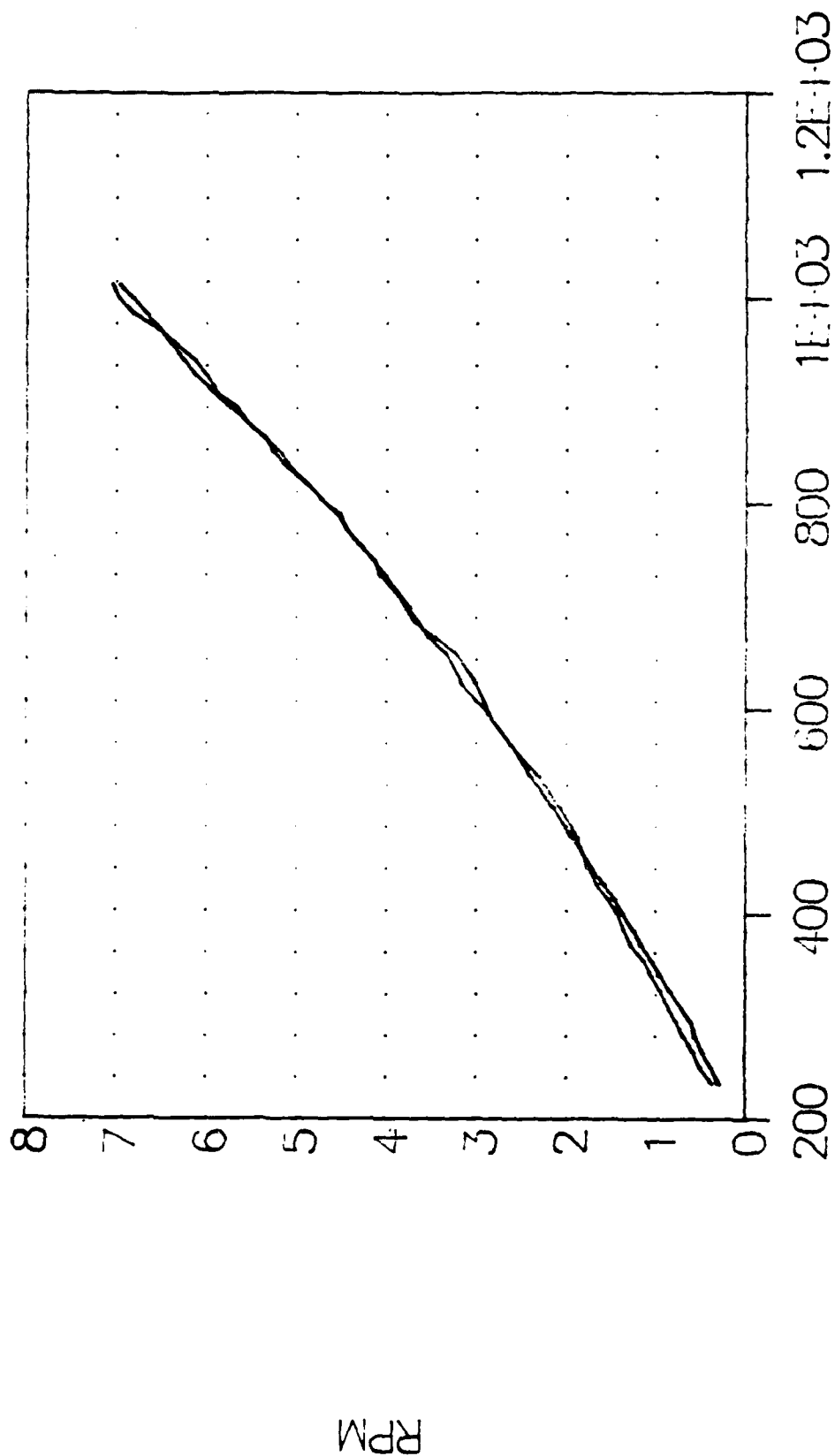
Calibration Curve

Motor C

RPM
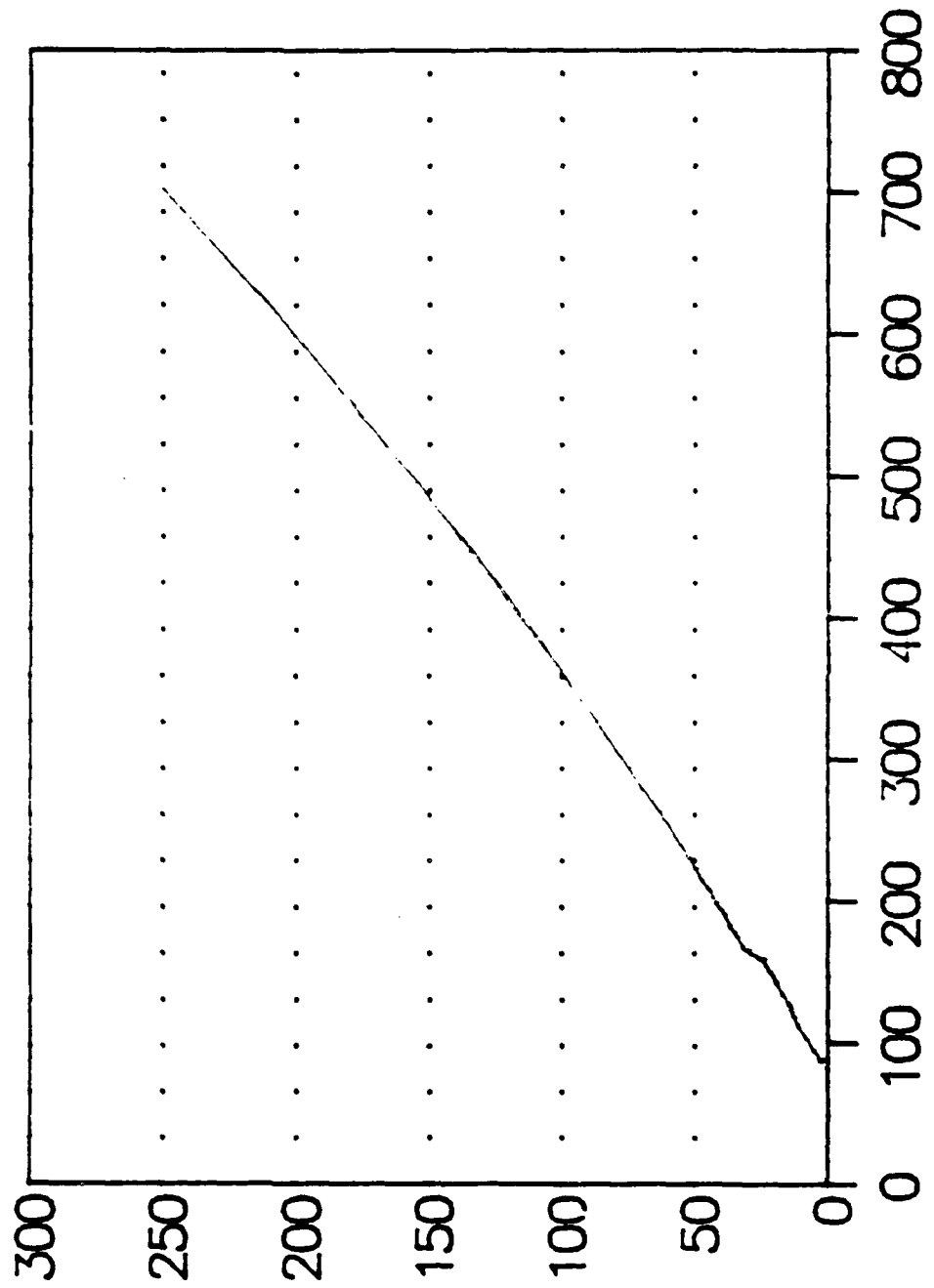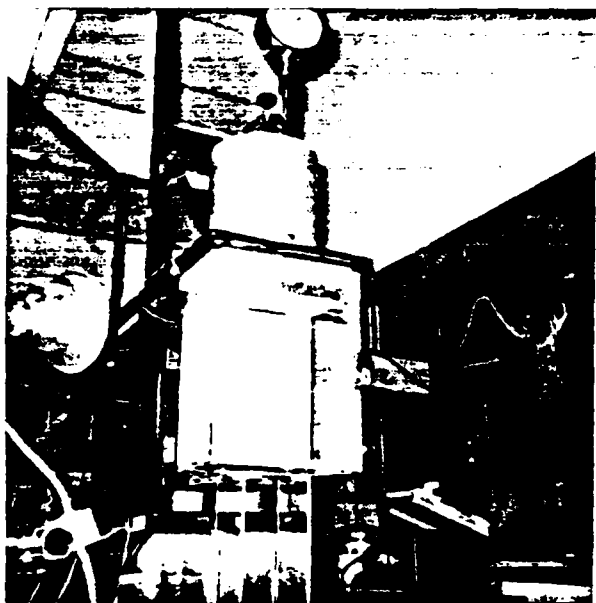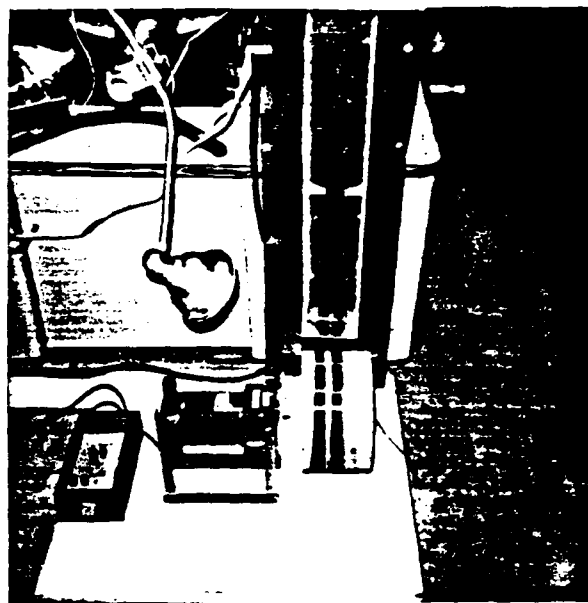
Figure 7

Figure 8

Figure 9

Figure 10

74-17
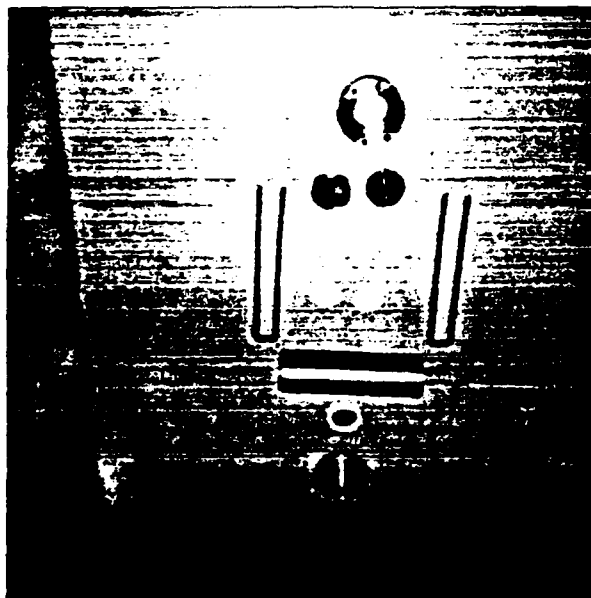
APPENDIX II.   DOCUMENTATION OF SOFTWARE DEVELOPMENT

```
>>C

create (devices)
cr .( loading DEVICES.SRC )

\
\   12-88 Modified version of AUT.SRC for fiber spinning
\

\ -------------------------------- DT2805 A/D D/A
CR .( loading DT2805 support .. )

\ DT2805 board parameters:
HEX
02EC         constant BASE.ADDR      BASE.ADDR 1+ constant DT.CMND.REG
BASE.ADDR constant DT.DATA.REG     BASE.ADDR 1+ constant DT.STAT.REG

\ DT2805 BOARD COMMAND CODE:
04 constant CMND.WAIT     02 constant WRITE.WAIT    05 constant READ.WAIT
0F constant CSTOP         01 constant CCLEAR        02 constant CERROR
03 constant CCLOCK        0D constant CSAD          0E constant CRAD
10 constant CDMA          05 constant DUMMY         05 constant CSOUT
0C constant CADIN            \ SINGLE A/D CONVERSION
08 constant CDAOUT           \ SINGLE D/A CONVERSION
07 constant CDIOOUT          \ OUTPUT DIGITAL BYTE

DECIMAL

: BINARY 2 BASE ! ;

\ DT2805 USER-SELECT PARAMETERS:
0 constant GAIN.CODE  ( GAIN IS SET TO 1 )

HEX
: CHECK.DT.STATUS ( -- TF )
  DT.STAT.REG PC@ 70 AND 0= NOT DUP
  IF   CR ." fatal error - illegal DT.STATUS register "
       CR ." DT.STATUS register value is " DT.STAT.REG PC@ .
  THEN ;
DECIMAL

: WAIT ( N -- ) BEGIN DT.STAT.REG PC@ OVER AND UNTIL DROP ;

: >DT.CMND.REG ( N -- ) CMND.WAIT WAIT   DT.CMND.REG PC! ;
: >DT.DATA.REG ( N -- )
  WRITE.WAIT WRITE.WAIT
  BEGIN SWAP >R DT.STAT.REG PC@ OVER XOR R@ AND R> -ROT UNTIL
  DROP DROP  DT.DATA.REG PC! ;

: <DT.DATA.REG ( -- N ) READ.WAIT WAIT   DT.DATA.REG PC@ ;
: <DT.STAT.REG ( -- N ) CMND.WAIT WAIT   DT.STAT.REG PC@ ;

: DTSTOP ( -- ) CSTOP DT.CMND.REG PC!   DT.DATA.REG PC@ DROP ;
: DTCLEAR ( -- )  CCLEAR >DT.CMND.REG ;
```

```
: SETFOR-DOUT ( -- ) CSOUT >DT.CMND.REG ;
: SETUP-A/D ( -- )  CADIN >DT.CMND.REG ;
: SETUP-D/A ( -- )  CDAOUT >DT.CMND.REG ;
: SETUP-DOUT ( -- ) CDIOOUT >DT.CMND.REG ;
: SEL-CHANNEL ( N -- )  >DT.DATA.REG :

: A/D-GAIN ( -- ) GAIN.CODE >DT.DATA.REG ;
: DO-A/D ( -- N )  <DT.DATA.REG  <DT.DATA.REG  256 * + ;
: DO-D/A ( N -- )  256 /MOD SWAP >DT.DATA.REG >DT.DATA.REG ;
: DO-DOUT ( N-- )  >DT.DATA.REG ;

HEX
VARIABLE DT.STATUS     VARIABLE ERROR1      VARIABLE ERROR2

: ?DT.ERROR ( -- TF )  <DT.STAT.REG DUP DT.STATUS ! 80 AND ;

: GET-DT-ERR ( -- )
  DTSTOP  CERROR >DT.CMND.REG
  <DT.DATA.REG ERROR1 !  <DT.DATA.REG ERROR2 ! ;

: .DT.ERROR ( -- )
  CR ." fatal DT board error" BELL BELL
  CR ." DT.STATUS register value is " DT.STATUS @ .
  GET-DT-ERR
  CR ." ERRORx register values are: "
  CR ."    byte 1 - " ERROR1 @ .
  CR ."    byte 2 - " ERROR2 @ . ;

DECIMAL

\ : ADIN ( N -- N )   \ ( CHANNEL -- 12-BIT VALUE )
\   DTSTOP DTCLEAR  SETUP-A/D  A/D-GAIN  SEL-CHANNEL
\   DO-A/D
\   ?DT.ERROR IF .DT.ERROR THEN ;

variable  ch#

: ADIN ( N -- N )   \ ( CHANNEL -- 12-BIT VALUE )
  ch# !   0   10 0 do
  DTSTOP DTCLEAR  SETUP-A/D  A/D-GAIN  ch# @ SEL-CHANNEL
  DO-A/D  ?DT.ERROR IF .DT.ERROR THEN  10 / + loop ;

: DAOUT ( N N -- )   \ ( 12-BIT VALUE, CHANNEL -- )
  DTSTOP DTCLEAR  SETUP-D/A  SEL-CHANNEL
  DO-D/A  ?DT.ERROR IF .DT.ERROR THEN ;

: DOUT ( N N -- )  \ ( 8-BIT VALUE,CHANNEL -- )
  DTSTOP DTCLEAR SETUP-DOUT SEL-CHANNEL DO-DOUT
  ?DT.ERROR IF .DT.ERROR THEN ;

: DA-OUT ( N N -- ) \ ( 16-BIT VALUE, CHANNEL -- )
  DTSTOP DTCLEAR SETUP-DOUT SEL CHANNEL DO-D/A
  ?DT.ERROR IF .DT.ERROR THEN ;
```

```
HEX

: STUFF-IT ( MOTOR-CHNL#, SPEED --- )
  03FF AND              \ mask out upper 6 bit
  SWAP                  \ get motor-chnl#
  0400 *                \ set chnl bit
  + DUP                 \ pack channel & data (16 bit)
  2 DECIMAL DA-OUT      \ write 16 bit to I/O port
  HEX -8000 OR DUP U.   \ set wr = 1
  2 DA-OUT ;

: st-go hex -8000 2 da-out ;

: TRY-IT ( MOTOR-CHNL#, SPEED --- )
  03FF AND              \ mask out upper 6 bit
  SWAP                  \ get motor-chnl#
  0400 *                \ set chnl bit
  +                     \ pack channel & data (16 bit)
  HEX -8000 AND U.      \ set wr = 1
  ;

: STUFF ( MOTOR-CHNL#, SPEED --- )
  03FF AND              \ mask out upper 6 bit
  SWAP                  \ get motor-chnl#
  0400 *                \ set chnl bit
  - DUP BINARY 16 .R    \ pack channel & data (16 bit)
  2 DECIMAL DA-OUT      \ write 16 bit to I/O port
  ;

DECIMAL

: dt-clr dtstop dtclear setfor-dout 2 sel-channel ;

\ -------------------------------------- OMEGA SUPPORT
CR .( LOADING OMEGA SUPPORT .. )

  80 constant #omegabuf
  create ^omegabuf #omegabuf 1+ allot        \ ^omegabuf has count
  ^omegabuf 1+ constant omegabuf             \ omegabuf is beginning

: clr.omegabuf ( -- )
  omegabuf #omegabuf 32 fill
  0 ^omegabuf c! ;

  defer omegaport
  defer clr.omegaport
  defer ?omegaport

: read.omega ( -- )        \ reads into omegabuf
  clr.omegabuf  begin show-time ?omegaport until
  omegabuf #omegabuf omegaport dos.read
  byte.cnt @ ^omegabuf c!
  clr.omegaport ;

  create <cr>  13 c,
  create <lf>  10 c,
  create hnd.omega  0 ,

: ?dos.write  ( buf, len, handle -- )
  ?dup if dos.write then ;
```

74-21

```
: echo.omega ( -- )
  ^omegabuf count
  2 - swap 1+ swap 2dup type     \ removing leading <lf> and ending <cr>
  hnd.omega @ ?dos.write
  <cr> 1 hnd.omega @ ?dos.write
  <lf> 1 hnd.omega @ ?dos.write ;    \ append <lf>

: TIMESTAMP ( -- )
  TIME$ 8 hnd.omega @ dos.write
  <CR> 1 hnd.omega @ ?dos.write
  <LF> 1 hnd.omega @ ?dos.write ;



\ OMEGA COMMANDS

create wpv0 ascii q string *0:WCSP/0000: q
create rpv0 ascii q string *0:RPV0: q
create  tmp.buff 50 allot

: str>omegaport  ( `adr -- )
  count 2dup - 1- 13 swap c! omegaport dos.write ;   \ append <cr>

: .RPV0 ( -- )
  rpv0 str>omegaport read.omega ;

: .WPV0 ( -- )
  wpv0 str>omegaport read.omega ;

: d/  ( d u --- a )
  SWAP OVER /MOD >R SWAP UM/MOD
  SWAP DROP R> ;

: omega-use-com1
  com1 filter.file.mode
  ['] com1 is omegaport
  ['] rsclear is clr.omegaport
  ['] rsthere? is ?omegaport ;

: omega-use-com2
  open.com2   com2 filter.file.mode
  ['] com2 is omegaport
  ['] com2clear is clr.omegaport
  ['] com2there? is ?omegaport ;

: INIT-OMEGA ( -- )
  omegaport com1 = if 0 else 1 then 1200 baud
  cr ." Omega Port is initialized to 1200 baud "
  bell clr.omegaport bell ;

  create dspbuf 40 allot

: clr.dspbuf ( -- )  dspbuf 40 32 fill ;
```

```
: >dspbuf ( -- )
  omegabuf 1+ dspbuf ^omegabuf c@ 2 - cmove ;

  defer (?dsport      defer dsport

: ?dsport ( -- tf )
  begin (?dsport until
  0 sp@ 1 dsport dos.read 11 =
  if true else 56 6 wat ." ***" false then ;

cr .( <devices, )

: (stat>dsport ( -- )
  ?dsport if d-comm  1 dsport dos.write then
  ?dsport if dspbuf 38 dsport dos.write then ;


  defer stat>dsport    ' noop is stat>dsport

: <devices ( -- )
  clr.dspbuf
  get-DT
  stat>dsport ;


: init-devices ( -- )
  cr cr ." checking DT2805"
  check.dt.status if abort" run aborted " then
  cr ." DT2805 OK"
  init-omega;

: nodata>dsport ( n -- )
  drop ;

: create.omega.file ( -- )
  cr ." create omega data storage file "
  ['] hnd.omega is file.handle
  create.a.file ;

: close.omega.file
  hnd.omega @ dos.close.file ;

: open-files
  create.data.file    create.omega.file
  ['] (record-data is record-data ;

: close-files
  close.data.file  close.omega.file  ;

: do-cleanup
  reset-controllers
  close-files ;
```

```forth
\
\  Omega 2010 Temperature Controller words
\

create temp 5 allot
5 temp c!

: display-temp                      \ display the temp received in number
  5 0 do temp i + c@ emit loop ;

: show-temp                         \ show the temp received in ASCII no.
  5 0 do temp i + c@ . loop ;

: use-devices ( -- )
  ['] (wait-for-clock is wait-for-clock
  ['] open-files is prep-data-files
  ['] do-cleanup is tidy-up
  ['] (init-setpoints is init-setpoints
  ['] <devices  is <monitors
  ['] (do-heat-up   is do-heat-up
  ['] (do-heat-hold is do-heat-hold
  ['] (do-heat-down is do-heat-down

: DEVICES ( -- )
  USE-DEVICES
  cr  ." enter RUN to start " ;

: extract-temp                      \ extract the temp received & store under
  ^omegabuf swap + 2 + temp 1 + 4 cmove> ;

: findcolon                         \ search for separator in the input string
  ^omegabuf swap + c@ 58 = ;

: get-temp                          \
  ^omegabuf count 0 do i findcolon
   if i extract-temp leave, then loop drop ;

: string ( c -- ) word c@ 1+ allot ;


: set-temp
  temp 1 + wpv0 9 + 4 cmove> ;

: display-setpt
  wpv0 count type ;

: r-display
  .rpv0 get-temp set-temp display-setpt ;

: send-auto ( -- )
  .rpv0 get-temp set-temp
  wpv0 str>omegaport read.omega ;

: send-manual ( -- )
  cr ." Enter set point xxxx : "
  wpv0 9 + 4 expect
  wpv0 str>omegaport read.omega ;

omega-use-com1
devices
```

FINAL TECHNICAL REPORT

REF. CONTRACT # F 49620-85-C-0013/SB 5851-0360
UES PROJECT NO. 760S-760-7MG-077

INFLUENCE OF MICROSTRUCTURAL VARIATIONS ON THE THERMOMECHANICAL
PROCESSING IN DYNAMIC MATERIAL MODELING OF TITANIUM ALUMINIDES

MARCH 15, 1989

BY

RAVINDER M. DIWAN, Ph.D.
PROFESSOR
DEPARTMENT OF MECHANICAL ENGINEERING
SOUTHERN UNIVERSITY
BATON ROUGE, LOUISIANA   70813

RESEARCH PROGRAM: PROCESSING SCIENCE, HIGH TEMPERATURE
MATERIALS BRANCH, MATERIALS LABORATORY, AFWAL,
MLLM, WPAFB, OHIO

SUBMITTED TO:

UNIVERSAL ENERGY SYSTEMS
4401 DAYTON-XENIA ROAD
DAYTON, OHIO 45432

PREPARED FOR:

AFWAL/MLLM
MATERIALS LABORATORY
WRIGHT PATTERSON AFB, OHIO 45433

FOREWORD

This technical report covers the work performed under contract #F49620-85-C-0013/SB 5851-0360, UES Project # 760 S-760-7MG-077 for the Processing Science Group AFWAL/MLLM. This research was proposed and coordinated with Dr. H. L. Gegel, and thereafter with Mr. J. T. Morgan, Mr. W. T. O'hara of the Processing Science Group, and Dr. S. M. Doraivelu and Mr. C. M. Lombard of the Universal Energy Systems, Inc. This research report is for technical information and is the required final technical report to the Universal Energy Systems, Inc.

Mr. J. T. Morgan served as the technical group leader and Mr. W. T. O'hara served as the program focal point. The overall program director is Mr. Rodney C. Darrah, of the Universal Energy Systems, Inc.

The author is grateful to all associated individuals, to the U. S. Air Force, AFWAL/MLLM Materials Laboratory and the UES, Inc. for their technical collaboration and financial support in this follow-on research effort of the referenced project.

In addition to this final report, interim input and progress reports have been periodically provided on this project.

Final Report Submitted: March 15, 1989.

ABSTRACT

Titanium aluminides with strong thermodynamically stable intermetallic phases are significantly potential advanced materials for high temperature applications. The gamma based titanium aluminides of the PREP-HIP Ti-48Al-1V, isothermal compression tested for several strain rate conditions and temperatures from 1000 to 1350 C were investigated for phase behavior and transformations to include the transformation at 1285 C in the TiAl system. Material characterizations were conducted using optical metallography, DIC methods and scanning electron microscopy. Working with the Air Force and the Processing Science Group of the Materials Laboratory, WPAFB, OH, and using MIS generated processing maps, the thermomechanical processing characteristics and the structural evolutions were analyzed and evaluated. Evaluations of influence of micro-structural variations were carried out for the CAST-HIP alloy system supplied and designated as alloy B . The research focused on characterization and evaluations of microstructural mechanisms for stable material flow conditions with maximum efficiency of power dissipation through metallurgical processes in these titanium aluminide alloy systems. Detailed examination of the microstructural and mechanical behavior was carried out as a part of understanding the constitutive behavior and unique deformation mechanisms in the γ titanium aluminide alloy systems.

INFLUENCE OF MICROSTRUCTURAL VARIATIONS ON THE THERMOMECHANICAL PROCESSING IN DYNAMIC MATERIAL MODELING OF TITANIUM ALUMINIDES

1.0 INTRODUCTION

The influence of microstructural variations on the thermomechanical processing in dynamic material modeling of titanium aluminides has been investigated for the following materials supplied by the Air Force, UES., Inc in case of two selected titanium aluminides systems:

1. the PREP-HIP Ti-48 Al-1V material; and

2. the CAST-HIP TiAl material, designated as alloy B.

The effects of the constituent phases and the processing conditions, including several temperature and strain rate kinematic variable conditions have been investigated to understand and analyze the microstructural mechanisms, and material stability in relation to the dynamic material modeling DMM maps, using the Material Information System MIS system generated stability maps. The DMM stability maps can be converted to devise conditions of stable constitutive material flow to shorten the cycle time of the alloy development and for selection of the more efficient processing conditions related to microstructural mechanisms and supported by metallurgical constituent phase conditions.

This research work and study of microstructural variations related to the dynamic material modeling of titanium aluminides was carried on as follow-on of the summer faculty research program in which the principal investigator participated in

the Processing Science Group of the Materials Laboratory, WPAFB, MLLM, Ohio. The summer faculty research work has been on some of the microstructural developments in the specific Ti-48Al-1V γ-aluminide under constant rate, isothermal, hot deformation compression conditions. However, the test temperature conditions had analyzed the material behavior only upto 1250 C. The results of that study had indicated the need to characterize the behavior of these γ-aluminides to include higher temperature test conditions, and to analyze in particular the microstructural developments in this Ti-Al system at and above the peritectoid transformation seen at $\approx$ 1285 C in this system.

In this on-going research, the main goal has been to better understand the power partitioning processes and carryout microstructural characterizations in the proposed titanium aluminide alloy systems. To that end, complete characterization of the PREP HIP Ti-48Al-1V model material has been carried out to higher temperatures, including to 1350 C at constant strain rates from $10^{0} - 10^{-3}$ s^{-1}. Another Ti-Al base composition material, and with TiB_2 additions were not available and with no Air Force test plan could not be analyzed; however, investigations for microstructural variations and their effects on dynamic material modeling behavior in the CAST-HIP TiAl material alloy B are carried out of their stability and microstructural mechanisms. The alloy B processing test conditions are in test regime for temperatures from 1000 to 1175 C and at strain rates from $10^{-0.5}$ to $10^{-2.5}$ s^{-1}.

2.0 APPROACH TO THERMOMECHANICAL MODELING AND STUDY OF MICROSTRUCTURAL DYNAMICS

The thermomechanical processing of materials can be analyzed using a knowledge of interrelation between their processing parameters and microstructural dynamics. The theoretical basis for these analyses is based on the approach [1-5] of dynamic material modeling DMM which is a significant tool to arrive at the "safe processing windows" and for designing material deformation processes. This approach has been utilized in the present research work and as seen in some of the earlier studies [6-10] for certain aluminum based 2024-SiC alloys, nickel based alloys, Ti6Al4V, Ti-based 6242 alloys, and titanium aluminide material systems. The development of microstructures and constitutive behavior of a work piece material depends on the effects of stress, temperature, strain levels and strain rates during processing.

The development of dynamic material modeling DMM approach is based on understanding the several irreversible thermodynamic processes which occur in the work piece material and are controlled by the rate of energy input and the subsequent dissipation of energy by dynamic metallurgical processes. In dual or multiphase systems, several atomic processes are possible which combine to create new structures and provide the degrees of freedom needed for stable plastic flows. Stability is determined by the condition that the excess entropy production rate, $1/2\ \delta^2\dot{S}$, is greater than zero. Simple compression testing can be used for the dynamic material modeling if a "steady" state can be approached asymptotically with time. This DMM approach is quite useful and differs from the mechanistic approach, for in the DMM

approach the mechanisms active in a particular region are determined after the processing maps have been constructed. This thermo-mechanical DMM approach thus allows a material systems approach, in which to view a material as an energy dispersal system and to analyze its behavior macroscopically, without making a priori determinations of the operating mechanisms.

This research project involved the study of effects of high temperature flow processes in gamma based titanium aluminides as affected by γ-grains, the α_2 phases, any transformed β phase at higher temperatures, interlamellar spacings variations in microstructure, and other microstructural effects in the specified titanium aluminide material alloy systems. The conditions in this referenced research are analyzed by carrying out the following:

(a) Study of the thermomechanical modeling DMM maps at certain strain levels of the PREP-HIP Ti-48Al-1V and of the alloy B CAST-HIP Ti-Al material

(b) Analyses of the operative microstructural mechanisms in relation to the stability maps in the α_2/γ microconstituents

(c) Material microstructural characterizations of the specific PREP-HIP Ti-48Al-1V and CAST-HIP Ti-Al material

(d) Analyze and catalog any observable differences in the two specific test materials and study of selected test material specimens

(e) Analysis of limiting critical strain level concept and evaluation and formalism of any microstructural mechanisms related to material flows in the specific test material alloy systems.

3.0   ANALYSIS OF THE PREP-HIP Ti-48Al-1V MATERIAL

This research work has been carried out in collaboration with Processing Science WPAFB, MLLM, Material Laboratory and conducted at Southern University, Baton Rouge, LA. After formulation of the specific research problem, and the microstructural analyses approaches, the PREP-HIP Ti-48Al-1V material system tested up to 1350 C for strain rates from 10^{0} to 10^{-3} S^{-1} was selected for analyses of microstructural variations and dynamic material modeling behavior.

Test data analyzed in the 1000-1250C of this PREP-HIP Ti-48Al-1V has been studied for its flow curves for different strain rate conditions. This part of the study has revealed flow curves approaching steady state or some flow softening. The typical slight barelling in some specimens was seen on microscopic examination to indicate microstructurally observed cracking at end regions. These studies were further carried out to study the stress-strain behavior of the PREP-HIP Ti-48Al-1V material at 1250 C plus 1275-1350 C. This testing was carried out by the Wright State University, and test data indicated continuous gradual flow softening.

3.1 ANALYSIS OF PROCESSING MAPS

The stress strain data were analyzed using the dynamic material modeling computer program MIS to produce the processing maps which are then used to provide the framework for micro-structural analyses to control the material flow characteristics. The stable processing regions marked with X are noted, and are to be analyzed in detail at temperatures of 1250, and 1275-1350 C.

This PREP-HIP Ti-48Al-1V material has been earlier analyzed and had indicated cracking at 10^0 S^{-1} strain rate, and therefore the higher temperature compression testing to 1350 C was carried out from 10^{-1} to 10^{-3} S^{-1} strain rate conditions. The as-received starting material PREP-HIP Ti-48Al-1V had been characterized in detail for identification of composition and starting microstructure.

The overall processing maps with plot of efficiency with stability maps at 0.4 strain level indicated intability near 1275 C which could be due to the peritectoid transformation temperature of $\cong$ 1285 C as seen in the Ti-Al phase diagram.[11] The study of the titanium aluminides system, it should be noted, is made difficult due to the limitation of unconfirmed information of phase boundaries and phase stabilities,[11,12] of the titanium-aluminum system. The processing maps are analyzed and thermo-mechanical modeling carried out in our specified γ based TiAl alloy systems.

3.2 MICROSTRUCTURAL DYNAMICS AND THERMOMECHANICAL MODELING IN PREP-HIP Ti-48Al-1V

The main objectives of this research are to identify and characterize the microstructural aspects in selected titanium aluminide materials related to their DMM stability processing maps. This research has been focussed on the study of the "as-received" and "processing" microstructures to understand the microstructural evolutions during stable material flow. This involved problem formulation for the TiAl system, relevant literature review and formulation of a program to determine the microstructural constituents and their behavior in titanium aluminides.

As formulated in the proposal, the PREP-HIP Ti-48Al-1V material system tested up to 1350 C for strain rates from 10^0 to 10^{-3} S^{-1} had to be analyzed for microstructural variations and dynamic material modeling behavior. Specimens TAV64WSU, TAV65WSU, TAV63WSU, TAV73WSU, TAV79WSU, TAV76WSU, TAV78WSU and TAV77WSU for different temperature and strain rates supplied by UES, Inc. were initially evaluated for their microstructural characterizations. In later discussions with Processing Science Group, MLLM, and during visit to the WPAFB Materials Laboratory, eight additional specimens were supplied. These specimens TAV71WSU, TAV67WSU, TAV69WSU, TAV66WSU, TAV68WSU, TAV72WSU, TAV74WSU, and TAV75WSU, were also analyzed for specific evaluation of their microstructural evolutions related to the DMM maps.

A program to determine the microstructural constituents and their behavior in titanium aluminides was set up. The following determinations were made;

Optical metallography, microstructural analysis using SEM techniques, microhardness measurements.

For metallographic specimens preparation, Kroll's Reagent with composition 3ml HF, 6 ml HNO_3, 100 ml H_2O, was found to be suitable for optical microstructural analysis. Test conditions of the material specimens are given in Table I of strain rates and temperatures during their controlled compression testing.

The "as-received" PREP-HIP material on metallographic examination as the starting structure indicated a large variability in the grain size of the γ-grains which could be due to the variability and distribution in this preconsolidated PREP-alloy powder size. The microstructure also revealed regions of possible interlamellar structure, in the dual $\gamma + \alpha_2$ phase regions, fine second phase α_2 particles, and twins in the matrix γ-phase as seen in figures 1a and 1b. In this PREP-HIP alloy powder using the transmission electron microscopy,[13] a number of widely separated γ grains were also observed which contained thin α_2 lamella. Some γ grains had also consisted of a high density of dislocations, twins, and stacking faults. It should be noted that since most of the contiguous γ grains did not contain the α_2 - phase, it is believed that the high temperature flow processes will be essentially governed by a large volume of γ grains.

Table 1: <u>PREP HIP TI48AllV MATERIAL TEST CONDITIONS</u>

$\dot{\varepsilon}$ \ Temp. (^{O}C)	1250	1275	13$\emptyset\emptyset$	1325	1350
$1\emptyset^{O}$	TAV7$\emptyset$WSU	TAV71WSU	TAV67WSU	TAV72WSU	TAV79WSU
$1\emptyset^{-1}$	TAV6$\emptyset$WSU	TAV64WSU	TAV69WSU	TAV73WSU	TAV76WSU
$1\emptyset^{-2}$	TAV62WSU	TAV65WSU	TAV66WSU	TAV74WSU	TAV78WSU
$1\emptyset^{-3}$	TAV61WSU	TAV63WSU	TAV68WSU	TAV75WSU	TAV77WSU

The analysis of the stability maps and plots of efficiency with stability maps, figure 2, on dynamic material modeling at 0.4 strain level are used to investigate the stable and unstable regions of the material flow conditions. It should be noted in these that there appears to be the presence of instability at about 1275 C. Close to this and at these higher temperatures near 1275 C as related to the TiAl phase diagram, figure 3, in which, the TiAl system shows a phase transformation at $\triangleq$ 1285 C. Close to this temperature, and up to 1350 C, the system has been investigated by microstructural analyses to identify the microstructural mechanisms during thermomechanical processing of the PREP-HIP Ti-48Al-1V. Several specimens, as shown in figure 2 have been investigated.

Overall microanalysis of a typical compression tested specimen confirmed on microprobe analysis the basic TiAl γ phase composition, the overall scan and microanalysis report results are included in figure 4a and b. In some isolated locations, regions with inclusions are seen. Also in certain strain rate temperature test conditions, using the DIC microscopic methods, some bright white phase particles are seen. These microscopic studies indicate the possibility of α_2, α, and of some transformed β phase particles. Analyses of these might require some transmission thin foil electron microscopy work and are recommended.
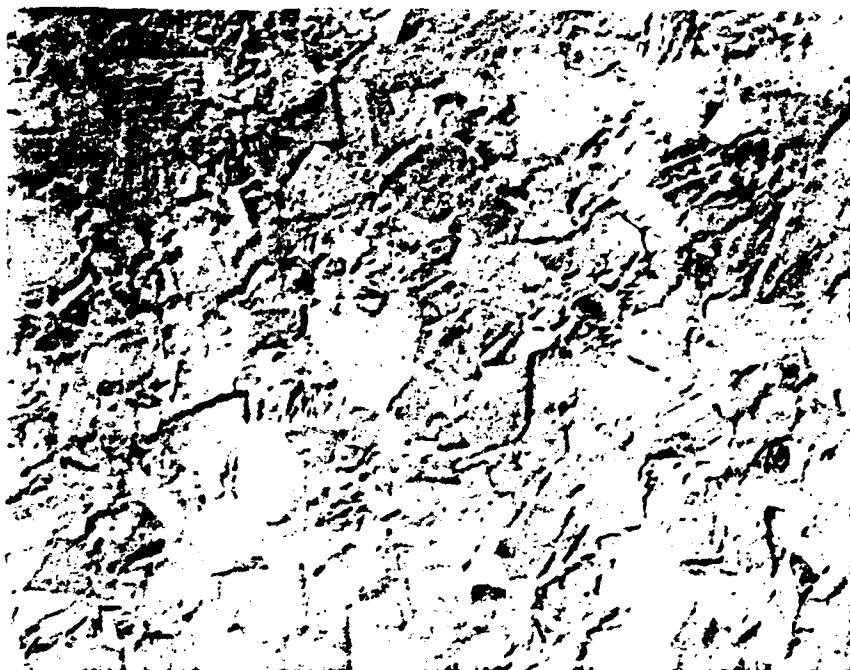
Figure 1a.   As received PREP-HIP Ti-48-Al-1V material showing regions of possible interlamellar structure, fine second phase particles, and twins in the matrix γ phase.   X400

Figure 1b.   SEM micrograph in the compositional mode of the as received PREP-HIP Ti-48-Al-1V material showing effects of stress and possible interlamellar arrangement.   X1000
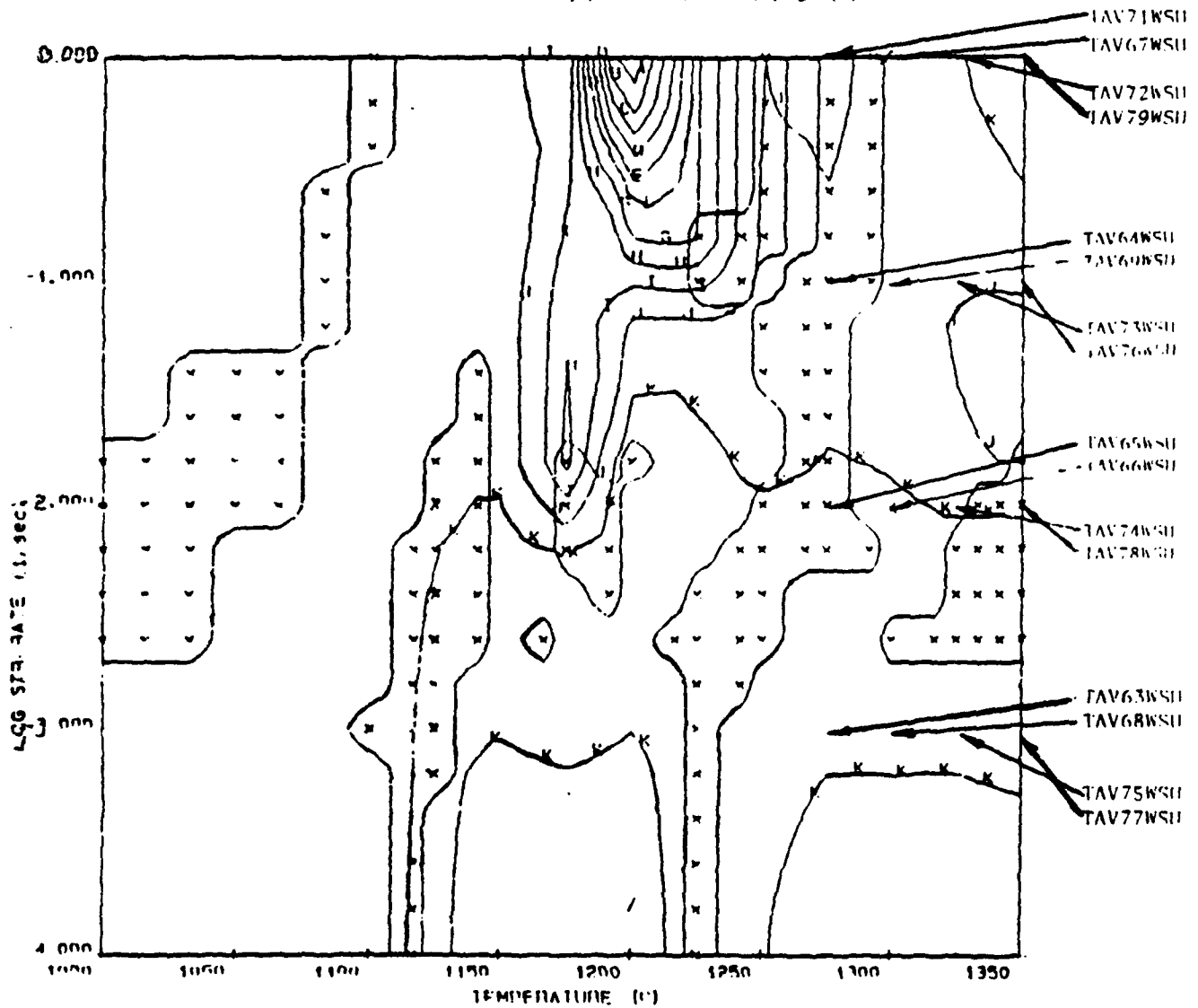
Figure 2.   Plot of efficiency with stability map of PREP-HIP
Ti-48Al-1V at Ø.4 strain.
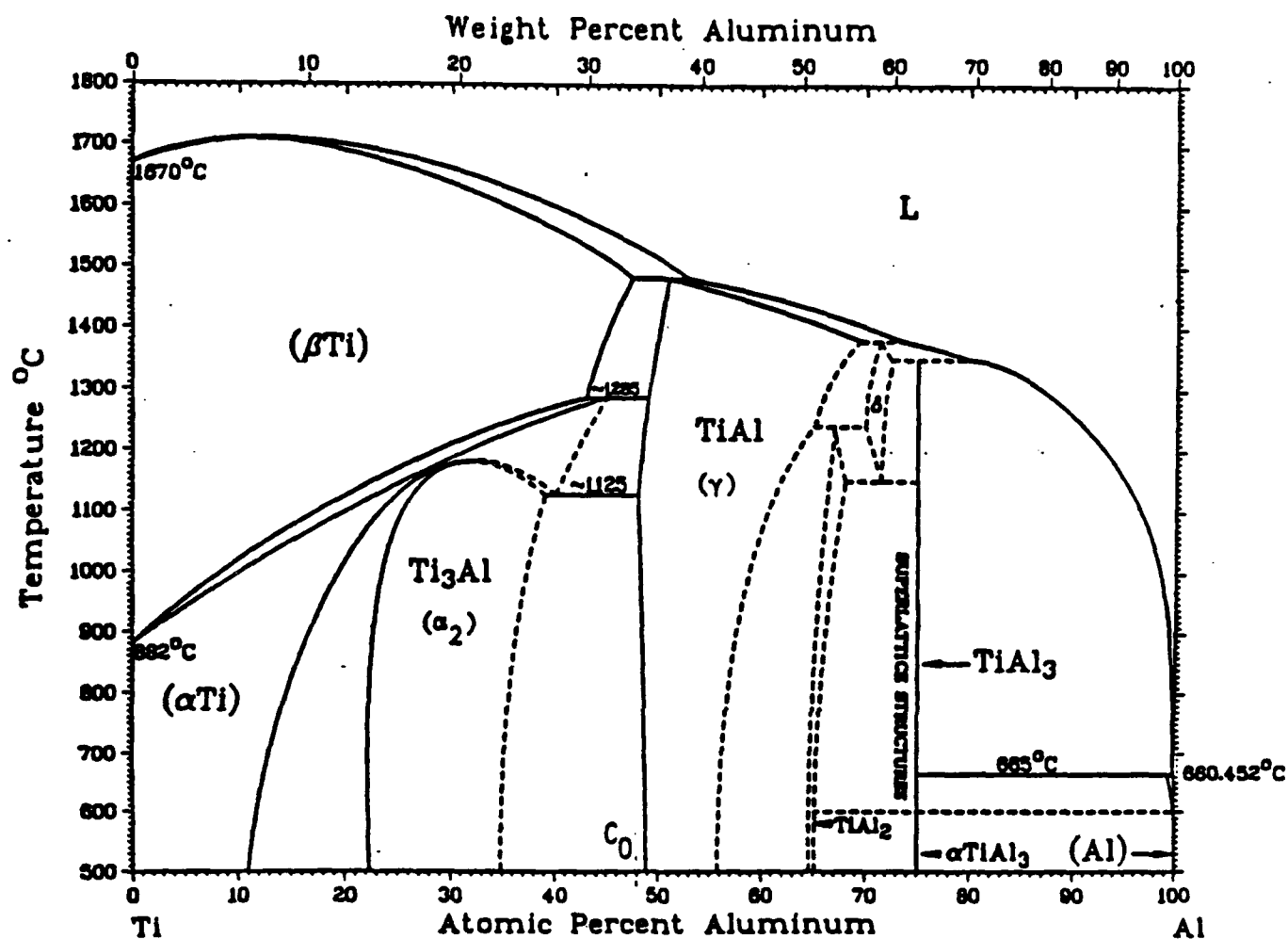
Figure 3.   Phase diagram of the Ti-Al system showing C_O, the base alloy composition with 48% Al.

```
                              EG&G ORTEC
                        ZAP MICROANALYSIS REPORT
                        VO2.14  29-JUN-89  09:51

    ID:#77

        ELEMENT      WEIGHT     ATOMIC      INTENSITY
                     PERCENT    PERCENT       (CPS)

         AL KA       29.97      43.18         356.18
         TI KA       70.03      56.82        1654.94

    ACCELERATING VOLTAGE:      25.0 KV
    SPECIMEN TILT X-AXIS:       0.0 DEGREES
                  Y-AXIS:     -25.0 DEGREES
    INCIDENCE ANGLE     :      94.63 DEGREES
    TAKEOFF ANGLE       :      35.37 DEGREES
    SAMPLE DENSITY      :       3.76 G/CC
```

Figure 4a: Microanalysis report of the TAV77WSU specimen.
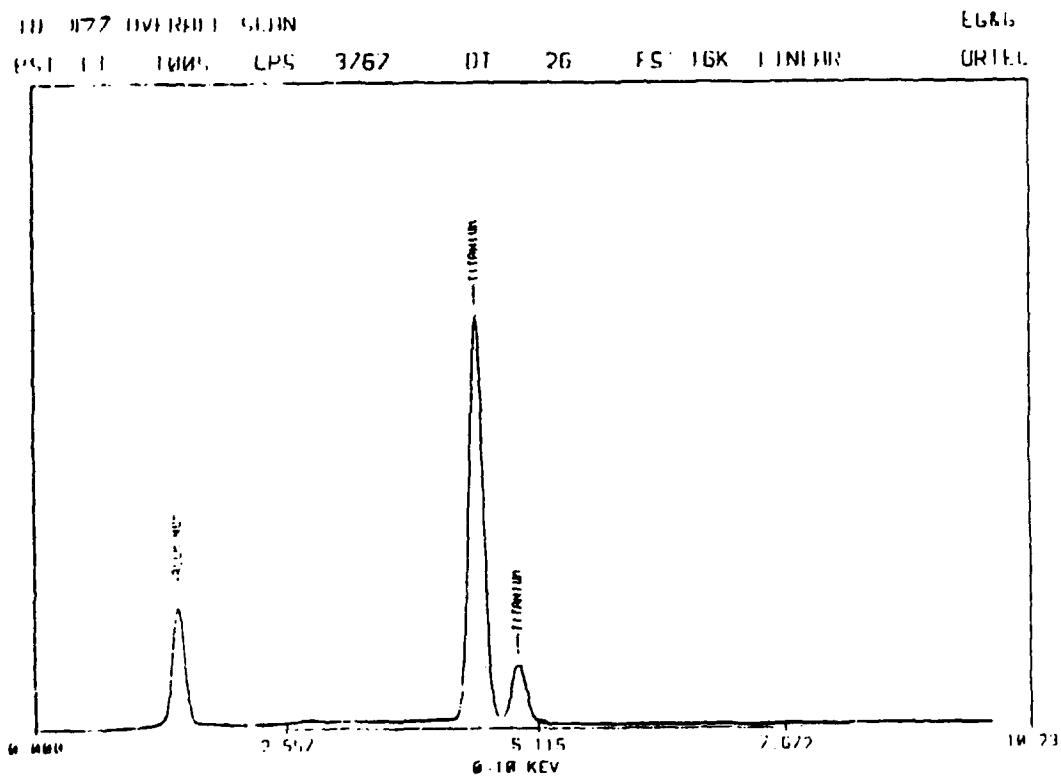
Figure 4b. Overall scan showing peaks on microprobe analysis
of Ti and Al, with corresponding microanalysis
report in Figure 4a. Specimen TAV77WSU.

Optical microscopy and SEM studies performed on the selected test specimens, at the higher temperature of 1350C at strain rates from 10^0 to 10^3 s^{-1}, have in different samples shown oxide scale on the flat ends and also presence of cracks as seen in figure 5a. This is for $\dot{\varepsilon} = 10^{-1}$ s^{-1} at 1350 C. Some cracks are seen on both sides and some inclusions are also seen. At the lower strain rate of $\dot{\varepsilon} = 10^{-2}$ s^{-1}, it appears that the possible formation of the α-2 transformed into coarse β-phase can be seen appearing in a lacy configuration. These β-phase particles seem to envelope the γ-grains at most locations. Some twinning is still seen in the interior of the γ grains as seen in figure 5b and 5c. Similar effects are also present in typical figure 5d and 5e at lower strain rate of $\dot{\varepsilon} = 10^{-3}$ s^{-1}. Interlameller features showing effects of deformation and high temperature are also seen. Partial recrystallization and dynamic strain effects can also be seen in these micrographs, as seen in figures 5f for 1325 C, 10^{-1} s^{-1} strain rate, and in figure 5g and 5h for 1325 C, 10^0 s^{-1} strain rate and 10^{-2} s^{-1} strain rate.

At the specimens close to $\cong$ 1285 C of the peritectoid transformation temperature, which for specimens at 1275 C, several strain rates form 10^0 to 10^{-3} s^{-1} were investigated, figures 6a, b, c, d, and e. Specimens tested at 1300 C, figures 6f through j, indicate very little film and cracks on flat end areas and show twinning and presence of some β phase is also seen. Nucleation of the β phase in seen at lower strain rates 1275 C, 10^{-2} and 10^{-3} s^{-1}. In some regions, presence of some blocky grains is also observed. Also seen is partial recrystallization at about 1300 C, and dynamic nucleation and growth of the β phase. Overall

microhardness values are about 24Ø-258 VHN, whereas near and inside blocky grains, the hardness values appear higher, the measurement of microhardness of the transformed β grains has been difficult due to their small size particles, figures 6i and 6j. It is also seen in certain 1300 C, 10^{-2} s^{-1} specimens that the center regions indicate fine grain structure with very little twinning, whereas the end portions show twinning and also dynamic recrystallization effects and possible transformed β grains formation, figures 6k and 6l.

Figure 5a.   1350 C, 10^{-1} s^{-1}.   X500
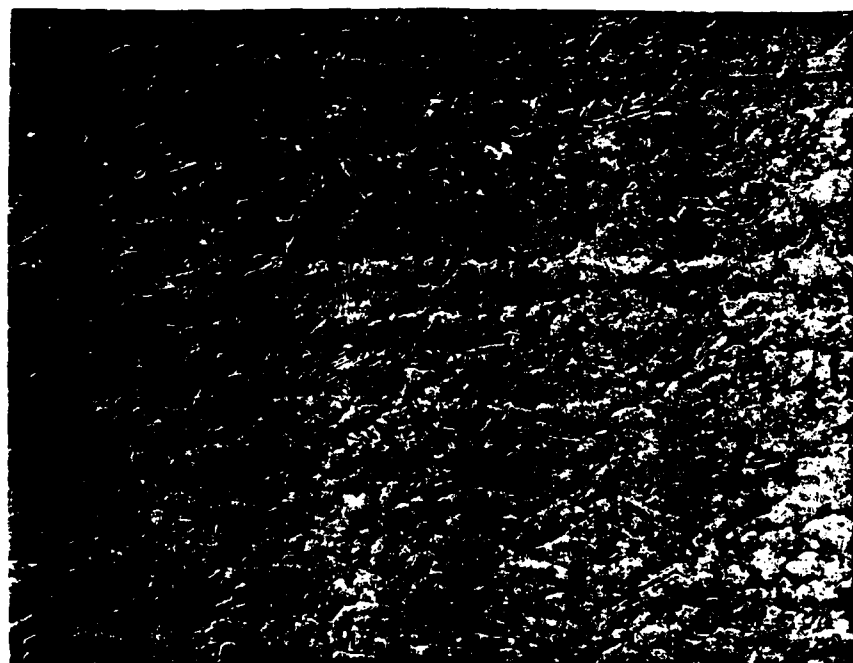
Figure 5b.   1350 C, 10^{-2} s^{-1}.   X500

Figure 5c.   1350 C, 10^{-2} s^{-1}.   X1250

Figure 5d.   1350 C, 10^{-3} s^{-1}.   X500

Figure 5e.   1350 C, 10^{-3} S^{-1}.   X200

Figure 5f.   1325 C, 10^{-1} S.   X500

Figure 5g.   1325 C, 10^0 s^{-1}.   X300

Figure 5h.   1325 C, 10^{-2}, s^{-1}.   X400

Figure 6a. 1275 C, 10^0 s^{-1}. X200
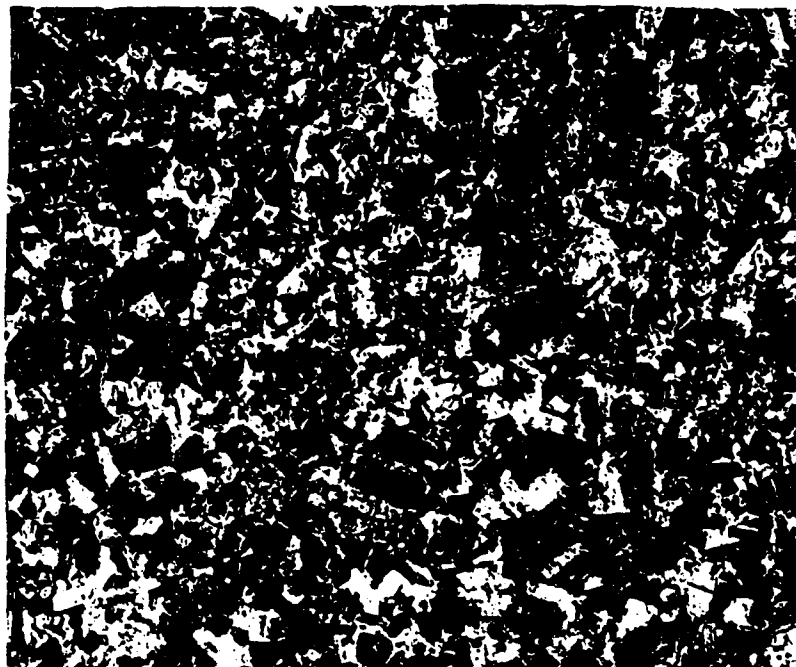
Figure 6b. 1275 C, 10^{-1} s^{-1}. X200
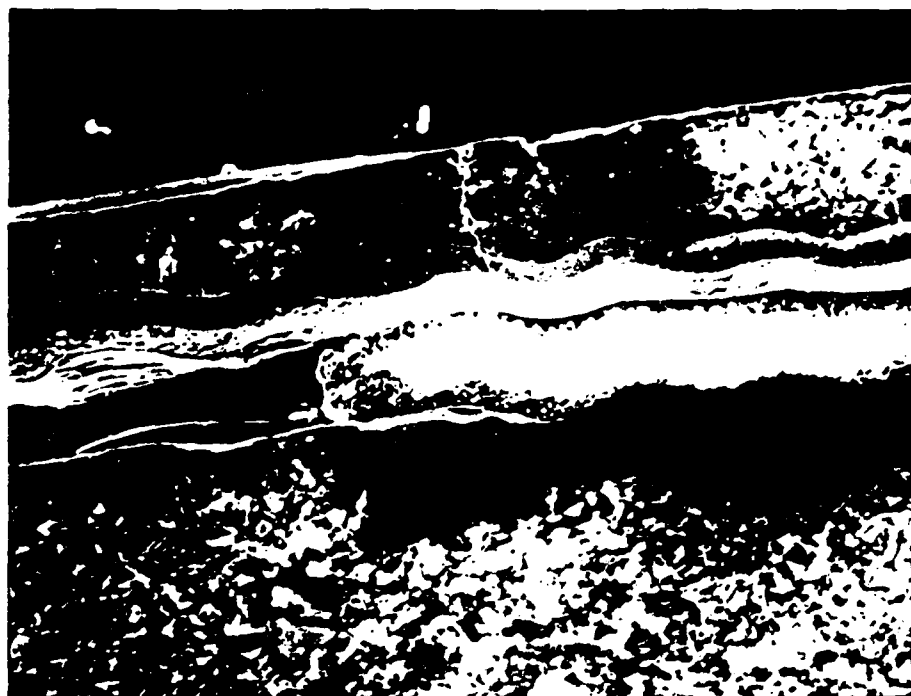
Figure 6c.   1275 C, 10^{-3} S^{-1}.   X100
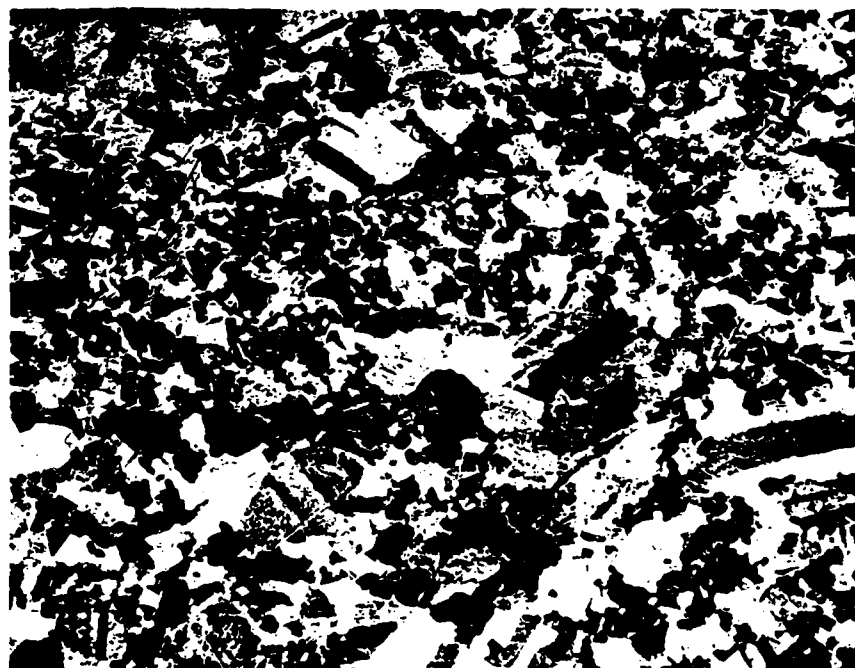
Figure 6d.   1275 C, 10^{-3} S^{-1}.   X200
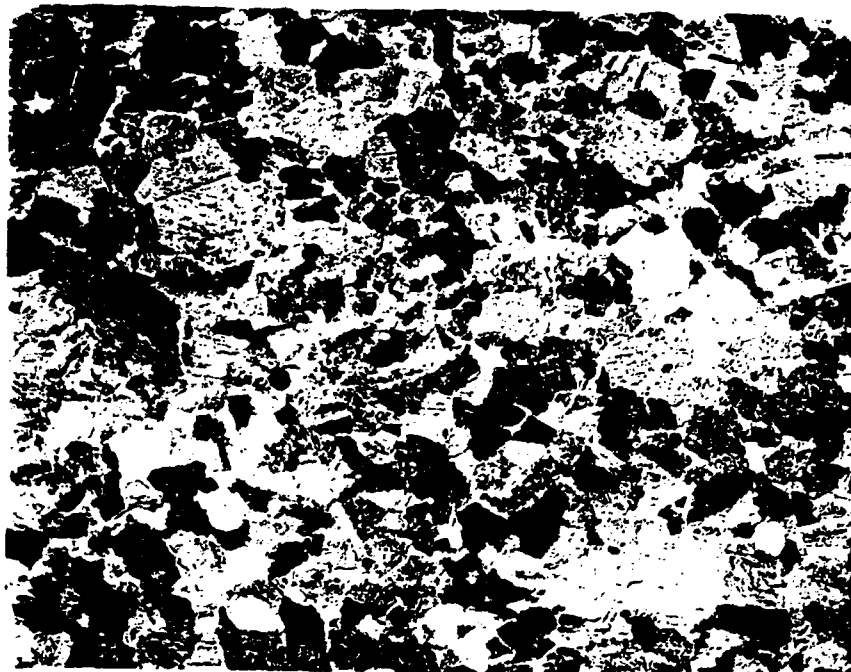
Figure 6e. 1275 C, 10^{-3}, s^{-1}. X500

Figure 6f. 13ØØ C, 10^{0} s. X4ØØ
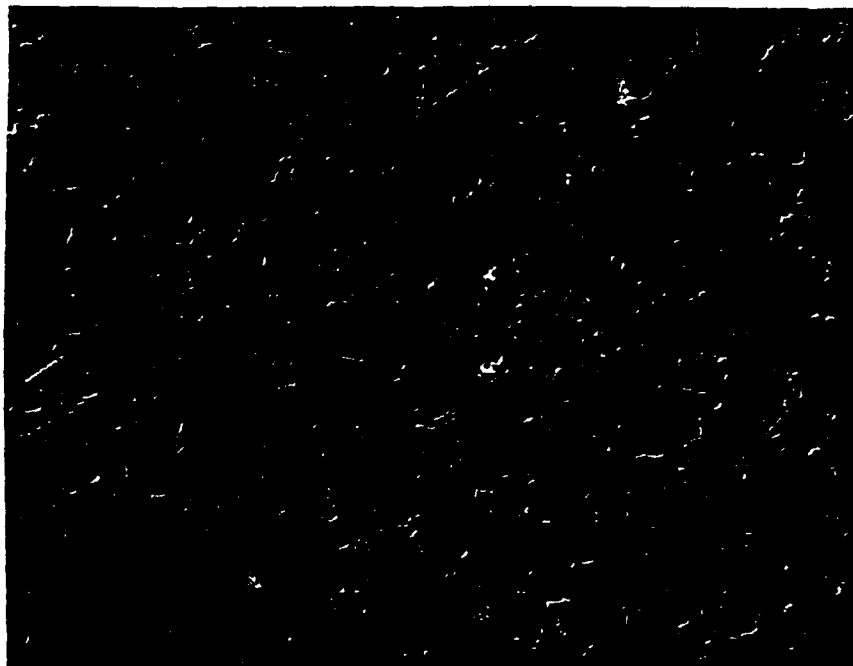
Figure 6g.   1300 C, 10^{-3} s^{-1}.   X300
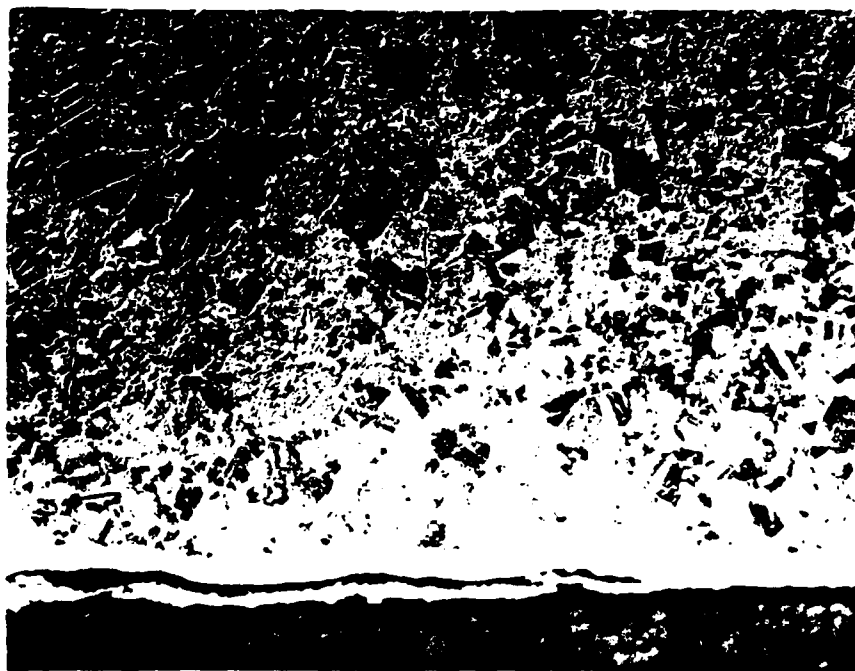
Figure 6h.   1300 C, 10° s^{-1}.   X200
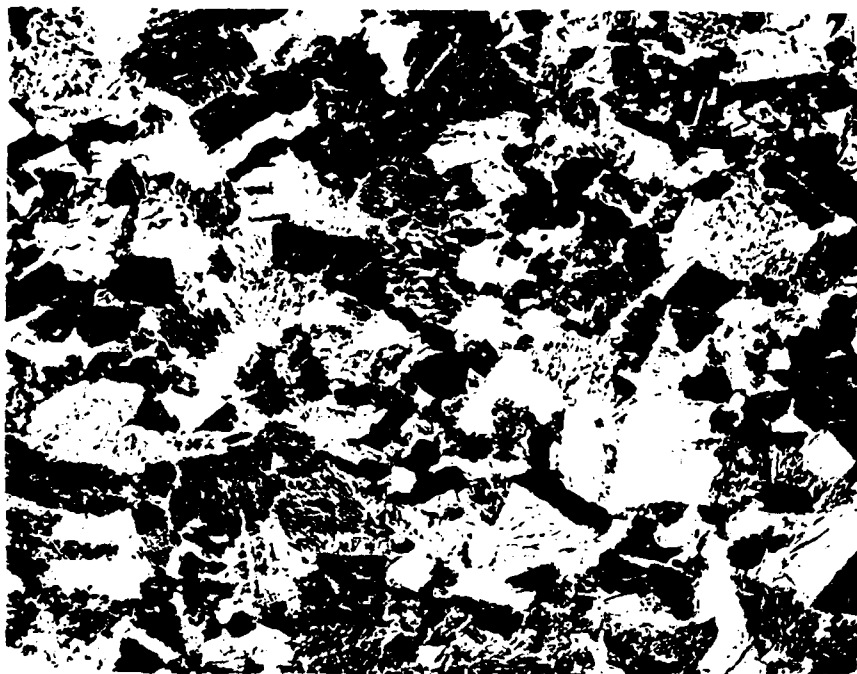
Figure 6i.   1300 C, 10^{-1} s^{-1}.   X400

Figure 6j.   1300 C, 10^{-1} s.   X400
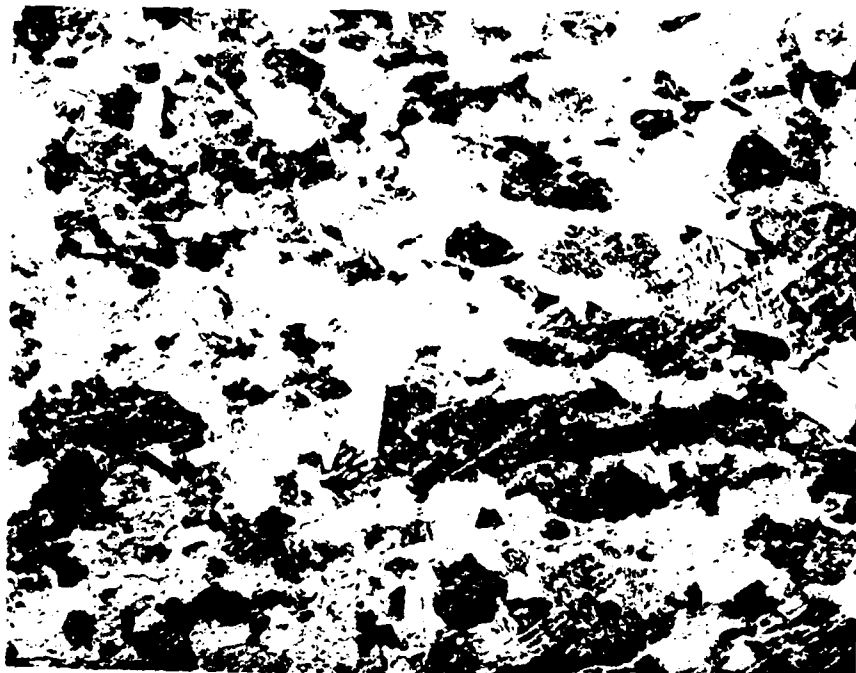
Figure 6k.   1300 C, 10^{-2} s^{-1}.   X400
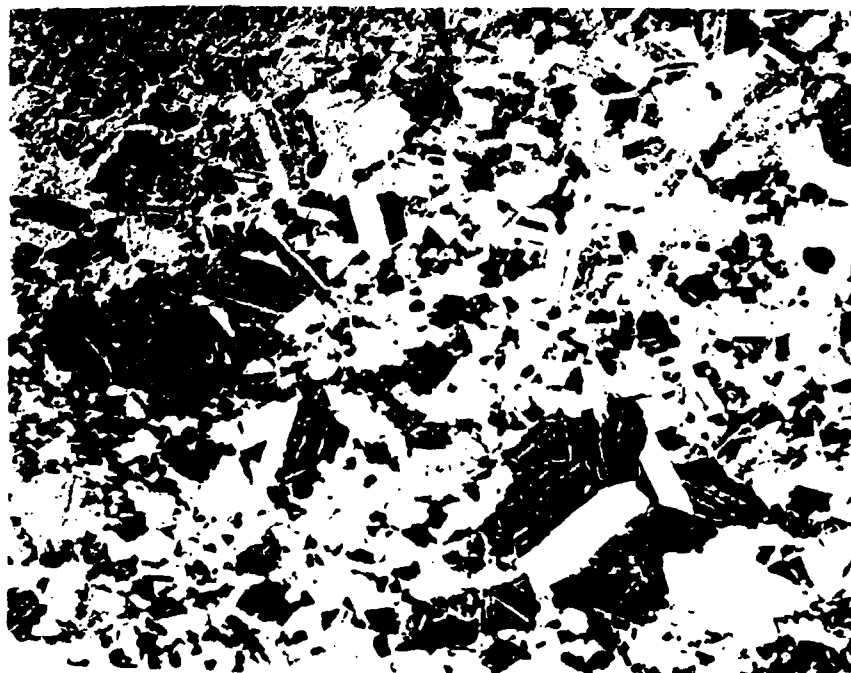
Figure 6l.   1300 C, 10^{-2} s^{-1}.   X200

4.0 ANALYSIS OF THE ALLOY B CAST-HIP Ti-Al MATERIAL

The CAST-HIP Ti-Al material was examined for microstructural evolution of specimens compression tested at temperatures from 1000-1175 C at strain rates from $10^{-0.5}$ to $10^{-2.5}$ s^{-1}. The several specimens analyzed for this study were labelled as per the following conditions, Table 2. The nominal composition of this alloy is similar to Ti 48Al base alloy, but the chemistry specifications and the casting and HIP procession specifications are proprietary and are thus not included. The microstructural evaluations were carried out in a similar manner as for the earlier PREP-HIP Ti-48Al-1V alloy.

Table 2   Conditions of Specimens Compression Tested for Alloy B CAST HIP Material

Temp. (°C)	Strain Rate (S^{-1})	Specimen Tested Identification
1000 C	10^{-1} s^{-1}	B-17
1000 C	10^{-2} s^{-1}	B-8
1050 C	10^{-1} s^{-1}	B-19
1125 C	10^{-2} s^{-1}	B-3
1150 C	$10^{-.5}$ s^{-1}	B-31
1150 C	$10^{-2.5}$ s^{-1}	B-39
1175 C	$10^{-1.5}$ s^{-1}	B-48
1175 C	$10^{-2.5}$ s^{-1}	B-40

4.1 ANALYSIS OF PROCESSING MAPS

The test data obtained on isothermal compression testing of the alloy B CAST-HIP TiAl material was used to compute the processing stability maps of this material. In these processing maps, for data from 1000 to 1175 C, stable regions are seen about 1000-1050 C, between 1150-1175 C, and also unstable regions are noted close to $\cong$ 1125 C. This could be due to the possible phase transformation seen at $\cong$ 1125 C in the Ti-Al phase diagram.

In this analysis, and based on samples analyzed, upto $\leqslant$ 1125 C temperature conditions are considered low temperature conditions and above 1125 to 1175 C are considered high temperature conditions. Combinations of these low temperature, high temperature conditions with several strain rate conditions are used to analyze the microstructural evolutions as seen and investigated in these alloy B cast material.

4.2 MICROSTRUCTURAL DYNAMICS AND THERMOMECHANICAL MODELING STUDIES IN CAST-HIP TiAl MATERIAL

The specimens as shown in Table 2 earlier were analyzed. The "as-received" CAST-HIP material revealed some twinning, variability in grain size of the matrix material, and possible interlamellar structure, figure 7a and 7b. The material exhibits variability in this cast product, and the interlamellar regions or any dual phases need to be identified using this foil transmission electron microscopy.

For specimens on compression testing at low temperature $\leqslant$ 1125 C and high strain rates conditions ($\dot{\varepsilon} \geqslant 10^{-2} s^{-1}$), the structures are seen to exhibit in general the presence of microcracks at one edge, usually isolated to one end corner. Detailed optical and scanning electron microscopy analysis revealed banded structure, possibility of interlamellar $\alpha_2 + \gamma$ phase lath type structure, α_2 phase particles, presence of porosity and effects of processing and deformation conditions as well as wide variability in microstructures in the interior compared to the end regions. Typical micrographs are shown in figures 8 and 9. It is seen that as the material deforms, power dissipation is mainly through stored energy as atomic defects, and in these specimens end corners have shown the presence of microcracks. Microstructures in these low temperature, high strain rate conditions would have significant dislocations interactions and hardening of the matrix phase. Study of behavior of the defect structures and recovery processes in these materials requires transmission electron microscopy work to confirm the mechanisms,

which could not be carried due to non availability of instrumentation and the techniques. Any subgrains formation or dynamic recrystallization effects would become possible depending on temperature and diffusional mechanisms, possibly with increasing temperature and at lower strain rates.

At strain rates from $10^{-.5}$ to $10^{-2.5}$ s^{-1}, and at the higher temperature conditions (T $\geqslant$ 1150 C) some typical microstructures of the CAST-HIP TiAl material are shown in figures 10 and 11. For 1150 C compression tested specimens, a lot of variation is seen for typical microstructures. Effects of banding and deformation in the $\alpha_2 + \gamma$ phase structures are still seen with a near end crack. This does not seem to agree with the location of stability regions at and close to 1150 C. At and above $\simeq$ 1125 C transformation temperature, under dynamic conditions and aided by lower strain rates there is possibility of the ordered α_2 phase to transform to the α phase. These and other energy dissipative processes can involve diffusional flows, transformations and recovery processes. It should be noted that this material exhibits much more variability in structure compared to the PREP-HIP Ti-48Al-1V and in typical structures has revealed mixed and somewhat polyhedral grains, with interlamellar structure towards end portions of the specimens, whereas in the interior, structures involved appear to be related to dynamic recovery and polygonization processes. Effects of banding and deformation are also seen in some of the specimens.

Figure 7a. As received CAST-HIP alloy B TiAl material showing some twinning, variability in the γ grain size of the matrix. X100
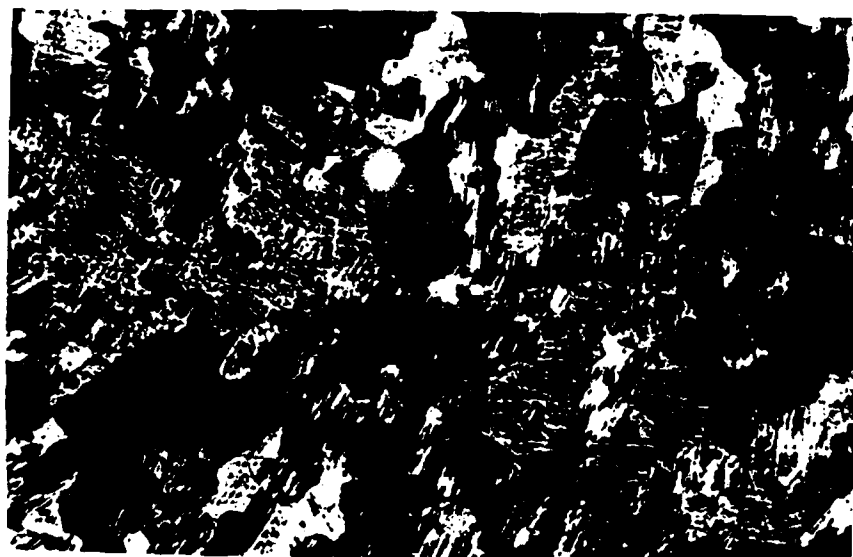
Figure 7b. As received CAST-HIP alloy B TiAl material side microstructural view with possible interlamellar structure, some twinning, and variability in grain size. X100
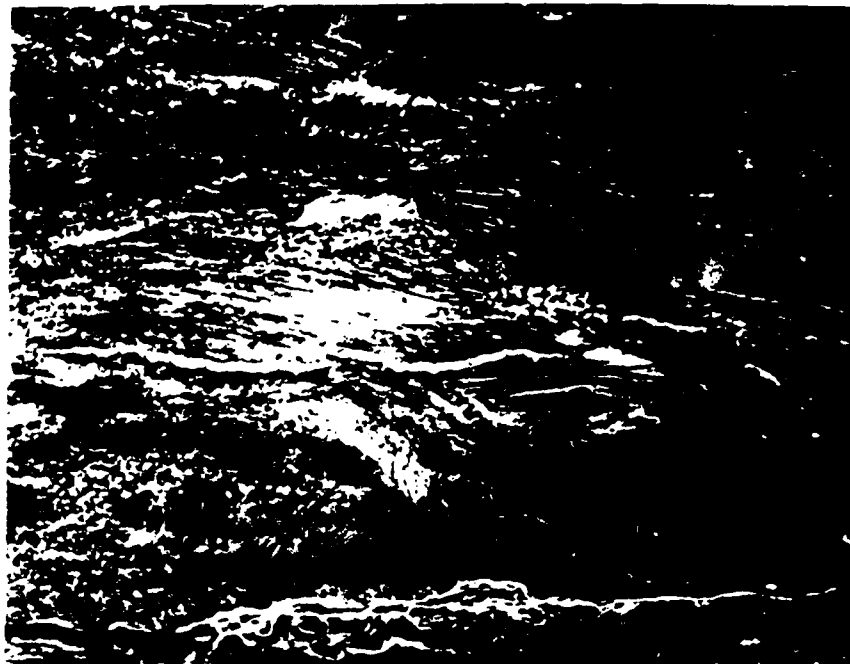
(a) X100
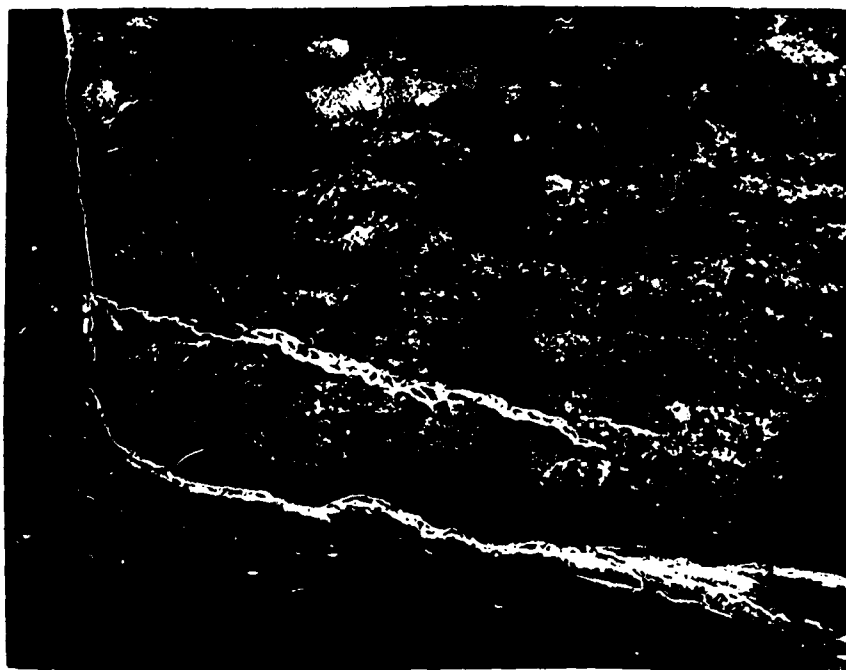
(b) X100

Figure 8. SEM Micrographs of CAST-HIP TiAl material for low temperatures, high strain rate compression tested conditions (a) 1000 C, 10^{-2} s^{-1} (b) 1125 C, 10^{-2} s^{-1} conditions.

(c)   X500
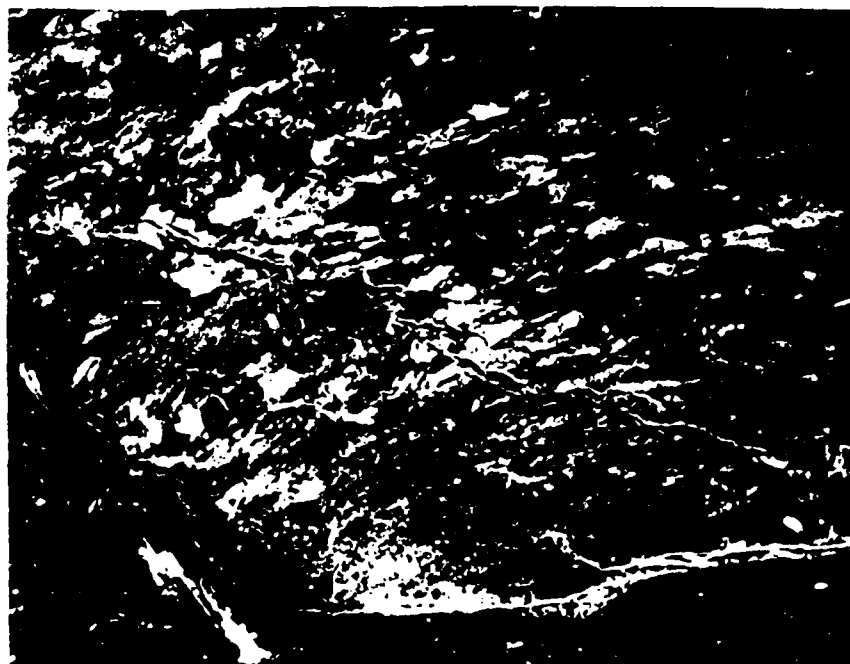
(d)   X100

Figure 8.   SEM micrographs of CAST-HIP TiAl material for low
temperature, high strain rate compression test
conditions (a) showing porosity and corner oriented
crack (b) 1050 C, 10^{-1} s^{-1} (c) 1000 C, 10^{-1} s^{-1}.

(a)   X100

(b)   X100

Figure 9.   Optical micrographs of CAST-HIP TiAl material
for low temperature, high strain rate compression
test conditions showing porosity, banding and
interlamellar structures (a) 1000 C, 10^{-2} s^{-1}
(b) 1000 C, 10^{-1} s^{-1}.

75-37
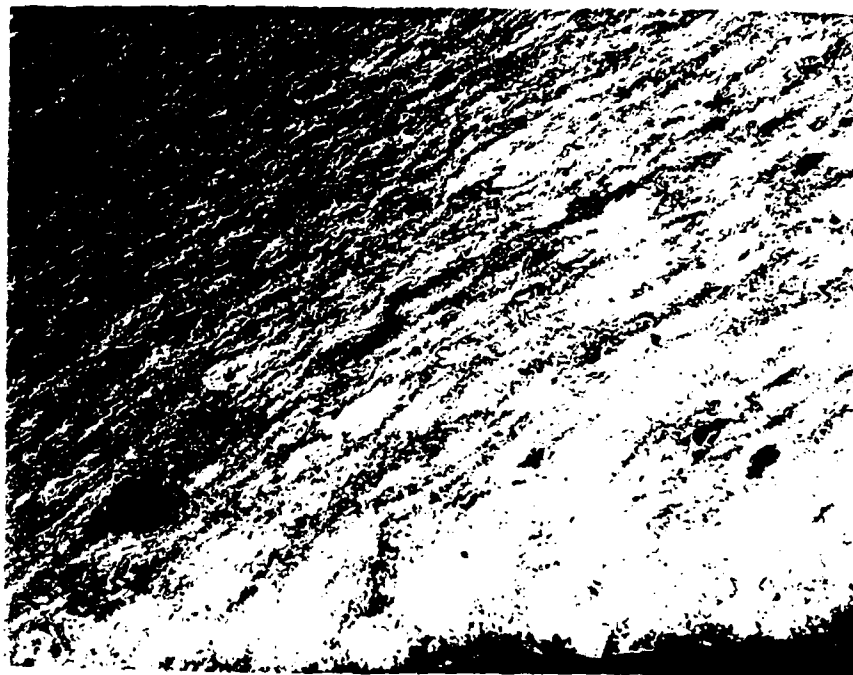
(c)   X100

(d)   X200

Figure 9.   Optical micrographs of CAST-HIP TiAl material
            for low temperatures, high strain rate compression
            test conditions showing banding, interlamellar
            structure and possible dynamic processing effects
            (c) 1050 C, 10^{-1} s^{-1} (d) 1125 C, 10^{-2} s^{-1}.

75-38

X400

Figure 9. Optical micrograph of CAST-HIP TiAl material for
low temperature, high strain rate compression
tested specimen (e) 1125 C, 10^{-2} S^{-1}.
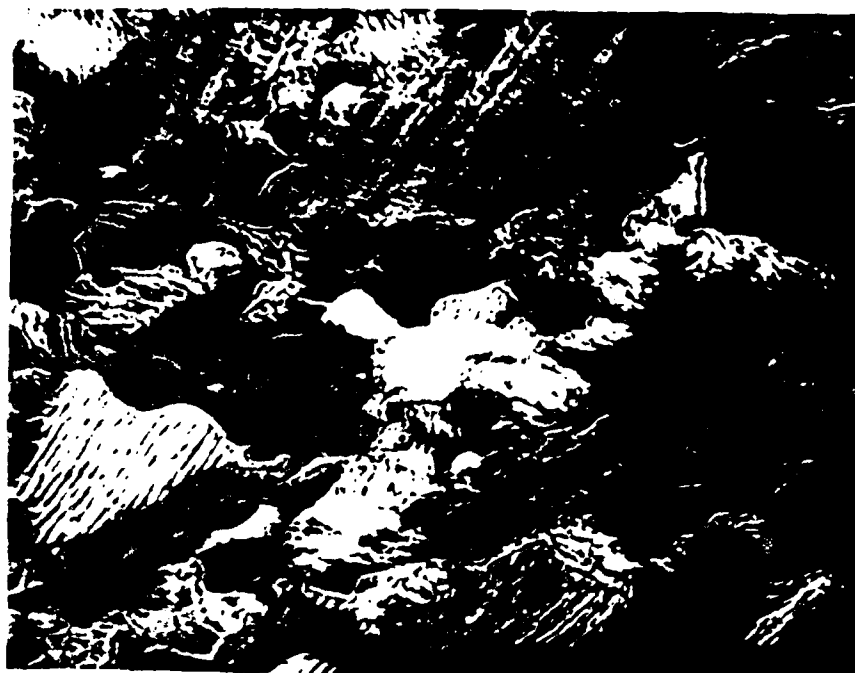
(a) X1000

(b) X50

Figure 10. SEM micrographs of CAST-HIP TiAl material for high temperature, low strain rate compression tested specimen at 1150 C, $10^{-2.5}$ s-1.
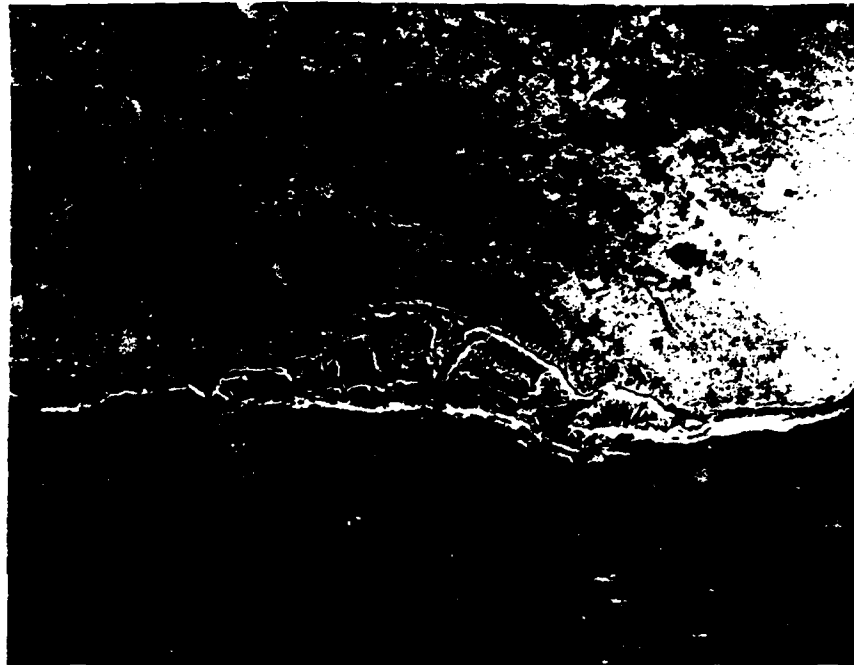
(c)   X200

Figure 10.   SEM micrograph of CAST-HIP TiAl material for high temperature, low strain compression tested specimen at 1175 C, $10^{-2.5}$ s^{-1}.

(a) X200
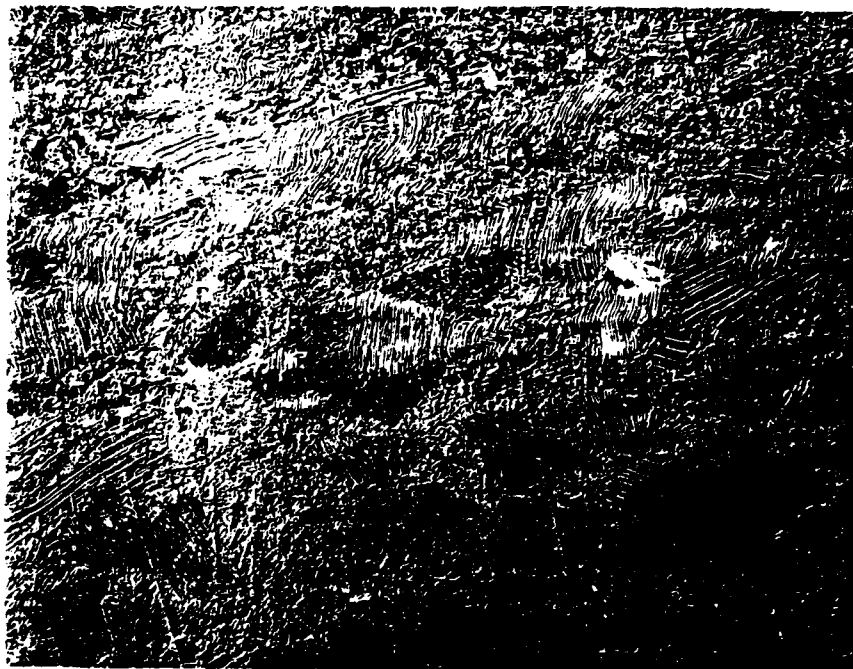
(b) X200

Figure 11. Optical micrographs of CAST-HIP TiAl material
for high temperature, high strain rate compression
tested specimens (a) 1150 C, $10^{-.5}$ S^{-1} (b) 1175 C,
$10^{-2.5}$ S^{-1}.

(c) X200

(d) X200

Figure 11. Optical micrographs of CAST-HIP TiAl material for high temperature, low strain rate compression tested specimen. Variability in the specimen structure seen for interior region in (c) and towards edge in (d) for 1175 C, $10^{-2.5}$ s^{-1}.

X200

Figure 11. Optical micrographs of CAST-HIP TiAl material for high temperature, low strain rate compression tested specimen (e) 1150 C, $10^{-2.5}$ s^{-1}.

5.0 DISCUSSION

The mechanistic modeling approach to understanding work-
ability is based on fracture and material behavior based on
atomistic models. Such studies of atomistic fracture mechanisms
as done by Ashby and Frost[14] and Raj[15] provide some basic under-
standing of microstructural operating mechanisms, but are not
completely suitable in case of complex engineering alloys
such as titanium aluminides. It should be further understood
that the workability of a material would be a function both
of the material as well as its thermomechanical processing
methods.

The material characteristics would be dependent upon phase
and compositional effects, grain size, grain distribution the
as-received structure and material dynamic effects. The thermo-
mechanical process characteristics would primarily include the
kinematic variables such as the strain rate and temperature
conditions, critical strain levels and other process considera-
tions.

A direct approach of understanding the microstructural
mechanisms is based upon studying the dynamic material modeling
DMM maps and evaluation of stability regions and controlling
microstructures. This approach was utilized in this research
by direct experimental structural characterizations, study of
DMM maps and microstructural analyses of the two types of
titanium aluminide alloy system as specified.

The microstructural dynamics studies have clearly shown the differences in the microstructural evolutions, and effects of different processing histories in case of the two specified titanium aluminide alloy systems. In case of PREP-HIP Ti-48Al-1V, power partitioning has been shown to be due to the dynamic recovery and polygonization processes related to subgrain formation. This system has not shown any grain boundary sliding, wedge cracking or superplasticity behavior mechanisms in these intermeltallic alloys. The system has indicated overall metallurgical stability, though mechanical instabilities are seen as porosity, and crack propagation in some specimens.

The dynamic material modeling approach has pointed out the conditions of stability in processing flow and has clearly shown a region of mechanical stability $\cong$ 1150 C. Furthermore, for the PREP-HIP Ti-48Al-1V material, transitions are seen in the stability, instability regions close to $\cong$1125 C and $\cong$ 1285 C, the regions close to transformation temperatures seen in the Ti-Al phase diagram. The effects of the higher temperatures phase in the study of the PREP-HIP Ti-48Al-1V are seen in the presence of any α_2, α , and transformed β . Close t 1350 C, the system has shown the dynamic nucleation and growth of the β phase This dynamic nucleation, dependent on the temperature and strain rate conditions, could have set in at $\cong$1275 C, with possibility of coarse β formation for 1350 C specimen conditions. Also, this alloy system has shown a transition in material flow conditions, such as in going

from stability regions in processing-stability maps at the 0.3 strain level to the 0.5 strain level which indicates that the deformation processing should be stopped at a certain "critical" strain level. More microstructural characterization and analyses are needed in this direction to fully evaluate this concept.

The effects of material flow conditions are largely dependent on the characteristics of the predominant matrix γ phase, with only small amounts of the α_2, α, or any transformed β phase. The microstructures have revealed twinning, microcracks, and dynamic recovery, polygonization, and partial dynamic recrystallization processes. Interlamellar features showing effects of deformation and high temperature are also seen. The microstructures also reveal oxide scale on flat ends and also presence of microcracks in some of the compression tested specimens.

In case of the PREP-HIP Ti-48Al-1V material, the high temperature deformation mechanisms are seen as leading to the possible formation of the α_2 transformed into coarse β phase in the lacy configuration at 1350C. It should be understood that dislocation interactions, creation and movement of dislocation boundaries, and creation and movement of transformed phase boundaries would be the operative steps in these mechanisms. These microstructural transformations appear to be surface controlled, rather than bulk volume diffusion controlled, and the amount or volume fraction of the transformed phase could be correlated to the nucleation and growth rates under the dynamic

process conditions. Such models can be then related to kinematic variables such as temperature and strain rates.

The enchanced effects of the second phase could be invoked by changing basic chemistry of the titanium aluminide alloy system. A possible study with hard particle dispersoids of TiB_2 was considered, but as such materials were not available, another formulation of the base alloy system was evaluated in form of the CAST-HIP TiAl material. These CAST-HIP TiAl compression tested specimens have shown presence of twinning; and in several temperature, strain rate conditions presence of shear bands. These shear bands are seen to be more pronounced in the central regions of high strains in these compression tested CAST-HIP materials. These shear bands could have further acted as sites for potential corner cracks which are seen in these materials.

The CAST-HIP TiAl material, in the specimens analyzed to 1175C show more pronounced non-uniform microstructural features compared to the PREP-HIP Ti-48Al-1V material. This suggests the possibility of hysteresis or memory effect related to the starting as-received structures in those CAST-HIP material.

In addition to effects of shear bands which are exhibited by these CAST-HIP TiAl materials these microstructures also reveal banding, interlamellar structure and possible dynamic processing effects. As the compression tested specimens are analyzed to 1175 C, no α_2/β transformation is expected. The presence is seen of the possible interlamellar $\alpha_2 + \gamma$ phase

lath type structure. The overall microstructures in these materials show wide variations in the interior compared to the end regions which could be due to the inhomogenity of deformation and the processing conditions of the CAST-HIP process.

--

6.0 CONCLUSIONS

1. The present research has evaluated the PREP-HIP Ti-48Al-1V, isothermal compression tested from 1000 - 1350 C for several strain rate conditions, and the CAST-HIP TiAl alloy system isothermal compression tested from 1000 - 1175 C from $10^{-.5}$ to $10^{-2.5}$ s^{-1} strain rate conditions, for their DMM maps and the microstructural behavior of these alloy systems.

2. The microstructural dynamics of the PREP-HIP Ti-48Al-1V and the CAST-HIP TiAl material in this study indicate that the presence of prior deformation structures and applied thermomechanical processing parameters have resulted in distinct, nonuniform microstructures and shear bands in case of the tested CAST-HIP TiAl material. However, for the CAST-HIP TiAl material these determinations are based on limited available materials tested to 1175 C.

3. The microstructural analyses in case of the PREP-HIP Ti-48Al-1V material have exhibited the nucleation and growth of the transformed β phase resulting with the peritectoid transformation at ≏ 1285 C. This β phase for compression tested conditions to 1350 C is seen in a lacy configuration appearing to envelope the γ grains in the matrix of the PREP-HIP Ti-48Al-1V. This is considered to be surface controlled and the extent of this growth transformation should be dependent both on the dynamic nucleation and growth rates of these new grains under the dynamic process condition.

4. The formation of metallurgical stable structures, dislocation
    related subgrain boundaries, their nucleation and growth
    rates and formation and growth rates of α_2/ α / and any
    transformed β phases is expected to be affected by changes
    in strain rates and temperatures. For constant temperature
    conditions, the dislocation densities, any stacking faults,
    related interactions and phase transformations related to
    the Ti-Al system could increase with increasing strain
    rates. These can be evaluated further with transmission
    electron microscopy and should be correlated with
    differential scanning calorimetry to confirm these
    dynamic microstructural aspects and the nucleation and
    growth of the transformed β phase at $\cong$ 1285 C.

5. The metallurgical synthesis attempted in the thermo-
    dynamically stable TiAl intermetallic alloy systems using
    quantitative microscopy methods, SEM techniques, optical
    metallography with differential interference contrast DIC
    procedures has shown the operative mechanisms of dynamic
    recovery, subgrain formation, polygonization and dynamic
    recrystallization in selected temperature, strain rate
    conditions in the PREP-HIP Ti-48Al-1V and CAST-HIP TiAl
    material.

6. Both specific systems that are studied in this research
    have shown metallurgical stability in different temperature,
    strain rate conditions. To 1175 C compression test
    conditions, it is seen that the presence of α_2 phase
    is very limited, and the hot deformation processes can be

controlled mainly by the γ-phase matrix. For the Ti-48Al-1V compression tested to 1350 C, this system has indicated the dynamic nucleation and growth of the β phase related to the peritectoid transformation in the Ti-Al system. For specimens compression tested at 1250 C and higher, the presence of α_2/ transformed β is seen as related to this dynamic nucleation and growth of the β phase and the reversion and the peritectoid transformation at $\simeq$ 1285 C. The structural evolutions and microstructural aspects for stable material flow conditions have been analyzed in the selected titanium aluminide alloy systems.

REFERENCES

1. E. W. Collings and H. L. Gegel Eds., "Physical Principles of Solid Solution Strengthening in Alloys, "Proc. ASM-TMS (AIME) Symposium, Plenum Press, New York, 1975, pp. 147-182.

2. E. A. Stern, "Application of Alloy Physics to Solution Strengthening," Proc. ASM-TMS (AIME) Symposium, Collings and Gegel, Eds., Plenum Press, 1975, pp. 183-197.

3. H. L. Gegel, J. C. Malas, S. M. Doraivelu, J. M. Alexander, J. S. Gunasekera, "Material Modeling and Intrinsic Workability for Simulation of Bulk Deformation," To be published, FGU 2nd International Conference for Applied Plasticity, University of Stuttgart, Germany, August 24-28, 1987.

4. H. L. Gegel, "Synthesis of Atomistics and Continuum Modeling to Describe Microstructure," Computer Simulation in Materials Science, ASM, Ed. by R. J. Arsenault, J. R. Beeler, Jr., and D. M. Esterling, 1988, pp. 291-344.

5. H. L. Gegel, "Material Behavior Modeling-An Overview, "American Society for Metals, Metals Park, in Conference Proceedings Experimental Verification of Process Models, Ed. by C. C. Chen, ASM 1983, pp. 3-32.

6. Y. V. R. K. Prasad, H. L. Gegel, J. C. Malas, J. T. Morgan, K. A. Lark, S. M. Doraivelu, and D. R. Barker, "Constitutive Behavior and Dynamic Modeling of Hot Deformation of a P/M 2024 Al Alloy with 20 Vol% SiC Dispersion," AFWAL/MLLM, Materials Laboratory, Wright-Patterson AFB, Ohio, Internal report: Final Report for the period May 1983-December 1983, AFWAL-TR-84-4076, November 1984.

7. General Electric IR&D - Research conducted by General Electric Company on nickel based alloys.

8. S. M. L. Sastry, R. J. Lederich, T. H. Mackay and W. R. Kerr, "Superplastic Forming Characterization of Titanium Alloys," Journal of Metals, 35, 48-53, 1983.

9. Y. V. R. K. Prasad, H. L. Gegel, S. M. Doraivelu, J. C. Malas, J. T. Morgan, K. A. Lark, and D. R. Barker, "Modeling of Dynamic Material Behavior in Hot Deformation: Forging of Ti-6242," Met. Trans. A, 15, 1883-1892, October 1984.

10. Summer Faculty Research Report - R. M. Diwan - Research conducted at WPAFB Materials Laboratory - Microstructural Developments in PREP-HIP Ti-48Al-1V in the study of Dynamic Material Modeling Behavior - August, 1987.

11. J. L. Murray, "The AlTi (Aluminum Titanium) System," 26.98154 Equilibrium Diagrams, published by the National Bureau of Standards.

12. C. McCullough, et al., "The High Temperature Field in the Titanium-Aluminum Phase Diagram," Scripta Metallurgica, Volume 22, 1988, pp. 1131-1136.

13. M. G. Mendiratta, Private Communication - transmission electron microscopy of the PREP-HIP Ti-48Al-1V, June-August 1987.

14. H. J. Frost and M. F. Ashby, "Deformation - Mechanism Maps" The Plasticity and Creep of Metals and Ceramics, Pergamon Press, 1982.

15. R. Raj, "Development of a Processing Map for Use in Warm-Forming Processes," Met. Trans. A, 12, 1089-1097, June 1981.

FINAL REPORT NUMBER 76
REPORT NOT AVAILABLE AT THIS TIME
Dr. Bruce A. Craver
760-7MG-097

FINAL REPORT NUMBER 77
REPORT NOT AVAILABLE AT THIS TIME
Dr. John W. Gilmer
760-7MG-013

FINAL REPORT NUMBER 78
REPORT NOT AVAILABLE AT THIS TIME
Dr. Gordon Johnson
760-7MG-075

STUDIES ON THE COMPATIBILITY OF

POTENTIAL MATRIX AND REINFORCEMENT MATERIALS IN

CERAMIC COMPOSITES FOR HIGH-TEMPERATURE,

AEROSPACE APPLICATIONS

Final Report
Submitted to

Universal Energy Systems

4401 Dayton-Xenia Road

Dayton, OH 45432

by

Gopal M. Mehrotra

Materials Science and Engineering Program

Wright State University, Dayton, OH 45435

Abstract

The mutual chemical compatibility of some of the potential matrix and reinforcement materials for ceramic-ceramic composites was analytically evaluated using the available thermodynamic data. The material combinations evaluated include AlN-TiB_2, AlN-ZrB_2, AlN-HfB_2, TiC-TiB_2, TiC-ZrB_2, TiC-HfB_2, TiN-Al_2O_3, TiN-ZrO_2 and TiN-HfO_2. In addition, the chemical stability of TiC, AlN and TiB_2 in a matrix of Al_2O_3, ZrO_2 or HfO_2 was assessed experimentally. Further, the oxidation behavior of the TiC-Al_2O_3, TiC-ZrO_2, AlN-Al_2O_3, AlN-ZrO_2, TiC-TiB_2 and ZrC-ZrB_2 composites was also studied.

I.   Introduction

The mutual chemical compatibility of the constituents of a ceramic composite material is one of the important considerations in developing such materials for high temperature, aerospace applications. Considerable effort is therfore currently being devoted to the study of the mutual chemical compatibility of potential matrix and reinforcement materials.

The present report describes the results of analytical evaluations of chemical compatibility of constituents of a few nitride-boride, carbide-boride and nitride-oxide material combinations and the results of experimental studies on a few nitride-oxide, carbide-oxide, boride-oxide and carbide-boride material combinations which were chosen on the basis of earlier screening studies and were described in the research proposal for this project.

II. Objectives of the Research Effort

The overall objective of the effort was to identify the pairs of materials which would be mutually compatible in the temperature range of 1200-2000°C. Specifically, the objectives were:

(i) To evaluate, analytically, the mutual chemical compatibility of some of the potential constituent materials for ceramic composites for high temperature applications. The materials chosen for evaluation included ZrB_2, HfB_2, TiB_2, TiC, $A\ell N$, TiN, $A\ell_2O_3$, ZrO_2, and HfO_2.

(ii) To experimentally study the mutual chemical compatibility of constituents in the composites of chosen material pairs, namely, $TiC-A\ell_2O_3$, $TiC-ZrO_2$, $TiC-HfO_2$, $A\ell N-A\ell_2O_3$, $A\ell N-ZrO_2$, $A\ell N-HfO_2$, $TiC-TiB_2$, $ZrC-ZrB_2$, $TiB_2-A\ell_2O_3$, TiB_2-ZrO_2 and TiB_2-HfO_2.

(iii) To study the oxidation behavior of $A\ell N$, TiC and ZrB_2 in the $TiC-A\ell_2O_3$, $TiC-ZrO_2$, $A\ell N-A\ell_2O_3$, $A\ell N-ZrO_2$, $TiC-TiB_2$, and $ZrC-ZrB_2$ composites

In the following, the progress made in each of the above areas will be described.

III. <u>Analytical Evaluation of Chemical Compatibility of Potential Matrix and Reinforcement Phases</u>

The analytical evaluations have been made on the basis of the results of thermodynamic calculations making use of the available thermodynamic data.[1-3] The material pairs thus evaluated include:

(1) $A\ell N$-TiB_2, $A\ell N$-ZrB_2, $A\ell N$-HfB_2 (examples of nitride-boride combinations)

(ii) TiC-TiB_2, TiC-ZrB_2, TiC-HfB_2, (examples of carbide-boride combinations), and

(iii) TiN-$A\ell_2O_3$, TiN-ZrO_2 TiN-HfO_2, (examples of nitride-oxide combinations).

The results obtained for these systems are described in the following:

(a) $A\ell N$ in a matrix of TiB_2, ZrB_2 or HfB_2 (or TiB_2, ZrB_2 or HfB_2 in a matrix of $A\ell N$)

Some of the possible reactions between the matrix and reinforcement materials are:

$$A\ell N + 6TiB_2 = A\ell B_{12} + TiN + 5Ti \qquad (1)$$

$$A\ell N + TiB_2 = A\ell B_2 + TiN \qquad (2)$$

$$2A\ell N + TiB_2 = TiA\ell + 2BN + A\ell \qquad (3)$$

$$A\ell N + TiB_2 = TiB + BN + A\ell \qquad (4)$$

$$A\ell N + ZrB_2 = ZrN + A\ell B_2 \qquad (5)$$

$$A\ell N + 6ZrB_2 = A\ell B_{12} + ZrN + 5Zr \qquad (6)$$

$$A\ell N + HfB_2 = A\ell B_2 + HfN \qquad (7)$$

$$A\ell N + 6HfB_2 = A\ell B_{12} + HfN + 5Hf \qquad (8)$$
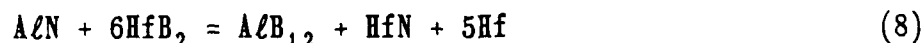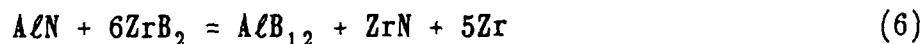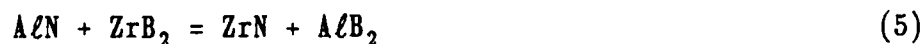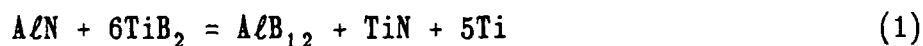
The feasibility of the above reactions has been evaluated

using the Gibbs energy of formation data for the various compounds involved in these reactions. The results of the thermodynamioc calculations are given in Table 1. In this table, and in all other tables, the subscript of ΔG^0 (standard free energy change) or K (the equilibrium constant) refers to the reaction number for which the value of ΔG^0 or K is given. All the values of ΔG^0 are in calories.

Table 1.   Thermodynamic Data for Reactions (1) - (8)

ΔG_i^0 or K_i	Temperature (K)		
	1873	2073	2273
ΔG_1^0	291,513	283,732	275,244
K_1	9.60×10^{-35}	1.21×10^{-30}	3.41×10^{-27}
ΔG_3^0	58,935	---	---
K_3	1.33×10^{-7}	---	---
ΔG_4^0	28,222	26,188	24,154
K_4	5.09×10^{-4}	1.73×10^{-3}	4.76×10^{-3}
ΔG_6^0	338,984	331,498	322,304

K_6	2.77×10^{-40}	1.12×10^{-35}	1.02×10^{-31}
ΔG_8^0	378,825	374,707	370,589
K_8	6.21×10^{-45}	3.11×10^{-40}	2.32×10^{-36}

In the above table, the data for reactions (2), (5) and (7) have not been included because the $A\ell B_2$ phase is not stable in the temperature range 1873-2273 K. Above 1248 K, it decomposes to give $A\ell B_{12}$ and a liquid $A\ell$-B phase. Below 1248 K, the reactions (2), (5) and (7) are not feasible. It must also be pointed out that the melting points of the $TiA\ell$ and $A\ell$ phases in reaction (3) are 1768 and 933 K, respectively, and the value of ΔG_3^0 at 1873 K has been calculated by extrapolating the data for the $TiA\ell$ phase.

It may be pointed out that the error bars in some of the thermodynamic data are rather large, especially in the case of the data for TiB (± 10 kcal). However, the data given in Table 1 indicate that the value of K is the largest for reaction (4). This reaction may therefore be feasible at high temperature. These data also indicate that $A\ell N$ should be compatible with ZrB_2 and HfB_2.

(b) TiC in a matrix of TiB_2, ZrB_2 or HfB_2

Some of the possible chemical reactions between the matrix

and reinforcement materials are:

$$TiC + 3TiB_2 = B_4C + 2TiB + 2Ti \tag{9}$$

$$TiC + 2TiB_2 = B_4C + 3Ti \tag{10}$$

$$TiC + ZrB_2 = ZrC + TiB_2 \tag{11}$$

$$TiC + HfB_2 = HfC + TiB_2 \tag{12}$$
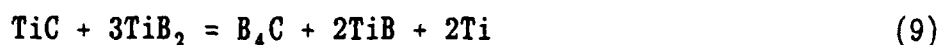
The thermochemical calculations for the above reactions yield the data given in Table 2.

Table 2 Thermodynamic Data for Reactions (9) - (12)

ΔG_i^0 or K_i	Temperature (K)		
	1873	2073	2273
ΔG_9^0	134,823	131,582	128,108
K_9	1.85×10^{-16}	1.34×10^{-14}	4.80×10^{-13}
ΔG_{10}^0	148,757	145,747	142,313
K_{10}	4.38×10^{-18}	4.30×10^{-16}	2.07×10^{-14}
ΔG_{11}^0	4,750	4,450	4,150
K_{11}	0.28	0.34	0.40
ΔG_{12}^0	3,108	3,316	3,524
K_{12}	0.44	0.45	0.46

The above data indicate that TiC and TiB_2 should be

mutually compatible. However, in view of the small positive values of ΔG_{11}^0 and ΔG_{12}^0, there is some possibility of reaction between the matrix and reinforcement phases, i.e., between TiC and ZrB_2 (or HfB_2).

(c)   TiN in a matrix of Al_2O_3, ZrO_2 or HfO_2

Some of the possible chemical reactions between TiN and the three oxide materials are:

$$2TiN + Al_2O_3 = Ti_2O_3 + 2AlN \tag{13}$$

$$3TiN + Al_2O_3 = 3TiO + 2AlN + \frac{1}{2}N_2 \tag{14}$$

$$TiN + Al_2O_3 = Al_2O + TiO_2 + \frac{1}{2}N_2 \tag{15}$$

$$TiN + ZrO_2 = ZrN + TiO_2 \tag{16}$$

$$TiN + HfO_2 = HfN + TiO_2 \tag{17}$$
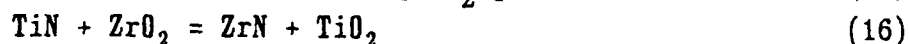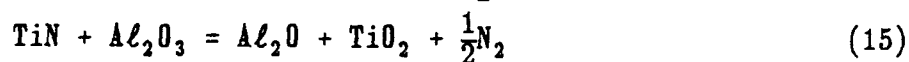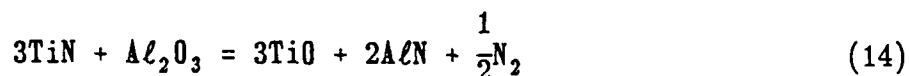
Using the available thermodynamic data for the phases involved in the above reactions, one obtains the data given in Table 3.

Table 3. Thermodynamic Data for Reactions (13) - (17)

ΔG_i^0 or K_i	Temperature (K)		
	1873	2073	2273
ΔG_{13}^0	37,835	36,677	*
K_{13}	3.84×10^{-5}	1.36×10^{-4}	---
ΔG_{14}^0	50,396	*	*
K_{14}	1.32×10^{-6}	---	---
ΔG_{15}^0	87,280	73,328	*
K_{15}	6.53×10^{-11}	1.86×10^{-8}	---

ΔG_{16}^{0}	26,302	25,952	*
K_{16}	8.52×10^{-4}	1.84×10^{-3}	---
ΔG_{17}^{0}	20,812	20,894	*
K_{17}	3.73×10^{-3}	6.27×10^{-3}	*

* TiO_2, Ti_2O_3 and β-TiO have melting points of 2143, 2115 and 2023 K, respectively,

The above data show that TiN should be chemically compatible with Al_2O_3, ZrO_2 and HfO_2. The chemical and microstructural studies of the AlN-TiO_2 system by Mocellin and Bayer[4] showed that at temperatures of 1400-1600°C a displacement type reaction took place and that the phases formed were TiN and Al_2O_3. This confirms the results of the thermodynamic calculations, shown in the above table.

IV. <u>Experimental Studies</u>

As stated earlier, the objectives of the experimental studies were:

(a) to assess the mutual chemical compatibility of the constituents

of chosen material combinations. These material combinations were TiC-$A\ell_2O_3$, TiC-ZrO_2, TiC-HfO_2, $A\ell$N-$A\ell_2O_3$, $A\ell$N-ZrO_2, $A\ell$N-HfO_2, TiB_2-$A\ell_2O_3$, TiB_2-ZrO_2, TiB_2-HfO_2, TiC-TiB_2, and ZrC-ZrB_2. The choice of most of these material pairs was based upon thermochemical evaluations of the mutual chemical compatibility of the materials in these pairs[5].

(b) to investigate the oxidation behavior of TiC and $A\ell$N, pure as well as embedded in the matrices of oxides ($A\ell_2O_3$, ZrO_2), and of TiC-TiB_2 and ZrC-ZrB_2 composites.

IV.a   Assessment of mutual chemical compatibility of constituents of the chosen material combinations.

For the purpose of obtaining information about their mutual chemical compatibility, the powders of the constituent materials of the chosen combinations were intimately mixed in various desired proportions. The powders used in the present investigations were purchased from commercial sources (AESAR-Johnson-Matthey). The purity of the powders is given below:

Material	Purity/Grade
AℓN	98+%
Aℓ$_2$O$_3$	99.99%
HfO$_2$	Reactor grade, Zr 1.5%
TiB$_2$	99.8%
TiC	99%
ZrB$_2$	97%
ZrC	98%, Hf 1.8%
ZrO$_2$	99.99%

The powder mixtures were hot pressed into dense compacts. The dies used were made of graphite, and were lined with graphoil. Hot pressing, in all cases (except for pure AℓN), was carried out in an evacuated chamber (p≃100-250μmHg). The compositions of the powders/powder mixtures that were hot pressed are given in Table 4. This table also gives the hot pressing temperatures for various compositions.

Table 4. Compositions of Powder Mixtures Hot Pressed and
The Hot Pressing Temperatures

Composition (wt%)	Maximum Temperature (^{0}C) during Hot Pressing
100 TiC	2270
10TiC-Aℓ$_2$O$_3$	1840,1930
20TiC-Aℓ$_2$O$_3$	1800
30TiC-Aℓ$_2$O$_3$	1805,1575
35.4TiC-Aℓ$_2$O$_3$	1830

90TiC-Al_2O_3	1980
20TiC-ZrO_2	2030
20TiC-HfO_2	2220
100 AlN	1900
10Aln-Al_2O_3	1740
20AlN-Al_2O_3	1600
44AlN-Al_2O_3	1700
80Aln-Al_2O_3	1820
90AlN-Al_2O_3	2040
30AlN-ZrO_2	1960, 2200
42AlN-ZrO_2	1475
80AlN-ZrO_2	2190
90AlN-ZrO_2	2250
80AlN-HfO_2	2230
100TiB_2	2370
20TiB_2-Al_2O_3	1800
20TiB_2-ZrO_2	2220
20TiB_2-HfO_2	2190
10TiC-TiB_2	2310
20TiC-TiB_2	1875, 2250
20TiB_2-TiC	2270
100 ZrC	2200
20ZrC-ZrB_2	1950

An interesting observation was made in the course of hot pressing of 30AlN-ZrO_2 and 80AlN-ZrO_2 powder mixtures at the temperatures given in Table 1. The slump (an indication of

decrease in volume) was unusually large. When the compacts were taken out of the dies, they appeared to be very thin. They had golden, metallic appearance. A large weight loss was also observed. This observation was not made in the case of the 42AℓN-ZrO_2 specimen which was hot pressed at a much lower temperature, 1475ºC, nor was it made in the case of the 90AℓN-ZrO_2 specimen.

The densities of hot pressed compacts, as estimated from their weights and dimensions, varied from ~88 to 98% of the theoretical density. The theoretical densities of the composites were calculated assuming that there was no reaction between the constituent materials of a composite during hot pressing. This assumption may or may not be valid. However, the validity of this assumption could be tested by characterizing the hot pressed specimens by x-ray diffraction (XRD). Since the composites were made from intimate mixtures of powders by hot pressing, the characterization of the composite specimens by XRD also yields information regarding the new phases formed, if any, as a result of a chemical reaction between the constituents and therefore about the mutual chemical compatibility of the constituent materials.

The results obtained from XRD of hot pressed specimens are given in Table 5.

Table 5. Phases Identified in Hot Pressed Compacts

Composition (wt%)	Phases Identified
100 TiC	TiC (Cubic)
10TiC-Al_2O_3	TiC, Al_2O_3
20TiC-Al_2O_3	TiC, Al_2O_3
30 TiC-Al_2O_3	TiC, Al_2O_3
35.4TiC-Al_2O_3	TiC, Al_2O_3
90TiC-Al_2O_3	TiC, Al_2O_3
20TiC-ZrO_2	TiC, ZrO_2 (monoclinic)
20TiC-HfO_2	TiC, HfO_2 (monoclinic)
AlN	AlN (hexagonal)
10AlN-Al_2O_3	AlN (hexagonal + cubic), Al_2O_3
20AlN-Al_2O_3	AlN (cubic + hexagonal), Al_2O_3
44AlN-Al_2O_3	AlN (hexagonal + cubic), Al_2O_3
42AlN-ZrO_2	AlN (hexagonal), ZrO_2 (cubic), ZrO_2 (monoclinic), ZrN (cubic)
90 AlN-ZrO_2	AlN (hexagonal), ZrO_2 (cubic), ZrN (cubic), & also aluminum oxynitride ($Al_{196}O_{287}N_4$ or $Al_{27}O_{39}N$)

80AℓN-HfO$_2$	AℓN,HfO$_2$
100TiB$_2$	TiB$_2$
20TiB$_2$-Aℓ_2O$_3$	TiB$_2$, Aℓ_2O$_3$
20TiB$_2$-ZrO$_2$	TiB$_2$, ZrO$_2$ (mono.)
	Ti$_3$B$_4$ (?)
20TiB$_2$-HfO$_2$	TiB$_2$, HfO$_2$
10TiC-TiB$_2$	TiB$_2$, TiC (very few
	peaks of TiC)
20TiC-TiB$_2$	TiB$_2$, TiC
20TiB$_2$-TiC	TiC, TiB$_2$
100ZrC	ZrC
20ZrC-ZrB$_2$	ZrC, ZrB$_2$

The XRD results indicate that the two constituent compounds in each of the systems TiC-Aℓ_2O$_3$, TiC-ZrO$_2$, TiC-HfO$_2$, AℓN-Aℓ_2O$_3$, AℓN-HfO$_2$, TiB$_2$-Aℓ_2O$_3$, TiB$_2$-HfO$_2$, TiC-TiB$_2$ and ZrC-ZrB$_2$ are mutually compatible upto approximately the temperature at which the respective material combination was hot pressed. The constituent compounds in the material combination AℓN-ZrO$_2$ (and possibly also in TiB$_2$-ZrO$_2$) do not appear to be mutually compatible as indicated by the XRD results given in Table 5. In the case of the hot-pressed AℓN-ZrO$_2$ specimens, the presence of the cubic and monoclinic zirconia, aluminum nitride, aluminum oxynitride and zirconium nitride phases was detected. The "d-values" reported in the JCPDS cards for the ZrO and ZrN phases are very close to each other. Therefore, there can be some question about the presence of ZrN in the hot-pressed AℓN-ZrO$_2$ samples. However, as the ZrO phase is reported to be gaseous at room temperature[3], it was concluded

that the observed peaks in the XRD traces must be of ZrN. The stabilization of cubic zirconia phase in the AℓN-ZrO$_2$ composites during hot pressing, as observed in the present studies, is somewhat similar to an earlier observation that cubic ZrN, upon partial oxidation, forms "amorphous" cubic ZrO$_2$ phase[11].

It may be pointed out that XRD cannot detect the presence of a phase if its volume fraction is very small. Therefore, if any new phases are formed as a result of a chemical reaction between the constituent compounds of a material pair, and if the rate of this reaction is extremely slow, the reaction products may not be detected by XRD of the hot pressed specimens. In such cases, thermal ageing experiment of longer durations would be necessary. However, in view of the high temperatures at which the powder mixtures were hot pressed, the likelihood of a reaction being slow is small.

IV. b Oxidation Studies

The study of the oxidation behavior of composites is important because the rate of oxidation of a non-oxide ceramic may be influenced by the presence of other materials (oxide or non-oxide) in the composite. The oxidation studies were therefore carried out on the hot-pressed specimens of TiC, AℓN, TiC-Aℓ$_2$O$_3$, TiC-ZrO$_2$, TiC-TiB$_2$ and ZrC-ZrB$_2$. A thermogravimetry setup was used for these studies. In most cases, the

samples were oxidized in an atmosphere of flowing (50-100 mℓ/min) air, and in some cases, in an atmosphere of flowing pure oxygen (technical grade). The gases were passed over Drierite ($CaSO_4$) and phosphorous pentoxide before they entered the reaction tube. Most of the experiments were carried out in the temperature range $\sim$800-1000°C. In the case of the TiC-TiB_2 and $A\ell N$-$A\ell_2O_3$ composites, studies were also carried out at $\sim$1430°C using a thermogravimetric analysis/ differential thermal analysis (TGA/DTA) apparatus. The products of oxidation were characterized using X-ray diffraction.

IV. b.1 Oxidation of the TiC-$A\ell_2O_3$ and TiC-ZrO_2 Composites

The results obtained from the oxidation of pure TiC as well as the TiC-$A\ell_2O_3$ composites of various compositions are shown in Fig. 1-3. These results show that the oxidation of TiC, pure as well as embedded in a matrix of alumina, is a strong function of temperature. The plots in Fig. 1-3, show that the rate of weight gain of a sample increases with increasing percent TiC in the composite. This, however, does not imply that the rate of oxidation of TiC is greater in the composites containing larger weight fraction of titanium carbide. This is merely due to the fact that in the calculation of the weight gain per unit area, the surface area of the entire sample has been considered. It is obvious that the surface area of the TiC is only a fraction of the total surface area of the sample and is proportional to the volume fraction of TiC in the composite.

The activation energy for the oxidation of TiC has been estimated to

be 59 ± 6 kcal/mole. This is greater than the values $(46-49 \pm 2$ kcal/mole) reported earlier[6,7]. The value of the activation energy obtained in this work is comparable to the activation energy for the self diffusion of oxygen in TiO_2[8].

The effect of the partial pressure of oxygen on the rate of oxidation of TiC is shown in Fig. 4 and 5. It is found that the rate of oxidation increases with increasing partial pressure of oxygen. This is in agreement with the results obtained earlier by other investigators[7,9].

The rate of oxidation of TiC when present in a matrix of ZrO_2 was found to be several times greater than its rates of oxidation when embedded in a matrix of Al_2O_3. The compact became very fragile and sometimes even powdery after oxidation for 6 hours. Fig. 6 shows the results obtained from our studies. It should be pointed out that for the calculations of weight gain/unit area, the surface area of the entire sample has been considered. The actual surface area will be different from this in view of the fact that only a fraction of the surface is covered by the TiC and that, as a result of rapid oxidation, the sample may be crumbling and thereby exposing fresh surface to the atmosphere.

The oxidized specimens were characterized by XRD. In the case of the TiC-Al_2O_3 composites, the phases identified were TiO_2 (rutile) and Al_2O_3, while those in the case of the TiC-ZrO_2 composites were TiO_2 (rutile) TiC and ZrO_2 (monoclinic).

IV. b.2 <u>Oxidation of the AℓN-Aℓ$_2$O$_3$ and AℓN-ZrO$_2$ Composites</u>

The oxidation rates of the AlN-Al$_2$O$_3$ composites were found to be slower than those of the TiC-Al$_2$O$_3$ composites. Figs. 7 and 8 show the results obtained for the various compositions studied. It can be seen that the weight gain/unit area in the case of the composites containing up to 44 weight percent AlN increases with increasing weight fraction of AlN. The weight gain/area is, however, greater for the composite containing 80 weight percent AlN than it is for pure AlN. These results are similar to those obtained for the TiC-Al$_2$O$_3$ composites, and therefore the discussion pertaining to the TiC-Al$_2$O$_3$ system applies in this case, too.

The XRD results showed that the phases present in the oxidized specimen were AlN and Al$_2$O$_3$. No surface cracks were detected upon microscopic (optical) examination of the oxidized specimens. If one calculates the ratio of the volume of the Al$_2$O$_3$ formed to the volume of AlN oxidized, one obtains a value of 1.02. Therefore, the change in volume of the composite as a result of oxidation of AlN is very small.

The rate of oxidation of the hot pressed composite made from AlN and ZrO$_2$ powders (44 wt % AℓN and balance ZrO$_2$) was very rapid. The product of oxidation was in the form of a powder. This, at first, seemed surprising in view of the fact that the rate of oxidation of pure AlN and of AlN-Al$_2$O$_3$ composites was very slow. However, as stated earlier, the presence of ZrN and aluminum oxynitride phases was detected in these hot pressed composites. The oxidation rates

of ZrN have been reported to be very rapid[10,11]. The observed high rates of oxidation may, therefore, be due to the presence of ZrN in the composites. The results are shown in Fig. 9.

The XRD results showed that the phases present in the oxidation product are Al_2O_3 and ZrO_2 (monoclinic). It is interesting to note that, though the hot pressed specimens showed the presence of cubic zirconia, the cubic zirconia phase was transformed to the monoclinic phase during oxidation of the composite. This would seem to suggest that the stabilization of the cubic phase may possibly be due to the incorporation of small amounts of nitrogen in the lattice of zirconia.

IV. b.3 Oxidation of $TiC-TiB_2$ and $ZrC-ZrB_2$ composites

The oxidation behavior of $TiC-TiB_2$ composites was studied at 995^oC and 1430^oC. The rate of oxidation of a 20 $TiC-TiB_2$ composite at 995^oC as well as at 1430^oC was faster than that of pure TiC at the same temperature. The results obtained from XRD of the oxidized specimens showed that the product of oxidation was TiO_2. The B_2O_3 phase could not be detected. The rate of vaporization of B_2O_3 above 1050^oC is reported to be high, especially in the presence of moisture. It is, therefore, surprising that it could not be detected in a sample which was oxidized at 995^oC in dry air. Similar results were obtained in the case of the $TiC-TiB_2$ specimens oxidized at 1430^oC. Fig. 10 shows the TGA results.

The results obtained from the oxidation of pure ZrC and a 20 ZrC-ZrB$_2$ composite in air at 995^{0}C are shown in Fig. 11. It can be seen that the rate of oxidation of the ZrC-ZrB$_2$ specimen is slower than that of pure ZrC. The only phase detected in the oxidized specimens by XRD was monoclinic zirconia.

V. Summary and Conclusions

1. Analytical evaluations based on thermodynamic calculations indicate that

    (i) AℓN should be chemically compatible with a matrix of ZrB$_2$ or HfB$_2$, and possibly with TiB$_2$ also.

    (ii) TiC is compatible with TiB$_2$, but there exists the possibility that it may react with ZrB$_2$ and HfB$_2$.

    (iii) TiN should be compatible with a matrix of Aℓ$_2$O$_3$, ZrO$_2$ or HfO$_2$.

    As there is a large uncertainty in some of the reported thermodynamic data, it is suggested that these conclusions be verified experimentally.

2. Experimental results indicate that (i) TiC is compatible with a matrix of Aℓ$_2$O$_3$, ZrO$_2$ or HfO$_2$, and (ii) AℓN and TiB$_2$ are compatible with a matrix of Aℓ$_2$O$_3$ or HfO$_2$. However, the AℓN-ZrO$_2$ composites showed the presence of new phases (cubic ZrO$_2$, ZrN and, in some cases, aluminum oxynitride).

3. The conditions prevalent during hot pressing of $A\ell N$ + ZrO_2 powder mixtures in vacuum seem to be favorable for the stabilization of the cubic zirconia phase in the composite.

4. The rate of oxidation of TiC or $A\ell N$ is much more rapid when it is embedded in a matrix of ZrO_2 than when it is embedded in a matrix of $A\ell_2O_3$.

5. The rate of oxidation of a ZrC-ZrB_2 composite at $995^\circ C$ in air is much slower than the rate of oxidation of pure ZrC under identical conditions. The oxidation rate of a TiC-TiB_2 composite is, however, faster than that of pure TiC.

References

1. Metallurgical Thermochemistry, Fifth Edition, by O. Kubaschewski and C.B. Alcock, Pergamon Press, 1979.

2. JANAF Thermochemical Tables, Third Edition, by M.W. Chase, Jr., C.A. Davies, J.R. Downey, Jr., D.J. Frurip, R.A. McDonald and A.N. Syverud, American Chemical Society and American Institute of Physics, 1986.

3. Physical Chemistry of High Temperature Technology, by E.T. Turkdogan, Academic Press, 1980.

4. A. Mocellin and G. Bayer, Journal of Materials Science, 20, 3697-3704 (1985).

5. G.M. Mehrotra, "Compatibility of Reinforcement and Matrix Phases in Composite Materials for High-Temperature, Aerospace Applications," Final Report, 1986 USAF-UES Summer Faculty Research Program.

6. E. Nikolaiski, Z. Physikalische Chemie, N.F., 24, 405-417 (1960).

7. M. Reichle and J.J. Nickl, Journal of Less Common Metals, 27, 213-236 (1972).

8. Nonstoichiometry, Diffusion, and Electrical Conductivity in Binary Metal Oxides, by Per Kofstad, Robert E. Krieger Publishing Company, 1983.

9. V.A. Lavrenko, L.A. Glebore, '..P. Pomitkin, V.G. Chuprina and T.G. Protsenko, Oxidation of Metals, 9(2), 171-179 (1975).

10. Engineering Property Data on Selected Ceramics, Vol. I (Nitrides), Metals and Ceramics Information Center, Battelle, Columbus, 1976.

11. D.R. Glasson and S.A.A. Jayaweera, J. Applied Chemistry, 19, 182-184 (1969).

12. M.P. Gordova, et al., Tr. Mosk. Khim-Technal. Inst., 82, 76-78 (1974).

Acknowledgement

I would like to thank the U.S. Air Force Office of Scientific Services, Bolling AFB, DC, for the sponsorship of this work, and the Universal Energy Systems, Dayton, Ohio, for the award of a contract to carry out this research. The laboratory facilities for hot pressing of ceramic powders and for high temperature TGA/DTA experiments were provided by the AFWAL/MLLM, Wright-Patterson Air Force Base, Dayton, Ohio, and I would like to thank all the staff members of the AFWAL/MLLM, especially Mr. E.E. Hermes and Drs. A.P. Katz and R. Kerans, for their help. I would also like to thank my students, Mr. M. Subramanian, Mr. M. Dennis Petry and Mr. Jeff McDowell for their assistance with the experimental work, and Mrs. Suellen Grieshop and Mrs. Nancy Lockwood for their help in typing this report.

A:TIC.AL2O3(10:90) B:TIC.AL2O3(20:80)
C:TIC.AL2O3(30:70) D:TIC.AL2O3(34.5:65.5)
E:TIC.AL2O3(90:10) F:TIC
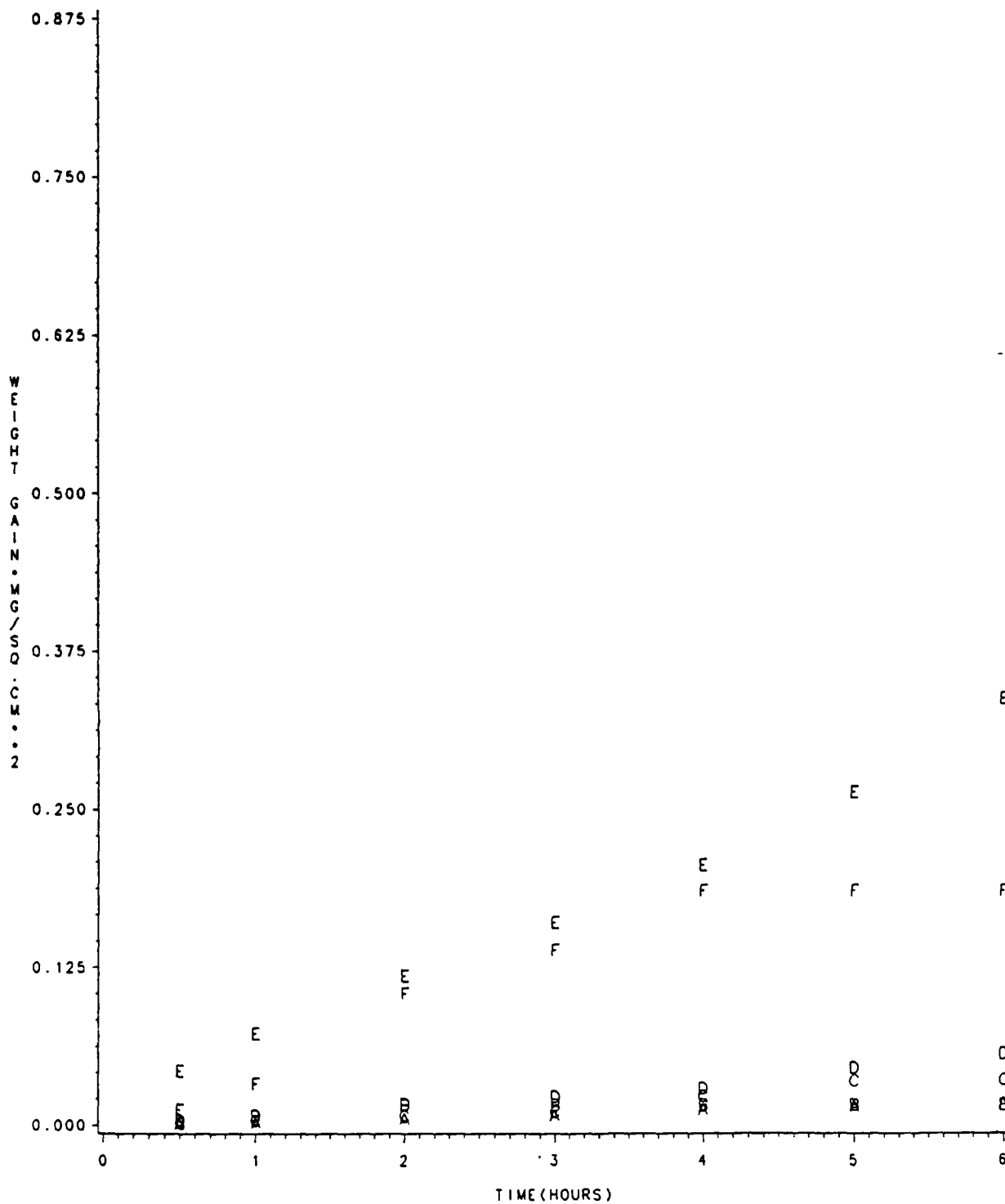
Fig.1. Oxidation of TiC- Al_2O_3 Composites in
air at 800°C.

A:TIC.AL2O3(10:90) B:TIC.AL2O3(20:80)
C:TIC.AL2O3(30:70) D:TIC.AL2O3(34.5:65.5)
E:TIC.AL2O3(90:10) F:TIC
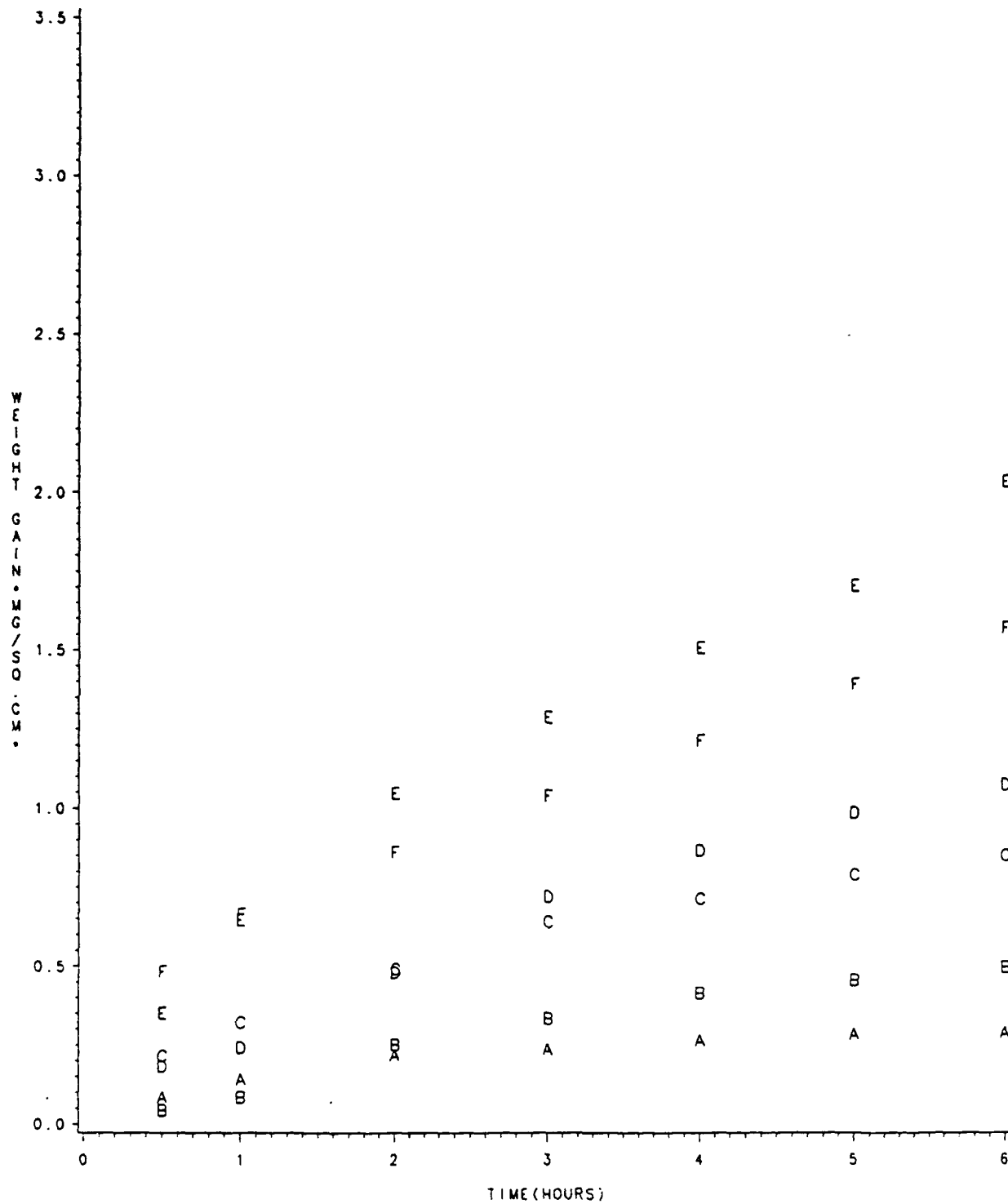
Fig.2. Oxidation of TiC - Al$_2$O$_3$ composites in air at 900°C.
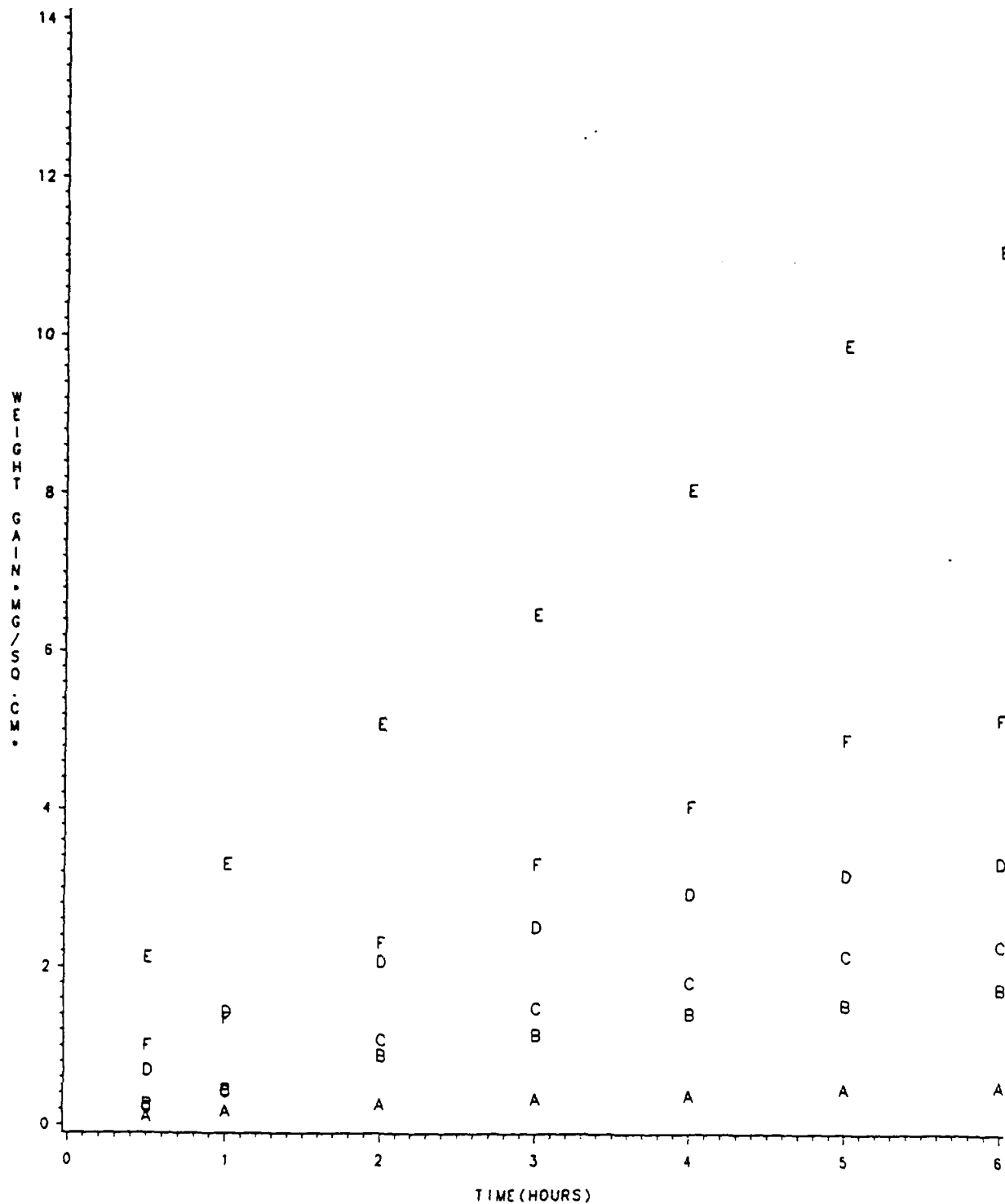
Fig.3. Oxidation of TiC- Al_2O_3 composites in air at 995°C.
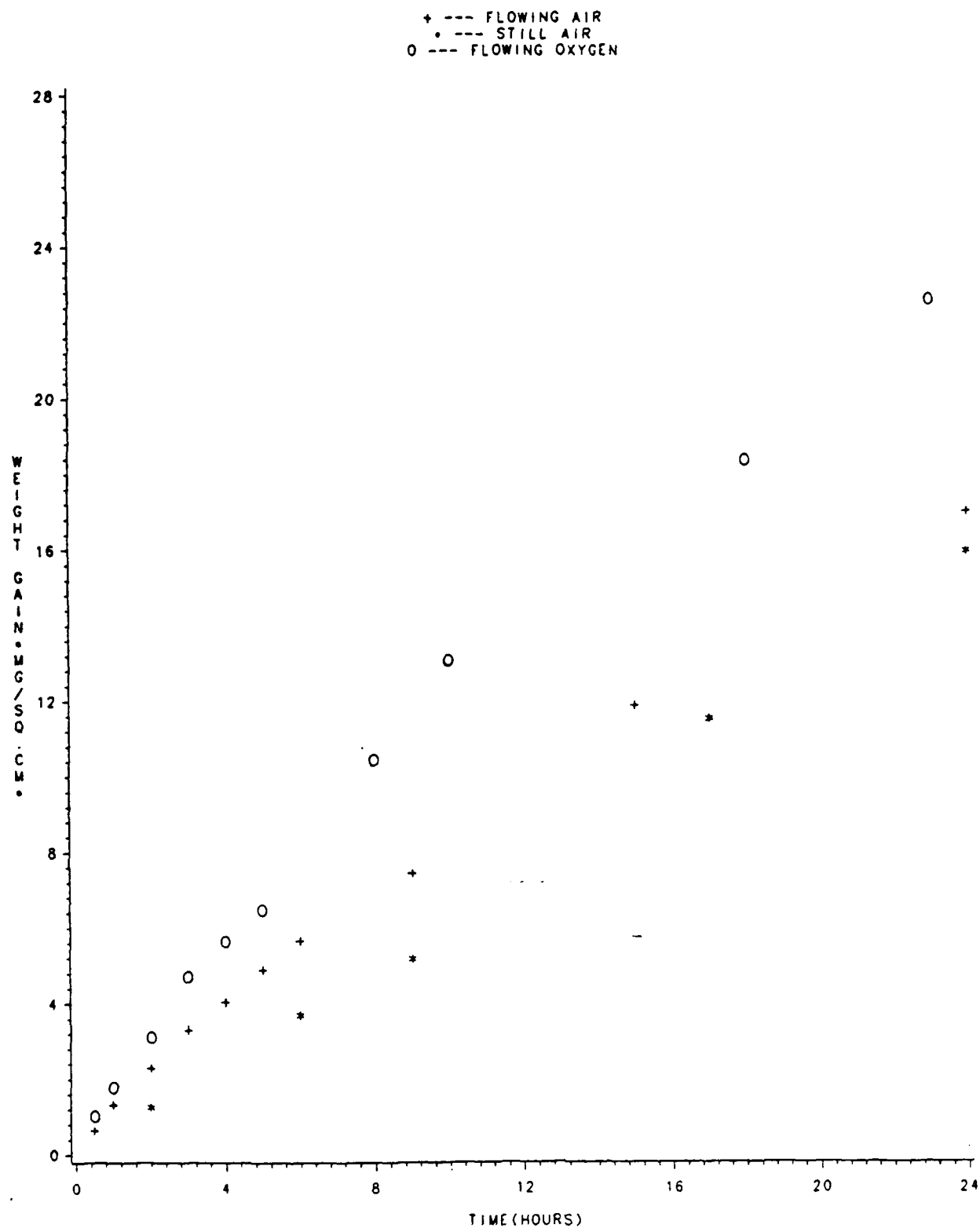
Fig.4. Oxidation of TiC at 995°C in Air and in Oxygen.

WEIGHT GAIN.MG/SQ.CM.

TIME(HOURS)
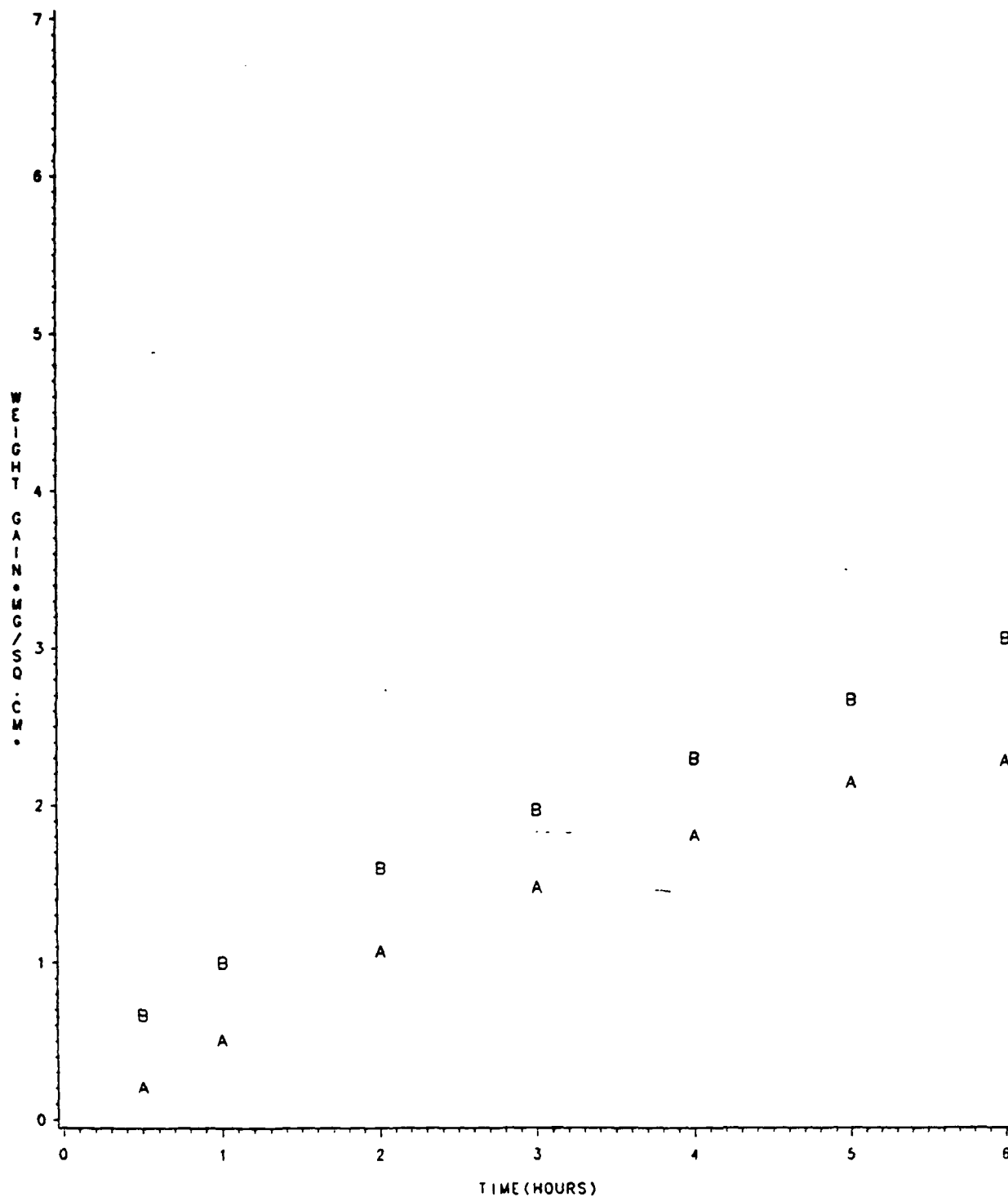
Fig.5. Oxidation of 30 wt% TiC-Al$_2$O$_3$ composite at 995°C
in Air and in Oxygen.
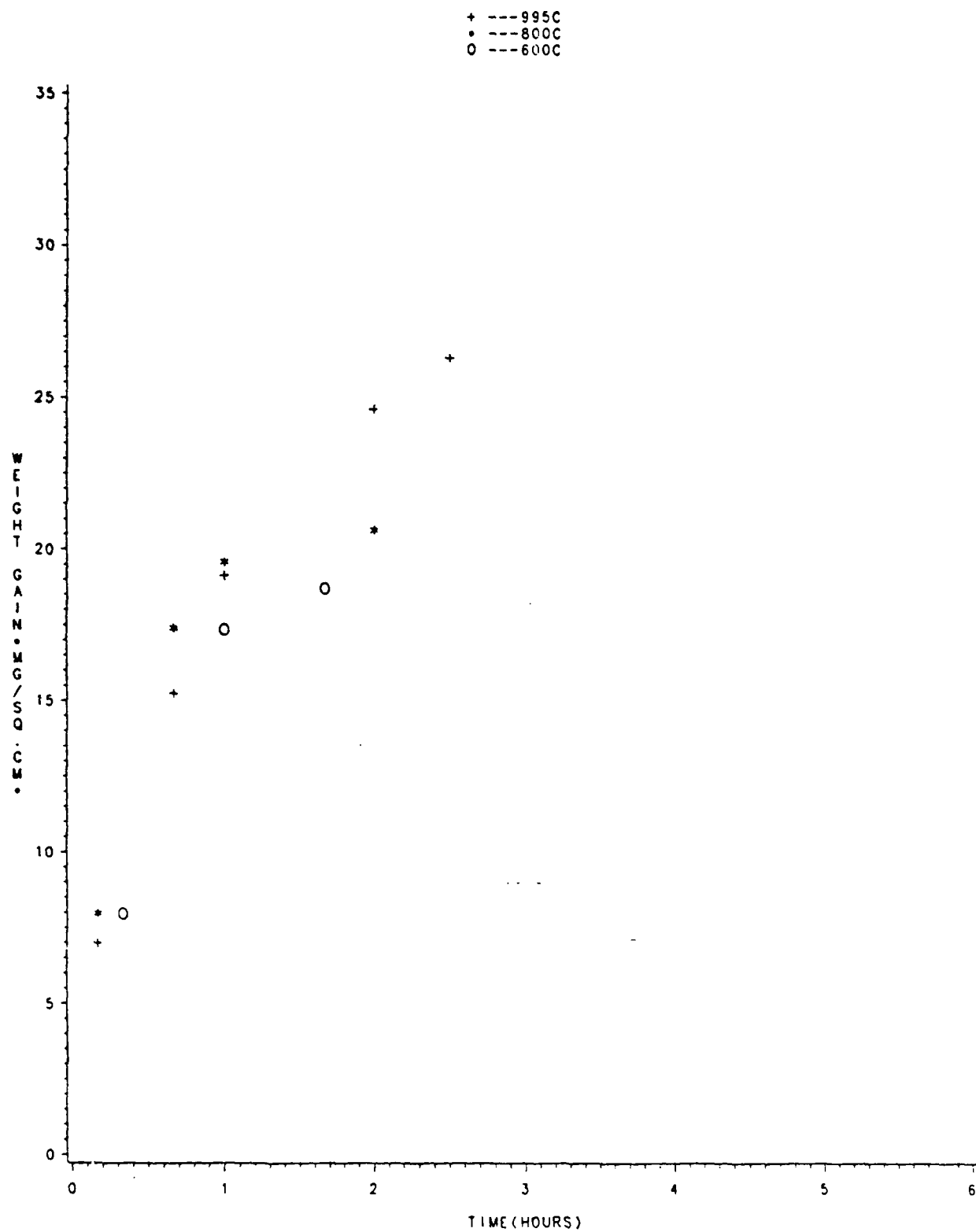
Fig.6.   Oxidation of a 20 wt% TiC-ZrO$_2$ composite in Air.

A:ALN.AL2O3(10:90) B:ALN.AL2O3(20:80)
C:ALN.AL2O3(44:56) D:ALN.AL2O3(80:20)
E:ALN
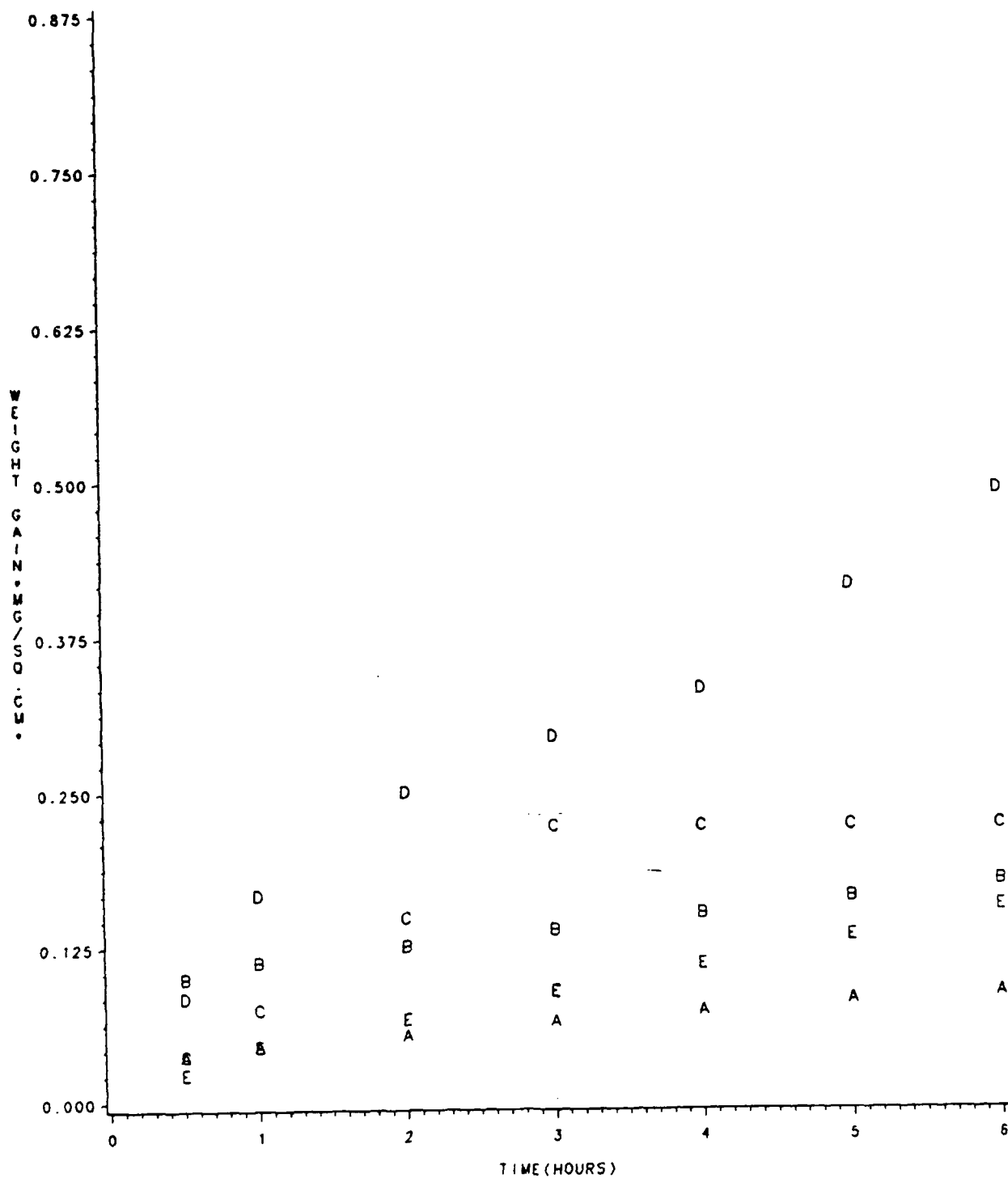
Fig.7.   Oxidation of AlN and AlN-Al$_2$O$_3$ composites at 900°C in air.

A:ALN.AL2O3(10:90) B:ALN.AL2O3(20:80)
C:ALN.AL2O3(44:56) D:ALN.AL2O3(80:20)
E:ALN
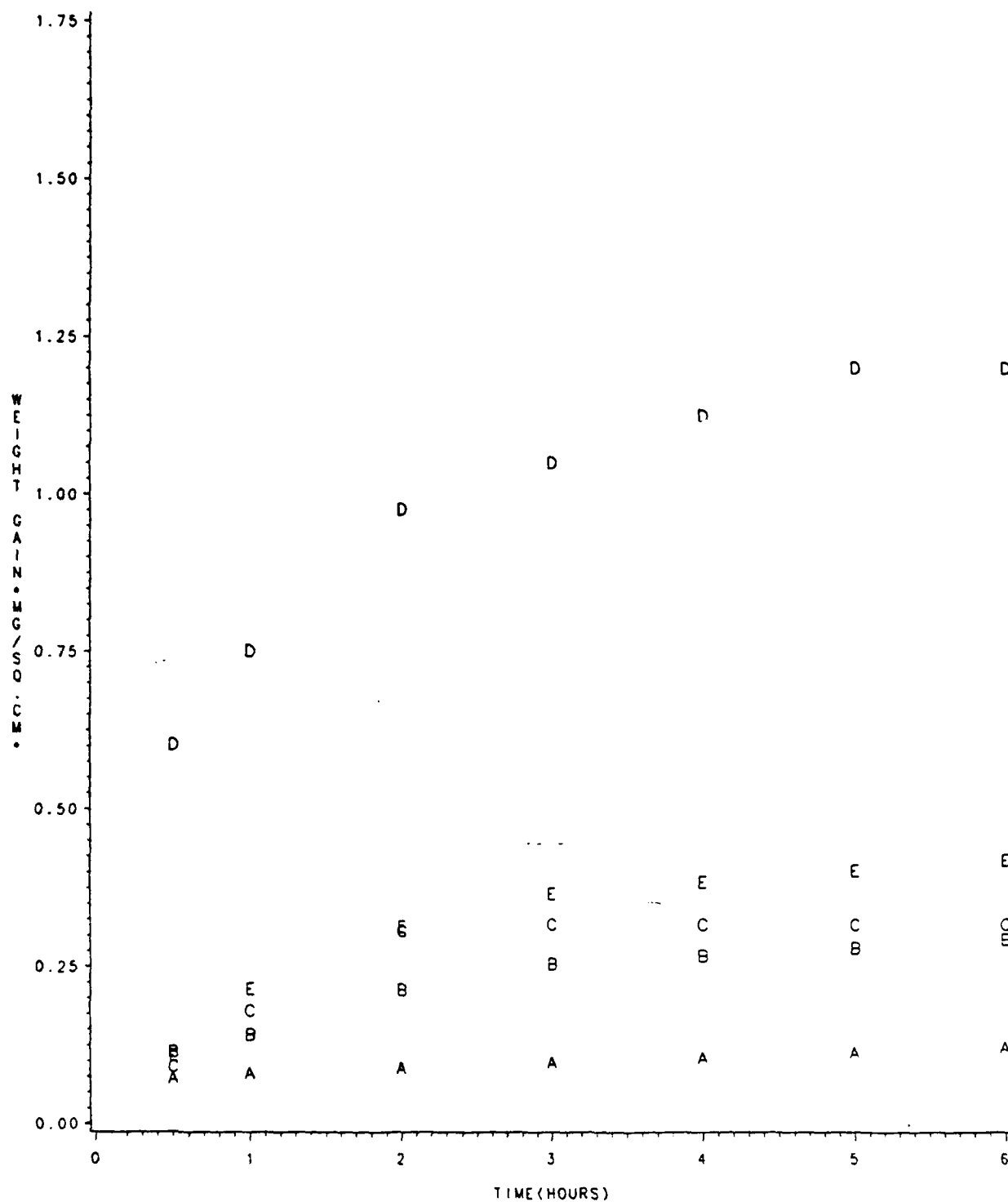
Fig.8. Oxidation of AlN and AlN-Al$_2$O$_3$ Composites in air at 995°C.
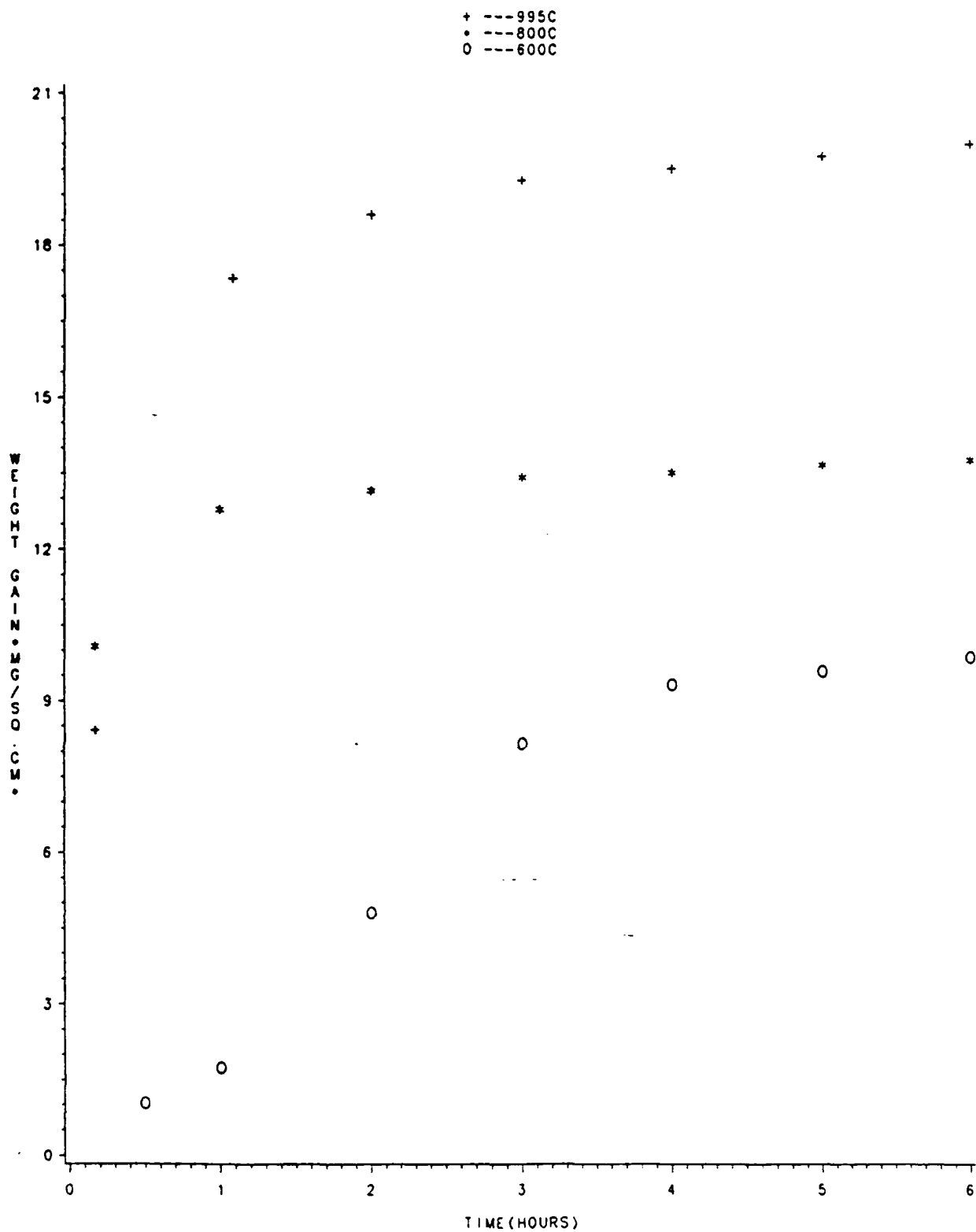
Fig.9. Oxidation of a 42 wt% AlN-ZrO$_2$ composite in air.
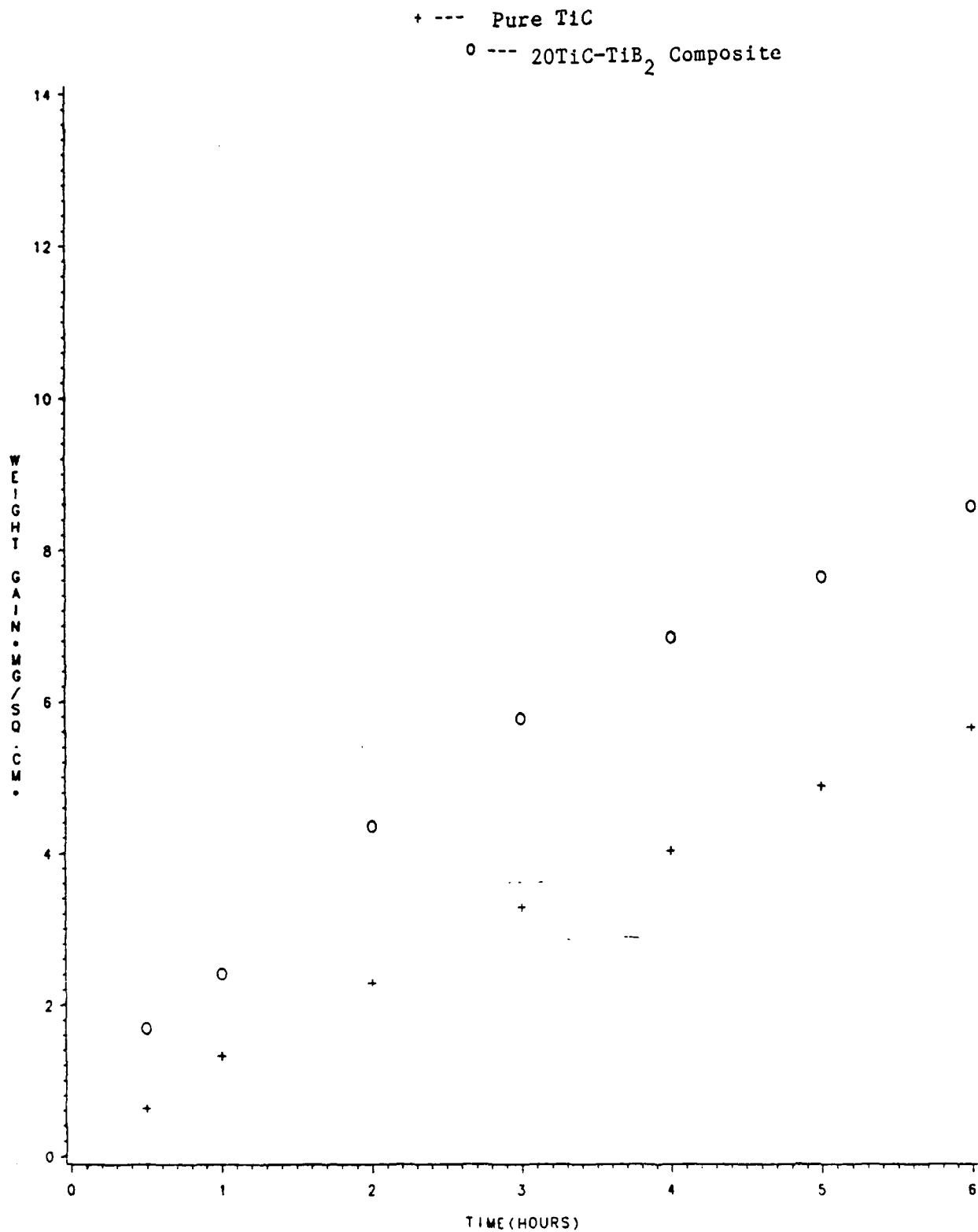
Fig.10. Oxidation of a TiC – TiB_2 composite at 995 $^\circ$C in air.
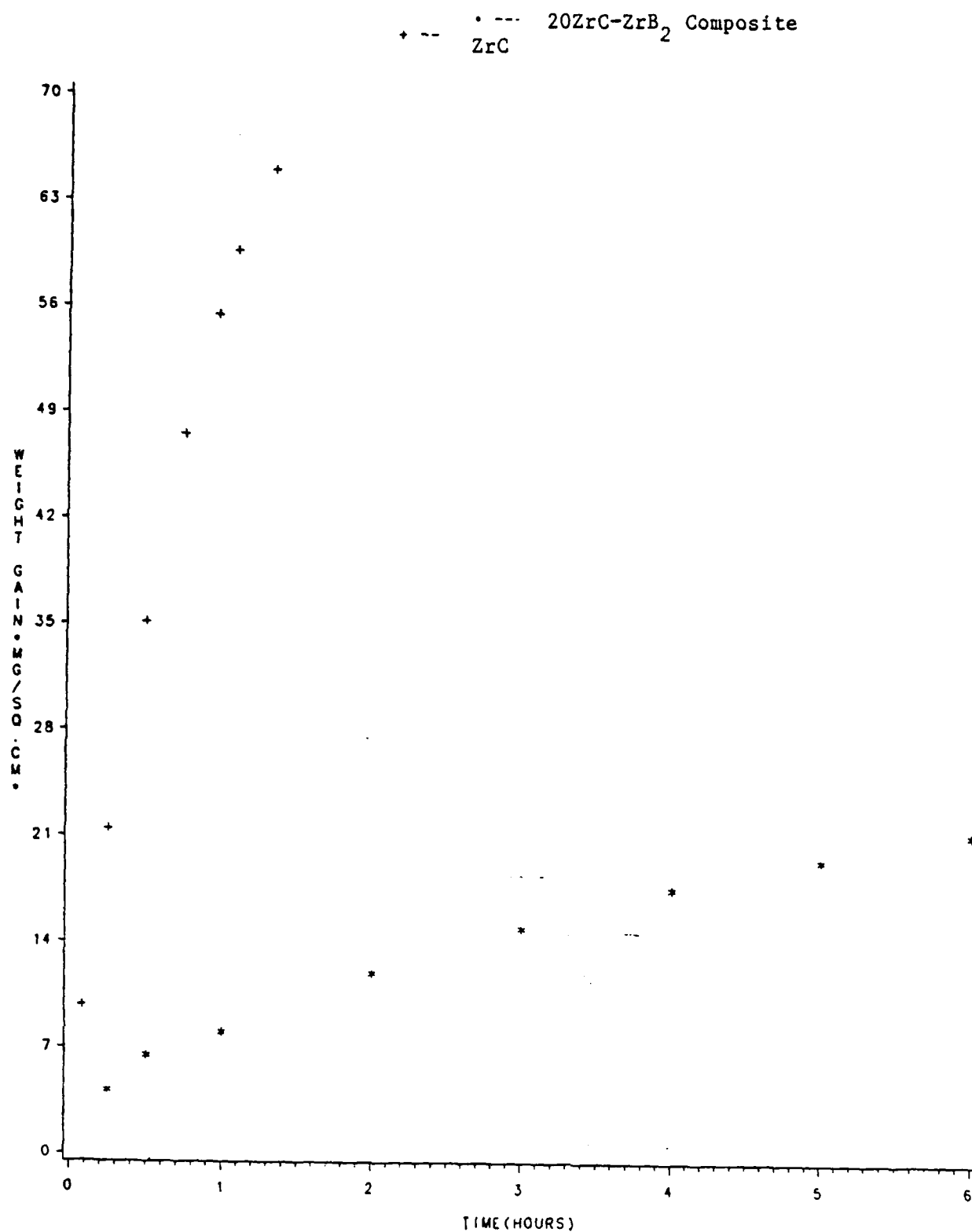
Fig.11. Oxidation of ZrC and a 20 wt% ZrC-ZrB$_2$ composite at 995 $^{\circ}$C in air.

RESEARCH INITIATION PROGRAM

F I N A L   R E P O R T

Synthesis of Compounds Capable of Intramolecular

Cyclization - Aromatization Reactions

Principal Investigator: Robert A. Patsiga

Home Institution: Indiana University of Pennsylvania

Award Period: January 1 to December 31, 1987

Supporting Agency: Air Force Office of Scientific Research

Administrative Agency: Universal Energy Systems

SUMMARY

This research is aimed at synthesizing two diene-yne compounds which are to be studied for their cylization-aromatization ability. The two compounds should give meta- and para-terphenyl if aromatization is successful. Future development of these systems is intended for the production of thermally stable polymers.

The diene-yne 1,5-diphenyl-1-hexyne-3-5-diene, a compound that should give m-terphenyl when heated, has been synthesized by two routes. One route converts atropaldehyde to 1-bromo-3-phenylbutadiene by a Wittig reaction and this product is then coupled with phenylacetylene. The second route involves only one step in which atropaldehyde reacts with the ylide based on 3-bromo-1-phenylpropyne. The second route gives the diene-yne in greater yield and in purer form although elemental analysis and mass spectral analysis indicate the presence of impurities.

The synthetic route to 1,4-diphenyl-1-hexyne-3,5-diene a compound that should give p-terphenyl when heated, has been only partially completed. Atropaldehyde has been successfully brominated to give 2,3-dibromo-2-phenylpropanal. The dehydrobromination of this compound is currently under study.

STUDENT-COLLEAGUES

Michael A. Buben, graduate student involved during summer 1987

Marty Stern, undergraduate student involved during summer 1987

Elizabeth M. Zippi, undergraduate student involved during spring 1987

I. INTRODUCTION

The thermal and chemical stability of aromatic systems has motivated considerable effort over the years toward the preparation of all-aromatic polymers. These are polymers which contain no aliphatic or other non-arylene linking units along the backbone of the polymer chain. In a sense, the epitome of these types of polymers is poly (paraphenylene), I, as well as its ortho and meta isomeric forms. Poly (p-phenylene) has been prepared by a number of routes. For example, most notably it has been obtained from the aromatization of poly (1,3-cyclohexadiene) by

I
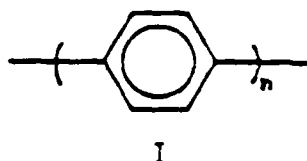
Marvel (1), by the coupling of benzidinetetrazonium chloride (2), by the reaction of 1,4-dilithiobenzene with titanium, vanadium or cobalt (3), and by the oxidative coupling of benzene (4); the latter an innovative method developed by Kovacic and co-workers.

Poly (p-phenylene) as generally prepared by the above methods has been found to be a brown, insoluble and infusible material having fiber-forming capability. It is stable in air to 500°C and to 700°C in an inert atmosphere (4). Reliable molecular weight values have not been obtained for these polymers owing to their insolubility.

There are a number of drawbacks to the above synthetic routes. Often the polymers are obtained having extraneous elements (nitrogen, chlorine) as the result of concurrent side reactions, or branching may occur. The mechanical properties have also been found to be disappointing which may be due to incomplete aromatization or to low molecular weight.

A continuing effort has been put forward at the Polymer Branch of the Materials Laboratory at Wright-Patterson Air Force Base toward the synthesis of polyarylene polymers. The objective has been the preparation of a pre-polymer that is soluble and processable and which upon heating (curing) would give an all-aromatic structure. An all-paraphenylene system would give a rigid rod configuration having the potential to act as internal reinforcement as discrete molecules (molecular composite concept). Certain proportions of meta or ortho configurations in the structure might improve processability. For maximum effectiveness the pre-polymer cure concept for preparation of arylene polymers demands certain requirements:

1) No volatile substances should be evolved during the curing process.

2) No catalysts (especially metals) should be required for the cure.

3) The curing reaction should involve as little translational molecular motion as possible.

Requirements 1) and 2) are needed so that residual artifacts of the curing process (gas bubbles, metals from a catalyst) do not cause weakness in the structure or promote chemical decomposition. Requirement 3) is a kinetic one. It results from the fact that the unreacted portion of the functional groups taking part in the curing reaction become immobilized as curing progresses. This can be compensated for only by increasing the temperature of the curing process so that chain translational mobility is increased. The result of this is that the use temperature of the polymer (glass temperature) can be no higher than the maximum cure temperature employed.

In order to minimize the translational motion required in the curing process, the concept at the WP Polymer Branch has been to investigate systems which possess reacting groups located in close proximity to each other. These groups are to be designed to yield aromatic structures by an intramolecular cyclization process.

Some success has been achieved (5) with 2,2'-bis(phenylethynyl) biaryl systems such as II. These have been found to cyclize upon heating to give dibenzoanthracene

$$\text{II} \quad\xrightarrow{\Delta}\quad \text{III} \qquad Eq. 1$$
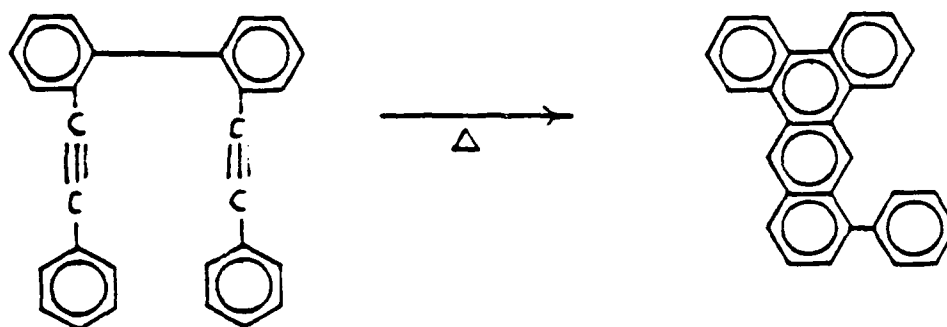
structures (III). When the diethynyl biaryls were incorporated into the backbone of poly(phenylquinoxalines), it was possible to obtain a cured polymer having a glass temperature at least one hundred degrees higher than the cure temperature.

Continued effort along these lines has been aimed at synthesizing certain model diene-yne systems which could be examined for intramolecular cyclization ability. During the summer of 1986, the writer was engaged at WPAFB in attempts to prepare compounds IV, V, and VI which were intended for study of cyclization-aromatization. It is hoped that these compounds will form the aromatic structures shown in equations 2, 3, and 4. The approaches taken to prepare these compounds are summarized in schemes 1 and 2.

$$Eg. 2$$

$$Eg. 3$$
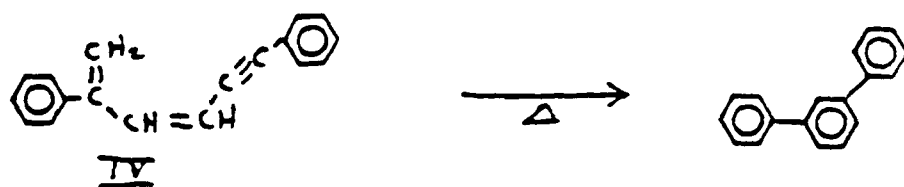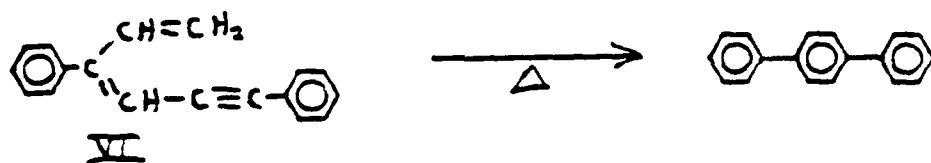
$$Eg. 4$$

These studies revealed that these approaches are generally not feasible. The attempt to convert the bromoketone, XI to the bromodiene, XIII, (Scheme 1) by a Wittig reaction resulted in dehydrobromination (reversion back to compound VIII).

Scheme 1

$$\text{Ph-C(=O)-Cl} + \text{HC}\equiv\text{C-R} \xrightarrow{\text{PdCl}_2(\phi_3P)_2} \text{Ph-C(=O)-C}\equiv\text{C-R}$$

$$\text{VII, } R = \text{SiMe}_3 \text{ ; } \text{VIII, } R = C_6H_5$$

$$\downarrow \text{HBr}$$

$$\text{Ph-C(=O)-C}\equiv\text{C-SiMe}_3 \xrightarrow{\text{K}_2\text{CO}_3} \text{Ph-C(=O)-C}\equiv\text{CH}$$

$$\text{VII} \qquad\qquad \text{IX}$$

$$\downarrow \text{HBr}$$

$$\text{CrO}_3 \nearrow$$

$$\text{Ph-C(=O)-CH=C(Br)-R'}$$

$$\text{Ph-C(=O)-H} \xrightarrow[\text{② } H_2O]{\text{① LiC}\equiv\text{CH}} \text{Ph-C(OH)(H)-C}\equiv\text{CH}$$

$$\text{XII} \qquad\qquad\qquad \text{X, } R' = H$$
$$\text{XI, } R' = C_6H_5$$

$$\phi_3P=CH_2 \searrow$$

$$\text{Ph-C(=CH}_2)\text{-CH=C(Br)-R'} \xrightarrow{\text{HC}\equiv\text{C-Ph, Pd catalyst}}$$

$$\text{XIII}$$

$$\text{Ph-C(=CH}_2)\text{-CH=C(R')-C}\equiv\text{C-Ph}$$

$$\text{IV, } R' = H$$
$$\text{I, } R' = C_6H_5$$
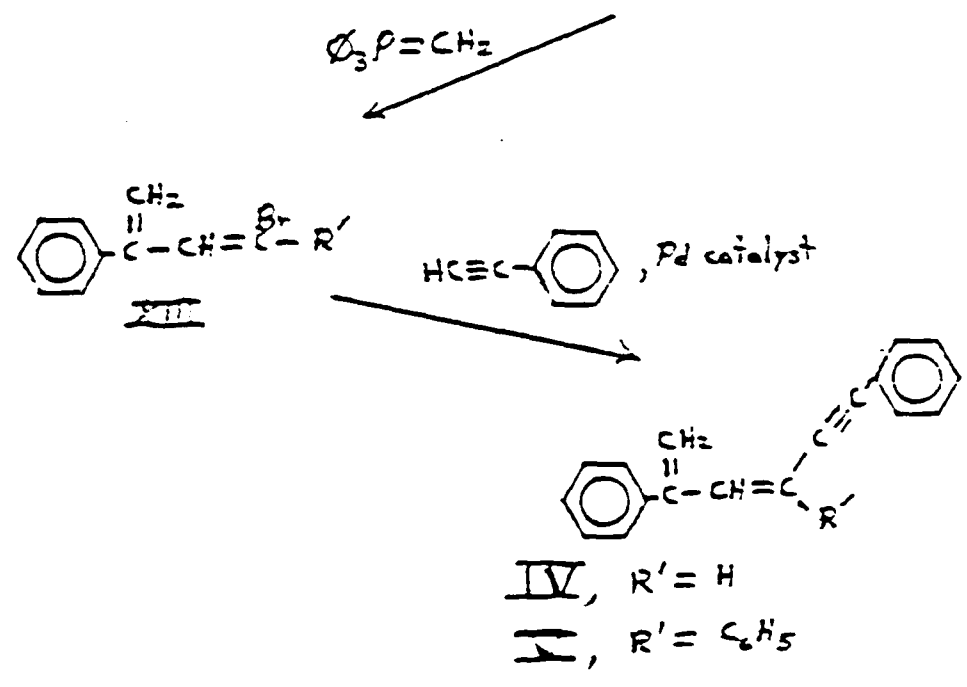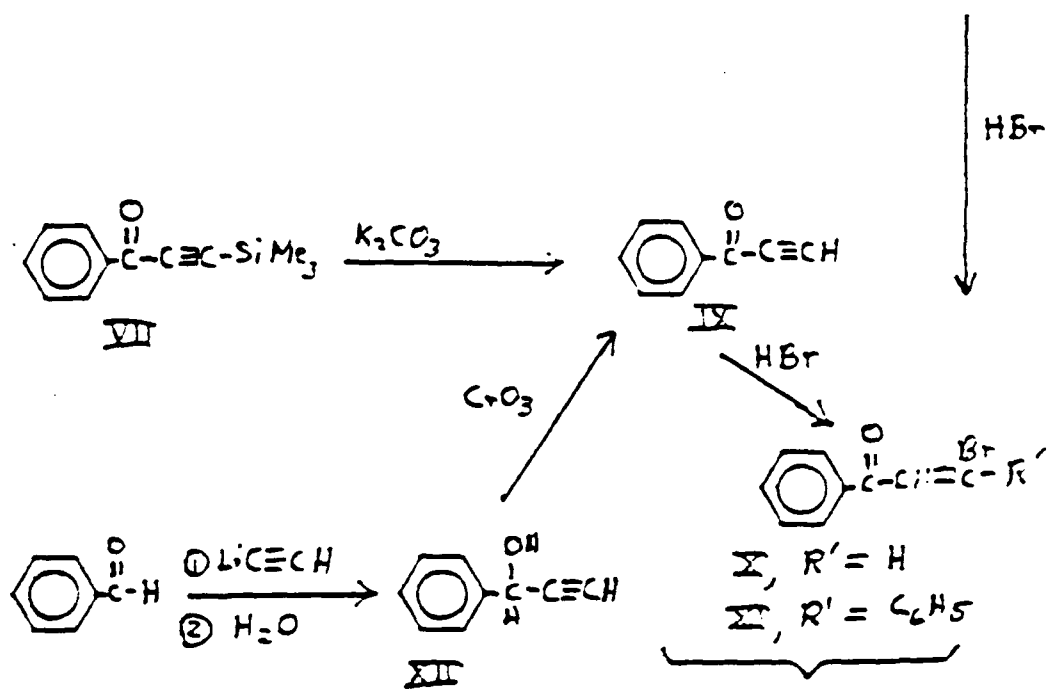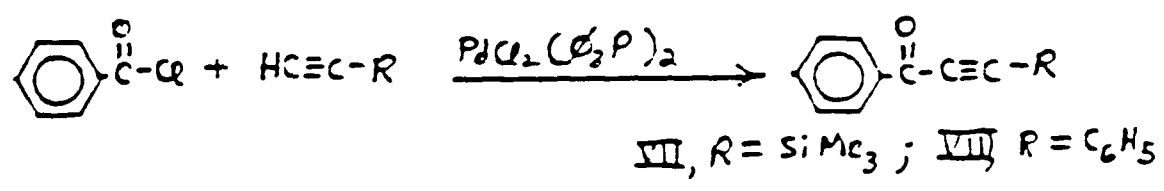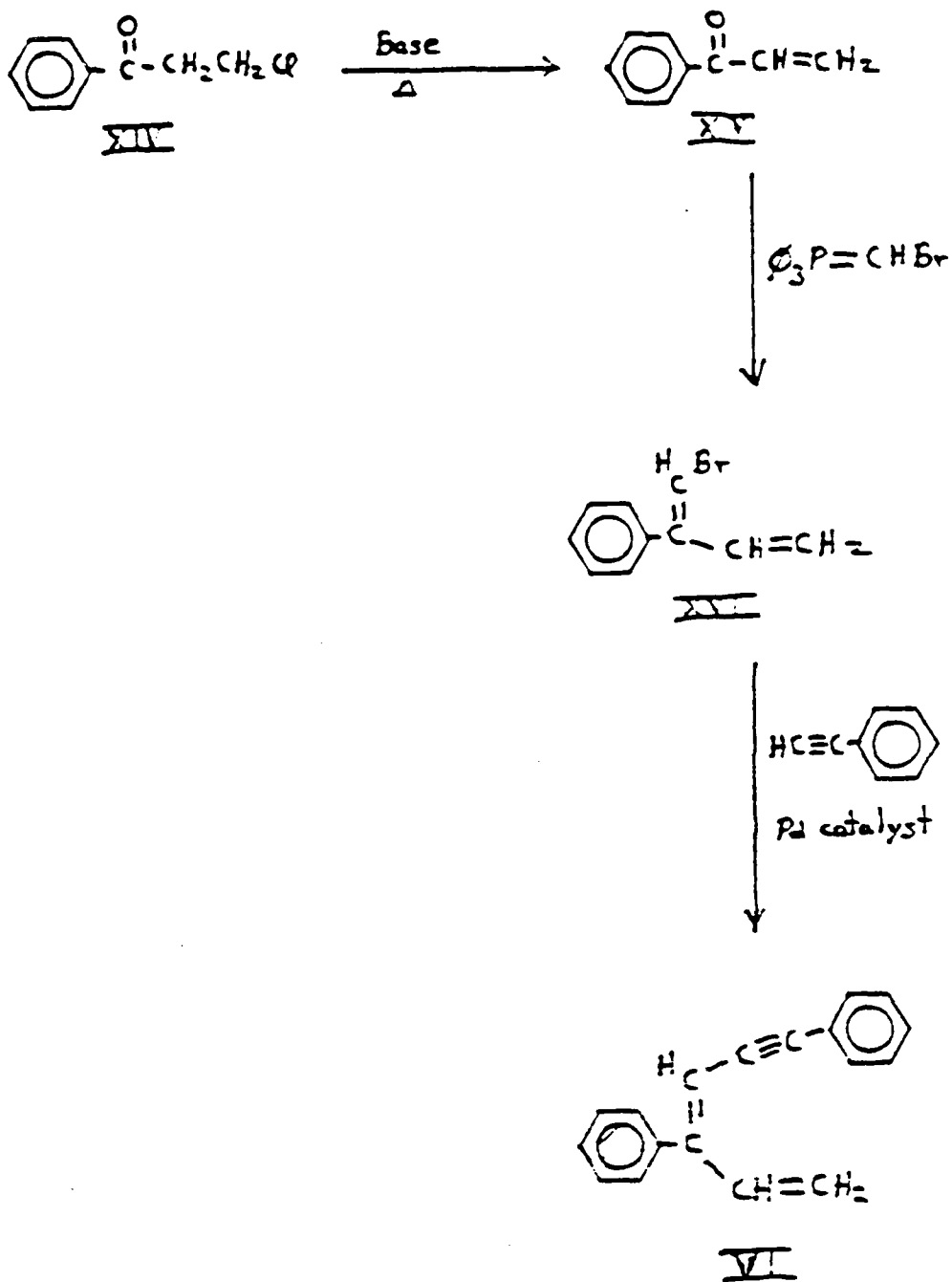
Scheme 2

Also, it was not possible to prepare the acetylenic ketone, IX. In Scheme 2,
viny'phenyl ketone, XV, proved to be so susceptible to polymerization that it was
not possible to carry out its conversion to the bromodiene, XVI, even when
performing the Wittig reaction at -78°.

Ketones behave in a much more sluggish manner in Wittig reactions than do
aldehydes. Also, the basic nature of the ylide used in the Wittig synthesis opens
a possibility for side reactions that become more likely vis-a-vis the desired
reaction with the ketone group. The proposed research is directed at preparing
compounds IV and VI by route: involving Wittig reactions with aldehydes rather than
ketones.

II. APPROACH

The synthesis of the diene-yne compounds IV and VI was attempted utilizing the
α, β-unsaturated aldehyde, atropaldehyde as the starting material (Schemes 3, 4,
and 5). This aldehyde is a white solid which tends to decompose (polymerize ?) if
kept for long times (> 4 hr.) at room temperature, but it can be stored up to three
weeks at -20°. Atropaldehyde can be prepared, as needed, utilizing the procedure
of Crossland (6) (see Scheme 6).

The preparation of compound IV followed two paths as shown in Schemes 3 and 5.
Scheme 3 begins with atropaldehyde and in two steps yields the desired diene-yne.
The first step is a Wittig reaction with bromomethylenephosphorane (ylide) to give
the bromodiene XVII. This is then coupled with phenylacetylene using a procedure
developed at WPAFB (7) to give diene-yne. The second path, shown in Scheme 5,
involves a Wittig reaction between atropaldehyde and the ylide obtained from
3-bromo-1-phenylpropyne (XXII and XXIII).

The approach to compound VI is shown in Scheme 4. This involves the
preparation of bromodiene XX by bromination of atropaldehyde followed by

Scheme 3

$$\underset{\text{Atropaldehyde}}{\phi\overset{\overset{CH_2}{\|}}{\underset{}{C}}-CHO} \quad \xrightarrow[\text{THF , } -78^\circ]{\phi_3 P=CHBr} \quad \underset{XVII}{\phi\overset{\overset{CH_2}{\|}}{\underset{}{C}}-CH=CHBr} \quad + \quad \phi_3 P=O$$

$$\downarrow \begin{array}{l} HC\equiv C-\phi \\ (\phi_3 P)_2 PdCl_2/CuI \\ Et_3 N , \text{ Room Temp} \end{array}$$

$$\underset{IX}{\phi\overset{\overset{CH_2}{\|}}{\underset{}{C}}-CH=CH-C\equiv C-\phi} \quad + \quad Et_3 NHBr$$

Scheme 4

$$\phi\overset{\overset{CH_2}{\|}}{\underset{}{C}}-CHO \quad \xrightarrow[CCl_4]{Br_2} \quad \underset{XVIII}{\phi\overset{\overset{CH_2Br}{|}}{\underset{Br}{C}}-CHO} \quad \xrightarrow{\text{Base}} \quad \underset{XIX}{\phi\overset{\overset{CHBr}{\|}}{\underset{}{C}}-CHO}$$

$$\downarrow \phi_3 P=CH_2$$

$$\underset{XX}{\phi\overset{\overset{CHBr}{\|}}{\underset{}{C}}-CH=CH_2} \quad + \quad \phi_3 P=O$$

$$\downarrow \begin{array}{l} HC\equiv C-\phi \\ (\phi_3 P)_2 PdCl_2/CuI \\ Et_3 N , \text{ Room Temp} \end{array}$$

$$\underset{XI}{\phi\overset{\overset{CH-C\equiv C-\phi}{\|}}{\underset{CH=CH_2}{C}}} \quad + \quad Et_3 NHBr$$

Scheme 5

$$
\underset{\substack{\text{(Ph)} \\ \|}}{\overset{\overset{CH_2}{\|}}{C}}\!\!-CHO \ + \ \emptyset_3 P = CH-C \equiv C-\text{(Ph)} \xrightarrow{\text{THF, 0°}}
$$

XXIII

$$
\underset{\substack{\text{(Ph)} \\ \|}}{\overset{\overset{CH_2}{\|}}{C}}\!\!-CH=CH-C \equiv C-\text{(Ph)}
$$

IV

$+ \ \emptyset_3 P = O$

$\emptyset_3 P$

$BrCH_2-C \equiv C-\text{(Ph)}$

XXII

PBr_3

$HO\text{-}CH_2-C \equiv C-\text{(Ph)}$

XXI
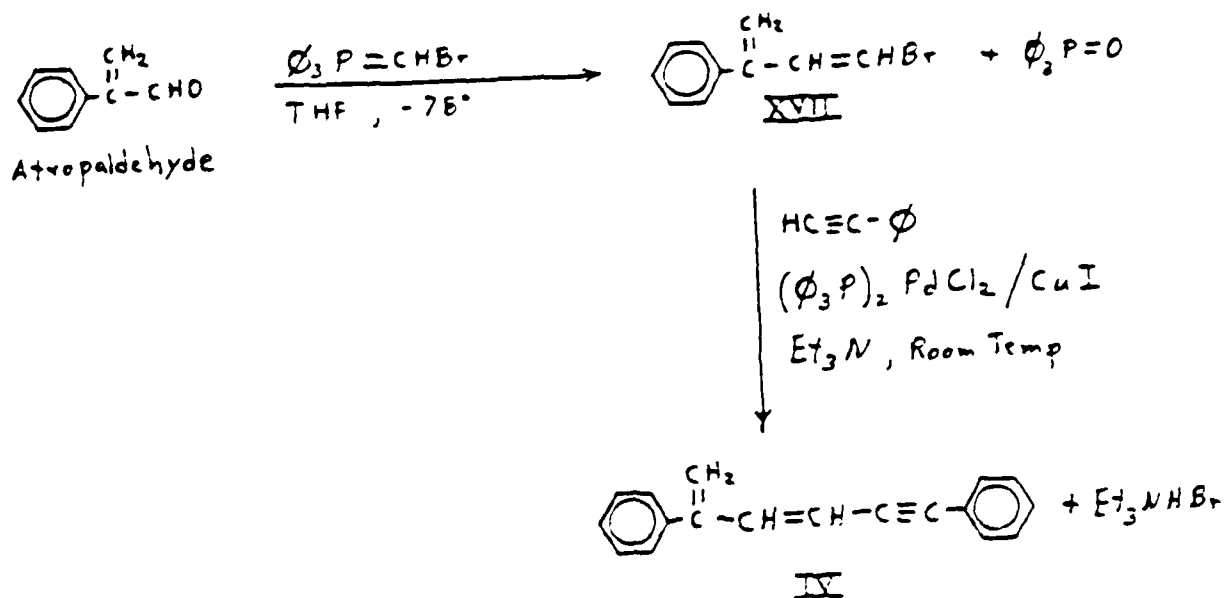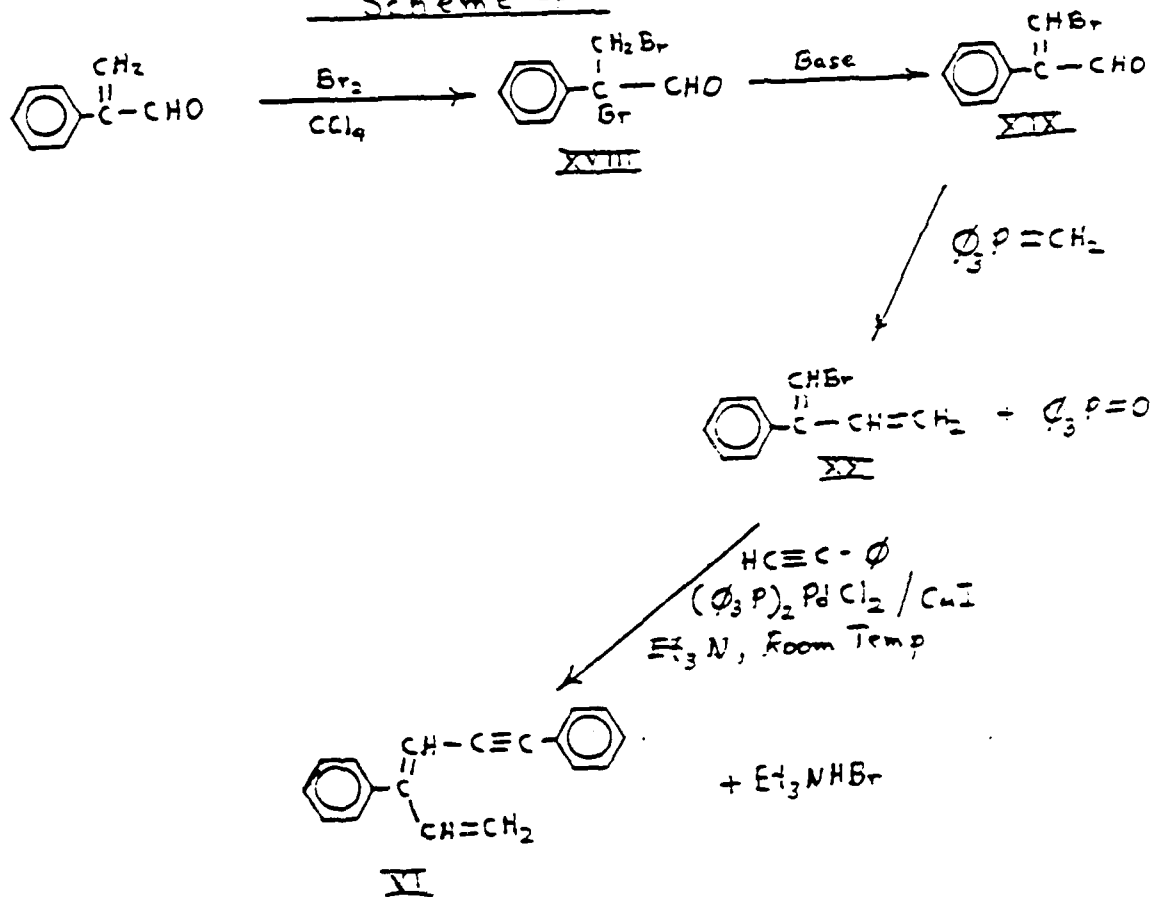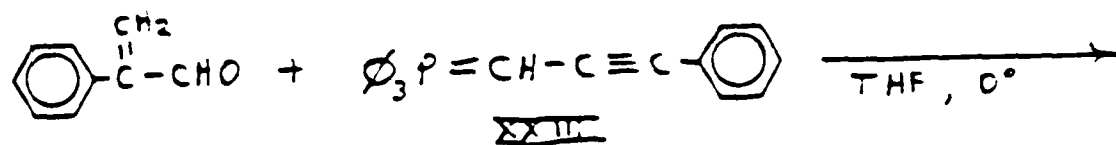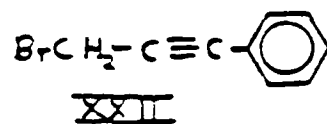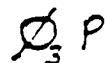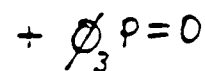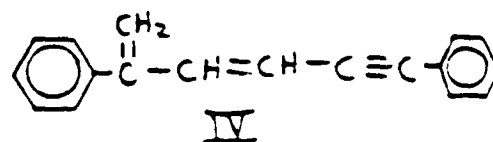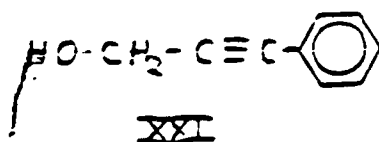
dehydrobromination and a Wittig reaction. The bromodiene is then coupled with
phenylacetylene as in Scheme 3.

Some of the intermediate and products occurring in these procedures contain
double bonds capable of existing in two geometric (cis-trans) forms. In these
preliminary experiments no attempt is made to determine stereochemical identity or
to perform stereospecific reactions.

III. EXPERIMENTAL PROCEDURES

Atropaldehyde: The procedure of Crossland (6) was followed without major
modification (Scheme 6). Infrared and proton NMR spectra of intermediates and
products were consistent with the expected structures. The last step, the
hydrolysis of the acetal with formic acid/water, had to be done quickly and all
reagents had to be pre-chilled before use. Crystallization of the atropaldehyde
from diethyl ether/petroleum ether was accomplished using a chloroform slush bath
(-63°). The white, crystalline solid melted at 33-38° (Lit.: 38-40°). Samples of
atropaldehyde were prepared in 8-10 g batches which were then stored at -18° until
used (storage generally not longer than two weeks).

Triphenylbromomethylphosphonium bromide: This salt was used in Scheme 3 to
prepare bromodiene XVII. The procedure of Wolinsky and Erickson was followed (8).
Dibromomethane (45.9 g, 0.264 moles), triphenylphosphine (30.1 g, 0.115 moles) and
250 mL dry toluene were refluxed for three hours. The mixture was cooled and
poured off from the small amount of dark brown oil that formed. The supernatant
was then refluxed for an additional 21 hours, cooled to room temperature and the
solid isolated by filtration. A second crop of solid could be obtained by an
additional 24 hour reflux. The combined solids were pumped for 4 hours at 48° to
give 21.7 g of tan solid (43%), mp 227-234° (Lit.: 240-241). Recrystallization
using acetone/water or isopropyl alcohol gave crystals with mp 238-243° and
237-244° respectively.

Scheme 6

Preparation of 2-Phenylpropenal ("Atropaldehyde") Procedure of
I. Crossland, "Organic Synthesis", vol 60, pp 6-10, 1981

$$\text{Ph-CH=CH}_2 + CHCl_3 + NaOH \xrightarrow[\text{H}_2\text{O}, 40\text{-}60°]{\varnothing CH_2(Et)_2 NCl} \quad \text{Ph-CH—CH}_2 \underset{\underset{CCl_2}{|\quad\quad|}}{} + NaCl$$

$$\underline{\text{XXIV}}$$

$$\downarrow \begin{array}{l} C_2H_5OH \\ NaOH \\ Reflux \end{array}$$

$$\text{Ph-}\underset{\underset{C}{||}}{\overset{CH_2}{}}\text{—CH}(OC_2H_5)_2$$

$$\underline{\text{XXV}}$$

$$\swarrow \begin{array}{l} HCOOH/H_2O \\ -4 \text{ to } -4° \\ 1 \text{ min} \end{array}$$

$$\text{Ph-}\underset{\underset{C}{||}}{\overset{CH_2}{}}\text{—CHO} + 2 C_2H_5OH$$

Atropaldehyde
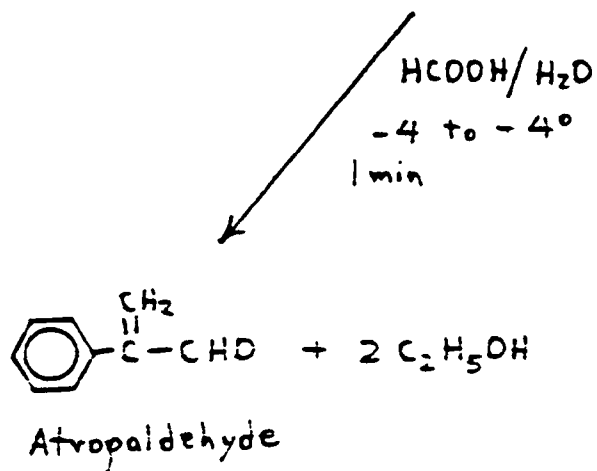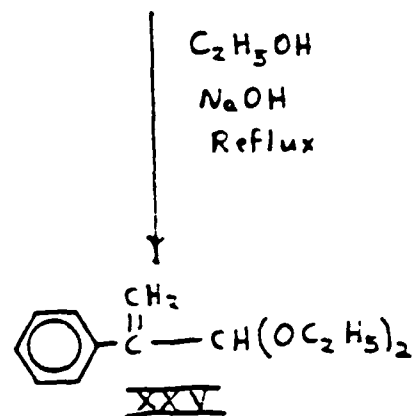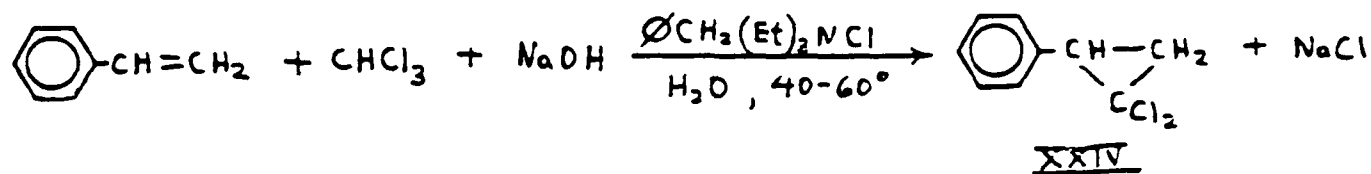
Preparation of Bromodiene XVII, Scheme 3: In a glove box (argon blanket) the following were prepared. Mixture A: this is a suspension of 28.3 g (0.065 moles) of triphenylbromomethylphosphonium bromide in 50 mL dry THF placed in a 250 mL three-neck flask along with a Teflon-coated stir bar. The necks of the flask were sealed with rubber serum caps. Mixture B: this is a solution of 7.28 g of potassium t-butoxide (0.065 moles) in 50 mL dry THF placed in a dropping funnel. Mixture C: is a solution of 8.0 g (0.060 moles) of atropaldehyde in 50 mL dry THF placed in a second dropping funnel. All containers were sealed with rubber septa and removed from the glove box. Using argon purging to minimize exposure to air, the dropping funnels (mixture B and C) were attached to the three-neck flask (mixture A). The flask was cooled to -78° using a dry ice-isopropanol bath while stirring and maintaining a slow argon purge. Mixture B was added slowly to A over a 30 min. period while stirring and maintaining argon purge and a temperature of -78°. The mixture was allowed to stir for an additional 30 min. (-78°). This procedure is similar to that of Matsumoto and Kuroda (9). The atropaldehyde solution (mixture C) was then added over 30 min., the mixture was allowed to stir an additional 50 min. and then vacuum filtered quickly through a large (150 mL) medium frit funnel (rinsed with 3x10 mL HPLC grade THF). Dry, filtered solid mass: 12.15 g.

The filtrate was poured, with stirring into 400 mL petroleum ether. A light brown precipitate (in some experiments a brown sticky paste formed) formed which was filtered off (dry solid mass: 16.50 g). The solvent in the filtrate was removed by rotary evaporation to give a dark amber oil (11.25 g). To this was added 50 mL petroleum ether which induced the formation of a bright yellow precipitate which was removed by filtration. The filtrate was again concentrated to 4.35 g of a cloudy-yellow oil.

The yellow oil was kneaded with 5.0 g powdered $AgNO_3$ and 10 mL petroleum ether (removes unreacted atropaldenyde) for 5-10 min. and using suction, the mixture was run through a short (1.5 cm) column of silica gel using elution by petroleum ether. Twenty mL of eluate were collected and this was vacuum concentrated to give 1.45 g of a nearly colorless (slightly yellow) oil. A second $AgNO_3$/silica gel column treatment yielded 0.70 g of the oil.

The proton NMR of the oil is consistent with the structure for the bromodiene XVII. The spectrum is shown in Figure 1. The principal absorptions are: 7.1 δ (singlet, 5H), 6.6 δ (doublet, 0.8 H), 6.3 δ (doublet, 0.8 H), 5.5 δ (doublet, 1.6 H). The infrared spectrum showed absorptions at 3090 cm^{-1} (olefinic C-H), 3040 cm^{-1} (aromtic C-H) anc 900 cm^{-1} (terminal - CH_2). This spectrum is shown in Figure 2.

Preparation of Diene-Yne IV by Scheme 3: Into a 25 mL three neck flask were placed: 0.0469 g Bis(triphenylphosphine) palladium(II) chloride, 0.0217 g cuprous iodide, 10 mL petroleum ether, 5 mL triethylamine (previously distilled from and stored over CaH_2) and a magnetic stir bar. The necks of the flask were sealed with rubber septa and the mixture was purged for 15 min. with argon. (Syringe needles used for argon inlet and exit). To the stirred mixture, 0.343 g (3.36 mmoles) of pnenylacetylene (vacuum distilled from and stored over CaH_2) was added by syringe. The mixture turned black and a black sticky solid adherec to the bottom of the flask. One neck of the flask was briefly opened (argon purge) to allow breaking up the solid with a spatula. To this mixture was added 0.616 g (2.94 mmoies) of bromodiene XVII (syringe injection petroleum ether rinse). The necks of the flask were stoppered and the mixture allowed to stir at room temperature for 50 hours (flask covered by black cloth).

The dark brown reaction mixture was diluted with 10 mL methylene chloride and run through a short (1.5 cm, 4.0 g) silica gel column using 15 mL methylene

chloride as rinse. The eluate was concentrated by rotary evaporation, additional methylene chloride was added and again evaporated (twice more) in order to remove most of the triethylamine. The residue remaining (a dark brown tar) had a mass of 0.92 g. This material was transferred to a 1.5 x 10 cm column of silica gel using a minimum amount of methylene chloride (2, 2, 1 mL rinses) and elution continued with this solvent. A dark brown band eluted between 6 and 15 mL of elution volume. A total of 25 mL was collected and this was evaporated and then pumped at 0.5 mm at room temperature for two hours leaving 0.75 g of residue. The proton NMR of this material showed at least three large, overlapping peaks at 7.3 δ (aromatic H) and many small peaks between 1 and 3 δ (aliphatic H) and between 5 and 7 δ (olefinic H).

An attempt was made to purify this product by selective solubility. It was found that a 30/70 THF/methanol mixture caused the precipitation of some dark brown material. Slow gravity filtration through a medium frit funnel and evaporation of the solvent (pumping at 0.5 mm 4 1/2 hrs.) gave 0.485 g of red-brown tar. The THF/methanol solid was similarly dried to give 0.052 g of brown tar. This latter material was not examined further.

The NMR and FTIR of the soluble portion are shown in Figure 3 and 4. Samples of this material were sent for C and H analysis, mass spectral analysis and DSC scan (see Results and Discussion).

Preparation of Diene-Yne IV by Scheme 5:

A. Preparation of 3-bromo-1-phenylpropyne (XXII): In a 250 mL three neck flask were placed 25 g (0.19 moles) of commercial 3-phenyl-2-propyn-1-ol, 90 mL diethyl ether, 10 ml pyridine, and a magnetic stir bar. To this stirred solution was added over 1 1/2 hours, a solution of 25.65 g (0.095 moles) phosphorous tribromide in 25 mL diethyl ether. The mixture was allowed to stir at room temperature for two hours and then refluxed for two hours. After cooling, the solution was poured into

500 mL ice water. The layers were separated. The water layer was given two washes with 50 mL ether. The ether layers were combined and given three washes with 2% aqueous sodium carbonate. The organic layer was dried with magnesium sulfate and then concentrated by rotary evaporation to give 19.86, of clear, nearly colorless liquid (50% yield). The proton NMR of the liquid is consistent with the structure of 3-bromo-1-phenylpropyne: singlet at 7.4 δ (aromatic H, 5H), singlet at 4.2 δ ($-CH_2Br$, 2H). (See Figure 5).

B. Preparation of Triphenylphosphonium salt of 3-bromo-1-phenylpropyne (precursor to ylide in Scheme 5): Into a 500 ml one neck flask were placed 12.0 g (0.06 moles) of the bromo compound prepared in Part A above, 21.0 g (0.08 moles) of triphenylphosphine, 175 mL dry toluene and a magnetic stir bar. The mixture was stirred and refluxed for 4 hours. The flask was stoppered and refrigerated overnight. To the mixture was added, with stirring, 70 mL cyclohexane. The slurry was run through a coarse frit funnel (slow gravity filtration) and the solid rinsed with 2 x 50 mL cyclohexane. The solid was then sucked dry by vacuum and then pumped at 0.5 mm 30-40° for 4 hours and then 2 1/2 hours at 50°. Mass of the tan salt was 28.15 g (100% yield). The melting point found was 200-210° (192° reported by WPAFB technician).

C. Preparation of diene-yne IV, Scheme 5: Into a 250 mL three neck flask were placed 13.26 g (0.029 moles) of the phosphonium salt of part B above, 100 mL dry THF, and a magnetic stir bar. An argon inlet was attached and the remaining necks were sealed with rubber septa (a syringe needle used as argon exit). The mixture was stirred and cooled to 0° and then 12 mL of a 2.5 M solution of n-butyllithium in hexanes (0.03 moles) was added by syringe over 35 minutes. The mixture turned a very dark red (almost black). The ice bath was removed and the mixture was allowed to warm to room temperature over 25 min. The ice bath was replaced and into one-neck of the flask was placed a dropping funnel containing 3.3 g (0.025 moles) of

atropaldehyde in 20 mL dry THF. This solution was added over 25 min. and then the mixture allowed to stir at 0° for 1 1/2 hrs. and then at room temperature for 4 hrs.

The mixture was poured with stirring into 350 mL "hexanes" to give a large lump of sticky material. The liquid phase was run through a large, coarse frit funnel. The mass of the air dried sticky solid was 15.4 g and this material was not examined further. The above filtrate was concentrated by rotary evaporation to give 3.75 g of a thick, red, tarry residue.

Partial purification of this material was accomplished by two column chromatography procedures. The first chromatography was performed on a 2.5 x 4 cm silica gel column and the material collected in 300 mL of 35/65 cyclohexane/CH_2Cl_2 gave 2.64 g of residue. This, in turn was run through a short (2.5 x 2.5 cm) column of silica gel, using first cyclohexane as solvent (200 mL eluted) and then a 50/50 cyclohexane/CH_2Cl_2 mixture (300 mL eluted). The cyclohexane elution gave approximately 0.5 g of dark brown tar (not examined further) and the solvent mixture elution gave 1.30 g of a yellow, crusty solid (23%). The proton NMR, ^{13}C NMR and FTIR of this material are shown in Figures 6, 7, and 8. Elemental analysis mass spectrometry and differential scanning calorimetry were also performed (see Results and Discussion).

Preparation of Dibromoatropaldehyde (compound XVIII, Scheme 4): Into a 100 mL flask were placed 7.15 g (0.054 moles) atropaldehyde, 25 mL CCl_4 and a magnetic stir bar. A dropping funnel containing 8.95 g (0.056 moles) bromine in 25 mL CCl_4 was attached to the flask. The flask was cooled to 0° and while stirring the mixture, the bromine solution was added over 40 min. The mixture was stirred for 30 min. and allowed to warm to room temperature. The red reaction mixture was washed with 3 x 30 mL 20% NaHSO$_3$ solution, 3 x 30 mL saturated NaHCO$_3$ solution, and 2 x 50 mL water. The organic layer was dried with Na$_2$SO$_4$ followed by MgSO$_4$ and

then rotary evaporated to give 12.03 g (76%) pale yellow liquid. The proton NMR and FTIR of this material are shown in Figures 9 and 10. Elemental analysis was obtained.

Attempted Preparation of Bromoaldehyde XIX (Scheme 4): A procedure similar to that of Bailey and Feng (10) was followed in which 1,8-diazabicyclo(5,4,0)undec-7-ene (DBU) was used as the base. Into a 250 mL 3 neck flask were placed 10.0 g (0.0342 moles) of the dibromoatropaldehyde (XVIII), 40 mL anhydrous diethyl ether and a magnetic stir bar. To this were attached an argon inlet and exhaust and a dropping funnel containing 5.21 g (0.0342 moles) DBU in 80 mL anhydrous ether. The flask was cooled to 0° and stirred while the DBU solution was added over 2 hrs. The mixture was then allowed to stir and warm to room temperature for an additional 1 1/2 hrs. The mixture was run through a medium frit funnel (ether rinse) and the filtrate rotary evaporated to give 2.9 g of residue (40% crude yield). The proton NMR spectrum of this material is shown in Figure 11.

IV. RESULTS AND DISCUSSION

A. Preparation of diene-yne, IV, by Scheme 3: The synthesis of the bromodiene, XVII, proved to be the most difficult step in the scheme. Numerous attempts were made using various modifications of the Wittig procedure. The most conspicuous and detrimental feature of this step was the tendancy of atropaldehyde to polymerize. This could be seen in the large amounts of sticky, brown material which precipitated when the filtered reaction mixture was poured into petroleum ether. Generally the mass of this material was greater than the amount of triphenylphosphine oxide expected from the reaction. Evidently the basicity of the ylide was sufficient to initiate the anionic polymerization of atropaldehyde.

In addition to the above handicap, some atropaldehyde remained unreacted and appeared in the crude product. This last trace of aldehyde could be removed by the

silver nitrate treatment (see Experimental Procedure). The final purified product was generally obtained as a colorless oil in small yields of 5-10%, however, the proton NMR and infrared spectra agree quite well with the structure of XVII (Figures 1 and 2). Elemental analysis on this compound was not obtained.

The coupling reaction of the bromodiene with phenyl acetylene catalyzed by the palladium complex and cuprous iodide gave 71% crude product. This material is a reddish-amber paste. The proton NMR (Figure 3) shows one large peak (overlapping peaks) at 7.4 δ (aromatic protons) a very weak absorption at 6.5 δ (olefinic protons) and several small peaks between 2 and 4 δ probably due to impurities. Olefinic proton peaks could not be discerned. The infrared spectrum (Figure 4) shows the expected absorption between 3000 and 3100 cm^{-1} for sp^2 C-H stretch, a weak (broad) absorption near 2280 cm^{-1} probably due to -C≡C- stretch, a moderate absorption of 912 cm^{-1} likely due to =CH$_2$, and certain other features (-C=C- stretch near 1600 cm and aromatic bend at 753 and 693 cm^{-1}) consistent with the structures.

The mass spectrogram of this material shows a great deal of 1,4-diphenylhexadiyne(mass 202 relative intensity = 100%) and some of the desired diene-yne, IV (mass 230, RA = 2.16%). The diyne is a by-product known to be created when phenylacetylene interacts in a reductive coupling reaction with palladium compounds (11). The elemental analysis showed: %C, 82.24, 82.24; %H, 5.50, 5.52 (Theoretical % C: 93.8; %H:6.1).

Thus, the synthetic route depicted in Scheme 3 is capable of giving the desired diene-yne, however, the overall yield is quite low and the final material is not pure. The synthetic steps would have to be greatly increased in scale in order to obtain enough material to explore various purification/separation procedures.

One additional aspect of Scheme 3 is that the Pd/Cu catalyzed coupling step may result in metal residues occurring in the final product. It was observed in this study that solutions of the material in deuterated chloroform (NMR samples) tended to give a small amount of fine, yellow precipitate on standing overnight. No attempt was made to analyze this material and identify it as metallic, however, all organic products (including by-products and impurities) were quite soluble in chloroform. If such metallic materials were to occur in the polymeric analog of the diene-yne, they might result in certain adverse consequences. For example, they may catalyze oxidative degradation of the polymer at high temperature.

B. Preparation of diene-yne, IV, by Scheme 5: This is a relatively simple procedure that can produce IV in one step. The disadvantage of this procedure is that the key step is a Wittig reaction which is notoriously poor in giving products in high yields. If used as a polycondensation reaction, this approach would not easily give rise to high molecular weight material. Nevertheless, the scheme does not utilize heavy metals and its simplicity makes it an attractive alternative to Scheme 3.

Compared to the procedure in Scheme 3, the one step procedure of Scheme 5 gives the final product in four times the quantity (based on atropaldehyde). Furthermore, the final product appears to be a more pure form of the diene-yne. The elemental analysis gave: %C, 85.21, 85.50; %H, 5.93, 5.99 (Theo: %C, 93.8, %H 6.1). The FTIR spectrum (Figure 8) gives absorptions which are in agreement with the structure of IV (3000-3100 cm^{-1} for sp^2 C-H stretch, 2247 cm^{-1} for $-C\equiv C-$ stretch, 1643 cm^{-1} for -C=C stretch and 912 cm^{-1} for =CH_2 bend) however, there are some absorptions that seem to be due to contaminants (2931 cm^{-1} sp^3 C-H stretch and 1722 cm^{-1} for C=O stretch). The proton NMR spectrum (Figure 6) is similar to that of the product of Scheme 3. This shows a very strong aromatic proton absorption (several overlapping peaks) at 7.5 δ but very weak absorptions in the 5-7 δ region

where the olefinic hydrogens are expected. One explanation (though, perhaps not valid) for the apparent lack of significant olefin hydrogen absorption is that these hydrogens are experiencing aromatic ring current deshielding effect that causes them to absorb in the aromatic region. Some peaks in the 6-7 δ region of the spectrum indeed seem to merge with the strong aromatic peak. The ^{13}C NMR spectrum (Figure 7) likewise shows primarily only the absorption due to aromatic carbons in the 120-130 ppm region. A small negative absorption is seen at 85 ppm which is in the region for acetylenic carbon absorption.

Thin-layer chromatography of this material (20/80 cyclohexane/chloroform on silica gel) shows what appears to be two intensly fluorescent overlapping spots (cis-trans isomers?) at R_f - 0.7 plus two, very faint spots .t R_f - 0.41 and 0.32. There was a slight tailing pattern behind the spots which may suggest some reaction occurring between the compound and the silica gel.

The mass spectrum for this compound shows a relative intensity of 25.78 (compared to $C_6H_5^+$ RA - 100) for mass 230 corresponding to the diene-yne. Actually mass 230 gives the most intense peak above 200.

C. Differential scanning calorimetry of diene-yne samples prepared by Schemes 3 and 5: DSC information on the diene-ynes should be very useful in determining whether cyclization is taking place. The DSC scan for the Scheme 3 product (designated as sample RP77-2) is shown in Figure 12. This shows a slight endotherm at 83.2° and then a large, broad exotherm at 100-250°. A second scan of this material (first scan taken to 450°) gives essentially a flat line with a very slight endothermic transition at 214°. No endotherm was observed at 86-87°, the melting region for m-terphenyl which is the expected product of cyclization.

The DSC scan for the Scheme 5 product (designated as sample RP80-1) is shown in Figure 13. A rather different behavior is observed in comparison to the Scheme 3 product. A weak endotherm appears at 53° which is immediately followed by a

broad exotherm from 90 to 170° and another very broad exotherm from 170 to 366°. The second scan shows no discernible transition; a disappointment in that the melting point for m-terphenyl was not detected.

Continued, more careful DSC work on this sample is to be carried out. It may be that since the first DSC scan was carried out to 450°, the m-terphenyl which formed may have decomposed or sublimed out of the sample holder. It has been suggested to the chemists at WPAFB that the first DSC scan be carried out to no higher than 300° before running the second scan.

D. Synthesis of diene-yne VI (Scheme 4): This sequence of steps is only partially complete. Atropaldehyde has been successfully brominated to give 2,3-dibromo-2-phenylpropanal (compound XVIII) in fair yield. The proton NMR and FTIR of this material (Figures 9 and 10) are consistent with the structure. Elemental analysis gave 38.88% C, 2.93%; H, 49.75% Br (Theo. 37.02% C, 2.76% H 54.74% Br).

The dehydrobromination of XVII to form 3-bromo-2-phenylpropenal (XIX) was attempted using a variety of bases such as hot, solid K_2CO_3, aqueous KOH (with phase transfer catalyst) and DBU. This latter organic base was used successfully by Bailey and co-workers (10) to perform a dehydrobromination in the synthesis of α,β-unsaturated esters. Only one attempt has been made at this type of dehydrobromination. The current material in hand has not been purified in any way. A proton NMR spectrum is shown in Figure 11. Further work is planned to purify this material by column chromatography and to repeat the synthesis on a larger scale.

V. CONCLUSIONS

Two routes to the synthesis of the diene-yne, IV, have been developed. The one-step route using a Wittig reaction on atropaldehyde gives the desired product in greater overall yield and in purer form. Although mass spectral data and

infrared spectra indicate the presence of tne diene-yne, tne proton and ^{13}C NMR spectra do not indicate the presence of olefinic or acetylenic hydrogens. This synthesis should be repeated on a larger scale in order to develop methods for purification and to more fully characterize the material.

Careful DSC studies should be performed on this compound in order to determine the region (temperature) of cyclization and the extent of formtion of m-terphenyl.

As an intermediate needed in the synthesis of diene-yne VI, 2,3-dibromo-2-phenylpropanal could be prepared in good yield from atropaldehyde. The dehydrobromination of this compound using DBU appears to be successful although purification procedures need to be conducted.

REFERENCES

1. a) C.S. Marvel and G.E. Hartzell, J. Am. Chem. Soc., 81, 448 (1959).
    b) D.A. Frey, M. Hasigawa, and C.S. Marvel, J. Polym. Sci., Part A, 1, 2057 (1963).

2. S. Hayama and S. Niino, J. Polym. Sci., Polym. Chem. Ed., 12, 357 (1974).

3. V. Ya. Bogomolnyi and B.A. Dolgoplosk, Isv. Akad. Nank SSSR, Otdel. Khim. Nank, 1912 (1961).

4. a) P. Kovacic and A. Kyriakis, Tetr. Lett., 467 (1962).
    b) P. Kovacic and A. Kyriakis, J. Am. Chem. Soc., 85, 454 (1963).
    c) P. Kovacic and R. Lange, J. Org. Chem., 28, 968 (1963). M.M. Koton. "Advances in Macromolecular Chemistry" Vol. 2; W.M. Pasika, ed., 175 (1970).

5. F.L. Hedberg and F.E. Arnold, Am. Chem. Soc. Prepr. Polym. Chem. Div., 16(1), 677 (1975).

6. I. Crosland, Org. Syn., 60, 6 (1981).

7. B.A. Reinhardt and F.E. Arnold, U.S. Patent 4,417,039, November 22, 1983.

8. J. Wolinsky and K.L. Erickson, J. Org. Chem., 30, 2208 (1965).

9. M. Matsumoto and K. Kuroda, Tet. Lett., 21, 4021 (1980).

10. W.J. Bailey and P. Feng, Polym. Prepr. 28(1), 154 (1987).

11. K. Sonogashira, Y. Tohda, and N. Hagihara, Tet. Lett., 50, 4467 (1975).

Figure 1 Proton NMR spectrum of Bromodiene

REMARKS: Bromodiene

$$\phi-C-CH=CHBr$$

(b) 1-Bromo-3-phenylbutadiene

SAMPLE:
SOLVENT: CDCl₃/27.1MS
DEG. LEVEL:

Offset 180 Hz

OPERATION: RAP

DATE: 8/13/87

80-25

Figure 2. IR Spectrum of Bromodiene
CH_3
$CH_2 = C - CH = CH_2$
Br

Figure 3 Proton NMR Spectrum of Diene-Yne

(Scheme 3)

$$\phi - \overset{\overset{\displaystyle CH_2}{\|}}{C} - CH = CH - C \equiv C - \phi$$
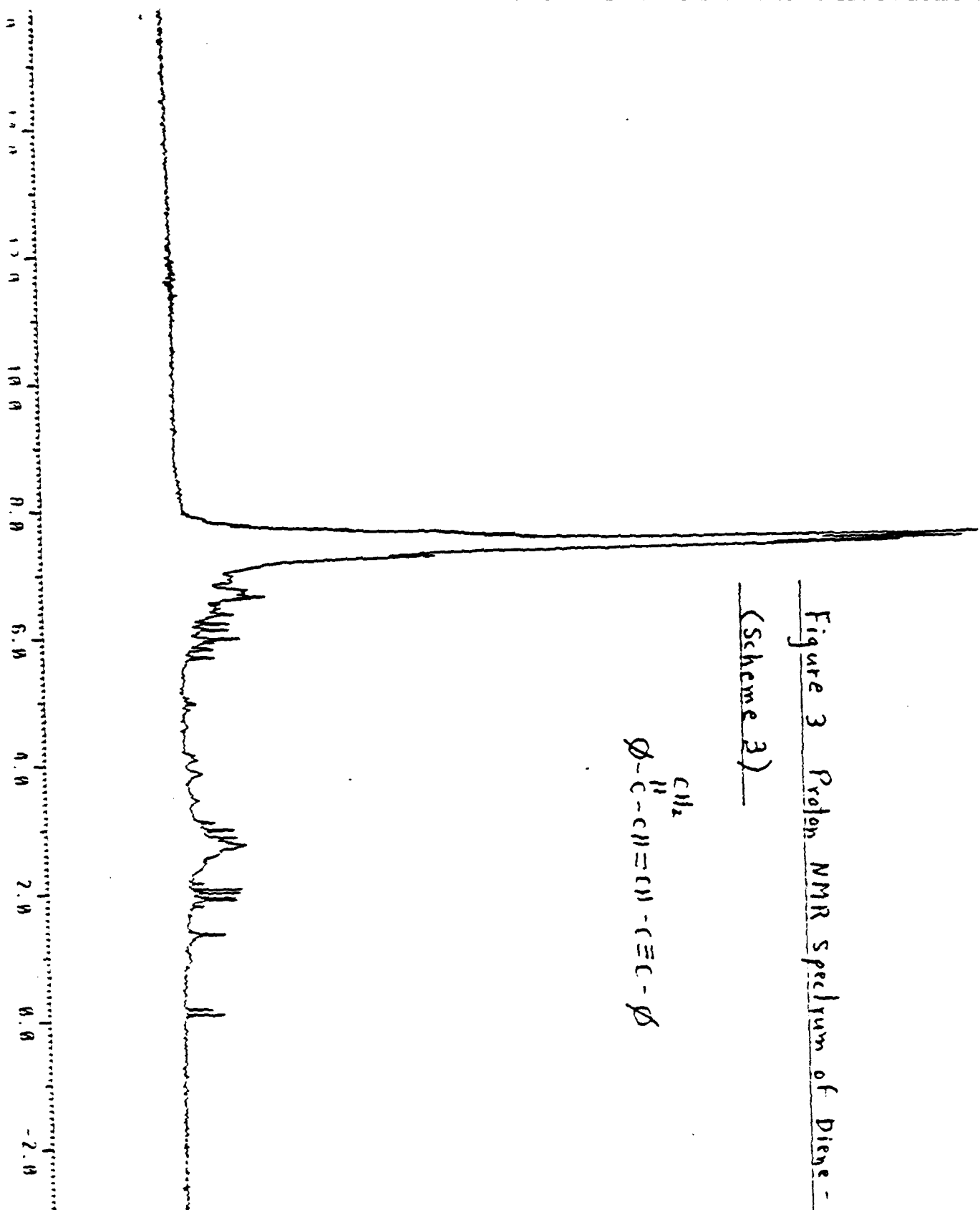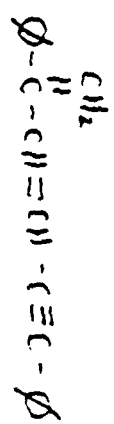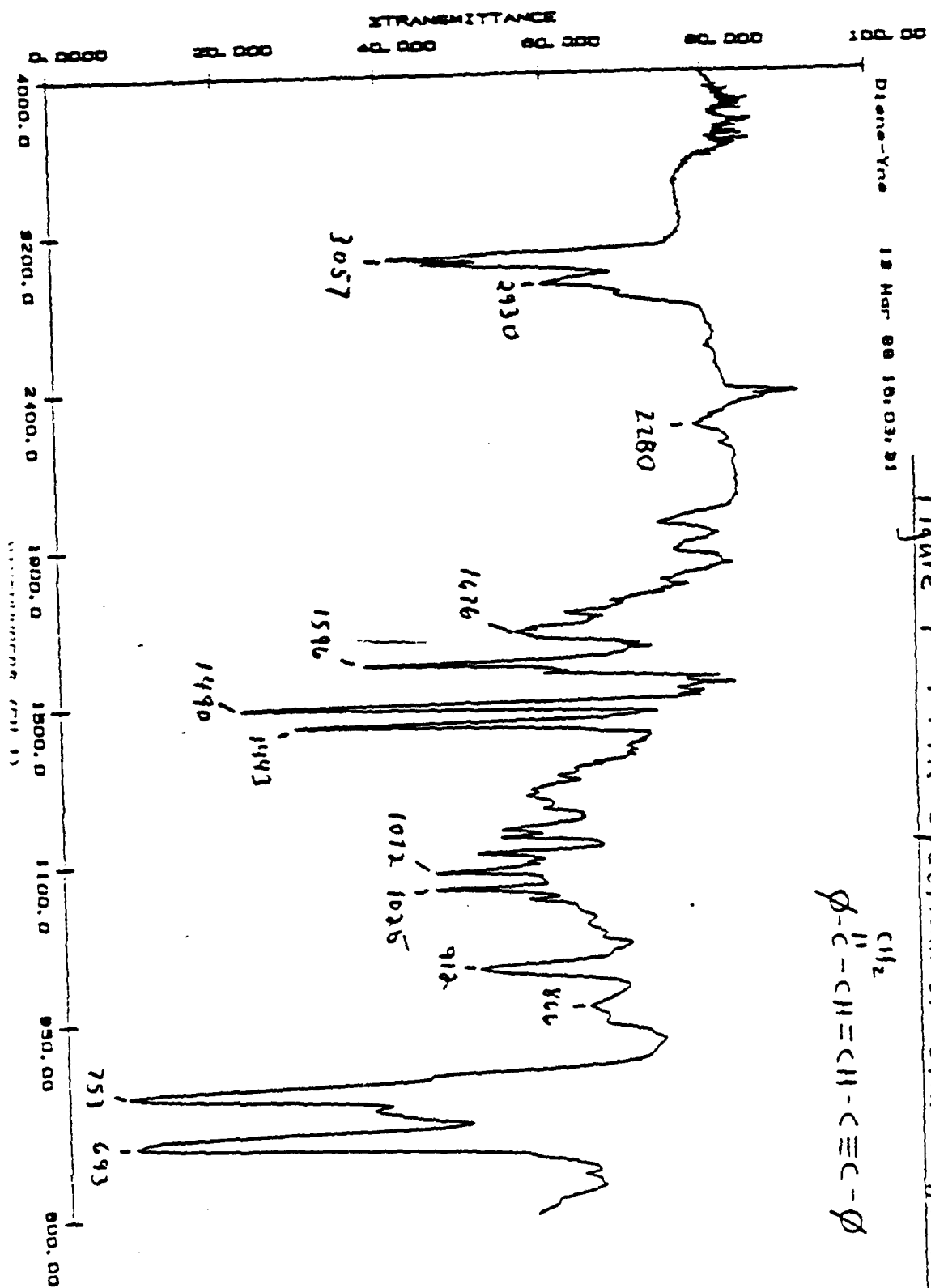
Figure 4 FTIR Spectrum of Diene-Yne (Scheme 3)

Figure 5 Proton NMR Spectrum of

3-Bromo-1-Phenylpropyne
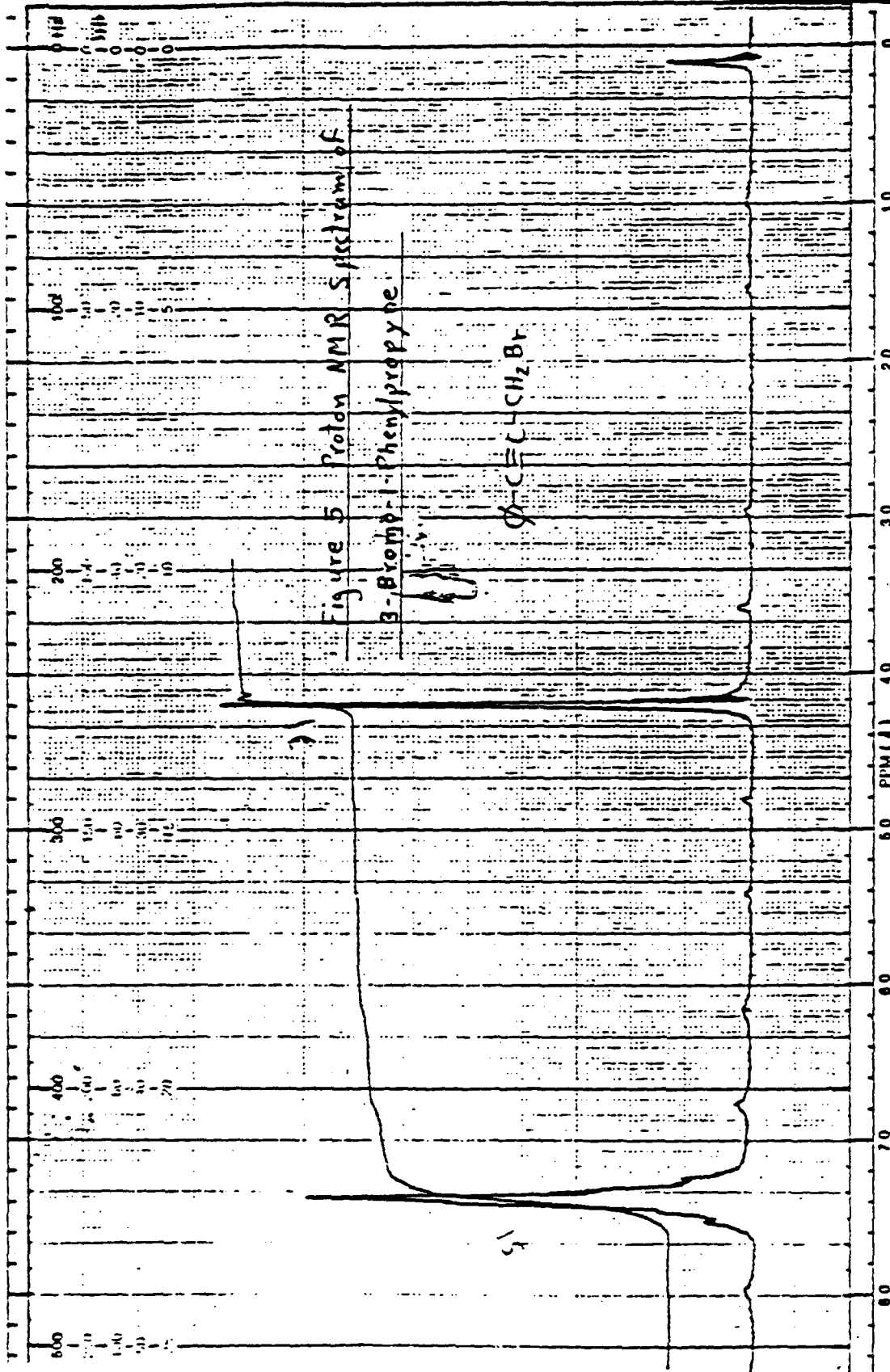
$\phi-C\equiv C-CH_2Br$

REMARKS: $\phi-C\equiv C-CH_2Br$ after chromatography (short silica gel column)

SAMPLE:
SOLVENT: $C_6H_6 / 1\% TMS$
DEC. LEVEL

OPERATOR: RAP

MANUAL
SWEEP TIME (SEC):
SWEEP WIDTH (Hz):
FILTER:
RF POWER LEVEL: 0.05

DATE: May 13, 1988

SWEEP OFFSET (Hz):
SPECTRUM AMPLITUDE: 2.5
INTEGRAL AMPLITUDE:
SPINNING RATE (RPS): 40

NORELL, INC.

Proton NMR Spectrum
of Diene - Yne

Notebook page 80

Figure 6   Proton NMR
Spectrum of Diene - Yne
(Scheme 5)

$$\phi-\overset{\overset{\displaystyle CH_2}{\|}}{C}-CH=CH-C\equiv C-\phi$$

14.2   12.2   10.2   8.2   6.2   4.2   2.2   0.
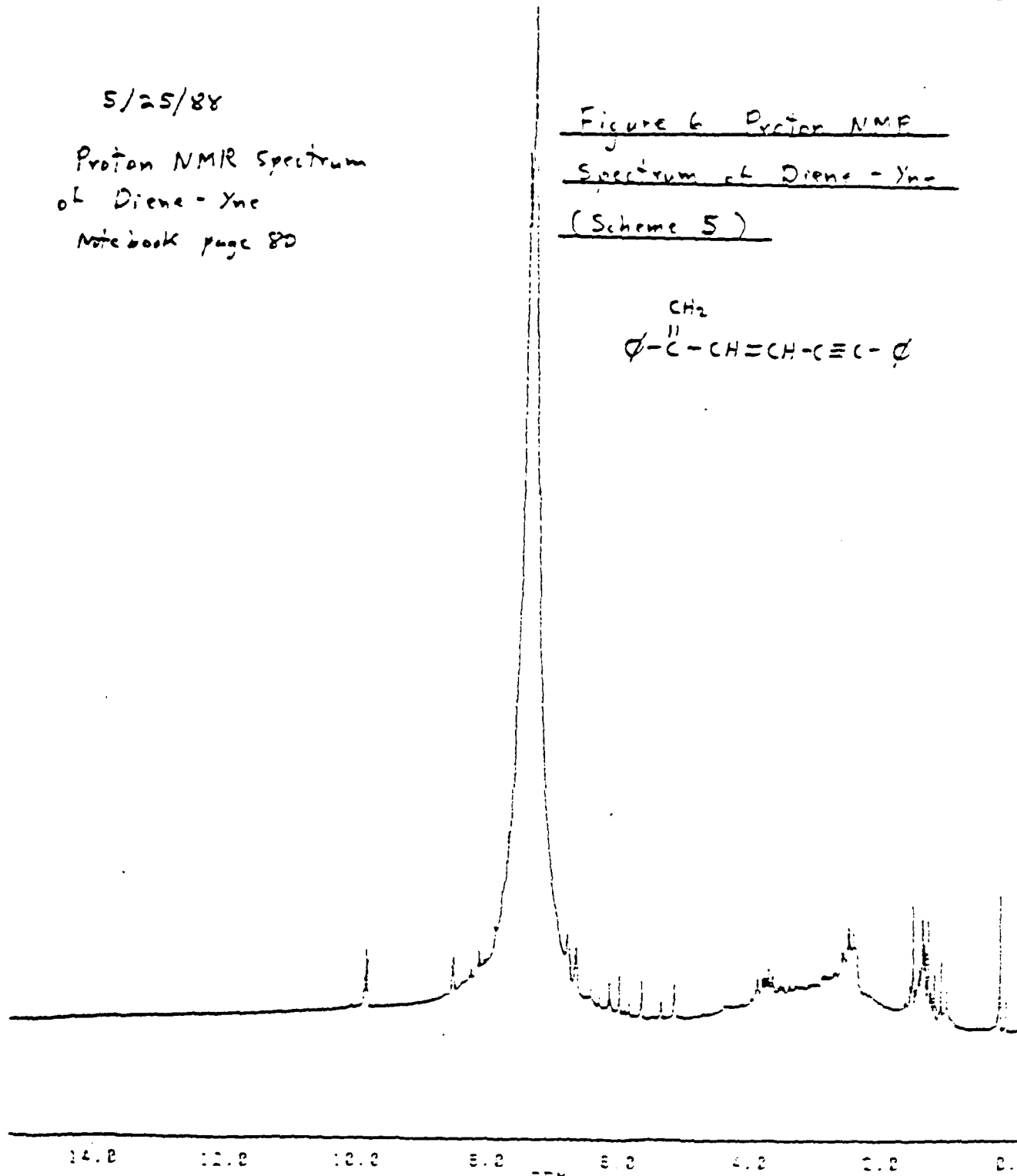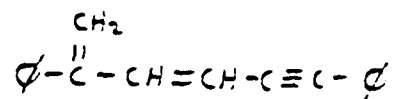
Figure 7 ^{13}C NMR spectrum for Diene-Yne
(Product of Scheme 5)

$$\phi-\overset{\overset{\displaystyle CH_2}{\|}}{C}-CH=CH-C\equiv C-\phi$$
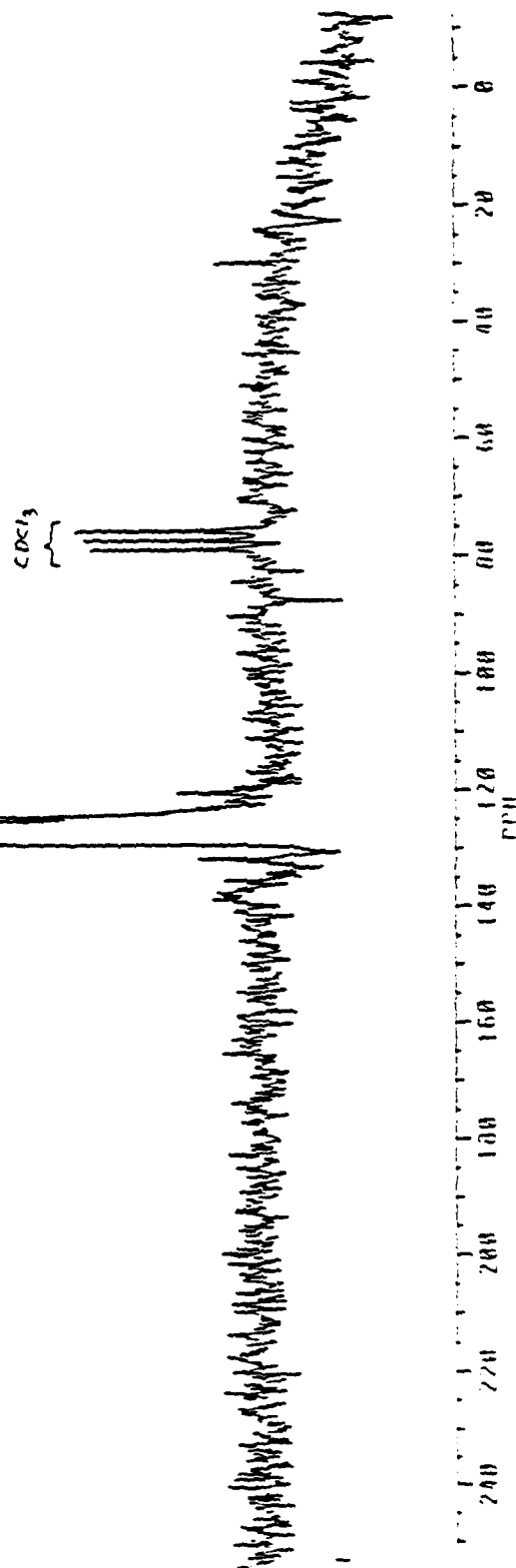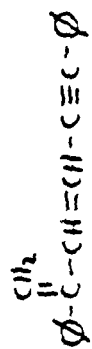
CDCl$_3$

Figure 8 FTIR of Diene-Yne (Scheme 5)
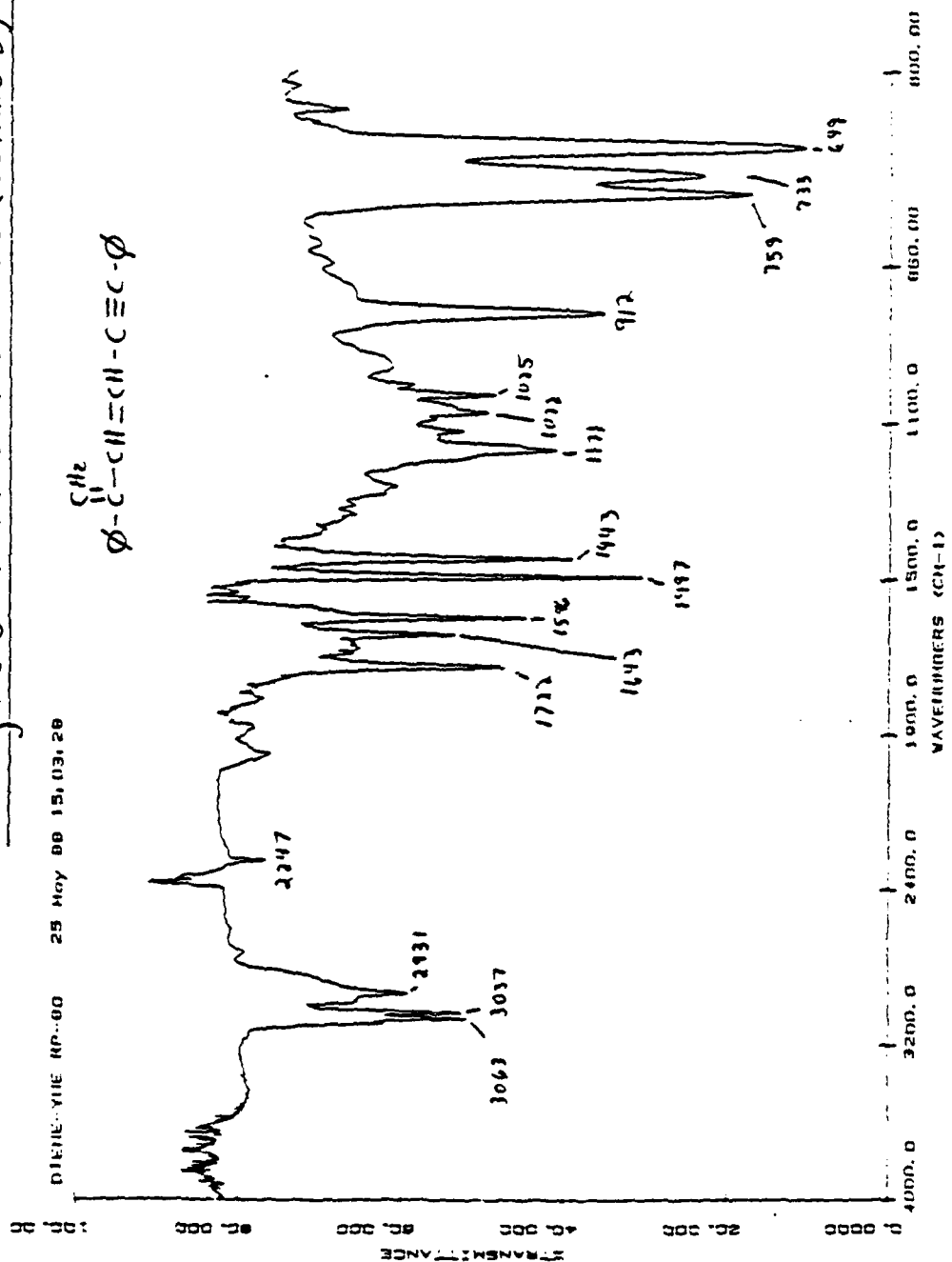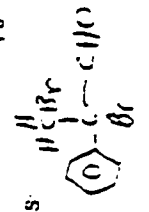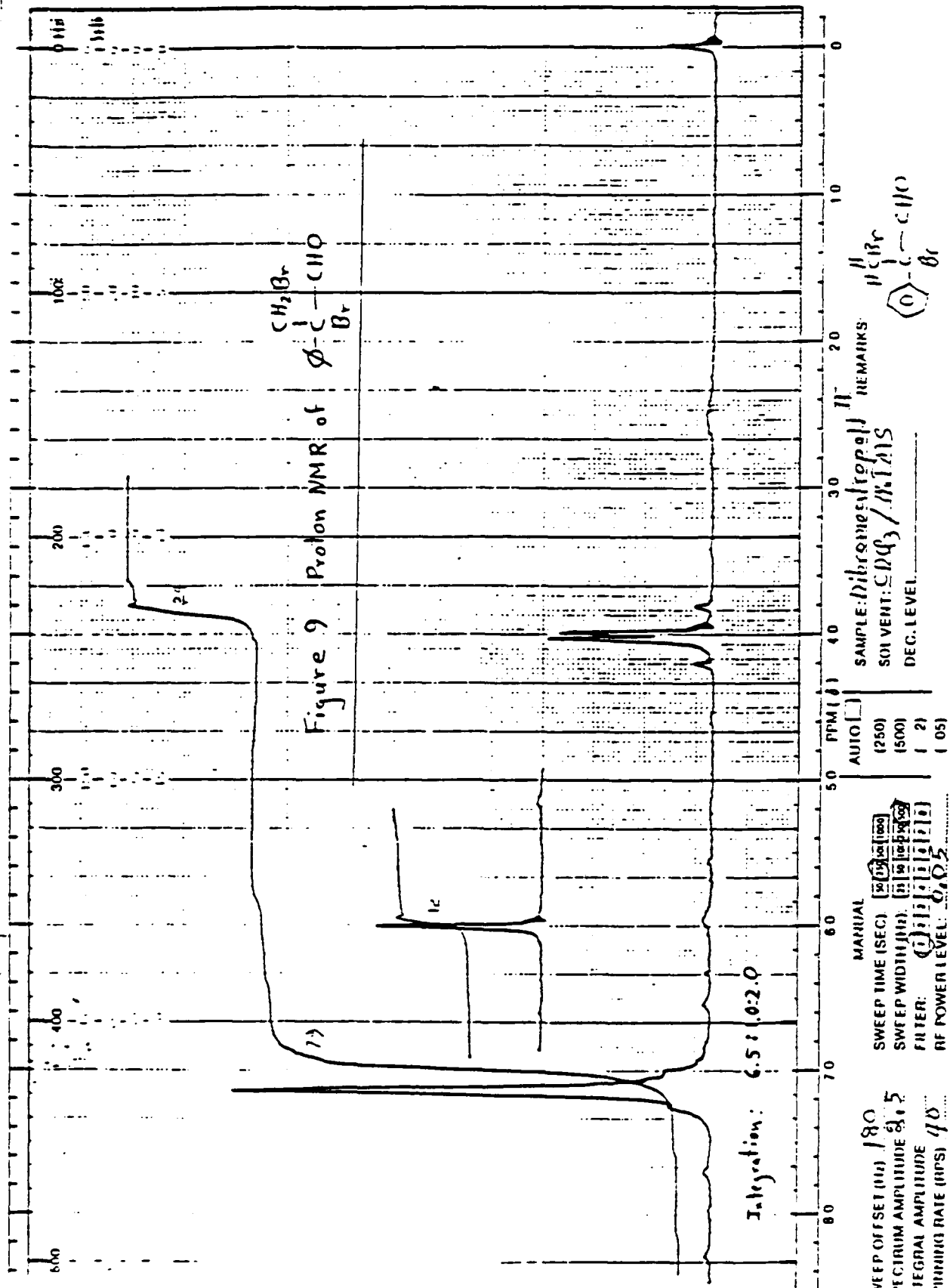
Figure 9 Proton NMR of $\phi-\overset{\overset{\displaystyle CH_2Br}{\displaystyle |}}{\underset{\displaystyle Br}{C}}-CHO$

Integration: $6.5 : 1.0 : 2.0$

SWEEP OFFSET (Hz) 180
SPECTRUM AMPLITUDE 8.5
INTEGRAL AMPLITUDE
SPINNING RATE (RPS) 18

MANUAL
SWEEP TIME (SEC)
SWEEP WIDTH (Hz)
FILTER:
RF POWER LEVEL 0.05

SAMPLE: Dibromostropal II
SOLVENT: CDCl₃ / JMTMS
DEG. LEVEL

REMARKS: $\underset{\displaystyle Br}{\overset{\displaystyle O}{\underset{\displaystyle |}{C}}\!Br_r}\overset{\displaystyle O}{-C}-CHO$

SPECTRUM NO

OPERATOR RAP

DATE 4/26/87

PERKIN, INC.

80-33

Figure 10 FTIR of $\phi-\overset{CH_2Br}{\underset{Br}{C}}-CHO$
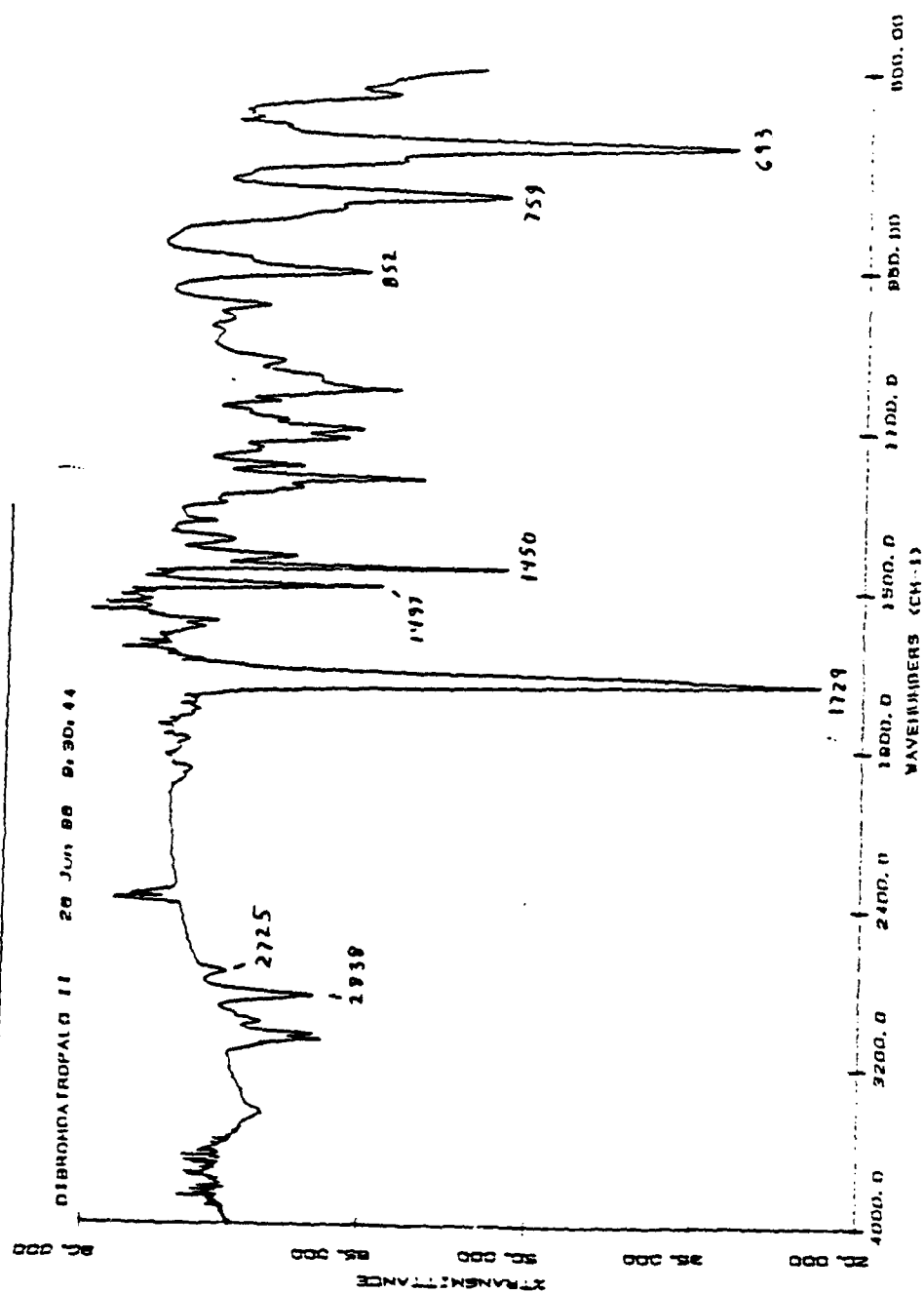
Figure 11 Proton NMR of Crude

$$\phi-\overset{\overset{\displaystyle CHBr}{\|}}{C}-CHO$$

14.2   12.2   12.0   8.2   6.2   4.0   2.2   0.0

ppm

DSC

OMNITHERM DATA SYSTEM

Sample: LST;RP '77-2
Size: 9.4. mg
Run No: #3057 (13)
Date: MAY/25/00 09:03
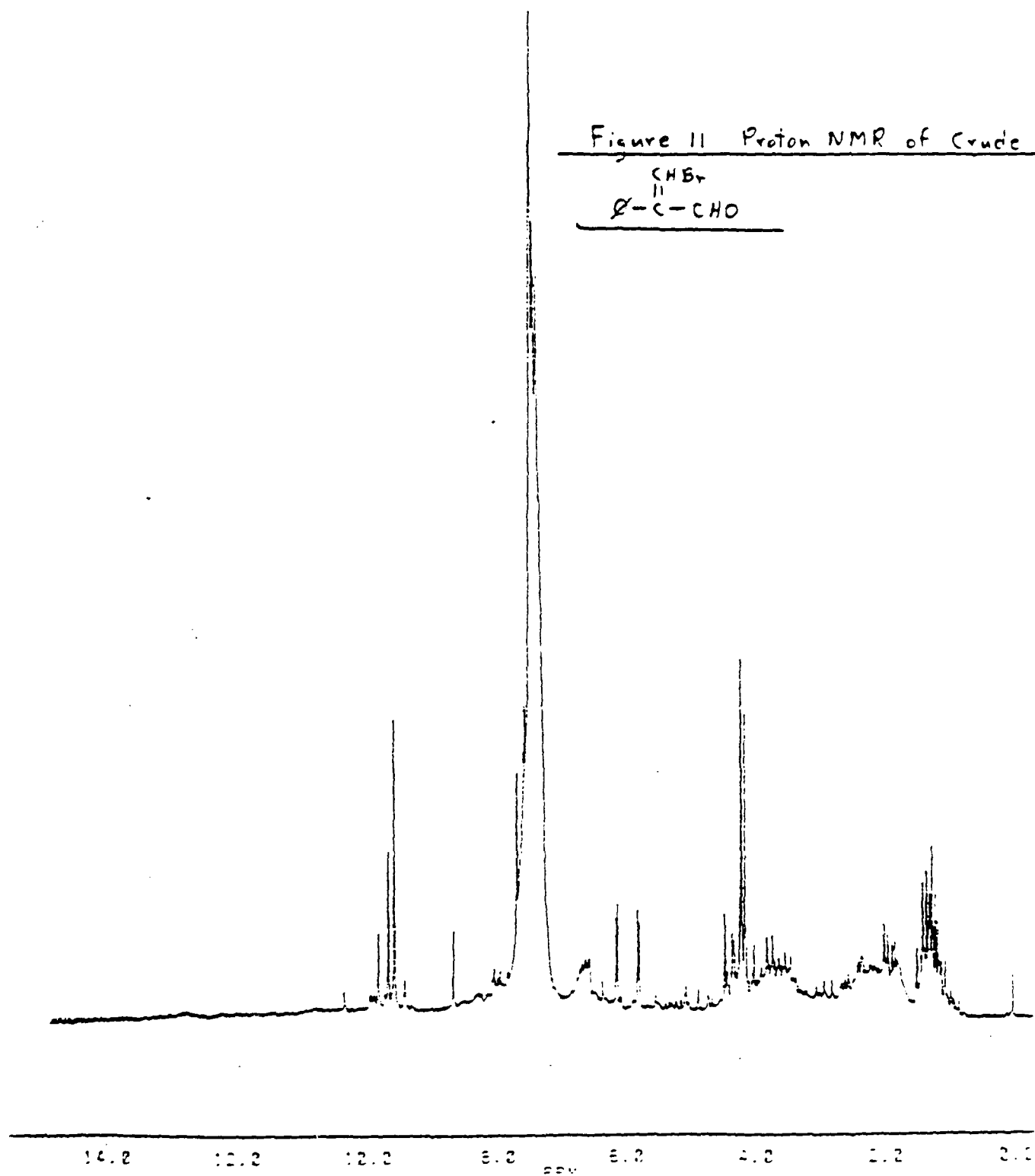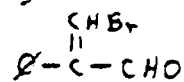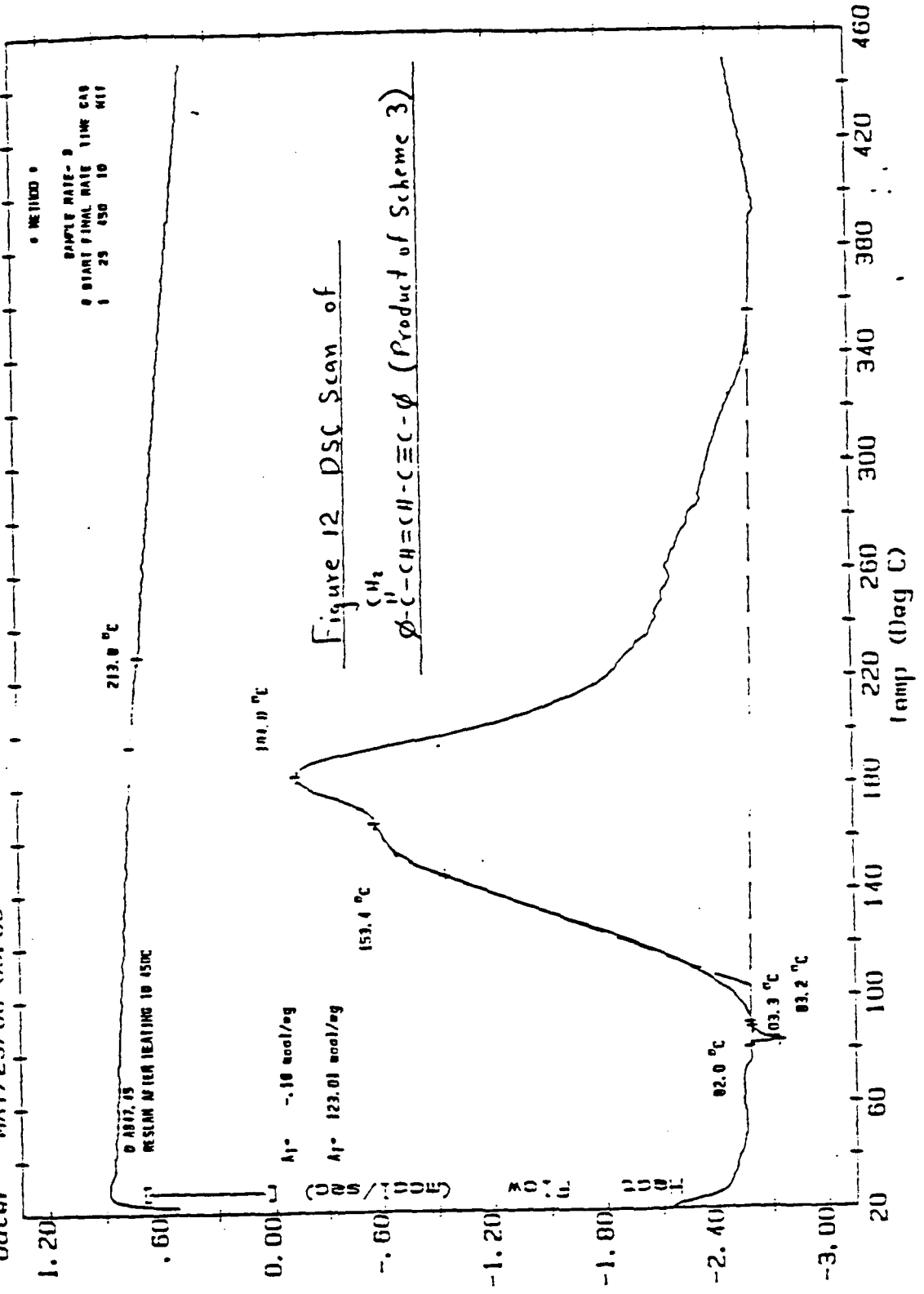
Operator: EJS
Disk ID: EJS DATA-47
File No: D 44.DAT V2.1
Plotted: MAY/25/00 14:37

● METHOD 0

SAMPLE RATE= 0
● START FINAL RATE TIME CAL
1 25 450 10 NII

213.0 °C

308.0 °C

153.4 °C

0 ABS2.15
RESCAN AFTER HEATING TO 450C

Ar= -.18 mcal/mg

Ar= 123.01 mcal/mg

82.0 °C

103.3 °C
83.2 °C

1.20

.60

0.00

-.60

-1.20

-1.80

-2.40

-3.00

(mcal/sec)

FLOW

HEAT

20 60 100 140 180 220 260 300 340 380 420 460

Temp (Deg C)

Figure 12 DSC Scan of

$$\phi-C-CH=CH-C\equiv C-\phi \text{ (Product of Scheme 3)}$$

with CH$_2$ substituent

Figure 13   DSC Scan of φ-C-CH=CH-C≡C-φ (Scheme 5 Product)
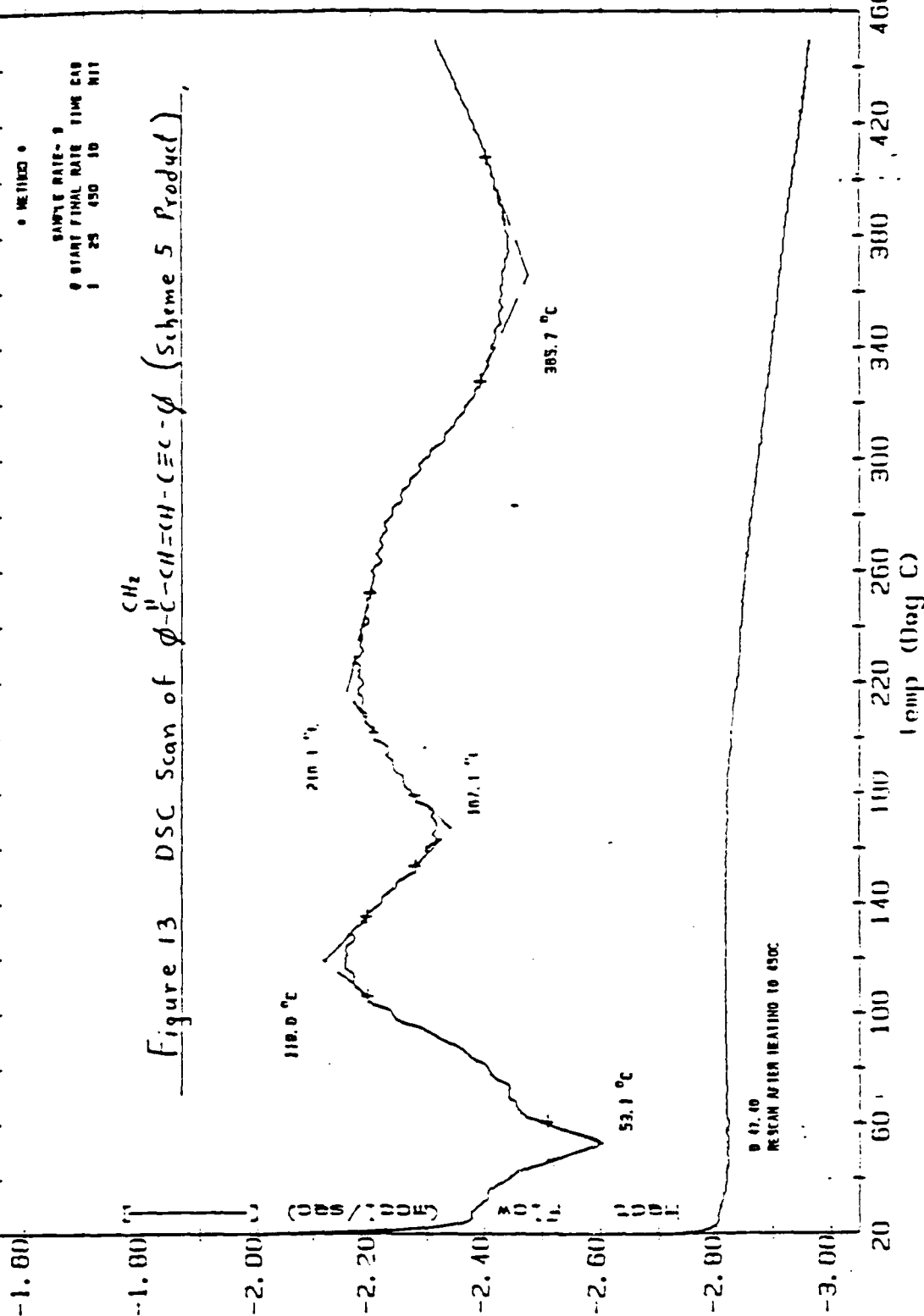
1988 USAF/UES MINI-GRANT

Sponsored by the

Air Force Office of Scientific Research

Conducted by the

Universal Energy Systems, Inc.

Final Report

Leaky Rayleigh And Lamb Waves On Composites

Prepared by: Nisar Shaikh

Academic Rank: Assistant Professor

Department   Engineering Mechanics Department
 and University: University of Nebraska-Lincoln
                           Lincoln, NE 68588-0347

Research Location: University of Nebraska and
                           NDE Branch - U.S. Air Force Wright
                           Aeronautical Laboratory

USAF Research: Dr. T. J. Moran

Date: May 31, 1988

Contract No: S-760-6MG-007

LEAKY RAYLEIGH AND LAMB WAVES ON COMPOSITES

by

Nisar Shaikh

ABSTRACT

A device was designed and constructed to generate leaky guided waves in the submerged composite materials, addressing some of the problems associated with the existing appartus. Particular featue of the design is that at different orientation of the transducers the point of insonification remains the same. The measurements were made with both the leaky surface and plate waves.

Experimental measurements of leaky Rayleigh waves on a fluid-composite solid interface are presented, and the results are compared with those of a mixture-continuum model. A laminated microstructure is simulated by fabricating a solid from a stack of alternating layers of stainless steel and copper sheets. Leaky Rayleigh waves are propagated in the lamination direction with their particle motion in the plane of the layers. At the intermediate frequencies the Rayleigh waves are observed to be dispersive, and the frequency dependence is related to the ratio of wave length and layer thickness (cell size). For long wavelengths the surface wavespeed attains the mixture value for the two constituents. For short wavelengths, the Rayleigh wave velocity asymptotically approaches the values for the constituent having the slower surface wave velocity in the absence of microstructure.

ACKNOWLDEGEMENTS

I would like to thank the NDE Branch of the Air Force Wright Aeronautical Laboratory and the Air Force Office of Scientific Research and the staff of Universal Energy System for their able assistance and efficient handling of the contract.

My thanks are first due to Doctors Moran and Chimenti for providing me the opportunity of participation in their ongoing research program in the exciting area of Nondestructive Evaluation using Leaky Lamb and Rayleigh Waves.

INTRODUCTION

The research undertaken here was continuation of the author's work at the materials laboratory (WPAT/AFB), which he visited during the summer of 1986 and subsequently in 1987. The principal interest was in launching and receiving the leaky guided waves in unidirectional fibrous composites. One of the problems encountered in the measurement system was that as the transducer orientation changed the point of insonification changed also. The transducer then has to be translated to reach to the original point. A simple device, though similar to goniometer, was devised to circumvent the above problem. The interest then was to study the off-angle propagation of Lamb waves in the unidirectional fibrous composites. Later this work was discontinued, under the instruction from the materials laboratory, for the surface wave studies.

The Rayleigh waves propagated in fibrous medium exhibit dispersion similar to the bulk waves. To aid in the studies of such composites, a simpler two dimensional model was suggested composed of layers of two different materials. Thus specimens exhibiting laminar microstructure were constructed and the dispersion studies were carried out.

OBJECTIVE OF THE RESEARCH EFFORT:

The overall objective of this particular program is to conduct basic research in acoustics and follow it up with the necessary technological developments for the advancement of NDE and imaging techniques to meet the nations's Air and Strategic

defense needs.

Our particular objective was to further the measurement technique for leaky Raleigh waves in dispersive media. The specific problems addressed were:

1. Design and construction of a device to launch and receive leaky waves without affecting the change of measurement location, a handicap of existing devices.

2. The construction of specimen exhibiting laminar microstructure, and measure Rayleigh wave dispersion.

INTRODUCTION TO THE TOPIC AND APPROACH

The measurement of Rayleigh wave velocity in dispersive media presents a challenge since the conventional technique of measuring time of flight with wedge transducers would require a different transducer for each frequency of the measurement. Even more troublesome is the distortion of the short tonebursts used. The dispersive media clutters the echo, making it difficult to measure the travel time with accuracy; the same difficulty is encountered in measuring dispersion of the bulk waves. A more efficient scheme employed by Chimenti [4,5] consists of resonant generation of leaky Rayleigh (and Lamb) waves by immersed transducers launching acoustic waves at critical incident angles to the liquid-solid interface. If conditions of frequency, beamwidth, and radiation damping coefficient are favorable, a bimodal reflected acoustic field is created, composed of a remnant specular reflection summed coherently with the radiating surface wave. In that case, a portion of the field distribution

shows a strong reduction in amplitude, due to phase cancellation of component fields. The technique of acoustically seeking a null zone in the reflected field, caused by phase cancellation between leaky surface energy and the specular reflection provides a convenient and clear means of establishing the presence of a surface wave at the appropriate frequency.

A new fixture was designed in which the transducer holder slides in a slotted arc such that the center of arc could be maintained on the surface of the transducer. In this case, at different orientation the point of insonification remains the same, considerably easing the measurements compared to the earlier set up. The details of the designs are described in the next section.

Various mixture-continua theories have been proposed to model elastodynamics of composite materials. Experimental support is needed both to aid in formulating as well as in verifying these models. It requires devising experiments and constructing practical specimens that would simulate the desired material characteristics. In what follows, a one-dimensional laminar microstructure is simulated by constructing samples with alternating layers of copper and stainless steel sheets. The dispersion of leaky Rayleigh waves is studied on such a sample.

DESIGN OF FIXTURE

The fixture consists of two aluminum support plates mounted on a channel across the tank as shown in Fig. 1. One of the plates is allowed to slide along the length of the channel, while

the other is held stationary. The channel is leveled with respect to the base plate of the tank to obtain proper alignment. The transducer assemblies are attached to the support plate at a curved slot which allows the assembly to rotate. Both the transmitting and receiving transducers are held by means of a tube which also serves as a conduit for the transducer cables. An O-ring between the tube and the transducer keeps the water from leaking into the tube. The receiving transducer is attached to the sliding support plate, and the transmitting transducer to the stationary one.

Motion of the sliding support plate is provided by a screw and nut attachment housed within the channel. Hence, the sliding plate with the receiving transducer effectively provides the horizontal movement required to locate the null energy region of the reflected field. Variable angle settings can be selected for each of the transducers by means of a rack and gear mechanism located in the curved slots of the support plates. The reference point for the measurement of the angle is the vertical axis, thus the point of insonification remains the same for all transducer positions. The curved rack is positioned on the back of each support plate where it is engaged with a gear wheel. By moving the gear wheel along the rack, the desired angle settings for the transducer can be achieved. The range of angles that can be attained with this arrangement is from 5 to 65 degrees with respect to the vertical axis. The angle settings are accurately marked on the front of the support plate. Therefore, this arrangement selects different angle settings precisely and

quickly. All the components of this fixture are anodized for corrosion-resistance.

The forerunner of this fixture had a thinner support plate and did not have the rack and gear mechanism for selection of different angles. It also did not have the nut and screw arrangement for the sliding motion of the support plate. Selection of different angle settings were not as quick, and there was always a chance of committing errors with a protractor.

A plexiglass base plate equipped with leveling screws is placed at the bottom of the tank. The specimen is then placed on the top of the base plate.

SAMPLE PREPARATION

At first, we considered fabricating the specimen out of the layers of urethane and epoxy. However, problems of accurately determining exact elastic properties of cured epoxy and the potential problem of the poor quality of the interfaces suggested using all-metal constituents. The best choice, considering their ready availability, was sheets of copper and stainless steel. A diffusion bond would have been an ideal choice for forming a solid out of these sheets, but the idea was found to be impractical. Instead, we constructed a clamping fixture to keep the plates pressed together, assuring uniform contact that would realize the welded- contact boundary condition for both the stresses and the displacements.

The sheets were degreased and etched. After clamping the plates tightly, the assembly was heated in an oven for two hours

at 250° centigrade. Considerable care in machining was taken to prepare the top surface without deforming the cells and to achieve a mirror finish. Fig. 2 shows the photograph of one of these samples, where the actual cell size is 0.787 mm. The sharp interfaces between the two constituents and the high degree of regularity in the laminates are clearly seen in this figure.

MEASUREMENT DESCRIPTION

A schematic of the experimental geometry is given in Fig. 3. An ultrasonic beam from a damped piston source insonifies the sample at selected incident angles, each of which corresponds (by Snell's law) to a particular trace velocity. At frequencies corresponding to the generation of Rayleigh waves in the sample, the reflected ultrasonic field will show the displacement and distortion characteristic of the presence of a propagating wave on the surface. At frequencies away from critical, the signal is dominated by the specular reflection. An initial set of measurements was made on a pulsed Schlieren system both to build confidence in our ability to launch surface waves on such a sample and to verify the presence of dispersion. Fig. 4 shows the Schlieren visualization, which also provides a vivid picture of the null zone described earlier. To study surface wave dispersion, data are acquired in a high-resolution ultrasonic scanning system by exciting a broadband ultrasonic transducer with low-level rf tonebursts from a function generator. The reflected acoustic beam is detected by a second matched transducer positioned at the same angle and about the same

distance to the sample. Spectra are accumulated by discretely stepping the frequency and recording the reflected signal. A typical experimental spectrum for an incident angle of 43° is shown in Fig. 5. The dashed curve is the unprocessed experimental signal, while the solid line shows the same data normalized to remove the transducer response. At 9.35 MHz, there is a strong reduction in amplitude, indicating the presence of a leaky Rayleigh wave. The test is repeated over a range of transducer angles, and the corresponding Rayleigh wave frequency is determined.

RESULTS AND DISCUSSION

The new design of transducer holder performed satisfactorily and provided ease in the measurements as expected. However there is room for improvement; the gear retards free motion, for finer adjustment.

The results of experimental measurements on ultrasonic reflection from the laminated sample and the results of the theoretical calculations showing the phase velocity dispersion versus frequency times cell size are displayed in Fig. 6 (the elastic properties used in the calculations are collected in [10]). Open circles have been recorded with the 2.0-MHz transducers, while the points denoted by the crosses correspond to the 10.0-MHz pair. The solid curve is the prediction of the approximate theory. At the low frequency end of the curve the normalized wavelength (λ/d) is equal to 3.4, with a value of 0.20 at the high frequency end. That is, the data and theory span

more than one order of magnitude. In spite of this large frequency range, over which the dispersion changes markedly in terms of the mechanical behavior, rather good agreement is seen across the Fd axis. In particular, the asymptotic approach at large Fd to the Rayleigh velocity of the more compliant material (in this case copper) is very accurately rendered by the prediction. Also, the wavespeed derived from the mixture elastic constants is well reproduced at low frequency, where the influence of the microstructure on dispersion is diminishing.

In summary, we have measured dispersion of leaky Rayleigh waves, where the dispersive behavior arises soley from microstructural features of solid. We find the limiting behavior at long wavelengths plausible.

CONCLUDING REMARKS

The measurement of dispersion is difficult, even for the bulk waves. The method for measurements of Rayleigh wave dispersion as presented here is quite efficient. However analytical results for comparisons are lacking. The results we have compared with are computed from mixture-continuum theories. Ideally an independent verification is necessary for the experimental results before they can be used to verify the computational models. Some preliminary studies made by the investigator, both for longitudinal and shear waves, show infinite dispersive modes exist, similar in nature to Lamb waves. It may be surmised that the surface waves in such layered material could also have several modes, possibly with regions of frequencies for which

real velocities do not exist. Without guidance from analysis some of the experimental data can be confusing. We are beginning this analysis by studying the wave reflections from a free surface in such materials.

ACKNOWLEDGEMENTS

REFERENCES

1. G. A. Hegemier, G. A. Gurtman and A. H. Nayfeh, Int. J. Solids and Struct. 9, 395 (1973).

2. C. T. Sun, J. D. Achenbach and G. Herrmann, J. Appl. Mech. 35, 467 (1968).

3. A. H. Nayfeh, "Acoustic Wave Reflection from Water/Laminated Composite Interfaces", (To appear in J. Appl. Phys.).

4. D. E. Chimenti, A. H. Nayfeh and D. L. Butler, J. Appl. Phys. 53, 170 (1982).

5. D. E. Chimenti and A. H. Nayfeh, J. Appl. Phys. 58, 4531 (1985).

6. Steel C_ℓ = 5.92 km/s,
          C_t = 3.2 km/s,
          ρ = 7.9 g/cm^3

    Copper C_ℓ = 4.76 km/s,
           C_t = 2.3 km/s,
           ρ = 8.9 g/cm^3
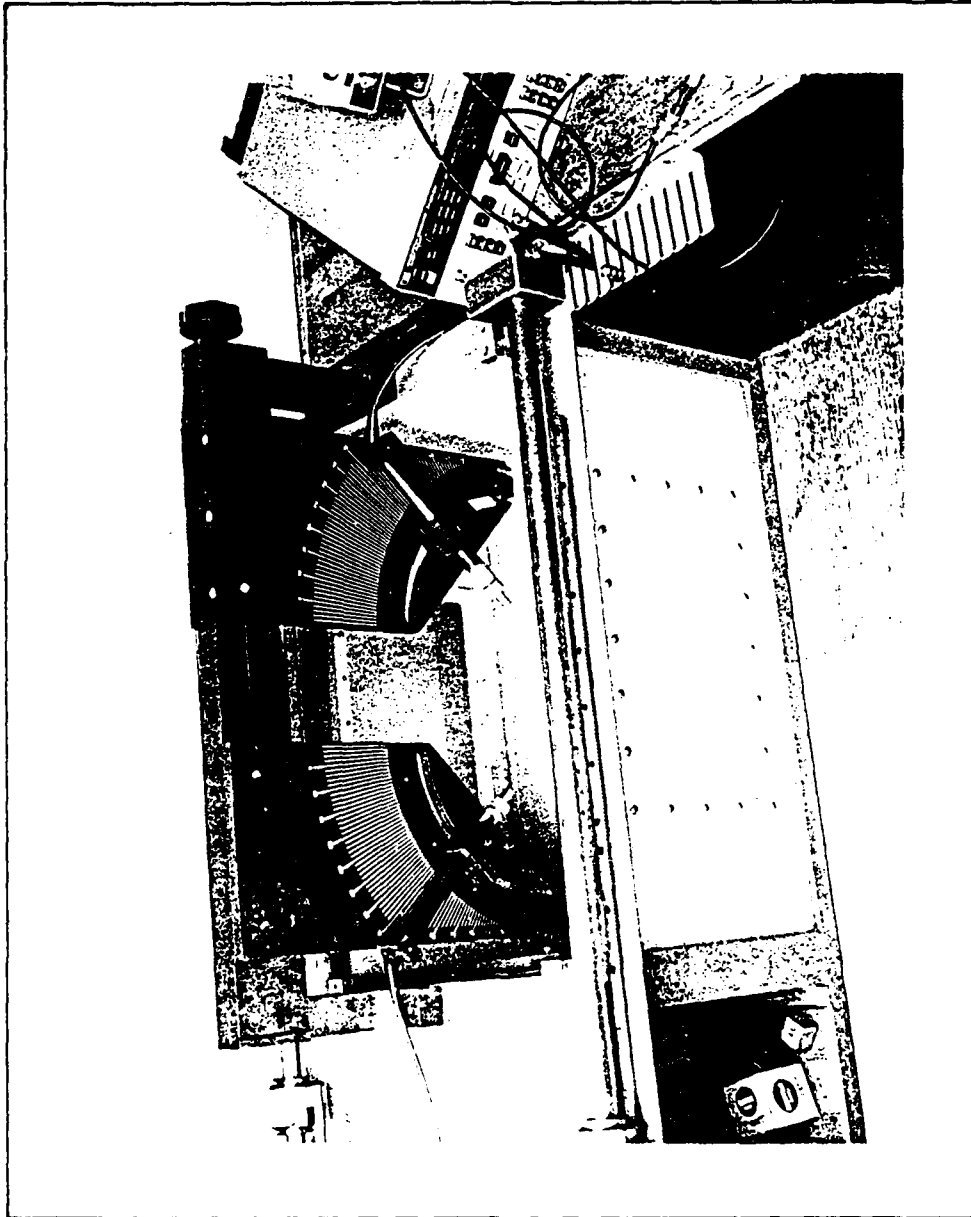
Figure 1. Transducer Fixture.
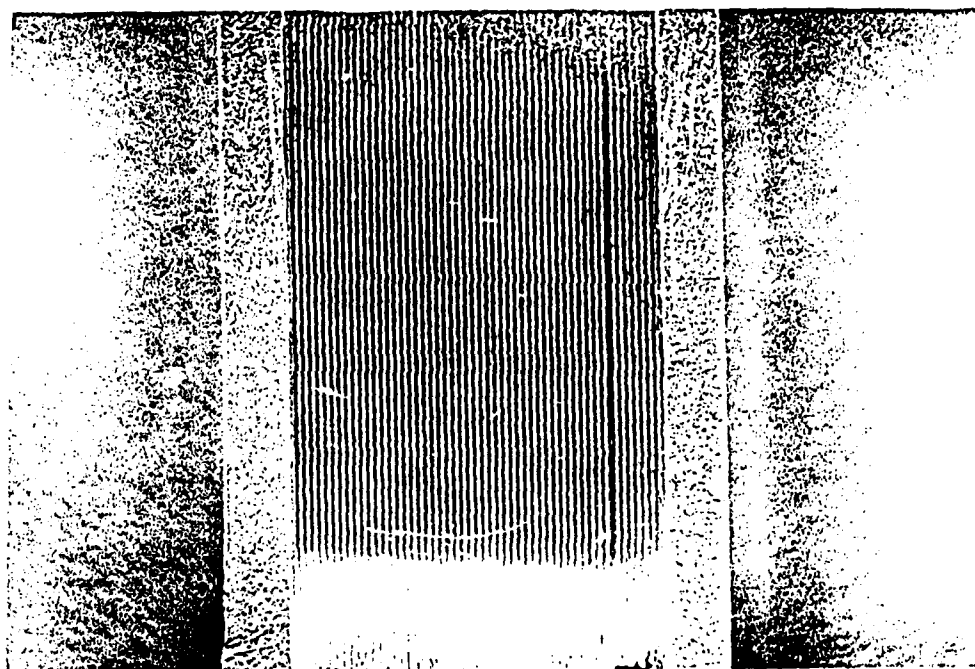
Figure 2. Copper-Stainless Steel Laminates. Arrows show the
Direction of propagation of Rayleigh Waves.
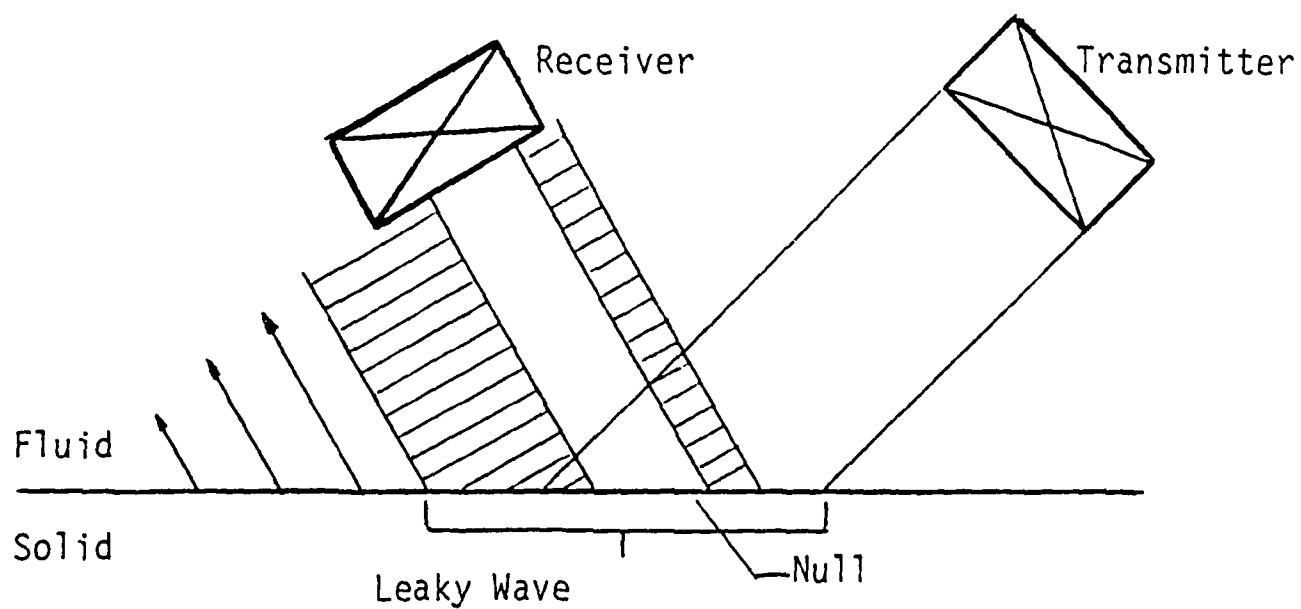
Figure 3. Schematic of Leaky-Rayleigh Wave experiment. Transmitter is fixed, while receiver scans along x-axis, which is collinear with the fluid interface. Dashed lines are supressed specular reflection. Shaded region contains most of the power.
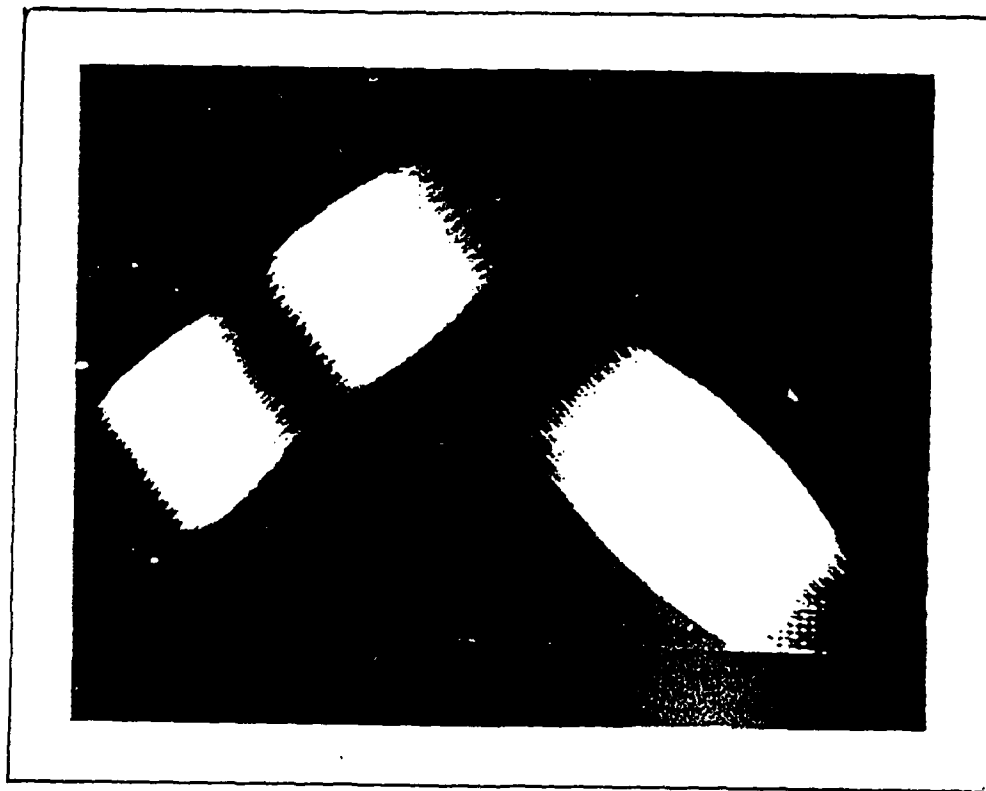
Figure 4.   Pulsed Schlieren Visualization of leaky Rayleigh
            Wave phenomena in a copper-stainless steel laminate.
            Incident tone-burst is at right, reflects from the
            surface, and appears distorted and displaced at the
            left of the frame. Null zone in reflected field is
            clearly visable.
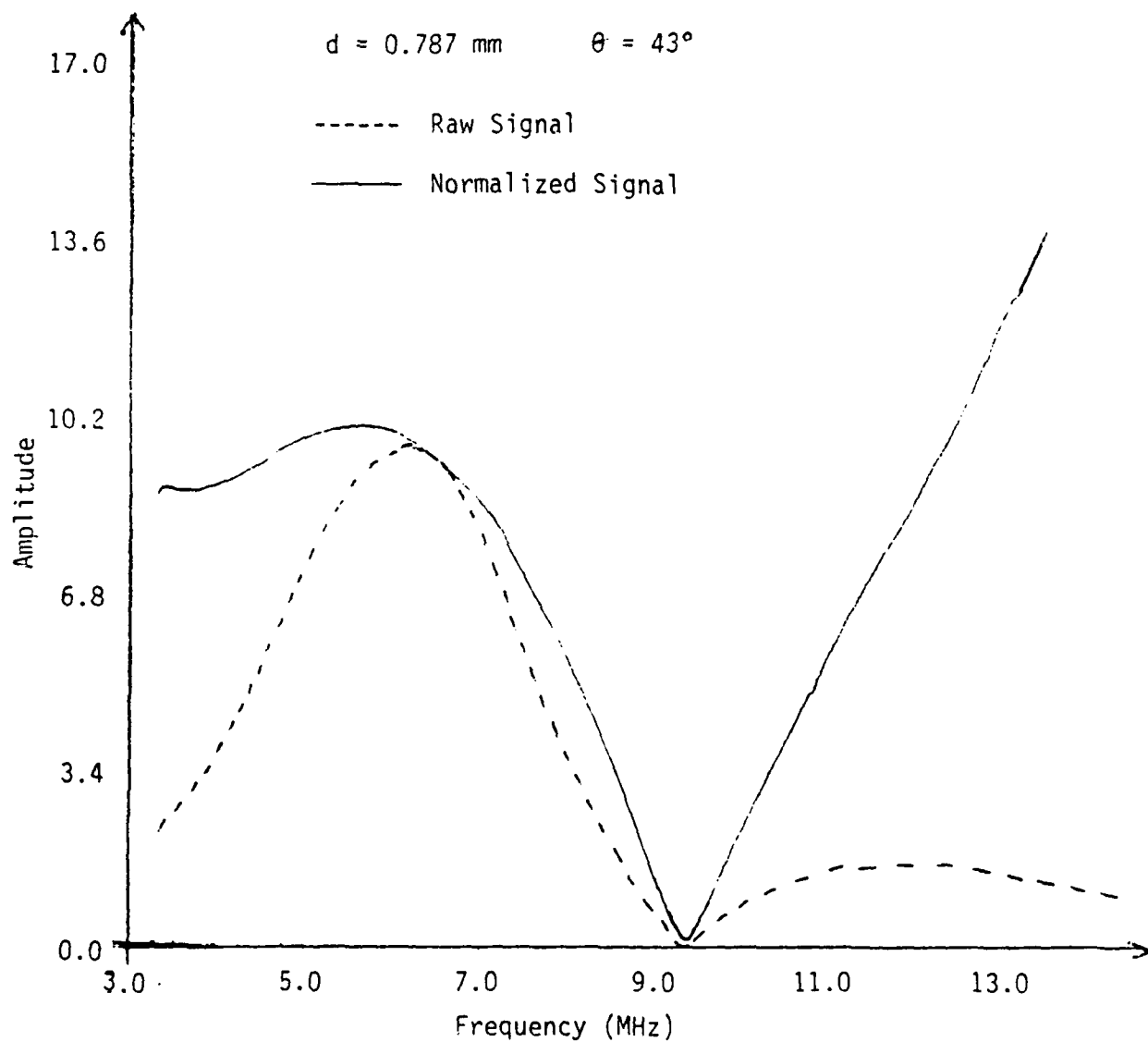
FIG. 5. Experimental Reflected Wave Signal versus Frequency x Cell size. Amplitude units are arbitrary
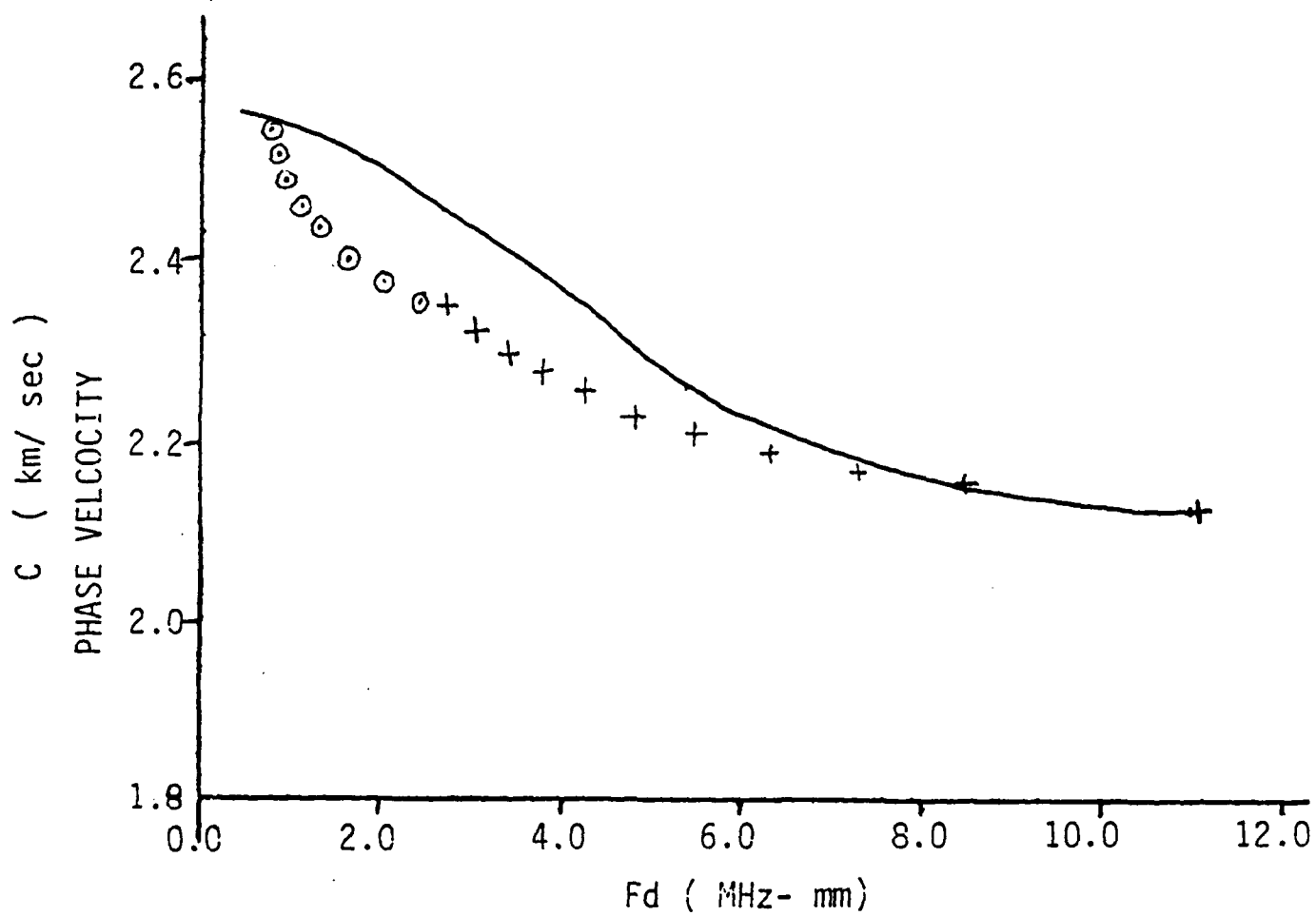
Figure 6. Experimental Reflected Wave Signal versus Frequency x Cell size. Amplitude units are arbitrary.

FINAL REPORT

PERFORMANCE IMPROVEMENT IN KNOWLEDGE-BASED

PROCESS CONTROL SYSTEMS
:

Submitted by
John M. Usher, Ph.D. Candidate - Principal Investigator
Gerald R. Graves, Ph.D. - Project Coordinator

December 1988

Department of Industrial Engineering
Louisiana State University
Baton Rouge, Louisiana 70803
(504) 388-5112

ABSTRACT

"Performance Improvement in Knowledge-Based Control Systems" is sponsored by the Air Force Office of Scientific Services under Contract No. F49620-85-C-0013/SB5851-0360, and administered under Universal Energy Systems Project 760. This research investigates improving system performance by using deterministic knowledge to enhance resolution of conflicts within the program. Different heuristic and numeric strategies of conflict resolution are presented. Each strategy is reviewed from the viewpoint of its usefulness within the process control environment. It is determined that use of deterministic knowledge is inappropriate for conflict resolution. However, alternative uses of this knowledge are presented.

FOREWORD

This report describes work completed under Contract Number F49620-85-C-0013/SB5851-0360 during the period from January 1 to December 31, 1988. This effort investigates the potential for using deterministic knowledge to enhance conflict resolution within knowledge-based process control systems.

The project is sponsored by the Air Force Office of Scientific Services, Bolling AFB, DC, administered by Universal Energy Systems, Dayton, Ohio, and conducted by researchers in the Department of Industrial Engineering at Louisiana State University in Baton Rouge, Louisiana. Major Steven LeClair of the AFWAL Materials Laboratory at Dayton, Ohio is the principal Air Force representative, and Mr. John M. Usher and Dr. Gerald R. Graves are the principal Louisiana State University researchers.

This report is divided into seven chapters. The first chapter introduces the concept of conflict resolution and identifies the major classes of resolution strategies. The next two chapters then present knowledge-based control and discuss the conflict resolution strategies from this viewpoint. In the remaining chapters, qualitative process automation is examined, and its method of conflict resolution is presented. Methods of improvement are discussed and conclusions provided.

CHAPTER 1

INTRODUCTION

This research report addresses the issue of performance improvement in real-time knowledge-based control systems. The objective of this effort was to enhance the technique for resolution of conflicts within the knowledge-based system. The targeted system for applying these improvements is the Qualitative Process Automation (QPA) controller developed and patented by Air Force researchers.

The proposed method of conflict resolution involved using deterministic knowledge to aid in the resolution process. The deterministic knowledge would be in the form of equations that could be solved by numerical methods. The results of the study found that it is not beneficial to use deterministic knowledge in conflict resolution. However, it could be used as one of the principle sources of object-level knowledge. In addition, it is proposed that QPA needs additional conflict resolution strategies in order to expand its usefulness.

This report is divided into seven chapters beginning with this introduction. Chapter 2 presents a definition of conflict resolution followed by a review of the different conflict resolution strategies now available. The next chapter, Chapter 3, introduces the knowledge-based process control system with a discussion of its functions, capabilities, and operational requirements. This is followed by Chapter 4 which addresses conflict resolution from the point of view of the process control environment. Chapter 5 then presents the theory of Qualitative Process Automation and discusses the operation of the QPA controller as applied to the process of laminating composites in an autoclave. This chapter concludes with a review of the current methods of conflict resolution used by QPA. Chapter 6 reviews the proposed methods of enhancing conflict resolution and discusses the problems with these methods. The last chapter, Chapter 7, presents concluding remarks and discusses future work.

CHAPTER 2

CONFLICT RESOLUTION

2.1 Introduction

In order to discuss the techniques of conflict resolution, it is necessary to understand the basic operation of a knowledge-based system. Knowledge-based systems can vary dependent on the type of control strategy applied (forward chaining, backward chaining, etc.) and the method used to represent the knowledge (frames, semantic nets, production rules, etc.). Since production systems are a common type of knowledge-based system, the following discussion will be based on the operational characteristics of these systems, but the concepts extend to all other types of knowledge-based systems.

A production system operates in cycles made up of the two operational phases: "recognize" and "act." The recognize phase can be further divided into two major steps, "match" and conflict resolution (see Figure 2.1). The "match" step employs some form of a control strategy (within the inference engine) to compare the contents of working memory with the rules in the knowledge-base. The objective of this step is to determine which rules are satisfied by the facts in working memory. When all the conditions of a rule are matched by data elements within working memory, the rule is instantiated. Since it is possible for the system to instantiate more than one rule in a single cycle, all the instantiated rules are placed in a set, called the "conflict set." In the next step, conflict resolution, the system will order the alternative instantiations within the conflict set and then select one or more of the instantiations to execute. The execution of the rule actions (consequents) is the function of the "act" phase of the operational cycle.

The objective of the conflict resolution step is to apply some specific strategy to differentiate, and therefore order the instantiations within the conflict set. The need for a conflict resolution strategy arises only in those systems where multiple solutions are possible. It is possible to construct a knowledge base such that multiple solutions will not occur in operation, this occurs when all the knowledge elements are applicable to mutually exclusive situations. Construction of such a knowledge base is a difficult task and reserved for use on knowledge bases of small size, or knowledge bases which use a highly-structured knowledge representation (e.g., semantic nets) where relationships between objects are more easily detected.

Sometimes even though there are several solutions possible, only one solution is acceptable. As an example, consider the two expert systems MYCIN and R1. MYCIN [1] is an expert system that diagnoses infectious diseases; therefore, it is important that the system consider all possible diseases in order to determine the patient's true disease. Then doctors can properly treat the
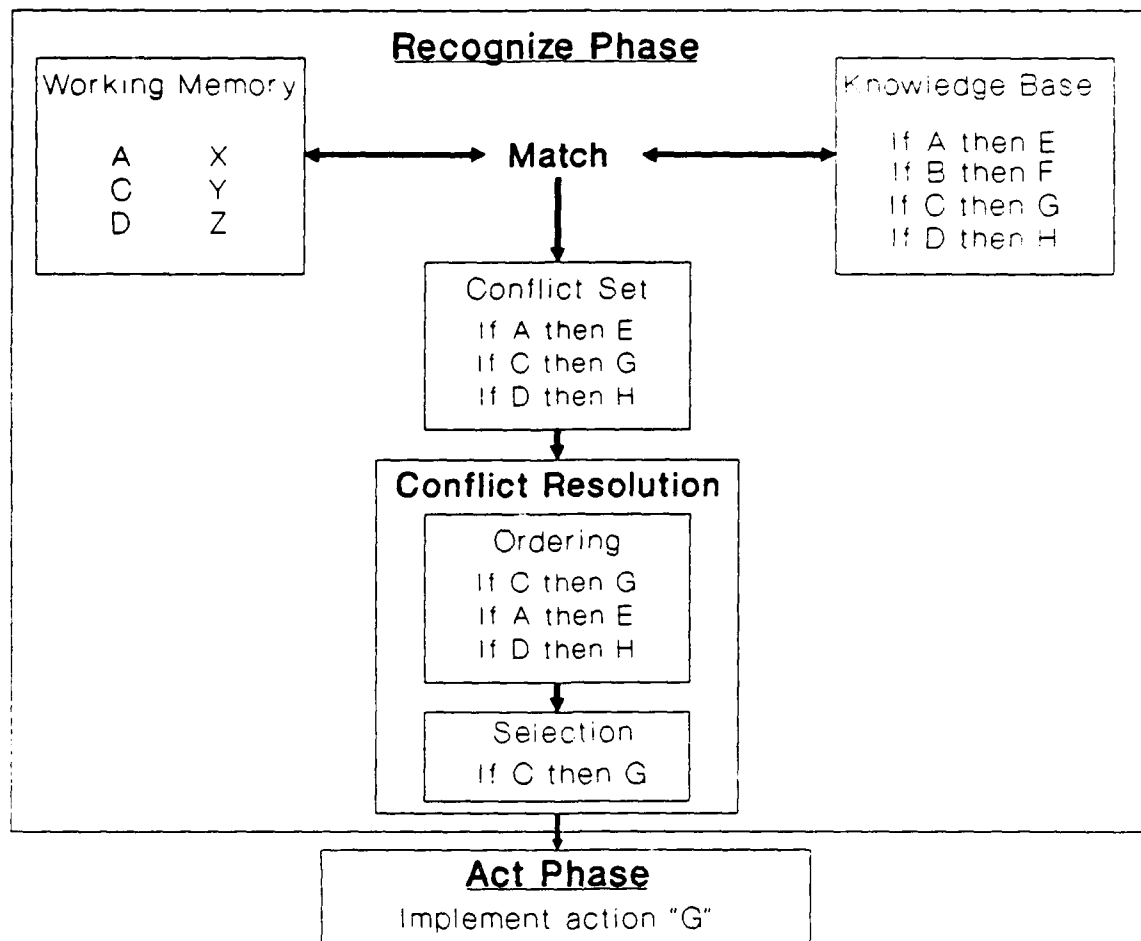
Figure 2.1: Production System Cycle.

patient. However, some systems do not need to consider all the possible solutions, even though they may exist. An example would be the expert system, R1 [2], that configures computer systems from customer orders. Any configuration that R1 determines, which meets the constraints, is acceptable. Therefore, conflict resolution is not required for all systems and is dependent on the application involved.

In the literature, the discussion of conflict resolution is limited to knowledge-based systems which use knowledge in the form of production rules (IF-THEN form). Production rules is one of the most widely used methods of knowledge representations. This representation lacks structure and as the size of the knowledge base grows so does the chance of the system arriving at conflicting alternatives. It is for this purpose that researchers developed the strategies of conflict resolution. In this chapter,

these different strategies for conflict resolution and the logic behind their use will be presented.

2.2 Literature Review

Conflict resolution has been of interest from the beginning of the development of knowledge-based systems. Just as humans arrive at several alternatives when reasoning about a solution, so will most knowledge-based systems. This results in a need to resolve the conflict between the alternative solutions and make a selection of the best solution based on some strategy. The following is a discussion of the conflict resolution strategies presented in the literature. These strategies are categorized as heuristic techniques, or numeric techniques. These techniques of conflict resolution represent the basic methods in use today.

2.2.1 Heuristic Techniques

One of the fundamental works on conflict resolution is that of McDermott and Forgy [3]. In this paper, McDermott and Forgy explore the requirements of conflict resolution strategies for production systems used within a dynamic environment. The important characteristics of the production system are its sensitivity to changes in the environment, and its stability in the face of these changes. A system's sensitivity is characterized by its ability to respond quickly to changes which occur in the environment. The system's stability is determined by how well it maintains continuity in its behavior. McDermott and Forgy state that "the function of the conflict resolution strategy is to provide a mechanism that can preserve sensitivity and stability without sacrificing production autonomy" [3].

McDermott and Forgy present five classes of strategies for conflict resolution. Each class of rules is characterized by the criteria it uses to judge the worth of an instantiation (see Table 2.1). Within each class, a variety of individual rules for resolving conflicts can be developed. These rules can be distinguished by their selectivity, and the source of knowledge they use to make their decision.

The selectivity of a rule is defined by its capability to differentiate the worth of each member within the conflict set. If a rule is capable of distinguishing between the worth of each member of the conflict set (no two are of equal worth), then it is possible for the system to order the alternatives and select the best. Such a rule would be considered strongly selective. As a conflict resolution rule decreases in selectivity, it capability to distinguish between the alternative's worth is decreased. This results in a greater chance that two or more alternatives will be viewed as having equal value as a solution. In order to make a selection, another rule will have to be applied to provide further clarification.

Table 2.1: Classes of Conflict Resolution Strategies.

CLASSES OF CONFLICT RESOLUTION STRATEGIES

Production Order Rules
Special Case Rules
Recency Rules
Distinctiveness Rules
Arbitrary Decision Rules

The possible knowledge sources that can be used to make a decision include the knowledge-base, working memory, and the inference engine's (control program's) state memory. The knowledge base provides information about the order in which the rules were added, or organized. Working memory provides information on the ages of the facts it contains, and the order those facts were received. The third source, state memory, can hold information about the decisions made in prior cycles.

The five classes of conflict resolution strategies, listed in Table 2.1, encompass a majority of the resolution techniques currently in use. In the following discussion the basic strategy of each of the five classes of rules is presented. For examples of some possible rules that can be developed within each class, the reader is referred to [3].

The first class of rules, referred to as "production order rules", uses the ordering of the rules within the knowledge-base as the criteria from which to make its selection. The order criteria can be based on the age of a rule or possibly its physical location within the knowledge base. This method requires that the user develop a scheme for classifying and correctly placing each rule within the knowledge-base. This complicates maintenance of the knowledge base.

The second class of rules, "special case rules", favors an instantiation which is a special case of another instantiation in the conflict set. The definition of a "special case" is left to the user that develops the explicit rule. As an example, consider a resolution rule that states:

A rule, R1, is a special case of rule, R2, if rule R1 has a greater number of preconditions than rule R2.

Then if the two rules,

Rule-1: IF (A) AND (B) AND (C) THEN (D)
Rule-2: IF (A) AND (B)   THEN (F)

are members of the conflict set, this strategy would favor Rule-1 over Rule-2, since Rule-1 has three preconditions, while Rule-2 only has two. An example of a related rule that is less selective is:

> A rule, R1, is a special case of rule, R2, if the preconditions of R2 match a subset of the preconditions of R1.

Using the two example rules above, this strategy would again select Rule-1 over Rule-2. All the preconditions of Rule-2 appear in Rule-1, therefore, Rule-1 can be considered a "special case" of Rule-2. Following the same basic strategy of this class, other variations of these rules are possible. This strategy class is considered weakly selective, in that it only eliminates those instantiations within the conflict set that are general cases of other instantiation in the conflict set.

A third strategy for conflict resolution, called "recency rules", bases the ordering of the alternative instantiations on the amount of time that the data elements of each instantiation have resided within working memory. Dependent on the application, a strategy rule could be developed that favors instantiations using old elements, or one that favors instantiations using the newer elements in working memory. The method used to measure the age of the data element also affects the ordering of the instantiations.

The fourth strategy, "distinctiveness rules", makes a selection based on the similarity or dissimilarity of the instantiations in the conflict set to those instantiations that the system selected in previous cycles. This strategy can be used to prevent any production from firing on consecutive cycles.

The final strategy class contains "arbitrary selection rules". In this class, the system performs the ordering of the alternatives using some method of random selection. This class of rules demonstrates strong selectivity since random selection guarantees that the system will be able to distinguish between the alternatives. Such a strategy should only be applied in cases where no other strategy can provide any further differentiation between the members of the conflict set. This strategy assumes that each alternative is approximately equivalent in its worth to the system; therefore, random selection of one will not cause a problem.

McDermott and Forgy [3] conclude that no simple conflict-resolution strategy can be completely satisfactory. They conclude that no single conflict resolution strategy is a strong supporter of both sensitivity and stability. Thus a combination of strategies is required to develop a sound technique for resolution of conflicts.

Barr and Feigenbaum [4] also discuss conflict resolution in production systems. They identify the conflict resolution phase as the time in the cycle of the system when "basic cognitive

traits like action sequencing, attention focusing, interruptibility, and control of instability are realized". Therefore, because of the capability of the conflict resolution strategy to control these traits, the knowledge base maintains a modularity that contributes to the stability of the system. They list seven common strategies used for conflict resolution. In the discussion to follow, each of these strategies is presented and related back to the five main classes of strategies proposed by McDermott and Forgy to demonstrate the comprehensive nature of these classes.

The first and simplest of the strategies instructs the system to use the first rule it instantiates. Therefore, the reasoning cycle terminates at the first instantiation of a rule. One could argue that this method is not a resolution strategy since it does not formulate a conflict set or deal with more than one alternative (no conflict ever arises). In such a system, the order in which the rules are placed in the knowledge base becomes the ruling factor in their worth. This strategy falls within the "production order" class of conflict resolution rules.

A second method involves selecting the rule from the conflict set which has the highest priority. This strategy requires the assignment of priority by the programmer according to the demands and characteristics of the task. The weakness of this method arises in the method used to determine the weights of each rule. This method can be considered to belong to the "production order" strategy class, in that the assignment of priority values to the contents of the knowledge base requires the same logic as ordering the knowledge base in terms of importance.

The third method listed belongs to the class of rules labeled "special case" rules. This strategy of resolving conflicts selects the rule that is the "most specific" of the rules in the conflict set. The term "most specific" means the rule which has the most detailed pre-conditions. This logic assumes that the more conditions satisfied by rule, the better it characterizes the current state of the system.

The fourth method for conflict resolution involves selecting the rule that refers to some fact most recently added to the contents of working memory, a "recency" class rule. This strategy has the effect of focusing the system. For example, suppose that on the first cycle two rules (R1 and R2) were instantiated and the system selected rule R1 to fire. In the next cycle, if the system instantiates rules R1, R2, and R3, then the resolution strategy would select R3 since this is evidently the action to finish what R1 started. This strategy has the effect of focusing the system on the results of the actions most recently taken.

The fifth approach involves selecting the rule in the conflict set which has not previously been instantiated by the system. This allows the system to give immediate attention to events that have not previously occurred. This strategy belongs to the "distinctiveness" class of rules. The next approach to conflict resolution is identical to the "arbitrary selection rules" class,

in that it just makes an arbitrary selection of a rule from among the conflict set.

The last method listed by Barr and Feigenbaum [4] involves not making a selection at all, but instead, exploring all the applicable rules in parallel. This is the strategy employed in the expert system, MYCIN [1]. In this technique, the resolution method is not based on the alternative instantiations, but on the effects that each alternative produces when fired. Such a strategy would be difficult to implement and would still require some means to differentiate the solutions that each line of reasoning determines. For physical systems, like a process control system, this strategy would require a simulator to explore the effects of each applicable rule in the conflict set. This strategy does not belong to any of the five main classes of conflict resolution strategies. However, it could be implemented using a technique based on meta-knowledge, the topic to be discussed next.

A new strategy class, not yet discussed, involves the use of meta-rules to resolve conflicts. A meta-rule is one form of meta-level knowledge [5]. Simply put, meta-knowledge is knowledge about the system knowledge (object-level knowledge). In the context of conflict resolution, the meta-rules would contain knowledge that could be used to make a selection from among the alternatives within the conflict set. In this regards, meta-rules would qualify as a selection strategy for conflict resolution.

The knowledge contained in the meta-rules can encompass general process knowledge or even address the current process state. Therefore, the meta-rules can be applied to reason about the usefulness of the knowledge that each alternative within the conflict set provides. This results in the selection of the alternative(s) most appropriate for the given context. Example meta-rules for a batch process might state:

```
IF   ( in the cooldown sequence )
THEN ( ignore all rules related to heat effects )
```

or possibly,

```
IF   ( current temperature > maximum )
THEN ( ignore all rules requesting temperature increases )
```

Meta-rules differ from the other heuristic strategies. The other strategies do not consider the usefulness of the alternative, they instead use a fixed set of rules that consider the characteristics possessed by each alternative (age, placement, number of preconditions, similarity to other knowledge elements, etc.).

One important point about meta-rules is that they do not make any conclusions about the validity of the alternative rules in the conflict set. They only make a decision based on the utility of the rules. Consequently, the knowledge provided by the meta-rules cannot be embodied within the object level rules

themselves. The meta-level knowledge used by the conflict resolution system would be separate from the object level knowledge in the knowledge base.

The selectivity of the meta-rules is dependent on the detail provided by the meta-knowledge they embody. It would be difficult to provide the knowledge necessary to deal with all possible conflicts; therefore, this strategy is best applied in combination with another. One advantage provided by the use of meta-rules, is that the resolution strategy is stated explicitly in rule form. This aids in the editing and maintenance of the system and provides a means for explaining system behavior.

In an article by Sauers and Walsh [6], they divide conflict resolution strategies into two major types: elimination strategies and selection strategies. Elimination strategies are those methods which rule out the consideration of certain alternatives based on some criteria. The selection strategies are those methods that will pick from among the alternatives those deemed acceptable. Using these definitions it is possible to further divide the six classes of conflict resolution strategies, defined earlier, into these two major categories (see Figure 2.2).

Sauers, and Walsh, believe that when a conflict resolution strategy is used in a real-time knowledge-based system (such as process control), it should possess additional capabilities to increase the efficiency of the system. They state that the standard methods of conflict resolution are flawed in that they are "unaware of the characteristics of the system environment, and are thus unresponsive to changes in this environment" [6]. If the conflict resolution system were to take into account system performance statistics, it could use these statistics to aid in selecting the optimum alternative. Sauers and Walsh [6], go on to mention that conflict resolution strategies "should also be allowed to address real-time constraints by enabling productions themselves to alter the conflict resolution strategy used in critical situations." They also propose the use of meta-conflict resolution procedures to test the validity of possible instantiations before they are placed within the conflict set, hoping to reduce the number of required instantiations. No detail is provided on how these capabilities would be implemented.

2.2.2 Numeric Techniques

In addition to the methods discussed above, there exist numeric methods of conflict resolution. Ferrante [7] states that "conflict resolution has been treated by a number of different authors who use various techniques and terminology such as reasoning about uncertainty or 'the integration of knowledge from disparate sources'." He found that most work in the area of conflict resolution has focused on the use of numeric approaches to conflict resolution, such as Bayesian or Dempster-Shafer techniques.

Conflict Resolution Strategies

```
Conflict Resolution Strategies
                    |
        +-----------+-----------+
        |                       |
Elimination Strategies    Selection Strategies
        |                       |
   +----+----+       +-----+----+----+----+
   |         |       |     |    |    |    |
+------+ +--------+ +----+ +-----+ +-----+ +--------+
|Special |Distinct | |Meta-| |Prod.| |Rec. | |Arbitr. |
|Case    |iveness  | |Rules| |Order| |Rules| |Decision|
|Rules   |Rules    | |     | |Rules| |     | |Rules   |
+------+ +--------+ +----+ +-----+ +-----+ +--------+
```
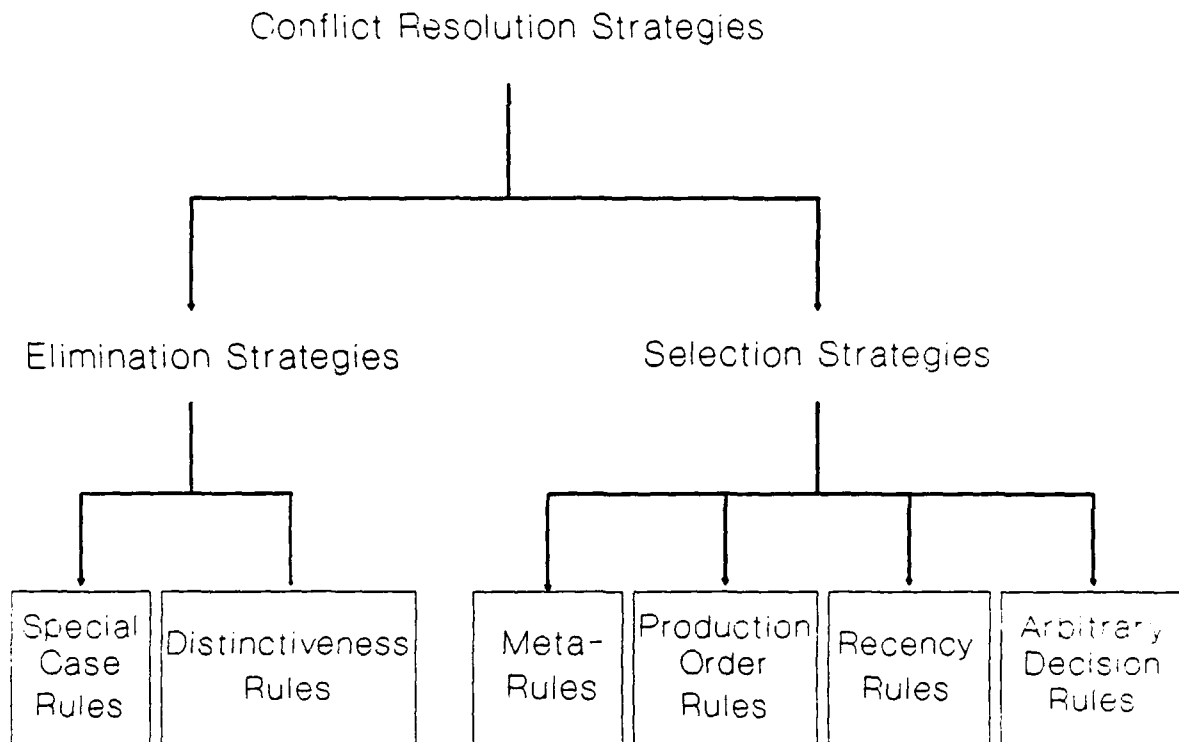
Figure 2.2: Classes of Heuristic Conflict Resolution Strategies.

The numeric methods of Bayesian and Dempster-Shafer are techniques for reasoning about the uncertainty of the knowledge applied to solve the problem. These techniques provide a method for propagating the certainty in a line of reasoning. Therefore, the result of using this type of numeric method would be a conflict set where each instantiation has a certainty value associated with it. These priority values can then be used to order the alternatives within the conflict set, and to perform the elimination and selection. Therefore, the conflict resolution method would encompass the Bayesian or Dempster-Shafer calculations along with a procedure used to order the alternatives.

These numeric methods of conflict resolution are similar to the "priority rule", mentioned in Barr and Feigenbaum [4]. The priority values represent the resulting belief values calculated for each alternative within the conflict set. Compared with the heuristic strategies discussed previously, these numeric methods

attempt to apply a more formalistic strategy for determining the worth of each alternative within the conflict set. These methods utilize belief functions to characterize the worth of a deducted conclusion (rule consequent). Using the belief value associated with each alternative in the conflict set, the members can be ordered. This idea is similar to the heuristic strategy which uses priority values as the criteria for ordering. The difference between the two is in the method used to obtain the criteria (belief values) for those rules within the conflict set. In the heuristic method, the priority values associated with a rule are constant and not dependent on the line of reasoning used to arrive at an alternative solution. In the numeric approach, the belief functions are dependent on the evidence provided. The system propagates the belief values through the reasoning and the final values obtained depend on the evidence used to arrive at the conclusions. Using the final belief values, the system will order the alternatives and then make a selection. Since the propagation of these belief values is part of the reasoning technique, the function of the conflict resolution system becomes more an integral part of the "recognize" phase and is not as distinct in its operation, as for the heuristic methods.

The difference among the various numeric methods of conflict resolution is the mathematical technique used to propagate the belief values used in the reasoning of the system. The two basic methods involve the use of the Bayesian or Dempster-Shafer technique for propagation of the belief values in the reasoning of the system [8][9]. Bayes' rule represents the belief function using statistical probabilities. Here, the probability establishes the belief in the deduction made based on the probabilities of the evidence used (i.e., preconditions). The weakness of this approach lies in the requirement that the conditional probabilities concerning system states be available 'a priori'.

Dempster-Shafer calculus provides a means for propagating belief values in a more general manner than the Bayesian approach. The Dempster-Shafer technique allows for multiple beliefs in that it does not require that:

Prob(event "a" occurs) + Prob(event "a" does not occur) = 1

as is the case in Bayes' approach. The disadvantage arises in that the Dempster-Shafer method is more complicated to apply than the Bayesian approach.

These two methods represent only the basic techniques that can be used for propagating belief functions. Examples of other numeric, and heuristic, strategies of conflict resolution will be given in the next section.

2.2.3 Implementations and Extensions of the Basic Strategies

In the following discussion, five example implementations of conflict resolution techniques are presented. These techniques represent possible extensions or combinations of the basic strategies discussed in the previous sections.

An automatic-programming system, PECOS, developed by David Barstow and discussed in Bar and Feigenbaum [4], uses a combination of techniques for conflict resolution. This implementation is unique in its approach to conflict resolution, in that it employs one of three strategies depending on the current situation. For example, if PECOS is interacting directly with the user, then the user has the power to resolve the conflict. If the user chooses not to make the selection, then PECOS will make a selection of one of the applicable rules using heuristics (meta-rules) to determine the alternative which produces the most efficient implementation. The heuristics are able to handle about two-thirds of all the possible cases which arise. In the event the user does not make a selection and the heuristics do not apply, then PECOS has the capability to apply each alternative in parallel. This results in several solutions which can be compared directly in terms of some goal criteria.

Another variation of the basic heuristic conflict resolution strategies can be found in the language YES/L1 [10]. YES/L1 is designed for use with real-time applications and provides a method for the integration of rule-based programming and procedural programming in IBM environments. In general, YES/L1 combines the heuristic strategies of production order, recency, special case, arbitrary decision, and distinctiveness, to formulate the overall method of resolving conflicts. As a first step the system employs the use of assigned priority values for each rule to provide initial ordering. If a tie results, then the system selects the instantiation that was most recently created. If a tie still exists, then the system selects the "most specific" rule, defined as the rule with the greater number of preconditions. As a last resort to resolving remaining conflicts, the system will make a random selection. After a rule is instantiated once, it is not allowed to fire again until the data in the instantiation changes in value. An instantiation is automatically re-enabled for firing only when its rule refers to an attribute (in the antecedent) that has changed since the previous firing. This eliminates the repeated firing of a rule and requires that the rule's precondition be found false before it can again be instantiated. In addition to these capabilities, YES/L1 allows the programmer to access the conflict set and program a custom strategy for conflict resolution.

Garvey, et al. [11], discusses a numeric approach to conflict resolution which is an extension of Shafer's mathematical theory of evidence. The resulting technique, like the Dempster-Shafer method, is more general than either a Boolean or Bayesian approach. Garvey's purpose was to develop a system which could interpret the important aspects of a system's state

based on information obtained from different sources, and integrate this knowledge to arrive at the appropriate conclusion.

Another possible method for conflict resolution, combines heuristic and numeric techniques for use in systems employing multiple knowledge sources [7]. The conflict resolution strategy integrates the concept of reasoning about uncertainty, to determine the relative validity of beliefs, with the concept of constraint propagation, which uses contradictions to restrict the range of applicable choices. This new strategy is termed "characteristic error" conflict resolution and is unique in its "method of treating each knowledge source as a separate entity whose validity is determined only from the information the knowledge source itself provides" [7]. The idea is that within a multi-source system, each individual knowledge source is, to some extent, the best judge of its own performance.

When a using a shell to develop a knowledge-based system, the user must contend with the strategies provided by the vendor. Sometimes the shell will allow the user to implement a custom strategy or develop a combination of strategies from those provided. As an example, consider GEST, a generic expert system tool, from Georgia Tech's Research Institute [12]. GEST allows the user to customize the conflict resolution strategy. GEST supports six different strategies and allows for prioritized combinations of these strategies to be employed. The conflict resolution strategies provided are [12]:

1. complexity - fire the most complex rule
2. simplicity - fire the simplest rule
3. recency - fire the most recently used rule
4. reverse recency - fire the least recently used rule
5. antecedent ordered - fire the rule with the highest antecedent priority.
6. consequent ordered - fire the rule with the highest consequent priority.

Each of these strategies can readily be categorized into the one of the six main classes as presented by McDermott and Forgy [3].

Based on the above findings, it is evident that there is no single method for conflict resolution. Many strategies are possible, and the selection of the appropriate strategy should be dependent on the application.

CHAPTER 3

KNOWLEDGE-BASED PROCESS CONTROL SYSTEMS

3.1 Introduction

The application of knowledge-based systems to process control is a relatively new area of research, but one that is gaining the attention of researchers in both the academic and industrial environments [13]. This interest arises because both the manufacturing and process industries have complex production management and control problems which current analytical methods are often unable to solve, or too difficult to deal with at the production level. The operation of these complex processes usually involves a human operator who relies on the use of empirical knowledge gained from operational experience. Due to their experience, it is possible for these operators to provide near-optimal operation in terms of the product's quality and consistency. Processing problems arise when more than one operator is responsible for a given process. The differences in the methods of control employed by each operator results in variations in product quality and material consumption. These variations in the product, and the inconsistency in the applied control strategy, are two primary reasons for seeking to automate the control of these ill-understood processes [14].

The knowledge-based process control system provides a way to implement a consistent control strategy that employs both the heuristic knowledge used by the operator and the deterministic knowledge from control theory. These knowledge-based control systems can be used to solve a whole host of problems where conventional methods are inadequate - for example, where no mathematical or algorithmic solution exists because data is inexact, uncertain, or based on probabilities.

In the discussion which follows, the general characteristics of a knowledge-based system, as applied to process control, will be presented. Discussion begins by defining the type of control applied to batch and continuous processes. This section is followed by a presentation of the functions that a knowledge-based program can perform when used in the process control environment. The last two sections include discussions on the structure of the knowledge-based control system, and the operational requirements for the knowledge-based program when used in the dynamic process control environment.

3.2 Continuous and Batch Control Systems

The purpose of a process control system is to maintain control of the process within specified operational constraints. The method used to control the process is dependent on whether the process operates in a continuous or batch mode. A continuous

process is perceived as a process that continues to operates until either no more product is desired, or some failure causes a shutdown. Once the process is up and running, the system will experience upsets in the process due to disturbances (e.g., changes in the feedrate, feed composition, and steam pressure, etc.). The controller compensates for these disturbances by changing the values of the manipulative variables. This type of control is referred to as "regulatory" control. The overall objective is to maintain the control variables at their set-points. For the start-up and shutdown of the process, the system requires different methods of control. These methods encompass techniques ranging from manual control to methods of "servo" control where the set-point is adjusted and used to drive the process to the desired state. Since these transient stages (start-up and shutdown) represent only a small percentage of the operating cycle of a continuous process, the strategies for these steps are not considered to be an integral part of the control system and are handled by the engineering staff.

On the other hand, in batch processes the transient phases of start-up and shutdown can be a major part of the process cycle, and therefore, control of these phases of the process become important. In addition, sometimes a batch process is sequenced, that is, the process is driven to proceed through a series of process steps from start to completion. For these processes servo control is the major method of control. Examples of batch processes include the blending of ingredients in the food industry, the mixing of chemicals to form a reaction in a reactor, and composite lamination in an autoclave.

3.3 Functions of the Knowledge-based Process Control System

In addition to fundamental control of the process, researchers have developed and commercialized methods for providing additional capabilities within the control system. These capabilities include techniques for self-tuning control and process optimization. Industry was and still is slow to accept these methods because they are rigorous and complex. With the introduction of knowledge-based systems in the area of process control, researchers immediately began to investigate using the new technology to provide these same extended capabilities (self-tuning control, process optimization) and more. The key was that instead of having to characterize the system mathematically, the system could be modeled heuristically and the knowledge used by the operator could be modeled and applied to control the process. The functions that these new knowledge-based systems can provide include:

1. self-tuning control of an inner loop controller,
2. optimization of the controlled process,
3. process monitoring, diagnosis, and alarm advising, and
4. assistance in process start-up and shut-down.

Therefore, the idea of applying knowledge-based systems to process control has prompted a reexamination of old problems.

Knowledge-Based Process Control System

Operational Constraints

Knowledge-Based Controller — Control Commands → Process

Sensor Values
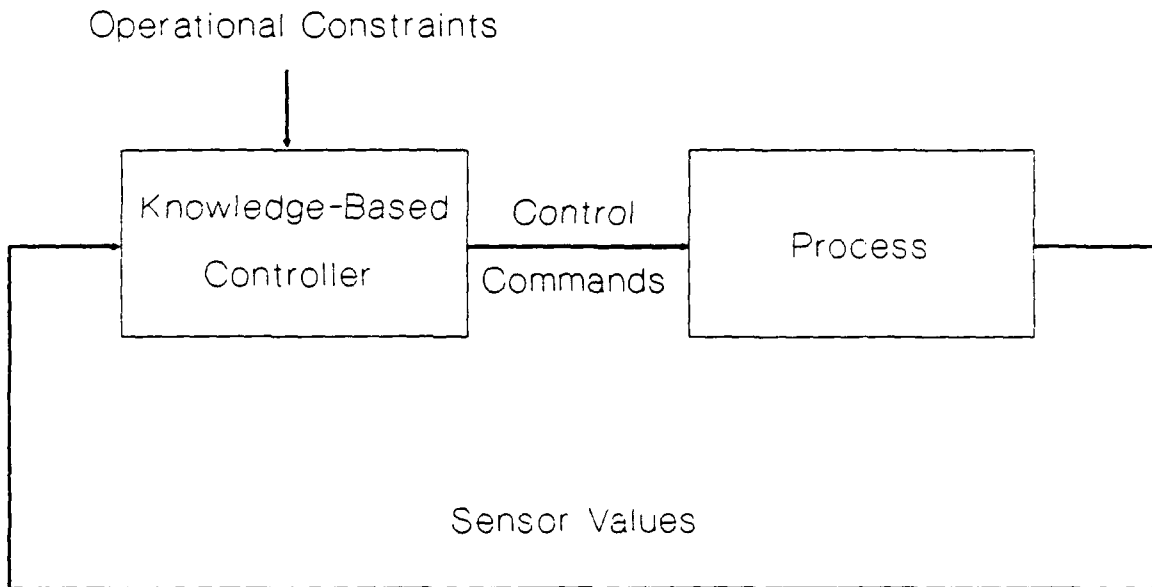
Figure 3.1: Block diagram of a knowledge-based process control system.

3.4 The Structure of a Knowledge-Based Process Control System

The fundamental structure of a knowledge-based process control system can be represented by the block diagram shown in Figure 3.1. The knowledge-based component is interconnected to the process in a feedback loop. The function of the knowledge-based component is to observe the output of the process (through the sensor values) and formulate a conclusion about the perceived state of the process. Then the knowledge-based program will make a decision on how to react (manipulate the process) to position the process at a desired state. The method in which these functions are implemented varies dependent on the application process, and the level of interaction between the process and the knowledge-based system.

Operational Constraints

```
                    |
                    v
         +---------------------+        Sensor
         |   Knowledge-Based   |
         |      Program        |        Values
         +---------------------+
                                        
    +----------------+    +-----------+         +-----------+
    |  Conventional  |    |  Control  |         |           |
    |   Controller   |----| Commands  |-------->|  Process  |
    +----------------+    +-----------+         +-----------+

                         Sensor Values
```
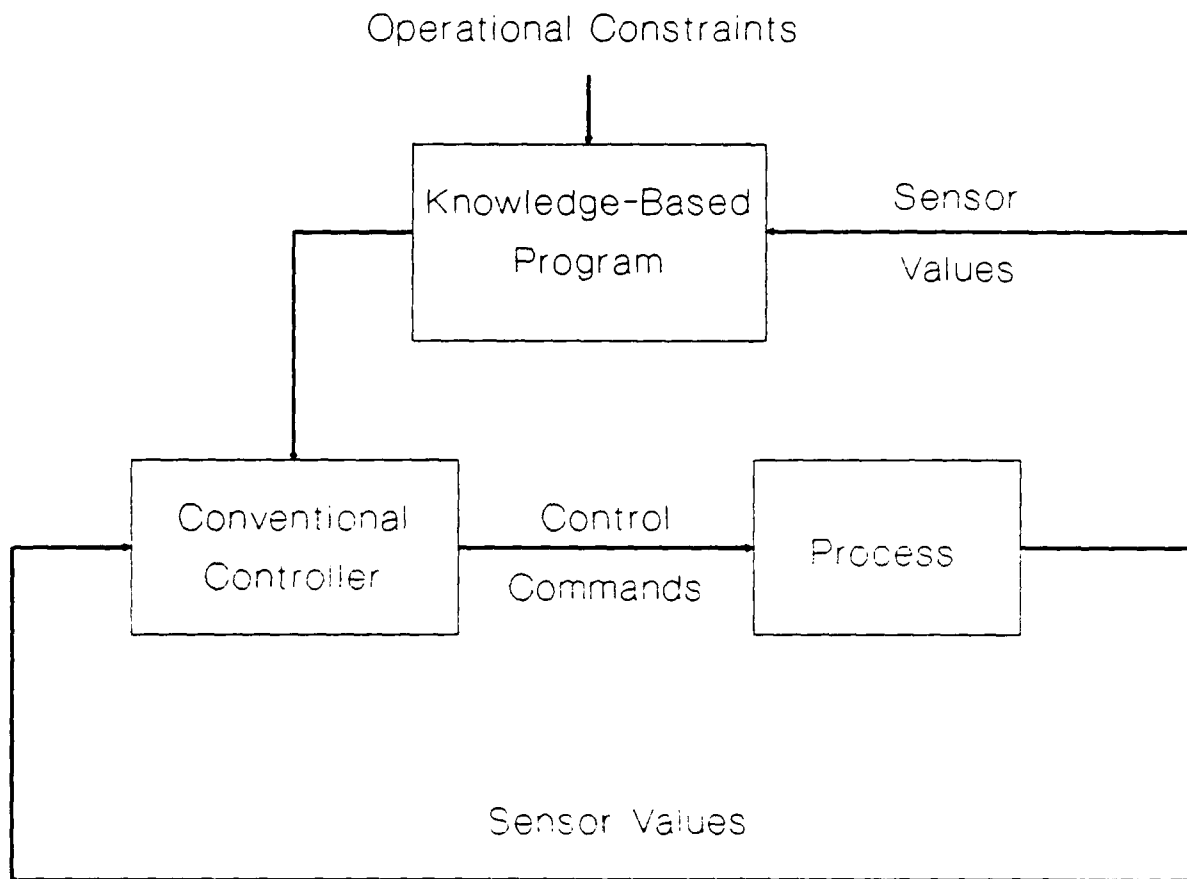
Figure 3.2: Block diagram of a knowledge-based process control system with the knowledge-based controller in a supervisory position.

For each type of process, continuous or batch, the knowledge-based component of the system can interact with the process at two different levels. At the lowest level, the knowledge-based component will directly control the process by manipulation of the final control elements through interface hardware. The second level of interaction, places the knowledge-based portion of the system outside of the feedback loop. The knowledge-based program then issues commands to a conventional controller within the feedback loop (see Figure 3.2). This places the knowledge-based program in a supervisory mode and alleviates some of the constraints on the design requirements of the knowledge-based program itself. In this configuration, the knowledge-based program will interact with the controller providing adjustments to set-point and/or tuning parameters. At either level of interaction, the knowledge-based program provides an interface for the operators to interact with the process.

The knowledge-based portion of the control system is composed of several major components which include the knowledge base, the control program, and working memory (see Figure 3.3). The control program directs the reasoning process of the system using the knowledge base and the evidence contained in working memory. This reasoning results in control actions that the program issues directly to the controller (or the control elements directly). The knowledge base is composed of facts and heuristics. "The 'facts' constitute a body of information that is widely shared, publicly available, and generally agreed upon by experts in a field. The 'heuristics' are mostly private, little-discussed rules of good judgment (rules of plausible reasoning, rules of good guessing) that characterize expert-level decision making in a field" [15]. Working memory is a dynamic database that is used to store evidence (proposed facts) about the system that are currently true. These facts can be anything from the variable values derived from the sensors to information about the process states that the system has obtained in its reasoning.
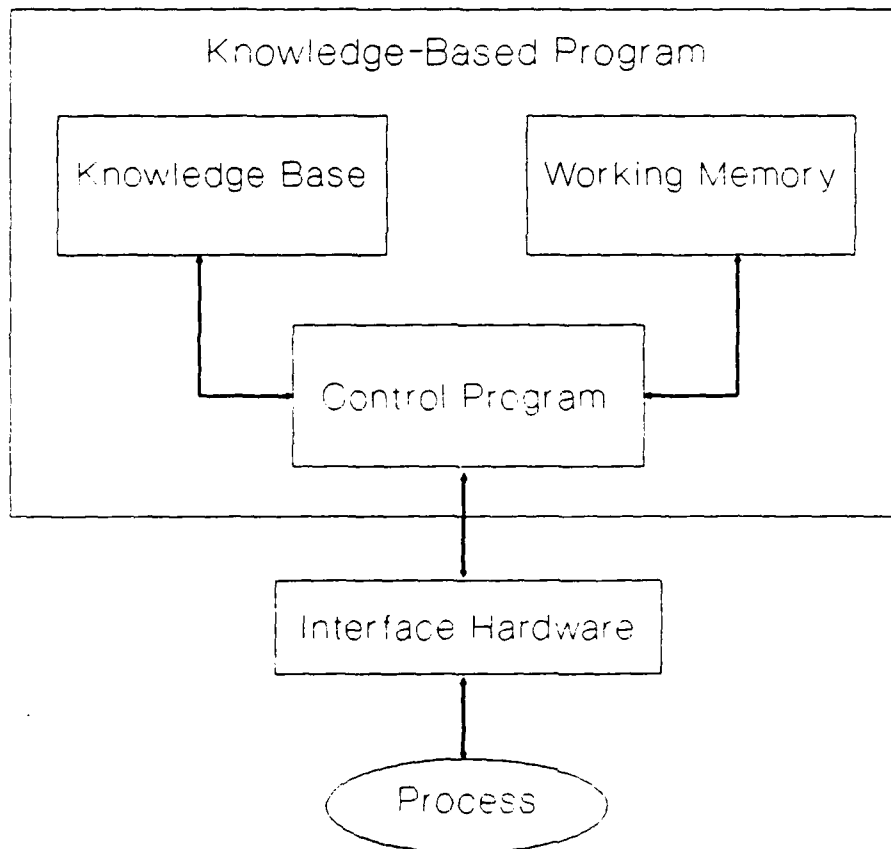
Figure 3.3: Block diagram of a knowledge-based program.

A knowledge-based process control system differs from a conventional control system in several ways. One difference is that a knowledge-based process control system, uses symbolic knowledge to reason about the process as opposed to the conventional means of mathematical equations. A second difference is that the knowledge is used to emulate the behavior of the operator rather than the process. A third difference is that the knowledge-based control system will operate in an event-driven mode as opposed to the data-driven mode of conventional controllers. Finally, in a conventional controller the knowledge pertinent to the process and the methods for using this knowledge are intertwined. Whereas, in a knowledge-based system, these two components are separate, thus allowing for ease in maintenance and modification.

The knowledge-based process control system provides a means of applying a consistent control strategy using experiential knowledge, assuming that such knowledge is available. This consistent control strategy satisfies the goal of reducing product variation and improving product quality.

3.5 Operational Requirements

In a production environment, the data used in controlling the process is dynamic in nature. This operating environment is different from that of other knowledge-based systems applications. Because of the differing environments, the knowledge-based program must possess additional capabilities in terms of its operating characteristics. These capabilities will include [13]:

- providing time critical responses,
- providing non-monotonic reasoning,
- performing in continuous operation,
- catering to asynchronous events,
- interfacing to external environments,
- dealing with missing information,
- providing temporal reasoning, and
- providing integration with procedural routines.

In the discussion that follows each of these characteristics is addressed with reference to a knowledge-based process control system.

A knowledge-based system must operate within the requirements set forth by the process. Some processes require response times in milliseconds while some can wait hours for a response. Therefore, the response time requirement for a knowledge-based control system will depend on the application of interest. When the knowledge-based system responds within the limits of the process, it can be considered to be a real-time system. This follows the description of Laffey, et al. [13]:

"If given an arbitrary input (or event) and an arbitrary state of the system, the system always produces a response by the time it is needed then the system is said to be real-time."

In a production process, the variables are continuously changing in value. Facts about the state of the process will change from one sample period to the next. Therefore, any facts that are derived based on a previous state may no longer hold. Thus the knowledge-based program must retract assertions from working memory that are no longer true. Such reasoning is labeled non-monotonic.

Most of the current applications of knowledge-based systems are in the form of expert systems that are used in a batch mode. That is, the program is executed for a specific purpose which has a definite stopping point. When a knowledge-based process control system is attached to a continuous process, it must operate continuously. If an error in processing arises, or insufficient data are available, the system must continue to provide consistent control of the process.

In a manufacturing process unscheduled events can occur at any time. These events include such problems as tool failure, equipment failure, and workpiece problems. Similarly, in a production environment unscheduled events can occur due to sensor failure, and certain process problems (e.g., fires, leaks, etc.). A knowledge-based process control system must be able to handle interrupts in its normal cycle of operation to attend to asynchronous (emergency) events.

In most current applications of knowledge-based systems, the system assimilates its data from a database or by querying the user. In a process control application, the knowledge-based system will obtain a majority of its data (some may still reside in databases or the user) through an interface to the external environment. The system must be able to read in sensor data, and store and manipulate this data for use in reasoning. This can present additional problems due to sensor degradation, or failure.

Since the process state changes over time, the knowledge-based system must have some capability to reason about the past, present, and future. Therefore, the knowledge-based process control system must be capable of dynamic and temporal reasoning. The system must reason about transient data and transient process states. The system must also accommodate delays in initiating actions and obtaining responses.

The knowledge-based system must also have access to procedural routines as provided in conventional programming. The system will use these procedural routines to perform such duties as data compression, signal processing, certain I/O related functions, and some numerical methods processing (equation solving, optimization, etc.).

These characteristics are not an all inclusive list of the required capabilities for a knowledge-based process control

system. Some system will require more capabilities than these, and some might require less. The needs of the system are dictated by the application of interest.

CHAPTER 4

CONFLICT RESOLUTION AND KNOWLEDGE-BASED PROCESS CONTROL

4.1 Introduction

This chapter will present and discuss the concepts of conflict resolution from the viewpoint of knowledge-based process control systems. The objective of this discussion is to provide the groundwork for evaluating current techniques for conflict resolution and for proposing new strategies.

The discussion begins with a brief explanation of why there is a need for conflict resolution. This is followed by a review of basic conflict resolution strategies and their application to knowledge-based process control systems. The chapter is concluded with a review of the strategies presented in the literature, along with an explanation for the trends discovered.

4.2 Conflict Resolution

Most knowledge-based control systems, in current use, include the human operator as an integral part of the outer loop, acting as the interface mechanism between the knowledge-based system and the process [16]. This configuration creates a knowledge-based control system which performs as an open-loop system for process diagnosis. Such knowledge-based control systems perform causal reasoning about process conditions using experienced-based heuristics developed by the experienced process and control engineers. These systems diagnose process anomalies and propose remedies (control actions). It is then the operator's decision to either implement one of the proposed remedies or use a solution of their own.

The next technological advancement involves closing the outer loop and allowing the knowledge-based system to provide direct control of the process (as was shown in Figures 3.1 & 3.2). This design transfers the decision-making responsibility from the human operator to the knowledge-based system. In this mode, however, multiple valid remedies about how to control a problem may exist. This results in a conflict in determining which alternative remedy to implement. Consequently, a conflict resolution system is needed.

4.3 Nature of the Conflicting Alternatives

A conflict resolution strategy operates on the alternatives within the conflict set. Therefore, the application of the strategy is dependent on the type of alternatives. Within the process control environment there are different types of alternatives dependent on the characteristics of the knowledge-

based program. In this section, these characteristics and the types of alternatives are presented.

The first question becomes: "Is the type of alternative dependent on the level of interaction (supervisory or direct) between the knowledge-based program and the process?" If the program is used in a supervisory position, then the alternatives will make absolute or relative changes to the set-point, or controller parameters. If the program is used directly in the feedback loop, then the alternatives will be commands to manipulate the final control elements. Again, these actions will be absolute or relative changes in the levels of those control elements. So, for both levels of control interaction, the nature of the alternatives is identical in that they both prescribe relative, or absolute, changes in a parameter. However, the nature of the alternatives would differ for knowledge-based programs that differ in:

- the number of levels of reasoning used by the system, and
- the capabilities implemented in the system (self-tuning control, optimization, alarm advising, etc.)

First, consider the number of levels of reasoning used by the system. The number of levels (depth) of reasoning is defined by how many "recognize-act" cycles the system uses to arrive at a conclusion based on the initial evidence obtained. For example, consider a rule-based knowledge representation where forward chaining is the method of inference. A part of the knowledge base might appear as follows:

```
RULE-1      IF   temperature        >  400.
            AND  viscosity          >  35.
            THEN process-problem-1 is true.

RULE-2      IF   process-problem-1 is true
            AND  process-problem-2 is false
            THEN decrease             heater-1.
```

Assume that working memory initially only contains the sensor readings:

. temperature = 425
. viscosity   = 35.5

Now, in the first "recognize-act" cycle, the system instantiates RULE-1 and adds the consequent "process-problem-1 is true" to working memory. On the second cycle, RULE-2 will be evaluated as true and its action, "decrease heater-1," will be fired. The difference is that the action "decrease heater-1" is a command that directly affects control of the process by reducing the heat to the process from the heater labeled "heater-1." The system required two cycles to go from the basic evidence (sensor values) to a conclusion (decrease heater-1) that directly affected the

control of the process. This is an example of multiple levels of reasoning.

When the consequent of the rule adds to, or changes, the contents of working memory, as RULE-1 did, then the consequent action is called an internal command. The term "internal" is derived from the fact that the consequent has no direct affect on any part of the system outside of the knowledge-based program. This differs from an external command which provides the control actions by direct manipulation of the final control elements (or movement of the set-point).

The use of a single level of reasoning or multiples levels of reasoning is dictated by the structure of the knowledge elements (productions, frames, etc.) in the knowledge base. A system would be limited to a single level of reasoning if every knowledge element's resulting action (consequent) was composed of only external commands that directly manipulate the process variables used for control (fuel flow, steam pressure, etc.). Since the external command does not directly affect working memory, the resulting action fired at one cycle can never directly participate as a precondition of the second cycle. In this type of knowledge structure, the preconditions of the knowledge elements would only use information obtained directly from sensory data. This information would take the form of numeric values of sensor readings, manipulated sensory values (calculated first and second differences between past and present values), and operating conditions input by the operators. For a knowledge-based system of this type (single level of reasoning), the alternatives within the conflict set will all be of the same type. That is, they will all be external commands that directly affect some external variable. This means that the conflict resolution system will be handling alternatives of the same type, thus reducing the complexity of comparing and ordering the alternatives.

In a system employing multiple levels of reasoning, the resulting actions of a knowledge element can be composed of either an external command, internal command, or both. Some cycles will produce external commands, and some will not. Therefore, the conflict resolution system must be designed to handle the possibility of a mixture of command types. This presents a problem in determining an appropriate means to compare the worth of alternatives that serve different purposes (the external command directly affect the process, while the internal commands affect the perceived state of the process).

The nature of the alternatives will also be different for systems that incorporate additional capabilities into the control system (like optimization, alarm advising, etc.). Again, these systems can be structured to reason on one or more level. Consider first a multiple level system. For this system, internal and external commands still exist, but now they serve different purposes (affect either control, optimization, or some other factor like shutdown). This creates a new mixture of alternatives within the conflict set. Some alternatives might be concerned

with control, some with optimization, and some with process advising. For the single level system, the conflict set only see external commands, but due to the additional capabilities, the purposes of these commands may also be different (might be for control, optimization, or process advising).

Therefore, the nature of the alternatives contained in the conflict set of a knowledge-based process control program will vary. They can range from a simple set of external commands with one purpose, to a complex set of internal and external commands with different purposes.

4.4 Applicable Strategies for Conflict Resolution

In this section, each of the numeric and heuristic classes of conflict resolution strategies, discussed in Chapter 2, will be examined for its applicability within the framework of a knowledge-based process control system. Because production rules and rule-based frames are the typical method for knowledge representation in knowledge-based process control applications, the discussion will be based on these representations.

4.4.1 Heuristic Strategies

PRODUCTION ORDER: In a process control system, the "production order" strategy class can be applied by constructing the knowledge base such that the most important rules are placed in a priority position (either first or last depending on selection criteria). For a single variable control system, a small knowledge base can be ordered to provide a system with strong selectivity. However, as the size of the knowledge base increases it becomes difficult to determine the exact placement of a rule in relation to all the others. This problem also makes maintenance of the knowledge base a difficult task. One possible solution is to divide the rules into groups based on the applicability of the rule to a part (or phase, or state) of the process. Then the rules can be prioritized within each group. Complications arise when a rule can be identified as belonging to more than one group.

For a multivariable control system, the task of prioritizing the rules in the knowledge base is also a problem. Compared to the single variable control system, the task is more complicated because of the possibility of the rules addressing more than one control variable. It is not an easy task to prioritize the knowledge to reveal all the correct priorities for every possible relationship that exists between the knowledge elements. Again, the grouping of rules would help, but it is still possible for a single rule to belong to more than one group. Prioritizing may be facilitated using some additional knowledge representation, such as a directed graph, to express the relationship between the

rules for the different domains. But even this method is difficult to implement.

The "production order" strategy is useful for applications involving knowledge bases which are small in size, and where the knowledge is static in nature and won't require much editing. This strategy also favors single variable control systems with limited amounts of knowledge; or, multivariable control systems, where it is possible to determine the relationships between the rules, and each rule is mutually exclusive.

Another "production order" strategy rule discussed earlier used confidence factors ("priority values") as the criteria for determining the order within the conflict set. In a process control application, the priority values assigned to a rule can represent several things depending on the designer. For example, a priority value can be assigned which is nothing more than a number which represents the importance of that rule in comparison to all other in the knowledge base. This implementation is identical to the production order strategy, where the production order is not based on physical location, but on the priority number assigned. Another means of using the priority value entails using it to represent the probability (confidence) that the affect stated by the rule is true given the evidence stated in the preconditions. In either case, this strategy requires that the knowledge engineer determine and assign the priority value prior to the use of the system. Assignment of the values themselves is not an easy task and leaves room for error in judging the worth of a rule. This produces the same weaknesses that the production order strategy possesses. The selectivity of this strategy is dependent on the method used to assign values. If not two rules possess the same probability, then the selectivity will be strong and definite. However, in a typical case it is not possible to ensure that no two rules possess the same value. The selectivity of the strategy will decrease as the chance of multiple values increases. However, this strategy is useful in that it provides a means for expressing the confidence that the designer has in each piece of knowledge used within the system. This information is useful the knowledge is examined at a later date, or by someone other than the designer.

SPECIAL CASE: The next conflict resolution strategy is the class of "special case" rules. The determination of the criteria for specifying a special case can make use of a rule's preconditions, and/or the instantiations of the rule that result from the "match" step. The selectivity of this strategy is dependent on the criteria employed. When the system arrives at two alternatives and one of the alternatives is a special case of the other, then it is safe to assume that the action taken by the more specific instantiation will also compensate for the more general instantiation. As an example, lets define the "special case" criteria to be the following [3]:

"Instantiation I_s is a special case of instantiation I_q, if I_s contains as a proper subset, all the data elements contained in I_g"

This criteria is only one of the many possible criterion that can be defined.

To demonstrate, consider an autoclave system that is in the process of laminating composite materials (a batch process). Assume that the knowledge-based process control system has detected an accelerated reaction within the laminate. This event is given by the rule:

```
IF      ( mid-layer-temp    *rising   )
   AND  ( top-layer-temp    *rising   )
   AND  ( mid-layer-slope > top-layer-slope )
   THEN ( heater             *decrease )
```

The action specified by the system is to reduce the heat to the autoclave to bring the reaction under control. Now if the system is also able to detect a fire using the (fictitious) rule:

```
IF      ( mid-layer-temp    *rising   )
   AND  ( top-layer-temp    *rising   )
   AND  ( mid-layer-slope > top-layer-slope )
   AND  ( temp            > fire-temp )
   THEN ( autoclave          *off      )
   AND  ( pressure           *off      )
   AND  ( alarm              *on       )
```

Then the system needs to stop processing and sound an alarm to prompt immediate action from the operator. Examination and comparison of the preconditions would reveal that all the instantiations of the "accelerated reaction" rule are a subset of the "fire" rule. Therefore, if both rules were present within the conflict set, the "fire" rule would be recognized as a "special case" of the "accelerated reaction" rule and would receive priority by elimination of the "accelerated reaction" rule from the conflict set. The action performed as a result of the firing of the special case rule will also provide the necessary control action for handling the problem noted in the general rule.

Since it is not likely that all the members of the conflict set will be a special case of other alternatives, this strategy can be labeled as being weakly selective. That is, the strategy only has the capability of eliminating instantiations within the conflict set that are general cases of other instantiation in the conflict set. This strategy would also require care in the construction of the rules for the knowledge base to ensure compatibility in the specification of the rule preconditions. It is necessary that the rule be constructed using only those preconditions that are absolutely pertinent to the identification and handling of that process condition. If a rule is constructed haphazardously and other preconditions are added that are not

necessary to define the state, then the selectivity of this strategy will be greatly reduced, since it will be rare that a special case will exist. For example, consider, again, the two rules above, "accelerated reaction" and "fire." If the "accelerated reaction" rule was rewritten as:

```
IF      ( mid-layer-temp    *rising   )
  AND   ( top-layer-temp    *rising   )
  AND   ( mid-layer-slope > top-layer-slope )
  AND   ( mid-layer-slope > 0         )
THEN    ( heater            *decrease )
```

Then the "fire" rule would not be a special case of this rule, due to the extra precondition "mid-layer-slope > 0." This precondition is not required since it is implicit in the fact that the mid-layer-temp is indicated as "rising." The poor construction of the rule led to a breakdown in the selectivity of the conflict resolution strategy. Although not easily detected, this problem can be avoided by careful construction and examination of the contents of each rule.

The "special case" class of conflict resolution is applicable to all knowledge-based systems in process control. The strategy essentially says that the system should favor those process states (problems) that are identified by rules that use more preconditions, because they are more exact in their identification of process states. This type of logic is applicable for systems which address physical processes.

RECENCY: The third strategy class of conflict resolution rules uses age as the basis for ordering alternatives within the conflict set. This class of rules, referred to as the "recency rules," keeps track of the amount of time that the data elements have been posted to working memory. Implementation of this strategy could favor older or newer data elements, depending on the needs of the system. The method of determining the age of an instantiation is dependent on the user. McDermott and Forgy [3], mention two possible methods for defining the age of a data element in working memory. The first defines the age based on the number of interpreter (recognize-act) cycles that have elapsed since that element was asserted. The second interprets age as the number of actions that have fired since the firing of the action that asserted that particular data element. The first definition of age is less selective since it is possible for more than one data element to be asserted in a single cycle. Therefore, two alternatives in the conflict set could be defined as having the same recency criteria. The second definition is more discriminating since no two data elements would share the same age.

The fundamental idea of this strategy is to provide continuity in the system operation. As an example, consider a process control system. The idea behind control is to maintain the specified control variable(s) at prescribed conditions (i.e.,

set-points). Therefore, the firing of an alternative will manipulate some process variable to correct a control variable. On the next cycle of the system, any new alternatives that are added to the conflict set will most likely represent process conditions that are the result of the application of the previous correction. If the new data elements are favored over the old, then the system continues to correct for the original problem. For the sake of clarity, the example used in the chapter on conflict resolution will be repeated:

> "Suppose that on the first cycle two rules (R1 and R2) were instantiated and the rule R1 was selected to fire. In the next cycle, if rules R1, R2, and R3 are instantiated, then the resolution strategy would select R3 since this is evidently the action to finish what R1 started. This strategy has the effect of focusing the system on the results of the actions most recently taken."

This idea of focusing the control system would be beneficial in a process control systems since it improves the operating efficiency of the system.

A problem can result in the use of this strategy for some cases. Since R1 was chosen over R2, it is deemed that R1 recognizes a more important problem than R2. In the next cycle when R3 and R2 appear in the conflict set, R3 is favored over R2. This assumes that the condition identified by R3 (considered to be a continuance of the correction begun in R1) is more important than R2. This might not always be true, depending on what condition R2 identifies. Therefore, the selectivity of this strategy is strong, but it's usefulness can be limited and would be more appropriate when applied in combination with some other conflict resolution rules. This would help to prevent the situation of focusing on a problem of less significance, than others in the conflict set.

When the recency strategy is applied to a knowledge-based control system that operates at only one level of reasoning, then no internal commands (posting of assertions to working memory) will be fired from the rules. The only changes to working memory will come as the result of changes in the sensory values and direct manipulation of these values. For these systems, the calculation of the age of the data elements in working memory is of no use since the contents of working memory are updated at each sample. The only real indication of age would be to track the time between significant changes in each value. This would be a complex task.

In a system employing multiple levels of reasoning, some of the rules will make assertions to working memory (fire internal commands). The knowledge base will contain a mixture of rules. Some rules will have preconditions that pertain only to sensory input. Other rules will have preconditions that are a mixture of sensory input and previously asserted commands. The question

becomes: how will the system determine the age of both types of rules? Is sensory input considered to be of age zero? If so, then rules composed of only sensory input preconditions will always be favored. Because of the confusion, the recency strategy based on the age of the data elements would not be applicable to systems which use sensory input (i.e., process control systems).

However, the strategy of recency could be applied to sensory based systems if the determination of age was based on some criteria other than the data elements. One logical choice would be to calculate the age of an alternative based on the amount of time that has transpired since it last fired. This criteria could be applied to rules with preconditions that contained either sensory data, internal commands, or a mixture of the two. Therefore, the capability to focus the system would still exist.

DISTINCTIVENESS: Distinctiveness rules make-up the fourth class of conflict resolution rules. The selection criteria can be based on differences or similarities that exist between the alternatives within the conflict set to those previously executed. In process control systems, operating in real-time, the state of the system will not always change drastically between samples. The amount of change in the process state recognized by the knowledge-base component will be dependent on the application (process time constants), the sample rate, and the disturbances affecting the process. If the program identifies a problem and makes a correction, there will be a time delay before the process responds to the correction. Also there will be an additional time delay before the process can be considered to have moved out of that problem state. Thus, it is likely that the program will continue to identify the problem in subsequent cycles. It would not be appropriate to prescribe the corrective action again since this would lead to overcompensation. This continual overcompensation could result in the process becoming unstable.

One solution is to increase the cycle time of the knowledge-based program. This allows for a greater chance of change between examination of the process states. However, if there exist other process conditions with smaller time constants, the system might not be able to react quickly enough to provide proper control. A better solution would be to recognize that the system fired the same rule previously and block it from firing again until some criteria is satisfied. This criteria would fall under the specification of the "distinctiveness" strategy of conflict resolution.

For application to continuous processes, this strategy would require placing limits on how far back in time the system would consider previous instantiations. The system would need to purge old information about instantiations to reduce the system memory requirements. Even though this strategy is weakly selective, it performs the necessary function of reducing the possibility of overcompensation in the control of the process.

ARBITRARY DECISION: The application of "arbitrary decision" rules to process control is valuable when combined with other strategies. This strategy will provide the necessary selection when other strategies fail. This occurs when there remains two or more alternatives in the conflict set that show no distinction from one another after all the other strategies have been applied. It is at this point that a random selection must be made.

META-RULES: The last class of heuristic strategies involves the use of meta-rules. Meta-rules possess knowledge about the utility of the object level knowledge contained in the knowledge base. This meta-knowledge is used to provide a selection from among the alternatives in the conflict set. Meta-rules can be advantageous to a knowledge-based process control system since they provide the opportunity to make a decision based on process knowledge. This allows the conflict resolution system to take into account the current process status when making its decision (see example Chapter 2).

4.4.2 Numeric Strategies

Numeric strategies are the most popular methods for providing conflict resolution in knowledge-based system for process control. These methods are similar to the priority strategy that uses confidence factors for priority values. Both provide a means to gain insight into the validity of a conclusion based on the evidence given. However, in the numeric strategies, the belief values are not static, but instead are propagated through the line of reasoning. These methods provide a means for relating the decisions made by the system, to the physical constraints of the process. For example, if the reliability of a sensory reading is low, then this fact can be incorporated into the decision making of the process. No heuristic technique provides this capability, except, the priority strategy (which could be placed in the numeric category).

It is for this reason that numeric strategies are so popular for knowledge-based systems used in physical processing applications. This method of conflict resolution incorporates reasoning about uncertainty to allow the system to indirectly deal with additional information about the process that is provided in numeric form (individual confidence factors).

4.4.3 Conclusions

Table 4.1 lists the major characteristic and strength of selectivity of each of the conflict resolution strategies discussed above. As can be seen, no one strategy provides all of the necessary characteristics that a process control system

needs. It will be necessary to construct a strategy which is a combination of these.

Table 4.1:   Conflict resolution strategies for knowledge-based process control systems.

Strategy	Selectivity	Characteristic
Recency	strong	Allows system to focus.
Arbitrary Decision	strong	Makes definite selection.
Production Order	strong	Easy to apply in small systems.
Confidence Factors	moderate	Provides understanding of confidence in knowledge.
Numeric Methods	moderate	Attaches physical signifi- cance to knowledge.
Meta-rules	moderate	Reasons about utility of alternatives.
Special Case	weak	Eliminates the general- case instantiations.
Distinctiveness	weak	Reduces chance of over- compensation.

Only the production order, recency, and arbitrary decision, strategies can be used by themselves (although the recency strategy is not recommended). Their strong selectivity provides a means of eliminating all other alternatives, ensuring that only a single alternative will remain for firing. These three strategies can also be used in combination with the other weakly selective strategies. This will ensure the selection of a single alternative. The simplest methods to implement are the "production order" and "arbitrary decision" strategies. The other strategies will require additional considerations in programming.

The strategies presented in this chapter represent the main classes of the techniques of conflict resolution. Changes in the criteria for a strategy class can result in a particular implementation that either enhances or reduces the selectivity of the technique. This tailoring of the applied strategies for a particular application is desirable to optimize the efficiency of the system.

4.5 Example Systems

A number of applications of knowledge-based systems in manufacturing have been reported. These applications include

monitoring, diagnosis, advising, scheduling, alarm handling, control, etc. In this review, only those articles which allude to methods for conflict resolution, within the framework of knowledge-based process control, will be presented.

Of ninety-six AI-based process control references, only five address the issue of conflict resolution, and these do not provide much detail on the methods used. These articles just mention in passing the need or use of some means to address the problem of conflicting alternatives. In the discussion that follows, the methods of these five articles are presented.

Burg, et.al. [17] developed a real-time knowledge-based process control system which controls a 5 Kw metal cutting laser. The system receives its sensory data from an image processing system and provides control of the laser power, the gas supply, and the velocity of the workpiece. The system uses production rules for knowledge representation and employs a priority scheme for resolution of conflicts. The priority strategy performs the ordering of the alternatives based on a weight function associated with each rule. The weight for each rule is defined using two parameters: the priority coefficient, and the execution time needed to perform the action specified. The conflict resolution system will order the rules according to their priority values and then check to see if the best one is able to fire within the time constraint. If not, then the system evaluates the next rule for firing, and so on. This scheme allows the system to operate within the time constraints of the process, but it does not guarantee that the constraint will be satisfied. Flexibility is provided by allowing the system to modify the parameter values during system operation. This scheme is not a numerical method because the weights are used directly and not propagated through the reasoning process. This approach is a priority-based heuristic technique that belongs to the "production order" class of conflict resolution strategies. The use of the execution time provides further selection, by eliminating those alternatives which don't satisfy a current process constraint.

Gallanti, et.al. [18], presents a new architecture which combines declarative knowledge, in the form of production rules, with procedural knowledge, in the form of event-graphs (also referred to as directed-graphs). The only mention of conflict resolution strategies is in reference to a "credibility value," which is defined for each active diagnosis/intervention event graph. The credibility value represents the probability that the event-graph is the most appropriate current means for explaining the ongoing phenomenon and for suggesting the right actions. Maintenance of the credibility values is performed at the control level, which embodies the declarative knowledge. No mention of the specific strategy for the use of these values is given. It is assumed that a priority ordering is the most likely method of employing these values to order the alternative diagnoses and to make a selection.

Moore and Hawkinson [19] present some of the details of the PICON system for process control. PICON is a knowledge-based system that runs on a LISP-class machine and is capable of providing control for processes involving large numbers of process variables. PICON uses both deep knowledge and heuristic knowledge with a frame-based representation. Within a frame, a certainty factor is included as a dynamic attribute. No further mention of the manipulation of these factors is given. It is possible that the certainty factors are used in some type of numeric or priority based strategy of conflict resolution.

In an article by Rao, Jiang, and Tsai [20], the authors present a new architecture for real-time intelligent control systems. The design of this architecture is based on the belief that the coordination of symbolic reasoning and numeric computation is essential to developing an intelligent process control system. This design couples several symbolic reasoning systems and numerical computation routines, and uses a meta system to control the selection, operation, and communication of these programs. The meta-system performs the task of finding the optimal solution when presented with conflicting facts and events from different expert systems. Again, no further information is provided about how the system handles conflicts, only the statement that the use of the certainty factors is "to aid in representing the imprecise knowledge and indicate the reliability of decision-making" [20].

HEXSCON, a Hybrid Expert System Controller, is a knowledge-based expert system intended to deal with control problems [21]. When multiple lines of reasoning arrive at conflicting alternatives, HEXSCON relies on a numerical based technique for conflict resolution based on the techniques of Dempster and Shafer.

A note worth making is that in these five references, each implementation makes use of either a numeric based technique or some form of a priority based method employing confidence factors. In the next section, a reason for this selection will be proposed.

4.6 Conflict Resolution in Knowledge-based Process Control

After examination of the literature dealing with knowledge-based process control systems, it appears that the favored method for conflict resolution is the use confidence factors. These confidence factors are employed in one of two ways. They can be used as static values which indicate the probability of a single deduction. A second possibility is to use them as dynamic values which indicate a degree of belief that will contribute to calculating the plausibility for an entire line of reasoning. As mentioned earlier, these methods allow the knowledge engineer to attach a degree of belief to the knowledge elements (rules). This provides a means for representing the actual characteristics of a particular process. In a typical process control system, not all

of the interfacing hardware (sensors, meters, etc.) has the same reliability or accuracy. Therefore, the evidence based on the data provided by sensors should not be weighted equally. In addition, it is possible that some rules within the system have not been proven, and it would be beneficial to be able to attach some degree of belief to the conclusions that they provide.

For a system using a single level of reasoning, it is not possible to implement dynamic confidence values. This is because the conclusion fired represents an external command that was directly deduced from the sensory data (or manipulations of this data). The conclusion reached is not dependent on some line of reasoning based on evidence obtained from some other rules. Therefore, for these single level reasoning systems, there is no need for consideration of dynamic confidence values.

The heuristic methods are still valid methods of conflict resolution. In fact, even the two methods above will require that a heuristic method (such as arbitrary decision, production order) be included to handle the possible case of a tie in the selection of an alternative. Any system that does not employ a strategy based on confidence factors must use heuristic strategies. It is these heuristic methods that are not mentioned in the literature pertaining to process control systems. Maybe the authors of those articles think it a trivial matter and not worth mentioning. The selection and combination of the different methods of conflict resolution, will be dependent on the desired characteristics of the overall system.

CHAPTER 5

QUALITATIVE PROCESS AUTOMATION (QPA)

5.1 Introduction

Qualitative process automation (QPA) is defined as qualitative physics applied to process control [22]. The idea of qualitative physics is:

> "Qualitative physics predicts and explains the behavior of mechanisms in qualitative terms, i.e., the goals for the qualitative physics are to be far simpler than the classical physics, yet retain all the important distinctions such as state, oscillation, gain, and momentum without invoking the mathematics of continuously varying quantities – differential equations, and produce causal accounts of physical mechanisms that are easy to understand." [23]

The use of qualitative techniques to model the process, as opposed to quantitative techniques, allows for the use of process knowledge within the framework of an AI-based program.

In this chapter the theory of qualitative process automation (QPA) is presented. The application of this theory is discussed in reference to autoclave-curing of graphite-epoxy composite materials. The presentation includes a discussion of the operation of the QPA controller, and a detailed discussion of the method of conflict resolution used by the system.

5.2 QPA as a Knowledge-Based Controller

QPA represents one example implementation of the theory of a knowledge-based process control (KBPC) system. QPA differs from most other systems in that it uses qualitative physics to describe the mechanics of the process under control. The functions of the QPA controller are to identify the process state and specify the set-point values for each process variable. Thus the QPA controller operates in a supervisory mode as a set-point scheduler. The ideal QPA controller can analyze trends in the process from knowledge of the process status, and can predict possible outcomes of the control actions using knowledge of the process behavior. The controller obtains knowledge of the process status from the sensory data, and from the temporal and spatial derivatives that are derived from manipulation of the data. The process behavior is determined by interpreting the sensory information. For example, if the first derivative of the laminate temperature is positive, the laminate temperature is increasing.

The basis of QPA's operation is to adapt the process (e.g., autoclave, rector, robot, machine tool, etc.) to meet a specified

goal. To provide for temporal reasoning, a process is broken down into a series of episodes. For each episode a goal is specified. It is the job of the QPA controller to drive the process to meet that goal by manipulating the controller set-points. A more detailed example will be presented in a later section.

5.3 Autoclave Lamination

The QPA controller was first applied to the curing of graphite-epoxy composites in an autoclave.

> "The particular process was selected not so much because it is beyond the state-of-the-art in adaptive control technology but because it is on the leading edge of conventional model-based process control technology . . .."[24]

The current method of curing composites relies on predetermined patterns (set-point schedules) that describe the variation of temperature and pressure during the process cycle. This method results in long processing times (cure cycles), variations in product quality, and poor yields. Employing the QPA controller eliminates the need for explicitly specifying these patterns. Instead, the QPA controller will monitor the process and use its knowledge of the process to automatically control the cure cycle.

The QPA controller receives sensory data from the autoclave. This data includes the temperature and pressure of the autoclave, the temperature of the top and middle layers of the composite, and a dielectric reading of the composite (used as an indication of the viscosity of the material). This sensory data is used by the system to determine the status of the process and to determine its behavior. The application of the QPA controller to the autoclave process has significantly reduced processing times for the curing of the composites [25][26].

5.4 Method of Operation

A block diagram of the QPA system is shown in Figure 5.1. From its supervisory position, the QPA controller drives the set-points of two conventional proportional-integral-derivative (PID) controllers. One controls the autoclave's temperature and the other its pressure. The QPA controller is composed of three expert system subsystems: the blackboard monitor, the Parser, and the Thinker (see Figure 5.2). A blackboard architecture is used to allow for communication between each of the subsystems. The blackboard monitor coordinates program control and provides an external interface to the process (sensory data and controllers). From the sensory data, the blackboard monitor derives information about the behavior of the process. This information is posted to the blackboard along with the raw data from the sensors. The
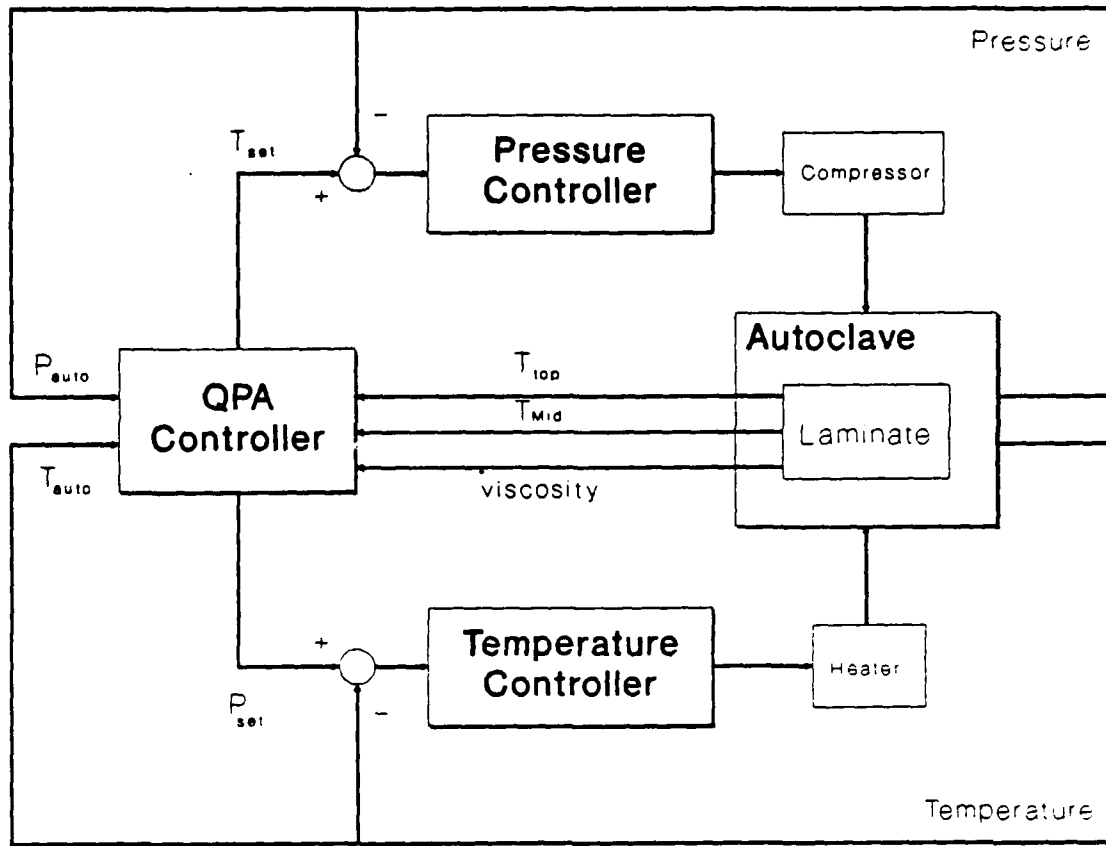
Figure 5.1: Block diagram of a knowledge-based process control system based on QPA theory.

second subsystem, the Parser, then uses this data to identify the process status. The Parser posts the results to the blackboard for use by the Thinker. The Thinker subsystem then determines the required commands for maintaining control of the process and for achieving the goal of the system. These commands are posted to the blackboard from where they will be sent out.

The knowledge within the subsystems is represented using frame-based rules. QPA defines two types of frames: process instance frames and episode frames. The frame used to represent each process instance is defined as:

```
FRAME: rule-name
       ISA   type
       PRECONDITIONS   rule-antecedents
       EFFECTS         rule-consequents
       ACTORS   nil    L;
```

Process   Expert Systems   Environment
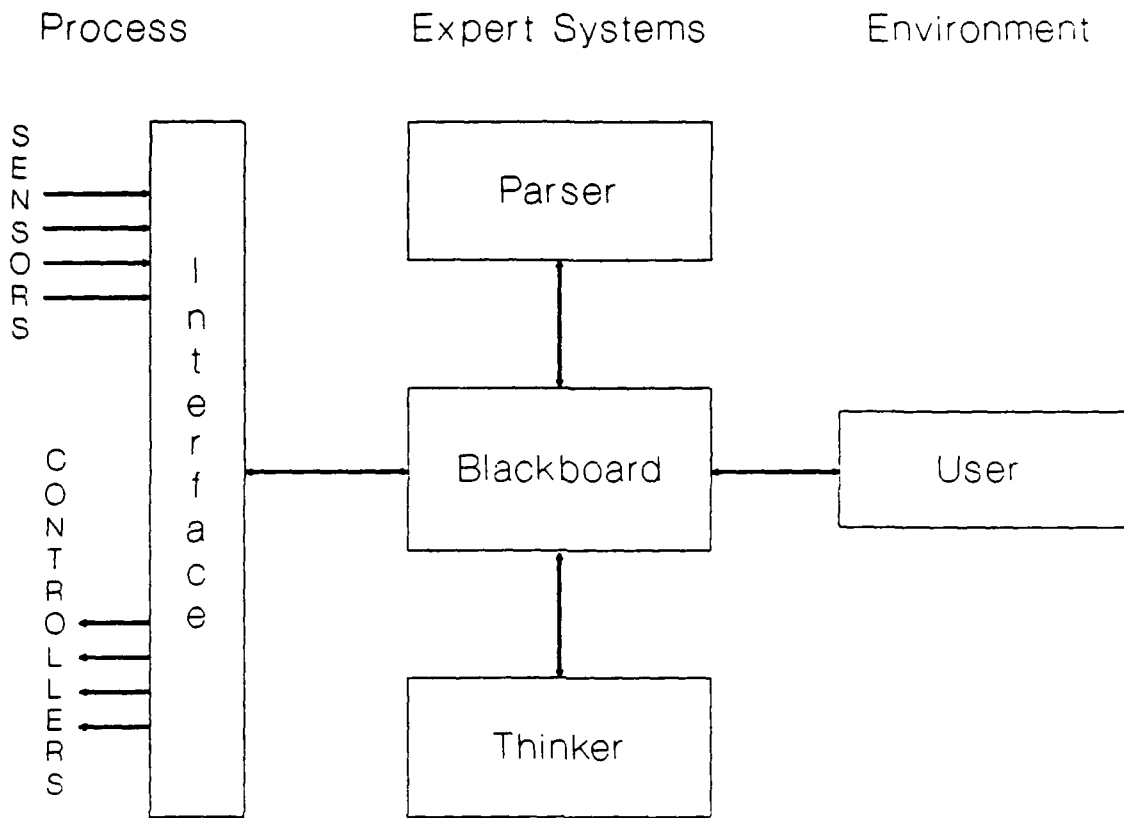
Figure 5.2: Block diagram of the QPA controller [24].

A process instance frame can represent a desirable process condition, an undesirable process condition (process problem), or a process condition denoting a transition between process episodes. In the current implementation, the ISA and ACTORS slots have no functional meaning. The PRECONDITIONS slot contains a list of process-related conditions that must be satisfied before the system (Parser) declares the frame as active (instantiated, true). The EFFECTS slot contains the consequents, or actions, for the rule specified by the process instance. These actions represent the control commands prescribed for dealing with the process state defined by the frame.

The episode frame is used to define each step or phase of the process. The frame is defined as:

```
FRAME:  episode-name
        SYMBOL        episode-symbol
        TRANSITION    episode-goal(s)
        AGENDA        process-conditions    L;
```

The episode SYMBOL slot is used by the system to label the currently active episode. The TRANSITION slot specifies which process instance frame dictates the behavior of the episode. This process instance frame that specifies the process conditions that identify when the episode is active and the goal, or goals, to be achieved during the episode. The AGENDA slot provides a list of the process instance frames that the system should examine during the episode. This list of specific process instances allows QPA to focus the system on a certain portion of the knowledge base, improving the efficiency of its operation. This is similar to the concept of "goal directedness" discussed by Sauers and Walsh [6].

In summary, the Blackboard monitor receives data from the external sources and derives behavioral information about the process. The data and information are posted to the blackboard and passed to the Parser. The Parser then determines the process status by identifying which process instance frames are active. These frames are labeled as active on the blackboard and the blackboard is passed to the Thinker. The Thinker then identifies the active episode and constructs a conflict set from the list of effects of each active frame. The Thinker then resolves the conflict, posts its decision on the blackboard, and passes it back to the Blackboard monitor. The Blackboard monitor will then execute the commands.

5.5 Conflict Resolution in QPA

5.5.1 Method of Conflict Resolution

As with other knowledge-based systems, QPA requires a means of conflict resolution when multiple rules (frames) have been instantiated and are applicable for firing. When a frame is declared as active, QPA places the effects (actions) of that rule in a list called PLANS, which represents a type of conflict set. (In actuality, the list PLANS contains the addresses of effect found to be active.) This list is then consulted to determine which effect to implement.

The effects prescribed by a frame are statements that will prescribe some change in a condition of the process. Examples of these effect statements include:

```
( laminate-mid-temperature    increase )
( degree-of-cure              increase )
( autoclave-temperature       decrease )
( pressure                    increase )
( heater                      hold     )
( heater                      decrease )
```

Notice that some of these prescribe changes in states that are not directly controllable (e.g., degree-of-cure, laminate-mid-temperature); whereas, some prescribe changes involving the direct manipulation of the final control elements (heater,

pressure). Each of the effects is passed through a routine which determines which manipulative variable relates to that change in state and how that change in state is influenced by the manipulative variable. This information is obtained from "influence" statements. Examples of these statements include:

```
I+( laminate-mid-temperature   degree-of-cure            )
I+( laminate-top-temperature   laminate-mid-temperature )
I+( autoclave-temperature      laminate-top-temperature )
I+( heater                     autoclave-temperature    )
```

Although none are shown, it is also possible to have negative influences (I-). In addition, the system will use the CONTROLLABLE statement to specify which process variables can be directly controlled. Examples of these statements are:

```
CONTROLLABLE( heater    message1 )
CONTROLLABLE( pressure message3 )
```

The "message1" and "message3" represent the particular blackboard slot associated with that controllable variable.

The influence statements are structured to provide information on how one process variable is affected by another. For example, assume that the action require increasing the DEGREE-OF-CURE. The system would scan the influence statements and determine, from the first statement above, that the LAMINATE-MID-TEMPERATURE positively influences DEGREE-OF-CURE. This tells QPA that if it wants to increase the degree of cure it must raise the temperature in the middle of the laminate. The system can't identify LAMINATE-MID-TEMPERATURE as a controllable variable, so it must address the influence statements again. The next influence statement reveals that LAMINATE-MID-TEMPERATURE can be increased by increasing the LAMINATE-TOP-TEMPERATURE. Again, this is not a controllable variable, and the system goes back to the influence statements. This action continues until the system reaches the statement identifying the HEATER as the variable that can positively influence the AUTOCLAVE-TEMPERATURE. Since HEATER is a controllable variable, the system appends the command to "increase" the HEATER (turn it up) to a list called VOTES. This external command is the EFFECT that will produce the desired result of increasing the DEGREE-OF-CURE.

The VOTES list, like the PLANS list mentioned earlier, is also a conflict set, except that VOTES contains the effects in terms of controllable variables. If the effect given is neither found on the positive or negative influence list, then the effect itself is directly appended to the list VOTES. This type of effect would represent a system characteristic which is not influenced by other system dynamics. It would be directly controlled without outside influence.

At this point in the execution of the program, the conflict set contains all the process instance effects that are applicable to the current condition of the process. The Thinker must now

decide which effect to implement. The strategy used to resolve the conflict involves assigning priorities to the type of action performed by the effect. In QPA, these priorities are specified apriori. Priorities are determined for the final control element associated with each manipulated variable and for each possible action that can be implemented for that control element. These priorities are specified by the use of a RESOLVES statement located in the knowledge base. As an example, consider the group of RESOLVES statements:

```
RESOLVES( heater    decrease  increase )
RESOLVES( heater    decrease  hold     )
RESOLVES( heater    hold      increase )
RESOLVES( pressure  increase  decrease )
```

Listed are all the possible combinations of effects that can be implemented for each final control element. The terms HEATER and PRESSURE represent the final control elements for the autoclave. The RESOLVES statement structure is such that the first argument represents the control element (controllable) and the next two arguments represent possible actions to be performed by that control element. The RESOLVES statement is constructed such that the first action argument is the one to favor in a conflict. For example consider the situation where a conflict exists in the control action prescribed for the heater. If the prescribed actions are both "decrease" and "increase," then from the RESOLVES statement it is known that whenever a choice between "decrease" and "increase" exists, it is best to select the "decrease" action.

The RESOLVES statements provide the knowledge used to resolve the conflicts within the system. Even though this knowledge exists in the knowledge base, it is the control program within the Thinker that decides how to apply this knowledge (favor the first of the two arguments in the statement) to resolve conflicts. This strategy falls under the "production order" class of heuristic strategies. Resolution of conflicts is dependent on the placement of frames within the knowledge base, and on preassigned priorities for alternatives. The only requirement for placement is that the process instance frames associated with the episodes be placed in front all other frames. The remaining process instance frames require no specific ordering. The assignment of priorities is similar to the method outlined in Chapter 2. The main difference is that instead of assigning priorities for all the rules in the system using some means such as confidence factors, the system only assigns priorities to the possible actions that a rule will prescribe. In this way, the system does not relate a specific action (in the conflict set) to the precondition(s) that prescribed that action. This simplifies the process of assigning priorities, but results in a loss of physical significance due to the generalization of the effects. This generality is not a problem unless the evidence (which make-up the preconditions) varies in certainty, or its

application is not consistent. For example, assume a system has decided that due to the evidence presented, it is 12% sure that a decrease in heat is needed, and 92% sure that an increase is needed. The RESOLVES statement would state that a decrease in heat is appropriate, but a process operator might decide to favor an increase for another sample or two. For these types of systems with varying degrees of confidence in the evidence, it would be necessary to use a numeric method to resolve the conflicts and to support uncertainty in the reasoning.

5.5.2 Types of Conflicts

In QPA, the alternatives that make-up the conflict set represent only external commands with the single purpose of driving the set-points of the process. However, the format of the conflicts that occur are different from what one would find in a typical knowledge-based system. This difference is due to the structure of the QPA system and its use of episodes. First, recall that under QPA control a process is represented as a series of episodes, where each episode has a process goal that the controller is trying to achieve. The episode goal is described as an effect (controller action) that is an external command to the controller. For example, in the "cure" episode of the lamination process, the goal is to increase the degree of cure of the laminate. Using knowledge of the process influences, this episode goal translates into a command to turn-up (increase) the heater. Therefore, throughout the "cure" episode, the controller will increase the temperature in the autoclave. The effect of this goal will continue to be applied until that episode ends, or a process problem occurs that requires a different controller action.

The types of conflicts that can occur in the QPA system can be described as:

1. Episode/Single problem - conflicts between the episode goal and a process problem that occurs during that episode, or,

2. Episode/Multiple-problems - conflicts between the episode goal and two or more process problems occurring simultaneously during that episode.

The main type of conflict that the occurs in the system is the "episode/single problem" type. This type of conflict results from the occurrence of a process instance that requires a control action which opposes the action prescribed by the episode goal. For example, assume the process is in the "cure" episode where the current control action (episode goal) requires that the heater be turned up. Then, during this episode, the knowledge-based system detects an accelerated reaction. The prescribed effect of the process instance frame identifying this problem is to decrease the heat. Therefore, the conflict set will contain

the two conflicting actions that the heater be increased or decreased. Using the RESOLVES statement, the system would decide to decrease the heat.

The "episode/single problem" conflict is a trivial conflict when one considers the logic used to control a process. During the control of any process, the purpose is to maintain control of the process in the face of disturbances. When a problem occurs then it is necessary to give it immediate attention, unless there is another problem occurring that has a higher priority. Therefore, any time the system detects only a single problem, there is really no need to consider it a conflict, the control action prescribed by the process problem should always be given priority attention.

The second type of conflict, "episode/multi-problem," can be further broken down into cases of conflicts:

Case-1: The controller actions prescribed by the episode goal, and two or more process problems are in conflict one with another.

Case-2: The controller actions for the two or more process problems are in conflict with each other, but not with the episode goal because they deal with a different manipulative variable.

The Case-1 conflict is similar to the "episode/single problem" type of conflict discussed above. The difference is that the system has detected two process problems, instead of just one. Just as before, the process problems have a higher priority than the episode goal. Therefore, the job of the conflict resolution strategy is to resolve the conflicts between the control actions prescribed by the process problems.

The Case-2 conflict is identical to Case-1, except that now the episode goal addresses a different manipulative variable than the process problems. For this situation, two control actions will be implemented, one from the episode goal (addressing one manipulative variable), and one which is the result of the resolution of the conflict between the process problems (addressing a different manipulative variable).

In addition, other combinations of conflicts are possible. However, the logic used to address these conflicts would be similar to that discussed above.

5.5.3 Distinctions of Conflict Resolution in QPA

The current implementation of the QPA theory is in its infancy. As was shown in the previous section, the QPA program employs a heuristic strategy for conflict resolution that provides complete selectivity, ensuring that all alternatives are distinguished from each other in terms of their worth. However,

there are several factors concerning the conflict resolution system that require further explanation.

As discussed in Chapter 4, overcompensation in the assignment of control actions might occur unless some method is provided to block alternatives that were previously fired. The current implementation of QPA does not require the blocking of previously fired alternatives. This is due to the structure of the conflict set in the QPA system. In each system cycle (Parse-Think) the conflict set will contain an alternative that is placed there by the episode goal EFFECT. Also, in each cycle QPA will send the PID controller a set-point scheduling command. When a process problem is detected, the EFFECT of the process instance frame associated with this problem will be added to the conflict set, and this EFFECT will have a higher priority than that of the episode goal. Therefore, the EFFECT of the process problem will fire and the controller will apply the correction to alleviate the problem. If this process problem alternative is blocked on the next cycle of the system, then unless another process problem occurs, the episode goal will be the only alternative in the conflict set. If the EFFECT of the episode goal is associated with the same manipulative variable as the EFFECT that is blocked, the control action of the episode EFFECT will be in direct opposition to the EFFECT prescribed in the previous cycle. This results in canceling the overall effect of the previous command (from the process problem), allowing it only one cycle to act in alleviating the process problem.

QPA overcomes this problem by not blocking alternatives. This absence of blocking will allow the alternative EFFECT posted by the process problem to remain a member of the conflict set until the system no longer recognizes the process problem. This results in the process problem alternative continually being selected over the episode goal (in essence blocking the episode goal), unless another process problem occurs that has even higher priority. In order for this method to work, it is necessary that the set-point be moved in small increments which are approximately equal to the time constant of the process that is associated with that variable. If the set-point is moved at a rate faster than the process can respond, then there will be some amount of overcompensation.

Consider the composite lamination process as an example. When the process is operating in the "cure" episode, the goal is to increase the degree of cure of the laminate. Using the list of "influences," this translates into a need to turn-up the heater. So at each Parse-Think cycle of the system the conflict set will contain the alternative to turn-up the heater. Assume that the system detects the process problem that an accelerated reaction is occurring in the laminate. The effect of this process problem is to turn-down the heater (the process problem and episode effect both pertain to the same manipulative variable - heater). The resultant conflict set will contain the two alternatives to turn-up and turn-down the heater. The alternative to turn-down the heater is selected. As long as the process problem is

detected, both of these alternatives will be present in the conflict set, and the action of turning down the heater will always be selected. If the set-point is moved ten degrees at each sample, where a sample is made every 30 seconds, then the overall driving of the process is 20 degrees/minute. If the process can actually only heat-up at a rate of 10 degrees/minute (in the operating range), the controller will get ahead of the process in its prescription of control. Then, when the process problem is alleviated, there is a good chance that the set-point value will be much less than the current process temperature. So, when QPA begins to prescribe an increase in the set-point value, there will be a delay until the value reaches the current level of the autoclave temperature. This effect can be lessened by setting maximum and minimum values for the set-point and more closely matching the movement of the set-point to the response time of the process.

The working memory of QPA is based on a blackboard structure composed an array of storage slots. Each of these slots are updated during each parse-think cycle of the system. Because of this updating scheme and the fact that QPA uses only one level of reasoning, there is no need for non-monotonic reasoning. There is no need to retract facts from working memory (blackboard) since they are updated during each cycle of the system.

Another feature of QPA is that it can be applied to multivariable control systems. In these systems, QPA is responsible for scheduling the set-points of two or more process controllers. During each program cycle QPA is unique in that it has the capability to select an EFFECT for each process set-point. In other knowledge-based programs the resolution process is restricted to making only a single selection from among the conflict set.

5.6 Other Methods of Conflict Resolution

The current implementation of QPA is limited in its application. One reason is because of the method it uses to resolve conflicts. The resolution method is applicable only to systems where the set-points can be moved in relative increments based on qualitative commands (increase, decrease, hold). If other methods of resolution were employed, this limitation could be removed.

The first addition to the resolution toolbox would be a numerical method of conflict resolution. The capability to reason about uncertainty and use this information to resolve conflicts would be beneficial in QPA. Instead of assuming that all the evidence (sensory input) provided by the process is equivalent, the system could take into account the peculiarities, and faults, of each piece of evidence. The resultant belief values obtained for each instantiated rule could be used directly for ordering the alternatives within a conflict set. This method, when coupled

with one or more heuristic strategies, could be used to provide an a robust conflict resolution strategy for process control.

It is important that the numeric methods be applied in combination with one or more heuristic techniques to ensure that the system selects only one alternative for implementation. The system must distinguish between each alternative within the conflict set in case several alternatives result in the same belief values. This can be accomplished with a heuristic strategy such as "arbitrary decision" or "production order."

Currently, only one heuristic strategy is employed in QPA. The implementation of this strategy is provided in FORTH code and is not easy to decipher. The best alternative would be to offer several strategies to the user and allow the user the freedom to select which ones to implement and the order in which they are to be applied to resolve conflicts.

5.7 Conclusions

The application of QPA theory has resulted in a system that possesses great potential. The QPA controller has worked well with the batch process of laminating composite materials in an autoclave. The knowledge-based program is capable of operating in real-time to identify process behavior and to provide appropriate control.

Although the method of conflict resolution employed by QPA is limited, it is capable of handling the conflicts that occur in the lamination process. However, the incorporation of numeric techniques and other heuristic methods of conflict resolution would strengthen the applicability of the controller to other processes in the industrial environment.

CHAPTER 6

METHODS FOR PERFORMANCE IMPROVEMENT IN QPA
THROUGH CONFLICT RESOLUTION

6.1 Introduction

The goal of this research was to improve the performance of knowledge-based process control systems by enhancing the methods used to resolve conflicts. The approach was to develop a coupled system that would combine heuristic knowledge about the process, in the form of experienced-based rules, with deterministic knowledge about process, in the form of numerical equations which model the process. The hypothesis was that a purely heuristic-based system overlooks the knowledge about the process that is provided by mathematical models. This additional knowledge source can be used to aid in the resolution of conflicts that arise in the system.

6.2 Improving Conflict Resolution

Three methods of improving system performance by changing conflict resolution include:

1. decreasing the number of times a conflict occurs,
2. reducing the time it takes to resolve a conflict, and
3. maximizing the capability of the system to make the best selection.

The first method derives performance improvements by reducing the number of calls to the conflict resolution system. This is implemented by structuring the knowledge base to minimize the number of rules fired in a single cycle. This requires identifying which rules might be triggered at the same time. This is a difficult task for physical processes because of the interactions that exist between the different variables. It is difficult to predict the conditions (combination of variable values) that will occur during processing. Once these rules are identified, then additional logic can be added to the preconditions to further justify their applicability. For example, consider the two rules:

OVERTEMP Rule:
```
IF    ( autoclave-temp > (temp-bandwidth + set-pt-limit) )
THEN  ( heater = hold )
```

LARGE-GRADIENT Rule:
```
IF    ( temp-gradient  > gradient-limit )
AND   ( autoclave-temp > low-layer-laminate-temp )
THEN  ( heater = decrease )
```

It is possible for these two conditions to occur simultaneously during the lamination process. When both rules are active, the conflict resolution system would always select the action to decrease the heat supplied by the heater. Therefore, the system should favor the LARGE-GRADIENT rule. To include this in the knowledge base, additional logic should be added to the OVERTEMP rule:

```
OVERTEMP Rule:
    IF      ( autoclave-temp > (temp-bandwidth + set-pt-limit) )
    ANDNOT( temp-gradient  > gradient-limit )
    ANDNOT( autoclave-temp > low-layer-laminate-temp )
    THEN   ( heater = hold )
```

This prevents the OVERTEMP rule from firing whenever the LARGE-GRADIENT rule is active. Using this approach throughout the knowledge base will result in a decrease in the number of possible conflicts that the system will encounter.

A problem arises when using this method. Examination of the rule to determine what physical condition it identifies would be misleading. The preconditions statement now contains statements which identify the process condition and which also block the rule at appropriate times. This results in a knowledge base that is cryptic, confusing, and difficult to maintain. To reduce the confusion, the rule may be restated as:

```
OVERTEMP Rule:
    IF      ( autoclave-temp > (temp-bandwidth + set-pt-limit) )
    ANDNOT( LARGE-GRADIENT )
    THEN   ( heater = hold )
```

This rule structure reduces some of the confusion, but it also requires that rules be evaluated by the system using a carefully prescribed order. This method does not eliminate the need for conflict resolution, but only reduces the number of times it is used. It changes the structure of the knowledge base, and hampers its construction and maintenance. These problems make this an unattractive solution.

The second method improves system performance by reducing the time required to make a selection. This method involves reprogramming the conflict resolution system such that it executes more efficiently. Improvement might also be achieved by employing a different strategy to obtain the same result, but one which is faster (possibly using less logic or a better elimination strategy).

The third method to improve system performance requires modifying the conflict resolution strategy to improve its capability to select the best alternative. This method is the subject of the following section.

6.3 Using Deterministic Knowledge in Conflict Resolution

The focus of this research is to improve conflict resolution in QPA. The approach selected is to incorporate deterministic techniques, such as mathematical and simulation models, into the conflict resolution strategy. The intent is to improve the outcome of conflict resolution. The following paragraphs discuss why this approach is not encouraging.

In Chapter 5 it was shown that QPA resolves conflicts using the RESOLVES statement. This technique provides a limited means for resolving conflicts. The RESOLVES statement is static and conservative, in that it always selects the alternative that is the safest, independent of other circumstances or interactions.

Research revealed that most of the conflicts handled by the RESOLVES statement are of the "episode/single-problem" type. For this type of conflict, independent of any resolution strategy, the correct decision is to select the EFFECT specified by the process problem (see discussion Chapter 5). Therefore, no real conflict exist. For the other conflict types mentioned in Chapter 5, the system selects from among alternative EFFECTs that are issued by active process instances (not including the episode goal). For these cases, the conflict set will contain only two, or three, alternative actions from which to choose. It is these types of conflicts that the system must be capable of resolving.

The proposed method for resolving these conflicts involves three steps. As each step was explored, it was found to be either not necessary or too complicated to be of any real use. The task of the first step is to verify the existence of the process state represented by each alternative within the conflict set. Recall that each of these alternatives represents actions that are necessary to eliminate some process problem (accelerated reaction, large temperature gradients, etc.), or to produce some desired effect (provide compaction to the laminate when the resin begins to gel). It was believed that some of these process states could be verified using quantitative calculations involving the process equations (deterministic knowledge). This verification step would eliminate any alternatives that the process calculations did not support. However, this requires that the user place a greater confidence in the deterministic knowledge than in the heuristic knowledge. This requirement may not always be true. Furthermore, if deterministic knowledge is available to accurately verify the process states, then it would be more efficient to use it as the object-level knowledge in the reasoning of the system. Thus, this is not a viable first step.

The second step involves using a process model to make a simulation run for each alternative in the conflict set. This produces a process response for each alternative. The system then examines the process responses and selects the alternative that produced the best response.

This step has several weaknesses. First, there is a question of the accuracy of the model. This accuracy will be dependent on the operating region under consideration and the process

variables of interest. Second, the development of a simulation model is a difficult task. It is not always possible to include in the model all the details of the process. This reduces the breadth of the application, thereby requiring that an alternative conflict resolution strategy be provided for those situation where the model is not appropriate. Last of all, in order for the system to pick the best alternative, it would have to possess the capability to rate each response dependent on the current episode, and then perform a comparison of these ratings so a selection could be made.

The complexity and difficulty of this step reduces its usefulness as an appropriate means for conflict resolution. Because of the complexity and intensity of the calculations, it is likely that this method would degrade, rather than enhance, the system's performance. It is for these reasons that the proposed research objective was not achieved. Although it seems simple to derive these conclusions, it is not until one begins to attempt these tasks that the faults within them appear.

6.4 Other Methods for Possible Performance Improvements

Even though the idea of using deterministic knowledge to aid in conflict resolution is not viable, it does not mean that the same knowledge can't be used to enhance the accuracy of the reasoning process of the knowledge-based program itself. In this section, several other methods are briefly discussed that could provide improvements in the performance of the QPA system.

6.4.1 Prediction of Process Variable Values

The first beneficial use of deterministic knowledge would be to predict the values of process variables that the sensory readings do not provide directly. These predictions would be obtained by quantitative calculations using the sensory data provided by the system. These additional process variables could provide a better understanding of the process and allow for simpler construction of the control heuristics. For example, in the current QPA system the viscosity of the system is predicted using the dielectric sensor reading. Using process equations it might be possible to use this dielectric sensor reading (e2) along with other sensory or calculated variable values to obtain a viscosity value. Then, instead of using the e2 value in the rules of the system, the "viscosity" value could be used. This would make the rules easier to understand and interpret, since one has a better understanding of the relationships of other variables with viscosity than with e2 values.

This type of calculation is currently provided in automatic control systems by the use of computing relays. However, these computational relays are limited in that they can only perform rudimentary mathematical functions (e.g., add, subtract,

multiply, divide, compare, etc.). In a knowledge-based program the calculations would be limited only by the time constraints of the process, or the hardware and programming constraints of the system. In a knowledge-based program it would be possible to perform complex computations, such as numerical integration, optimization, etc. The results of the these calculations would be available for use within the knowledge base of the system.

In QPA, this type of system would provide for the best of both worlds, qualitative and quantitative descriptions of the process. To a limited extent, this capability is provided in the current implementation. QPA currently performs calculations using the sensory readings to obtain qualitative terms, such as derivatives and averages. These calculations are limited to simple manipulations involving addition, subtraction, multiplication, and division. This limitation is due to the restrictions of the hardware and software of the current implementation and will be rectified in the next release. Therefore, with the new release of the system, it would be beneficial for QPA to incorporate more complex numerical capabilities into the system. These calculations would be performed by the blackboard monitor and used by the Parser and Thinker.

6.4.2 A Coupled System Approach

One problem with the method described in the previous section is that it requires time to perform calculations. The time required might exceed that allowed by the system in order to conform to the real-time response constraints set by the process. One method of reducing the time would be to off-load the calculations to a separate processor and to perform only those calculations that the system needs. Within each episode of QPA the process is only concerned with certain process instance frames. Therefore, it would be necessary to perform the calculation of only those process variables that are used within the process instance frames specified by the current episode. This reduces the number of calculations that the system performs. The resulting system might be considered a coupled system.

A coupled system is one which combines numeric and symbolic computing (see Figure 6.1). Even though some of the current knowledge-based systems use some form of numeric processing they are not necessarily coupled systems. To be considered a coupled system, the "system must have some knowledge of the numeric processes embedded within them and must reason about the application or results of these numeric processes" [27]. For example, even though the system described in the previous section uses both symbolic and numeric computing, it would not be a coupled system. This is because the numeric calculations are performed during every cycle, and the system has no control over the application of them. Whereas, in the proposed system of this section, the system determines which calculations to perform
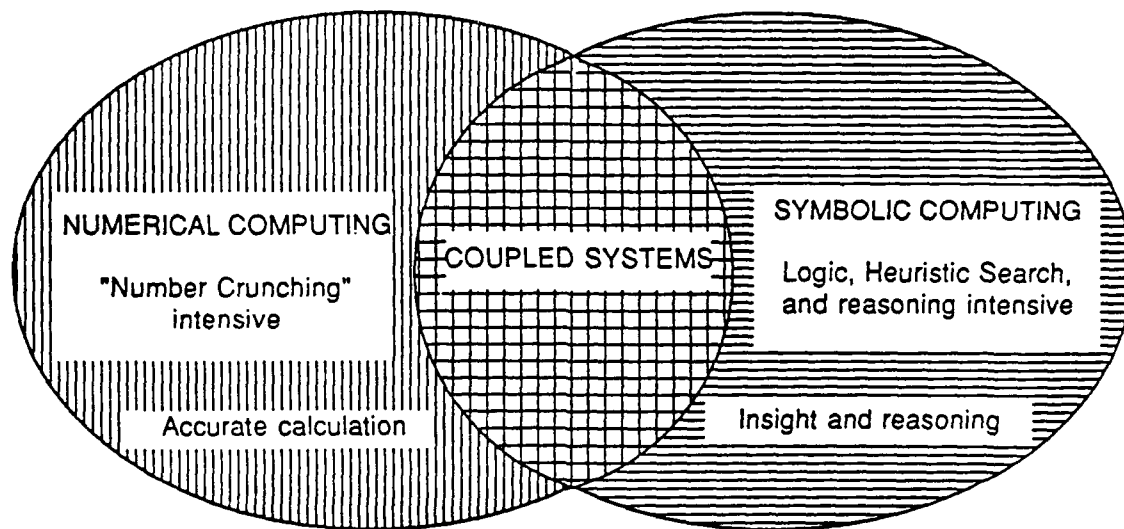
Numerical Computing
- Data processing & reduction
- Simulation & quantitative models
- Statistics and probability
- Numerical Algorithms
Appilcation: algorithmically tractable problems

Symbolic Computing
- Data interpretation
- Cognitive & qualitative models
- Search and heuristics
- Non-deterministic solution strategies,
Application: problems intractable algorithmically

Figure 6.1: Computing Techniques [27].

based on the episode information contained in the knowledge base. The results of the calculations are then used in the heuristics to determine the proper control action.

The resulting system would provide speed improvements unless every calculation is needed in every episode. For such a case, the number of calculations would be identical for each episode. Specification of which calculations to perform would be contained with the episode frame using a new slot.

CHAPTER 7

CONCLUDING REMARKS

This research investigated improving the performance of knowledge-based process control systems. The method involved using deterministic knowledge to enhance conflict resolution within the system.

During the investigation it became evident that conflict resolution has not received much attention in the literature. Based on the articles reviewed, the strategies of conflict resolution can be categorized as either numeric or heuristic. Within the heuristic category six different classes of strategies were identified. Each class possesses different advantages in their capability to order the conflict set. In process control applications, the numeric strategies are the favored technique for conflict resolution. But in order to provide a robust method of conflict resolution it is necessary to combine both numeric and heuristic strategies.

Examination of the QPA system revealed that its technique for conflict resolution falls under the "production order" class of strategies. To make a selection, It relies on the correct placement of certain frames within the knowledge base, and on the use of preestablished priorities for rule effects. In order to extend its applicability to other processes, QPA will need to make available to the user other heuristic techniques. In addition, it would be beneficial if QPA provided numeric techniques to provide for reasoning about the uncertainty of the evidence used by the frame-based rules. This would provide a physical link between the resolution process and the peculiarities of the process.

Application of deterministic knowledge to resolve conflicts within QPA is not appropriate. Attempts to use deterministic knowledge to resolve conflicts results in a partial redundancy of process knowledge and the need to perform complex calculations. The correct use of deterministic knowledge would be as an additional source of object-level knowledge, possibly within a coupled system design.

Additional research is needed to answer the following questions:

1. What combination of conflict resolution techniques is best for process control?
2. Can each resolution strategy be related to specific characteristics of a process control systems?
3. What is the appropriate combination of resolution techniques needed to handle each of the possible types of conflicts that arise (see Chapter 4)?
4. When is it proper to use multiple levels of reasoning?

Answers to these questions are not found in the literature. To answer these questions, a trial system will have to be constructed and demonstrated.

REFERENCES

1. Shortliffe, E.H., Computer-based Medical Consultations: MYCIN, Elsevier, New York, 1976.

2. McDermott, J., "R1: A Rule-based Configurer of Computer Systems," Artificial Intelligence, Vol. 19, pp. 39-88, Sept. 1982.

3. McDermott, J. and C. Forgy, 1978, "Production System Conflict Resolution Strategies". In Waterman, D. A., and Hayes-Roth, F. (Eds.). 1978. Pattern-directed Inference Systems. New York: Academic Press, pp. 177-199.

4. Barr, A. and Feigenbaum, E.A., The Handbook of Artificial Intelligence, William Kaufmann, Inc., 1981, Vol 1, p. 197.

5. Davis, R., and Buchanan, B.G., "Meta-Level Knowledge: Overview and Applications," Proc. of the 5th Int. Joint Conf. on Artificial Intelligence, 1977, pp. 920-927.

6. Sauers, R. and R. Walsh, "On the Requirements of Future Expert Systems," Proc. of the 8th Int. Joint Conf. on Artificial Intelligence, Vol. 1, 1983, pp. 110-115.

7. Ferrante, R.D., "The Characteristic Error Approach to Conflict Resolution," Int. Joint Conf. on Artificial Intelligence, 1985, pp. 331-334.

8. Tanimoto, S.L., The Elements of Artificial Intelligence: An Introduction Using LISP, Computer Science Press, 1987.

9. Charniak, E., and McDermott, D., Introduction to Artificial Intelligence, Addison-Wesley Pub. Co., 1985.

10. Cruise, A., Ennis, R., et.al., "YES/L1: Integrating Rule-Based, Procedural, and Real-time Programming for Industrial Applications," Third Conf. on AI Applications, IEEE 1987, pp. 134-139.

11. Garvey, T., Lowrance, J.D., and Fischler, M.A., "An Inference Technique For Integrating Knowledge From Disparate Sources," Proceedings of the 7th Int. Joint Conf. on AI., Vancouver, British Columbia, Canada, 1981.

12. "GEST - The Anatomy of an Expert System Tool," Product Literature, Georgia Tech Research Institute.

13. Laffey, T.J., Cox, P.A., Schmidt, J., Kao, S., and Read, J., "Real-Time Knowledge-Based Systems," AI Magazine, Spring 1987, pp. 27-45.

14. Efstathiou, J., "Rule-based Process Control Using Fuzzy Logic," In Approximate Reasoning in Intelligent Systems, Decision and Control, Sanchez & Zadeh (eds.), Pergamon Press, 1987, pp. 145-158.

15. Davis, R., and Lenat, D.B., Knowledge-based Systems in Artificial Intelligence, McGraw-Hill Book Co., 1982.

16. Baur, P.S., "Development Tools Aid in Fielding Expert Systems," InTech, April 1987, pp. 7-15.

17. Burg, B., Foulloy, L., Heudin, J., and Zavidovique, B., "Behavior Rule Systems for Distributed Process Control," Proc. of the 2nd Conf. on Artificial Intelligence Appl., 1985, pp. 198-203.

18. Gallanti, M., et.al., "Representing Procedural Knowledge in Expert Systems: An Application to Process Control," Proc. of the 9th Int Joint Conf. on Artificial Intelligence, pp. 345-352.

19. Moore, R.L., and Hawkinson, L.B., "Progress Report on Expert System Installations," Proc. of ISA 1985, pp. 549-552.

20. Rao, M., Jiang, T.-S., and Tsai, J., "Integrated Environment for Intelligent Control," Proc. of the 1st Int. Conf. on IEA/AIE 1988, pp. 466-474.

21. Wright, M.L., Green, M.W., Fiegl, G., and Cross, P.F., "An Expert System for Real-Time Control," IEEE Software, March 1986, pp. 16-24.

22. Garrett, P., Lee, C.W., and LeClair, S.R., "Qualitative Process Automation .VS. Quantitative Process Control," Proc. of American Control Conf., 1987.

23. Bobrow, D.G., Qualitative Reasoning About Physical Systems, The MIT Press, Cambridge, Mass, 1985.

24. LeClair, S.R., "SENSOR FUSION: The Application of Artificial Intelligence Technology to Process Control," 86 Rochester Forth Conf., June 1986, pp. 15-22.

25. Lee, C.W., "Composite Cure Process Control by Expert Systems," First Conf. on Composite Materials, American Society for Composites, Dayton, OH, Oct. 7-9, 1986.

26. Matejka, R.F., and Lagnese, T.J., "A Representational Language for Qualitative Process Control," Proc. of the First Int. Conf. on Industrial and Engineering Applications of Artificial Intelligence and Expert Systems, 1988, pp. 475-482.

27. Kitzmiller, C. T., Kowalik, J. S., "Coupling Symbolic and Numeric Computing in Knowledge-Based Systems," AI Magazine, Summer, 1987, pp. 85-90.